Transactions of the ASME

PUBLISHING STAFF
Mng. Dir., Pub., J. J. FREY
Director, Technical Publishing
JOS. SANSONE
Managing Editor,
CORNELIA MONAHAN
Production Editor, SUZANNE MAGIDA
Prod. Asst., BETH DARCHI

Journal of Applied Mechanics (ISSN 0021-8936) is edited and published quarterly at the offices of The American Society of Mechanical Engineers, United Engineering Center, 345 E. 47th St., New York, N.Y. 10017. ASME-TWX No. 710-581-5267, New York. Second Class postage paid at New York, N.Y., and at additional mailing offices.

CHANGES OF ADDRESS must be received at Society headquarters seven weeks before they are to be effective. Please send old label and new address.

PRICES: To members, $30.00, annually; to nonmembers, $60.00. Single copies, $20.00 each. Add $5.00 for postage to countries outside the United States and Canada.

STATEMENT from By-Laws. The Society shall not be responsible for statements or opinions advanced in papers or . . . printed in its publications (B7.1, Par. 3).

INDEXED by the Engineering Index, Inc.

Journal of Applied Mechanics

Published Quarterly by The American Society of Mechanical Engineers

VOLUME 49 • NUMBER 3 • SEPTEMBER 1982

(Contents continued on Inside Back Cover)

CONTENTS (CONTINUED)

DESIGN DATA AND METHODS

BRIEF NOTES

DISCUSSIONS

BOOK REVIEWS

Two-Dimensional Apparent Masses for Cross-Flow Sections of Wing-Store Configurations

M.-K. Huang[1]
Associate Professor,
Nanjing Aeronautical Institute,
Nanjing, Jiangsu,
People's Republic of China

On the basis of the assumption that the external stores are small compared with the wing, an approximate method has been developed for estimation of two-dimensional apparent masses for the cross-flow sections of wing-store combinations. The results obtained may be applicable to the analysis of the effects of the stores on the aerodynamic stability derivatives in slender-body theory. The theory has also been applied to estimate the rolling moment due to sideslip for high-wing configurations. The presented results are in agreement with those of other investigations.

1 Introduction

In view of the increasing variety of stores used on current combat aircraft, the problems of the interference among the aircraft and the external stores have received considerable attention in the last decade. Some of the recent investigations were reported in [1-6]. It is well known that the estimation of aerodynamic stability derivatives based on slender-body theory is not very accurate except possibly for small aspect ratio and low supersonic Mach number. However, other methods to achieve quantitative results for wing-body store configurations, such as the numerical methods based on singularly distribution, would be considerably more complicated. Moreover, a comparison of the various combinations on the basis of slender-body theory would possibly still show the trend of their relative behavior.

As indicated by Nielson [7], in slender-body theory most of the stability derivatives for certain classes of slender configurations can be calculated by means of apparent mass coefficients. The apparent masses for some simple cross sections have been given by Nielsen [7] and Sedov [8]. Some of the complex wing-body combinations were investigated by Portnoy [9], Andrens [10], Crowell and Crowe [11], Keldysh [12], and Huang [13]. However, the estimation of the apparent masses for very complex cross sections, such as those of wing-store configurations, is by no means a simple matter. It is the purpose of this paper to consider these kind of cross sections. The method is based on the assumption that the stores are small compared with the wing, so that the stores in a cross-flow plane can be simulated by two-dimensional doublets. The result obtained is written as a ratio of the increment of the apparent mass produced by the stores to that of the wing alone, which may be used to analyze the effects of the stores on the aerodynamic stability derivatives for aircrafts.

In addition, the two-dimensional apparent mass theory relates closely to the least-induced drag theory. In many cases, the results of these two theories can be applied to one another. Some of the exact results calculated numerically by Jundry and Lissaman [14] will be used for comparison with the present approximate results.

2 The Analogy Between a Doublet and an Arbitrary Cross Section

Let yoz be a cartesian coordinate system. With the same notation as that of [7], we represent apparent masses by m_{ij}, $i, j = 1, 2, 3$, where 1 and 2 denote, respectively, the y and z directions, and 3 the rotation. The cross-sectional area is denoted by S_a and the density of the fluid by ρ. We have $m_{12} = m_{21} = 0$ if the cross section has at least one axis of symmetry.

Suppose that there is an incompressible flow past a two-dimensional body with oncoming velocity components U_1 and U_2 along y and z directions, respectively. The complex potential of the flow can be expressed by

$$W(Z) = (U_1 - iU_2)Z + \sum_{n=1}^{\infty} \frac{A_n}{Z^n} \tag{1}$$

where $Z = y + iz$ is the complex variable and A_n is the complex constant. The constant A_1 relates to the apparent masses of the body section by (see [7])

$$2\pi A_1 = U_1\left(\frac{m_{11}}{\rho} + S_a\right) + iU_2\left(\frac{m_{22}}{\rho} + S_a\right) \tag{2}$$

It is obvious that the term A_1/Z of the expression (1) is nothing else but the contribution due to a doublet, which may be used to approximate the perturbation effect due to the body if its cross section is small. The doublet strength A_1 is determined once the apparent masses of the body section are known.

---

[1] Currently, Visiting Associate Professor, Department of Aerospace Engineering Sciences, University of Colorado, Boulder, Colo. 80309

Contributed by the Applied Mechanics Division for publication in the JOURNAL OF APPLIED MECHANICS.

Discussion on this paper should be addressed to the Editorial Department, ASME, United Engineering Center, 345 East 47th Street, New York, N.Y. 10017, and will be accepted until two months after final publication of the paper itself in the JOURNAL OF APPLIED MECHANICS. Manuscript received by ASME Applied Mechanics Division, October, 1981; final revision, May, 1982.

Table 1 Doublet analogy and apparent mass increments for a variety of configurations

CONFIGURATION	1	2	3	4	5
$Z=Y+iZ$ PLANE	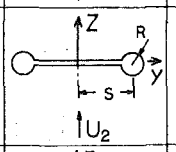	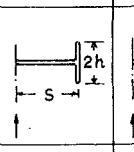	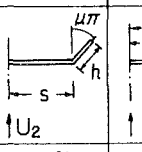	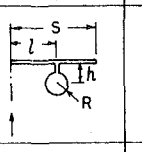	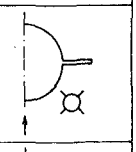
$\sigma=\xi+i\eta$ PLANE	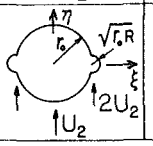	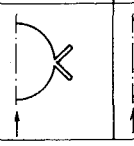	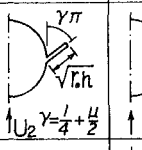	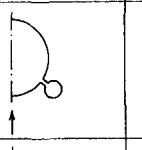	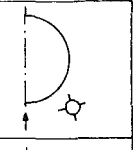
$\sigma=\xi+i\eta$ PLANE DOUBLET ANALOGY	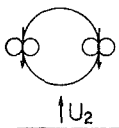			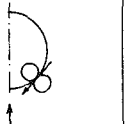	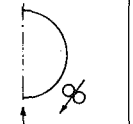
$\frac{\Delta m_{22}}{(m_{22})_{WING}}$	$4\frac{R}{S}$	$2\frac{h}{S}$	$2\frac{h}{S}\left(\frac{\gamma}{1-\gamma}\right)^{1-2\gamma}$	EQ.(5)	EQ.(13)
$\frac{\Delta m_{33}}{(m_{33})_{WING}}$	$8\frac{R}{S}$	$4\frac{h}{S}$	$4\frac{h}{S}\left(\frac{\gamma}{1-\gamma}\right)^{1-2\gamma}$		

3 m_{22} for Wing-Body Store Configurations

We first consider the configuration 1, a wing carrying two small stores of circular cross section at wing tips, shown in Table 1. Suppose that there is an incompressible flow past the wing store in a cross-flow plane with oncoming velocity U_2 along the direction z. As shown in Table 1, the use of the transformation $Z=\sigma+s^2/4\sigma$ turns the wing into a circle of radius $r_0=s/2$ in σ-plane, where s is the local semispan of the wing. The stores are turned into half circles with radius $\sqrt{r_0R}$ under the assumption of small stores. It is obvious that in σ-plane the velocity of the local oncoming flow past the stores is $2U_2$. The strength of the doublets for simulating the stores in σ-plane can be determined by equation (2), so that the complex potential can be written as

$$W(\sigma)=-iU_2\left(\sigma-\frac{r_0^2}{\sigma}\right)+2iU_2r_0R\left(\frac{1}{\sigma-r_0}+\frac{1}{\sigma+r_0}\right) \quad (3)$$

Turning back to the Z-plane and expanding in series, we can find the coefficient of the term containing $1/Z$. Then, m_{22} for the combination is found by equation (2).

The same procedure has been applied to the configurations 2 and 3. The approximate formulas derived for estimating the apparent mass increment Δm_{22} due to the stores are given in Table 1, where $(m_{22})_{\text{wing}}$, the apparent mass for a single wing alone, is equal to $\pi\rho s^2$. In derivation for the configuration 3, the wing with winglets, it was required to know the apparent mass for a V-form section in which each wing makes an angle of $\gamma\pi$ with the symmetry plane. By using the conformal mapping given in Section 39 of [15] and the equation (2), it can be shown that the apparent mass for such V-form section is

$$m_{22}=\pi\rho s_1^2\left(\frac{\gamma}{1-\gamma}\right)^{1-2\gamma} \quad (4)$$

where s_1 is the semispan measured in each wing plane.

Figure 1 presents the approximate results for three configurations and the exact ones calculated numerically in [12, 14]. The comparison demonstrates that a correlation is achieved even when the stores are small.

For configuration 4, the wing-pylon store combinations, we first assume that the store pylons are not close to the wing tips, and are very small compared with the wing. It is well known from the conformal mapping theory that the shape of the store pylons in σ-plane would be the same as that in Z-plane, but their scale is changed by a factor of

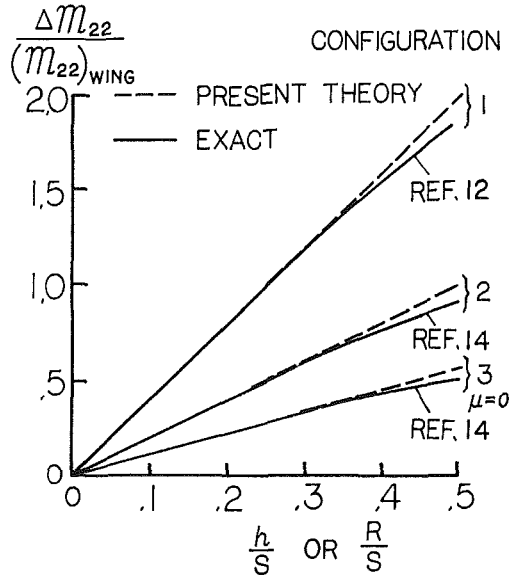

Fig. 1 Apparent mass increment Δm_{22} for the configurations 1, 2, and 3

$$\left|\frac{d\sigma}{dZ}\right|_A=\frac{1}{2\sqrt{1-(l/s)^2}}$$

where l is illustrated in Table 1.

A similar procedure yields

$$\frac{\Delta m_{22}}{(m_{22})_{\text{wing}}}=\left[\frac{(m_{22})_{\text{store}}}{\pi\rho h^2}\left(\frac{h}{s}\right)^2+2\left(\frac{R}{s}\right)^2\right]\frac{l^2}{s^2-l^2}-2\left(\frac{R}{s}\right)^2 \quad (5)$$

where $(m_{22})_{\text{store}}$ is the apparent mass for the section that consists of the store-pylon section and its mirror image with reference to the wing plane. The value of $(m_{22})_{\text{store}}$ can be found in Fig. 1.

If there are only pylons of height h beneath the wing, equation (5) becomes

$$\frac{\Delta m_{22}}{(m_{22})_{\text{wing}}}=\left(\frac{h}{s}\right)^2\frac{l^2}{s^2-l^2} \quad (6)$$

This formula fails as $s\to l$. In fact, $|d\sigma/dZ|_A\to\infty$ in this extreme case.

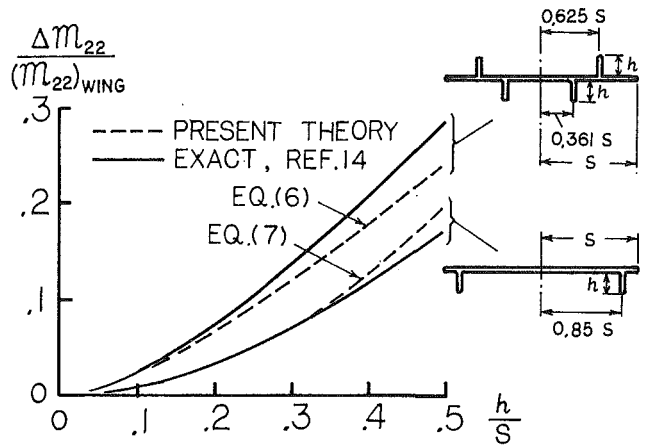

Fig. 2 Apparent mass increment Δm_{22} due to pylons and fences

By matching the expression (6) with that for the configuration 3 with $\mu=0$, a unified approximation, valid for both cases that the pylons are close to the wing tips or not, can be obtained as

$$\frac{\Delta m_{22}}{(m_{22})_{\text{wing}}} = \left(\frac{h}{s}\right)^2 \frac{l^2}{\left(s+\frac{\sqrt{3}h}{4}\right)^2 - l^2} \tag{7}$$

Figure 2 shows the application of equations (6) and (7). The first application is to the case where there are two pylons mounted beneath the wing and two fences on its upper surface. Suppose that they are not close to the wing tips, so that equation (6) could be used. The total increment of the apparent mass is a simple superposition of the contributions from the pylons and the fences. The second example is the case when the pylons are close to the wing tips, so that equation (7) should be used. Both of the results are close to the exact ones even if h/s is as high as 0.5.

For a wing-body store combination, there may be some cross-flow sections without pylons, which is the case named by configuration 5 shown in Table 1. The complex coordinates of the centers of the stores are denoted by Z_0 and $-\bar{Z}_0$. $\sigma=f(z)$ is an analytical function mapping the region outside the wing-body combination in Z-plane into that outside the circle of radius r_0 in σ-plane, which has the property that $f'(\infty)=1$.

Let

$$W_0(Z)=W_0(\sigma)=-iU_2\left(\sigma-\frac{r_0^2}{\sigma}\right)$$

be a complex potential of the flow past the combination without stores, and the stores are replaced by two doublets at $\sigma=\sigma_0=f(Z_0)$ and $\sigma=-\bar{\sigma}_0$. The circle theorem [16] is employed to keep the transformed circle to be a stream line, so that the total complex potential can be written by

$$\Omega=W_0(\sigma)+\frac{B}{\sigma-\sigma_0}-\frac{\bar{B}}{\sigma+\bar{\sigma}_0}+\frac{\bar{B}}{\frac{r_0^2}{\sigma}-\bar{\sigma}_0}-\frac{B}{\frac{r_0^2}{\sigma}+\sigma_0} \tag{8}$$

where B, the strength of the doublets in σ-plane, is to be determined.

Note that

$$\frac{B}{\sigma-\sigma_0}=\frac{B}{f'(Z_0)}\frac{1}{Z-Z_0}+\cdots$$

The strength of the doublets in Z-plane is then $B/f'(Z_0)$. The use of equation (2) yields

$$\frac{B}{f'(Z_0)}=\frac{V_1}{2\pi}\left[\frac{(m_{11})_a}{\rho}+S_a\right]+i\frac{V_2}{2\pi}\left[\frac{(m_{22})_a}{\rho}+S_a\right] \tag{9}$$

where the subscript a refers to a single store alone. V_1 and V_2,

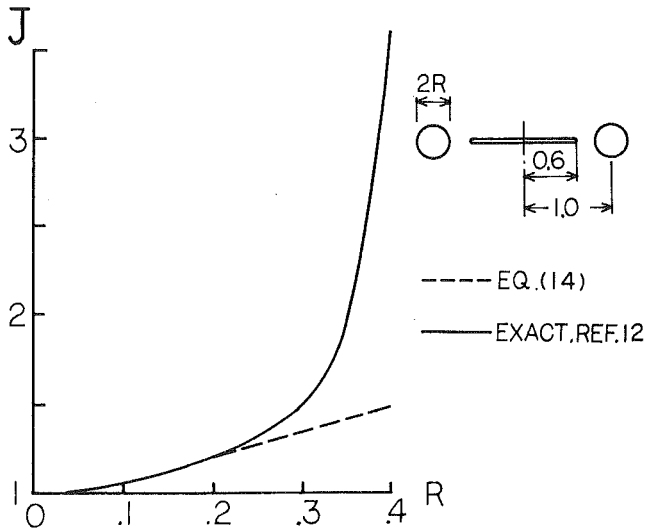

Fig. 3 The ratio of the apparent mass m_{22} for the wing-necelle cross section to the sum of the apparent masses for the wing and necelles as they are alone

the local velocity components of the flow past the wing body without stores, can be evaluated by

$$V_1-iV_2=\left(\frac{dW}{dZ}\right)_{Z=Z_0}=-iU_2\left(1+\frac{r_0^2}{\sigma_0^2}\right)f'(Z_0) \tag{10}$$

By applying equation (2) to the wing-body store combination, the increment of the apparent mass, produced by two stores located symmetrically, can be obtained as

$$\Delta m_{22}=\frac{2\pi\rho}{iU_2}\Delta A-2\rho S_a \tag{11}$$

where ΔA is given by

$$\Delta A=\frac{1}{2\pi i}\oint_C(\Omega-W_0(\sigma))\frac{dZ}{d\sigma}d\sigma$$

Here the integration path C is around the wing-body store section. The integral is then evaluated by the residue theorem. We obtain

$$\Delta A=2i\,Im\left[B\left(1+\frac{r_0^2}{\sigma_0^2}\right)\right] \tag{12}$$

where Im denotes the imaginary part. Substituting the equation (12) into equation (11), the final result is

$$\frac{\Delta m_{22}}{\rho}=2\left[\left(\frac{V_2}{U_2}\right)^2\frac{(m_{22})_a}{\rho}+\left(\frac{V_1}{U_2}\right)^2\frac{(m_{11})_a}{\rho}\right]+2S_a\left[\left(\frac{V_2}{U_2}\right)^2+\left(\frac{V_1}{U_2}\right)^2-1\right] \tag{13}$$

As a simple example, consider the case in which the stores are of circular cross section. We have

$$\frac{\Delta m_{22}}{\rho}=2\pi R^2\left[2\left(\frac{V_2}{U_2}\right)^2+2\left(\frac{V_1}{U_2}\right)^2-1\right] \tag{14}$$

where R is the radius of the store sections.

In view of the fact that, according to slender-body theory, the lift of a configuration is proportional to m_{22}, we conclude from equation (14) that the maximum increment of the lift would be achieved if the stores are located at the places where the local cross-flow velocity is maximum. Another extreme case is where the store is located just beneath the body, where the cross flow is stationary. The lift increment would be a minimum in this case.

Figure 3 presents an example for a particular wing-store configuration in which the centers of the stores lie in the wing plane. In the figure, J denotes the ratio of the apparent mass for the wing-store combination to the sum of the apparent

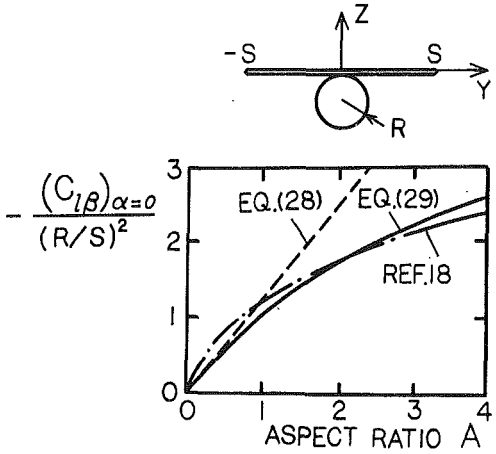

Fig. 4 High-wing configurations and their stability derivatives for the rolling moment due to sideslip

masses for the individual wing and stores, the dashed line is the result calculated by equation (14), and the solid line is the exact one given by Keldysh [12]. It is shown that there is close agreement when the stores are far from the wing tips.

4 m_{33} for Wing-Store Combinations

It is well known that in slender-body theory the rolling moment in roll is proportional to the apparent mass m_{33}. However, the evaluation of m_{33} is very difficult except for some simple cases. An approximate method will be suggested here for a wing carrying stores at its tips.

For a single wing alone, we have seen from [7] that

$$(m_{22})_{\text{wing}} = \pi\rho s^2, \quad (m_{33})_{\text{wing}} = \frac{\pi\rho s^4}{8}$$

Suppose that the semispan of the wing has a small increment δ. The corresponding increments of the apparent masses can be calculated to the first order by

$$\frac{\Delta m_{22}}{(m_{22})_{\text{wing}}} = 2\frac{\delta}{s}, \quad \frac{\Delta m_{33}}{(m_{33})_{\text{wing}}} = 4\frac{\delta}{s} \tag{15}$$

An equivalent increment of the semispan can be found for a wing with stores at its tips such that it has the same increment of m_{22} as given by (15). Then the increment Δm_{33} follows immediately from equation (15). The results obtained in such a way are also shown in Table 1 for the three configurations considered. Unfortunately, we have no other theories for comparison.

5 m_{13} for Wing-Store Configurations

m_{13} is another one of the apparent masses which is difficult to evaluate. To begin, consider a high-wing configuration shown in Fig. 4. According to [7], m_{13} is defined by

$$m_{13} = -\rho \oint_c \phi_3 \frac{\partial \phi_1}{\partial n}\, dt \tag{16}$$

where ϕ_1 and ϕ_3 are the potentials due to the motion of the cross section with unit velocities in translation along y and in rotation, respectively. $\mathbf{n}$ is the outward normal. The integration path C is around the cross section of the wing-body combination, and dt is the contour element. The boundary condition shows that $\partial\phi_1/\partial n = 0$ on the wing surface, so that we need only to evaluate the integral around the body.

Let

$$\phi_3 = \varphi_3 + \Delta\phi_3 \tag{17}$$

where φ_3 is the corresponding potential for the single wing alone, and $\Delta\phi_3$ is the increment due to the body. Inserting equation (17) into (16), we have

$$m_{13} = -\rho \int_{\text{body}} \varphi_3 \frac{\partial \phi_1}{\partial n}\, dt - \rho \int_{\text{body}} \Delta\phi_3 \frac{\partial \phi_1}{\partial n}\, dt \tag{18}$$

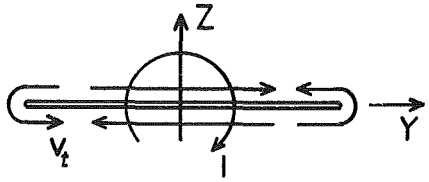

Fig. 5 Flow direction around the wing rotated with unit angular velocity

The exact φ_3 for a rotated plate has been given in [16]. The corresponding tangential velocity of the flow on the lower surface of the plate is thus obtained as

$$(V_t)_{z=-0} = \frac{\partial \varphi_3}{\partial y} = -\frac{1}{2}\frac{s^2 - 2y^2}{\sqrt{s^2 - y^2}} \tag{19}$$

The flow direction around this plate is shown in Fig. 5, and we have

$$(V_t)_{z=-0} = -\frac{s}{2}$$

at $y = 0$.

The assumption is made that the body section is much smaller than that of the wing. As a consequence, ϕ_1 can be approximated by the potential of the flow with unit oncoming velocity past the configuration consisting of the body and its image with reference to the wing plane if the wing is considered as a reflected plate. $\Delta\phi_3$ can be considered as the potential of the flow with oncoming velocity $(V_t)_{\substack{z=-0\\y=0}}$ past such a configuration, so that

$$\Delta\phi_3 \approx (V_t)_{\substack{z=-0\\y=0}} \phi_1 = -\frac{s}{2}\phi_1$$

The second integral of equation (17) can be evaluated as follows

$$-\rho \int_{\text{body}} \Delta\phi_3 \frac{\partial \phi_1}{\partial n}\, dt = \frac{s}{2}\rho \int_{\text{body}} \phi_1 \frac{\partial \phi_1}{\partial n}\, dt = \frac{s}{2}\frac{(m_{11})_{\text{body}}}{2} \tag{20}$$

where $(m_{11})_{\text{body}}$ is the apparent mass for the section that is made up of the body section and its image. For the body of the circular cross section, $(m_{11})_{\text{body}}$ refers to eight-form section. Using the complex potential given in Section 6.52 of [16], the apparent mass for this section can be obtained by the use of equation (2) as

$$(m_{11})_{\text{body}} = 2\left(\frac{\pi^2}{3} - 1\right)\pi\rho R^2 \tag{21}$$

where R is the radius of the body section.

To perform the first integration in equation (18), we first expand φ_3 into Taylor series

$$\varphi_3 = \text{constant} + (V_t)_{\substack{z=-0\\y=0}} y + \cdots$$

By taking into account the boundary condition

$$\frac{\partial \phi_1}{\partial n}\, dt = \cos(n,y)\, dt = dz,$$

we have

$$\int_{\text{body}} \frac{\partial \phi_1}{\partial n}\, dt = 0 \quad \text{and} \quad \int_{\text{body}} y \frac{\partial \phi_1}{\partial n}\, dt = \int_{\text{body}} y\, dz = S_{\text{body}}$$

where S_{body} is the area of the body section.

Thus,

$$-\rho \int_{\text{body}} \varphi_3 \frac{\partial \phi_1}{\partial n}\, dt = -\rho (V_t)_{\substack{z=-0\\y=0}} S_{\text{body}} \tag{22}$$

Substitution of equations (20) and (22) into (18) yields

$$m_{13} = \frac{s}{2}\left[\rho S_{\text{body}} + \frac{(m_{11})_{\text{body}}}{2}\right] \tag{23}$$

Two special cases will be considered. The first one is that the body has a circular cross section. By using equation (21), we have

$$m_{13} = \rho \frac{\pi^3 s R^2}{12} \tag{24}$$

The second one is that the body has a square cross section with the width denoted by a. $(m_{11})_{\text{body}}$ of this case refers to a rectangular section, which can be evaluated by the formula given in [10]. Thus we have

$$m_{13} = \frac{1.23\pi^3 s a^2}{12} \tag{25}$$

The other cases, such as the wing mounted at any height above the central line of the body, can be considered as the superposition of the contributions from the portions of the body above and below the wing.

This approach can be easily extended to configuration 4 shown in Table 1. We have

$$m_{13} = -2(V_t)_{z=-0}\left[\rho S_{\text{store}} + \frac{(m_{11})_{\text{store}}}{2}\right] \tag{26}$$

where S_{store} is the cross-sectional area for a single store, $(m_{11})_{\text{store}}$ refers to the section that consists of the store-pylon section and its image, and $(V_t)_{z=-0}$ evaluated at $y=l/2$ by equation (19) is

$$(V_t)_{z=-0} = \frac{1}{2}\frac{s^2 - 2l^2}{\sqrt{s^2 - l^2}} \tag{27}$$

Since the assumption has been made that the planar wing can be considered as a reflected plane, the results obtained apply only to the case where the store pylons are not close to the wing tips.

6 Applications

Two examples of application will be presented for their practical interest.

As a first example, we consider a combination that consists of a high delta wing and body of revolution. The angle of attack is assumed to be zero ($\alpha=0$). Let $C_{l\beta}$ be the stability derivative for the rolling moment due to sideslip. By use of the relationship given in [7] between the stability derivative $C_{l\beta}$ and the apparent mass m_{13}, we have

$$(C_{l\beta})_{\alpha=0} = -\frac{\pi^3}{24} A \left(\frac{R}{s}\right)^2 \tag{28}$$

where A is the aspect ratio. Unfortunately, this expression applies only to slender configurations. As indicated by Nielsen [7], lift-curve slopes are overestimated by slender-body theory if the configurations are not slender. However, this fact does not preclude the use of slender-body theory for nonslender configurations since, in certain instances, the ratio of the lift of the wing-body combination to that of the wing alone can be accurately predicted by slender-body theory, even though the magnitude of the lift-curve slope might be incorrect. As a consequence, Piter et al. [17] proposed that the ratio of the accurate lift-curve slope $C_{L\alpha}$ for the wing alone to that predicted by slender-body theory could be used as a modification factor to nonslender configurations. It is thus proposed that, with the same modification factor for non-slender configurations, equation (28) is modified as

$$(C_{l\beta})_{\alpha=0} = -\frac{\pi^2}{12} C_{L\alpha} \left(\frac{R}{s}\right)^2 \tag{29}$$

Figure 4 presents the results given by equations (28) and (29) and those by an empirical formula of [18]. In Fig. 4, the calculation by equation (29) was carried out for delta wings at low speeds because the empirical formula was demonstrated by experiment in this speed range for such wings. The comparison shows that the modified results agree very well with the empirical ones.

The second application is to the configuration 4. We know from equation (27) that $(V_t)_{z=-0} \approx 0$ when $l/s \approx 0.7$. For such a case, $(C_{l\beta})_{\beta=0}$ is nearly zero according to equation (26). Otherwise, the negative dihedral effect results when the store pylons move inward and the positive effect results when they move outward. The same tendency has been shown experimentally in [20].

7 Conclusions

The approximate formulas derived in this paper for estimating the apparent mass increments due to stores represent the leading approximations if the characteristic scale of the stores is assumed to be a small parameter. These formulas apply to cases where the stores are very small, but the comparison with the exact results shows that the theory provides a fair estimation of the apparent mass increments even when the stores are not small.

References

1 "Aerodynamic Interference," *AGARD Conference Proceedings*, No. 71, 1970.

2 Meyer, R., Cenko, A., and Yaros, S., "An Influence Function Method for Predicting Store Aerodynamic Characteristics During Weapon Separation," Paper Presented at the 12th Navy Symposium on Aeroballistics, David Taylor Naval Ship Research and Development Center, May 1981.

3 Tessitore, F., Cenko, A., Meyer, R., Dyer, R., and Waskiewicz, J., "A New Approach to Weapon Separation Aerodynamics," AIAA Paper 81-1654, Aug. 1981.

4 Waskiewicz, J., DeJongh, J., and Cenko, A., "Application of Panel Methods to the Aerodynamic Analysis of Proximity and Mutual Interference Effects on Store Separation at Supersonic Speeds," AIAA Paper 81-1653, Aug. 1981.

5 Vore, D. A., "Wind Tunnel Test of Advanced Configurations and Various Weapons for Mach Numbers 0.6 to 1.6," AEDC TSR 79-P69, 1979.

6 Cenko, A., and Tinoco, E. N., "PANAIR-Weapons, Carriage and Separation," AFFDL-TR 79-3142, Sept. 1979.

7 Nielsen, J. N., *Missile Aerodynamics*, McGraw-Hill, New York, 1960.

8 Sedov, L. I., *Two-Dimensional Problems in Hydrodynamics and Aerodynamics*, Wiley, New York, 1965.

9 Portnoy, H., "The Slender Wing with a Half Body of Revolution Mounted Beneath," *Aeronautical Journal of the Royal Aeronautical Society*, Vol. 72, No. 693, 1968, pp. 803–807.

10 Andrews, R. D., "The Lift of a Slender Combination of a Fuselage of Rectangular Cross-Section with a High Wing," *Aeronautical Journal*, Vol. 74, No. 719, 1970, pp. 903–906.

11 Crowell, K. R., and Crowe, C. T., "Prediction of the Lift and Moment on a Slender Cylinder-Segment Wing-Body Combination," *Aeronautical Journal*, Vol. 77, 1973, pp. 295–298.

12 Keldysh, V. V., "Application of Slender Body Theory to the Calculation of Aerodynamic Properties of Low Aspect Ratio Wings With Necelles at Their Tips," *Prikladnaia Matematika i Mekhanika*, Vol. 22, No. 1, 1958, pp. 126–132.

13 Huang, Ming-Chu (Huang, Ming-Ke), "Aerodynamic Interference of Wing-Body-Store Combinations," *ACTA MECHANICA SINICA*, No. 3, 1979 (in Chinese).

14 Jundry, J. L., and Lissaman, P. B. S., "A Numerical Solution for the Minimum Induced Drag of Nonplanal Wings," *Journal of Aircraft*, Vol. 5, No. 1, 1968, pp. 17–21.

15 Lavrentiev, M. A., and Shabat, B. V., *The Methods in the Theory of Functions of Complex Variables*, 3rd ed., Fizmatgiz, Moscow, 1965 (in Russian).

16 Milne-Thompson, L. M., *Theoretical Hydrodynamics*, 2nd ed., Macmillan, New York, 1950.

17 Pitts, W. C., Nielsen, J. N., and Kaattari, G. E., "Lift and Center of Pressure of Wing-Body-Tail Combinations at Subsonic, Transonic and Supersonic Speeds," NACA Report 1307, 1957.

18 Campbell, J. P., and Mckinney, M. C., "Summary of Methods for Calculating Dynamic Lateral Stability and Response and for Estimating Lateral Stability Derivatives," NACA Report 1098, 1952.

19 Goodman, A., and Thomas, D. F., "Effects of Wing Position and Fuselage Size on the Low-Speed Static and Rolling Stability Characteristics of a Delta-Wing Model," NACA Report 1224, 1955.

20 Spearman, M. L., "Some Effects of External Stores on the Static Stability of Fighter Airplanes," NASA TN D-6775, 1972.

On the Mean Reynolds Equation in the Presence of Homogeneous Random Surface Roughness

N. Phan-Thien
Department of Mechanical Engineering,
University of Sydney,
N.S.W. 2006 Australia

Assuming that the surface roughness is of small amplitude and can be modeled by a homogeneous random function in space, the classical Reynolds equation is averaged using a method due to J. B. Keller. The mean Reynolds equation is accurate up to terms of $0(\epsilon^2)$, where ϵ is the dimensionless amplitude of the surface roughness and has a nonlocal character. Furthermore, by exploiting the slowly varying property of the mean film thickness, this nonlocal character is eliminated. The resulting mean Reynolds equation depends on the surface roughness via its spectral density and, in the limits of either parallel or transverse surface roughness, it reduces to Christensen's theory.

1 Introduction

Thin-film hydrodynamic lubrication of rough surfaces has been a subject of intense research during the past two decades. A recent summary of the state of the arts can be found in Wilcock [1] where two types of surface roughness are recognized: the Reynold roughness and the Stokes roughness. In the former case the classical Reynolds equation [2] applies and in the latter case the full solution to the Stokes equations must be sought.

Basically, a surface roughness is said to be of the Reynolds type when its amplitude is considerably less than, and its characteristic wavelength is considerably greater than the mean film thickness [3]. More quantitatively, for a squeeze-film [4] or a slider bearing [5] with parallel surface roughness an error of about 10 percent is made when using the Reynolds equation to correct for the presence of the surface roughness provided that $\omega_n h \leq 0.5$, where ω_n is a characteristic frequency of the surface roughness and h is the mean film thickness. Furthermore if $\omega_n h > 2$, the predictions of the Reynolds equation cannot be trusted even qualitatively [4–5].

Most of the existing work in the lubrication of rough surfaces concerns the Reynolds roughness where the Reynolds equation is averaged using some heuristic or "dishonest" (in the terminology of Keller [6]) arguments. An "honest" [6] approach using Keller's [6] method has recently been advanced by the writer [7, 8] to obtain the mean Reynolds equation which is correct up to $0(\epsilon^2)$, where ϵ is the dimensionless amplitude of the surface roughness. In [7] and [8] the mean Reynolds equation was used to correct the surface roughness in a two-dimensional squeeze-film bearing and slider bearing with exponential mean film thickness, respectively. In particular it was shown in [8] that the theory of Christensen [9] accurately predicts the load enhancements when the surface roughness is either transverse or parallel to the flow, the only two cases intended for the theory to apply [9]. It was conjectured in [8] that Christensen's theory is correct to $0(\epsilon^2)$ for two-dimensional bearings with parallel or transverse surface roughness.

One of the purposes of this communication is to prove this conjecture. Furthermore, neglecting terms of the order $0(\epsilon^4, \epsilon^2 h/l)$, a new mean Reynolds equation is derived which correctly yields Christensen's [9] theory when the surface roughness is either parallel or transverse to the flow.

2 Surface Roughness

The geometry of any rough surface is so irregular that it requires a statistical description [10]. In general, the probability of the surface height must be known to fully specify the surface roughness. However, in practice this complete statistical information is expensive to obtain and only the rms, or at most second-order statistics of the surface roughness are measured. Partly to reflect this practice and partly to simplify the analysis we assume a homogeneous surface roughness with the consequence that only second-order statistics enter in the calculations. That is, the only quantity that we need is the spatial correlation of the surface roughness or equivalently its Fourier transform, commonly known as the spectral density of the surface roughness.

Specifically we consider the quasi-static and isothermal flow of an incompressible viscous fluid in a bearing whose surfaces are described by

$$z_1 = \epsilon a m_1(x,y); \quad z_2 = h(x,t) + \epsilon a m_2(x,y), \tag{1}$$

where a is a length scale, ϵ is the dimensionless amplitude of

Contributed by the Applied Mechanics Division for presentation at the Winter Annual Meeting, Phoenix, Ariz., November 14–19, 1982 of THE AMERICAN SOCIETY OF MECHANICAL ENGINEERS.

Discussion on this paper should be addressed to the Editorial Department, ASME, United Engineering Center, 345 East 47th Street, New York, N.Y. 10017, and will be accepted until two months after final publication of the paper itself in the JOURNAL OF APPLIED MECHANICS. Manuscript received by ASME Applied Mechanics Division, October, 1981; final revision, February, 1982. Paper No. 82-WA/APM-8.

Copies will be available until July, 1983.

the surface roughness, h is a given function of x and time t, $m_k(x, y)$; $k = 1, 2$ are surface profiles and x, y, z are cartesian coordinates, with x being the primary direction of flow. In writing (1), we wish to leave ϵ and m_k dimensionless; a is thus a dummy length scale.

As a consequence of adopting the Reynolds equation as our starting point, only the total film thickness

$$H = z_2 - z_1 = h + \epsilon a m; \quad m \equiv m_2 - m_2 \tag{2}$$

enters in the governing equation. From now on we call m the total film roughness, or simply the surface roughness.

Without loss of generality $m_k(x,y)$ are assumed meanless; the mean film thickness is $<H> = h$, with the angular brackets denoting either an ensemble average or a spatial average if m_k are ergodic or periodic in space.

As mentioned previously, m_k (and thus m) are assumed to be homogeneous in space when the film roughness can be represented as (the spectral representation of m [11])

$$m(x,y) = \int_{-\infty}^{\infty}\int_{-\infty}^{\infty} e^{i(\lambda x + \mu y)} Z(d\lambda d\mu) \equiv \int e^{i\lambda \cdot \mathbf{r}} Z(d\lambda). \tag{3}$$

In (3) r and λ are two-dimensional vectors (x, y) and (λ, μ), respectively, and, in the interest of brevity we write the double Fourier-Stieltjes integral as indicated in the second equality of (3) where $Z(d\lambda)$ is an interval random function of $d\lambda \equiv d\lambda d\mu$ which satisfies

$$<Z(d\lambda)> = 0, \tag{4}$$

$$<Z(d_i\lambda)\, Z^*(d_j\lambda)> = \delta_{ij}\, \Omega(\lambda_i)\, d_i\lambda. \text{ (not sum)} \tag{5}$$

Here x^* denotes the complex conjugate of x, $d_i\lambda$, a two-dimensional interval center at λ_i, δ_{ij} is the Kronecker delta, and $\Omega(\lambda)$ is the spectral density of $m(\mathbf{r})$, defined by the Wiener-Khintchine relations [11]:

$$R(\mathbf{s}) = <m(\mathbf{r}+\mathbf{s})m(\mathbf{r})> = \int e^{i\lambda \cdot \mathbf{s}} \Omega(\lambda)\, d\lambda, \tag{6}$$

$$\Omega(\lambda) = \frac{1}{(2\pi)^2} \int e^{-i\lambda \cdot \mathbf{s}} R(\mathbf{s})\, d\mathbf{s} \tag{7}$$

3 Christensen's Theory

Consider a bearing whose surfaces are given by (1) and the upper bearing plate moves with velocity $(U(x), 0, V(t))$. Assuming that the surface roughness is of the Reynolds type, the pressure distribution obeys the following Reynolds equation [2]

$$\nabla \cdot (H^3 \nabla P) = 6\eta \frac{\partial}{\partial x}(UH) + 12\eta V, \quad \nabla \equiv \mathbf{i}\frac{\partial}{\partial x} + \mathbf{j}\frac{\partial}{\partial y}, \tag{8}$$

$$P(0,y) = P(l,y) = 0, \tag{9}$$

where η is the fluid (constant) viscosity.

Owing to the stochastic nature of H, equations (8)–(9) become a stochastic differential equation. Since only mean bearing performance is required, various attempts have been made to average (8). A notable success is due to Christensen [9] who was concerned with two special cases of surface roughness:

For a parallel surface roughness, where $m = m(y)$, Christensen [9] gives

$$\frac{\partial}{\partial x}\left(<H^3>\frac{\partial <P>}{\partial x}\right) + \frac{\partial}{\partial y}\left(<H^{-3}>^{-1}\frac{\partial <P>}{\partial y}\right) = 6\eta U \frac{\partial <H>}{\partial x} + 12\eta \frac{\partial <H>}{\partial t} \tag{10}$$

and for a transverse surface roughness, where $m = m(x)$, Christensen's theory gives

$$\frac{\partial}{\partial x}\left(<H^{-3}>^{-1}\frac{\partial <P>}{\partial x}\right) + \frac{\partial}{\partial y}\left(<H^3>\frac{\partial <P>}{\partial y}\right) = 6\eta U \frac{\partial}{\partial x}\left(\frac{<H^{-2}>}{<H^{-3}>}\right) + 12\eta \frac{\partial <H>}{\partial t} \tag{11}$$

In both cases the boundary conditions are

$$<P(0,y)> = <P(l,y)> = 0 \tag{12}$$

For the film thickness given by (2), and keeping only terms up to $0(\epsilon^2)$ it can be easily shown that (10) and (11) reduce to, respectively,

$$\frac{\partial}{\partial x}\left[\left(h^3 + 3\epsilon^2 a^2 h <m^2>\right)\frac{\partial <P>}{\partial x}\right] + \frac{\partial}{\partial y}\left[\left(h^3 - 6\epsilon^2 a^2 h <m^2>\right)\frac{\partial <P>}{\partial y}\right] = 6\eta \frac{\partial}{\partial x}(Uh) + 12\eta V, \tag{13}$$

and

$$\frac{\partial}{\partial x}\left[\left(h^3 - 6\epsilon^2 a^2 h <m^2>\right)\frac{\partial <P>}{\partial x}\right] + \frac{\partial}{\partial y}\left[\left(h^3 + 3\epsilon^2 a^2 h <m^2>\right)\frac{\partial <P>}{\partial y}\right] = 6\eta \frac{\partial}{\partial x}\left[U\left(h - 3\epsilon^2 \frac{a^2}{h} <m^2>\right)\right] + 12\eta V \tag{14}$$

Nomenclature

a = length scale
$G(\mathbf{r}, \mathbf{r}')$ = Green function of the operator L, defined in (17)
h = mean film thickness
H = total film thickness, $h + \epsilon am$
I_1, I_2 = defined by (20)–(22)
L, L_1, L_2 = differential operators defined by (15)
l = bearing length
m_1, m_2 = surface corrugations on the bearing plates
$m = m_2 - m_1$ = total film, or surface roughness
P = pressure distribution
P_0 = pressure distribution if the surface roughness was not present ($\epsilon = 0$)
$R(\mathbf{s})$ = correlation of the surface roughness, $<m(\mathbf{r})\, m(\mathbf{r}+\mathbf{s})>$
U, V = bearing velocities
$\mathbf{r}, \mathbf{r}'$ = two-dimensional vectors (x, y) and (x', y')
x, y, z = Cartesian coordinates, with x being the primary direction of flow
$Z(d\lambda)$ = random interval function of $d\lambda = d\lambda d\mu$
∇ = two-dimensional gradient operator, $\mathbf{i}\,\partial/\partial x + \mathbf{j}\,\partial/\partial y$
δ_{ij} = Kronecker delta
ϵ = dimensionless amplitude of the surface roughness
$\lambda = (\lambda, \mu)$ = two-dimensional Fourier wavenumbers; they take values in (real numbers)^2
ω_n = a characteristic frequency of the surface roughness
$\Omega(\lambda)$ = spectral density of $m(\mathbf{r})$, defined in (7)
ϕ_1, ϕ_2 = functions defined in (23)
η = lubricant constant viscosity
$<\bullet>$ = ensemble average of $(\bullet)$
$0(\bullet)$ = order symbol
$\mathbf{1}$ = unit tensor

4 Mean Reynolds Equation

4.1 Two-Dimensional Bearing. The mean Reynolds equation, which is correct up to $0(\epsilon^2)$, has been derived in [7]. For continuity we record the essential steps leading to the final result.

First we denote by L, L_1, L_2 the differential operators

$$L = \nabla \cdot h^3 \nabla, \quad L_1 = 3a \nabla \cdot h^2 m \nabla, \quad L_2 = 3a^2 \nabla \cdot m^2 h \nabla. \tag{15}$$

then (8) is formally equivalent to, in symbolic notation,

$$P = P_0 + 6\epsilon\eta a L^{-1} \frac{\partial}{\partial x}(mU) - L^{-1}(\epsilon L_1 + \epsilon^2 L_2)P + 0(\epsilon^3), \tag{16}$$

where P_0 is the pressure distribution if the film roughness was not present ($\epsilon = 0$) and by L^{-1} we mean the integral operator

$$L^{-1} f(\mathbf{r}) = \int G(\mathbf{r}, \mathbf{r}') f(\mathbf{r}')\, d\mathbf{r}'$$

with $G(\mathbf{r}, \mathbf{r}')$ being the Green function of the self-adjoint operator L which has the relevant boundary conditions (9) embedded in it.

A successive iteration can be made on (16) and we have

$$(L + \epsilon L_1 + \epsilon^2 L_2 + 0(\epsilon^3))\, P = 6\eta \frac{\partial}{\partial x}(hU) + 12\eta V + 6\eta\epsilon a \frac{\partial}{\partial x}(mU) \tag{17}$$

Noting that $<L_1> = 0$ we find that $<P> = P_0 + 0(\epsilon^2)$. Equation (17) is then averaged. Also in any term of $0(\epsilon^2)$, $<P>$ may be replaced by P_0 with a resulting error of $0(\epsilon^4)$. We finally obtain [7]

$$\begin{aligned} &\nabla \cdot [(h^3 + 3a^2 h\epsilon^2 <m^2>) \nabla <P>] \\ &\quad - 9\epsilon^2 a^2 < \nabla \cdot [h^2 m \nabla \int G(\mathbf{r}, \mathbf{r}') \\ &\nabla \cdot (h^2(x') m(\mathbf{r}') \nabla <P(x')>) d\mathbf{r}'] > \\ &\quad = 6\eta \frac{\partial}{\partial x}(Uh) + 12\eta V \\ &\quad - 18\epsilon^2 \eta a^2 < \nabla \cdot \left[h^2 m \nabla \int G(\mathbf{r}, \mathbf{r}') \right. \\ &\quad \left. \frac{\partial}{\partial x'}(m(\mathbf{r}') U(x')) dr' \right] > \end{aligned} \tag{18}$$

where the relevant boundary conditions are (12) and, as before, we have written $\mathbf{r}, \mathbf{r}'$ for (x, y) and (x', y'), respectively. It should be noted that (18) is correct up to $0(\epsilon^2)$. Alternatively, noting that $<P>$ can be replaced by P_0 in any term of the order $0(\epsilon^2)$ we have, in place of (18)

$$\begin{aligned} &\nabla \cdot [(h^3 + 3a^2 h\epsilon^2 <m^2>) \nabla <P>] \\ &\quad - 9\epsilon^2 a^2 < \nabla \cdot (h^2 m \nabla I_1) > \\ &= 6\eta \frac{\partial}{\partial x}(Uh) + 12\eta V - 18\epsilon^2 \eta a^2 < \nabla \cdot (h^2 m \nabla I_2) >, \end{aligned} \tag{19}$$

where, using the definition of $G(\mathbf{r}, \mathbf{r}')$ and noting that $P_0 = P_0(x)$, I_1 and I_2 are given by

$$\nabla \cdot h^3 \nabla I_1 = \frac{\partial}{\partial x}\left(h^2 m \frac{dP_0}{dx}\right), \tag{20}$$

$$\nabla \cdot h^3 \nabla I_2 = \frac{\partial}{\partial x}(mU), \tag{21}$$

$$I_1(0,y) = I_1(l,y) = I_2(0,y) = I_2(l,y) = 0. \tag{22}$$

Equations (19)–(22) and (12) are the mean Reynolds equations and boundary conditions.

We now show that the mean Reynolds equation (19) includes as special cases Christensen's theories (13)–(14), if terms of order $0(h/l)$ are neglected in I_1 and I_2. (This leads to an error of $0(\epsilon^2 h/l)$ in the final results because terms involved I_1 and I_2 in (19) are of order $0(\epsilon^2)$.)

Since m can be represented by (3) and in anticipating that I_1 and I_2 are stationary in y we write

$$I_k = \int e^{i\mu y} \phi_k(x)\, Z(d\lambda); \quad k = 1, 2, \tag{23}$$

where a direct substitution of (23) into (20)–(22) yields

$$\frac{d}{dx}\left(h^3 \frac{d\phi_1}{dx}\right) - \mu^2 h^3 \phi_1 = \frac{d}{dx}\left(h^2 e^{i\lambda x} \frac{dP_0}{dx}\right), \tag{24}$$

$$\phi_1(0) = \phi_1(l) = 0, \tag{25}$$

and

$$\frac{d}{dx}\left(h^3 \frac{d\phi_2}{dx}\right) - \mu^2 h^3 \phi_2 = \frac{d}{dx}\left(U e^{i\lambda x}\right), \tag{26}$$

$$\phi_2(0) = \phi_2(l) = 0. \tag{27}$$

In (24)–(27) we note that $h(x)$, dP_0/dx and U are slowly varying functions of x (otherwise Reynolds equation will not be applicable); and $\exp(i\lambda x)$ is a fast varying function of x. The latter is due to the fact that $\lambda h \approx 0.5$ and thus $\lambda x \sim 0(x/h)$. These suggest that we should look for a solution of the form

$$\phi_k = \phi_k^{(0)} + \delta\phi_k^{(1)} + \ldots, \quad k = 1, 2, \tag{28}$$

where $\delta = 0(h/l)$ is the slope of the bearing (say $h = h_0 e^{\delta\chi(x)}$ for some function $\chi(x)$).

Neglecting terms of $0(h/l)$ (that is, treat all slowly varying functions of x as constants) the solutions to (24) and (26) are

$$\begin{aligned} \phi_1 &= -\frac{1}{\lambda^2 + \mu^2}\left[\frac{1}{h^3}\frac{d}{dx}\left(h^2 \frac{dP_0}{dx}\right) + \frac{i\lambda}{h}\frac{dP_0}{dx}\right] e^{i\lambda x} \\ &\quad + A_1 \frac{\sinh \mu x}{\sinh \mu l} + B_1 \frac{\cosh \mu(l-x)}{\cosh \mu l} + 0(h/l), \end{aligned} \tag{29}$$

$$\begin{aligned} \phi_2 &= -\frac{1}{\lambda^2 + \mu^2}\left[\frac{1}{h^3}\frac{dU}{dx} + \frac{i\lambda U}{h^3}\right] e^{i\lambda x} \\ &\quad + A_2 \frac{\sinh \mu x}{\sinh \mu l} + B_2 \frac{\cosh \mu(l-x)}{\cosh \mu l} + 0(h/l), \end{aligned} \tag{30}$$

where A_k, B_k, $k = 1, 2$ can be found from (25) and (27); but we have no need of them here. This is because the terms involved A_k and B_k are also slowly varying functions of x; they only contribute to the mean Reynolds equation through terms of $0(h/l)$.

Now we are ready to calculate the terms involving I_1 and I_2 in (19). First we have

$$\begin{aligned} < \nabla \cdot h^2 m \nabla I_k > &= < \int\int \nabla \\ &\cdot [h^2 e^{-i\lambda' \cdot \mathbf{r}'} \nabla \phi_k e^{i\mu y}] Z(d\lambda)\, Z^*(d\lambda') > + 0(h/l), \end{aligned}$$

which gives, owing to (5),

$$< \nabla \cdot h^2 m \nabla I_k > = \int \frac{d}{dx}\left(h^2 e^{-i\lambda x} \frac{d\phi_k}{dk}\right) \Omega(\lambda)\, d\lambda + 0(h/l). \tag{31}$$

Next, using (29) and (30) in (31) we obtain

$$\begin{aligned} < \nabla \cdot h^2 m \nabla I_1 \geq &= \frac{d}{dx}\left(h \frac{dP_0}{dx}\right) \int \frac{\lambda^2}{\lambda^2 + \mu^2} \Omega(\lambda)\, d\lambda \\ &- \frac{d}{dx}\left(\frac{1}{h}\frac{d}{dx}\left(h^2 \frac{dP_0}{dx}\right)\right) \int \frac{i\lambda}{\lambda^2 + \mu^2} \Omega(\lambda)\, d\lambda + 0(h/l), \end{aligned} \tag{32}$$

and

$$< \nabla \cdot h^2 m \nabla I_2 \geq = \frac{d}{dx}\left(\frac{U}{h}\right) \int \frac{\lambda^2}{\lambda^2 + \mu^2} \Omega(\lambda)\, d\lambda$$

$$-\frac{d}{dx}\left(\frac{1}{h}\frac{dU}{dx}\right)\int\frac{i\lambda}{\lambda^2+\mu^2}\Omega(\lambda)\,d\lambda+0(h/l). \tag{33}$$

In deriving (32) and (33) we have used the result that the x-derivative of a slowly varying function of x is of the order $0(h/l)$ (i.e., the slope of that function). Furthermore the second terms on the right-hand sides of (32) and (33) vanish because $\Omega(\lambda, \mu)$ is even in its first argument.

Thus the mean Reynolds equation (19) becomes, noting that $<P> = <P>(x)$,

$$\frac{d}{dx}\left[(h^3+3a^2h\epsilon<m^2>)\frac{d<P>}{dx}\right]$$

$$-9\epsilon^2a^2\frac{d}{dx}\left(h\frac{dP_0}{dx}\right)\int\frac{\lambda^2}{\lambda^2+\mu^2}\Omega(\lambda)\,d\lambda$$

$$=6\eta\frac{\partial}{\partial x}(Uh)+12\eta V$$

$$-18\epsilon^2\eta a^2\frac{d}{dx}\left(\frac{U}{h}\right)\int\frac{\lambda^2}{\lambda^2+\mu^2}\Omega(\lambda)\,d\lambda. \tag{34}$$

It should be noted that the error in (34) is of the order $0(\epsilon^4, \epsilon^2h/l)$. Finally, in place of P_0 we can write $<P> + 0(\epsilon^2)$ and recognizing that

$$<m^2> = \int\Omega(\lambda)\,d\lambda,$$

we obtain

$$\frac{d}{dx}\left[\left(h^3-3\epsilon^2a^2h\int_{-\infty}^{\infty}\int_{-\infty}^{\infty}\frac{2\lambda^2-\mu^2}{\lambda^2+\mu^2}\Omega(\lambda,\mu)\,d\lambda d\eta\right)\frac{d<P>}{dx}\right]$$

$$=6\eta\frac{\partial}{\partial x}(Uh)+12\eta V$$

$$-18\epsilon^2a^2\frac{\partial}{\partial x}\left(\frac{U}{h}\right)\int_{-\infty}^{\infty}\int_{-\infty}^{\infty}\frac{\lambda^2}{\lambda^2+\mu^2}\Omega(\lambda,\mu)\,d\lambda d\mu$$

$$+0(\epsilon^4, \epsilon^2h/l). \tag{35}$$

Subjected to the boundary conditions (12), this is the mean Reynolds equation that is sought.

For a parallel surface roughness $\Omega(\lambda, \mu) = \delta(\lambda)\,\Omega(\mu)$ and (35) reduce to equation (13) of Christensen's [9] theory. On the other hand if the surface roughness is transverse to the flow $\Omega(\lambda, \mu) = \delta(\mu)\,\Omega(\lambda)$ and (35) reduce to equation (14) of Christensen's [9] theory. Thus Christensen's theory is correct to $0(\epsilon^2)$.

In a squeeze-film bearing, $h = h(t)$ and (35) reduce to

$$\left(h^3-3\epsilon^2a^2h\int\frac{2\lambda^2-\mu^2}{\lambda^2+\mu^2}\Omega(\lambda)\,d\lambda\right)\frac{d^2}{dx^2}<P>$$

$$=12\eta V+0(\epsilon^4, \epsilon^2h/l) \tag{36}$$

thus the effective gap thickness H_{eff} is given through

$$H_{\text{eff}}^3=h^3\left(1-3\epsilon^2\frac{a^2}{h^2}\int\frac{2\lambda^2-\mu^2}{\lambda^2+\mu^2}\Omega(\lambda)\,d\lambda\right). \tag{37}$$

Since the normal load is proportional to H_{eff}^{-3}, there will be a load enhancement factor of

$$1+3\epsilon^2\frac{a^2}{h^2}\int_{-\infty}^{\infty}\int_{-\infty}^{\infty}\frac{2\lambda^2-\mu^2}{\lambda^2+\mu^2}\Omega(\lambda,\mu)\,d\lambda\,d\mu$$

which was found in [7] using equation (19).

4.2 General Bearings. If the mean film thickness is a function of x and y and/or the boundary ∂s of the bearing is a closed curve in x-y plane, then instead of (13) the relevant boundary condition for the mean pressure is

$$<P(\mathbf{r})>=0 \quad \text{for} \quad \mathbf{r}\in\partial s \tag{38}$$

Also the boundary conditions for (22) I_k must be replaced by

$$I_k(\mathbf{r})=0 \quad \text{for} \quad \mathbf{r}\in\partial s, \quad k=1, 2.$$

Thus I_k are not homogeneous in y anymore and the representation (23) is not appropriate. Instead one can only write that

$$I_k=\int\phi_k(x, y)\;Z(d\lambda), \tag{39}$$

with $\phi_k(x, y)$ now being functions in both x and y. The equations for $\phi_k(\mathbf{r})$ read

$$\nabla\cdot(h^3\nabla\phi_1)=\nabla\cdot(h^2e^{i\lambda\cdot\mathbf{r}}\nabla P_0); \quad \phi_1=0 \text{ on } \partial s \tag{40}$$

$$\nabla\cdot(h^3\nabla\phi_2)=\partial(Ue^{i\lambda\cdot\mathbf{r}})/\partial x; \quad \phi_2=0 \text{ on } \partial s \tag{41}$$

Again $\exp(i\lambda\cdot\mathbf{r})$ is a fast-varying function of x and y while h, ∇P_0, and U are slowly varying functions of x and y. Thus regarding the slowly varying functions to be constants, the solutions to (40) and (41) are

$$\phi_1=-\frac{1}{(\lambda^2+\mu^2)h^3}(\nabla\cdot h^2\nabla P_0+i\lambda\cdot P_0h^2)e^{i\lambda\cdot x}$$

$$+\text{ homogeneous slowly varying terms,} \tag{42}$$

$$\phi_2=-\frac{1}{(\lambda^2+\mu^2)h^3}\left(\frac{\partial U}{\partial x}+i\lambda U\right)e^{i\lambda\cdot x}$$

$$+\text{ homogeneous slowly varying terms,} \tag{42}$$

where the homogeneous terms in (42)–(43) satisfy the homogeneous equations (40)–(41) where the right-hand sides are zero. Thus we obtain instead of (32) and (33)

$$<\nabla\cdot h^2m\nabla I_1>=$$

$$\nabla\cdot\left(h\int\frac{\lambda\lambda}{\lambda^2+\mu^2}\Omega(\lambda)\,d\lambda\,\nabla P_0\right)+0(h/l) \tag{44}$$

and

$$<\nabla\cdot h^2m\nabla I_2>=\nabla\cdot\left(\frac{U}{h}\int\frac{\lambda\lambda}{\lambda^2+\mu^2}\Omega(\lambda)\,d\lambda\right)+0(h/l) \tag{45}$$

Then the mean Reynolds equation becomes

$$\nabla\cdot\left(\left[(h^3+3\epsilon^2a^2h<m^2>)\,\mathbf{1}\right.\right.$$

$$\left.\left.-9\epsilon^2a^2h\int_{\infty}^{\infty}\int_{\infty}^{\infty}\frac{\lambda\lambda}{\lambda^2+\mu^2}\Omega(\lambda,\mu)\,d\lambda d\mu\right]\cdot\nabla<P>\right)$$

$$=6\eta\frac{\partial}{\partial x}(Uh)+12\eta V$$

$$-18\epsilon^2a^2\eta\nabla\cdot\left(\frac{U}{h}\int_{-\infty}^{\infty}\int_{-\infty}^{\infty}\frac{\lambda\lambda}{\lambda^2+\mu^2}\Omega(\lambda,\mu)\,d\lambda d\mu\right) \tag{46}$$

with an error of the order $0(\epsilon^4, \epsilon^2h/l)$.

Again, for a transverse surface roughness we can integrate μ out in (46) and obtain (14). On the other hand, for a parallel surface roughness we integrate λ out in (46) and obtain (13). That is, Christensen's [9] theory is correct to the order $0(\epsilon^2)$ in the surface roughness amplitude. For a surface roughness of a general two-dimensional form a naive approach of combining (13) and (14) additively will not yield the correct answer, which is equation (46).

5 Conclusions

In summary, we have derived a mean Reynolds equation that is accurate to terms of order $0(\epsilon^2)$, where ϵ is the dimensionless amplitude of the film roughness defined in (2). The final result is given in (46) and is dependent on the spectral density Ω of the surface roughness defined in (6)–(7). It is noteworthy that the new mean Reynolds equation reduces

to Christensen's theory in the appropriate limits where either the film roughness is parallel or transverse to the flow direction. In these cases only the mean square of the film thickness, $<m^2>$, enters in the final equation, cf. (13) and (14).

The mean Reynolds equation (46) is intended to be used for small-amplitude surface roughness. This is not seen as a stringent restriction since the application of the Reynolds equation requires that $\epsilon a \omega_n << 1$ (ratio of surface roughness amplitude to wavelength). Also from the Stokes solutions to squeeze-film and slider bearing with parallel surface roughness [4–5] we require that $\omega_n h \leq 0.5$. This means $\epsilon a/h << 1$ or that $\epsilon << 1$, which was assumed in this paper.

Acknowledgment

The support of the Australian Research Grants Committee (ARGC grant F7915597R) is gratefully acknowledged.

References

1 Wilcock, D. F., "Effects of Surface Roughness in Lubrication," ASME *Journal of Lubrication Technology,* Vol. 100, 1978, pp. 6–11.

2 Reynolds, O., "On the Theory of Lubrication and Its Application to Mr. Beauchamp Tower's Experiments," *Phil. Trans. Roy. Soc.,* Vol. A 177, 1886, pp. 157–234.

3 Sun, D.-C., and Chen, K.-K., "First Effects of Stokes Roughness on Hydrodynamic Lubrication," ASME *Journal of Lubrication Technology,* Vol. 99, 1977, pp. 2–9.

4 Phan-Thien, N., "On the Effects of Parallel and Transverse Stationary Random Surface Roughness in Hydrodynamic Lubrication," *Proc. Roy. Soc. London,* Vol. A 374, 1981, pp. 569–591.

5 Phan-Thien, N., "On the Effects of Reynolds and Stokes Surface Roughness in a Two-Dimensional Slider Bearing," *Proc. Roy. Soc. London,* Vol. A 377, 1981, pp. 349–362.

6 Keller, J. B., "Wave Propagation in Random Media," *Proc. Symp. Appl. Math.,* Vols. 13 and 16, Amer. Math. Soc., Providence, R.I., 1962 and 1964.

7 Phan-Thien, N., "On the Mean Reynolds Equation in the Presence of Surface Roughness: Squeeze-Film Bearing," ASME JOURNAL OF APPLIED MECHANICS, Vol. 48, 1981, pp. 717–720.

8 Phan-Thien, N., "On the Effects of Homogeneous Reynolds Roughness in a Two-Dimensional Slider Bearing With Exponential Film-Thickness," ASME *Journal of Lubrication Technology* (in press).

9 Christensen, H., "Stochastic Models for Hydrodynamic Lubrication of Rough Surfaces," *Proc. Inst. Mech. Eng.,* Vol. 184, 1969–70, pp. 1013–1026.

10 Longuet-Higgins, M. S., "The Statistical Geometry of Random Surfaces," *Proc. Symp. Appl. Math.,* Vol. 13, American Math. Soc., Providence, R.I., 1962.

11 Yaglom, A. M., *An Introduction to the Theory of Stationary Random Functions,* translated and edited by R. A. Silverman, Prentice-Hall, Englewood Cliffs, N.J., 1965.

Theory of Maximum Tensile Stresses in the Solidifying Shell of a Constrained Rectangular Casting

R. H. Tien
Associate Research Consultant.

O. Richmond

U.S. Steel Corporation,
Research Laboratory,
Monroe, Pa. 15146

A theoretical model is derived for determining the stresses that develop during the early stages of solidification in flat-sided ingot molds. The model requires flatness of the solidifying skin and is strictly valid only up to the time when an air gap begins to form at the corners. Here it is argued that the model continues to provide a valid estimate of the maximum stresses in the central portion of the flat sides, where mold contact is maintained long after the first appearance of an air gap at the corners. This argument is supported by the fact that the lateral contraction of this portion is inhibited both by mold friciton and by tensile forces transmitted through the contracted corners from adjacent faces of the skin. Specific calculations are made for low-carbon steel by using physical property data from the literature. The maximum tensile stresses occur at the outer face and have values between 500–1500 psi, depending on the cooling rate. The theory is believed to be relevant to the interpretation of "center-line" cracking.

Introduction

The stresses that develop in the solid shell during solidification are of considerable practical importance because when sufficiently large, they may cause longitudinal cracking. It is the objective of the present work to describe a method for estimating such stresses and to give some actual numerical results for the solidification of steel in a mold with flat sides.

If the solidifying shell is subjected to uniform but nonsteady surface temperature and pressure, and if it remains flat during solidification, then the theoretical problem in the early stages reduces to a one-dimensional nonsteady problem on each side of the ingot except for small corner effects. Weiner and Boley [1] have considered such a problem for a square mold. They assumed that the newly formed solid behaved as a rate-independent elastic-plastic material. This led to contraction immediately upon cooling, causing an "air gap" between the mold and the solid shell (Fig. 1(*a*)). Continued flatness of the skin was nevertheless assumed on the basis that fluid pressures and inelastic corner rotations were negligible. The resultant lateral strain in the shell was negative (contracting) and the resultant lateral force was zero.

Richmond and Tien [2] took a different approach. They assumed that the newly formed shell behaved as a viscoelastic material and that the fluid pressure was not negligible. This caused the shell to remain in contact with the mold for some time after cooling began (Fig. 1(*b*)). The fluid pressure forced the shell against the mold, causing the resultant lateral force

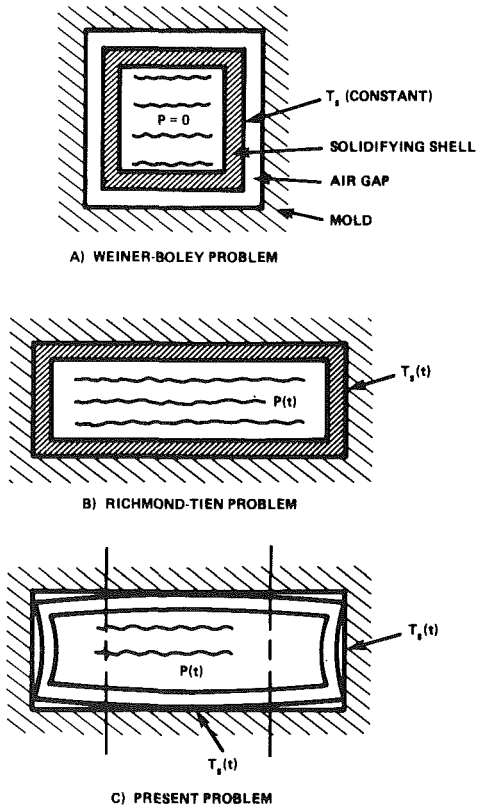

Fig. 1 Illustration of solidification problems

Contributed by the Applied Mechanics Division for publication in the JOURNAL OF APPLIED MECHANICS.

Discussion on this paper should be addressed to the Editorial Department, ASME United Engineering Center, 345 East 47th Street, New York, N.Y. 10017, and will be accepted until two months after final publication of the paper itself in the JOURNAL OF APPLIED MECHANICS. Manuscript received by ASME Applied Mechanics Division, October, 1981, final revision, March, 1982.

to be compressive in the early stages and the lateral strain to be zero. If the cooling rate was sufficiently rapid, however, the lateral force changed in time from compressive to tensile, and the time of this transition was taken as the beginning of air-gap formation at the corners. After this time the solution was considered invalid because the shell would no longer remain flat.

It is the contention of the present work, however, that the approach of Richmond and Tien can be used to obtain an estimate of the stresses in the central portion of the face of the ingot even after the air gap begins to form. As illustrated in Fig. 1(*c*), the air gap is visualized as growing from the corners, but the central portion of the skin is kept flat against the mold by the fluid pressure. Furthermore, lateral contraction of this portion is inhibited both by mold friction and by the tensile forces transmitted through the contracted corners from adjacent faces of the skin. Thus, continued application of the solution is believed to give a reasonable estimate of the stresses at the center of the faces even after air-gap formation at the corners, and up to the time of complete breakaway of the faces from the mold. These stresses are probably significant for the understanding of the formation of center-line cracks. The formation of corner cracks, on the other hand, is probably intimately associated with the occurrence of the air gap itself.

In the next section, the rheological model of Richmond and Tien is reviewed and compared with specific experimental results on the mechanical behavior of low-carbon steels at very high temperatures. Then the theoretical problem for flat-sided molds is reviewed and the method of solution briefly described. Finally, actual results for the solidification of low-carbon steel are presented and discussed.

The Rheological Model Compared With the Behavior of Low-Carbon Steel at High Temperatures

A general viscoelastic model for solids at temperatures that are high relative to their melting points was proposed by Richmond and Tien [2], and is used here. In Cartesian components it is given by,

$$\dot{\epsilon}_{ij} = (1+\nu)\left(\frac{\dot{s}_{ij}}{E}\right) + \left[\left(\frac{1-2\nu}{3}\right)\left(\frac{\dot{\sigma}_{kk}}{E}\right) + \alpha\dot{T}\right]\delta_{ij} + \frac{s_{ij}}{\mu}, \quad (1)$$

where the strain-rate components $\dot{\epsilon}_{ij}$ are related to the velocity components v_i by

$$\dot{\epsilon}_{ij} = \frac{1}{2}(v_{i,j} + v_{j,i}), \quad (2)$$

and the deviator stress components s_{ij} are related to the full stress components σ_{ij} by

$$s_{ij} = \sigma_{ij} - \frac{1}{3}\sigma_{kk}\delta_{ij}. \quad (3)$$

The thermal-expansion coefficient α and Poisson's ratio ν are assumed to be material constants, whereas Young's modulus E is taken to be a function of temperature, and viscosity μ is a function of both temperature and stress. The dot operator, although generally a Jaumann rate [3], is taken as a simple time derivative $\partial/\partial t$ because convection terms are assumed to be negligible.

The thermal expansion coefficient α used in the present model is assumed to be constant. This is justified by the experimental measurements obtained by Tammann and Bandel [4] which indicated the linear relationship between temperature and specific volume at temperatures up to the melting point.

No direct measurements of Poisson's ratio have been reported for low-carbon steels at high temperatures. However, Garber and Kovalev [5] did measure both Young's modulus and the shear modulus in an 0.04 percent C steel at temperatures below 1000°C and inferred from these data that Poisson's ratio increases with increasing temperatures from a value of 0.28 at room temperature. Because this result was obtained indirectly and at temperatures considerably below the melting point, and because the maximum possible value of ν is 0.5, it has been assumed for the purposes of this work simply that ν has a constant value of 0.3.

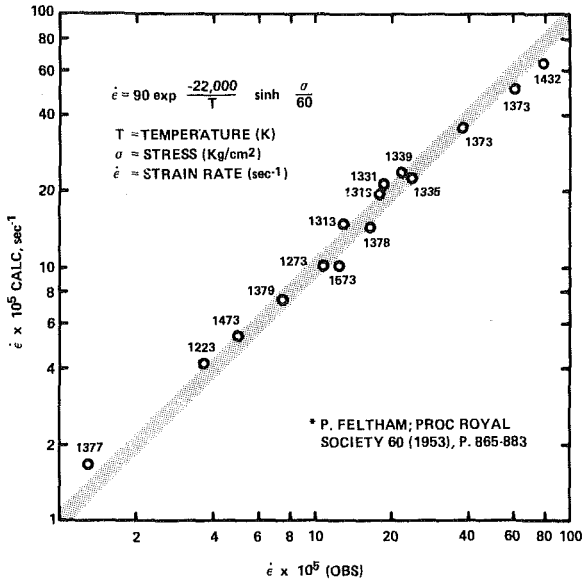

Fig. 2 Companion with Feltham's* data for 0.05 percent C Steel

The dependence of Young's modulus on temperature appears to be linear from the measurements on iron by Köster [6] and by Hub [7] and is represented by

$$E = F - GT, \quad (4)$$

where F and G are material constants. It should be noted that atomistic theories [8] also generally agree with equation (4) at high temperatures.

The temperature and stress dependence of viscosity are assumed to be given by

$$\mu = \frac{2e^{C/T}}{3A'}\frac{J}{\sinh(BJ)}, \quad (5)$$

where A', B, and C are material constants and where the second stress invariant J is given by

$$J = \sqrt{\frac{3}{2}s_{ij}s_{ij}}. \quad (6)$$

For a simple tension test under a stress, σ, it is readily seen from equations (3) and (6) that $J = \sigma$. If the test also is conducted at constant stress and constant temperature, equations (1) and (5) show that the strain rate $\dot{\epsilon}$ in the tensile direction is given by

$$\dot{\epsilon} = A' e^{-C/T}\sinh(B\sigma). \quad (7)$$

Comparisons of this equation with creep-test measurements on an 0.05 percent C steel by Feltham [9] are shown in Fig. 2, and the agreement is seen to be quite good. It should be noted that this equation can be derived from absolute reaction-rate theory [10, 11], in which case A' is proportional to T. This is the form that was proposed in [3], and it would provide even better agreement with Feltham's data. However, the simpler form (7) with A' as a constant is considered to be adequate.

The Solidification Problem and Method of Solution

The problem is illustrated at a general stage of

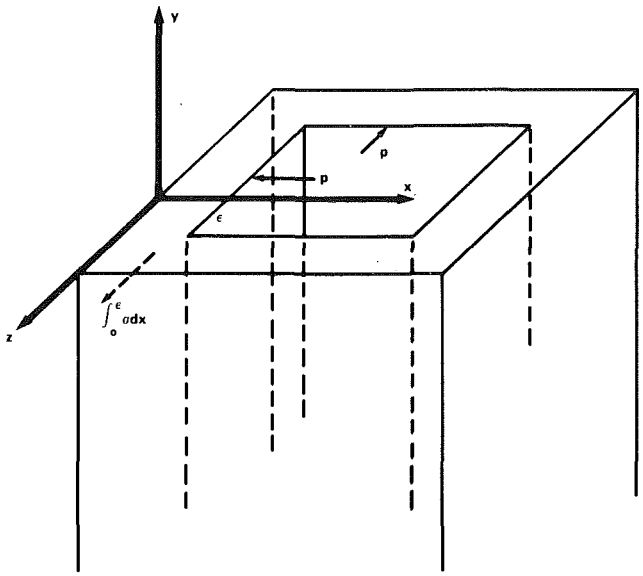

Fig. 3 Physical representation of the problem and the coordinate system

solidification in Fig. 3, where x represents the space coordinate normal to an ingot face. Initially the melt is assumed to be at a uniform temperature, T_m, just above the melting point and at a uniform pressure, P, caused by the liquid head. Subsequently, the surface temperature of the ingot is decreased uniformly over the entire ingot surface while the melt pressure is held constant.[1] The problem is to calculate the thickness of the solid shell and the temperature, stress, and strain distributions within the shell during solidification. The thickness and the temperature distribution are obtained from the heat conduction equation

$$\dot{T}=kT_{,ii'} \tag{8}$$

where k is thermal diffusivity, assumed to be a material constant. The stresses must satisfy the equations of mechanical equilibrium

$$\sigma_{ij,j}=0 \tag{9}$$

as well as the rheological equations (1), (4), and (5).

In general, even though the surface temperature and pressure are uniform, the shell will become distorted during solidification, leading to a difficult three-dimensional problem. For a viscoelastic material, however, and a rigid mold, the newly formed shell will be pressed against the mold in the early stages, preventing distortion and allowing a much simpler solution. For this case the only nonzero velocity component is $v_x = v\ (x,t)$, and the only nonzero stress components are $\sigma_{xx} = -P$ and $\sigma_{yy} = \sigma_{zz} = -P + \tau\ (x,t)$. The temperature, too, is a function only of x and t, and consequently the entire problem becomes one dimensional. The heat-conduction equation (8) then reduces to

$$\frac{\partial T}{\partial t}=k\frac{\partial^2 T}{\partial x^2}, \tag{10}$$

or, if a modified heat of fusion is used (12), an approximate solution can be obtained from the still simpler equation

$$\frac{\partial^2 T}{\partial x^2}=0. \tag{11}$$

The accuracy of this approximation was discussed in a previous paper [12]. The equilibrium equation (9) is identically satisfied and the rheological equations (1), (4), ,and (5) give

$$\frac{\partial \tau}{\partial t}=\left[\left(\frac{(1-2\nu)}{1-\nu}P-\tau\right)\frac{G}{F-GT}-\frac{(F-GT)}{1-\nu}\right]\frac{\partial T}{\partial t}$$
$$-\frac{A'(F-GT)e^{-C/T}\sinh(B\tau)}{2(1-\nu)} \tag{12}$$

and

$$\frac{\partial v}{\partial x}=\frac{2(1-2\nu)}{(F-GT)^2}\frac{\partial \tau}{\partial t}+\left[\frac{(1-2\nu)G\ (2\tau-3P)}{(F-GT)^2}+3\alpha\right]\frac{\partial T}{\partial t}. \tag{13}$$

Equations (11)-(13) are the three field equations for the three dependent variables, T, τ, and v, in the resulting one-dimensional, nonsteady problem.

Initially, $v = \tau = 0$ and $T = T_m$. The boundary conditions on temperature are given by the circumstances that the outer surface of the skin is subject to a specified temperature history, while the inner surface remains at the melting temperature, and also that heat is generated at the inner surface in an amount required by the modified heat of fusion [12]. More precisely,

$$T(x=0)=T_m-T_a(1-e^{-(Rt)^2})$$
$$T(x=X(t))=T_m \tag{14}$$

and

$$\frac{\partial T}{\partial x}(x=X(t))=\frac{\rho l'}{k}\frac{dX}{dt},$$

where $X(t)$ is the thickness of the solid shell and l' is the modified heat of fusion. These boundary conditions are sufficient to determine $T(x,t)$ from equation (11). Once $T(x,t)$ is determined, $\tau(x,t)$ can be determined from equation (12) and the condition that it is zero at the solidifying interface. Finally, $v(x,t)$ can be determined from equation (13) and the condition that it is initially zero and remains zero at the outer surface of the shell. Actually, $v(x,t)$ is not computed here because it is of no particular interest, but $T(x,t)$ and $\tau(x,t)$ are computed from the reasonable cooling history given by the first part of equation (14).

The problem is first restated in dimensionless variables by using the following substitutions:

$$\left.\begin{aligned}\bar{t} &= \mathrm{Rt},\ \bar{x}=x/D,\ \bar{X}=X/D,\ \bar{T}=T/T_m,\ \bar{\tau}=B\tau\\ \bar{T}_a &= T_a/T_m,\ \bar{L}=\frac{\rho D^2 R l'}{kT_m},\ \bar{P}=BP,\ \bar{F}=BF,\ \bar{G}=BT_mG\\ \bar{\alpha} &= \alpha T_m,\ \bar{A}'=A'/R,\ \bar{C}=C/T_m\end{aligned}\right\} \tag{15}$$

where D is unit length. The thermal problem then becomes

$$\left.\begin{aligned}&\frac{\partial^2 \bar{T}}{\partial \bar{x}^2}=0\\ &\text{subject to the boundary conditions}\\ &\bar{T}(\bar{x}=0)=1-\bar{T}_a(1-e^{-\bar{t}^2})\\ &\bar{T}(\bar{x}=\bar{X}(\bar{t}))=1\\ &\text{and}\\ &\frac{\partial \bar{T}}{\partial \bar{x}}(\bar{x}=\bar{X}(t))=\bar{L}\frac{d\bar{X}}{d\bar{t}},\\ &\text{where}\\ &\bar{X}(t=0)=0.\end{aligned}\right\} \tag{16}$$

And the mechanical problem becomes

[1] The more general case of uniform but nonsteady pressure was treated in [2].

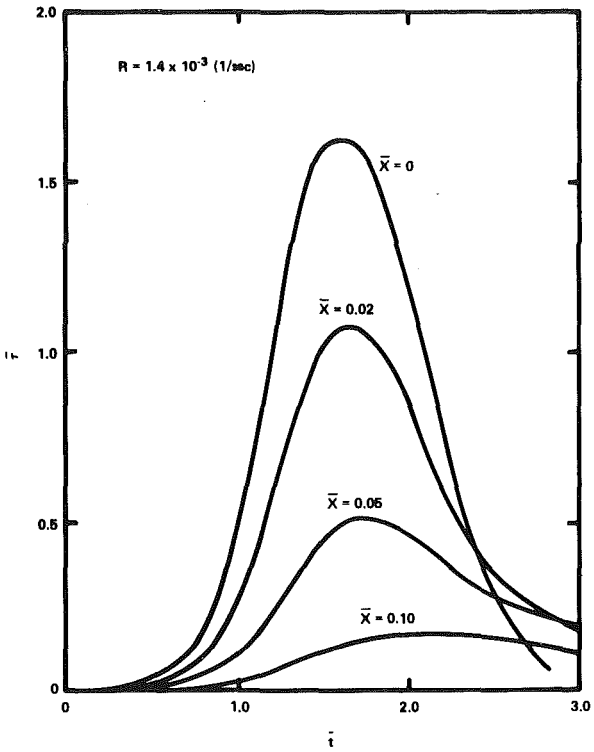

Fig. 4 Development of stress at various locations

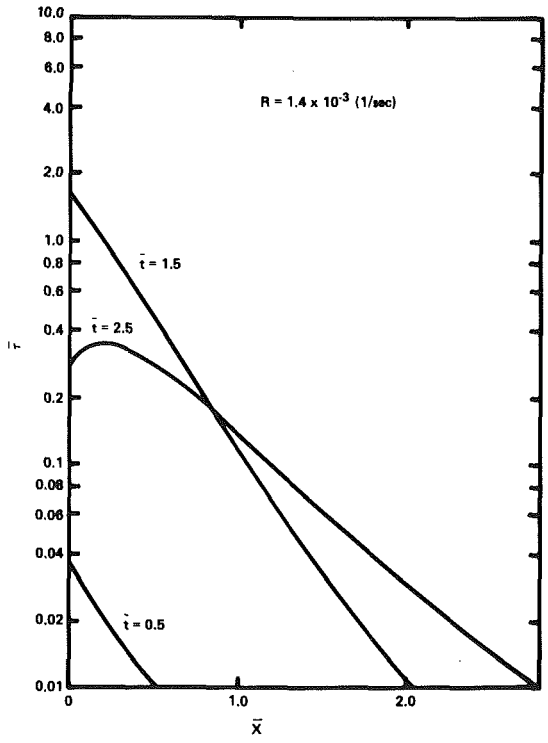

Fig. 5 Distribution of stress at various times

$$\frac{\partial\bar{\tau}}{\partial\bar{t}} = \left[\left(\frac{(1-2\nu)}{1-\nu}\bar{P}-\bar{\tau}\right)\frac{\bar{G}}{\bar{F}-\bar{G}\bar{T}} - \frac{\bar{\alpha}(\bar{F}-\bar{G}\bar{T})}{1-\nu}\right]\frac{\partial\bar{T}}{\partial\bar{t}} - \frac{A'(\bar{F}-\bar{G}\bar{T})e^{-\bar{C}/\bar{T}}}{2(1-\nu)}\sinh\bar{\tau} \tag{17}$$

subject to the condition that $\bar{\tau}$ is zero at the solidification front.

It is readily verified that the solution to the thermal problem is given by

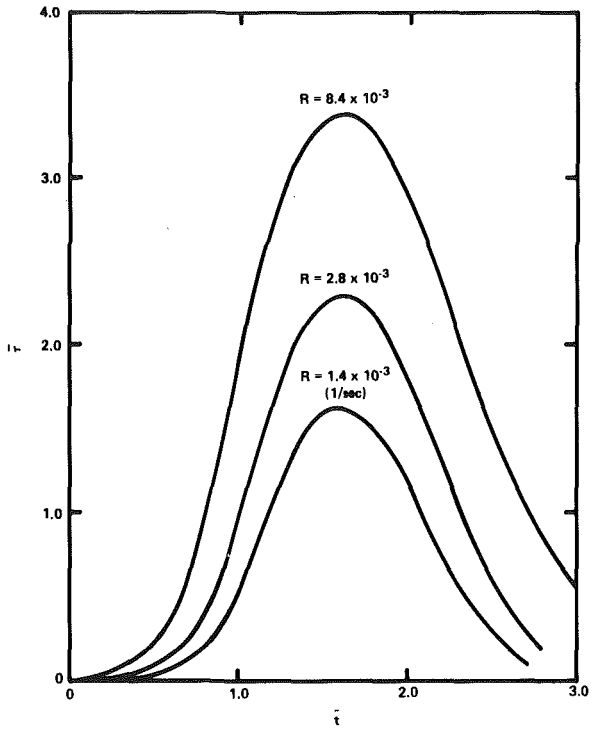

Fig. 6 Development of stress at surface $\bar{X} = 0$

$$\left.\begin{aligned}\bar{T} &= 1-\bar{T}_a\left(1-\frac{\bar{x}}{\bar{X}}\right)(1-e^{-\bar{t}^2})\\ \bar{X} &= \sqrt{\frac{2\bar{T}_a}{\bar{L}}\left(\bar{t}-\frac{\sqrt{\pi}}{2}\operatorname{erf}\bar{t}\right)}\end{aligned}\right\} \tag{18}$$

where

The mechanical problem is solved by using this result in the right-hand side of equation (17). Specifically, the dimensionless stress $\bar{\tau}$ is computed at various specific positions, $\bar{x}_n$, by using the simple but reliable Runge-Kutta [13] integration procedure with the condition

$$\bar{\tau}(\bar{t}=\bar{t}_n)=0, \tag{19}$$

where $\bar{t}_n$ is computed from the second part of equation (18) when $\bar{x}_n = \bar{X}$.

Numerical Calculations and Figures

The following data that are appropriate for 0.05 percent C steel were used in equations (17) and (18) to calculate the stresses developed during solidification:

$A' = 1.55\times10^5$ (1/sec)
$B = 2.05\times10^{-5}$ (cm²/gr)
$C = 3.2\times10^4$ (°C)
$\alpha = 1.8\times10^{-5}$ (1/°C)
$G = 0.88\times10^6$ (gr/cm²°C)
$F = 0.002$ (gr/cm²)
$\nu = 0.3$
$T_a = 538$ (°C)
$T_m = 1550$ (°C)
$\rho = 8$ (gr/cm³)
$l' = 65$ (cal/gr)
$k = 0.07$ (cal/sec°C cm)

The development of stress at various positions is shown in Fig. 4 by using $R = 1.4 \times 10^{-3}$ (1/sec), which corresponds to the case where surface temperature decreases from melting temperature to 1100 °C within 16 min. It is seen that at any position the stress starts to build up when solidification begins

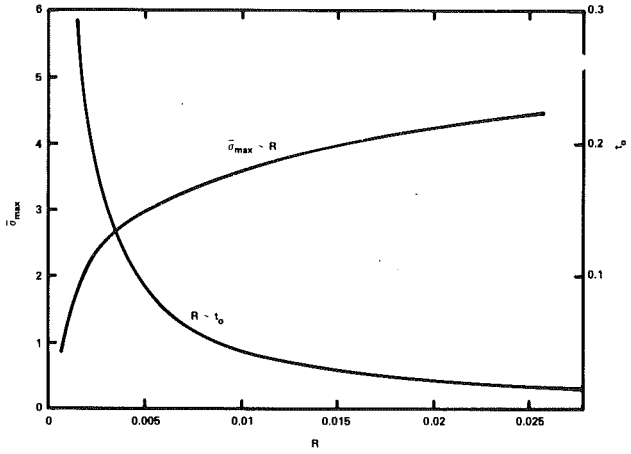

Fig. 7 Effect of cooling rate on maximum stress

because of thermal contraction. During the initial stages, the temperature is high and the stress is low. Hence the inelastic strain rate is low, and the stress accumulates from thermal contraction at a rate faster than stress relaxation from the inelastic behavior. The overall stress is therefore increasing. At a later stage, the temperature is low and the stress is high, and the inelastic effect overpowers that of thermal contraction. Then the stress is gradually relaxed. The overall maximum stress occurs at the cooling surface ($\bar{x} = 0$), but at any particular instant the stress may be higher elsewhere. This is shown in Fig. 5, where the stress distribution within the solidifying shell is given at various times. The maximum stress is at the surface up to $\bar{t} = 2.0$, but then the stress level decreases and the location of the maximum stress moves inward toward the liquid side. The stress history at the surface $\bar{x} = 0$ is given in Fig. 6 for various values of R, which implies different rates of cooling. It is seen that the maximum stress can be three times higher when the time required to drop the surface temperature to 1100°C decreases from about 16 min to 2.7 min ($R = 1.4 \times 10^{-3}$ to 8.4×10^{-3} sec^{-1}). The maximum stress and the time t^* when it occurs are plotted against R in Fig. 7. This plot indicates that the maximum stress is very sensitive to R only when R is small than about 0.005.

The integration of stress

$$\int_0^{\bar{\epsilon}} \bar{\sigma} d\bar{x}$$

is equivalent to the total transverse force in the shell. It is also the force required at the ends and by friction buildup to prevent overall contraction. This force obtained from graphical integration of the curves in Fig. 5, is shown in Fig. 8 as a function of R. The total force, like the stress at a particular location, increases, reaches a maximum, and then decreases. In a recent publication by Fröber and Oeters [14], the forces in a solidified shell are directly measured through an experimental setup. Some typical results shown in Fig. 9 are consistent with present predictions.

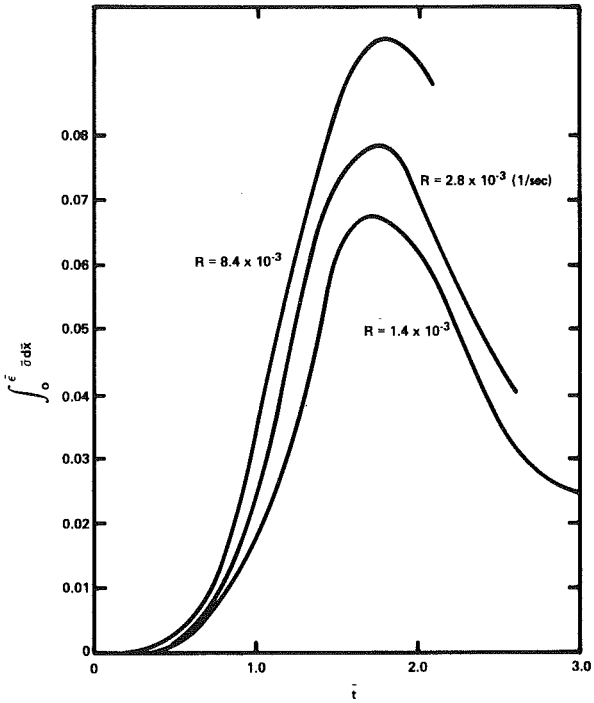

Fig. 8 Total force ($\int_0^{\bar{\epsilon}} \bar{\sigma} d\bar{x}$) versus time ($\bar{t}$)

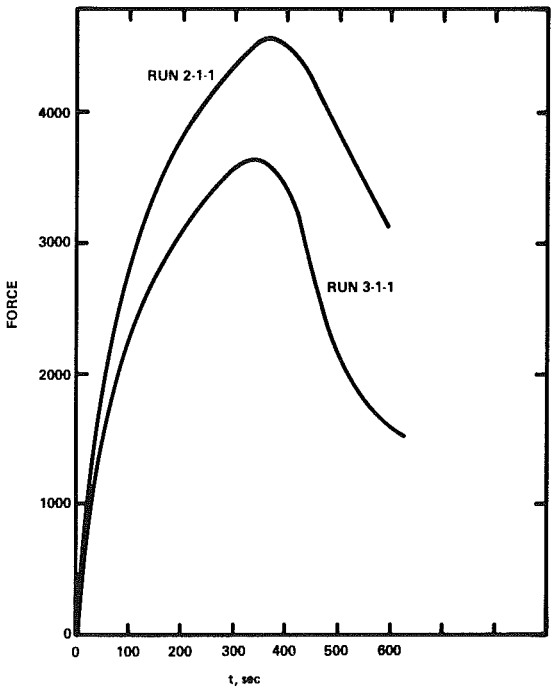

Fig. 9 Experimental measurement of forces in a solid shell

Concluding Remarks

The maximum transverse stress that can occur in the center of a flat face of a solidifying steel casting has been estimated by examining the case when the ferrostatic pressure and the mold-friction forces completely inhibit contraction. For normal cooling histories the maximum tensile stress occurs at the outer surface of the solidifying shell, next to the mold face. This stress first increases because of the effect of the thermal contraction coefficient, but later decreases because of inelastic (creep) effects. The maximum stress is, as expected, very sensitive to cooling rate. These results should be useful in interpreting the effect of cooling history on center-line cracking when accurate yield stresses at elevated temperatures becomes available.

References

1 Weiner, J. H., and Boley, B. A., "Elasto-Plastic Thermal Stresses in a Solidifying Body," *Journal of Mechanics and Physics of Solids*, Vol. 2, 1963, pp. 145-154.

2 Richmond, O., and Tien, R. H., "Theory of Thermal Stresses and Air-Gap Formation During the Early Stages of Solidification in a Rectangular

Mold," *Journal of Mechanics and Physics of Solids*, Vol. 19, 1971, pp. 273–284.

3 Jaumann, G., *Grundlagen der Bewegungslehra*, Leipzig, 1905.

4 Tammann, V. G., and Bandel, G., "Specific Heat and Specific Volume of Iron-Carbon Alloy," *Arch. Eisenhüttenwesen*, Vol. 7, 1934, p. 571.

5 Garber, R. I., and Kovalev, A. L., "Investigation of the Temperature Dependence of the Modulus of Elasticity of Iron," *Zavodsic Laboratory*, Vol. 24, 1958, p. 539.

6 Koster, W., "Elastic Modulus and Damping of Iron and Iron Alloys," *Arch. Eisenhüttenwesen*, Vol. 14, 1940, p. 271.

7 Hub, D. R., "Measurement of Velocity and Attenuation of Sound in Iron Up to the Melting Point," Paper No. 551 in the *Proceedings of the 4th International Congress on Acoustics*, Copenhagen, 1962.

8 Leibfried, G., and Ludwig, W., "Temperature Dependence of Elastic Constants of Alkali Halide Crystals," *Solid State Physics*, Vol. 12, 1961, p. 276.

9 Feltham, P., "The Plastic Flow of Iron and Plain Carbon Steels Above the A_s Point," *Proceedings of Roy. Soc.*, Vol. 66, 1952, pp. 865–85.

10 Eyring, H., "Activated Complex and the Absolute Rate of Reaction," *Journal Chem. Phys.*, Vol. 4, 1936, p. 283.

11 Eyring, H., and Ree, T., "Theory of Plasticity Involving the Virial Theorem," *Proceedings of the National Academy of Science*, Vol. 41, 1955, p. 118.

12 Tein, R. H., "A Modified Heat of Fusion for Use in the Mathematical Formulation of Solidification Process," *Trans. ASME*, Vol. 242, 1968, pp. 1289–1292.

13 Hildebrand, F. B., *Introduction to Numerical Analyses*, McGraw-Hill, New York 1956, p. 237.

14 Frober, J., and Oeters, F., "On the Mechanical Behavior of Steel During Solidification," *Arch. Eisenhüttenwesen*, Vol. 51, 1980, pp. 43–48.

Relaxation of Thick-Walled Cylinders and Spheres

N. S. Ottosen
Research Engineer,
Engineering Department,
Risø National Laboratory,
DK-4000 Roskilde,
Denmark

Using the nonlinear creep law proposed by Soderberg, closed-form solutions are derived for the relaxation of incompressible thick-walled spheres and cylinders in plane strain. These solutions involve series expressions which, however, converge very quickly. By simply ignoring these series expressions, extremely simple approximate solutions are obtained. Despite their simplicity these approximations possess an accuracy that is superior to approximations currently in use. Finally, several physical aspects related to the relaxation of cylinders and spheres are discussed.

Introduction

Creep problems are encountered in many situations, in particular when high temperatures are present. When the creep strains depend nonlinearly on stresses, the solution becomes complex and numerical solutions are most often necessary. This also applies to relaxation problems, where displacements are known in advance. Often, however, relaxation problems are somewhat simpler than the corresponding creep problems, as the constitutive conditions become differential equations in which all terms are known explicitly. This situation arises for incompressible cylinders and spheres.

However, only a few closed-form solutions are known for such thick-walled structures. For an arbitrary Poisson ratio, solutions have been obtained by Davis [1] for the linear viscoelastic cylinder, and by Wierzbicki [2] for the linear viscoplastic sphere, but apart from these solutions all other contributions seem to resort to numerical solutions. This applies, for instance, to the investigation of Davis [3] dealing with incompressible cylinders and to the work of Spence and Hult [4] treating incompressible spheres. To avoid the tedious numerical calculations, the latter two investigations also discuss several simple approximations to the considered problems.

The present paper deals with relaxation of thick-walled cylinders in plane strain and with thick-walled spheres. The material is considered incompressible and the creep strains are assumed to follow Soderberg's [5] creep law, which involves nonlinear stress dependency. From this basis, closed-form solutions are derived. Even though these solutions are quite easy to work with, extremely simple but very accurate approximate expressions are suggested and compared with the exact solutions. Moreover, the exact closed-form solutions are applied to discuss physical aspects related to relaxation problems.

Constitutive Equations

Assuming small strains and deformations, the total strains are composed of the elastic and the creep strains, i.e.,

$$\dot{\epsilon} = \dot{\epsilon}^e + \dot{\epsilon}^c \tag{1}$$

where a dot indicates the time rate. The elastic strains follow from Hooke's law. The creep strain rates are assumed to be of the usual associated von Mises type, i.e.,

$$\dot{\epsilon}^c_{ij} = \frac{3\dot{\epsilon}_e}{2\sigma_e} s_{ij} \tag{2}$$

where $\dot{\epsilon}_e = (2\dot{\epsilon}^c_{ij}\dot{\epsilon}^c_{ij}/3)^{1/2}$ and $\sigma_e = (3s_{ij}s_{ij}/2)^{1/2}$ are the effective creep strain rate and effective stress, respectively, whereas $s_{ij} = \sigma_{ij} - \delta_{ij}\sigma_{kk}/3$ is the deviatoric stress tensor. Usual tensor notation is applied.

Due to its simplicity we will adopt time hardening here and express the time dependence in terms of a power function. The stress dependence is frequently assumed to be of the Norton power law type. Here, however, we shall make use of the exponential form proposed by Soderberg [5], i.e.,

$$\dot{\epsilon}_e = mA(e^{B\sigma_e} - 1)t^{m-1} \tag{3}$$

where A, B, and m are parameters and t is the time. According to both Soderberg [5] and Popov [6], this expression provides close fits to experimental data. Moreover, for practical purposes, it gives almost identical results as the hyperbolic sine relation suggested, for instance, by Nadai [7]. Nadai and McVetty [8] and McVetty [9] found that the hyperbolic sine relation provides a better fit to experimental data than the power law, whereas Pickel et al. [10] found almost the same accuracy. Here, we could also make use of the hyperbolic sine relation, but the results are somewhat more complicated and will therefore not be given.

Thick-Walled Cylinder

Consider a thick-walled cylinder in plane strain with inner radius r_1 and outer radius r_2. The condition of plane strain

Contributed by the Applied Mechanics Division for publication in the JOURNAL OF APPLIED MECHANICS.
Discussion of this paper should be addressed to the Editorial Department, ASME, United Engineering Center, 345 East 47th Street, New York, N.Y. 10017, and will be accepted until two months after final publication of the paper itself in the JOURNAL OF APPLIED MECHANICS. Manuscript received by ASME Applied Mechanics Division, August, 1981; final revision, January, 1982.

provides $\dot{\epsilon}_z = 0$. Therefore, as the inner surface is given a specific fixed displacement, it follows from the assumption of material incompressibility that

$$\dot{\epsilon}_\theta = 0 \tag{4}$$

in familiar notation. Incompressibility implies that Poisson's ratio equals ½. Therefore, from $\epsilon_z = 0$ follows $\sigma_z = (\sigma_r + \sigma_\theta)/2$ which results in

$$\sigma_e = T\frac{\sqrt{3}}{2}(\sigma_\theta - \sigma_r) \tag{5}$$

where $T = 1$ or $T = -1$ holds, if the inner surface is expanded or contracted, respectively.

By the preceding observations we are left with only one constitutive equation of interest which, using equations (1)-(5), reads

$$\dot{\sigma}_e + mA\mathrm{E}(e^{B\sigma_e} - 1)t^{m-1} = 0 \tag{6}$$

where E is Young's modulus. This equation together with the equilibrium equation

$$r\frac{\partial \sigma_r}{\partial r} + \sigma_r - \sigma_\theta = 0 \tag{7}$$

constitute the governing equations of the problem.

The cylinder is loaded by a constant external pressure and the inner surface is given a fixed displacement, i.e., the boundary conditions are

$$r = r_1; \quad u = u_1 = \text{constant} \tag{8}$$

$$r = r_2; \quad \sigma_r = -p_2 = \text{constant} \tag{9}$$

Using the transformation $y = e^{-B\sigma_e}$, the solution of (6) follows straightforward. This solution involves an arbitrary function $f(r)$, which is determined so that for $t = 0$ the isothermal elastic solution follows. The result is

$$\sigma_e = -\frac{1}{B}ln\left(a + be^{-\frac{M}{r^2}}\right) \tag{10}$$

where the two time-dependent functions a and b are defined by

$$a(t) = 1 - b(t); \quad 0 \le a < 1$$

$$b(t) = e^{-Nt^m}; \quad 0 < b \le 1$$

and where the positive parameters M and N are defined by

$$M = T\frac{2}{\sqrt{3}}\mathrm{E}Bu_1r_1; \quad N = AB\mathrm{E}$$

Inserting (10) into (7) and integrating from r to r_2 gives

$$\sigma_r = \frac{2T}{B\sqrt{3}}\int_r^{r_2}\frac{ln\left(a + be^{-\frac{M}{x^2}}\right)}{x}dx - p_2 \tag{11}$$

where the boundary condition (9) has been used. Integration of this expression is performed after the numerator of the integrand has been expanded into a Taylor series. However, this expansion depends on the magnitude of the positive term $be^{-\frac{M}{x^2}}/a$, and it becomes convenient to define the time-dependent radius r_0 so that $be^{-\frac{M}{r_0^2}}/a = 1$, i.e.,

$$r_0 = \left(\frac{M}{ln\frac{b}{a}}\right)^{1/2}$$

This expression can be used only for $b/a > 1$, otherwise r_0 is defined to be infinitely large. Depending on the value of r_0 we are now in a position to determine the radial stress using (11).

If $r_2 \le r_0$ then

$$ln\left(a + be^{-\frac{M}{x^2}}\right) = lna - \sum_{n=1}^{\infty}\frac{1}{n}\left(-\frac{be^{-\frac{M}{x^2}}}{a}\right)^n$$

Equation (11) now becomes

$$\sigma_r = \frac{2T}{B\sqrt{3}}\left[lna\ ln\frac{r_2}{r} - \sum_{n=1}^{\infty}\frac{1}{n}\left(-\frac{b}{a}\right)^n\int_r^{r_2}e^{\frac{Mn}{x^2}}\frac{dx}{x}\right] - p_2$$

Using the transformation $z = Mn/x^2$ this expression yields

$$\sigma_r = \frac{T}{B\sqrt{3}}\left\{2\,lna\ ln\frac{r_2}{r} - \sum_{n=1}^{\infty}\frac{1}{n}\left(-\frac{b}{a}\right)^n\left[\mathrm{E}_1\left(\frac{M}{r_2^2}n\right) - \mathrm{E}_1\left(\frac{M}{r^2}n\right)\right]\right\} - p_2 \tag{12}$$

where Mn/r^2 is a positive quantity and the exponential integral is defined by

$$\mathrm{E}_1(z) = \int_z^{\infty}\frac{e^{-v}}{v}dv$$

and is extensively tabulated, for instance, by Abramovitz and Stegun [11].

Similarly, if $r_0 \le r$ then

$$ln\left(a + be - \frac{M}{x^2}\right) = lnb - \frac{M}{x^2} - \sum_{n=1}^{\infty}\frac{1}{n}\left(-\frac{a}{be^{-\frac{M}{x^2}}}\right)^n$$

Use of this expression in equation (11) and proceeding as in the foregoing yields

$$\sigma_r = \frac{T}{B\sqrt{3}}\left\{2lnb\ ln\frac{r_2}{r} + M\left(\frac{1}{r_2^2} - \frac{1}{r^2}\right) - \sum_{n=1}^{\infty}\frac{1}{n}\left(-\frac{a}{b}\right)^n\left[\mathrm{E}i\left(\frac{M}{r^2}n\right) - \mathrm{E}i\left(\frac{M}{r_2^2}n\right)\right]\right\} - p_2 \tag{13}$$

where the exponential integral is defined by

$$\mathrm{E}i(z) = \int_{-\infty}^{z}\frac{e^v}{v}dv$$

and is tabulated, for instance, by Abramowitz and Stegun [11]. The initial elastic solution follows from (13) with $a = 0$, $b = 1$ and therefore $r_0 = 0$.

Finally, if $r \le r_0 \le r_2$ then by completely analogous calculations we obtain

$$\sigma_r = \frac{T}{B\sqrt{3}}\left\{2lna\ ln\frac{r_0}{r} - \sum_{n=1}^{\infty}\frac{1}{n}\left(-\frac{b}{a}\right)^n\left[\mathrm{E}_1\left(\frac{M}{r_0^2}n\right)\right.\right.$$

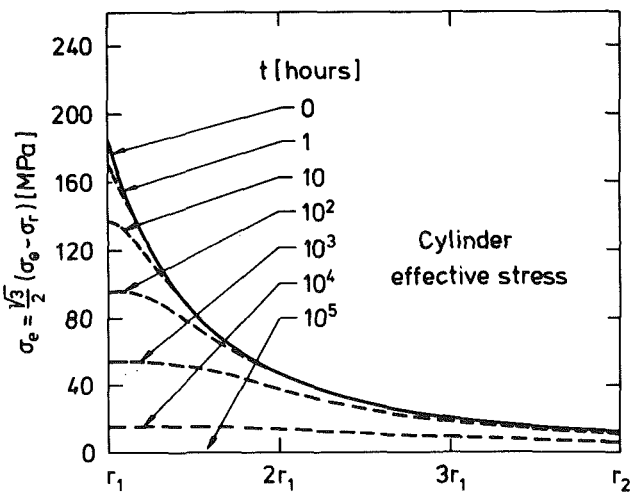

Fig. 1 Development with time of effective stress in cylinder

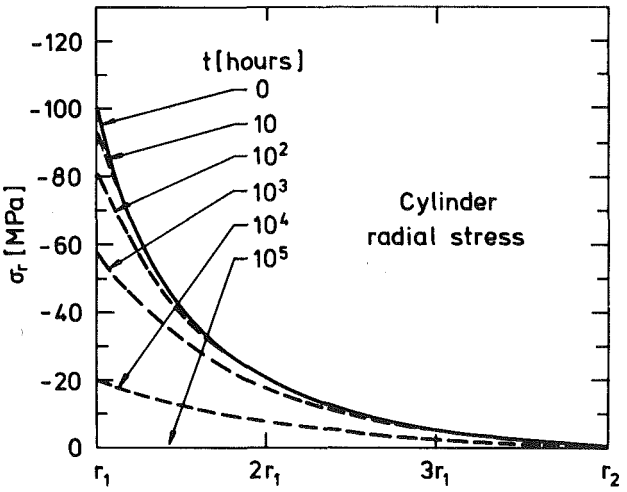

Fig. 2 Development with time of radial stress in cylinder

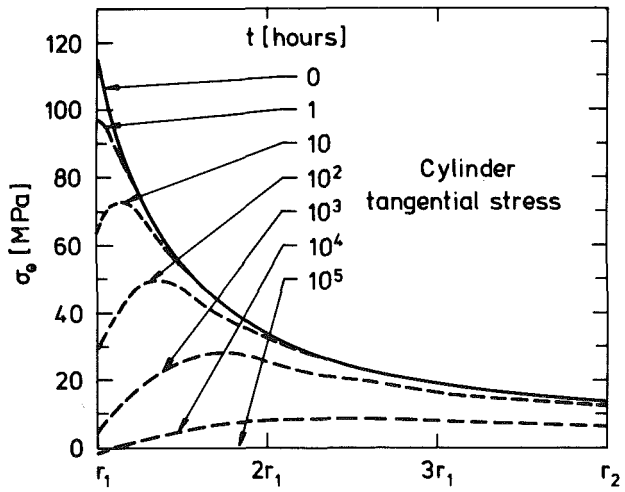

Fig. 3 Development with time of tangential stress in cylinder

$$-E_1\left(\frac{M}{r^2}n\right)\Big]$$

$$+2lnb\,ln\frac{r_2}{r_0}+M\left(\frac{1}{r_2^2}-\frac{1}{r_0^2}\right)$$

$$-\sum_{n=1}^{\infty}\frac{1}{n}\left(-\frac{a}{b}\right)^n\left[\mathrm{Ei}\left(\frac{M}{r_0^2}n\right)-\mathrm{Ei}\left(\frac{M}{r_2^2}n\right)\right]\Big\}-p_2 \qquad (14)$$

The closed-form solution for σ_r given by either (12), (13), or (14) is very easy to work with noting that only a, b, and r_0 depend on time. Moreover, the series present in the solution converge very quickly. In addition to that, these terms are small compared to the other terms. This means that in preliminary calculations the radial stress can be determined with close accuracy by completely ignoring the series expressions and considering just the first term in the series will raise the accuracy to a very high level. These important aspects are demonstrated in the section on applications.

Thick-Walled Sphere

Consider now a thick-walled sphere of incompressible material and with inner radius r_1 and outer radius r_2. The boundary conditions are again given by (8) and (9). The calculations are completely similar to those of the cylinder problem and we shall therefore merely state the final results.

Define the positive quantity Q by

$$Q=T2\mathrm{E}Bu_1r_1^2$$

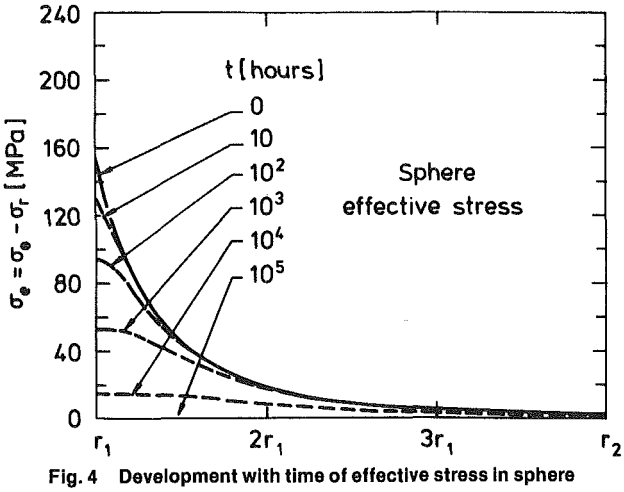

Fig. 4 Development with time of effective stress in sphere

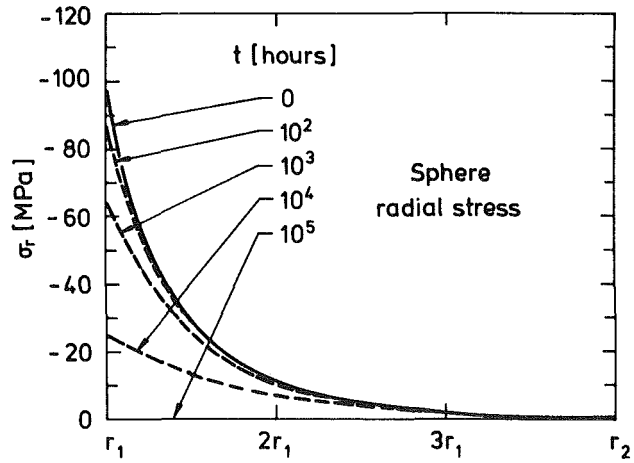

Fig. 5 Development with time of radial stress in sphere

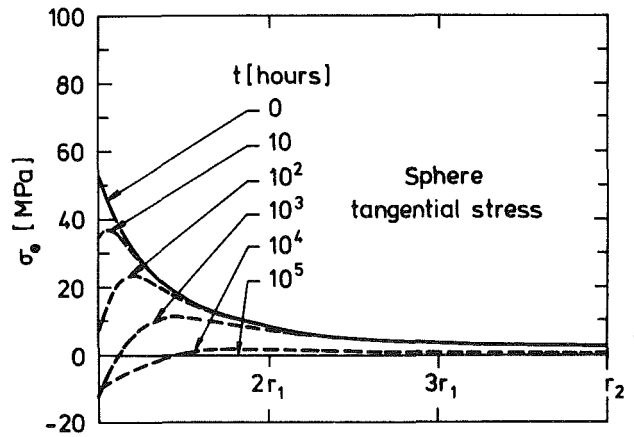

Fig. 6 Development with time of tangential stress in sphere

where $T=1$ or $T=-1$ if the inner surface is expanded or contracted, respectively. The effective stress is then given by

$$\sigma_e=T(\sigma_\theta-\sigma_r)=-\frac{1}{B}ln\left(a+be^{-\frac{Q}{r^3}}\right) \qquad (15)$$

Define the time-dependent radius r_* so that $be^{-\frac{2}{r_*^3}}/a=1$, i.e.,

$$r_*=\left(\frac{Q}{ln\frac{b}{a}}\right)^{1/3}$$

This expression applied only so long as $b/a>1$; otherwise r_* is

defined to be infinitely large. Depending on the value of r_* the following expressions hold for the radial stress.

If $r_2 \le r_*$ then

$$\sigma_r = \frac{2T}{3B}\left\{3lna\ ln\frac{r_2}{r} - \sum_{n=1}^{\infty}\frac{1}{n}\left(-\frac{b}{a}\right)^n\left[\mathrm{E_1}\left(\frac{Q}{r_2^3}n\right) - \mathrm{E_1}\left(\frac{Q}{r^3}n\right)\right]\right\} - p_2 \quad (16)$$

If $r_* \le r$ then

$$\sigma_r = \frac{2T}{3B}\left\{3lnb\ ln\frac{r_2}{r} + Q\left(\frac{1}{r_2^3} - \frac{1}{r^3}\right) - \sum_{n=1}^{\infty}\frac{1}{n}\left(-\frac{a}{b}\right)^n\left[\mathrm{Ei}\left(\frac{Q}{r^3}n\right) - \mathrm{Ei}\left(\frac{Q}{r_2^3}n\right)\right]\right\} - p_2 \quad (17)$$

The initial elastic solution follows from this equation with $a=0$, $b=1$, and therefore $r_*=0$.

If $r \le r_* \le r_2$ then

$$\sigma_r = \frac{2T}{3B}\left\{3lna\ ln\frac{r_*}{r} - \sum_{n=1}^{\infty}\frac{1}{n}\left(-\frac{b}{a}\right)^n\left[\mathrm{E_1}\left(\frac{Q}{r_*^3}n\right) - \mathrm{E_1}\left(\frac{Q}{r^3}n\right)\right] + 3lnb\ ln\frac{r_2}{r_*} + Q\left(\frac{1}{r_2^3} - \frac{1}{r_*^3}\right) - \sum_{n=1}^{\infty}\frac{1}{n}\left(-\frac{a}{b}\right)^n\left[\mathrm{Ei}\left(\frac{Q}{r_*^3}n\right) - \mathrm{Ei}\left(\frac{Q}{r_2^3}n\right)\right]\right\} - p_2 \quad (18)$$

Applications and Approximations

Consider an austenitic stainless steel at a temperature of around 600 deg C. In the secondary creep range, where $m=1$ applies, typical parameters in the creep law, equation (3), might be $A = 7 \cdot 10^{-9}$ [1/h] and $B = 5.4 \cdot 10^{-2}$[1/MPa]. For a stress range between 50–150 MPa, this B-value corresponds to an exponent of around five in Norton's creep law. Young's modulus is assumed to be $E = 1.5 \cdot 10^5$ MPa.

The first applications concern a thick-walled cylinder and sphere both with $r_1 = 0.01$ m and $r_2 = 0.04$ m, and with external pressure $p_2 = 0$. The initial internal pressure in both cases is 100 MPa. Assuming a rigid mandrel this pressure corresponds to the shrink-fit pressure.

Figures 1, 2, and 3 show the development with time of the effective, radial, and tangential stresses, respectively, for the cylinder. Figures 4, 5, and 6 provide the corresponding results for the sphere.

It appears that the stresses decrease considerably with time especially immediately after the initial loading and adjacent to the inner surface in particular. As the driving force in the creep process is the effective stress, the decrease of the stresses as well as the zone affected by relaxation is smaller at a given time for the sphere than it is for the cylinder due to the more favorable structural behavior of the sphere.

In addition to the decrease of stresses, a considerable stress redistribution takes place. This is especially pronounced for the tangential stress, cf., Figs. 3 and 6. The stress redistribution is a result of creep being a nonlinear function of effective stress. To illustrate this effect, consider a cylinder of incompressible viscoelastic material, where creep depends linearly on stress. This case arises from equation (3), when B is very small resulting in $\dot{\epsilon}_e \simeq mAB\sigma_e t^{m-1}$. Within the same approximation $e^{-M/r^2} \simeq 1 - M/r^2$ applies, which, by means of (10), yields $\sigma_e \simeq -ln(1 - bM/r^2)/B$. As $0 < b \le 1$ holds, this expression can be approximated by $\sigma_e \simeq \sigma_{e,\mathrm{elast.}}\, b(t)$ where $b(t)$ is equal to e^{-Nt^m} as before. For secondary creep, where m equals unity, the equation for σ_e corresponds to uniaxial relaxation of a Maxwell material. Now, using this expression in the equilibrium condition given by (7), we derive $\sigma_r \simeq \sigma_{r,\mathrm{elast.}}\ b(t)$ and similarly for the tangential stress. Therefore, when creep depends linearly on stress, the stress distribution itself is similar to that of an elastic material,

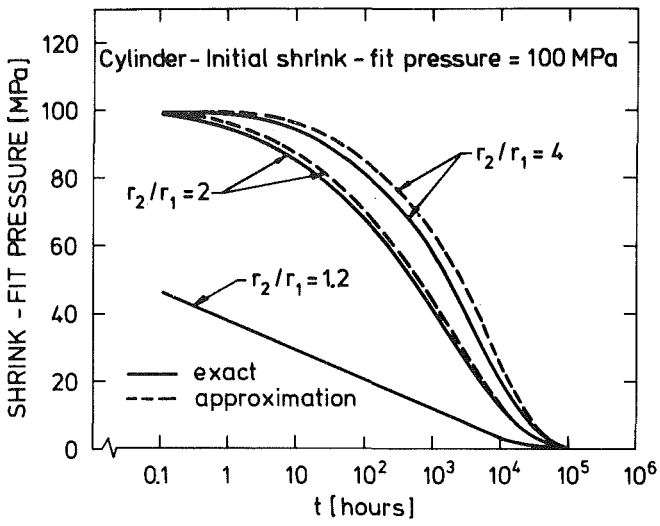

Fig. 7 Development with time of shrink-fit pressure in different cylinders

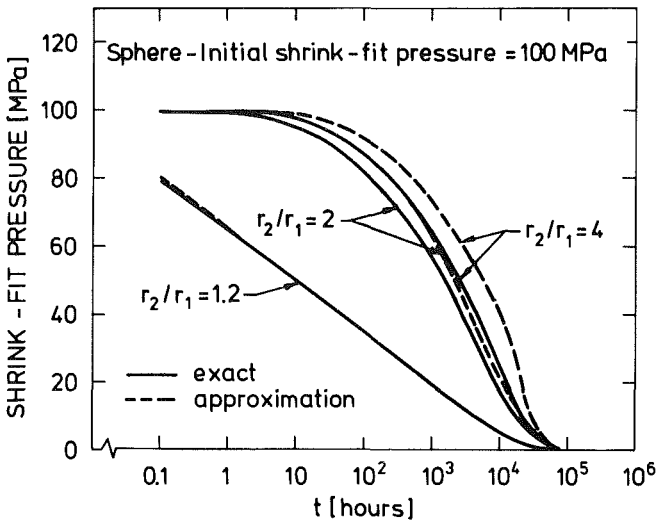

Fig. 8 Development with time of shrink-fit pressure in different spheres

whereas the stresses decay as if uniaxial relaxation were involved. These conclusions were originally derived by Davis [1].

Let us now consider the item of most practical interest, namely the development with time of the shrink-fit pressure p at the inner surface. For thin-walled vessels very simple expressions can be derived directly from the equilibrium conditions resulting in $\sigma_r = -p = -2T/\sqrt{3}\sigma_e h/r - p_2$ for the cylinder and $\sigma_r = -p = -2T\sigma_e h/r - p_2$ for the sphere. However, when the wall thickness increases, the problem becomes much more complex.

Figure 7 gives the development with time of the shrink-fit pressure for three different cylinders with $r_2/r_1 = 1.2$, 2, and 4. The material properties are identical to those previously used and the initial shrink-fit pressure is again 100 MPa. Figure 8 provides similar results for the sphere.

It appears that the wall thickness has a considerable influence on the results and in accordance with the previous discussion, this influence is a result of creep being a nonlinear function of stress. Physically, as the inner region is most subject to creep and as the outer region tends to restrain these creep deformations, it is obvious that the thicker the vessel the slower the loss of shrink-fit pressure. Similarly, the shrink-fit pressure decreases more slowly for the sphere than for the cylinder.

Different attempts to approximate the development with time of the shrink-fit pressure have been proposed in the past. When creep depends linearly on stress, the previous discussion shows that this development is identical to that of uniaxial relaxation. In [3] Davis proposed to also apply this concept to nonlinear creep. The approximation leads to the conclusion that for a given initial shrink-fit pressure, the development with time should be identical for all wall thicknesses. Comparisons with Figs. 7 and 8 discourage such an approach.

More recently, Spence and Hult [4] investigated the approximations currently in use, namely the Kachanov approximation and the reference stress concept and compared them with the exact, numerical solution for relaxation of incompressible spheres consisting of materials in which creep follows Norton's law. Here, we make use of the extremely simple formulas, which follow if we ignore all series terms present in equations (12), (13), and (14) for the cylinder problem and present in equations (16), (17), and (18) for the sphere problem. The resulting approximations are shown in Figs. 7 and 8. It appears that the predictions of the approximations become better the more thin-walled the vessel is. Compared with the approximations currently in use, cf., Spence and Hult [4], the approximations suggested here provide a much closer and even simpler estimate to the exact solution.

Apart from these advantages, the approximations shown here also demonstrate that the exact solutions are very easy to work with as the series converge very quickly. Indeed, if only the first term in the series is considered, the accuracy obtained is close to the drawing accuracy. The exact solution in all the figures shown is that obtained using the first four terms in the series.

Conclusions

Considering incompressible material behavior and assuming that creep is determined by the exponential expression proposed by Soderberg [5], closed-form solutions for the relaxation of thick-walled cylinders and spheres have been derived. These solutions contain terms in the form of series expressions. Approximative formulas that simply ignore these series have been proposed and have been demonstrated to be in close agreement with the exact solutions.

Apart from providing extremely simple and even more accurate predictions than approximations currently in use, the effectiveness of the proposed approximations also demonstrate that only a few terms in the series present in the closed-form solution have to be considered to obtain a solution close to the exact one. In addition, several physical aspects related to the relaxation of cylinders and spheres have been discussed.

Acknowledgment

Discussions with Dr. H. Schmidt, Risø National Laboratory, Denmark, are greatly appreciated.

References

1 Davis, E. A., "Relaxation of Stress in a Heat-Exchanger Tube of Ideal Material," *Transactions of the ASME*, Vol. 74, 1952, pp. 381–385.

2 Wierzbicki, T., "A Thick-Walled Elasto-Visco-Plastic Spherical Container Under Stress and Displacement Boundary Value Condition," *Archiwum Mechaniki Stosowany*, Vol. 15, 1963, pp. 297–308.

3 Davis, E. A., "Relaxation of a Cylinder on a Rigid Shaft," ASME JOURNAL OF APPLIED MECHANICS, Vol. 27, 1960, pp. 41–44.

4 Spence, J., and Hult, J., "Simple Approximations for Creep Relaxation," *International Journal of Mechanical Sciences*, Vol. 15, 1973, pp. 741–755.

5 Soderberg, C. R., "The Interpretation of Creep Tests for Machine Design," *Transactions of the ASME*, Vol. 58, 1936, pp. 733–743.

6 Popov, E. P., "Correlation of Tension Creep Tests with Relaxation Tests," *Transactions of the ASME*, Vol. 69, 1947, pp. A135–A142.

7 Nadai, A., "The Influence of Time Upon Creep. The Hyperbolic Sine Creep Law," in: *Stephen Timoshenko Anniversary Volume*, The Macmillan Co., New York, 1938, pp. 155–170.

8 Nadai, A., and McVetty, P. G., "Hyperbolic Sine Chart for Estimating Working Stresses of Alloys at Elevated Temperatures," *American Society for Testing and Materials, Proceedings*, Vol. 43, 1943, pp. 735–745.

9 McVetty, P. G., "Creep of Metals at Elevated Temperatures–the Hyperbolic-Sine Relation Between Stress and Creep Rate," *Transactions of the ASME*, Vol. 65, 1943, pp. 761–767.

10 Pickel, T. W., Sidebottom, O. M., and Boresi, A. P., "Evaluation of Creep Laws and Flow Criteria for Two Metals Subjected to Stepped Load and Temperature Changes," *Experimental Mechanics*, Vol. 11, 1971, pp. 202–209.

11 Abramowitz, M., and Stegun, I. A., *Handbook of Mathematical Functions*, Dover, New York, 1968.

Transient Response of a Fluid-Saturated Poroelastic Layer Subjected to a Sudden Fluid Pressure Rise

M. Kurashige
Assistant Professor,
Department of Mechanical Engineering II,
Faculty of Engineering,
Tohoku University,
Sendai 980, Japan

The transient response of a fluid-saturated poroelastic layer resting on a very porous rigid foundation and subjected to a sudden fluid pressure rise on its upper surface is analyzed on the basis of Biot's theory of poroelasticity. Compaction of the layer and fluid outflux from its bottom surface are calculated for five typical poroelastic materials: alundum and Ohio sandstone saturated with water, compact bone, and Albany felt and polyurethane foam filled with silicone fluid. For each of these materials, the numerical results are compared with those estimated by the "incompressible model" as well as the "rigid skeleton model" in order to examine the validity of these models.

1 Introduction

There are many mathematical formulations describing the mechanical behaviors of a fluid-saturated poroelastic body, taking into account various aspects of its behavior. Among these formulations, Biot's linear one [1-3] is one of the simplest theories and it suffices to describe various phenomena in various real situations.

Regarding experimental data on several material constants appearing in the Biot theory, Fatt [4] reported in 1959 his experimental results for Boise sandstone saturated with kerosene. After a long absence of reports on the material constants, some reports [5-7] were published for poroelastic materials such as bone, sandstone and sinter containing water, and foam rubber and felt filled with silicone fluid.

On the other hand, there are also a number of papers dealing with mathematical analysis of the mechanical response of a fluid-saturated poroelastic body. Many of these papers, however, do not base their numerical calculations on the experimental data of material constants but on assumed values. Furthermore, many of them base their analysis on a simplified model in which both the matrix material of the poroelastic body and the contained pore fluid are assumed to be incompressible so that the volume change of the body is equal to the amount of the pore fluid squeezed out. (We refer to this simplified model as the "incompressible model.") This incompressible model is supposed to be suitable for describing the consolidation of soil.

In the present paper, we consider the transient response of a fluid-saturated poroelastic layer resting on a very porous rigid foundation and subjected to a sudden fluid pressure rise on its upper surface. Because of the reasons mentioned in the first paragraph, we adopt the Biot theory. This theory contains the "incompressible model" as well as the "rigid skeleton model" as special cases. (The latter model has been used to examine the flow through porous media in various fields [8].) Our numerical calculations are based on the experimental data for five selected typical kinds of poroelastic materials.

Our main objectives are as follows: (1) to make clear qualitative distinctions, if any, in the transient response of the layer between the five typical poroelastic materials; (2) to determine which of the five allows us to estimate the compaction (consolidation) of the layer and the outflux of the pore fluid by the incompressible model; and (3) to make clear whether or not it is appropriate for each of the five to estimate the fluid outflux by the rigid skelton model.

It should be added that another objective at the outset of this research was to explain by the Biot theory of poroelasticity the decrease in the fluid flux with the progress of compaction (consolidation) of a reverse osmosis membrane when sea water is desalted by the reverse osmosis method [9]. However, this attempt was not successful. We conjecture that we should take into account the finite deformation (compaction) of the membrane and/or its viscoelastic nature.

2 Basic Equations

Let us begin by summarizing Biot's linear theory of poroelasticity which takes into account the compressibility of both the matrix material and the contained fluid. We shall refer to this theory as "Biot's full model."

Equilibrium equations and modified Darcy's law are, in Cartesian tensor notation,

Contributed by the Applied Mechanics Division for publication in the JOURNAL OF APPLIED MECHANICS.
Discussion on this paper should be addressed to the Editorial Department, ASME, United Engineering Center, 345 East 47th Street, New York, N.Y. 10017, and will be accepted until two months after final publication of the paper itself in the JOURNAL OF APPLIED MECHANICS. Manuscript received by ASME Applied Mechanics Division, July, 1981; final revision, February, 1982.

$$(\sigma_{ij}+\sigma\delta_{ij})_{,j}=0, \tag{1}$$

$$\sigma_{,i}=b(\dot{U}_i-\dot{u}_i), \tag{2}$$

where σ_{ij} and $\sigma\delta_{ij}$ are the solid and fluid partial stress tensors, respectively, and u_i and U_i the solid and fluid displacement vectors. Flow resistance coefficient b in equation (2) is related to permeability k and fluid kinematic viscosity μ by

$$b=\mu\beta^2/k, \tag{3}$$

with β denoting the porosity. The following shows relation between σ and pore pressure p:

$$\sigma=-\beta p. \tag{4}$$

Solid strain tensor e_{ij}, solid dilatàtion e, and fluid dilatation ϵ are expressed in terms of u_i and U_i as follows:

$$e_{ij}=\frac{1}{2}(u_{i,j}+u_{j,i}), \quad e=u_{i,i}, \quad \epsilon=U_{i,i}. \tag{5}$$

Constitutive equations are given by

$$\sigma_{ij}=2Ne_{ij}+(Ae+Q\epsilon)\delta_{ij}, \ \sigma=Qe+R\epsilon, \tag{6}$$

where N, A, Q, and R are the elastic constants. The first one is the shear modulus and the other three are expressed in terms of measurable parameters as follows [10]:

$$A=\{\gamma/\kappa+\beta^2+(1-2\beta)(1-\delta/\kappa)\}/(\gamma+\delta-\delta^2/\kappa)-(2/3)N,$$

$$Q=\beta(1-\beta-\delta/\kappa)/(\gamma+\delta-\delta^2/\kappa), \quad R=\beta^2/(\gamma+\delta-\delta^2/\kappa), \tag{7}$$

where κ and δ are the so-called "jacketed" and "unjacketed" compressibility coefficients, respectively. Parameter γ is a coefficient of fluid content and is given by

$$\gamma=\beta(c-\delta) \tag{8}$$

with c being the fluid compressibility.

3 Problem Formulation and Results of Analysis

A fluid-saturated poroelastic layer of an infinite extent and having thickness h is laid on a porous rigid foundation which has very large permeability compared with that of the layer. Fluid pressure is suddenly applied on the upper surface of the layer and thereafter varies according to time-dependent function $\pi(t)$.

If we take the x-coordinate downward and its origin on the upper layer surface, it is clear that

$$u_1=u(x,t), \quad U_1=U(x,t), \tag{9}$$

and that all other displacement components vanish.

Table 1 Initial and final values of layer compaction and fluid outflux

	Biot's Full Model	Rigid Skelton Model	Incompressible Model
u(0,0)	α_3 for $\nu\to\infty$	0	0
	0 for finite ν		
$u(0,\infty)$	$\alpha_3+\alpha_2(\alpha_2-\beta/2)$	0	$\beta^2/2$
V(1,0)	∞ for $\nu\to\infty$	0	∞ for $\nu\to\infty$
	0 for finite ν		0 for finite ν
$V(1,\infty)$	β	β	β

Since the fluid-saturated poroelastic layer is completely at rest before the fluid pressure is applied, the initial conditions are

$$u=U=0 \quad \text{at} \quad t=0. \tag{10}$$

From the condition of a sudden fluid pressure rise on the upper layer surface follow

$$\sigma_x+\sigma=-\pi(t), \quad p=\pi(t) \quad \text{at} \quad x=0. \tag{11}$$

Assuming for simplicity's sake that the layer rests on the bed that has very large permeability and very large rigidity compared with those of the layer, we can write the boundary conditions on the bottom layer surface as follows:

$$u=0, \quad p=0 \quad \text{at} \quad x=h. \tag{12}$$

In order to solve the preceding one-dimensional consolidation problem, we have introduced the following nondimensional quantities and material parameters:

$$(\bar{\sigma}_x,\bar{\sigma},\bar{p},\bar{\pi})=(\sigma_x,\sigma,p,\pi)/p_0,$$

$$(\bar{u},\bar{U})=(u,U)/(p_0h/K), \tag{13}$$

$$\bar{x}=x/h, \quad \bar{t}=t/(bh^2/K),$$

$$\alpha_1=(P+Q)/H, \quad \alpha_2=(Q+R)/H, \quad \alpha_3=K/H, \tag{14}$$

where $P=A+2N$, $H=P+2Q+R$, and $K=(PR-Q^2)/H$. In the first and second equations of (13), p_0 stands for the reference pressure. For simplicity's sake, the bars on the nondimensional quantities are omitted in the following.

In the course of the analysis, the applied fluid pressure has been specified to have the form

$$\pi(t)=1-\exp(-\nu t), \tag{15}$$

with ν being the parameter of the pressure rise rate. The analysis is very easy. We shall present only the results for the compaction, $u(0,t)$, of the layer and the fluid outflux, $V(1,t)=\dot{U}(1,t)$:

$$u(0,t)=\{\alpha_3-\alpha_2(2\alpha_2-\beta)(\cos\sqrt{\nu}-1)/(\sqrt{\nu}\sin\sqrt{\nu})\}(1-e^{-\nu t})$$

$$+2\alpha_2(2\alpha_2-\beta)\sum_{n=1}^{\infty}\nu/\{(n\pi)^2\{\nu-(n\pi)^2\}\}\times$$

$$\times\{1-(-1)^n\}\{1-e^{-(n\pi)^2 t}\}, \tag{16}$$

$$V(1,t)=\beta-(\sqrt{\nu}/\sin\sqrt{\nu})\{\alpha_2\cos\nu-(\nu_2-\beta)\}e^{-\nu t}$$

$$+2\sum_{n=1}^{\infty}(-1)^n\nu/\{\nu-(n\pi)^2\}\{\alpha_2(-1)^n$$

$$-(\alpha_2-\beta)\}e^{-(n\pi)^2 t}. \tag{17}$$

4 Rigid Skeleton and Incompressible Models

For the layer whose porous skeleton has very large rigidity, we may estimate the fluid flow through the layer by the rigid skeleton model. This model is a limiting case of Biot's full model. For the rigid skeleton, it follows from their definitions that

$$N\to\infty, \quad \kappa\to 0, \quad \delta\to 0, \quad \gamma\to\beta c. \tag{18}$$

Table 2 Material constants

	N (Pa)	A (Pa)	Q (Pa)	R (Pa)	β	b(N·s/m^4)
Alundum/Water	2.5E10	1.5E10	5.7E08	6.3E08	0.32	3.7E07
Ohio Sandstone/Water	6.8E09	6.7E09	9.5E08	3.3E08	0.19	6.6E09
Compact Bone	6.2E09	2.2E10	4.4E09	1.7E09	0.14	2.7E13
Albany Felt/Silicon Fluid	5.3E05	2.4E06	6.3E06	2.1E07	0.70	6.5E10
Polyurethane Foam/Silicon Fluid	3.1E03	3.2E03	9.4E04	8.7E06	0.93	4.4E07
Water: c = 5.1E-10 (Pa^{-1})		Silicone Fluid: c = 1.0E-09 (Pa^{-1})				

In these limits, we find

$$\alpha_1 \to 1, \quad \alpha_2 \to 0, \quad \alpha_3 \to 0. \tag{19}$$

On the other hand, both the matrix material of porous body and the contained pore fluid are often assumed to be incompressible so that the volume change of the body is equal to the amount of the pore fluid squeezed out. This is the case for soil. This incompressible model is also obtained as another limiting case of Biot's full model. For the incompressible matrix material and the incompressible pore fluid, it follows from their definitions that

$$\delta \to 0, \quad \gamma \to 0. \tag{20}$$

Jacketed compressibility κ remains finite. Thus, we obtain

$$\alpha_1 \to 1-\beta, \quad \alpha_2 \to \beta, \quad \alpha_3 \to 0, \tag{21}$$

for the incompressible model.

The layer compaction and the fluid outflux can be evaluated by equations (16) and (17). Especially, those at $t=0+$ and at $t\to\infty$ can be expressed in closed forms by recourse to the mathematical formulas in [11, p. 36]. Those are shown in Table 1 for Biot's full model as well as for the rigid skeleton and incompressible models. The latter two may serve the purpose of comparison.

For $\nu\to\infty$, that is, for the step pressure load, $u(0,0)=\alpha_3$. This means that the layer has "instantaneous elasticity" and presents a striking contrast to the incompressible model for which $u(0,0)=0$ even for $\nu\to\infty$. That is, not to mention the rigid skeleton model, the incompressible model is not appropriate to estimate the compaction of the layer immediately after the application of the step pressure, unless the layer material has a negligible value of α_3.

The layer compaction in the steady state is given by $u(0,\infty)=\alpha_3+\alpha_2(\alpha_2-\beta/2)$, which reduces to $u(0,\infty)=\beta^2/2$ for the incompressible case.

For $\nu\to\infty$, $V(1,0)\to\infty$ for both Biot's full model and the incompressible model, while $V(1,0)=0$ for the rigid skeleton model. This means that the deformation of the skeleton due to instantaneous elasticity causes a very large fluid outflux. This phenomenon will be discussed again in terms of the pore fluid pressure gradient in the next section.

The fluid outflux in the steady state is the same for all the models, that is, $V(1,\infty)=\beta$.

5 Numerical Examples and Discussion

To cast further light on the transient response of the layer, we carried out some numerical computations for the five typical kinds of fluid-saturated poroelastic materials; alundum and Ohio sandstone saturated with water, compact bone, and polyurethane foam and Albany felt filled with silicone fluid. For these five materials, we summarized the

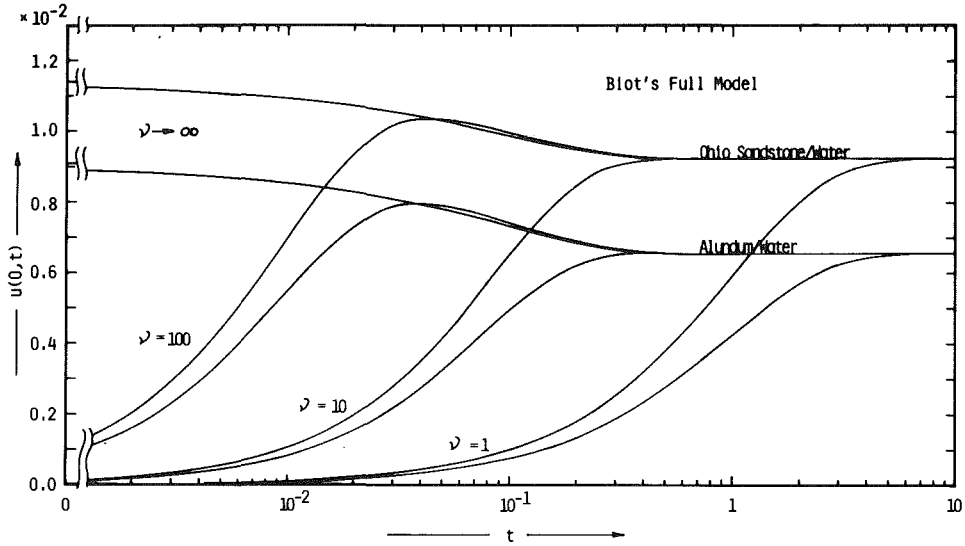

Fig. 1 Compaction history for Ohio sandstone and alundum layers containing water

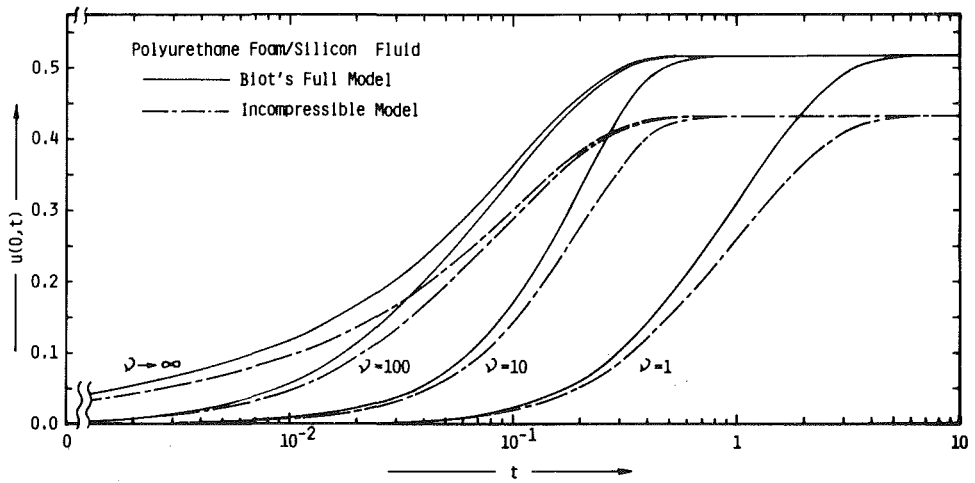

Fig. 2 Compaction history for polyurethane foam layer containing silicone fluid

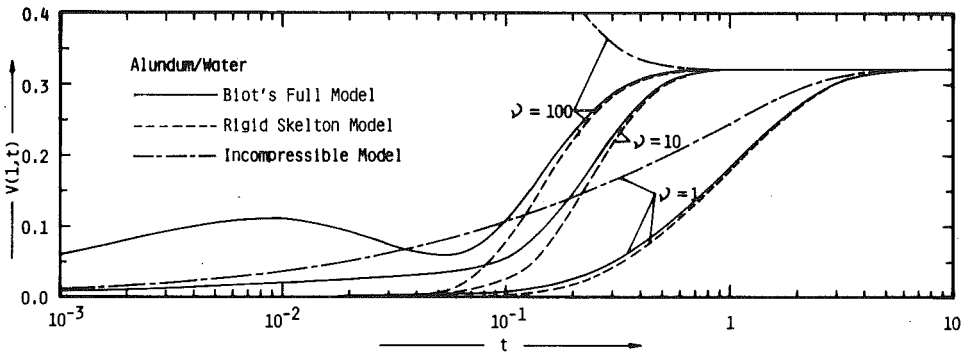

Fig. 3 Outflux history for water from alundum layer

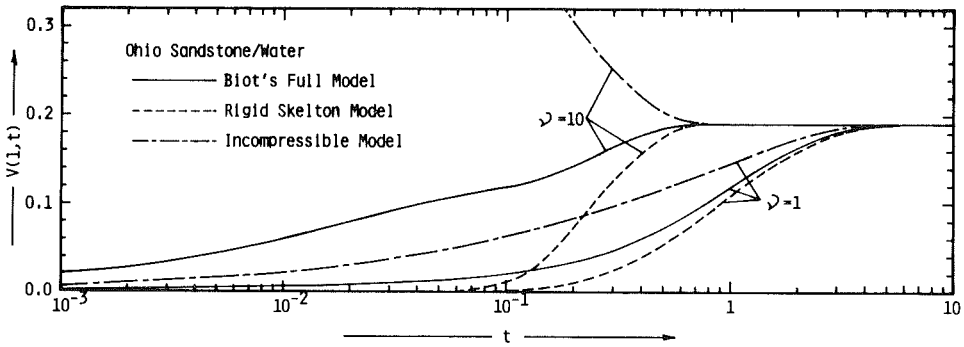

Fig. 4 Outflux history for water from Ohio sandstone layer

values of material constants, N, A, Q, R, β, b in Table 2. Some of these values were computed from those of other material constants. Units were reduced to SI units, when necessary.

The values of b in the last column of Table 2 are not necessary in computing the layer compaction and fluid outflux in the nondimensional form, but they are tabulated for the convenience of calculating real time from nondimensionalized time through the last equation of (13).

In Figs. 1–6, the solid curves correspond to Biot's full model, the chain curves to the incompressible model, and the dashed ones to the rigid skeleton model.

5.1 Compaction of the Layers. Figure 1 shows the compaction histories of the alundum/water and Ohio sandstone/water layers subjected to fluid pressure. For the larger ν, the compaction increases up to its peak and then goes down asymptotically to its steady state value $\alpha_3 + \alpha_2(\alpha_2 - \beta/2)$ (Refer to Table 1). Especially for the step pressure rise ($\nu \to \infty$), compaction happens instantaneously. That is, both the layers present a distinct "instantaneous elasticity." This instantaneous compaction is significantly larger than that in the steady state.

No curves of the estimates by the incompressible model are depicted in Fig. 1, because there is too much difference from those of Biot's full one.

Although not depicted for the sake of space saving, the compact bone layer also presents distinct instantaneous elasticity, but its instantaneous compaction is a little smaller than that in the steady state. The whole aspect of the compaction variation is similar to that of applied pressure for all ν. The estimates of the layer compaction by the incompressible model are far from being a good approximation.

The instantaneous compactions of the Albany felt and polyurethane foam layers containing silicone fluid are calculated at $u(0,0+) = 0.024$ and 0.00092 ($\nu \to \infty$), respectively. Therefore, their instantaneous elasticity is negligible. For the larger ν (including the case of $\nu \to \infty$), the response of both layers is delayed compared with the applied pressure rise. This is shown in Fig. 2 for the polyurethane foam layer. This figure also shows that the incompressible model gives a rough estimate of the compaction, although there is considerable discrepancy in the steady state compaction. This is the case also for the Albany felt layer.

5.2 Outflux From the Layers. Regarding the fluid outflux from the layers, its estimates by Biot's full model are compared with those by the incompressible model as well as by the rigid skeleton one in Figs. 3–5. It follows from the bottom row of Table 1 that the steady outfluxes estimated by the latter two models are the same as that calculated by the former one.

The chain curves in Fig. 3 are far from the solid curves for $\nu = 1$ as well as for $\nu = 100$, so that the incompressible model is useless to estimate the outflux from the alundum layer. However, the rigid skeleton model gives fairly good approximations except for $\nu = 100$ and for $t < 0.1$.

For the Ohio sandstone layer, neither of the simplified models yields good approximations, especially for the rapid pressure rise, as seen in Fig. 4.

Figure 5 shows that, in contrast with the rigid skeleton model being useless, the incompressible model gives very good approximation for the fluid outflux obtained by Biot's full model for the compact bone. This holds true also for the Albany felt and polyurethane foam. This approximation is good for all ν and from the outset of fluid pressure loading to the steady state.

5.3 Pore Pressure Distribution. In Figs. 4 and 5, the dashed curves are far from the solid curves except in the steady state. Especially for the compact bone and for $\nu = 100$ (Fig. 5), the rigid skeleton model indicates almost zero outflux in the early stages, but Biot's full model predicts such a large outflux that the curve extends out of the diagram in Fig. 5. Figure 6 is devoted to an explanation of this essential discrepancy between these two models.

Figure 6 designates the spatial distribution of pore pressure $p(x,t)$ for the various times for the compact bone. The left half is by Biot's full model and the right one by the rigid

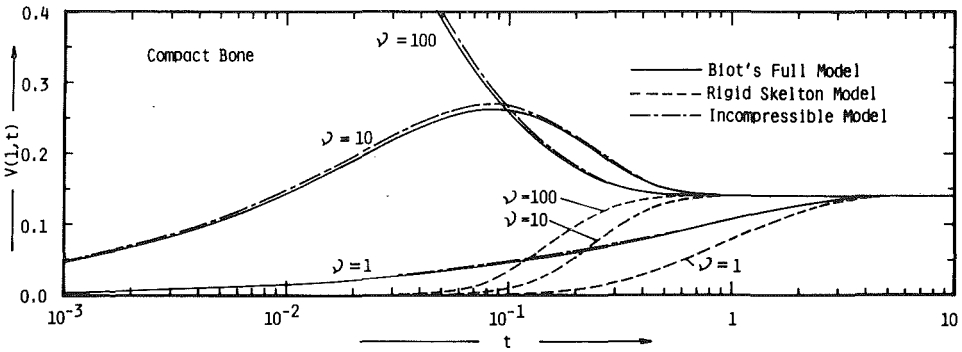

Fig. 5 Outflux history for pore fluid from compact bone layer

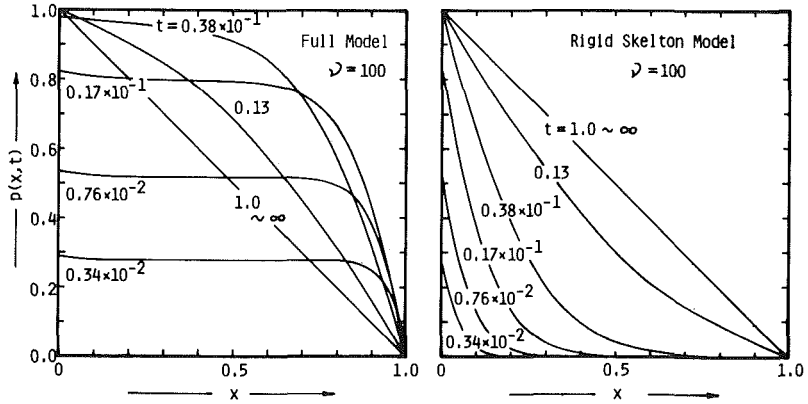

Fig. 6 Pore fluid pressure distribution for compact bone layer for various times using Biot's full model (left) and the rigid skeleton model (right)

skeleton model. Since the former model allows the skeleton to deform elastically and the elastic deformation propagates at infinite velocity in the case of quasi-static analysis, the pore pressure instantly penetrates into the layer near its bottom surface, as seen in the left half. In contrast to this, the latter model suppresses any skeleton deformation and the pore pressure gradually penetrates into the layer from the top surface that is suddenly subjected to the fluid pressure, as shown on the right. Therefore, near the bottom surface, the pore pressure gradients for Biot's full model are very steep in the early stages. These steep gradients result in a large fluid outflux. the circumstances for the rigid skelton model are completely contrary to this.

Acknowledgment

The author wishes to express his sincere gratitude to Professor A. Atsumi of Tohoku University for his valuable advice and encouragement.

References

1 Biot, M. A., "General Theory of Three-Dimensional Consolidation," *Journal of Applied Physics*, Vol. 12, 1941, pp. 155–164.

2 Biot, M. A., "Theory of Elasticity and Consolidation for a Porous Anisotropic Solid," *Journal of Applied Physics*, Vol. 26, 1955, pp. 182–185.

3 Biot, M. A., "General Solutions of the Equations of Elasticity and Consolidation for a Porous Material," ASME JOURNAL OF APPLIED MECHANICS, Vol. 23, 1956, pp. 91–96.

4 Fatt, I., "The Biot-Willis Elastic Coefficients for a Sandstone," ASME JOURNAL OF APPLIED MECHANICS, Vol. 26, 1959, pp. 296–297.

5 Yew, C. H., and Jogi, P. N., "The Determination of Biot's Parameters for Sandstones, Part I: Static Test," *Experimental Mechanics, Journal of SESA*, Vol. 18, No. 5, 1978, pp. 167–172.

6 Kim, Y. K., and Kingsbury, H. B., "Dynamic Characterization of Poroelastic Materials," *Experimental Mechanics, Journal of SESA*, Vol. 19, No. 7, 1979, pp. 252–258.

7 Kingsbury, H. B., "Applications of the Theory of Poroelasticity in Biomechanics," *Proc. Mech. Eng. Congress*, Pahlavi University, Shiraz, Iran, 1975, pp. 990–1006.

8 Scheidegger, A. E., *The Physics of Flow Through Porous Media*, University of Toronto Press, Toronto, Canada, 1972.

9 Kurokawa, Y., and Yui, N., "Separation by Reverse Osmosis (Fundamentals and Applications)," *Kagaku no Ryoiki*, Vol. 29, No. 1, 1975, pp. 12–26, (in Japanese).

10 Biot, M. A., and Willis, D. G., "The Elastic Constants of the Theory of Consolidation," ASME JOURNAL OF APPLIED MECHANICS, Vol. 24, 1957, pp. 594–601.

11 Gradshteyn, I. S., and Ryzhik, I. M., *Table of Integrals, Series, and Products*, Academic Press, New York, 1965.

Gravity-Induced Density Discontinuity Waves in Sand Columns[1]

S. C. Cowin[2]
Fellow ASME

W. J. Comfort III
Mem. ASME

University of California,
Lawrence Livermore National Laboratory,
Livermore, Calif. 94550

Formulas are obtained for the speeds of propagation of gravity-induced rarefaction and condensation density discontinuities in vertical sand columns. A rarefaction wave is induced in a column of sand at rest by removing the support at the bottom of the column. A condensation shock is induced by reintroducing the support, which stops the sand from falling. The theoretical prediction of the speed of propagation of the leading edges of the rarefaction wave corresponds well with the speed measurements obtained in a preliminary experiment.

Introduction

We are concerned here with the dynamics of sand columns. A sand column is a volume of sand contained within a rigid right cylinder of arbitrary cross section. The long axis of the cylinder is coincident with the direction of gravity, and the internal surface of the cylinder is rough. We use sand in a generic sense and we thereby include all dry, cohesionless granular materials in which pneumatic effects are not significant. Examples of sand columns satisfying this definition include hopper sections of bulk material handling equipment, silos for the storage of bulk agricultural products, and standpipes that supply granular materials to certain chemical production processes.

In the next section we briefly present the well-known formula of Janssen for the equilibrium intergranular stress in a sand column. In the following three sections, formulas are obtained for the speeds of propagation of rarefaction waves and condensation shocks in vertical sand columns. The formula for the speed of propagation of the leading edge of a rarefaction wave is of greatest interest. Although speed of propagation varies with the depth of the rarefaction wave in the sand column, the predicted speed of propagation of the leading edge of a rarefaction wave agrees well with the speed measured in a preliminary experiment.

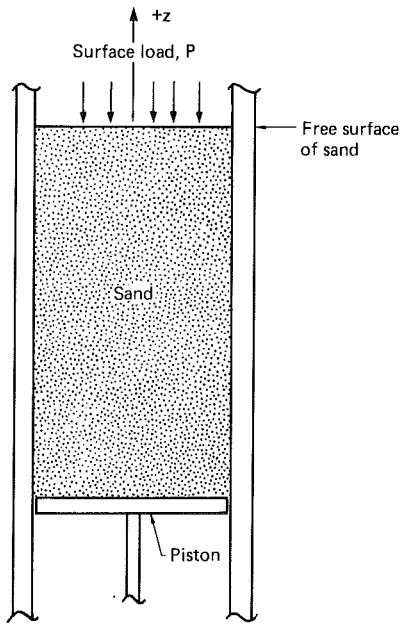

Fig. 1 The sand column and piston

The Sand Column in Equilibrium

We consider the column of sand illustrated in Fig. 1. The sand is in equilibrium in a cylinder of arbitrary cross section. It is subjected to a surface surcharge stress of magnitude P. The sand is supported from below by a piston. The cross-sectional area of the cylinder is denoted by A and the perimeter of the cross-sectional area by L. A coordinate axis z with positive direction upward from the free surface is used, as shown in Fig. 1. This selection of coordinate direction means that the sand column is located along the negative z axis; thus all material stations are located by negative z coordinates. The bulk density ρ of the sand is written as a product of the density of the sand grains γ and the solid volume fraction ν of the grains,

$$\rho = \gamma\nu. \tag{1}$$

The average value of a quantity $f(x,y,z)$ over the cross section z = constant is denoted by $\bar{f}(z)$ and is defined by:

$$\bar{f}(z) = \frac{1}{A}\int\int_A f(x,y,z)\, dxdy. \tag{2}$$

[1] This work was performed under the auspices of the U.S. Department of Energy by Lawrence Livermore National Laboratory under Contract W-7405-Eng-48.

[2] Consultant to Lawrence Livermore National Laboratory. Permanent adddress: School of Engineering, Tulane University, 6823 St. Charles Avenue, New Orleans, La. 70118.

Contributed by the Applied Mechanics Division for publication in the JOURNAL OF APPLIED MECHANICS.

Discussion on this paper should be addressed to the Editorial Department, ASME United Engineering Center, 345 East 47th Street, New York, N.Y. 10017, and will be accepted until two months after final publication of the paper itself in the JOURNAL OF APPLIED MECHANICS. Manuscript received by ASME Applied Mechanics Division, July, 1981; final revision, February, 1982.

The average value of $f(x, y,z)$ over the perimeter L of the cross section is defined by:

$$f^*(z) = \frac{1}{L}\int_C f(x,y,z)\, ds. \tag{3}$$

A formula for the stress in the sand was obtained by Cowin [1], improving the well-known formula of Janssen [2]. This formula involves the Janssen coefficient K defined by

$$K = \frac{T^*_{nn}}{\bar{T}_{zz}}, \tag{4}$$

where T_{nn} is the stress acting normal to the column boundary at the perimeter and T^*_{nn} is the average perimeter stress. $\bar{T}_{zz}$ is the cross-sectional average of the vertical stress T_{zz}. We are denoting tensile stresses as positive in this work. The coefficient K is constant for many granular materials. A summary of K values is given by Sundaram and Cowin [3]; see also Cowin and Sundaram [4].

The improved formula of Janssen (see Cowin [1]) gives the following bound on the average vertical stress $\bar{T}_{zz}$:

$$-\bar{T}_{zz} \geq \gamma\nu g l_0 + (P - \gamma\nu g l_0)e^{z/l_0}, \tag{5}$$

where

$$l_0 = \frac{A}{\mu L K}, \tag{6}$$

g is the acceleration of gravity, and μ is the static coefficient of friction between the cylinder and the sand. This bound on $-\bar{T}_{zz}$ becomes an equality when the friction between the sand and the cylinder wall is fully mobilized. It should be kept in mind that the last term in equation (5) represents an exponential decay because the admissible values of z are all negative.

Conservation of Mass and Momentum Across the Discontinuity

Statements of the conservation of mass and momentum across a one-dimensional discontinuity obtained in this section are well known. Our derivation, which is based on Lamb's [5] presentation of the original results of Rankine [6], emphasizes the applicability of these classical results to void volume changes in sand as well as to density changes in gases. The notation we introduce is generally that of Truesdell and Toupin [7].

Consider a discontinuity, for example a rarefaction wave moving up the sand column as illustrated in Fig. 2. The leading surface of the discontinuity is denoted by s^+ and the trailing surface by s^-. Let the normal stress, solid volume fraction, and particle velocity at the leading surface be denoted by T^+_{zz}, ν^+, and $\dot{z}^+$, respectively. At the trailing surface the same quantities are denoted by T^-_{zz}, ν^-, and $\dot{z}^-$, respectively. The spatial velocity of the wave is denoted by u. The material speeds of propagation of the two surfaces s^+ and s^-, denoted by U^+ and U^-, respectively, are related to u, $\dot{z}^+$, and $\dot{z}^-$ by

$$U^+ \equiv u - \dot{z}^+, \quad U^- \equiv u - \dot{z}^- \tag{7}$$

To obtain the desired statement of mass balance, the wave velocity u is superposed on the two surfaces s^+ and s^- to reduce the problem to one of steady motion. Since the same amount of mass crosses the surfaces s^+ and s^- in unit time:

$$\gamma\nu^+(u - \dot{z}^+) = \gamma\nu^-(u - \dot{z}^-) \tag{8}$$

which, using (7) can be rewritten as

$$\gamma\nu^+ U^+ = \gamma\nu^- U^- \equiv M \tag{9}$$

where M is the mass per unit area entering or leaving the wave front per unit time. Rankine [6] called M the "mass velocity" of the wave. Equation (9) is the desired statement of mass conservation across the discontinuity. It can also be written in the form

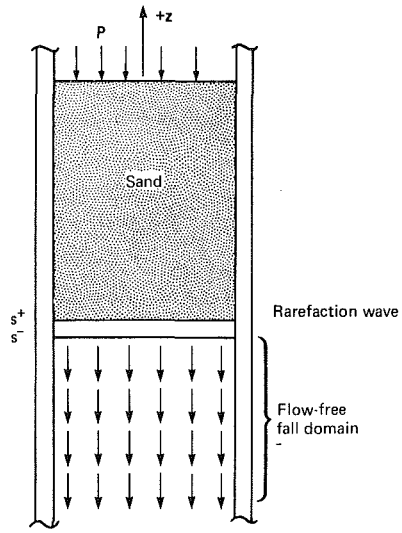

Fig. 2 A rarefaction wave in the sand column. The wave is bounded by the surfaces s^+ and s^-.

$$[\nu U] = 0 \tag{10}$$

where the square brackets denote the jump in the indicated quantity across a shock; i.e.,

$$[\nu U] = \nu^+ U^+ - \nu^- U^-. \tag{11}$$

To obtain a statement of momentum conservation across the discontinuity, the change in normal stress, given by $[T_{zz}] = T^+_{zz} - T^-_{zz}$, is equated to the rate at which the mass is gaining momentum:

$$[T_{zz}] = M(u - \dot{z}^+) - M(u - \dot{z}^-) = -M[\dot{z}]. \tag{12}$$

Thus, from (12) and (7), momentum balance requires that

$$[T_{zz}] = M[U]. \tag{13}$$

An expression for $(U^+)^2$ is obtained from (13) using (11) and (9),

$$(U^+)^2 = -\frac{\nu^-}{\gamma\nu^+}\frac{[T_{zz}]}{[\nu]}. \tag{14}$$

Thus, using (9) and (14), the speeds U^+ and U^- of the shock surfaces are determined by the normal stress jump $[T_{zz}]$ and values of the solid volume fractions ν^+ and ν^- at the shock surfaces, and are independent of other factors.

The Rarefaction Wave

We consider now what happens when the piston in Fig. 1 is suddenly dropped at an acceleration greater than that of gravity. Such an action leaves the bottom level of the sand unsupported. The sand will become less densely packed and begin to fall freely, creating a rarefaction wave. The surface s^+ is the lowest surface that is still in static equilibrium. Below the surface s^+, the shear stress sustained by friction between the sand and the wall diminishes in a short distance to zero. The surface s^- is defined to be the sand plane where the sand has become sufficiently disperse that it can no longer sustain intergranular stresses.

At the surface s^+, the stress is given by the equality in equation (5), which assumes that the full friction force is mobilized; thus,

$$-\bar{T}_{zz} = \gamma\bar{\nu}_r g l_0 + (P - \lambda\bar{\nu}_r l_0 g)e^{z/l_0}, \tag{15}$$

where $\bar{\nu}_r$ is the reference value of the volume fraction established by the initial packing. At the surface s^-, the normal stress $\bar{T}^-_{zz}$ is zero and the reference volume fraction ν^- is $\bar{\nu}_0$, the value of ν at which intergranular stress disappears.

When appropriate values for $[T_{zz}]$, $[\nu]$, ν^+, and ν^- are substituted into (14), the square of the material speed of

propagation of the leading surface of the shock is given by

$$(U^+)^2 = v_o^2 + (v_1^2 - v_0^2)e^{z/l_0}$$

where v_0 and v_1 are velocities defined by

$$v_0 = \sqrt{\frac{g l_0 \bar{\nu}_0}{\bar{\nu}_r - \bar{\nu}_0}}, \quad v_1 = \sqrt{\frac{\bar{\nu}_0}{\bar{\nu}_r(\bar{\nu}_r - \bar{\nu}_0)} \frac{P}{\gamma}}. \tag{17}$$

Equation (16) shows that far away from the free surface, the material speed of propagation of the leading edge of the rarefaction wave is v_0, where

$$\lim_{z \to -\infty} U^+ = v_0. \tag{18}$$

The result also shows that very near the free surface of the material, the material speed of propagation of the leading edge is v_1, where

$$\lim_{z \to 0^-} U^+ = v_1. \tag{19}$$

In particular, if the free surface has no surcharge (i.e., $P = 0$), the material speed of propagation of the leading edge of the shock (i.e., the velocity of the wave relative to the material) will go to zero as the free surface is approached.

The time for a shock wave to travel from a location $-z_0$ to the free surface can be calculated using the formula (16). From (16) we write that

$$U^+ = \frac{dz}{dt} = [v_0^2 + (v_1^2 - v_0^2)e^{z/l_0}]^{1/2}. \tag{20}$$

Thus,

$$t = \int_{-z_0}^{0} [v_0^2 + (v_1^2 - v_0^2)e^{z/l_0}]^{1/2}\, dz. \tag{21}$$

Integration yields

$$t = \frac{l_0}{v_0} ln\left(\frac{2v_0^2}{(v_0 + v_1)} e^{z_0/l_0} + \frac{v_1 - v_0}{v_1 + v_0}\right), \tag{22}$$

and, in the special case when the free surface is unstressed ($P = 0$, hence $v_1 = 0$),

$$t = \frac{l_0}{v_0} ln(2e^{z_0/l_0} - 1). \tag{23}$$

Equation (22) is a general expression for the time t that it takes a rarefaction wave to travel from a depth z_0 to the free surface. Equation (23) is an expression for the same time t in the special case of an unstressed free surface.

The Condensation Shock

Suppose now that the piston is suddenly stopped. The piston surface will be covered by sand rather quickly, and sand that has come to rest will be separated from the still-falling sand by an interface. This interface, which moves up the sand column, is here considered as a condensation shock. This situation is illustrated in Fig. 3. The leading edge of the condensation shock, s^+, is defined as the horizontal plane where the intergranular stress T_{zz} changes from zero to some nonzero value; hence, by definition the solid volume fraction is $\bar{\nu}_0$. Sand grains crossing the surface s^+ have a velocity $-v$. The surface s^- is the surface where all motion of the sand grains vanish; the value of ν^- is denoted by $\bar{\nu}_s$. To determine the speed of propagation U^-, the mass fluxes at the surfaces s^+ and s^- are set equal:

$$\bar{\nu}_s \gamma A U^- dt = -\gamma \nu_0 A \bar{v} dt. \tag{24}$$

Thus

$$U^- = -\frac{\nu_0}{\nu_s} \bar{v}. \tag{25}$$

An expression for the stress at the surface s^- can be obtained from (14) using (25), $T_{zz}^+ = 0$, $\nu^+ = \nu_0$, and $\nu^- = \bar{\nu}_s$; thus

$$\bar{T}_{zz} = -\left(1 - \frac{\bar{\nu}_0}{\bar{\nu}_s}\right) \gamma \bar{\nu}_0 \bar{v}^2. \tag{26}$$

Equation 26 shows that the jump in intergranular stress across the condensation shock is proportional to the square of the velocity of sand grains entering the shock.

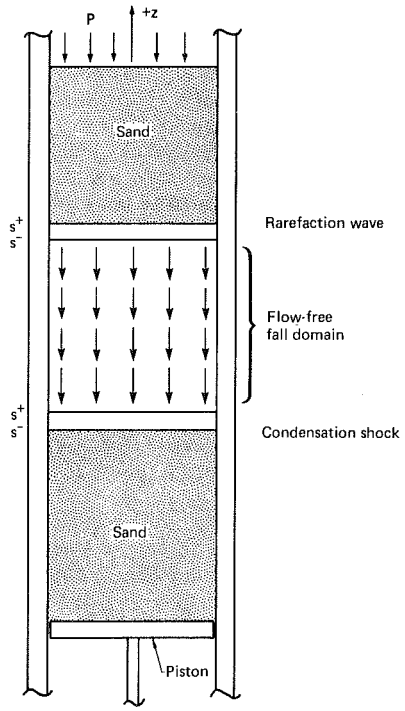

Fig. 3 The sand column containing both a rarefaction wave and a condensation shock

Comparison of Theory With Observations

Several years prior to the development of the theory reported here, a small-scale experimental investigation studied the movement of voids of a sand column. We will here report the results of this early experiment and compare them with the theory. In the experiment, a vertical, rough-walled cylinder of rectangular cross section was filled with sand. The cylinder was fitted with a piston that could be displaced downward a specified distance with an acceleration greater than that of gravity. Moving the piston downward by a specified amount created a void whose magnitude and dimensions were known. Static radiographs of the cylinder were taken before and after each downward displacement of the piston. Microswitches and an electronic timer were used to measure the time lapse between the beginning of downward movement of the piston and the initiation of downward movement of the free surface of the sand.

The test cylinder had a rectangular cross section 152.4 mm by 76. 2 mm and a height of 990 mm. The walls were made of perspex (plexiglass), and were covered internally with burlap to produce high friction surfaces. Both 76.2 mm perspex walls were perforated with many holes to eliminate pneumatic effects from the air entrained in the voids. The piston was released with a solenoid, was driven downward with a spring, and was stopped hydraulically. The mechanism was designed so that the piston could be moved up to a maximum of 76.2 mm.

The first step in the experimental procedure was to load the test device with dry sand. The sand was discharged from a loading hopper through a plastic tube into the cylindrical chamber. The flexible plastic tube was moved about to keep the free surface of the sand horizontal. A slow loading rate ensured that the sand would be densely packed in the cylinder. This method of loading the sand is described in detail by Lee, Cowin, and Templeton [8]. The total length of the completed sand column was 908 mm.

Next, the cylindrical chamber was placed in position and leveled. Three overlapping static x-rays were taken of the

cylindrical chamber on Kodak type M film (5M3M10), which was attached to one of the wider external faces of the chamber. A 2.44 m source-to-film distance was used. The bottom x-ray included the piston, the second one the middle region of the cylinder, and the top one the upper region and free surface of the sand. A tube voltage of 150 KV with a tube current of 4 mA and exposure time of 5 minutes was used. The system was then ready for use in studying the effect of piston motion.

In the first experiment, the piston was dropped 19.1 mm, after which three more static x-rays of the cylinder were taken. During this experiment the timer, which was designed to be activated by a microswitch associated with the piston and stopped by a microswitch measuring the beginning of motion of the free surface, did not stop because the free surface did not move. We feel that the free surface failed to move because the rarefaction wave was diffused to an amplitude below that which is required for propagation before reaching the free surface.

The static x-rays taken before the first experiment showed a smooth layering structure in the sand, characteristic of the manner in which the sand was deposited. Static x-rays taken after the first movement of the piston looked essentially like those taken before, even though the volume fraction of solids had changed from the initial packing fraction of $\bar{\nu}^*$ to 0.98 $\bar{\nu}^*$. The initial packing fraction $\bar{\nu}^*$ is unknown; the packing fraction after the movement of the piston, 0.98 $\bar{\nu}^*$, is calculated from the change in the total volume of the sand. Because the x-ray tube had to be moved to take the upper two x-rays after the first experiment, it was repositioned at the lowest position and another static x-ray was taken. This was done to obtain a before and after x-ray of the second experiment with the x-ray tube in the same position. This same process preceded the second and third experiments.

In the second experiment, the initial positions of the sand column and piston were their final positions at the end of the first experiment. The second experiment consisted of dropping the piston an additional 38.2 mm. The timers (a second one was employed as a backup) measured 0.182 s in both cases. The free surface was estimated to have dropped only 19 mm during the experiment. The static x-rays taken after this experiment showed changes to be more pronounced than for the first experiment. Recall that in the second experiment the piston dropped twice as far, 38.2 mm. In the second experiment, sand in the first 500 mm directly above the piston and the top 150 mm directly below the free surface of the sand appear on the static radiographs to be undisturbed by the piston motion. However, in a region about 300 mm long between these two undisturbed regions there is an interesting change. The region contained many rupture zones, that is, zones of increased porosity or reduced solids volume fraction from 1 to 8 mm wide and from 50 to 100 mm long. These rupture zones made angles of 25–30 deg with the horizontal and tended to cross at the middle of the cylinder. Patterns in the radiograph were very similar to those of Luders bands observed in metals. The average solid volume fraction in the second experiment was $0.98\nu^*$, as compared to $0.95\nu^*$, in the first experiment. The volume of $0.95\nu^*$ was calculated from the change in total volume occupied by the sand.

We now compare the results of the second experiment with the theory presented. By using equation (23) and numerical values associated with the experiment, we determined a theoretical transit time t. To make these calculations, values of $\mu = 0.5$ and $K = 0.6$ were chosen as being representative of the sand used. A survey of K values for various materials is given in [3]. Values directly related to the physical dimensions of the experimental equipment were:

$$A = 0.0116\ \text{m}^2 \qquad L = 0.0457\ \text{m} \qquad z_0 = 0.927\ \text{m}.$$

Using these values and equation (15), the value of $l_0 = 0.0846$ was calculated. With $g = 9.81\ \text{m/s}^2$ and the values of $\bar{\nu}_r = 0.98\ \nu^*$ and $\bar{\nu}_0 = 0.96\ \nu^*$, equation (17) yielded $v_0 = 6.31$ m/s. Substitution of z_0, l_0, and v_0 into equation (23) gave a transit time of 0.156 s. The agreement between this theoretical value of the transit time and the experimentally measured time of 0.182 s is quite acceptable when experimental precision is considered. In the experiment, the values of $\bar{\nu}_0$ and $\bar{\nu}_r$ were determined from the changes in total sand volume as a result of the wave passage and the values of μ and K were estimated from other data [3].

In the third experiment the initial positions of the sand column and piston were their final positions at the end of the second experiment. The third experiment consisted of dropping the piston an additional 19.1 mm. The timers measured 0.0885 s in both cases during the third experiment. Again, the free surface was estimated to have dropped 19 mm during the experiment. Static x-rays taken after the third experiment showed only slight changes from those taken after the second experiment. The principal change was that the rupture zones generated in the second experiment, which are still present, had become slightly diffuse and less distinct. A few new rupture zones were generated below the previously formed ruptured zones during the third experiment. The average solid volume fraction did not change noticeably from that after the second experiment.

The fact that measurements were not sufficiently precise to determine a change in the solid volume fraction in the third experiment prohibit the calculation of a theoretical transit time to compare with the experimental transit time.

Conclusion

The theoretical formula developed for the leading edge of a rarefaction wave up a sand column appears to be consistent with a preliminary experiment. The factors influencing the speed of propagation near the free surface of the sand column are different from the factors influencing the speed deep in the column. Deep in the column, the speed is determined by the cross sectional area, the perimeter of the cross section, the coefficient of friction between the wall and the sand, Jassen's coefficient K, the acceleration of gravity, and the volume fractions in front and behind the wave. Near the free surface the speed is determined by the surcharge stress on the free surface, the weight density of sand grains, and the volume fraction in front and behind the wave.

Both theoretical and experimental results suggest that the speed of propagation of the leading edge of a rarefaction shock is faster in looser sands.

Acknowledgments

The authors thank K. R. Johnson, R. N. Prudencio, R. D. Rikard, L. E. Sandy, and L. I. Starrh for assistance with the preliminary experiment reported in this work, and H. Keedy for his editing of this manuscript.

References

1 Janssen, H. A., "Versuche uber Getreidedruck in Silozellen," *Zeitschrift Verein Deutscher Ingenieure*, Vol. 39, Aug. 31, 1895, pp. 1045–1049.

2 Cowin, S. C., "The Theory of Static Loads in Bins," ASME JOURNAL OF APPLIED MECHANICS, Vol. 44, 1977, pp. 409–412.

3 Sundram, V., and Cowin, S. C., "A Reassessment of Static Bin Pressure Experiments," *Powder Technology*, Vol. 22, 1979, pp. 23–32.

4 Cowin, S. C., and Sundaram, V., "The Effect of Material Compressibility on State Bin Pressures," *Powder Technology*, Vol. 25, 1980, pp. 225–227.

5 Lamb, H., *Hydrodynamics*, 6th Ed., Dover, New York, 1932, pp. 484–485.

6 Rankine, W. J. M., "On the Thermodynamics of Waves of Finite Longitudinal Disturbance," *Phil. Trans. Royal Soc.*, Vol. 160, 1870, p. 277.

7 Truesdell, C., and Toupin, R. A., "The Classical Field Theories," in *Handbuch der Physik*, S. Flugge, ed., Springer Verlag, Vol. III/1, pp. 522 and 546.

8 Lee, J., Cowin, S. C., and Templeton, J. S. III., "An Experimental Study of the Kinematics of Flow Through Hoppers," *Trans. Soc. Rheology*, Vol. 18, 1974, pp. 247–269.

E. Nakamachi
Yatsushiro National College of Technology,
Yatsushiro, Japan

S. Takezono
Kumamoto University,
Kumamoto, Japan
Mem. ASME

R. Sowerby
Professor,
Department of Mechanical Engineering,
McMaster University,
Hamilton, Ontario,
Canada L85 4L7

A Numerical Analysis of the Hydraulic Bulging of Circular Disks Into Axisymmetric Dies

The hydraulic bulging of peripherally clamped, thin, circular disks into axisymmetric dies is studied by means of an incremental finite element method, based on membrane shell theory and formulated to account for finite strains and rotations. The material is treated as an isotropic, elastic-plastic solid obeying the von Mises yield criterion and plastic-potential flow law. The analysis was first performed for a flat-bottomed die, assuming Coulomb friction between the material and the die base. Experimental data were gathered from aluminium disks deformed into a die having a flat, thick glass base. The glass permitted a continuous assessment of the deformation profile and the contact boundary between the aluminium and the glass, using Moiré topography. The agreement between the experimental observations and theoretical predictions is good.

Introduction

The literature dealing with the nonlinear numerical analysis of thin plates and shells undergoing finite plastic deformation is extensive, and will not be reviewed here. The most favored test case to assess the numerical technique has been the axisymmetric bulging or stretching of a peripherally clamped thin, circular plate [1–7].

The present paper also deals with the axisymmetric bulging of a clamped circular disk, but here the material is being forced into an axisymmetric die. Calculations are provided herein for a cylindrical, flat-bottomed die, where the material is assumed to be an elastic-plastic solid obeying the von Mises yield criterion and associated flow rule. An incremental finite element method is employed, based on the membrane approximation for thin shells, and formulated to account for geometric nonlinearities [8]. The frictional conditions between the material and the die were assumed to be of the Coulomb type.

The predictions were checked against experimental observations when bulging a 0.31-mm-thick disk of pure aluminum into a flat-bottomed die. The die base was made of thick glass and this permitted the use of Moiré topography [9], to determine the profile of the deforming blank. The specimens were also gridded, and the principal surface strains could be determined by removing the specimens from the bulging apparatus and measuring the distorted grids. The agreement between experimental observations and theoretical predictions was very favorable.

Contributed by the Applied Mechanics Division for publication in the JOURNAL OF APPLIED MECHANICS.

Discussion on this paper should be addressed to the Editorial Department, ASME, United Engineering Center, 345 East 47th Street, New York, N.Y. 10017, and will be accepted until two months after final publication of the paper itself in the JOURNAL OF APPLIED MECHANICS. Manuscript received by ASME Applied Mechanics Division, August 1981; final revision, January, 1982.

Finite Element Formulation

The present analysis considers the finite deformation of thin circular disks, where over the major portion of the material a stretching mode is predominant and hence the disk may be assumed to behave approximately as a membrane. Since the loading and deformation is axisymmetrical, a ring-plate element is employed.

Figure 1 shows a ring-plate element in a known state C after finite deformation from the undeformed configuration C_0; there follows an *incremental* deformation and C is mapped into $\bar{C}$. An embedded (convected) coordinate system θ^i is adopted [7, 8, 10], where θ^1 and θ^2 are attached to the middle surface of the element and θ^3 is perpendicular to the $\theta^1 - \theta^2$

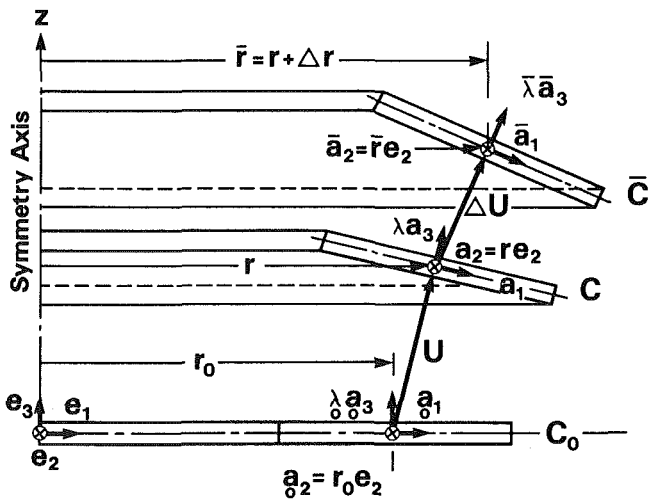

Fig. 1 Displacement of a ring-plate element, showing the coordinate systems

plane. The incremental kinematic relationships are described with reference to the base vectors $\mathbf{a}_i\,(i=1,\ 2,\ 3)$, of the coordinate system θ^i, at the center of gravity of the element in state C.

In the incremental deformation from C to $\bar{C}$, a generic point P in the plate is displaced by $\Delta\mathbf{u}$ where

$$\Delta\mathbf{u}=\Delta u^{\alpha}\mathbf{a}_{\alpha}+\Delta u^{3}\lambda\mathbf{a}_{3}, \tag{1}$$

and $\lambda=h/h_0$, the ratio of the thickness of the plate in C and C_0. The incremental displacement field in the finite element is considered to be given from the nodal values Δu^i_N by the Lagrangian interpolation function $\psi^N(\theta^{\alpha})$ as follows:

$$\Delta u^{i}=\sum_{N}\psi^{N}(\theta^{\alpha})\,\Delta u^{i}_{N},\quad (N=1,2) \tag{2}$$

where $\psi^N(\theta^{\alpha})=\phi^N+\beta^N_1$, and ϕ^N and β^N_1 are constants. The authors follow the convention that Greek indices range over the values 1, 2 and Latin indices over 1, 2, and 3.

The covariant differentiation of the incremental displacements is represented by

$$\left.\begin{aligned}\Delta u_j\,|_s &= {}_N\Psi^k_{js}\,\Delta u^N_k\\ \Delta u^i\,|_s &= N\Phi^i_{ks}\,\Delta u^k_N.\end{aligned}\right\} \tag{3}$$

The nonvanishing coefficients are

$$\begin{aligned}
&{}_N\Psi^1_{11}=\beta_{N1},\ {}_N\Psi^1_{22}={}_N\Pi^1_{22},\ {}_N\Psi^1_{33}=A^{11}_{33}\beta_{N1}+A^{22}_{33}\,{}_N\Pi^1_{22},\\
&{}_N\Psi^3_{31}=\beta_{N1},\ {}_N\Psi^3_{22}={}_N\Pi^3_{22},\ {}_N\Psi^3_{33}=A^{22}_{33}\,{}_N\Pi^3_{22},\\
&{}_N\Phi^1_{11}=\beta^N_1,\ {}_N\Phi^2_{12}=a^{22\,N}\Sigma_{221},\ {}_N\Phi^3_{31}=\beta^N_1,\\
&\qquad {}_N\Phi^3_{33}=A^{22}_{33}\,{}_N\Sigma_{223}/\lambda^2,\\
&{}_N\Phi^3_{13}=(a_{11}A^{11}_{33}\beta^N_1+A^{22}_{33}\,{}_N\Sigma_{221})/\lambda^2,\ {}_N\Phi^2_{32}=a^{22\,N}\Sigma_{223}.
\end{aligned}$$

The quantities $A^{\alpha\alpha\alpha}_{33}$ are the coefficient tensors in the constitutive equation of the material given later in the text by equation (21). The coefficients ${}^N\Sigma_{22k}$, ${}_N\Pi^k_{22}$ are expressed as

$${}^N\Sigma_{22k}=\frac{r^N}{2}\,\theta^1_k,\quad {}_N\Pi^k_{22}=\frac{r_N}{2}\,\Omega^k_1, \tag{4}$$

where r^N and r_N are the radius of a circle through the nodal point N. The terms θ^i_k and Ω^i_k are transformation coefficients which relate the base vectors $\mathbf{a}_i$ to the reference Cartesian coordinates $\mathbf{e}_j$ as follows:

$$\left.\begin{aligned}\mathbf{a}_{\alpha} &= \theta^j_{\alpha}\mathbf{e}_j,\\ \mathbf{a}^{\alpha} &= \Omega^{\alpha}_i\,\mathbf{e}_i,\\ \mathbf{a}_3 &= \theta^j_3\mathbf{e}_j/\lambda=\mathbf{a}^3=\lambda\Omega^3_j\mathbf{e}_j,\end{aligned}\right\} \tag{5}$$

where $|\mathbf{a}^3|=|\mathbf{a}_3|=1$ and $\mathbf{a}^{\alpha}$ is the contravariant base vector.

The Green strain increments at the center of gravity of the ring-plate element are expressed by

$$\left.\begin{aligned}\Delta\gamma_{11} &= \Delta u_1\,|_1=\beta_{N1}\,\Delta u^N_1=\beta^N_1 a_{11}\,\Delta u^1_N,\\ \Delta\gamma_{22} &= \Delta u_2\,|_2={}^N\Sigma_{22k}\,\Delta u^k_N={}_N\Pi^k_{22}\,\Delta u^N_k,\\ \Delta\gamma_{33} &= \lambda\Delta\lambda=A^{11}_{33}\Delta\gamma_{11}+A^{22}_{33}\Delta\gamma_{22}\\ \Delta\gamma_{ij} &= 0 \text{ when } i\neq j.\end{aligned}\right\} \tag{6}$$

It is convenient to introduce a traction per unit length of plate defined in terms of the true stress, $\tau^{\alpha\beta}$, and its increment, $\Delta\tau^{\alpha\beta}$ as follows,

$$\left.\begin{aligned}n^{\alpha\beta} &= \tau^{\alpha\beta}h\\ \Delta n^{\alpha\beta} &= \Delta\tau^{\alpha\beta}h\\ n^{\alpha\beta} &= \Delta n^{\alpha\beta}=0,\quad \alpha\neq\beta,\\ n^{33} &= \Delta n^{33}=0.\end{aligned}\right\} \tag{7}$$

Under hydraulic pressure the force is directed normal to the surface of the element. The increment of surface force, ΔT^i, is related to the increment of pressure, Δp, in the following way

$$\left.\begin{aligned}\Delta T^1 &= -p/\lambda(\beta^N_1\lambda^2 a^{11}\,\Delta u^3_N),\\ \Delta T^2 &= 0\\ \Delta T^3 &= \Delta p/\lambda+p/\lambda\{(\beta^N_1+a^{22\,N}\Sigma_{221})\Delta u^1_N\\ &\quad +a^{22\,N}\Sigma_{223}\,\Delta u^3{}_N\}.\end{aligned}\right\} \tag{8}$$

We now introduce the virtual velocity

$$\mathbf{v}=v_{\alpha}\mathbf{a}^{\alpha}+v_3\mathbf{a}^3/\lambda, \tag{9}$$

and in the absence of inertia and body forces the principle of virtual work in incremental form can be derived as

$$\begin{aligned}
&-\textstyle\int_A\sqrt{a}[\Delta n^{\alpha\beta}v_{\beta|\alpha}+n^{\alpha\beta}\,(\Delta u^{\nu}\,|_{\nu}+\Delta\lambda/\lambda)\,v_{\beta|\alpha}\\
&+n^{\alpha\beta}\Delta u^{m}\,|_{\beta}v_{m|\alpha}]dA+\textstyle\int_A\sqrt{a}\Delta T^k v_k\,dA=0.
\end{aligned} \tag{10}$$

When the material makes contact with the die the frictional resistance has been incorporated into the virtual work equation. The frictional forces in the direction of the meridion, $\mathbf{a}_1$, in C and $\bar{C}$ are derived from Coulomb's law as follows

$$\text{and}\qquad \left.\begin{aligned}&\mu p\frac{\tilde{\mathbf{a}}_1}{\sqrt{a_{11}}}\,dA \quad \text{in } C\\ &\mu\bar{p}\frac{\tilde{\mathbf{a}}_1}{\sqrt{\tilde{a}_{11}}}\,d\bar{A} \quad \text{in } \bar{C},\end{aligned}\right\} \tag{11}$$

where μ is the coefficient of friction and a_{11} is the metric tensor. The incremental frictional force can now be obtained with the aid of (11) in the following manner

$$\begin{aligned}
\Delta\tau dA &= (\Delta\tau^{\alpha}\mathbf{a}_{\alpha}+\Delta\tau^3\lambda\mathbf{a}_3)dA\\
&= \mu(p+\Delta p)\,(\mathbf{a}_1+\Delta u^3\,|_1\lambda\mathbf{a}_3)(1+\Delta u^{\alpha}\,|_{\alpha})\\
&\quad dA/\sqrt{a_{11}}-\mu p\mathbf{a}_1 dA/\sqrt{a_{11}}\\
&= \mu\{\Delta p\mathbf{a}_1+p(\Delta u^{\alpha}\,|_{\alpha}\mathbf{a}_1+\Delta u^3\,|_1\lambda\mathbf{a}_3)\}dA/\sqrt{a_{11}}.
\end{aligned} \tag{12}$$

If (12) is incorporated into the virtual work expression, equation (10) is modified to the extent of an additional term

$$-\textstyle\int_A\sqrt{a}\Delta\tau^k v_k\,dA,$$

appearing on the left-hand side of the equation.

The virtual work equation leads to the equation of motion of the finite element in the following incremental form[1],

$$(K^{iM}_{kN}+{}_{(G)}K^{iM}_{kN}+{}_{(\sigma)}K^{iM}_{kN}+{}_{(S)}R^{iM}_{kN})\,\Delta u^k_M=\Delta P^i_N. \tag{13}$$

In equation (13) the coefficients in the brackets on the left-hand side are the incremental stiffness matrix, the initial rotation matrix, the initial stress matrix, and the initial load matrix, respectively [7, 8]. The term on the right-hand side of the equation represents the incremental generalized nodal forces. The quantities are evaluated according to

$$\begin{aligned}
K^{iM}_{kN} &= \sum_{\alpha=1}^{2}\sum_{\beta=1}^{2}E^{\alpha\alpha\beta\beta}a_{\beta\beta}\,{}^M\Phi^{\beta}_{k\beta N}\Psi^i_{\alpha\alpha}\lambda h_0 A_e,\\
{}_{(G)}K^{iM}_{kN} &= \sum_{\alpha=1}^{2}n^{\alpha\alpha\,M}\Phi^q_{kq\,N}\Psi^i_{\alpha\alpha}A_e,
\end{aligned}$$

[1] (13) refers to the local coordinate system and must ultimately be transformed to the reference coordinates $\mathbf{e}_i$.

$$
\begin{aligned}
{}_{(\sigma)}K^{iM}_{kN} &= \sum_{\alpha=1}^{2} n^{\alpha\alpha M}\Phi^{q}_{k\alpha N}\Psi^{j}_{q\alpha}A_e,\\
{}_{(S)}R^{iM}_{kN} &= -p/\lambda({}^{M}\Phi^{\alpha}_{k\alpha}\delta^{i}_{3}-{}^{M}\Phi^{3}_{k\alpha}a^{\alpha j}\lambda^{2})A_N,\\
\Delta P^{i}_{N} &= (\Delta p/\lambda)\delta^{i}_{3}A_N,
\end{aligned}
$$

$$a=\det(a_{\alpha\beta}),A_e=\sqrt{a}\int_{A_0}dA \text{ and } A_N=\sqrt{a}\int_{A_0}\psi_N dA.$$

In the foregoing A_0 is the area of the finite element in C_0. Note that in the presence of friction two more coefficients have to be embodied into (13). The contribution to the right-hand side of the equation is the additional nodal force

$${}_{(\tau)}\Delta P^{i}_{N}=-\sqrt{a}\int_{A_0}\mu\Delta p\delta^{i}_{1}\psi_N dA/\sqrt{a_{11}},$$

while to the brackets on the left-hand side the stiffness matrix is supplemented by

$${}_{(\tau)}K^{iM}_{kN}=\sqrt{a}\int_{A_0}\mu p({}^{M}\Phi^{3}_{k1}\delta^{i}_{3}+{}^{M}\Phi^{\alpha}_{k\alpha}\delta^{i}_{1})\psi_N dA/\sqrt{a_{11}}.$$

Once the contact occurs with the die base, the displacement component normal to the surface is zero, and for the case of full friction the displacement component tangential to the surface is also zero. It is convenient to transform the components of the incremental, displacement $\Delta\bar{u}^i$ and nodal force $\Delta\bar{P}^i$, with respect to the reference coordinates $\mathbf{e}_i$, to directions normal and tangential to the contact surface. It follows that

$$\begin{vmatrix}\Delta w^1\\ \Delta w^3\end{vmatrix}=\begin{vmatrix}\cos\xi & -\sin\xi\\ \sin\xi & \cos\xi\end{vmatrix}\begin{vmatrix}\Delta\bar{u}^1\\ \Delta\bar{u}^3\end{vmatrix},$$

with a similar expression linking the nodal forces. In the preceding expression ξ is the angle between the tangent to the meridional direction and the reference direction $\mathbf{e}_1$. The equations are capable of solution for either frictionless, Coulomb friction or full sticking conditions.

Constitutive Equation

As already mentioned, an isotropic, elastic-plastic material is assumed, which deforms in an axisymmetric mode under plane stress conditions. It is further assumed that an increment of strain can be obtained as the sum of the elastic and plastic increments

$$\Delta\gamma_{ij}=\Delta\gamma^{e}_{ij}+\Delta\gamma^{p}_{ij} \tag{14}$$

The elastic strain increment $\Delta\gamma^{e}_{ij}$ is related to the Jaumann stress increment ${}_J\Delta\tau^{ij}$ by Hooke's law, and the plastic strain increment $\Delta\gamma^{p}_{ij}$ is derived from the von Mises plastic potential. The elastic relationships are

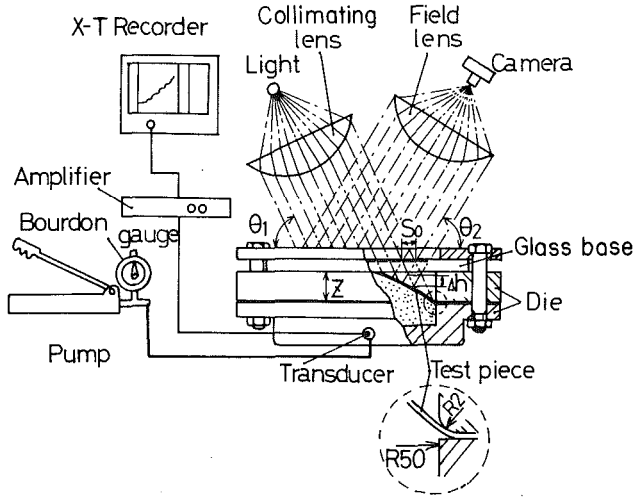

Fig. 2 Schematic view of apparatus

$$\begin{vmatrix}{}_J\Delta\tau^{11}\\ {}_J\Delta\tau^{22}\end{vmatrix}=\mathbf{B}\begin{vmatrix}\Delta\gamma^{e}_{11}\\ \Delta\gamma^{e}_{22}\end{vmatrix} \tag{15}$$

The elastic matrix $\mathbf{B}$ is given by

$$\mathbf{B}=\frac{2\mu}{1-\nu}\begin{vmatrix}a^{11}a^{11} & \nu a^{11}a^{22}\\ \nu a^{22}a^{11} & a^{22}a^{22}\end{vmatrix} \tag{16}$$

where μ is the shear modulus and ν is Poisson's ratio. The plastic strain increment is derived from the von Mises plastic potential in the usual manner

$$\Delta\gamma_{ij}{}^{p}=d\eta\partial f/\partial\tau^{ij},$$

where

$$\begin{aligned}
f &= 1/2\tau'^{ij}\tau'_{ij}=\bar{\sigma}^2/3,\\
\tau'^{ij} &= \tau^{ij}-a^{ij}a_{kl}\tau^{kl}/3\\
\tau'_{ij} &= \tau'^{kl}a_{ik}a_{jl}.
\end{aligned}$$

After some manipulation [8] the incremental stress-strain relationship for the elastic-plastic material can be expressed as

$$\begin{vmatrix}{}_J\Delta\tau^{11}\\ {}_J\Delta\tau^{22}\end{vmatrix}=\mathbf{D}\begin{vmatrix}\Delta\gamma_{11}\\ \Delta\gamma_{22}\end{vmatrix}, \tag{17}$$

where

$$\mathbf{D}=\mathbf{B}-\frac{1}{\hat{F}}\begin{vmatrix}F^{11}F^{11} & F^{11}F^{22}\\ F^{22}F^{11} & F^{22}F^{22}\end{vmatrix}. \tag{18}$$

In equation (18)

$$(F^{11}F^{22})^{T}=B(\tau'^{11}\tau'^{22})^{T},$$

$$\hat{F}=\frac{2}{3}F'\bar{\sigma}^2+F^{11}\tau'_{11}+F^{22}\tau'_{22}.$$

$\hat{F}$, $F^{\alpha\beta}$, and F' denote the characteristics of the material; F' is the derivative of the function of the plastic work, W^p, where

$$f=F(W^p),$$

and can be determined from a uniaxial tensile test.

The Jaumann stress increment can be expressed in terms of $\Delta\tau^{\alpha\beta}$ as

$$\begin{vmatrix}\Delta\tau^{11}\\ \Delta\tau^{22}\end{vmatrix}=\begin{vmatrix}{}_J\Delta\tau^{11}\\ {}_J\Delta\tau^{22}\end{vmatrix}-\mathbf{H}\begin{vmatrix}\Delta\gamma_{11}\\ \Delta\gamma_{22}\end{vmatrix} \tag{19}$$

where

$$\mathbf{H}=\begin{vmatrix}2\tau^{11}a^{11} & 0\\ 0 & 2\tau^{22}a^{22}\end{vmatrix}.$$

Equation (19) can be expressed in the alternative form

$$\begin{vmatrix}\Delta\tau^{11}\\ \Delta\tau^{22}\end{vmatrix}=\mathbf{E}\begin{vmatrix}\Delta\gamma_{11}\\ \Delta_{22}\end{vmatrix} \tag{20}$$

where

$$\mathbf{E}=\mathbf{D}-\mathbf{H}.$$

Under plane stress conditions the thickness strain increment $\Delta\gamma_{33}$ is given by

$$\Delta\gamma_{33}=A^{\alpha\beta}_{33}\,\Delta\gamma_{\alpha\beta}, \tag{21}$$

where

$$A^{\alpha\beta}_{33}=-\nu/Ea_{\xi\mu}D^{\xi\mu\alpha\beta}\lambda^2+\tau'_{33}F^{\alpha\beta}/\hat{F}.$$

Analysis of the Bulge Forming of Circular Plates

a Experimental Method. Pure aluminum disks, 0.31 mm thick were clamped around their periphery and deformed under hydraulic pressure. The diameter of the disk exposed to

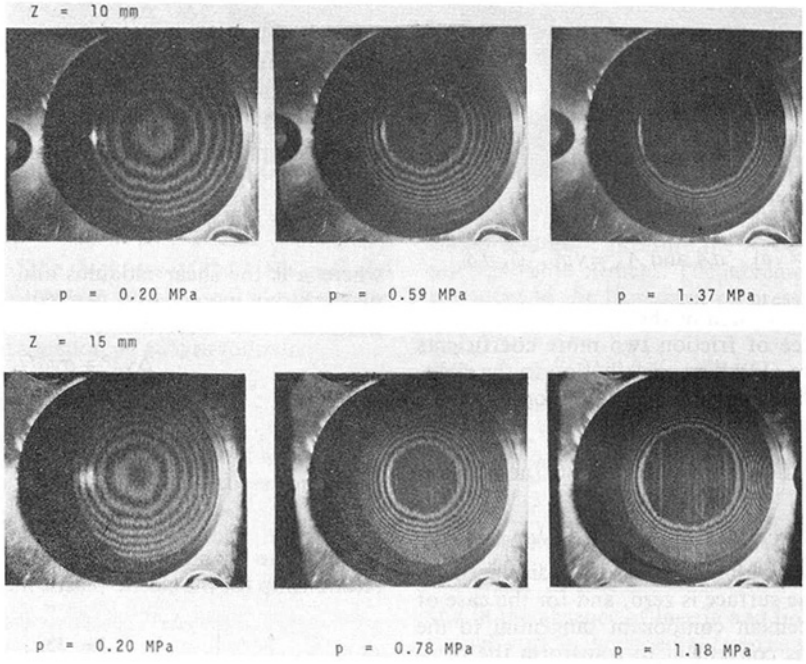

Fig. 3 Moiré fringe patterns

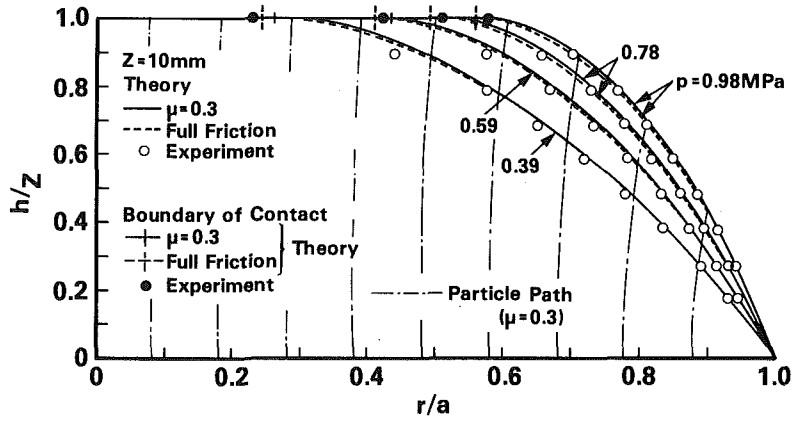

Fig. 4(*a*) $Z = 10$ mm

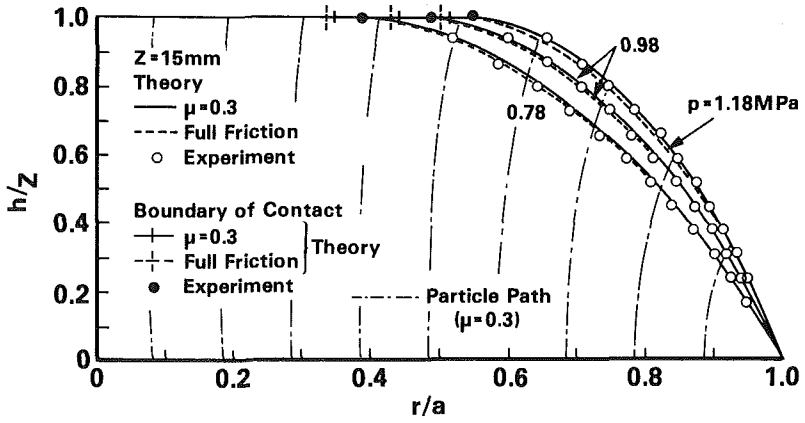

Fig. 4(*b*) $Z = 15$ mm

Fig. 4 Calculated and measured blank shapes when forming into a flat-bottomed die

the oil was 100 mm. At a distance, Z, above the flat blank was located a glass plate, 10 mm thick, which restricted the depth of the deforming blank. Hence the blank is being deformed into a flat-bottomed cylindrical die. The deflection of the central portion of the glass was minimal, being less than 0.04 mm with the highest pressure employed.

An array of lines was scribed on the surface of the glass plate to form a square grid of side, $S = 1.0$ mm. Moiré

Table 1 Material properties

Young's modulus	$E = 68650$ MPa
Yield stress	$\sigma_y = 22.05$ MPa
Poisson's ratio	$\nu = 0.314$
True stress-strain relationship	$\bar{\sigma} = 156.4(0.0011542 + \bar{\epsilon}^p)^{0.29}$ MPa

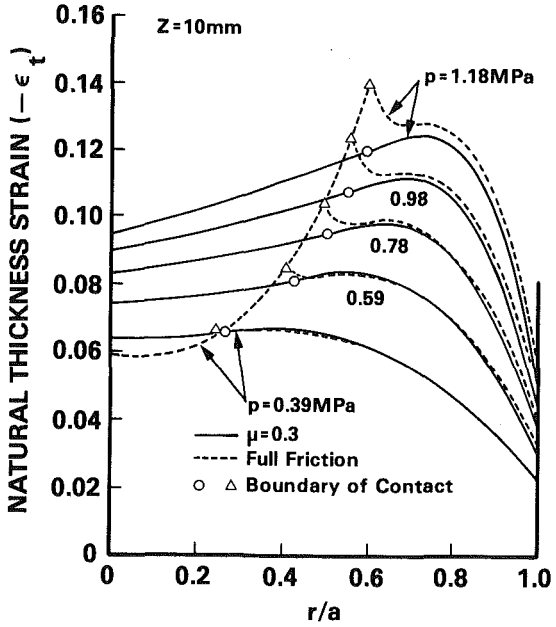

Fig. 5 Calculated thickness strain distributions for the die geometry of Fig. 4(*a*)

topography, [9] was utilized to determine the contour of the deforming disk. A pattern of interference fringes is revealed when viewed through the glass plate; the fringes represent contour lines of equal height difference, Δh, as shown in Fig. 2. In the present experiments Δh was 0.75 mm and is given by the following expression [9]

$$\Delta h = S \tan\theta_1 \tan\theta_2 / (\tan\theta_1 + \tan\theta_2), \qquad (22)$$

where θ_1 and θ_2 are the incident and viewing angles, respectively (see Fig. 2). Two distinct sets of experiments were performed with the lower surface of the glass plate set at either $Z = 10$ mm or 15 mm, above the upper surface of the flat blank. The oil pressure was applied by a hand pump, and at pressure intervals of 0.05 MPa a photograph of the interference pattern was taken after holding the line pressure constant for about 90 s. Typical Moiré patterns are shown in Fig. 3. As the pressure increases the fringes grow in number, and come closer together as the slope of the contour of the deforming specimen increases. The fringe pattern disappears when the material touches the glass, and the area of contact is apparent from the photographs of Fig. 3. It is to be noted that since $\theta_2 \neq 90$ deg, the fringes are elliptic rather than circular in shape. However, the difference is small as was found to be about 2 percent in region of the steepest slope of the bulge, and a correction was made for this. The maximum line pressure employed in these experiments was 1.40 MPa. This pressure was not sufficient to burst the specimen when the glass plate was set 10 mm above the blank, but with $Z = 15$ mm, rupture did take place.

Across the diameter of each circular blank, lines were scribed at 5.0 mm intervals. At different stages in the deformation process the blank was removed from the bulging apparatus and the principal surface strains were derived from measurements of the fiducial markings. The thickness strain was computed on the assumption of material incompressibility.

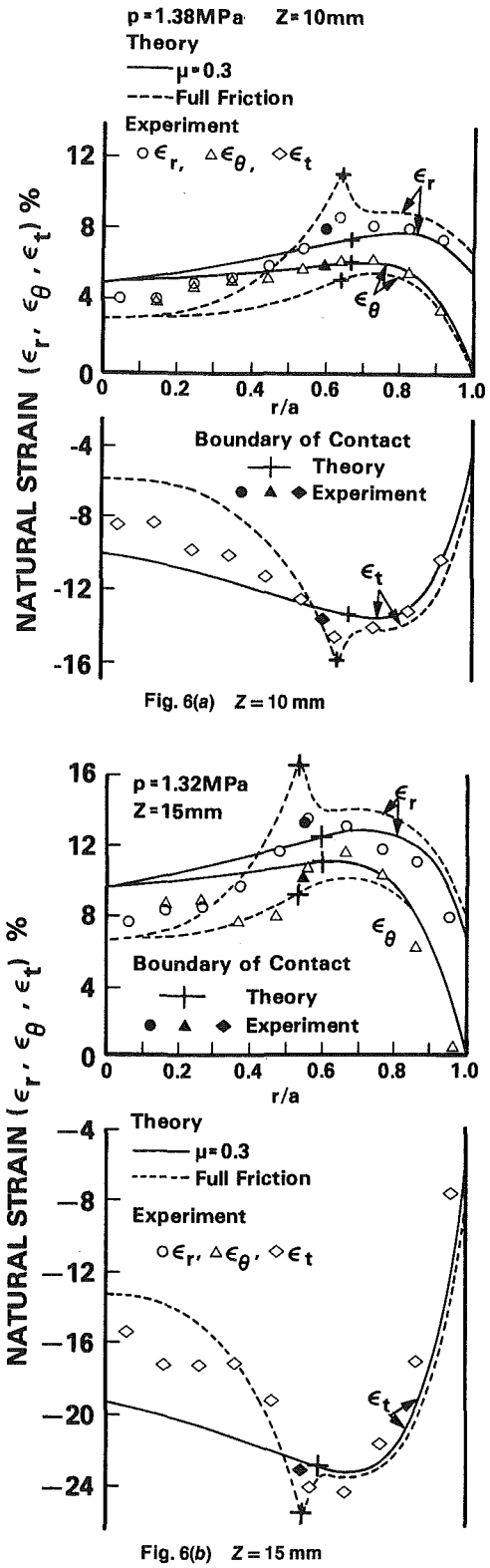

Fig. 6(*a*) $Z = 10$ mm

Fig. 6(*b*) $Z = 15$ mm

Fig. 6 Comparison of the calculated and measured strain distribution at one specific pressure

b Comparison Between Theory and Experiment. Uniaxial tensile tests performed on the aluminum revealed the property data given in Table 1. This was used as the material constitutive equation in the finite element analysis. The coefficient of friction between the aluminum and the glass was assessed experimentally. A series of weights were loaded onto aluminum strips which were attached to a

spring scale and pulled across the glass plate. A value of $\mu = 0.3$ was determined under dry conditions, and this value was used in the subsequent analysis. An alternative procedure was also employed in the calculations, by assuming that once the material contacted the glass plate no relative motion of the interface occurred. This condition is referred to as *fixed* or *full friction* in the following text.

The disk was divided into 50 ring-plate elements of equal width. To compensate for the radiused corner of the hold-down ring (see Fig. 2), the deforming blank was assumed to be of 51 mm radius. Figures 4(*a*) and (*b*) show the calculated and measured profiles of the bulge for $Z = 10$ mm and 15 mm, respectively. Calculations were performed for both friction conditions and there was little to choose between either method. In general the theoretical results agreed quite well with the experimental observations. Figure 5 shows the calculated thickness strain distribution for each friction condition, as a function of hydraulic pressure with $Z = 10$ mm. Under full friction conditions, the maximum thickness strain is calculated as occurring at the contact boundary of the workpiece and the glass base, while for $\mu = 0.3$ the maximum strain is deemed to occur just away from the contact boundary in the free surface of the bulge. Upon repeating the calculations for pressures in excess of those shown in Fig. 4, it was revealed that beyond a certain pressure, a dramatic increase in the thickness strain occurred. In analytical terms the enormous increase in the incremental displacements is caused by the determinant of the stiffness matrix in equation (13) going to zero. In physical terms this signifies plastic instability in the material in the form of a localized neck, and the onset of fracture. It was not straightforward to adjust the pressure increment so that the determinant of the stiffness matrix went exactly to zero. Some calculations were performed for the full friction condition and it was established that rapid increases in thickness strain were occurring at a pressure of $p = 1.57$ MPa and 1.42 MPa at $Z = 10$ mm and 15 mm, respectively. These values were regarded as being close to the instability pressure. Note that the full friction condition predicts the lowest instability pressure in this type of test.

A comparison of the calculated and measured strain distribution at one specific pressure is shown in Fig. 6(*a*) and (*b*) for $Z = 10$ mm and 15 mm, respectively. In general the agreement is satisfactory. The experimental results tend to lie between the predicted values using $\mu = 0.3$ and the full friction condition.

Some calculations were also performed when bulging into a cylindrical die with a sinusoidal base. The two friction conditions discussed in the foregoing were employed, and two distinct sinusoidal contours were utilized. The objective was to assess the applicability of the numerical procedure to the study of the forming of more complex parts. The predictions for the deformation modes, and the influence of friction and die geometry on the die filling capabilities were eminently sensible.

Conclusions

The incremental finite element method formulated to account for geometric nonlinearities and based on the membrane approximation, appears to be a suitable analytical tool for studying certain axisymmetric stretch forming processes of thin, elastic-plastic, circular plates. Experimental data have been gathered from the hydraulic bulging of a clamped, circular plate, into a cylindrical flat-bottomed die. The theoretical predictions agree well with the measured values of strain distribution and deformed blank profile. The calculations based on two assumed friction conditions straddle the actual results. At a certain stage in the deformation process the analysis reveals a very rapid increase in the strain components at some point in the diaphragm, for minor changes in the pressure. This was considered as being close to the point of instability in the process, and in the present case the full friction condition predicted the lowest instability pressure. The physical manifestation of the bifurcation phenomenon is the occurrence of a localized neck, which signifies the onset of fracture.

The theoretical exercise of analyzing the bulging of a clamped, circular disk into an axisymmetric die with a sinusoidal base confirmed the applicability of the numerical technique to the study of the forming of more complex parts.

References

1 Wang, N. -M. "Large Plastic Deformation of a Circular Sheet Caused by Punch Stretching," ASME JOURNAL OF APPLIED MECHANICS, Vol. 37, 1970, pp. 431-440.

2 Mehta, H. S., and Kobayashi, S., "Finite Element Analysis and Experimental Investigation of Sheet Metal Stretching," ASME *Journal of Engineering for Industry*, Vol. 95, 1973, pp. 874-880.

3 Key, S. W., Krieg, R. D., and Bathe, K. J., "On the Application of the Finite Element Method to Metal Forming Process," *Comp. Meth. in Applied Mech. and Eng.*, Vol. 17, 1979, pp. 597-608.

4 Chu, C. C., "An Analysis of Localized Necking in Punch Stretching," *Int. J. of Solids and Structures*, Vol. 16, 1980, pp. 913-931.

5 Wang, N. -M., and Budiansky, B., "Analysis of Sheet Metal Stamping by a Finite Element Method," ASME JOURNAL OF APPLIED MECHANICS, Vol. 45, 1978, pp. 73-82.

6 Kitagawa, H., Nakamachi, E., and Tomita, Y., "Static and Dynamic Analysis of Large Deflections of an Elastic-Plastic Thin Plate," *Proceedings of the Sixth North American Metalworking Conference*, 1978, pp. 236-243.

7 Takezono, S., Nakamachi, E., and Yamaguchi, T., "Elastic/Viscoplastic Analysis of Thin Circular Plates Under Large Strains and Large Deformations," ASME JOURNAL OF APPLIED MECHANICS, Vol. 47, 1980, pp. 741-747.

8 Kitagawa, H., and Tomita, Y., "An Incremental Finite Element Analysis of Two-Dimensional Large Strain and Large Displacement Problems for Elasto-Plastic Material," *Proceedings of the 21st Japan Nat. Cong. Applied Mech.*, 1971, pp. 243-255.

9 Takasaki, H., "Moire Topography," *Applied Optics*, Vol. 9, 1970, pp. 1467-1472.

10 Green, A. E., and Zerna, W., *Theoretical Elasticity*, Oxford University Press, London, 1954.

The Large Elastic-Plastic Deflection With Springback of a Circular Plate Subjected to Circumferential Moments

T. X. Yu[1]

W. Johnson

University Engineering Department,
Trumpington Street,
Cambridge CB2 1PZ, England

The large deflection elastic-plastic bending of a circular plate subjected to radially outward acting bending moments uniformly distributed around its circumference is analyzed, and computer programs are given to facilitate the determination of the distributions of bending moments, in-plane forces, and displacements during the bending and ***after unloading*** *or springback. Computed examples are given, and the errors developed by small deflection theory are discussed.*

1 Introduction

In reference [1], the biaxial elastic-plastic pure bending and springback of rectangular and circular plates after subjecting them to loading and unloading by edge moments was examined. However, the elementary theory of the bending of thin plates which forms the basis of that paper [1] was restricted to the maximum plate deflection being less than about the plate thickness. With this limitation in mind, reference [2] was provided to delineate the range of applicability of the results provided by [1].

In cases in which the deflections are no longer small by comparison with the thickness of the plate, but are still small as compared with other dimensions of the plate, analysis must be extended to include strains in the middle plane of the plate.

References [3] and [4] parallel [1] and [2] but treat work-hardening materials. Paper [5], in part, addresses itself to the problems that confront the manufacturer of large water tower containers, e.g., of ½ million gallon capacity. The many plates (typically 10 ft × 8 ft and thickness ⅜–1 in.) which make up a tower must be so pressed as to have predetermined biaxial curvatures. These curvatures are those to which the plate elastically springs back after plastic pressing. Thus the *ultimate* purpose behind this and papers [1–5] is to be able to contribute to assessing the radii to which relatively thick plate must be elastically-plastically pressed so that after removal from between the pressing tools and undergoing springback, the plate possesses any specific double curvature required.

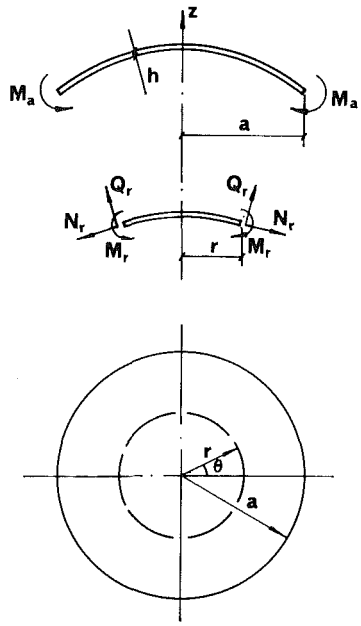

Fig. 1 A circular plate subjected to bending moments uniformly distributed along its circumference

2 Assumptions and Basic Relationships

Consider a circular plate of radius a, subjected to bending moments M_a uniformly distributed along its circumference (see Fig. 1). If the plate is elastic, then the large deflection problem may be treated as it was by Timoshenko in reference [6]. In the following, a similar approach is made to deal with the large deflection of an elastic perfectly plastic circular plate.

Assume that:

(*i*) the material of the plate is elastic perfectly plastic;

[1] On leave from the Research Institute of Construction Machinery, Tianjin, China.

Contributed by the Applied Mechanics Division for publication in the JOURNAL OF APPLIED MECHANICS.

Discussion on this paper should be addressed to the Editorial Department, ASME, United Engineering Center, 345 East 47th Street, New York, N.Y. 10017, and will be accepted until two months after final publication of the paper itself in the JOURNAL OF APPLIED MECHANICS. Manuscript received by ASME Applied Mechanics Division, November, 1981; final revision, February, 1982.

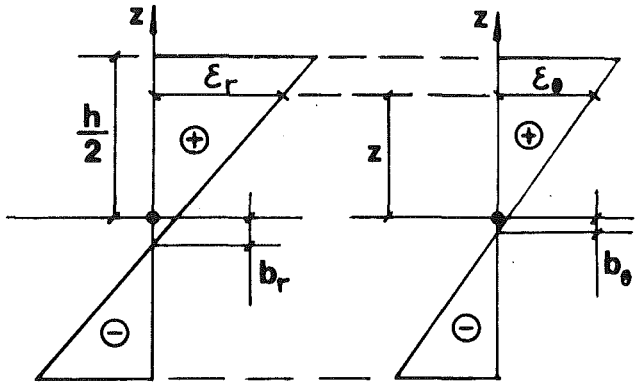

Fig. 2 The distributions of ϵ_r and ϵ_θ along a normal-to-the-middle plane of the plate

(*ii*) points of the plate lying initially on a normal-to-the-middle plane of the plate remain on the normal-to-the-middle surface of the plate after bending;

(*iii*) the normal stresses in the direction transverse to the plate can be disregarded;

(*iv*) in plastic zones, the material obeys Tresca's yield criterion.

Since the deflection surface in our problem is symmetrical with respect to the center of the plate, *the displacement of a point in the middle plane of the plate* can be resolved into two components: a component u in the radial direction and a component w perpendicular to the initial plane of the plate.

Referring to [6], we take the strain in the radial direction to be[2]

$$\epsilon_r^* = \frac{du}{dr} + \frac{1}{2}\left(\frac{dw}{dr}\right)^2, \tag{1}$$

and the strain in the tangential direction as

$$\epsilon_\theta^* = \frac{u}{r}, \tag{2}$$

where the superscript * denotes a value at the middle plane of the plate.

Similarly, the principal curvatures of the deflected middle plane can be expressed as[3]

$$\kappa_r^* = -\frac{d^2w}{dr^2} \tag{3}$$

and

$$\kappa_\theta^* = -\frac{1}{r}\frac{dw}{dr}. \tag{4}$$

It is convenient to introduce nondimensional parameters as follows:

$$\xi = \frac{u}{h}, \quad \zeta = \frac{w}{h}, \quad \rho = \frac{r}{h}, \tag{5}$$

$$\phi_r = \frac{\kappa_r^*}{\kappa_e} \quad \text{and} \quad \phi_\theta = \frac{\kappa_\theta^*}{\kappa_e}, \tag{6}$$

where h is the thickness of the plate and

$$\kappa_e = \frac{2Y(1-\nu^2)}{h\mathrm{E}}. \tag{7}$$

κ_e denotes the curvature in the initial yield state; E denotes Young's modulus, ν Poisson's ratio, and Y the yield stress of the material. Thus, expressions (1)–(4) can be rewritten as

$$\epsilon_r^* = \xi' + \frac{1}{2}\zeta'^2, \tag{1}'$$

$$\epsilon_\theta^* = \frac{\xi}{\rho}, \tag{2}'$$

[2] In the case of very large deflection we have [7] $\epsilon_r = du/dr + \frac{1}{2}[(dw/dr)^2 + (du/dr)^2]$. For our computed examples when $w_{max} \cong h$, $(du/dr)/(dw/dr) \simeq 0.01 \sim 0.03$, i.e., $(du/dr)^2/(dw/dr)^2 \simeq 0.0001 \sim 0.001$, so that the term in $(du/dr)^2$ is negligible at this level of deflection.

[3] In the case of very large deflections we have $\kappa_r^* = -d^2w/dr^2\ [1 - 3/2(dw/dr)^2]$. However, for our computed examples, when $w_{max} \simeq h$, $(dw/dr)_{max} \simeq 0.08$, i.e., $3/2(dw/dr)^2 < 0.01$, so that the term $(dw/dr)^2$ is negligible at this level of deflection.

Nomenclature

a = radius of the circular plate
b = distance in Fig. 2
c = distance in Fig. 3
d = distance in Fig. 3
E = Young's modulus
f = material constant, $E/2Y(1-\nu^2)$
h = thickness of plate
i = number of computing steps
M = bending moment
M_a = edge moment
M_e = initial yield bending moment, $Yh^2/6$
m = nondimensional bending moment, M/M_e
N = in-plane force
N_e = initial yield tensile force, Yh
n = nondimensional in-plane force, N/N_e
R = radius of curvature
r = radial coordinate
s = nondimensional quantity defined by (18)
u = component of displacement in the r-direction
w = component of displacement in the z-direction
Y = yield stress
z = direction perpendicular to the middle plane of the plate
α = nondimensional radius of plate, a/h
β = nondimensional distance, $b/(h/2)$
γ = nondimensional distance, $c/(h/2)$
δ = nondimensional distance, $d/(h/2)$
ϵ = strain
ζ = nondimensional displacement in the z-direction, w/h
κ = curvature
κ_e = curvature at the initial yield state
ν = Poisson's ratio
ξ = nondimensional displacement in the r-direction, u/h
ρ = nondimensional radial coordinate, r/h
$\Delta\rho$ = nondimensional increment in radial coordinate
σ = stress
ϕ = nondimensional curvature, κ/κ_e
ψ = nondimensional quantity defined by (30)

Superscripts

e = elastic
p = elastic-plastic
s = springback
SDT = small deflection theory
* = value at the middle plane of the plate
′ = differentiation, $d/d\rho$

Subscripts

a = value at the edge of the plate
i = value at the circle of radius $\rho_i = (i-1)\Delta\rho$
0 = value at the center of the plate
r = radial
θ = circumferential

$$\phi_r = -f\zeta'' \tag{3}'$$

and

$$\phi_\theta = -f\frac{\zeta'}{\rho}, \tag{4}'$$

where $' = d/d\rho$, so that

$$f = \frac{1}{h\kappa_e} = \frac{E}{2Y(1-\nu^2)}, \tag{8}$$

which is a constant dependent only on the material properties.

As in the theory of elastic plates, from the basic assumption (*ii*) it can be assumed that the distribution of the principal strains is as shown in Fig. 2. Thus, for any point in the plate, the strains are

$$\epsilon_r = \frac{z+b_r}{R_r+b_r} \simeq \frac{\left(1-\frac{b_r}{R_r}\right)z+b_r}{R_r} - \left(\frac{b_r}{R_r}\right)^2$$

$$\cong \frac{z+b_r}{R_r} = (z+b_r)\kappa_r \tag{9}$$

and

$$\epsilon_\theta = \frac{z+b_\theta}{R_\theta+b_\theta} \simeq \frac{z+b_\theta}{R_\theta} = (z+b_\theta)\kappa_\theta, \tag{10}$$

where R_r and R_θ are the radii of curvature in the middle plane, and it is reasonable to suppose that $R_r >> b_r$ and $R_\theta >> b_\theta$; b_r and b_θ are quantities defined in Fig. 2.

By taking $z = 0$ in (9) and (10), the strains at the middle plane are found to be

$$\left.\begin{aligned}\epsilon_r^* &= b_r\kappa_r = \beta_r\phi_r/2f\\ \text{and}\quad \epsilon_\theta^* &= b_\theta\kappa_\theta = \beta_\theta\phi_\theta/2f,\end{aligned}\right\} \tag{11}$$

where

$$\beta_r = \frac{b_r}{(h/2)} \quad \text{and} \quad \beta_\theta \equiv \frac{b_\theta}{(h/2)}, \tag{12}$$

so that

$$\beta_r = 2f\epsilon_r^*/\phi_r \quad \text{and} \quad \beta_\theta = 2f\epsilon_\theta^*/\phi_\theta. \tag{13}$$

In each principal direction (i.e., the r and θ directions), for different combinations of bending moment and in-plane force (i.e., (M_r, N_r) or (M_θ, N_θ)), the distribution of the corresponding principal stresses (σ_r or σ_θ) is of three different types, as shown in Fig. 3 (see [8] and [9]), that is

(*i*) a wholly elastic stress distribution, Fig. 3(*a*), such that no fiber yields in a specified principal direction;

(*ii*) a primary plastic stress distribution, Fig. 3(*b*), such that there is partial yield on one side with fibers yielding in a specified direction:

(*iii*) a secondary plastic stress distribution, Fig. 3(*c*), such that yielding occurs on both sides in the given direction.

It should be noted that when the distribution of one principal stress (say, σ_r) embraces just one of these three types, the other principal stress (say, σ_θ) may be another of these types. For example, when σ_r is of type (*iii*), σ_θ may be any one among types (*i*), (*ii*), and (*iii*).

However, in any case, there is always an elastic zone in the plate so that from Hooke's law we have

$$\left.\begin{aligned}\sigma_r &= \frac{E}{1-\nu^2}(\epsilon_r+\nu\epsilon_\theta) = \frac{E}{1-\nu^2}[(z+b_r)\kappa_r+\nu(z+b_\theta)\kappa_\theta]\\ \text{and}\quad \sigma_\theta &= \frac{E}{1-\nu^2}(\epsilon_\theta+\nu\epsilon_r) = \frac{E}{1-\nu^2}[(z+b_\theta)\kappa_\theta+\nu(z+b_r)\kappa_r].\end{aligned}\right\} \tag{14}$$

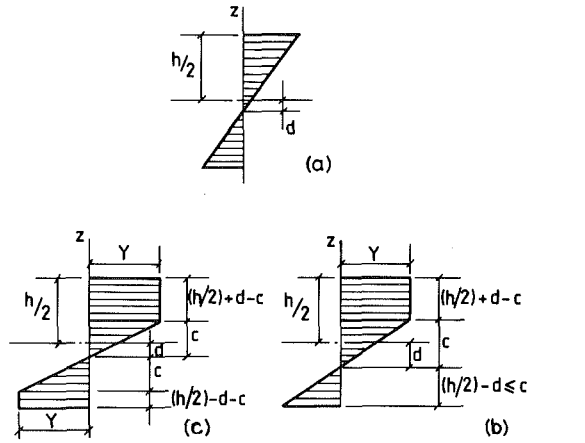

Fig. 3 The distribution of a principal stress (σ_r or σ_θ) along a normal-to-the-middle plane of the plate. Three different types are: (*a*) a wholly elastic stress distribution; (*b*) a primary plastic stress distribution; and (*c*) a secondary plastic stress distribution.

Since $\sigma_r = 0$ at $z = -d_r$ and $\sigma_\theta = 0$ at $z = -d_\theta$, it is found that

$$\left.\begin{aligned}&(-d_r+b_r)\kappa_r+\nu(-d_r+b_\theta)\kappa_\theta = 0\\ \text{and}\quad &(-d_\theta+b_\theta)\kappa_\theta+\nu(-d_\theta+b_r)\kappa_r = 0.\end{aligned}\right\} \tag{15}$$

Since, from (9) and (10),

$$b_r\kappa_r = \epsilon_r^* \quad \text{and} \quad b_\theta\kappa_\theta = \epsilon_\theta^*,$$

then

$$d_r = \frac{b_r\kappa_r+\nu b_\theta\kappa_\theta}{\kappa_r+\nu\kappa_\theta} = \frac{\epsilon_r^*+\nu\epsilon_\theta^*}{\kappa_r+\nu\kappa_\theta},$$

or

$$\delta_r \equiv \frac{d_r}{(h/2)} = 2f\frac{\epsilon_r^*+\nu\epsilon_\theta^*}{\phi_r+\nu\phi_\theta}, \tag{16}$$

and similarly,

$$\delta_\theta \equiv \frac{d_\theta}{(h/2)} = 2f\frac{\epsilon_\theta^*+\nu\epsilon_r^*}{\phi_\theta+\nu\phi_r}. \tag{16}'$$

By comparing (16), (16)', and (13), it is clear that in the general case $\delta_r \neq \beta_r$ and $\delta_\theta \neq \beta_\theta$, i.e., the fiber at which the stress vanishes may have a different location from that at which each strain vanishes; in other words, in the two-dimensional stress state discussed, there will not be a common neutral surface for both stress and strain.

Since $\sigma_r = Y$ at $z = c_r - d_r$, it is found from (14) that

$$(c_r-d_r+b_r)\kappa_r+\nu(c_r-d_r+b_\theta)\kappa_\theta = Y(1-\nu^2)/E = \kappa_e.h/2,$$

or by using (15),

$$c_r(\kappa_r+\nu\kappa_\theta) = \kappa_e.h/2.$$

Hence, by noting (3)' and (4)',

$$\gamma_r \equiv \frac{c_r}{(h/2)} = \frac{1}{\phi_r+\nu\phi_\theta} = -\frac{1}{f\left(\zeta''+\nu\frac{\zeta'}{\rho}\right)}, \tag{17}$$

and similarly,

$$\gamma_\theta \equiv \frac{c_\theta}{(h/2)} = \frac{1}{\phi_\theta+\nu\phi_r} = -\frac{1}{f\left(\frac{\zeta'}{\rho}+\nu\zeta''\right)}. \tag{17}'$$

Then, by writing

$$s_r \equiv \epsilon_r^* + \nu\epsilon_\theta^* = \xi' + \tfrac{1}{2}\zeta'^2 + \nu\frac{\xi}{\rho}$$

and

$$s_\theta \equiv \epsilon_\theta^* + \nu\epsilon_r^* = \frac{\xi}{\rho} + \nu\xi' + \frac{\nu}{2}\zeta'^2, \qquad (18)$$

it is found from (16) and (17) that

$$\delta_r = 2fs_r\gamma_r = \frac{2\xi' + \xi'^2 + 2\nu\dfrac{\xi}{\rho}}{\zeta'' + \nu\dfrac{\zeta'}{\rho}}$$

and

$$\delta_\theta = 2fs_\theta\gamma_\theta = \frac{2\dfrac{\xi}{\rho} + 2\nu\xi' + \nu\zeta'^2}{\dfrac{\zeta'}{\rho} + \nu\zeta''}. \qquad (19)$$

Expressions (17) and (19) show that the distributions of σ_r and σ_θ are determined by the components of the displacement of points in the middle plane of the plate and their derivatives.

For the different types of stress distribution, expressions (17), (18), and (19) remain the same, but the corresponding relationships between (γ, δ) and (m, n) will be different from each other; m denotes the nondimensional bending moment and n is the nondimensional in-plane force. In paper [9], it is proved that the three types of stress distribution correspond with three different regimes in the (m, n) plane, respectively, as shown in Fig. 4, where

(*i*) E_R is the elastic régime corresponding to Fig. 3(*a*);
(*ii*) *PI* is the primary plastic régime corresponding to Fig. 3(*b*);
(*iii*) *PII* is the secondary plastic régime corresponding to Fig. 3(*c*).

Now write down the relationships between (γ, δ) and (m, n) according to the results in [9] and use the following symbols,

$$m_r = \frac{M_r}{M_e}, \quad m_\theta = \frac{M_\theta}{M_e}, \qquad (20)$$

and

$$n_r = \frac{N_r}{N_e}, \quad n_\theta = \frac{N_\theta}{N_e}, \qquad (21)$$

where

$$M_e = \frac{1}{6}Yh^2 \qquad (22)$$

is the initial yield bending moment per unit width. Also,

$$N_e = Yh, \qquad (23)$$

is the initial yield force per unit width in tension or compression.

(*i*) If

$$\gamma_r - |\delta_r| \geqq 1, \qquad (24)$$

then (m_r, n_r) must be in régime E_R, and

$$m_r = \frac{1}{\gamma_r} \qquad (25)$$

and

$$n_r = \frac{\delta_r}{\gamma_r}. \qquad (26)$$

Similarly, if

$$\gamma_\theta - |\delta_\theta| \geq 1, \qquad (24)'$$

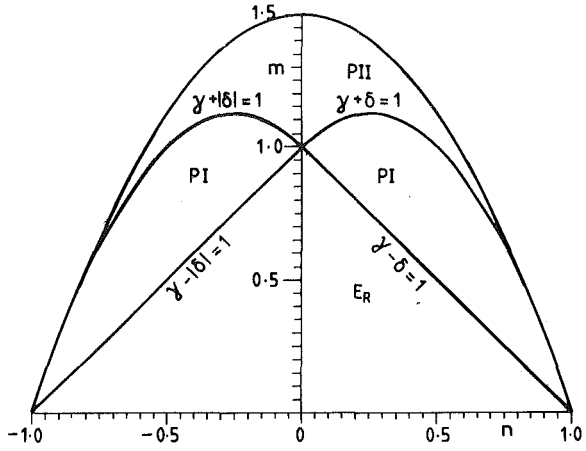

Fig. 4 Three different régimes in the (m, n) plane

then (m_θ, n_θ) must be in régime E_R, and

$$m_\theta = \frac{1}{\gamma_\theta} \qquad (25)'$$

and

$$n_\theta = \frac{\delta_\theta}{\gamma_\theta}. \qquad (26)'$$

(*ii*) If

$$\left.\begin{aligned}\gamma_r - |\delta_r| &< 1\\ \gamma_r + |\delta_r| &\geq 1,\end{aligned}\right\} \qquad (27)$$

but

then (m_r, n_r) must be in régime *PI*, and

$$m_r = \frac{\psi_r^2}{4\gamma_r}(3 - \psi_r) \qquad (28)$$

and

$$n_r = \frac{\delta_r}{|\delta_r|}\cdot\left\{1 - \frac{\psi_r^2}{4\gamma_r}\right\}, \qquad (29)$$

where

$$\psi_r = 1 - |\delta_r| + \gamma_r. \qquad (30)$$

Similarly, if

$$\left.\begin{aligned}\gamma_\theta - |\delta_\theta| &< 1\\ \gamma_\theta + |\delta_\theta| &\geq 1,\end{aligned}\right\} \qquad (27)'$$

but

then (m_θ, n_θ) must be in régime *PI*, with

$$m_\theta = \frac{\psi_\theta^2}{4\gamma_\theta}(3 - \psi_\theta) \qquad (28)'$$

and

$$n_\theta = \frac{\delta_\theta}{|\delta_\theta|}\cdot\left\{1 - \frac{\psi_\theta^2}{4\gamma_\theta}\right\}, \qquad (29)'$$

where

$$\psi_\theta = 1 - |\delta_\theta| + \gamma_\theta. \qquad (30)'$$

(*iii*) If

$$\gamma_r + |\delta_r| < 1, \qquad (31)$$

then (m_r, n_r) must be in régime *PII*, and

$$m_r = \frac{3}{2}(1 - \delta_r^2) - \frac{1}{2}\gamma_r^2 \qquad (32)$$

and

$$n_r = \delta_r. \tag{33}$$

Similarly, if

$$\gamma_\theta + |\delta_\theta| < 1, \tag{31}'$$

then (m_θ, n_θ) must be in régime *PII*, and

$$m_\theta = \frac{3}{2}(1-\delta_\theta{}^2) - \frac{1}{2}\gamma_\theta{}^2 \tag{32}'$$

and

$$n_\theta = \delta_\theta. \tag{33}'$$

For any one of the three types of stress distribution, the equilibrium equations for this problem are [6]

$$\frac{dN_r}{dr} + \frac{N_r - N_\theta}{r} = 0 \tag{34}$$

and

$$\frac{dM_r}{dr} + \frac{M_r - M_\theta}{r} + N_r \frac{dw}{dr} = 0, \tag{35}$$

or in nondimensional form,

$$n_r' = -\frac{1}{\rho}(n_r - n_\theta) \tag{36}$$

and

$$m_r' = -\frac{1}{\rho}(m_r - m_\theta) - 6n_r\zeta', \tag{37}$$

so that when n_r, n_θ, m_r, m_θ, and ζ' are known, n_r' and m_r' can be calculated. In the next step, they can be used for finding ξ'' and ζ''', but again there is a need to discuss three different cases.

(*i*) When (m_r, n_r) is in régime E_R, from (25), (26), (17), and (19) we find that

$$m_r' = -f\left(\zeta'' + \nu\frac{\zeta'}{\rho}\right)' = -f\left(\zeta''' + \nu\frac{\zeta''}{\rho} - \nu\frac{\zeta'}{\rho^2}\right)$$

and

$$n_r' = 2f\left(\xi' + \frac{1}{2}\zeta'^2 + \nu\frac{\xi}{\rho}\right)' = 2f\left(\xi'' + \zeta'\zeta'' + \nu\frac{\xi'}{\rho} - \nu\frac{\xi}{\rho^2}\right),$$

so that

$$\zeta''' = -\frac{m_r'}{f} - \nu\frac{\zeta''}{\rho} + \nu\frac{\zeta'}{\rho^2} \tag{38}$$

and

$$\xi'' = \frac{n_r'}{2f} - \zeta'\zeta'' - \nu\frac{\xi'}{\rho} + \nu\frac{\xi}{\rho^2}. \tag{39}$$

(*ii*) When (m_r, n_r) is in régime *PI*, since in this problem $\delta_r > 0$ (this can be verified by reference to all of the numerical results given later), expressions (28) and (29) become

$$n_r = 1 - \frac{\psi_r{}^2}{4\gamma_r} \tag{29}''$$

and

$$m_r = (1-n_r)(3-\psi_r). \tag{28}''$$

Thus, from (28)″,

$$m_r' = -n_r'(3-\psi_r) - (1-n_r)\psi_r'$$

or

$$\psi_r' = \{-n_r'(3-\psi_r) - m_r'\}/(1-n_r), \tag{40}$$

and from (29)″,

$$n_r' = -\frac{\psi_r\psi_r'}{2\gamma_r} + \frac{\psi_r{}^2}{4\gamma_r{}^2}\gamma_r' = \frac{1}{\gamma_r}\left\{-\frac{\psi_r\psi_r'}{2} + (1-n_r)\gamma_r'\right\}$$

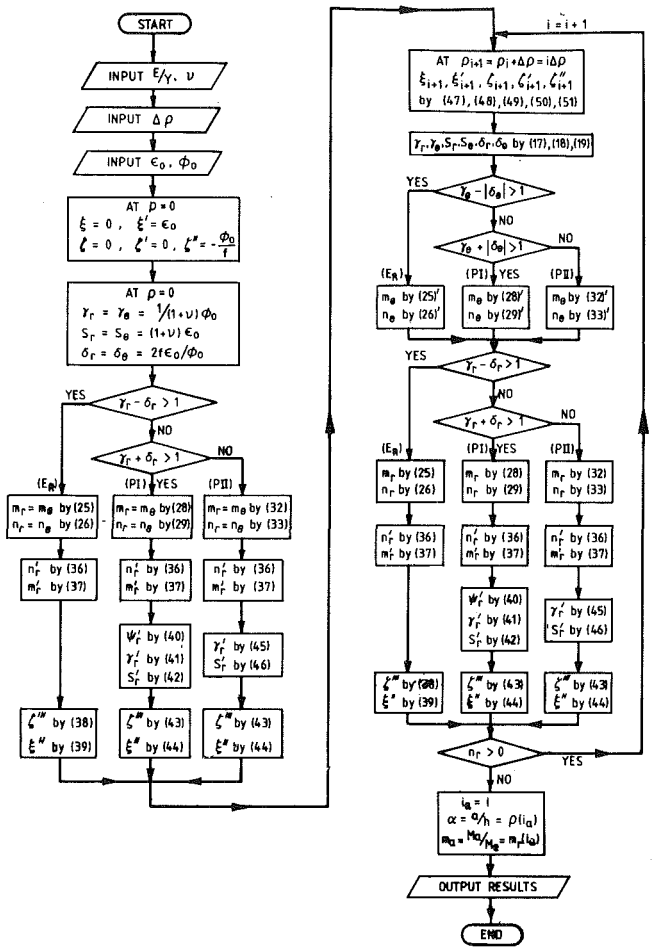

Fig. 5 The flow chart for the computing program from ϵ_0 and ϕ_0 to α, m_a, and so on

or

$$\gamma_r' = \left\{n_r'\gamma_r + \frac{1}{2}\psi_r\psi_r'\right\}/(1-n_r). \tag{41}$$

From (30), we have

$$\psi_r' = -2f(s_r\gamma_r' + s_r'\gamma_r) + \gamma_r',$$

so that

$$s_r' = \left\{\frac{\gamma_r' - \psi_r'}{2f} - s_r\gamma_r'\right\}/\gamma_r. \tag{42}$$

Lastly, from (17) and (18) we obtain

$$\zeta''' = \frac{\gamma_r'}{f\gamma_r{}^2} - \nu\frac{\zeta''}{\rho} + \nu\frac{\zeta'}{\rho^2} \tag{43}$$

and

$$\xi'' = s_r' - \zeta'\zeta'' - \nu\frac{\xi'}{\rho} + \nu\frac{\xi}{\rho^2}. \tag{44}$$

(*iii*) When (m_r, n_r) is in régime *PII*, from (32) and (33),

$$m_r' = -3n_r n_r' - \gamma_r\gamma_r'$$

and

$$n_r' = 2f(s_r\gamma_r' + s_r'\gamma_r),$$

so that

$$\gamma_r' = (-3n_r n_r' - m_r')/\gamma_r \tag{45}$$

and

$$s_r' = \left(\frac{n_r'}{2f} - s_r \gamma_r' \right) / \gamma_r. \tag{46}$$

Then, from (17) and (18) expressions for ζ''' and ξ'', which are similar to (43) and (44), are obtained.

At this point, all the basic equations required for a full solution to our problem have been obtained.

3 Computing Procedure

The problem discussed in this paper is one of geometrical and material nonlinearity, but the basic equations can be solved numerically by starting from the center of the plate and advancing by small increments in the radial direction.

By assuming a certain radial strain at the center, say,

$$\epsilon_r^* |_{\rho=0} = \epsilon_\theta^* |_{\rho=0} = \epsilon_0$$

and a certain uniform curvature at the center

$$\phi_r |_{\rho=0} = \phi_\theta |_{\rho=0} = \phi_0,$$

where ϵ_0 and ϕ_0 are chosen constants, then

$$\xi = 0, \quad \xi' = \epsilon_0$$

and

$$\zeta = \zeta' = 0, \quad \zeta'' = -\phi_0 / f$$

at $\rho = 0$.

Then $\gamma_r, \gamma_\theta, s_r, s_\theta, \delta_r, \delta_\theta, m_r, m_\theta, n_r, n_\theta, n_r', m_r', \xi''$, and ζ''' can be calculated in order, by means of the expressions obtained in Section 2.

As long as the values of $\xi, \xi', \xi'', \zeta, \zeta', \zeta''$, and ζ''' are known around the circle $\rho_i = (i-1)\Delta\rho$ $(i = 1, 2, 3, \ldots)$, a radial step of length $\Delta\rho$ can be made and the values of ξ, ξ', ζ, ζ', and ζ'' at $\rho_{i+1} = i\Delta\rho = \rho_i + \Delta\rho$ can be calculated approximately by means of Taylor's expansion, thus,

$$\xi_{i+1} = \xi_i + \xi_i' \Delta\rho + \frac{1}{2} \xi_i'' (\Delta\rho)^2, \tag{47}$$

$$\xi_{i+1}' = \xi_i' + \xi_i'' \Delta\rho, \tag{48}$$

$$\zeta_{i+1} = \zeta_i + \zeta_i' \Delta\rho + \frac{1}{2} \zeta_i'' (\Delta\rho)^2 + \frac{1}{6} \zeta_i''' (\Delta\rho)^3, \tag{49}$$

$$\zeta_{i+1}' = \zeta_i' + \zeta_i'' \Delta\rho + \frac{1}{2} \zeta_i''' (\Delta\rho)^2, \tag{50}$$

and

$$\zeta_{i+1}'' = \zeta_i'' + \zeta_i''' \Delta\rho. \tag{51}$$

According to the chosen length of step, $\Delta\rho$, the preceding procedure is repeated, until at a certain value of $\rho = \alpha = a/h$, the radial force vanishes, i.e.,

$$n_r |_{\rho=\alpha} = 0. \tag{52}$$

If

$$m_r |_{\rho=\alpha} = m_a \equiv \frac{M_a}{M_e}, \tag{53}$$

then the solution for the circular plate of radius $a = \alpha h$ bent by moments $M_a = m_a M_e$ and distributed uniformly around the plate periphery has been obtained.

Figure 5 shows the flow diagram for the computing procedure from ϵ_0 and ϕ_0 to α, m_a and so on.

In most practical cases, the radius of a plate and the bending moment along its circumference are given, i.e., α and m_a, but it remains to find the corresponding values of ϵ_0 and ϕ_0 in order to calculate the distributions of bending moments, in-plane forces, and displacements in the whole plate. To meet this requirement another program is produced, as shown in Fig. 6.

A parallel program to handle the unbending problem has been developed. As pointed out in [9], it can be proved that only if $(m + n) > 2$, can some fibers reyield during unloading; but this does not occur. Hence, the unbending process is entirely elastic and the parallel computing program can be easily set up. By assuming that the unbending results can be simply subtracted from the bending results, the distributions of $m_r, m_\theta, n_r, n_\theta, \xi$, and ζ after unloading can be obtained so that the springback is determined in detail.

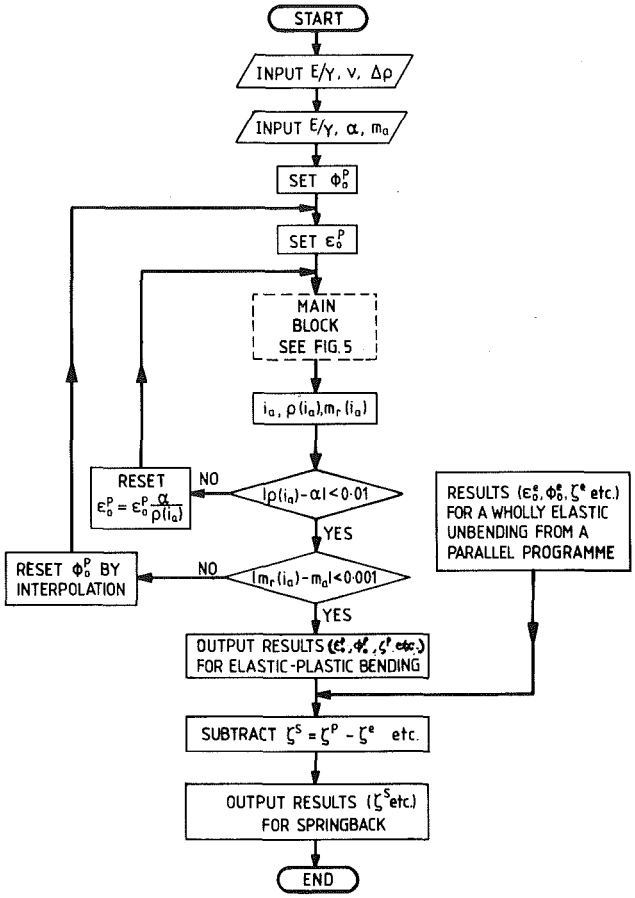

Fig. 6 The flow chart for the computing program from α, m_a to all results for elastic-plastic bending and springback

4 Numerical Examples

By taking $E/Y = 500$, $\nu = 0.3$, and $\Delta\rho = 0.1$ or 0.2—which imply a computing step length of 1/10 or 1/5 of the thickness of the plate, respectively—many interesting examples can be given. The computed results show that the differences between the results for $\Delta\rho = 0.2$ and for $\Delta\rho = 0.1$ are only between about 1 and 2 percent, so that there is good reason to believe that the computed results for these lengths of step are already relatively accurate.

Figure 7 shows results for a plate for which $\alpha = a/h = 20$ and for edge moment $m_a = M_a/M_e = 1.165$. In Fig. 7(*a*), the distributions of the bending moments (m_r and m_θ), the in-plane forces (n_r and n_θ), and the displacement components (ξ and ζ) are shown as functions of $\rho = r/h$. The divisions between the elastic and plastic zones in the plate are shown in Figs. 7(*b*) and (*c*), where dimensions in the z-direction are enlarged relative to the dimensions in the r-direction. Obviously, the "neutral surfaces," i.e., the surface for $\sigma_r = 0$ and the surface for $\sigma_\theta = 0$ are displaced from the middle plane toward the upper surface of the plate, but for the r-direction and the θ-direction there are different "neutral surfaces" and different plastic zones. In Fig. 7(*d*) of the figure

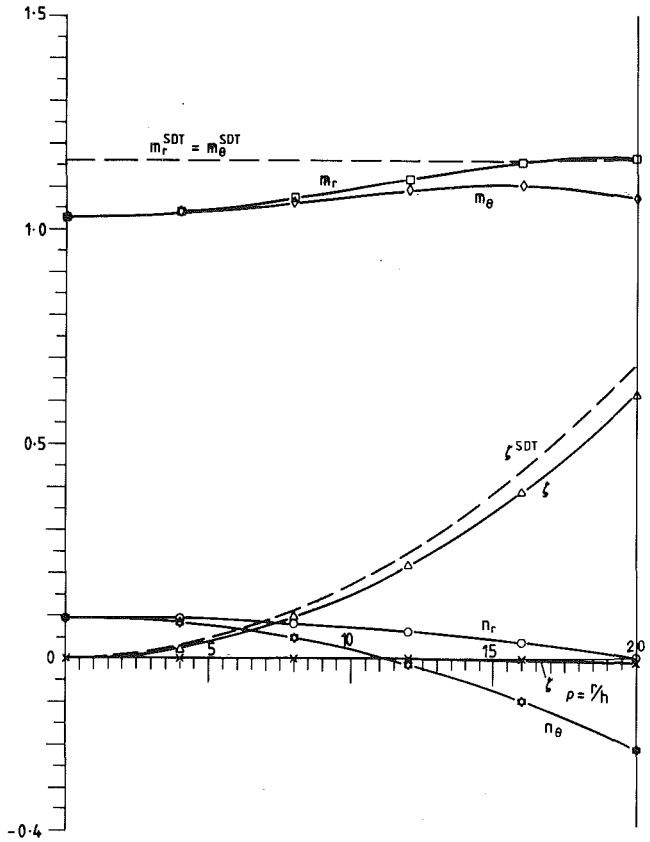

Fig. 7(*a*) The distributions of the bending moments, in-plane forces, and displacements; —— large deflection theory; ---- small deflection theory

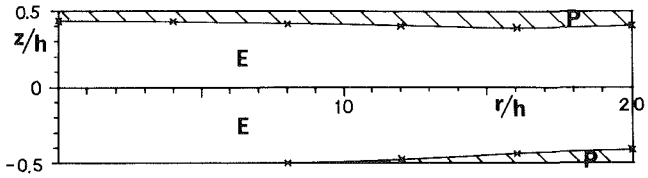

Fig. 7(*b*) The divisions between the elastic and plastic zones in the *r*-direction. *E* = elastic; *P* = plastic.

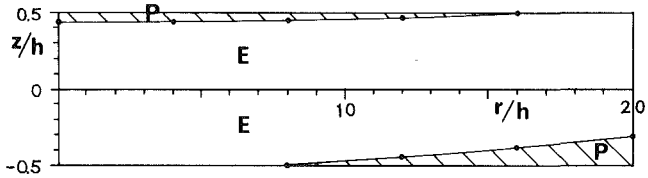

Fig. 7(*c*) The divisions between the elastic and plastic zones in the θ-direction. *E* = elastic; *P* = plastic.

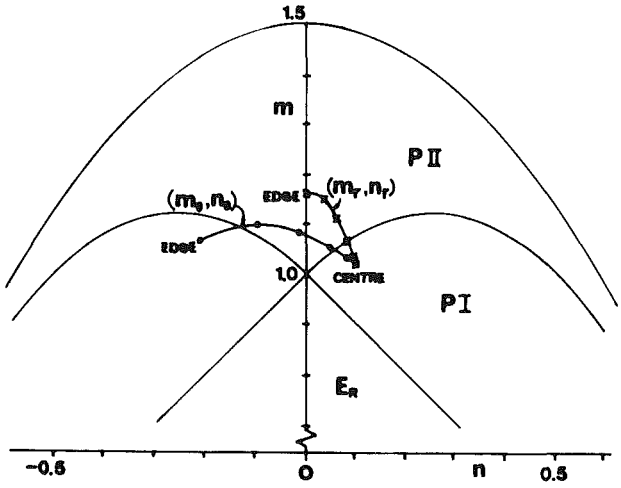

Fig. 7(*d*) The loci of (m_r, n_r) and (m_θ, n_θ) in the (m, n) plane

Fig. 7 The computed results for $\alpha = a/h = 20$ and $m_a = M_a/M_e = 1.1623$

Table 1 Principal results for various a/h and M/M_e ratios

Radius of plate $\alpha = a/h$	20 (Fig. 7)	20	30	30
Edge moment $m_a = M/M_e$	1.1623	1.4001	1.1652	1.400
ϵ_0^p	0.00013775	0.0002000	0.0002050	0.00022943
ϕ_0^p	0.80	1.00	0.60	0.6857
$(m_r)_{max}$	1.1647	1.4029	1.1694	1.4050
$(m_r)_{min}$, at center	1.0268	1.1860	0.7800	0.8889
$(m_r)_{min}/m_a$	0.8834	0.8471	0.6694	0.6349
$(m_\theta)_{max}$	1.1008	1.3080	0.9904	1.1864
$(n_r)_{max}$, at center	0.0938	0.1099	0.1464	0.1630
$(n_r)_{min}$, at edge	0	0	0	0
$(n_\theta)_{min}$, at edge	−0.2105	−0.2708	−0.3487	−0.4122
$\lvert(n_\theta)_{min}\rvert/m_a$	0.1811	0.1934	0.2993	0.2944
ζ_{max}	0.6135	0.8453	1.1408	1.4236
ζ_{max}^{SDT} (Small Deflection Theory)	0.6822	1.2578	1.5398	2.8189
$\zeta_{max}^{SDT}/\zeta_{max}$	1.1120	1.4880	1.3498	1.9801
ξ_{max}	0.0005	0.0007	0.0013	0.0013
ξ_{min}, at edge	−0.0099	−0.0204	−0.0241	−0.0413
$\lvert\xi_{min}\rvert/\zeta_{max}$	0.0161	0.0241	0.0211	0.0290
regimes for (m_r, n_r)	$PI \rightarrow PII$	PII	$E_R \rightarrow PI \rightarrow PII$	$PI \rightarrow PII$
regimes for (m_θ, n_θ)	$PI \rightarrow PII \rightarrow -PI$	PII	$E_R \rightarrow -PI$	$PI \rightarrow PII \rightarrow -PI$

the corresponding loci in the (m, n) plane are shown. At the center of the plate always $m_r = m_\theta$ and $n_r = n_\theta$, but with increasing values of $\rho = r/h$, the loci of (m_r, n_r) and (m_θ, n_θ) pass through different regimes in the (m, n) plane.

Some principal results obtained are assembled in Table 1.

5 Comparison With Small Deflection Theory

In the elementary or small deflection theory for an elastic perfectly plastic circular plate bent by an uniform edge moment, (see [1]), the bending moments m_r and m_θ are distributed uniformly throughout the whole plate, there is no

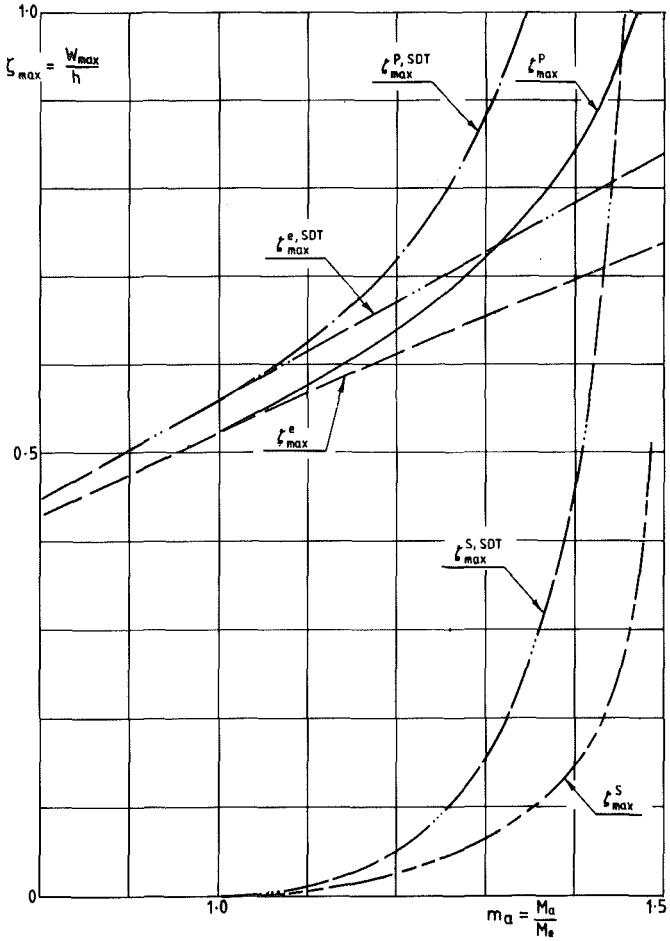

Fig. 8 The relationship between the maximum deflection of a plate and the edge moment for $\alpha = a/h = 20$. *e* = elastic; *p* = plastic bending; *s* = springback; *SDT* = small deflection theory.

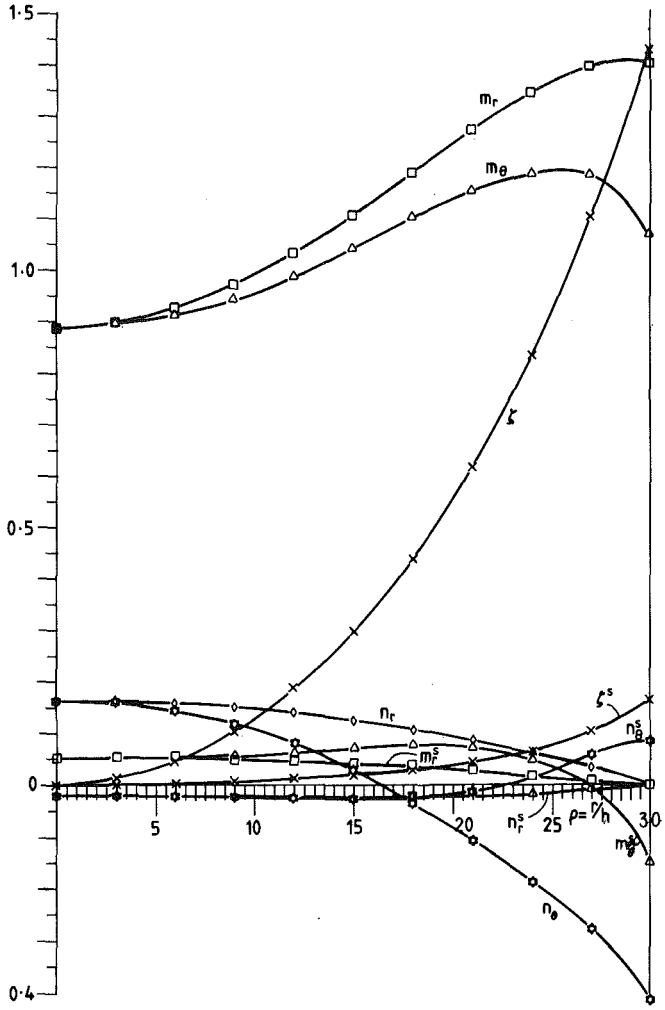

Fig. 9 The distribution of bending moments, in-plane forces, and deflection before and after unloading

in-plane force in the plate, and the deformed plate has an uniform curvature in any direction.

Comparison of results based on the small deflection theory and those based on large deflection theory as obtained in this paper has the following obvious features:

(*a*) The bending moments are no longer distributed uniformly in the plate, and the larger the plate ratio a/h, the smaller the bending moments at the center.

(*b*) Significant in-plane forces appear, especially around the center where it is tensile in both directions; the in-plane forces may play a vital role in the buckling of the plate. See [10] for experimental examples.

(*c*) Deflections of the plate according to large deflection theory are smaller than that for small deflection theory. Also, the larger the radius-thickness ratio of the plate and the edge moments, the larger the difference between these deflections.

According to small deflection theory [1], the radius of curvature of the deformed circular plate subjected to edge moments is

$$R^{SDT} = \frac{Eh}{2Y(1-\nu)} \cdot \sqrt{3-2m_a}, \tag{54}$$

and the maximum deflection is

$$W^{SDT}_{max} \simeq \frac{a^2}{2R^{SDT}} = \frac{a^2 Y(1-\nu)}{Eh} \cdot \frac{1}{\sqrt{3-2m_a}}, \tag{55}$$

or in nondimensional form,

$$\zeta^{SDT}_{max} \equiv \frac{W^{SDT}_{max}}{h} = \frac{\alpha^2 Y(1-\nu)}{E} \cdot \frac{1}{\sqrt{3-2m_a}}; \tag{56}$$

the superscript *SDT* refers to the "small deflection theory".

Figure 8 compares ζ^{SDT}_{max} and ζ_{max}, for $a/h = 20$, as based on the large deflection theory. It has been found that for $\alpha = a/h = 10$, ζ^{SDT}_{max} gives a good approximation to ζ_{max}; for $\alpha = a/h = 20$ (Fig. 8) when $m_a \leq 1.2$, the relative error of ζ^{SDT}_{max} is less than 13 percent; and for $\alpha = a/h = 30$, ζ^{SDT}_{max} is much larger than ζ_{max}. Thus small deflection theory may only be applied for plates of small a/h ratio, say, $a/h \leq 20$; this coincides with the conclusion in [2].

6 On Springback

Following the flow chart in Fig. 6, some of the numerical calculations have been carried out to arrive at distributions of bending moments, in-plane forces, and displacements. A portion of the results is shown in Table 2. Results for $\alpha = a/h = 30$ and $m_a = 1.400$ are as plotted in Fig. 9, where m^s_r, m^s_θ, n^s_r, n^s_θ, and ζ^s show the distributions after unbending. If needed, the residual stresses in the plate can easily be calculated from these values.

In small deflection theory, $m^s_r = m^s_\theta = n^s_r = n^s_\theta = 0$ in the plate after unbending. Then, the final deflection of the plate is determined by (see [1]),

$$\zeta^{s,SDT}_{max} = \frac{\alpha^2 Y(1-\nu)}{E} \left\{ \frac{1}{\sqrt{3-2m_a}} - m_a \right\}. \tag{57}$$

Taking $E/Y = 500$, $\nu = 0.3$, and $\alpha = a/h = 20$, some calculated results are as shown in Fig. 8 and Tables 1 and 2. It can be seen that the small deflection theory cannot well ap-

Table 2 Principal results for springback for different a/h and M/M_e ratios

Radius of plate α		20	20	30	30
Edge moment m_a		1.1623	1.4001	1.1652	1.4001
ϵ_0^p		0.00013775	0.00020000	0.00020500	0.00022943
ϕ_0^p		0.8000	1.0000	0.6000	0.6857
ϵ_0^e		0.00013960	0.00018830	0.00020650	0.00025640
ϕ_0^e		0.7848	0.9040	0.5894	0.6432
ϵ_0^s		−0.00000185	0.00001170	−0.00000150	−0.00002697
ϕ_0^s		0.0152	0.0960	0.0106	0.0425
	m_r^s	0.0066	0.0108	0.0138	0.0527
final values	m_θ^s	0.0066	0.0108	0.0138	0.0527
after unloading	n_r^s	−0.0059	−0.0246	−0.0011	−0.0201
at the center	n_θ^s	−0.0059	−0.0246	−0.0011	−0.0201
	ζ^s	0	0	0	0
	m_r^s	0	0	0	0
final values	m_θ^s	−0.0505	−0.0797	−0.0950	−0.1472
after unloading	n_r^s	0	0	0	0
at the edge	n_θ^s	0.0203	0.0478	0.0309	0.0838
	ζ^s	0.0171	0.1479	0.0256	0.1626
$\zeta^p_{\max}$		0.6135	0.8453	1.1408	1.4236
$\zeta^s_{\max}/\zeta^p_{\max}$		0.0279	0.1750	0.0224	0.1142

proximate the final deflection $\zeta^s_{\max}$, even when a/h is as small as about 20.

7 Conclusions

(*i*) By using the formulation in this paper and the corresponding computing procedure, the large deflection of an elastic-perfectly plastic circular plate subjected to edge moments can be arrived at. Our method and programs can be applied to any plate with various dimensions and various edge moments and also can be applied to determine its springback.

(*ii*) In the large deflection theory, the in-plane forces play an important role, and the distributions of bending moments and in-plane forces are no longer uniform as they are with the small deflection theory.

(*iii*) Computed examples show that small deflection theory can only be applied for the plates with small a/h ratios, say $a/h \leq 20$, and this coincides with the conclusion in [2]; when springback is concerned, its range of application is smaller, say $a/h \leq 15$. Beyond these ranges, in general, the large deflection theory developed in this paper must be applied for metal plates.

References

1 Johnson, W., and Yu, T. X., "Springback After the Biaxial Elastic-Plastic Pure Bending of a Rectangular Plate,—I," *Int. J. Mech. Sci.*, Vol. 23, 1981, pp. 619–630.

2 Johnson, W., and Yu, T. X., "On the Range of Applicability of Results for the Springback of an Elastic/Perfectly Plastic Rectangular Plate After Subjecting it to Biaxial Pure Bending—II," *Int. J. Mech. Sci.*, Vol. 23, 1981, pp. 631–637.

3 Johnson, W., and Yu, T. X., "On Springback After the Pure Bending of Plates of Elastic Work-Hardening Material—III," *Int. J. Mech. Sci.*, Vol. 23, 1981, pp. 687–695.

4 Johnson, W., and Yu, T. X., "On the Range of Applicability of Results for the Springback of an Elastic/Linear Work-Hardening Rectangular Plate After Subjecting it to Biaxial Pure Bending—IV," *Int. J. Mech. Sci.*, Vol. 23, 1981, pp. 697–701.

5 Johnson, W., "The Mechanics of Some Industrial Pressing, Rolling and Forging Processes," In: *Mechanics of Solids: The Rodney Hill 60th Anniversary Volume*, H. G. Hopkins and M. J. Sewell, eds., Pergamon Press, New York, 1982, pp. 303–355.

6 Timoshenko, S., and Woinowsky-Kreiger, S., *Theory of Plates and Shells*, McGraw-Hill, New York, 1959.

7 Reissner, E., *Proc. Symposia Appl. Math.*, Vol. 1, 1949, p. 213.

8 Chen, W. F., and Atsuta, T., *Theory of Beam-columns*, McGraw-Hill, New York, 1976.

9 Yu, T. X., and Johnson, W., "The Influence of Axial Force on the Elastic-Plastic Bending and Springback of a Beam," *Journal of Mechanical Working Technology*, Vol. 6, 1982, pp. 5–23.

10 Johnson, W., and Singh, A. N., "Springback in Circular Blanks," *Metallurgia*, May 1980, pp. 275–280.

R. T. Shield
Professor and Head,
Department of Theoretical
and Applied Mechanics,
University of Illinois
at Urbana-Champaign,
Urbana, Ill. 61801
Mem. ASME

Uniqueness for Elastic Crack and Punch Problems

Uniqueness of solution is shown for equilibrium states for elastic bodies in smooth contact. The cases considered include a body with a crack that may open only partially under load with parts of the faces in frictionless contact. Indentation of a body by a smooth rigid punch and contact with an elastic foundation are also treated.

Introduction

The proofs of the uniqueness theorems of linear elastostatics are straightforward for mixed boundary-value problems in which the portions of the bounding surface where the various types of boundary conditions apply are known in advance. They rest on the positive-definiteness of the strain energy function and Clapeyron's work identity (equation (2)) (see [1], for example). For some problems, the portions of the surface where one boundary condition holds rather than another must be determined in solving the problem. Thus in the indentation of an elastic half space by a smooth rigid spherical punch, the radius of the contact area is chosen so that the solution involves only pressure on the contact area and so that outside the contact area there is no movement of material into the region occupied by the punch. This leads to a unique solution on the reasonable assumption that contact occurs over the entire portion of a circular area. Other problems with contact between elastic bodies or with bodies resting on elastic foundations can be more complex (for references see [2]), and uniqueness of a solution may not be so apparent. For a body with a nonplanar crack, only parts of the crack may open under load. For a crack on the interface between two elastic solids, Comninou [3] has derived a solution for tension applied normal to the interface under the assumption that the crack only opens partially with the faces in frictionless contact near the crack tips. Again it is of interest to know if such a solution is unique.

In the following we show through the work identity that positive-definiteness of the strain energy is sufficient to ensure uniqueness for problems involving smooth contact between surfaces of elastic bodies. We first consider a body containing a crack and then treat smooth contact between elastic bodies. Indentation by a smooth rigid punch is a limiting case but is treated separately. Uniqueness for an elastic body which can come into contact with a rigid body of known shape has been shown previously by Knops and Payne [4], and their proof covers identation by a rigid punch when the movement of the punch is known. Here we also treat the case when the loading applied to the die is specified instead of the displacement and rotation of the punch. Finally we consider an elastic body with support from an elastic foundation. Villaggio [5] has proved uniqueness for an elastic body with a plane face in contact with a plane elastic foundation. His proof is similar to that given here and does not depend on the formulation of the problem given in [5].

To apply the work identity (2), we require that any improper integrals that arise in the left-hand side of (2) from the solutions that we consider, be convergent (with a similar restriction on body force integrals), and so have uniqueness for states with finite total-strain energy. Knowles and Pucik [6] have shown that for plane crack problems, boundedness of displacement is sufficient to guarantee uniqueness.

Elastic Body With a Crack

We consider an elastic body, which may be inhomogeneous, with strain-energy density W given by

$$2W = c_{ijkl}\, e_{ij}\, e_{kl} \quad (c_{ijkl} = c_{klij} = c_{jikl}), \tag{1}$$

where e_{ij} are the infinitesimal strains. The components of displacement are $u_i(x)$ referred to rectangular Cartesian axes $x_i\,(i=1,\ 2,\ 3)$, and the usual summation convention is assumed for a repeated index. For equilibrium states with no body force we have

$$\int_S \mathbf{T}\cdot\mathbf{u}\, ds = \int_V c_{ijkl}\, e_{ij}\, e_{kl}\, dV, \tag{2}$$

where $\mathbf{T}$ is the surface traction on the boundary S of the region V occupied by the body. If the body is a composite, equilibrium will require the surface tractions to be continuous across interfaces and with continuous displacements the identity (2) will still hold.

In the reference state the body is unstressed and it contains a crack defined by a surface C interior to V, but possibly extending to the boundary of V, across which the material has no cohesion. A particular case would be a crack on an interface in a composite. We use $\mathbf{n}$ to denote the unit normal to one side of the surface C. The displacements and stresses may be discontinuous across C in an equilibrium state of the body and we use $\pm$ signs to indicate values on the two sides of C,

Contributed by the Applied Mechanics Division for publication in the JOURNAL OF APPLIED MECHANICS.

Discussion on this paper should be addressed to the Editorial Department, ASME, United Engineering Center, 345 East 47th Street, New York, N.Y. 10017, and will be accepted until two months after final publication of the paper itself in the JOURNAL OF APPLIED MECHANICS. Manuscript received by ASME Applied Mechanics Division, December, 1981.

with the + sign referring to the side of C with exterior normal $\mathbf{n}$. Thus if we were to suppose that C were part of the boundary of the body, the normal $\mathbf{n}$ would point out of the body for the material surface on the positive side of C and the exterior normal for the other crack surface would be $-\mathbf{n}$.

Under loading of the body, we assume that separation can occur over the crack or that portions of the two sides can remain in smooth contact with no tangential traction. Thus on the surface C equilibrium states satisfy either (*i*) separation with no traction transmitted across C or (*ii*) continuous normal displacement with pressure transmitted across C. We therefore require either

$$\left.\begin{array}{ll} (i)\ \ \mathbf{T}^+ = -\mathbf{T}^- = 0 & \text{when } (\mathbf{u}^+ - \mathbf{u}^-)\cdot n < 0 \\ \text{or} & \\ (ii)\ \ \mathbf{T}^+ = -\mathbf{T}^- = -p\mathbf{n} & \text{when } \mathbf{u}^+ \cdot \mathbf{n} = \mathbf{u}^- \cdot \mathbf{n} \end{array}\right\} \quad (3)$$

at each point of C, where $p(x)$ is the pressure transmitted across C. We extend the definition of $p(x)$ so that it is zero at points of C where (*i*) holds.

The loading of the body is supposed to be caused by a body force field $\mathbf{F}$ and prescribed surface loading in which at each point of S, each component of the surface traction or the corresponding component of the displacement is specified. If $\mathbf{u}_1$ and $\mathbf{u}_2$ are two possible displacement fields for the loading, the difference field

$$\mathbf{u} = \mathbf{u}_1 - \mathbf{u}_2$$

will be an equilibrium field for zero body force with each component of traction or the corresponding component of displacement zero on S. Because the solutions $\mathbf{u}_1$, $\mathbf{u}_2$ each satisfy (3) on C, we will have $\mathbf{T}^+ = -\mathbf{T}^-$ everywhere on C for the field $\mathbf{u}$.

If we use the identity (2) for the state $\mathbf{u}$ we must include the contribution from the crack surfaces to the left-hand side. There is zero contribution from S, so the left-hand side of (2) is

$$\int_C (\mathbf{T}^+ \cdot \mathbf{u}^+ + \mathbf{T}^- \cdot \mathbf{u}^-) dS = \int_C \mathbf{T}^+ \cdot (\mathbf{u}^+ - \mathbf{u}^-) dS.$$

The integrand of the latter integral can be written as

$$(p^{(2)} - p^{(1)})\{(\mathbf{u}_1^+ - \mathbf{u}_1^-)\cdot\mathbf{n} - (\mathbf{u}_2^+ - \mathbf{u}_2^-)\cdot\mathbf{n}\},$$

where $p^{(1)}$, $p^{(2)}$ are the crack surface pressures for the two solutions (zero where (*i*) holds). On portions of C where $\mathbf{u}_1$ and $\mathbf{u}_2$ either both satisfy (*i*) of (3) or both satisfy (*ii*) of (3), the integrand is zero. On a part of C where $\mathbf{u}_1$ satisfies (*i*) and $\mathbf{u}_2$ satisfies (*ii*) the integrand is

$$p^{(2)}(\mathbf{u}_1^+ - \mathbf{u}_1^-)\cdot\mathbf{n},$$

which is less than or equal to zero in view of (3). Similarly the integrand is nonpositive where $\mathbf{u}_1$ satisfies (*ii*) and $\mathbf{u}_2$ satisfies (*i*). Thus the left-hand side of (2) is less than or equal to zero but the right-hand side will be non-negative for a positive-definite strain energy W so that both sides must vanish in this case. It then follows that the fields $\mathbf{u}_1$, $\mathbf{u}_2$ generate the same strain field and the solution for the given loading is unique, except possibly for a rigid displacement, depending on the conditions on S.

The result also holds if the body has more than one crack. With the approach of the next section, the analysis can also be extended to include loading by contact with other elastic bodies.

Smooth Contact Between Elastic Bodies

For simplicity we consider contact between two elastic bodies over a nearly plane area, as in the Hertz theory. However the approach can be generalized to smooth contact between curved surfaces of bodies, such as occurs between a body with a cylindrical hole and a closely fitting lubricated pin, and contact between several bodies can be treated.

In the unstressed reference configuration, the bodies touch at the origin of coordinates with a common tangent plane $x_3 = 0$. The bodies occupy regions V_1 and V_2 and the $x_3 - $axis points into region V_2. Under loading contact may occur over surfaces C_1 and C_2 of the two bodies, defined as the nearly plane surfaces

$$C_1: \quad x_3 = f(x_1, x_2), \quad C_2: \quad x_3 = g(x_1, x_2),$$

where x_1, x_2 lie in a region C of the $x_1 - x_2$ plane enclosing the origin and the shape functions f and g satisfy

$$f(x_1, x_2) \le g(x_1, x_2).$$

The tangential tractions are zero on C_1 and C_2 and we denote the common value of T_3^2 and $-T_3^1$ by $p(x_1, x_2)$, where superscripts refer to the fields for the two bodies. The bodies do not penetrate each other so that

$$u_3^2 - u_3^1 \ge f - g \text{ on } C,$$

and we require

$$\left.\begin{array}{l} p = 0 \text{ when } u_3^2 - u_3^1 > f - g, \\ u_3^2 - u_3^1 = f - g \text{ when } p > 0 \end{array}\right\} \quad (4)$$

at each point of C.

On the remaining portions S_1 and S_2 of the surfaces of the bodies, we suppose that each component of the traction or the corresponding component of the displacement is prescribed. If we have two possible displacement fields $\mathbf{u}_1$ and $\mathbf{u}_2$ for the given loading over S_1 and S_2 and for a given body force field, the difference field

$$\mathbf{u} = \mathbf{u}_1 - \mathbf{u}_2$$

will be an equilibrium field for no body force and such that each component of the traction or the corresponding component of the displacement vanishes on S_1 and S_2.

If we use the identity (2) for the state $\mathbf{u}$, the contribution to the left-hand side comes only from the region of possible contact and it is

$$\int_{C_1 + C_2} \mathbf{T}\cdot\mathbf{u}\, dS = \int_C T_3^2 (u_3^2 - u_3^1) dx_1\, dx_2.$$

The integrand can be written

$$(p^{(1)} - p^{(2)})\{u_3^{2(1)} - u_3^{1(1)} - (u_3^{2(2)} - u_3^{1(2)})\},$$

where the superscripts in parentheses indicate values for the two solutions while the other superscripts refer to the two bodies as before. The integrand is zero on the parts of C where both solutions have no contact between the bodies (zero $p^{(1)}$ and $p^{(2)}$) or both have contact (the expression in the curly bracket vanishes). Where one solution, say $\mathbf{u}_1$, has contact and the other does not, the integrand is

$$p^{(1)}\{f - g - (u_3^{2(2)} - u_3^{1(2)})\}$$

and is therefore less than or equal to zero because $\mathbf{u}_2$ satisfies (4) and p is non-negative. Thus the left-hand side of (2) is less than or equal to zero so that both sides of (2) must be zero when the strain energy is positive-definite. Uniqueness of solution to within a rigid body displacement then follows.

Indentation by a Smooth Rigid Punch

The indentation of an elastic body by a smooth rigid punch can be treated as a limiting case of two elastic bodies in contact. Alternatively we can use a direct approach as indicated here for the case when the possible area of contact is a region C of the $x_1 - x_2$ plane enclosing the origin. The exterior normal to the body at the origin is along the x_3-axis, and the

remainder of the surface of the body is denoted by S. When the movement of the punch is known, the location of the punch surface after indentation has occurred will be known. We will then have

$$u_3 \leq f(x_1, x_2) \text{ on } C, \tag{5}$$

where f is a known function, and we require

$$\begin{aligned} p &= 0 \text{ when } u_3 < f, \\ u_3 &= f \text{ when } p > 0 \end{aligned}$$

at each point of C, where p is the contact pressure. On the remaining surface S each component of the traction or the corresponding component of the displacement is known.

If we have two possible displacement fields $\mathbf{u}_1$ and $\mathbf{u}_2$ for the given surface loading and a given body force field and examine (2) for the difference field $\mathbf{u} = \mathbf{u}_1 - \mathbf{u}_2$, the contribution to the left-hand side comes only from C and it is

$$\int_C (p^{(2)} - p^{(1)})(u_3^{(1)} - u_3^{(2)}) dx_1\, dx_2, \tag{6}$$

where the superscripts indicate values for the two solutions. Where both solutions have no contact or both have contact the integrand is zero. At points of C where $\mathbf{u}_1$ has contact and $\mathbf{u}_2$ does not, the integrand is

$$-p^{(1)}(f - u_3^{(2)})$$

and this is less than or equal to zero because p is non-negative and $\mathbf{u}_2$ satisfies (5). Thus for a positive-definite strain energy we are again led to uniqueness of the strain field. The proof has been given previously by Knops and Payne [4] for the case when contact with a smooth rigid body whose location is known may occur over a curved portion C of the surface of the body.

Instead of prescribing the movement of the punch, the downward force L on the punch and the moments M_1 and M_2 of the force about the x_1 and x_2 axes may be given. In this case for a known punch shape $f(x_1, x_2)$ the solution will satisfy

$$u_3 \leq f(x_1, x_2) - \delta + \alpha x_2 - \beta x_1 \text{ on } C,$$

where the constants α, β, δ are to be determined. The contact pressure must satisfy

$$L = \int_C p\, dx_1\, dx_2, \quad M_1 = -\int_C p x_2\, dx_1\, dx_2,$$

$$M_2 = \int_C p x_1\, dx_1\, dx_2. \tag{7}$$

(If the punch is constrained to indent without tilting, the constants α, β are zero and the values of M_1 and M_2 are not prescribed.)

If we apply (2) to the difference of two possible solutions, the left-hand side will be equal to (6). We now define $v^{(1)}$ and $v^{(2)}$ for points on C through

$$v^{(n)} = u_3^{(n)} + \delta^{(n)} - \alpha^{(n)} x_2 + \beta^{(n)} x_1 (n = 1, 2) \tag{8}$$

for the two solutions. Because the contact pressures both satisfy (7), if we substitute (8) into (6) the terms involving the constants will go out and the integral becomes

$$\int_C (p^{(2)} - p^{(1)})(v^{(1)} - v^{(2)}) dx_1\, dx_2,$$

where now $v^{(1)}$ and $v^{(2)}$ are less than or equal to f on C. The integral can now be seen to be less than or equal to zero and uniqueness follows as before.

Uniqueness for problems involving contact with several rigid dies or punches is similar and essentially amounts to extending the definition of the contact region C.

Smooth Contact With an Elastic Foundation

We now consider the case when a portion of the elastic body can receive support from an elastic foundation. For simplicity we assume that the foundation is plane but curved supports can also be treated. The portion C of the surface of the body that can come into contact with the body is the nearly plane surface

$$x_3 = f(x_1, x_2)$$

touching the plane $x_3 = 0$ but entirely above it and (x_1, x_2) lying in a region C of the $x_1 - x_2$ plane. The elastic foundation occupies part of the half space $x_3 \leq 0$, and the x_3-axis points into the elastic body. The foundation reacts only in compression with a reactive pressure proportional to the normal displacement of the surface, so that on C we require

$$\left.\begin{aligned} &p = 0 \text{ when } u_3 > -f, \\ &p = -K(u_3 + f) \text{ when } u_3 < -f, \end{aligned}\right\} \tag{9}$$

where $p(x_1, x_2)$ is the contact pressure and the positive constant K is the stiffness of the foundation. Boundary conditions on the remaining surface S of the body and a body force field are specified as before.

For the difference field of two possible solutions, the left-hand side of (2) again reduces to an integral over C. If we write the integrand as

$$(p^{(1)} - p^{(2)})\{(u_3^{(1)} + f) - (u_3^{(2)} + f)\}$$

we see that in view of (9) the integrand is less than or equal to zero where one or both solutions have contact with the foundation and is zero otherwise. Uniqueness of the strain field then follows as before for a positive-definite strain energy.

Acknowledgment

The author would like to thank Dr. I. Choi for reading the manuscript. The question of uniqueness of solution of elastic crack problems arose in a conversation with Dr. Colin Atkinson.

References

1 Sokolnikoff, I. S., *Mathematical Theory of Elasticity*, 2nd Ed., McGraw-Hill, New York, 1956.

2 Gladwell, G. L. M., *Contact Problems in the Classical Theory of Elasticity*, Sijthoff and Noordhoff, Alpen aan den Rijn, 1980.

3 Comninou, M., "The Interface Crack," ASME JOURNAL OF APPLIED MECHANICS, Vol. 44, 1977, pp. 631-636.

4 Knops, R. J., and Payne, L. E., *Uniqueness Theorems in Linear Elasticity*, Springer-Verlag, New York, 1971.

5 Villaggio, P., "A Unilateral Contact Problem in Linear Elasticity," *Journal of Elasticity*, Vol. 10, 1980, pp. 113-119.

6 Knowles, J. K., and Pucik, T. A., "Uniqueness for Plane Crack Problems in Linear Elastostatics," *Journal of Elasticity*, Vol. 3, 1973, pp. 155-160.

M. Kishida
Professor.

K. Sasaki
Graduate Student.

Department of Mechanical Engineering,
Hokkaido University,
North 13, West 8, Kita-ku,
Sapporo 060, Japan

H. Hanzawa
Rector,
Tomakomai Technical College,
443, Nishikioka,
Tomakomai 059-12, Japan

One Solution of Three-Dimensional Boundary Value Problems in the Couple-Stress Theory of Elasticity

This paper describes a numerical approach for elastic boundary value problems in the linear, couple-stress theory on the basis of the "indirect fictitious-boundary integral method." In this approach we introduce appropriate potentials corresponding to those for a concentrated force and a couple in an infinite medium, and reduce the problem to solving the simultaneous Fredholm type integral equations of the first kind.

As an example, the stress concentration problem is analyzed for a circular cylinder with a semicircular annular groove under uniaxial tension. The results are obtained for various values of parameters such as Poisson's ratio ν, characteristic length l, and the ratio η_r of bending, twisting moduli.

Introduction

Continuum mechanics introducing couple-stresses has been proposed by Mindlin and Tiersten [1], Truesdell and Toupin [2], and Koiter [3] to explain some discrepancies between theoretrical predictions and experimental results. Many researchers have applied this theory to fundamental elastic boundary value problems [4–6], but almost all of these works have been restricted to those for two or three-dimensional infinite media. As a matter of fact, to determine the new material constants adopted in the couple-stress theory, it is necessary to compare theoretical results with experiments. For this reason, we should examine three-dimensional, finite, elastic boundary value problems which can be easily confirmed by experiments.

By the way, many investigators have developed the boundary integral methods as an attractive method to analyze boundary value problems in classical elasticity. These may be classified into two types. One is the indirect boundary integral method [7, 8], which takes the density functions as the unknowns, and the other is the direct boundary integral method [9, 10], which takes boundary displacements and tractions as the unknowns. In addition, some researchers have introduced the concept of a fictitious boundary to obtain more accurate solutions by the simplest numerical quadrature [11, 12]. Also, one of authors and his collaborators have been analyzing many two and three-dimensional boundary value problems by direct and indirect boundary integral methods together with and without a fictitious boundary [12–16]. Through these analyses we know:

i The direct boundary integral method has the advantage of being able to obtain boundary displacements and tractions directly; on the other hand the use of a fictitious boundary doubles the number of unknown functions.

ii The indirect boundary integral method with fictitious boundary has the advantages that the potential field becomes smooth and continuous in the region under consideration, that stresses and their gradients on a real boundary and in its neighborhood can be obtained accurately by analytical differentiation, and that the convergence of a solution with the increase of subdivisions is rapid.

In this paper, we propose one method to attack three-dimensional boundary value problems in the couple-stress theory of elasticity. This method is based on the "indirect fictitious-boundary integral method," in which we get no jumps and no singularities in the potential and can obtain the solution with high accuracy. This analysis may also be understood as a method where concentrated forces and couples are distributed over a fictitious boundary in an infinite medium so as to satisfy the conditions on a real boundary.

As a numerical example, the stress concentration problem is analyzed for a circular cylinder with a semicircular annular groove under uniaxial tension. From the results obtained, it is verified that the present method is very effective for solving three-dimenisonal boundary value problems in the linear, couple-stress theory of elasticity.

Basic Equations

The fundamental equations governing the linear, couple-stress theory of homogeneous and istropic elastic solids were presented by Mindlin and Tiersten [1]. The stress equation of equilibrium is given by

$$\nabla \cdot \tau^S + \frac{1}{2} \nabla \times \nabla \cdot \mu^D = 0 \tag{1}$$

where τ^S is the symmetric part of a force-stress dyadic τ, μ^D is

Contributed by the Applied Mechanics Division for publication in the JOURNAL OF APPLIED MECHANICS.

Discussion on this paper should be addressed to the Editorial Department, ASME, United Engineering Center, 345 East 47th Street, New York, N.Y. 10017, and will be accepted until two months after final publication of the paper itself in the JOURNAL OF APPLIED MECHANICS. Manuscript received by ASME Applied Mechanics Division, March 1981; final revision, February, 1982.

the deviatric part of a couple-stress dyadic μ, and ∇ is the spatial gradient. Let $\mathbf{u}$ be the displacement vector, τ^S and μ^D then are given by

$$\tau^S = \lambda \nabla \cdot \mathbf{u} \mathbf{I} + \mu(\nabla \mathbf{u} + \mathbf{u} \nabla)$$
$$\mu^D = 2\mu l^2 (\nabla \nabla \times \mathbf{u} + \eta_r \nabla \times \mathbf{u} \nabla) \tag{2}$$

where λ and μ are Lamé's constants, l and η_r are the material constants adopted in the couple-stress theory, and $\mathbf{I}$ is the unit spatial dyadic. Also, l has a dimension of length and η_r is dimensionless. Substituting equations (2) into equation (1), one can obtain the displacement equation of equilibrium

$$(\lambda+\mu) \nabla \nabla \cdot \mathbf{u} + \mu \nabla^2 \mathbf{u} + \mu l^2 \nabla^2 \nabla \times \nabla \times \mathbf{u} = 0 \tag{3}$$

Any solution $\mathbf{u}$ of equation (3) is representable as [1]

$$\mathbf{u} = \mathbf{B} - l^2 \nabla \nabla \cdot \mathbf{B} - \frac{(\lambda+\mu)}{2(\lambda+2\mu)} \nabla [\mathbf{r} \cdot (1 - l^2 \nabla^2)\mathbf{B} + B_0] \tag{4}$$

where $\mathbf{r}$ is the spatial position vector, and $\mathbf{B}$ and B_0 are the vector and scalar functions, respectively, characterized by

$$(1 - l^2 \nabla^2) \nabla^2 \mathbf{B} = 0 \quad \text{and} \quad \nabla^2 B_0 = 0 \tag{5}$$

Let τ^A be the antisymmetric part of τ and $(\mu:\mathbf{I})$ the scalar of μ. Neither of them appears in the equation of equilibrium (1), and they are only related by

$$\tau^A = \frac{1}{2} \mathbf{I} \times [2\mu l^2 \nabla^2 \nabla \times \mathbf{u} + \frac{1}{3} \nabla (\mu:\mathbf{I})] \tag{6}$$

Namely, τ^A and $(\mu:\mathbf{I})$ cannot be determined independently. This is the reason why the couple-stress theory is said to be indeterminate.

Analysis

Consider a homogeneous and isotropic medium that occupies a "real-domain" R bounded by a closed smooth "real-boundary surface" S and is subjected to a force traction $\mathbf{T}$ and a couple traction $\mathbf{M}$ on S. We now suppose a closed Liapunov "fictitious-boundary surface" S^* outside S not intersecting each other, and extend a domain form R to a "fictitious-domain" R^* bounded by S^*. Hereafter we asterisk the quantities defined on S^*. A displacement vector $\mathbf{u}$ in R then satisfies equation (3) and is given by equation (4). When $l = 0$, equations (3) and (4) agree with a well-known equation of equilibrium and its Boussinesq-Papkovich solutions in the classical theory.

Now we can get the solution of a concentrated force $\mathbf{F}$ acting at the origin in an infinite medium [1] by

$$\mathbf{B} = \mathbf{F}[(1 - e^{-r/l})/r], \quad B_0 = 0$$

where r is a magnitude of a spatial position vector, and also that of a concentrated couple $\mathbf{C}$ [1] by

$$\mathbf{B} = -\mathbf{C} \times \nabla [(1 - e^{-r/l})/r], \quad B_0 = 0$$

In the linear, couple-stress theory, we can superpose these solutions. Therefore, according to the "indirect fictitious-boundary integral method," a continuous distribution of surface densities $\xi^*(\mathbf{q}^*)$ and $\zeta^*(\mathbf{q}^*)$, corresponding to concentrated force and couple, over a surface S^* generates the potential $\mathbf{B}$ for the present solution as follows:

$$\mathbf{B}(\mathbf{P}) = \int_{S^*} [\xi^*(\mathbf{q}^*)(1 - e^{-r_0/l})/r_0] dS^*(\mathbf{q}^*)$$
$$+ \int_{S^*} \zeta^*(\mathbf{q}^*) \times \nabla^* [(1 - e^{-r_0/l})/r_0] dS^*(\mathbf{q}^*) \tag{7}$$
$$B_0(\mathbf{P}) = 0$$

where $\xi^*(\mathbf{q}^*)$ and $\zeta^*(\mathbf{q}^*)$ are Hölder continuous vector densities at $\mathbf{q}^*$, $\mathbf{P}$ and $\mathbf{q}^*$ are the vector variables specifying points in R and on S^*, respectively, r_0 is the distance between $\mathbf{P}$ and

Nomenclature

a = radius of groove
h_i^* = length of the ith segment on Γ^*
l = characteristic length
m = number of segments
$\mathbf{n}$ = outward unit normal vector on S
$\mathbf{p}$ = vector variable specifying points on S
$\mathbf{p}_i$ = vector variable specifying point of intersection of normal line at $\mathbf{q}_i^*$ and Γ
$\mathbf{q}^*$ = vector variable specifying points on S^*
$\mathbf{q}_i^*$ = vector variable specifying nodal point on the ith segment on Γ^*
$\mathbf{q}_{i\pm 1/2}^*$ = vector variable specifying interval points of the ith segment on Γ^*
r_0 = distance between two points $\mathbf{P}$ and $\mathbf{q}^*$
$\mathbf{u}$ = displacement vector
x_1, x_2, x_3 = coordinates of the point $\mathbf{p}$
x_1^*, x_2^*, x_3^* = coordinates of the point $\mathbf{q}^*$
r, θ, z = cylindrical coordinates
$\mathbf{B}$ = vector function
B_0 = scalar function
D = diameter of cylinder
$\mathbf{I}$ = unit spatial dyadic
L = length of cylinder
$\mathbf{M}$ = couple traction on S
M_i = components of $\mathbf{M}$ in Cartesian coordinates ($i=1,2,3$)
$\mathbf{P}$ = vector variable specifying points in R including S
R = real domain
R^* = fictitious domain
S = real-boundary surface
S^* = fictitious-boundary surface
$\mathbf{T}$ = force traction on S
T_i = components of $\mathbf{T}$ in Cartesian coordinates ($i=1,2,3$)
$S.C.F.$ = stress concentration factor
X_1, X_2, X_3 = Cartesian coordinates
α_1 = $S.C.F.$ with respect to the first principal stress
α_2 = $S.C.F.$ with respect to the second principal stress
α_i = coefficient of fictitious-boundary distance
ζ^* = vector density on S^*
$\zeta_1^*, \zeta_2^*, \zeta_3^*$ = components of ζ^* in Cartesian coordinates
$\zeta_r^*, \zeta_\theta^*, \zeta_z^*$ = components of ζ^* in cylindrical coordinates
η_r = ratio of bending-twisting moduli
λ, μ = Lamé's constants
μ = couple-stress dyadic
μ^D = deviatric part of μ
$\mu:\mathbf{I}$ = scalar of μ
ν = Poisson's ratio
ξ^* = vector density on S^*
$\xi_1^*, \xi_2^*, \xi_3^*$ = components of ξ^* in Cartesian coordinates
$\xi_r^*, \xi_\theta^*, \xi_z^*$ = components of ξ^* in cylindrical coordinates
τ = force-stress dyadic
τ^A = antisymmetric part of τ
τ^S = symmetric part of τ
$\bar{\tau}$ = mean normal stress on minimum cross section of cylinder
Γ = contour of S in the plane of $\theta = 0$
Γ^* = contour of S^* in the plane of $\theta = 0$
∇ = spatial gradient
∇^2 = Laplace's operator
∞ = infinity
$\binom{n}{i}$ = combination

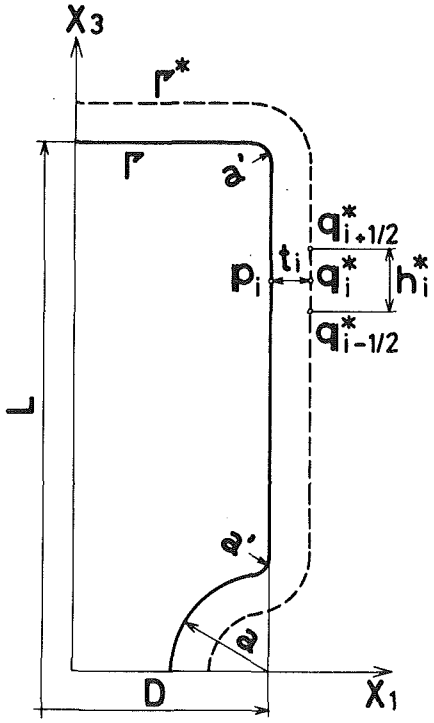

Fig. 1 Geometry of example problem

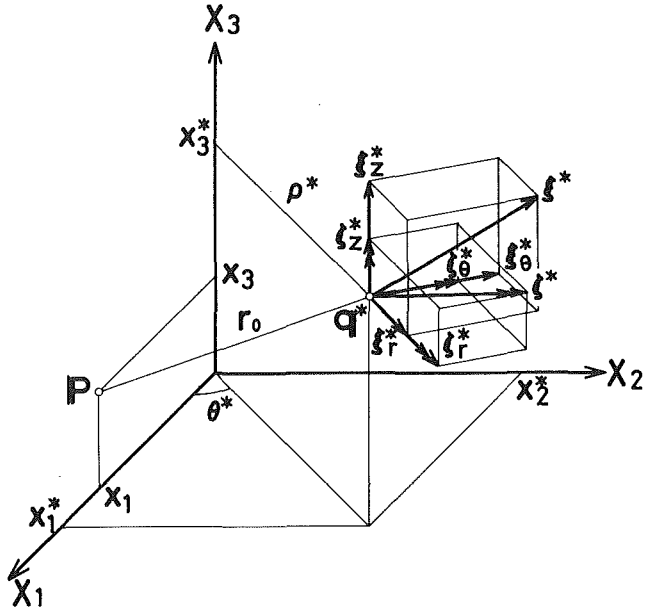

Fig. 2 Coordinate systems and sign convention

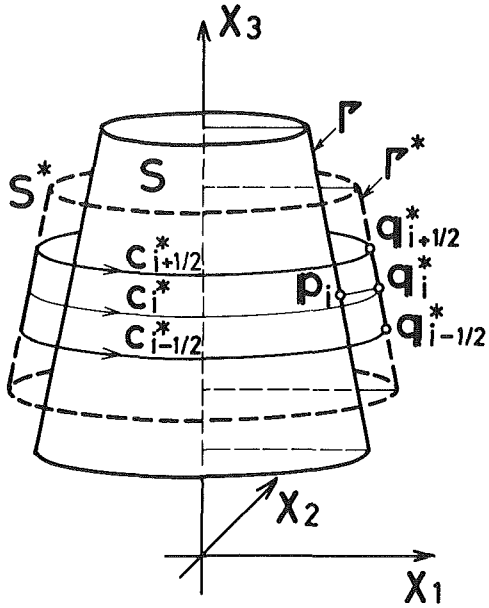

Fig. 3 Subdivision of fictitious-boundary surface S^*

$\mathbf{q}^*$, and ∇^* is the spatial gradient with respect to $\mathbf{q}^*$. As noted before, τ^A and $(\mu:\mathbf{I})$ remain indeterminate, but we can take $(\mu:\mathbf{I})$ to be identically zero without loss in generality [3], since they are not governed by the equation of equilibrium (1). Thus substituting equations (7) into equation (4), then into equations (2) and (6), we can obtain a force-stress $\tau = \tau^S + \tau^A$ and couple-stress $\mu = \mu^D$ in the forms of integral equations for $\xi^*(\mathbf{q}^*)$ and $\zeta^*(\mathbf{q}^*)$.

In this way, the present problem is reduced to solving the simultaneous integral equations for ξ^* and ζ^* on S^* under the boundary conditions

$$\mathbf{n}\cdot\tau=\mathbf{T} \quad \text{and} \quad \mathbf{n}\cdot\mu=\mathbf{M} \qquad \text{on } S \tag{8}$$

where $\mathbf{n}$ is the outward unit normal vector on S. Since $\mathbf{P}$ and $\mathbf{q}^*$ never coincide with each other, the relevant integral equations have no singularity. To solve these equations analytically is, generally speaking, very difficult, so it is rather convenient to solve them numerically.

Numerical Analysis

As a numerical example, we consider the stress concentration problem for a circular cylinder with a semicircular annular groove subjected to uniaxial tension parallel to X_3 axis as shown in Fig. 1. The problem being axisymmetric, we take a cylindrical coordinate system related to the Cartesian one as shown in Fig. 2, and formulate the problem in the plane of $\theta = 0$.

We define Γ and Γ^*, respectively, to be the contours of S and S^* in the plane of $\theta = 0$ (Figs. 1 and 3). For the sake of convenience, we divide Γ into m segments with equal length h and set the distance between Γ and Γ^* by t_i, and then define the coefficient of fictitious-boundary distance [12] by $\alpha_i = t_i/h$. The coefficient α_i is the most important parameter that affects the accuracy of solution, so that it should be determined with extreme care. Similarly we divide Γ^* into m segments, the ith segment being the length of $h_i{}^*$ and centered about a nodal point $\mathbf{q}_i{}^*$ midway between the interval points $\mathbf{q}^*_{i\pm1/2}$, and also S^* into m rings corresponding to m segments on Γ^* as in Fig. 3. On each ring, we suppose that the components of ξ^* and ζ^* in cylindrical coordinates $(\xi_r^*, \xi_\theta^*, \xi_z^*)$ and $(\zeta_r^*, \zeta_\theta^*, \zeta_z^*)$, are constant. We determine the position $\mathbf{p}_i$ such as a point of intersection of normal line at the nodal point $\mathbf{q}_i{}^*$ and Γ.

The foregoing simultaneous integral equations are reduced to simultaneous algebraic equations as follows:

$$\sum_{i=1}^{m}\int_{\Delta S_i^*}[\xi_k^*(\mathbf{q}_i^*)E_{kj}+\zeta_k^*(\mathbf{q}_i^*)F_{kj}]dS^*(\mathbf{q}_i^*)-T_j(\mathbf{p})=0$$

$$\sum_{i=1}^{m}\int_{\Delta S_i^*}[\xi_k^*(\mathbf{q}_i^*)G_{kj}+\zeta_k^*(\mathbf{q}_i^*)H_{kj}]dS^*(\mathbf{q}_i^*)-M_j(\mathbf{p})=0 \tag{9}$$

where $\mathbf{p}$ is a vector variable specifying points on S, ξ_k^* and ζ_k^* are the components of ξ^* and ζ^* in Cartesian coordinates, T_j and M_j are those of tractions $\mathbf{T}$ and $\mathbf{M}$, ΔS_i^* represents the area element of the ith ring, and E_{kj}, F_{kj}, G_{kj}, and H_{kj} are given in the Appendix. In these equations we assume the summation convention over repeated indices. The surface

integral around the ith ring can be calculated numerically by Simpson's rule, the simplest quadrature,

$$\int_{\Delta S_i^*} f^*(\mathbf{q}^*)\, dS^*(\mathbf{q}^*) = h_i^*(f_{i-1/2}^* + 4f_i^* + f_{i+1/2}^*)/6 \qquad (10)$$

where f_i^* and $f_{i\pm1/2}^*$ are contour integral values along the circles C_i^* and $C_{i\pm1/2}^*$, respectively (Fig. 3).

The components of ξ^* and ζ^* in cylindrical coordinates are independent on θ^* and related to those in Cartesian coordinates by

$$\begin{Bmatrix} \xi_1^* \\ \xi_2^* \\ \xi_3^* \end{Bmatrix} = [N] \begin{Bmatrix} \xi_r^* \\ \xi_\theta^* \\ \xi_z^* \end{Bmatrix} \text{ and } \begin{Bmatrix} \zeta_1^* \\ \zeta_2^* \\ \zeta_3^* \end{Bmatrix} = [N] \begin{Bmatrix} \zeta_r^* \\ \zeta_\theta^* \\ \zeta_z^* \end{Bmatrix} \qquad (11)$$

where

$$[N] = \begin{bmatrix} \cos\theta^* & -\sin\theta^* & 0 \\ \sin\theta^* & \cos\theta^* & 0 \\ 0 & 0 & 1 \end{bmatrix}$$

Since we now deal with the axisymmetric tensile problem, we can take ξ_θ^*, ζ_r^*, and ζ_z^*, density functions related to the torsion problem, to be zero. The coordinates x_i $(i = 1, 2, 3)$ at $\mathbf{p}$ on Γ and $x_i^*(i = 1, 2, 3)$ at $\mathbf{q}^*$ on S^* are represented as follows:

$$x_1 = x_1, \quad x_2 = 0, \quad x_3 = x_3$$
$$x_1^* = \rho^* \cos\theta^*, \quad x_2^* = \rho^* \sin\theta^* \quad \text{and} \quad x_3^* = x_3^* \qquad (12)$$

Then, from equations (9), (11), and (12) it is found that the contour integrals in equation (10) generally take the forms

$$\int_{-\pi}^{\pi} [\cos^{n_1}\theta^*/r_0^{n_2}]\rho^* d\theta^*$$

and

$$\int_{-\pi}^{\pi} [\cos^{n_1}\theta^*/r_0^{n_3}] e^{-r_0/l}\rho^* d\theta^* \qquad (13)$$

where $n_1 = 0,1,2,3,4$, $n_2 = 3,5,7$, and $n_3 = 1,2,3,4,5,6,7$. Letting $x_1^{\,2} + \rho^{*2} + (x_3 - x_3^*)^2 = A$ and $2x_1\rho^* = B$, we can write $r_0 = (A - B\cos\theta^*)^{1/2}$, so that

$$\cos^{n_1}\theta^* = [(A - r_0^{\,2})/B]^{n_1} = B^{-n_1} \sum_{i=0}^{n_1} (-1)^i \binom{n_1}{i} A^{n_1-i} r_0^{\,2i}$$

The functions r_0 and $e^{-r_0/l}$ being even with respect to θ^*, expressions (13) beomce

$$2B^{-n_1} \sum_{i=0}^{n_1} (-1)^i \binom{n_1}{i} A^{n_1-i} (A+B)^{i-n_2/2} \rho^* \int_0^{\pi} [1 - k^2\cos^2(\theta^*/2)]^{i-n_2/2} d\theta^*$$

$$2B^{-n_1} \sum_{i=0}^{n_1} (-1)^i \binom{n_1}{i} A^{n_1-i} (A+B)^{i-n_3/2} \rho^* \int_0^{\pi} [1 - k^2\cos^2(\theta^*/2)]^{i-n_3/2} e^{-r_0/l} d\theta^* \qquad (14)$$

where the relations $r_0 = \{(A + B)[1 - k^2\cos^2(\theta^*/2)]\}^{1/2}$ and $k^2 = 2B/(A + B)$ are used.

The integral in the first of expressions (14) is the elliptic integral and denoted as

$$I_n = \int_0^{\pi} [1 - k^2\cos^2(\phi/2)]^{-n/2} d\phi$$

by replacing $(2i - n_2)$ with $(-n)$. By successive use of the recurrence formula

$$I_n = [(n-2)(k^2-1)]^{-1}[(n-3)(k^2-2)I_{n-2} + (n-4)I_{n-4}] \qquad (15)$$

the integral I_n can be reduced to the sum of complete elliptic integrals of the first and second kinds

$$K(k) = I_1/2 = \int_0^{\pi/2} (1 - k^2\sin^2\phi)^{-1/2} d\phi$$

$$E(k) = I_{-1}/2 = \int_0^{\pi/2} (1 - k^2\sin^2\phi)^{1/2} d\phi \qquad (16)$$

Here we note that n is an odd number. Similarly the integral in the second of expressions (14) can be denoted as

$$H_{n'} = \int_0^{\pi} [1 - k^2\cos^2(\phi/2)]^{-n'/2} e^{-r_0/l} d\phi$$

and reduced to the sum of five integrals H_{-2}, H_{-1}, H_0, H_1, and H_2 by

$$H_{n'} = [(n'-2)(k^2-1)]^{-1}\{-k'(k^2-1)H_{n'-1} + (k^2-2)[(n'-3)H_{n'-2} + k'H_{n'-3}] + (n'-4)H_{n'-4} + k'H_{n'-5}\} \qquad (17)$$

where $k' = (A + B)^{1/2}/l$. These five integrals, $H_{-2} \sim H_2$, are obtained numerically.

Thus the numerical computation of the present problem is reduced to solving simultaneous algebraic equations of $2m$ unknown vector densities $\xi^*{}_{(i)}$ and $\zeta^*{}_{(i)}$ on S^* so as to satisfy the boundary conditions at m points $\mathbf{p}_i$ on Γ. Here $\xi^*{}_{(i)}$ and $\zeta^*{}_{(i)}$ are the vector densities on the ith ring. In the boundary integral method with a fictitious boundary, the lack of strong diagonal dominance may give rise to a little difficulty in solving the simultaneous algebraic equations; therefore, we use double precision, which gives satisfactory results.

Numerical Results

The estimates of accuracy for the numerical computation are

$$|T_j^n - T_j^e|/\bar{\tau} \leqq 0.5 \times 10^{-2} \text{ and}$$
$$|M_j^n - M_j^e|/[\bar{\tau}(D/2)] \leqq 0.5 \times 10^{-2}$$

midway between each neighboring collocation point on Γ. Here $\bar{\tau}$ is the mean normal stress on the minimum cross section of the cylinder, T_j^n and M_j^n are the components of

Table 1 Stress concentration factors for various values of parameters

		$\eta_r = -1.0$		$\eta_r = 0.0$		$\eta_r = 1.0$	
	$(D/2)/l$	α_1	α_2	α_1	α_2	α_1	α_2
$\nu = 0.1$	∞	1.451	0.214	–	–	–	–
	10	1.328	0.127	1.350	0.142	1.380	0.162
	8	1.295	0.103	1.318	0.119	1.352	0.143
	5	1.224	0.050	1.246	0.066	1.284	0.095
	2	1.137	−0.020	1.155	−0.013	1.178	0.015
$\nu = 0.3$	∞	1.411	0.260	–	–	–	–
	10	1.336	0.198	1.351	0.209	1.372	0.225
	8	1.313	0.178	1.329	0.191	1.353	0.210
	5	1.260	0.134	1.276	0.147	1.304	0.171
	2	1.193	0.072	1.201	0.078	1.222	0.100
$\nu = 0.45$	∞	1.390	0.286	–	–	–	–
	10	1.339	0.240	1.350	0.249	1.365	0.262
	8	1.321	0.225	1.333	0.235	1.351	0.251
	5	1.282	0.190	1.294	0.201	1.315	0.219
	2	1.241	0.139	1.246	0.145	1.259	0.161

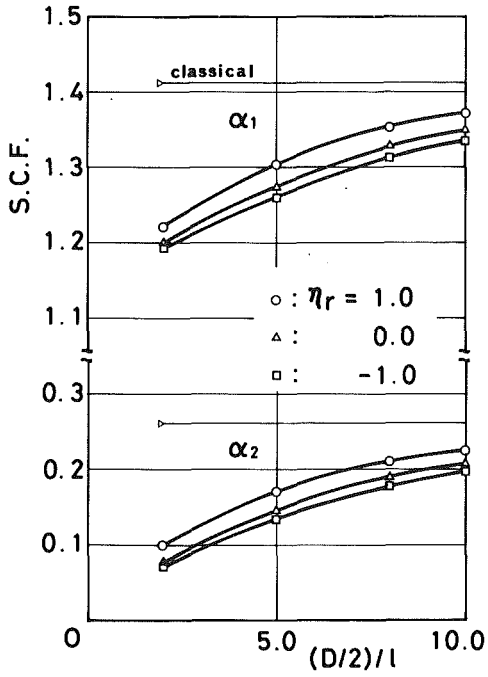

Fig. 4 Stress concentration factors, α_1 and α_2, versus (D/2)/ l for various value of η_r with $\nu = 0.3$

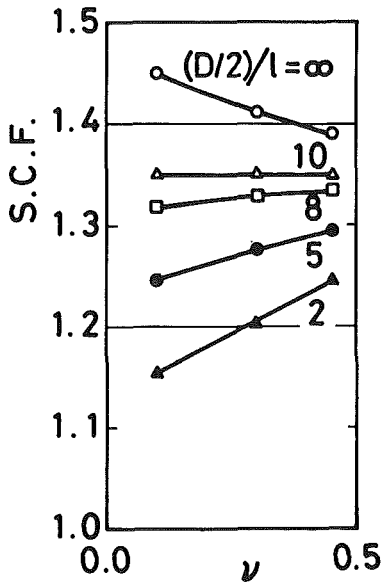

Fig. 5 Stress concentration factor, α_1, versus ν for various values of (D/2)/ l with $\eta_r = 0.0$

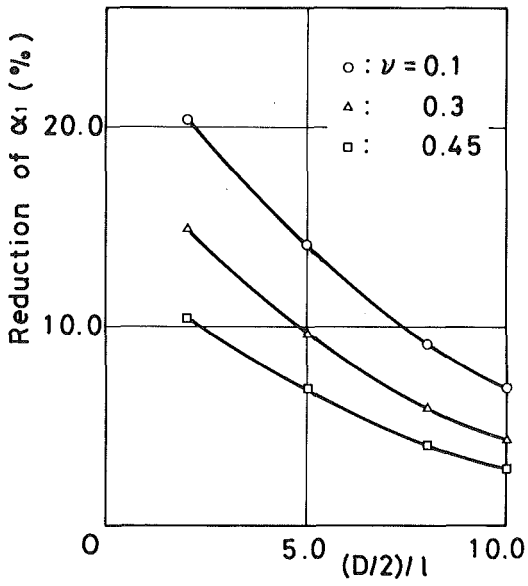

Fig. 6 Reduction ratio of stress concentration factor, α_1, to that in classical theory versus (D/2)/ l for various values of ν with $\eta_r = 0.0$

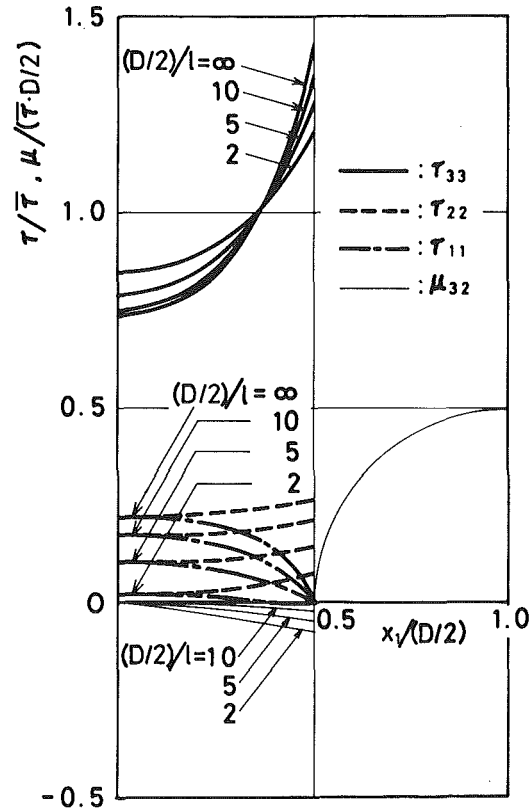

Fig. 7 Stress distributions along X_1 axis for various values of (D/2)/ l with $\nu = 0.3$ and $\eta_r = 0.0$

force and couple tractions obtained numerically, and T_j^e and M_j^e are those given on Γ, respectively.

The geometries of the cylinder analyzed here are $L/D = 3.0$, $a/D = 0.25$, and $a'/D = 0.05$. The coefficient of the fictitious-boundary distance α_i and number of subdivisions m are determined so as to satisfy the foregoing estimates of accuracy. In practice, the storage capacity of a computer limits the number of subdivisions m. We determine the suitable values of α_i first for a simple problem, e.g., bar and sphere, and then for the present problem by a few trials. Here, $\alpha_i \doteqdot 3.0$ and $m/2 = 63$. From the necessary and sufficient conditions for positive definiteness of a strain energy [1], we can obtain the parameter ranges as

$$\mu > 0, \quad 3\lambda + 2\mu > 0, \quad l \geqq 0 \quad \text{and} \quad -1 \leqq \eta_r \leqq 1 \qquad (18)$$

Noting that $\lambda = [2\nu/(1 - 2\nu)]\mu$, where ν is Poisson's ratio, we can find $-1 < \nu < 1/2$ from the second of equations (18).

Stress concentration factors are shown in Table 1, where α_1 and α_2 are those with respect to the first and second principal stresses, τ_{33} and τ_{22}, respectively. Figure 4 shows the stress concentration factors against $(D/2)/l$ for various values of η_r with $\nu = 0.3$. All results approach asymptotically to the values obtained by the classical theory, shown by thin lines, when $(D/2)/l \to \infty$. When ν is small, the magnitudes of α_2 at the center in the minimum cross section tend to be larger than

those at the surface. The difference between them is, however, very small, so that it is not mentioned here. Figure 5 shows the values of α_1 against Poisson's ratio, and Fig. 6 shows the reduction ratios of α_1 to that in the classical theory, $[(\alpha_{1_{\text{class}}} - \alpha_1)/\alpha_{1_{\text{class.}}}] \times 100(\%)$, against $(D/2)/l$, with $\eta_r = 0.0$. The stress distributions along X_1 axis are shown in Fig. 7 for various values of $(D/2)/l$ with $\nu = 0.3$ and $\eta_r = 0.0$, where the dimensionless force-stress $\tau/\bar{\tau}$ and couple stress $\mu/[\bar{\tau}(D/2)]$ are used.

Conclusions

In the present paper, we have given one method to solve three-dimensional elastic boundary value problems in the linear, couple-stress theory, which are difficult to analyze. This method is based on the "indirect fictitious-boundary integral method" which the authors have been using. Its advantages are:

1. Accurate solutions can be obtained by numerical quadrature with the simplest approximation.

2. The stresses and their gradients on a real boundary and in its neighborhood can be calculated by analytical differentiation of vector potentials on a fictitious boundary.

As a numerical example, we have treated a cylinder with a semicircular annular groove under uniaxial tension and shown the influence of the parameters, ν, l, and η_r on the stress concentration. The results are summarized as follows:

i The reduction ratio about α_1 increases with decreasing ν. That is, as Poisson's ratio ν becomes small, the couple stresses affect the stress concentrations significantly.

ii In the classical theory, the magnitude of α_1 decreases with increasing ν. But in the couple-stress theory, the relationship is reversed, i.e., the magnitude of α_1 increases with ν, under a certain value of $(D/2)/l$.

iii So far, there are many papers that show the influence of ν and l by solving two-dimensional problems, but none that show that of η_r since that can be obtained only by analyzing three-dimensional problems. In this paper, it is shown that the effect of η_r on stress concentrations is substantially smaller than that of ν.

This method cannot be applied, however, to the problems with complicated shapes, such as sharp notches and cracks. In these cases, we must use the analysis based on indirect and direct boundary integral methods without a fictitious boundary, which is now under consideration.

References

1 Mindlin, R. D., and Tiersten, H. F., "Effects of Couple-Stresses in Linear Elasticity," *Archives for Rational Mechanics and Analysis*, Vol. 11, 1962, pp. 415–448.

2 Truesdell, C., and Toupin, R. A., "The Classical Field Theories," *Encyclopedia of Physics*, Berlin-Göttingen-Heidelberg, Springer, 1960, Sections 200, 203, and 205.

3 Koiter, W. T., "Couple-Stresses in the Theory of Elasticity," *Proceedings Koninkljke Nederlandsche Akademie van Wetenschappen*, Amsterdam, Vol. 67, Series B, No. 1, 1964, pp. 17–44.

4 Mindlin, R. D., "Influence of Couple-Stresses on Stress Concentrations," *Experimental Mechanics*, Vol. 3, No. 1, 1963, pp. 1–7.

5 Weitsman, Y., "Couple-Stress Effects on Stress Concentration Around a Cylindrical Inclusion in a Field of Uniaxial Tension," ASME JOURNAL OF APPLIED MECHANICS, Vol. 32, 1965, pp. 424–428.

6 Wang, T. T., "The Effect of Couple-Stress on Maximum Stress and Its Location Around Spherical Inclusions," ASME JOURNAL OF APPLIED MECHANICS, Vol. 37, 1970, pp. 865–868.

7 Jaswon, M. A., "Integral Equation Methods in Potential Theory. I," *Proceedings of the Royal Society*, Series A., Vol. 275, 1963, pp. 23–32.

8 Symm, G. T., "Integral Equation Methods in Potential Theory. II," *Proceedings of the Royal Society*, Series A, Vol. 275, 1963, pp. 33–46.

9 Rizzo, F. J., "An Integral Equation Approach to Boundary Value Problems of Classical Elastostatics," *Quarterly of Applied Mathematics*, Vol. 25, 1967, pp. 83–95.

10 Cruse, T. A., "Numerical Solutions in Three-Dimensional Elastostatics," *International Journal of Solids and Structures*, Vol. 5, 1969, pp. 1259–1274.

11 Oliveira, E .R. A., "Plane Stress Analysis by a General Integral Method," *Proceedings of the American Society of Civil Engineers, Journal of the Engineering Mechanics Division*, Vol. 94, 1968, pp. 79–101.

12 Kishida, M., "On Fictitious-Boundary Method in Boundary-Integral Methods," *Theoretical and Applied Mechanics*, Vol. 28, 1980, pp. 139–151.

13 Kishida, M., et al., "Application of the Fictitious Boundary Method—Integral Equation Method to the Torsion Problem (Thin I, L and Cruciform Beams)," *Transactions of the Japan Society of Mechanical Engineers*, Vol. 46, No. 408A, 1980, pp. 901–906 (in Japanese).

14 Kishida, M., and Matsuda, T., "Axisymmetric Problem of Circular Shaft with Central Enlarged Section (Application of the Fictitious-Boundary Method to Direct Boundary Integral Method)," Preprint of the *Japan Society of Mechanical Engineers*, No. 800-10, 1980, pp. 156–158 (in Japanese).

15 Kishida, M., and Ozawa, H., "Three-Dimensional Elastic Stresses in Pressure Vessels with Torispherical Drumheads (Comparison of Elasticity, Photoelasticity and Shell Theory Solutions)," *Transactions of the Japan Society of Mechanical Engineers*, Vol. 47, No. 418A, 1981, pp. 626–634 (in Japanese).

16 Kishida, M., and Fujimura, K., "One Solution of Three-Dimensional Boundary Value Problems in Classical Elasticity," *Transactions of the Japan Society of Mechanical Engineers*, Vol. 48, No. 427A, 1982, pp. 358–366 (in Japanese).

APPENDIX

$$E_{kj} = \mu n_h \{ \delta_{hj} x_k' [-1 + 2\alpha - 6\beta^{-2} + 2(3\beta^{-2} + 3\beta^{-1} + 1)e^{-\beta}]/r_0^3$$
$$+ (\delta_{kh} x_j' + \delta_{kj} x_h')[-1 + 2\alpha' - 6\beta^{-2}$$
$$+ (6\beta^{-2} + 6\beta^{-1} + 3 + \beta)e^{-\beta}]/r_0^3$$
$$+ 2x_h' x_j' x_k' [15\beta^{-2} - (15\beta^{-2} + 15\beta^{-1} + 6 + \beta)e^{-\beta}]/r_0^5$$
$$+ 2\alpha' x_k (\delta_{hj} - 3x_h' x_j'/r_0^2)/r_0^3 + (\delta_{hk} x_j' - \delta_{jk} x_h')(1 + \beta)e^{-\beta}/r_0^3 \}$$

$$F_{kj} = \mu n_h \epsilon_{kmn} \{ (\delta_{hm} x_j' + \delta_{jm} x_h') x_n' [3(1 - 2\alpha')$$
$$- (3 + 3\beta + \beta^2)e^{-\beta}]/r_0^5$$
$$+ 6\alpha' x_m [-(\delta_{hn} x_j' + \delta_{nj} x_h' + \delta_{jh} x_n') + 5x_h' x_j' x_n'/r_0^2]/r_0^5 \}$$
$$+ \mu n_h \epsilon_{jhm} \{ \delta_{km} (1 + \beta + \beta^2)e^{-\beta}/r_0^3 - x_k' x_m' (3 + 3\beta + \beta^2)e^{-\beta}$$
$$/r_0^5 \}$$

$$G_{kj} = 2n_h \{ \epsilon_{hkj} (\eta - \eta')[-1 + (1 + \beta)e^{-\beta}]/r_0^3$$
$$+ (\eta \epsilon_{kjm} x_h' + \eta' \epsilon_{khm} x_j') x_m' [3 - (3 + 3\beta + \beta^2)e^{-\beta}]/r_0^5 \}$$

$$H_{kj} = -2n_h (\eta \delta_{kj} x_h' + \eta' \delta_{kh} x_j')(1 + \beta)\beta^2 e^{-\beta}/r_0^5$$
$$+ 2n_h (\eta + \eta') \{ (\delta_{kj} x_h' + \delta_{jh} x_k' + \delta_{hk} x_j')[3 - (3 + 3\beta + \beta^2)$$
$$e^{-\beta}]/(r_0^5 + x_h' x_j' x_k' [-15 + (15 + 15\beta + 6\beta^2 + \beta^3)e^{-\beta}]/r_0^7 \}$$

where δ_{ij} is the Kronecker delta, ϵ_{ijk} the permutation symbol, $\alpha = \mu/(\lambda + 2\mu)$, $\alpha' = (\lambda + \mu)/[2(\lambda + 2\mu)]$, $\beta = r_0/l$, $\eta = \mu l^2$, $\eta' = \mu l^2 \eta_r$, $x_i' = x_i - x_i^*(i = 1,2,3)$, x_i and x_i^* are the components of the vector variables $\mathbf{p}$ and $\mathbf{q}^*$, respectively, and n_i the components of the outward unit normal vector $\mathbf{n}$ at $\mathbf{p}$.

The Contact of a Cuspidal Crack

C. H. Wu
Professor,
Department of Materials Engineering,
University of Illinois at Chicago Circle,
Chicago, Ill. 60680
Mem. ASME

A simplified airfoil mapping is used to define a cuspidal crack. The objective is to investigate the effects of compressive loads on an infinite solid containing crack-like flaws. Such an objective cannot be achieved by using the conventional line crack to characterize the flaws. The associated contact problem is solved exactly by assuming that the contact region is small in comparison to the crack length. It is shown that the well-known Barenblatt model is just the present contact problem in reverse. Moreover, a specific functional form is determined to describe the so-called cohesive force which was assumed to be a material function by Barenblatt.

1 Introduction

The determination of the effects of compressive load on solids containing crack-like flaws is an important and intricate problem. It is important because it is still an open problem in that the several theoretical models [1, 2] do not lead to the experimentally determined high compressive strength. It is intricate because the convenient line-crack flaw is practically useless for this purpose. Moreover, internal contact is an inherent phenomenon to this problem. Compressive loads may be classified into two categories, crack-parallel loads and crack-perpendicular loads. For the former category the effects can again be divided into two distinct classes depending on whether the flaw is a line crack or a cuspidal hole. The line-crack case leads to the nonlinear buckling phenomenon discussed in [3, 4] and a cuspidal hole can be easily handled by the standard complex variable method [5, 6].

For the class of crack-perpendicular compressive loads, the effects can only be studied by introducing smooth holes or cuspidal cracks. Griffith used an elliptic hole and showed that the compressive strength is exactly eight times the tensile strength [1], but the experimentally obtained ratios are much higher. The inclusion of a coefficient of a friction does not change the picture much either [2]. It would seem to be more effective and reasonable to introduce a hole with initial internal contact, such as a figure-eight shaped hole. This problem is now under our investigation. The purpose of this paper is to investigate the effects of compression when the flaw is modeled by a cuspidal crack. With the expectation of a contact problem to solve in mind, the cuspidal crack must be chosen or constructed in such a way that it does not lead to additional complication. This is, of course, motivated by our desire to obtain a closed-form solution so that the result may be used for many meaningful parametric studies. A crack is said to be simple if the associated elasticity problem has a closed-form solution. Several methods are described in [5, 6] for the purpose of generating simple cracks.

The cracks generated by the well-known symmetric airfoil mapping are simple. This mapping, however, has two poles and the needed algebraic manipulation is still too involved. An offspring of the airfoil mapping is then derived. This new mapping has only a single pole of higher order. The class of cuspidal cracks considered in this paper is defined by this latter mapping.

The formulation of the problem expressed in terms of the complex variable method is outlined in Section 2. Many equations are taken directly from what we believe to be the most concise book on the subject by England [7]. The solution for the noncontact problem solved in [6] is summarized in Section 3. The contact problem is solved in Section 4. A formal asymptotic approach, using the contact length as the small parameter, is adopted as a matter of preference. We find it more convenient this way to trace the orders of magnitude of various terms. Finally, Barenblatt's theory is examined in Section 5. It amounts to a simple switch of the signs involved.

2 Statement of the Problem and Governing Equations

We consider the plane elasticity problem in the (x_1, x_2)-plane and shall use a complex formulation in terms of the complex variable $z = x_1 + ix_2$. The displacements $u_\alpha(x_1, x_2)$ and stresses $\tau_{\alpha\beta}(x_1, x_2)$ may be written in terms of two complex functions $W(z)$ and $w(z)$, viz.,

$$2\mu(u_1 + iu_2) = \kappa W(z) - z\overline{W'(z)} - \overline{w(z)} \tag{2.1}$$

$$\tau_{11} + \tau_{22} = 2[W'(z) + \overline{W'(z)}] \tag{2.2}$$

$$\tau_{22} - i\tau_{12} = W'(z) + \overline{W'(z)} + \overline{w'(z)} \tag{2.3}$$

In the preceding equations and throughout this paper prime denotes complex differentiation; W' and w' are holomorphic functions; μ is the shear modulus; and

$$\kappa = \begin{cases} 3 - 4\nu & \text{plane stress} \\ (3-\nu)/(1+\nu) & \text{plane strain} \end{cases} \tag{2.4}$$

where ν is Poisson's ratio. We will be dealing with an infinite body R_z loaded at infinity by the uniform stresses

$$\tau_{\alpha\beta} = \sigma_{\alpha\beta} \text{ (constant) as } |z| \to \infty \tag{2.5}$$

Contributed by the Applied Mechanics Division for presentation at the Winter Annual Meeting, Phoenix, Ariz., November 14-19, 1982, of the AMERICAN SOCIETY OF MECHANICAL ENGINEERS.

Discussion on this paper should be addressed to the Editorial Department, ASME, United Engineering Center, 345 East 47th Street, New York, N.Y. 10017, and will be accepted until two months after final publication of the paper itself in the JOURNAL OF APPLIED MECHANICS. Manuscript received by ASME Applied Mechanics Division, September, 1981; final revision, January 1982. Paper No. 82-WA/APM-5.

Copies will be available until July, 1983.

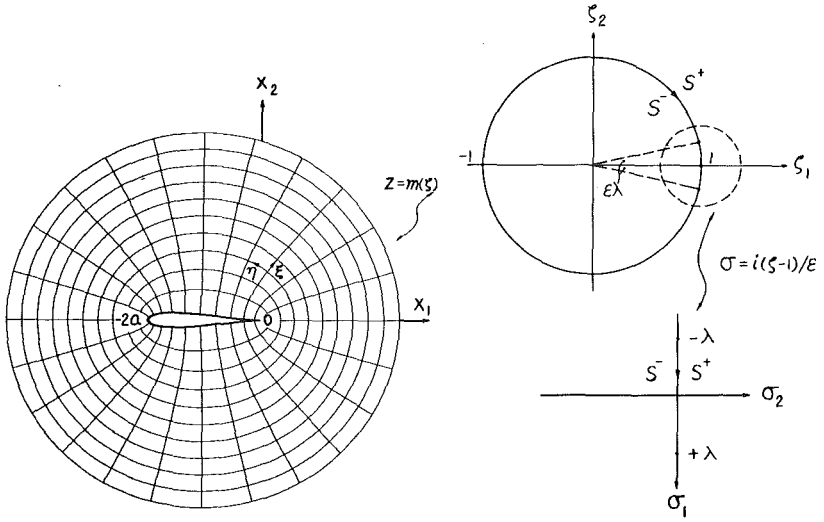

Fig. 1 Crack configuration in z-plane, together with curvilinear coordinates ξ and η, and two auxiliary complex planes ζ and σ

so that

$$W(z)=W_1 z+W_{-1}z^{-1}+\ldots, \quad W_1=\tfrac{1}{4}(\sigma_{11}+\sigma_{22}), \tag{2.6}$$

$$w(z)=w_1 z+w_{-1}z^{-1}+\ldots, \quad w_1=\tfrac{1}{2}(\sigma_{22}-\sigma_{11})+i\sigma_{12}, \tag{2.7}$$

as $|z|\to\infty$.

The infinite body R_z is assumed to be the image of $|\zeta|>1$ under the mapping

$$z=m(\zeta)=\frac{a}{2}\left[(1+\delta)\zeta+\frac{1-\delta}{\zeta}+\frac{\delta}{\zeta^2}-2-\delta\right] \quad |\zeta|>1 \tag{2.8}$$

where $\zeta=\zeta_1+i\zeta_2$ is an auxiliary complex plane, a is a length scale, and δ a parameter satisfying

$$0<\delta<1. \tag{2.9}$$

The mapping (2.8) is a derivative of the thin airfoil mapping discussed in [5]. It is simpler than the airfoil mapping because it contains only a single pole of order 2 at $\zeta=0$. The complete class of configurations defined by (2.8) may be found in [5]. The image of the unit circle $|\zeta|=1$ in the z-plane defines a crack C_z and

$$C_z: x(\eta)+iy(\eta)=m(e^{i\eta}) \tag{2.10}$$

where

$$x(\eta)=-a[1-\cos\eta+\delta\sin^2\eta], \tag{2.11}$$

$$y(\eta)=a\delta\sin\eta(1-\cos\eta). \tag{2.12}$$

It is noted that the crack C_z has a cusp of zero cusp angle at $z=0$ and

$$x(0)-x(\pi)=2a, \quad y_{\max}=y\left(\frac{2\pi}{3}\right)=\frac{3\sqrt{3}}{4}\delta a. \tag{2.13}$$

The crack configuration for $\delta=0.1$ is shown in Fig. 1. Near the cusp tip, i.e., $\eta<<1$,

$$x(\eta)=-\frac{1+2\delta}{2}a\eta^2, \quad y(\eta)=\tfrac{1}{2}a\delta\eta^3 \tag{2.14}$$

or

$$x_2=Y_t(x_1)=\tfrac{1}{2}a\delta\left(\frac{2}{1+2\delta}\right)^{3/2}\left(-\frac{x_1}{a}\right)^{3/2}. \tag{2.15}$$

We note in passing that $Y_t'(0)=0$ and $Y_t''(0)=\infty$.

Before proceeding, it is convenient to introduce curvilinear coordinates (ξ,η) in the z-plane by the coordinate curves (Fig. 1)

$$z=m(\xi e^{i\eta}). \tag{2.16}$$

Then,

$$2\mu(u_1+iu_2)=\kappa\Omega(\zeta)-\frac{m(\zeta)}{\overline{m'(\zeta)}}\overline{\Omega'(\zeta)}-\overline{\omega(\zeta)} \tag{2.17}$$

$$\tau_{\xi\xi}+\tau_{\eta\eta}=2\left[\frac{\Omega'(\zeta)}{m'(\zeta)}+\frac{\overline{\Omega'(\zeta)}}{\overline{m'(\zeta)}}\right] \tag{2.18}$$

$$\tau_{\xi\xi}+i\tau_{\xi\eta}=\frac{\Omega'(\zeta)}{m'(\zeta)}+\frac{\overline{\Omega'(\zeta)}}{\overline{m'(\zeta)}}-\left\{\frac{m(\zeta)}{\overline{m'(\zeta)}}\frac{\overline{d}}{d\zeta}\left[\frac{\overline{\Omega'(\zeta)}}{\overline{m'(\zeta)}}\right]+\frac{\overline{\omega'(\zeta)}}{\overline{m'(\zeta)}}\right\}\frac{\overline{\zeta m'(\zeta)}}{\zeta m'(\zeta)} \tag{2.19}$$

where

$$\Omega(\zeta)=W(m(\zeta)), \quad \omega(\zeta)=w(m(\zeta)). \tag{2.20}$$

The conditions (2.6) and (2.7) now become

$$\Omega(\zeta)=\Omega_1\zeta+\Omega_{-1}\zeta^{-1}+\ldots, \quad \Omega_1=\frac{(1+\delta)a}{2}W_1, \tag{2.21}$$

$$\omega(\zeta)=\omega_1\zeta+\omega_{-1}\zeta^{-1}+\ldots, \quad \omega_1=\frac{(1+\delta)a}{2}w_1. \tag{2.22}$$

It is assumed that the crack periphery is subjected to no externally applied load and, as a result, there are the following two possible boundary conditions:

(a) Traction-Free Crack

$$\Omega(\zeta)+\frac{m(\zeta)}{\overline{m'(\zeta)}}\overline{\Omega'(\zeta)}+\overline{\omega(\zeta)}=0, \quad |\zeta|=1. \tag{2.23}$$[1]

(b) Contact Problem

$$\tau_{\xi\xi}+i\tau_{\xi\eta}=0 \quad \text{for} \quad \zeta=e^{i\eta} \quad (|\eta|>\sin^{-1}\epsilon\lambda) \tag{2.24}$$

$$\begin{cases}\tau_{\xi\eta}=0 & (2.25)\\ u_2=-\tfrac{1}{2}a\delta\eta^3 & (2.26)\end{cases} \quad \text{for} \quad \zeta=e^{i\eta} \quad (|\eta|<\sin^{-1}\epsilon\lambda)$$[2]

It is implicitly assumed that the contact region is small so that (2.14) applies. The contact region in the physical z-plane is defined by (c.f. (2.14))

[1] This is the integrated form of $\tau_{\xi\xi}+i\tau_{\xi\eta}=0$.

[2] u_2 is taken from (2.14) and $\epsilon<<1$.

$$-c \le x \le 0 \quad \text{and} \quad c = \frac{1+2\delta}{2} a\epsilon^2 \lambda^2 \tag{2.27}$$

within which the condition

$$\tau_{\xi\xi} < 0 \tag{2.28}$$

must be satisfied.

To facilitate the solution, it is convenient to introduce the stress continuation through the introduction of a single function $\Omega_H(\zeta)$ defined by [7]

$$\Omega_H(\zeta) = \begin{cases} \Omega(\zeta) & \zeta \in S^+ [\,|\zeta| > 1] \\ -\dfrac{m(\zeta)}{\overline{m'(1/\bar{\zeta})}}\,\overline{\Omega'(1/\bar{\zeta})} - \overline{\omega(1/\bar{\zeta})} & \zeta \in S^- [\,|\zeta| < 1] \end{cases} \tag{2.29}$$

In terms of $\Omega_H(\zeta)$ and another new function

$$\Omega_m(\zeta) = \Omega_H'(\zeta)/m'(\zeta) \tag{2.30}$$

(2.17)–(2.19) become

$$2\mu(u_1 + iu_2) = \kappa\Omega_H(\zeta) + \Omega_H(1/\bar{\zeta}) - [m(\zeta) - m(1/\bar{\zeta})]\overline{\Omega_m(\zeta)}, \tag{2.31}$$

$$\tau_{\xi\xi} + \tau_{\eta\eta} = 2[\Omega_m(\zeta) + \overline{\Omega_m(\zeta)}], \tag{2.32}$$

$$\tau_{\xi\xi} + i\tau_{\xi\eta} = \Omega_m(\zeta) - \frac{m'(1/\bar{\zeta})}{\zeta\bar{\zeta}m'(\zeta)}\,\Omega_m(1/\bar{\zeta}) + \left[1 - \frac{m'(1/\bar{\zeta})}{\zeta\bar{\zeta}m'(\zeta)}\right]\overline{\Omega_m(\zeta)} + [m(1/\bar{\zeta}) - m(\zeta)]\,\frac{\overline{\zeta\Omega_m'(\zeta)}}{\zeta m'(\zeta)}. \tag{2.33}$$

Moreover, along the crack boundary $\zeta = e^{i\eta}$

$$2\mu\frac{d}{d\eta}(u_1 + iu_2) = [\kappa\Omega_H'^{+}(e^{i\eta}) + \Omega_H'^{-}(e^{i\eta})]ie^{i\eta} \tag{2.34}$$

where, and throughout the paper, F^+ and F^- are the values of F approached from S^+ and S^-.

Since the contact region characterized by $\epsilon\lambda$ (c.f. (2.26)) is assumed to be small, the behavior of the solution near the cusp tip $z = 0$ ($\zeta = 1$) is best described by introducing a boundary-layer complex variable defined by

$$\sigma = \sigma_1 + i\sigma_2 = i\frac{\zeta - 1}{\epsilon}, \quad \zeta - 1 = -i\epsilon\sigma. \tag{2.35}$$

The positive σ_1 and σ_2 directions are, respectively, the negative $x_2(\zeta_2)$ and positive $x_1(\zeta_1)$ directions (Fig. 1). The mapping function (2.8) now becomes

$$m(1 - i\epsilon\sigma) = -\frac{a(1+2\delta)}{2}\epsilon^2\sigma^2 + \frac{a(1+3\delta)}{2}i\epsilon^3\sigma^3 + \ldots. \tag{2.36}$$

Moreover, for $|\zeta| = |1 + i\epsilon\sigma| = 1$,

$$\sigma = \sigma_0(\sigma_1, \epsilon) = \sigma_1 - i\frac{\epsilon}{2}\sigma_1^2 + \ldots \tag{2.37}$$

In terms of σ, we may define $h(\sigma, \epsilon)$ by

$$\Omega_H(1 - \epsilon i\sigma) = -iq(\epsilon)h(\sigma,\epsilon) + \text{const.} \tag{2.38}$$

where $q(\epsilon)$ is a scaling factor to be determined. Then

$$\frac{d\Omega_H}{d\zeta} = \frac{q(\epsilon)}{\epsilon}\frac{dh}{d\sigma} = \frac{q(\epsilon)}{\epsilon}h'(\sigma,\epsilon) \tag{2.39}$$

Substituting (2.35), (2.36), (2.38), and (2.39) into (2.31)–(2.33) and keeping only the leading terms, we obtain

$$\frac{2\mu}{q(\epsilon)}(u_1 + iu_2) = -i\left[\kappa h(\sigma,0) + h(\bar{\sigma},0) + \frac{\bar{\sigma}^2 - \sigma^2}{2\sigma}h'(\sigma,0)\right], \tag{2.40}$$

$$\frac{\epsilon^2 a(1+2\delta)}{q(\epsilon)}(\tau_{\xi\xi} + \tau_{\eta\eta}) = 2i\left[\frac{h'(\sigma,0)}{\sigma} - \overline{\frac{h'(\sigma,0)}{\bar{\sigma}}}\right], \tag{2.41}$$

$$\frac{\epsilon^2 a(1+2\delta)}{q(\epsilon)}(\tau_{\xi\xi} + i\tau_{\xi\eta}) = i\left\{\frac{h'(\sigma,0)}{\sigma} - \frac{h'(\bar{\sigma},0)}{\sigma} - \left(\frac{1}{\bar{\sigma}} - \frac{1}{\sigma}\right)\overline{h'(\sigma,0)} + \frac{\sigma^2 - \bar{\sigma}^2}{2\sigma}\left[\overline{\frac{h''(\sigma,0)}{\bar{\sigma}}} - \overline{\frac{h'(\sigma,0)}{\bar{\sigma}^2}}\right]\right\}. \tag{2.42}$$

3 Traction-Free Crack

If we make the artificial assumption that the crack boundary is always free of traction, regardless of the load applied at infinity, then Ω_H defined by (2.29) must be determined in such a way that (2.23) is satisfied. It follows that Ω_H is holomorphic in the whole plane. This is just the problem solved in [5] and the result is

$$\Omega_H(\zeta) = \frac{a(1+\delta)}{2}\left[W_1\zeta - \left(\bar{w}_1 + \frac{1-\delta}{1+\delta}W_1\right)\frac{1}{\zeta} - \frac{\delta}{1+\delta}\frac{W_1}{\zeta^2}\right] \tag{3.1}$$

The stress-intensity factors are

$$(K_1, K_2) = (\sigma_{22}, \sigma_{12})(\pi a)^{1/2}\frac{1+\delta}{(1+2\delta)^{1/2}}. \tag{3.2}$$

The displacements at a point $z = m(e^{i\eta})$ along the crack boundary are just

$$u_1 + iu_2 = \frac{\kappa+1}{2\mu}\Omega_H(\zeta), \tag{3.3}$$

and

$$u_1 = \frac{(\kappa+1)a}{8\mu}\left\{-\frac{\delta}{2}(\sigma_{11} + \sigma_{22}) + [(1+2\delta)\sigma_{11} - \sigma_{22}]\cos\eta + \delta(\sigma_{11} + \sigma_{22})\sin^2\eta\right\} + \frac{(\kappa+1)(1+\delta)}{4\mu}a\sigma_{12}\sin\eta, \tag{3.4}$$

$$u_2 = \frac{(\kappa+1)(2+\delta)a}{8\mu}\left\{\left(\sigma_{22} - \frac{\delta}{2+\delta}\sigma_{11}\right) + \frac{\delta}{2+\delta}(\sigma_{11} + \sigma_{22})\cos\eta\right\}\sin\eta + \frac{(\kappa+1)(1+\delta)}{4\mu}a\sigma_{12}\cos\eta. \tag{3.5}$$

Near the cusp tip, we have

$$u_2 = \frac{(\kappa+1)(2+3\delta)}{8\mu}a\sigma_{22}\eta \tag{3.6}$$

An estimate for the contact length may now be computed from (2.14) and (3.6). It is

$$\frac{\text{Estimated Contact Length}}{a} = \frac{(\kappa+1)(1+2\delta)(2+3\delta)}{\delta}\left(-\frac{\sigma_{22}}{\mu}\right). \tag{3.7}$$

4 The Contact Problem

We now turn our attention to the problem defined by (2.24), (2.25), and (2.26). Since the contact region is assumed to be small, it is most convenient to express the solution in terms of an outer expansion and an inner expansion so that the relative orders of magnitude may be easily checked. We

shall use the variables ζ and σ for the outer and inner expansions, respectively. The leading terms of the two expansions will be explicitly determined. They are to be considered as an asymptotic solution of the *linear governing equations* of the theory of linear elasticity. At the same time, however, they are to be treated as the exact solution of the *theory of linear elasticity* in that it would be meaningless to include the higher order terms without also raising the accuracy of the governing equations.

4.1 Outer Expansion ($|z| >> 0$ or $|\zeta-1| >> 0$). In terms of the variable ζ, the contact region defined by (2.26) is an ϵ-segment centered at $\zeta=1$. It follows from (2.29) and (2.24), which is essentially the same as (2.23), that $\Omega_H'(\zeta)$ is holomorphic for $|\zeta-1|>0$. The solution is just

$$\Omega_H'(\zeta)=H'(\zeta,\epsilon)$$
$$=\frac{a(1+\delta)}{2}\left[W_1+\left(\bar{w}_1+\frac{1-\delta}{1+\delta}W_1\right)\frac{1}{\zeta^2}+\frac{2\delta}{1+\delta}\frac{W_1}{\zeta^3}\right]$$
$$+\sum_{n=2}^{\infty}\sum_{m=0}^{\infty}\frac{F_{-n}^{(m)}\epsilon^{n+m}}{(\zeta-1)^n}+\frac{\kappa\epsilon^2 P_x(\epsilon)}{2\pi(1+\kappa)}\frac{1}{\zeta} \tag{4.1}$$

A few comments regarding this solution are in order. For $\epsilon = 0$, there is no contact region and $H(\zeta, 0)$ becomes (3.1). The double sum follows from the fact that $H'(\zeta, \epsilon)$ is holomorphic only for $|\zeta-1| > 0$. The last term is added because the anticipated contact pressure is to be identified with $\tau_{\xi\xi}$ according to (2.26) and hence the horizontal resultant force on the crack is not zero. With these comments then (4.1) may now be formally considered as the complete outer expansion of the linear equations of the theory of elasticity.

To facilitate matching, we need the inner expansion of the outer expansion. It is

$$H'(1-\epsilon i\sigma,\epsilon)$$
$$=\left[\frac{a(1+\delta)}{2}(\sigma_{22}-i\sigma_{12})i+\sum_{n=2}^{\infty}\frac{F_{-n}^{(0)}}{(-i\sigma)^n}\right]+\ldots \tag{4.2}$$

4.2 Inner Expansion ($|z| << a$ or $|\zeta-1| << 1$). For the inner expansion, we use the independent variable σ defined by (2.35). Then, using (2.39) and (4.2) we write

$$\Omega_H'(1-\epsilon i\sigma)=\frac{q(\epsilon)}{\epsilon}h'(\sigma,\epsilon) \tag{4.3}$$

By comparing (4.2) and (4.3), we conclude that

$$q(\epsilon)=a|\sigma_{22}|\epsilon. \tag{4.4}$$

The stress continuation (2.29) and the boundary condition (2.24) imply that $h'(\sigma, \epsilon)$ is holomorphic in the whole ζ-plane cut along the ϵ-circular arc defined by

$$\zeta=e^{i\eta} \quad (|\eta|\geq\sin^{-1}\epsilon\lambda) \tag{4.5}$$

which, in terms of (2.35), (2.37), and (2.26), is just

$$\sigma=\sigma_0(\sigma_1,\epsilon)=\sigma_1-\epsilon\frac{i}{2}\sigma_1^2+\ldots \qquad (|\sigma_1|\leq\lambda). \tag{4.6}$$

Then, in the limit as $\epsilon \to 0$, the function

$$h_0'(\sigma)\equiv h'(\sigma,0)$$

must be holomorphic in the whole σ-plane cut along the real axis (c.f., Fig. 1)

$$\sigma=\sigma_0(\sigma_1,0)=\sigma_1 \qquad (|\sigma_1|\leq\lambda). \tag{4.7}$$

The function $h_0(\sigma)$ must now be determined to satisfy (2.25) and (2.26).

We first examine the property of $h_0'(\sigma)$ as $\sigma \to \infty$. This is determined by the inner expansion of the outer expansion. It follows from (4.2) and (4.4) that

$$h_0'(\sigma)=\frac{1+\delta}{2|\sigma_{22}|}(\sigma_{22}-i\sigma_{12}) \quad \text{as} \quad |\sigma|\to\infty \tag{4.8}$$

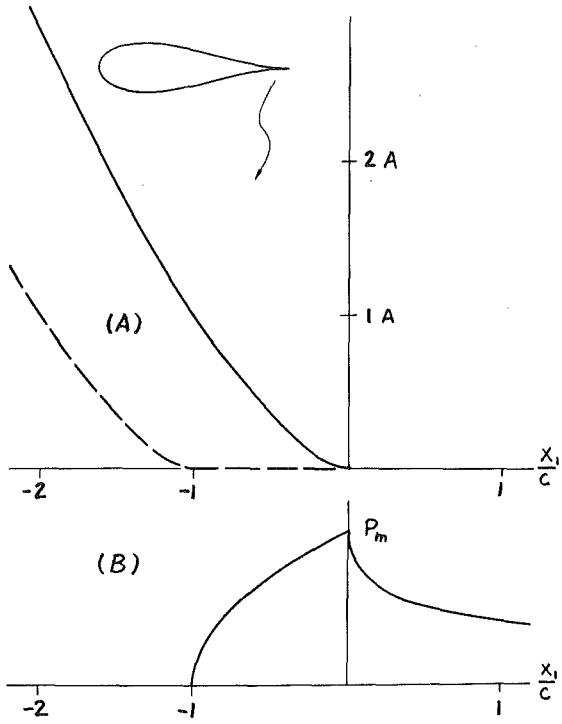

Fig. 2 *(a)* **Cusp shapes before and after deformation; and** *(b)* **contact pressure and normal stress ahead of cusp tip**

Substituting (2.37) into (2.42), we find

$$\frac{\epsilon(1+2\delta)}{|\sigma_{22}|}(\tau_{\xi\xi}+i\tau_{\xi\eta})=i\frac{1}{\sigma_1}[h_0'^{+}(\sigma_1)-h_0'^{-}(\sigma_1)] \tag{4.9}$$

where $h_0'^{\pm}(\sigma_1)=h_0'(\sigma_1 \pm i0)$. Equation (2.25) now becomes

$$h_0'^{+}(\sigma_1)+\overline{h_0'^{+}(\sigma_1)}-\overline{h_0'^{-}(\sigma_1)}-h_0'^{-}(\sigma_1)=0 \tag{4.10}$$

or

$$\lim_{\sigma=\sigma_1+i0}[h_0'(\sigma)-\overline{h_0'(\bar{\sigma})}]=\lim_{\sigma=\sigma_1-i0}[h_0'(\sigma)-\overline{h_0'(\bar{\sigma})}] \tag{4.11}$$

Since both $h_0'(\sigma)$ and $\overline{h_0'(\bar{\sigma})}$ are holomorphic in the whole plane cut along $|\sigma_1| \leq \lambda$, the preceding condition, together with (4.8), yields

$$h_0'(\sigma)-\overline{h_0'(\bar{\sigma})}=-i(1+\delta)\frac{\sigma_{12}}{|\sigma_{22}|}. \tag{4.12}$$

Substituting (2.37) and (2.38) into (2.40), we obtain

$$\frac{d}{d\sigma_1}(u_1+iu_2)=$$
$$-i\frac{q(\epsilon)}{2\mu}[\kappa h_0'^{+}(\sigma_1)+h_0'^{-}(\sigma_1)] \quad (|\sigma_1|<\lambda) \tag{4.13}$$

which, in view of (4.12), yields the relation

$$\frac{du_2}{d\sigma_1}=$$
$$-\frac{q(\epsilon)}{4\mu}(\kappa+1)\left[h_0'^{+}(\sigma_1)+h_0'^{-}(\sigma_1)+i(1+\delta)\frac{\sigma_{12}}{|\sigma_{22}|}\right] \tag{4.14}$$

Equation (2.26), with η replaced by $-\epsilon\sigma_1$, now yields

$$h_0'^{+}(\sigma_1)+h_0'^{-}(\sigma_1)=-\frac{6}{\kappa+1}\sigma_1^2-i(1+\delta)\frac{\sigma_{12}}{|\sigma_{22}|}, \tag{4.15}$$

$$q(\epsilon)=\mu a\delta\epsilon^3. \tag{4.16}$$

We conclude from (4.4) and (4.16) that

$$\epsilon^2 = \frac{|\sigma_{22}|}{\mu\delta} << 1. \tag{4.17}$$

The solution for (4.15) and (4.8) is just

$$h_0'(\sigma) = \frac{X(\sigma)}{2\pi i}\int_{-\lambda}^{\lambda} \frac{-\left[\frac{6t^2}{\kappa+1} + i(1+\delta)\frac{\sigma_{12}}{|\sigma_{22}|}\right]}{X^+(t)(t-\sigma)}\,dt$$

$$+X(\sigma)\sigma\frac{1+\delta}{2|\sigma_{22}|}(\sigma_{22}-i\sigma_{12}) \tag{4.18}$$

where the Plemelj function

$$X(\sigma) = (\sigma^2-\lambda^2)^{-1/2} \tag{4.19}$$

has been chosen so that $\sigma X(\sigma) \to 1$ as $|\sigma| \to \infty$. The integration of (4.18) is straightforward and the result is

$$h_0'(\sigma) = -i\frac{1+\delta}{2}\frac{\sigma_{12}}{|\sigma_{22}|} - \frac{3}{\kappa+1}\sigma^2$$

$$+\frac{3}{\kappa+1}\frac{\sigma}{(\sigma^2-\lambda^2)^{1/2}}\left\{\sigma^2 - \left[\frac{\lambda^2}{2} - \frac{(\kappa+1)(1+\delta)}{6}\frac{\sigma_{22}}{|\sigma_{22}|}\right]\right\} \tag{4.20}$$

The requirement that the contact pressure vanishes at $\sigma = \lambda$ leads to the conclusions:

$$\sigma_{22} < 0, \quad \lambda^2 = \frac{1}{3}(\kappa+1)(1+\delta), \tag{4.21}$$

and hence

$$h_0'(\sigma) = -i\frac{1+\delta}{2}\frac{\sigma_{12}}{|\sigma_{22}|} - \frac{3}{\kappa+1}[\sigma^2 - \sigma(\sigma^2-\lambda^2)^{1/2}]. \tag{4.22}$$

The contact pressure may now be computed from (4.9) and (4.22). It is

$$\tau_{\xi\xi} = -p_m\left[1-\left(\frac{\sigma_1}{\lambda}\right)^2\right]^{1/2} \quad (|\sigma_1| < \lambda) \tag{4.23}$$

$$= -p_m\left[1+\frac{x_1}{c}\right]^{1/2} \quad (-c \le x_1 \le 0) \tag{4.24}$$

where the maximum contact pressure p_m and the contact length c defined by (2.27) are

$$p_m = \frac{2}{1+2\delta}\left[\frac{3(1+\delta)\delta\mu|\sigma_{22}|}{\kappa+1}\right]^{1/2}, \tag{4.25}$$

$$\frac{c}{a} = \frac{1}{6}(\kappa+1)(1+\delta)(1+2\delta)\frac{|\sigma_{22}|}{\delta\mu} << 1. \tag{4.26}$$

We note that the estimate given by (3.7) is off by the factor

$$5/3 \le (2+3\delta)/(1+2\delta) \le 2. \tag{4.27}$$

The resultant contact force P is

$$P = \frac{2}{3}cp_m$$

$$= \frac{2}{3}\left[\frac{(\kappa+1)(1+\delta)|\sigma_{22}|}{3\delta\mu}\right]^{1/2}(1+\delta)|\sigma_{22}|a, \tag{4.28}$$

and the resultant horizontal force on the crack, a consequence of interpreting $\tau_{\xi\xi}$ as the "vertical" contact pressure, is (c.f., (4.1))

$$\epsilon^2 P_x(0) = \frac{\pi(\kappa+1)(1+\delta)^2\delta}{4(1+2\delta)}|\sigma_{22}|a\epsilon^2. \tag{4.29}$$

The constants $F_n^{(0)}$ involved in (4.2) may be identified with the expansion of $h_0'(\sigma)$ at infinity. In particular

$$F_2^{(0)} = \frac{q(\epsilon)}{\epsilon}\frac{3\lambda^4}{8(\kappa+1)} = \frac{1}{24}(\kappa+1)(1+\delta)^2 a|\sigma_{22}| \tag{4.30}$$

We have thus completed a solution accurate to the order of ϵ^2 in terms of the linear equations of elasticity. The solution, however, is actually exact in terms of the accuracy of the linear theory of elasticity.

The following summary is provided (see Fig. 2):

Contact Length

$$\frac{c}{a} = \frac{1}{6}(\kappa+1)(1+\delta)(1+2\delta)\frac{|\sigma_{22}|}{\delta\mu} << 1 \quad (\sigma_{22} < 0) \tag{4.31}$$

Maximum Contact Pressure

$$p_m = \frac{2}{1+2\delta}\left[\frac{3(1+\delta)\delta\mu|\sigma_{22}|}{\kappa+1}\right]^{1/2} \tag{4.32}$$

Contact Pressure

$$\tau_{\xi\xi} = -p_m\left(1+\frac{x_1}{c}\right)^{1/2} \quad (-c \le x_1 \le 0) \tag{4.33}$$

Normal Stress Along x_1-axis

$$\tau_{22}(x_1,0) = -p_m\left[\left(1+\frac{x_1}{c}\right)^{1/2} - \left(\frac{x_1}{c}\right)^{1/2}\right] \quad (0 \le x_1) \tag{4.34}$$

Cusp Shape Before Deformation ($x_2 = +0$)

$$x_2 = Y_t(x_1) = A\left(-\frac{x_1}{c}\right)^{3/2} \quad (x_1 \le 0) \tag{4.35}[3]$$

Displacement Near Cusp Tip ($x_2 = +0$)

$$u_2 = \begin{cases} \operatorname{sgn}(\sigma_{22})Y_t(x_1) & (-c \le x_1 \le 0) \\ \operatorname{sgn}(\sigma_{22})[Y_t(x_1) - Y_t(x_1+c)] & (x_1 \le -c) \end{cases} \tag{4.36}$$

Cusp Shape After Deformation ($x_2 = +0$, $\sigma_{22} < 0$)

$$x_2 = y_t(x_1) = \begin{cases} 0 & (-c \le x_1 \le 0) \\ Y_t(x_1+c) & (x_1 \le -c) \end{cases} \tag{4.37}$$

"Amplitude" of Cusp Opening

$$A = Y_t(-c) = y_t(-2c) = \tfrac{1}{2}a\delta\left[\frac{2c}{(1+2\delta)a}\right]^{3/2}. \tag{4.38}$$

It is noted that the change from (4.35) to (4.37) is merely a translation to the left. If we denote K_1 by

$$K_1(\sigma_{22},a,\delta) = \sigma_{22}(\pi a)^{1/2}\frac{1+\delta}{(1+2\delta)^{1/2}}, \tag{4.39}$$

which is just the stress-intensity factor defined by (3.2) but has no special implication in the present nonsingular stress field, then

$$K_1(|\sigma_{22}|,a,\delta) = \left(\frac{c\pi}{2}\right)^{1/2}p_m. \tag{4.40}$$

As $x_1 \to \infty$, in the sense of the outer expansion of the inner expansion, (4.34) becomes

$$\tau_{22}(x_1,0) = -p_m\frac{c^{1/2}}{2}x_1^{-1/2} = \frac{K_1(\sigma_{22},a,\delta)}{(2\pi x_1)^{1/2}} \quad (x_1 >> c) \tag{4.41}$$

which indicates that the present regular stress field approaches

[3] Same as (2.15).

the singular stress field obtained without including the effect of contact. We conclude this section by noting from (4.31) and (4.32) that

$$p_m = \left\{ \frac{2}{1+2\delta} \frac{3(1+\delta)}{\kappa+1} \frac{\delta\mu}{|\sigma_{22}|} \right\}^{1/2} |\sigma_{22}| >> |\sigma_{22}| \quad (0<\delta<1). \tag{4.42}$$

5 Barenblatt's Theory – The Contact Problem in Reverse

To set the stage for the ensuing discussion, we first deduce from (4.31), (4.32), (4.38), and (4.39) the following identities:

$$p_m = \frac{\kappa+1}{3\pi} \frac{K_1^2(|\sigma_{22}|,a,\delta)}{\mu A}, \tag{5.1}$$

$$c = \frac{2}{\pi}\left[\frac{3\pi\mu A}{(\kappa+1)K_1(|\sigma_{22}|,a,\delta)} \right]^2. \tag{5.2}$$

The values of p_m and c evaluated at $\delta = 0$ are denoted by

$$p_0 = \frac{\kappa+1}{3\pi} \frac{K_1^2(|\sigma_{22}|,a)}{\mu A} \tag{5.3}$$

$$c_0 = \frac{2}{\pi}\left[\frac{3\pi\mu A}{(\kappa+1)K_I(|\sigma_{22}|,a)} \right]^2 \tag{5.4}$$

where

$$K_I(\sigma_{22},a) = K_1(\sigma_{22},a,0) \tag{5.5}$$

Consider now a straight crack defined by $(-2a \le x_1 \le 0, x_2 = \pm 0)$. The infinite region containing the crack is loaded by a remote crack perpendicular tension $+\sigma_{22}$ and the crack-surface tension

$$\tau_{yy}(x_1, \pm 0) = +p_0\left(1+\frac{x_1}{c_0}\right)^{1/2} \quad (-c_0 \le x_1 \le 0) \tag{5.6}$$

where p_0 and c_0 are defined by (5.3) and (5.4) in which the amplitude A is assumed to be given. The solution to this problem may be easily obtained from the results of Section 4 by replacing (δ, p_m, c) by $(0, p_0, c_0)$. In particular, the displacement of the crack surface $x_2 = +0$ near $x_1 = x_2 = 0$ is just (4.6), i.e.,

$$u_2(x_1,+0) = \begin{cases} A\left(-\dfrac{x_1}{c_0}\right)^{3/2} & (-c_0 \le x_1 \le 0) \\ A\left\{\left(-\dfrac{x_1}{c_0}\right)^{3/2} - \left[\left(-\dfrac{x_1}{c_0}\right)-1\right]^{3/2}\right\} & x_1 \le -c_0) \end{cases} \tag{5.7}$$

Before proceeding we first review the hypotheses of the Barenblatt Theory [8, 9]:

(H-1) The molecular attractions across a crack near the ends are not insignificant. These attractions denoted by $g(x)$ are called cohesive forces. The positive singularity caused external load and the negative singularity caused by the cohesive forces cancel each other so that the net result is a stress field without singularity.

(H-2) The cohesive force distribution $g(x)$ is confined to a small zone extending inward for a distance c_c from the crack tip.

(H-3) Crack becomes unstable when $g(x) = g_m(x)$ and $g_m(x)$ is a material property.

These hypotheses lead to the conclusion that [9]

$$\int_0^{c_c} g_m(-t)\, t^{-1/2}\, dt = C = \left(\frac{\pi}{2}\right)^{1/2} K_I(\sigma_{22},a) \tag{5.8}$$

where C is a material constant called the modulus of cohesion. It takes at least two constants, $g_m(0)$ and c_c, to define the "material function" $g_m(x_1)$. The modulus of cohesion gives only one condition, and the other condition is the qualitative statement that c_c must be small. The equivalence of the Barenblatt theory and the K_{IC}-criterion has been established in many occasions [9, 10] but, to the best of our knowledge, no specific form of $g_m(x_1)$ has been determined or suggested. Equations (5.3)-(5.8) enable us to restate (H-3) as follows:

(H-3′) crack becomes unstable when

$$g_m(x) = p_c\left(1+\frac{x_1}{c_c}\right)^{1/2} \quad (-c_c \le x_1 \le 0) \tag{5.9}$$

$$p_c = \frac{\kappa+1}{3\pi} \frac{K_{IC}^2}{\mu A_c} \tag{5.10}$$

$$c_c = \frac{2}{\pi}\left[\frac{3\pi\mu A_c}{(\kappa+1)K_{IC}} \right]^2 \tag{5.11}$$

where K_{IC} is the fracture toughness and A_c a material length. Substituting the foregoing into (5.8), we conclude that the modulus of cohesion is just

$$C = \left(\frac{\pi}{2}\right)^{1/2} K_{IC} \tag{5.12}$$

and the fracture criterion is simply

$$K_I = K_{IC}. \tag{5.13}$$

Our statements preceding (H-3′) seem to have implied that (H-3′) is more complete than (H-3), but what is A_c? One may argue that there is no need to know A_c since the objective of the theory (5.12) and (5.13), is completed without the knowledge of A_c. Still the thrust of the theory lies in its assumption that the stress field is nonsingular, and it is of interest to know the magnitude of the cohesive force. If one insists on interpreting the cohesive forces as molecular attractions then, since $2A_c$ is just the separation at the end of the attraction, A_c must be of the order of the distance between atoms. It follows from

$$K_{IC} = 0(10^5)\text{psi}\sqrt{\text{in.}}, \quad \mu = 0(10^7)\text{psi}, \quad A_c = 0(10^{-8})\text{in.} \tag{5.14}$$

that

$$p_c = 0(10^{11})\text{psi} >> \text{theoretical strength} = 0(10^6)\text{psi}. \tag{5.15}$$

This estimate is obviously unrealistic even though the stress field is now finite.

References

1 Griffith, A. A., "The Theory of Rupture," *Proc. Ist. Int. Congr. Appl. Mech.*, Delft, 1924, pp. 55-63.

2 McClintock, F. A., and Walsh, J. B., "Friction on Griffith Cracks in Rocks Under Pressure," *Proc. 4th U.S. Congr. Appl. Mech.*, Berkeley, Calif., 1962, pp. 1015-1021.

3 Wu, C. H., "Plane-Strain Buckling of a Crack in a Harmonic Solid Subjected to Crack-Parallel Compression," ASME JOURNAL OF APPLIED MECHANICS, Vol. 46, 1979, pp. 597-604.

4 Wu, C. H., "Plane-Strain Buckling of Cracks in Incompressible Elastic Solids," *J. Elasticity*, Vol. 10, 1980, pp. 163-177.

5 Wu, C. H., "Unconventional Internal Cracks Part 1: Symmetric Variations of a Straight Crack," ASME JOURNAL OF APPLIED MECHANICS, Vol. 49, 1982, pp. 62-68.

6 Wu, C. H., "Unconventional Internal Cracks Part 2: Method of Generating Simple Cracks," submitted to ASME JOURNAL OF APPLIED MECHANICS.

7 England, A. H., *Complex Variable Methods in Elasticity*, Wiley-Interscience, New York, 1971.

8 Barenblatt, G. I., "Mathematical Theory of Equilibrium Cracks in Brittle Fracture," *Advances in Applied Mechanics*, Vol. 7, Academic Press, 1962, pp. 55-129.

9 Goodier, J. N., "Mathematical Theory of Equilibrium Cracks," *Fracture Vol. 2*, Liebowitz, H., ed., Academic Press, New York, 1970.

10 Rice, J. R., "A Path Independent Integral and the Approximate Analysis of Strain Concentration by Notches and Cracks," ASME JOURNAL OF APPLIED MECHANICS, Vol. 35, 1968, pp. 379-386.

A. Atsumi
Professor.

Y. Shindo
Associate Professor.

Department of Mechanical Engineering II,
Faculty of Engineering,
Tohoku University,
Sendai 980, Japan

Torsional Impact Response in an Infinite Cylinder With a Circumferential Edge Crack

The problem of torsional impact response in an infinite cylinder with a circumferential edge crack is solved. Using Laplace and Fourier transforms the problem is reduced to a singular integral equation of the first kind that has Cauchy-type, logarithmic and generalized Cauchy-type singularities. The kernel of the integral equation is improved in order that the calculation may be made easy. Dynamic stress-intensity factors are estimated with good accuracy.

Introduction

In the structure having pre-existing crack under dynamic loading, the waves are transmitted to all parts of the structure and are reflected and refracted at the crack, causing higher stress elevation than that of similar type of static loading. Therefore, since the crack problem concerning transient response in the elastic body has been considered as one of the most important problems in fracture mechanics, various research has been done up to date. Regarding three-dimensional axisymmetric crack problems, we may mention the work analyzed by Sih and Embley [1] for the problem of the dynamic stresses around a penny-shaped crack in an infinite elastic body under torsional impact in which the maximum stress-intensity factor has been determined to be about 1.19 times as large as the factor of the corresponding static problem. In the case of finite elastic body, there appears a reflected wave from the boundaries and a scattered wave from the crack, and the analysis becomes complicated. Chen [2] studied the problem of an infinite cylinder having a penny-shaped crack under torsional impact loading by solving the Fredholm integral equation of the second kind, and clarified the impact and geometry effect on the dynamic stress-intensity factor. In these researches, however, since the estimation of the kernels involved in the Fredholm integral equation of the second kind was not performed, the numerical evaluations are to be laborious in order that the accurate results may be obtained.

The present paper deals with the problem of the torsional impact response in an infinite cylinder with a circumferential edge crack. By the method of integral transforms, the problem is reduced to that of solving a singular integral equation of the first kind transformed from a dual integral equation. The solution of the integral equation is expanded in terms of the Jacobi polynomials with unknown coefficients which are solved by an infinite system of linear algebraic equations for the coefficients [3]. In the treatment, the integrals concerning Cauchy-type and logarithmic singularities involved in the singular integral equation of the first kind are estimated analytically, and the slow convergency of two sorts of integrands in the equation is improved by using contour integrations and asymptotic expansions. The expression of singular stress near the crack tip is given by a closed form and the solution is transformed into the physical plane by using the numerical Laplace inversion technique [4]. The stress-intensity factors subjected to time-dependent loadings are shown in a figure for various crack depths. The related static problem has been studied by Shibuya, et al. [5]. The results

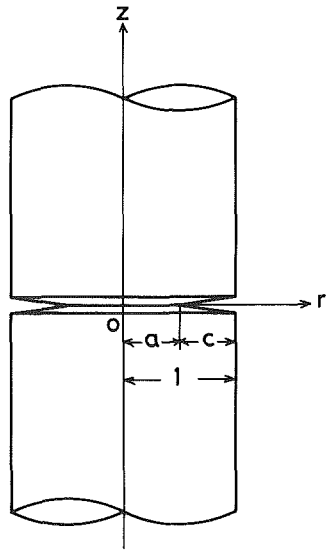

Fig. 1 Geometry and coordinate system

Contributed by the Applied Mechanics Division for publication in the JOURNAL OF APPLIED MECHANICS.

Discussion on this paper should be addressed to the Editorial Department, ASME, United Engineering Center, 345 East 47th Street, New York, N.Y. 10017, and will be accepted until two months after final publication of the paper itself in the JOURNAL OF APPLIED MECHANICS. Manuscript received by ASME Applied Mechanics Division, December, 1981; final revision, February, 1982.

are also obtained from the present solution by taking a limiting case. Both results are compared and made good use of for clarifying the impact effect on the dynamic stress-intensity factor. In addition, it may be mentioned that the present solution is identical to that for the sudden appearance of a crack in an infinite cylinder under stationary twisting.

Formulation of the Problem

Let us take cylindrical coordinates and the z-axis as the axis of symmetry of a circular cylinder which is made from homogeneous and isotropic material. For convenience, r and z will be regarded as dimensionless quantities referring to the radius of the cylinder b. The present problem is, as shown in Fig. 1, that of an infinite circular cylinder of radius 1 having a circumferential edge crack of depth c lying in the plane $z=0$.

The displacement field in the r, θ, and z-directions is denoted as u_r, u_θ, and u_z, respectively. For torsional motion, we have

$$u_r = u_z = 0, \quad u_\theta = u_\theta(r,z,T) \tag{1}$$

where T is time. The corresponding stress field is as follows:

$$\tau_{r\theta}(r,z,T) = \mu(u_\theta, r - u_\theta/r) \tag{2}$$

$$\tau_{\theta z}(r,z,T) = \mu u_{\theta,z} \tag{3}$$

where μ is the shear modulus of elasticity and a comma denotes partial differentiation with respect to coordinate variables. The other stress components are all vanishing. Hence, two of the equations of motion are identically satisfied and the remaining one gives

$$\frac{\partial^2 u_\theta}{\partial r^2} + \frac{1}{r}\frac{\partial u_\theta}{\partial r} - \frac{u_\theta}{r^2} + \frac{\partial^2 u_\theta}{\partial z^2} = \frac{1}{c_2^2}\frac{\partial^2 u_\theta}{\partial T^2} \tag{4}$$

where $c_2 = (\mu/\rho)^{1/2}$ and ρ is the mass density of the material.

In the present problem, a circular cylinder is initially at rest and a stress $\tau_{\theta z} = -\tau_0 r$, with τ_0 having the dimension of stress, is prescribed at the crack surface for $T \geq 0$. That is, a torque M_0 of magnitude of $\pi\tau_0/2$ is prescribed suddenly at $|z| = \infty$. For the resulting problem of scattering field of a normally incident torsional impact wave by the crack, the boundary condition is given as follows

$$\tau_{r\theta}(1,z,T) = 0 \tag{5}$$

$$\tau_{\theta z}(r,0,T) = -\tau_0 r H(T), \quad a < r \leq 1 \tag{6}$$

$$u_\theta(r,0,T) = 0, \quad 0 \leq r \leq a \tag{7}$$

where $a = 1 - c$ and $H(T)$ is the Heaviside step function.

Analysis

The time variable is removed by the Laplace transform relations

$$f^*(p) = \int_0^\infty f(T)e^{-pT}dT, \quad f(T) = \frac{1}{2\pi i}\int_{Br} f^*(p)e^{pT}dp \tag{8}$$

The path of integration in the second equation of (8) is the Bromwich path, which is a line on the right-hand side of the p-plane and parallel to the imaginary axis. Applying the first equation of (8) to equation (4) results in the transformed equation

$$\frac{\partial^2 u_\theta^*}{\partial r^2} + \frac{1}{r}\frac{\partial u_\theta^*}{\partial r} - \frac{1}{r^2}u_\theta^* + \frac{\partial^2 u_\theta^*}{\partial z^2} = \frac{p^2}{c_2^2}u_\theta^* \tag{9}$$

Referring to the upper half space $z>0$, solution of equation (9) can be written as

$$u_\theta^* = \int_0^\infty A(\alpha,p)J_1(\alpha r)e^{-\gamma z}d\alpha + \int_0^\infty B(\alpha,p)I_1(\gamma r)\sin(\alpha z)d\alpha + c_0 r\frac{1}{p}e^{-(p/c_2)z} \tag{10}$$

where $J_n(\ )$ and $I_n(\ )$ denote the n-order Bessel function and the modified Bessel function of the first kind, respectively, $A(\alpha)$, $B(\alpha)$, and c_0 are unknown functions and coefficients to be determined later, and γ denote

$$\gamma = (\alpha^2 + p^2/c_2^2)^{1/2} \tag{11}$$

The relation between unknown functions is determined from the Laplace and Fourier sine transforms of the boundary condition (5), by using equations (2) and (10), in the form

$$\gamma I_2(\gamma)B(\alpha,p) = \alpha\int_0^\infty \frac{\eta A(\eta,p)J_2(\eta)}{\alpha^2+\beta^2}d\eta \tag{12}$$

Similarly, from the boundary conditions (6) and (7) in the transformed plane, a pair of dual integral equations is obtained as

$$-\int_0^\infty A(\alpha,p)\gamma J_1(\alpha r)d\alpha + \int_0^\infty B(\alpha,p)I_1(\gamma r)\alpha\, d\alpha = -\tau_0 r/\mu p + c_0 r\frac{1}{c_2}, \quad a<r\leq 1 \tag{13}$$

$$\int_0^\infty A(\alpha,p)J_1(\alpha r)d\alpha + c_0 r\frac{1}{p} = 0, \quad 0\leq r\leq a \tag{14}$$

In order to solve the equation, the following definition is made on the crack surface displacement:

$$r\frac{d}{dr}\left(\frac{1}{r}u_\theta^*\right) = \varphi^*(r,p), \quad a<r\leq 1$$

$$= 0 \quad 0\leq r\leq a \tag{15}$$

From equation (15), $A(\alpha,p)$ is determined by the form

$$A(\alpha,p) = -\int_a^1 t\varphi^*(t,p)J_2(\alpha t)dt \tag{16}$$

Substituting equation (16) into equation (13), and using equation (12), a singular integral equation of the first kind is obtained as

$$\int_a^1 t\varphi^*(t,p)[R_0(r,t) + R_1(r,t) + R_2(r,t)]dt = -\tau_0 r/\mu p + c_0 r\frac{1}{c_2}, \quad a<r\leq 1 \tag{17}$$

where

$$R_0(r,t) \equiv \int_0^\infty \alpha J_2(\alpha t)J_1(\alpha r)d\alpha$$

$$= \frac{4}{\pi t^2}[K(t/r) - E(t/r)] + \frac{2}{\pi}\frac{1}{(t^2-r^2)}E(t/r), \quad t<r$$

$$= \frac{4}{\pi r t}[K(r/t) - E(r/t)] + \frac{2}{\pi r t}\left[\frac{t^2}{(t^2-r^2)}E(r/t) - K(r/t)\right], \quad t>r \tag{18}$$

$$R_1(r,t) = \int_0^\infty (\gamma-\alpha)J_2(\alpha t)J_1(\alpha r)d\alpha \tag{19}$$

$$R_2(r,t) = -\frac{2}{\pi}\int_0^\infty \frac{\alpha^2}{\gamma I_2(\gamma)}I_2(\gamma t)K_2(\gamma)I_1(\gamma r)d\alpha \tag{20}$$

where K and E are complete elliptic integrals of the first and second kind, respectively, and K_n denotes the n-order modified Bessel function of the second kind. Similarly, from equation (14), unknown coefficient c_0 is determined as

$$c_0 = p\int_a^1 \frac{1}{t}\varphi^*(t,p)dt \tag{21}$$

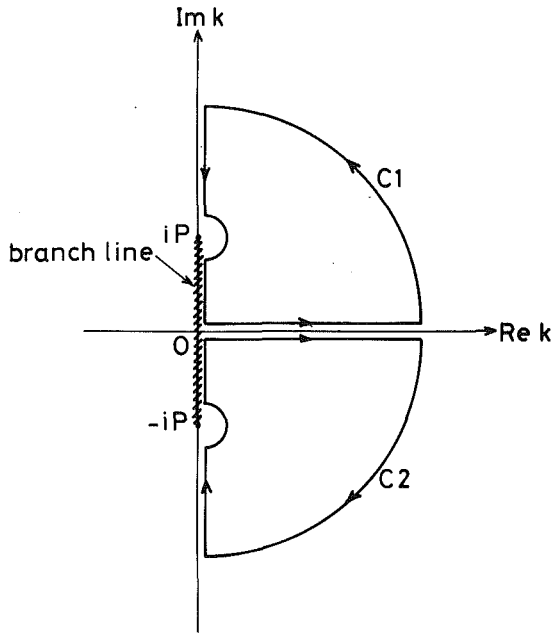

Fig. 2 Contours of integration for integrals in equations (29) and (30)

The kernel $R_0(r,t)$ in equation (17) has Cauchy-type and logarithmic singularities and can be written in the following form by separating the singularities:

$$t^2R_0(r,t)=\frac{r}{\pi(t-r)}-\frac{3}{2\pi}\log\left|\frac{2(t-r)}{1-a}\right|+L_0(r,t) \tag{22}$$

where $L_0(r,t)$ is the Fredholm kernel which has no singularities and is written as

$$L_0(r,t)=\frac{1}{\pi}\left[\frac{r^2}{t(t+r)}-2\right]E(t/r)+\frac{r\left[\frac{r}{t}E(t/r)-1\right]}{\pi(t-r)}$$

$$+\frac{4K(t/r)}{\pi}+\frac{3}{2\pi}\log\left|\frac{2(t-r)}{1-a}\right|,\quad t<r$$

$$=\frac{1}{\pi}\left[\frac{r}{t+r}-2(t/r)\right]E(r/t)+\frac{r[E(r/t)-1]}{\pi(t-r)}$$

$$+\frac{2\frac{t}{r}K(r/t)}{\pi}+\frac{3}{2\pi}\log\left|\frac{2(t-r)}{1-a}\right|,\quad t>r \tag{23}$$

For the sake of convenience of analysis, we perform the following change of variables and function:

$$r=\frac{1}{2}[(1-a)s+1+a],\quad t=\frac{1}{2}[(1-a)\tau+1+a] \tag{24}$$

$$P=p/c_2 \tag{25}$$

$$\varphi^*(t,p)/(\tau_0/\mu p)t=\Phi^*(\tau,p)\left(\frac{1-\tau}{1+\tau}\right)^{1/2} \tag{26}$$

Then, equation (17) is written as

$$\frac{1}{\pi}\int_{-1}^{1}\left[\frac{1}{\tau-s}-\frac{3(1-a)}{4r}\log|\tau-s|\right.$$

$$\left.+K(s,\tau)\right]\left(\frac{1-\tau}{1+\tau}\right)^{1/2}\Phi^*(\tau,p)\,d\tau=-1+c_0\frac{1}{c_2}p\mu/\tau_0 \tag{27}$$

where

$$K(s,\tau)=\frac{1-a}{2r}\pi[L_0(r,t)+t^2R_1(r,t)+t^2R_2(r,t)] \tag{28}$$

Next, let us consider the kernels $R_1(r,t)$ and $R_2(r,t)$, respectively. First, regarding $R_1(r,t)$ expressed by equation (19), it is a form of integral of bad convergency. To evaluate the integral accurately, we consider the contour integrals

$$I_{c1}=\oint_{c1}L(\gamma,k)J_2(kt)H_1^{(1)}(kr)\,dk,\quad t<r \tag{29}$$

$$I_{c2}=\oint_{c2}L(\gamma,k)J_2(kt)H_1^{(2)}(kr)\,dk,\quad t<r \tag{30}$$

where

$$L(\gamma,k)=k-\gamma=k-(k^2+P^2)^{1/2} \tag{31}$$

In equations (29) and (30), contours $c1$, $c2$ are defined in Fig. 2 and $H_1^{(1)}$, $H_1^{(2)}$ are the first-order Hankel functions of the first and second kind, respectively. The integrals in equations (29) and (30) satisfy Jordan's lemma on the infinite quarter circles, so that

$$I_{c1}=\int_0^\infty(\alpha-\gamma)J_2(\alpha t)H_1^{(1)}(\alpha r)\,d\alpha$$

$$+\int_\infty^P(i\alpha-i\nu')J_2(i\alpha t)H_1^{(1)}(i\alpha r)id\alpha$$

$$+\int_P^0(i\alpha-\nu)J_2(i\alpha t)H_1^{(1)}(i\alpha r)\,id\alpha \tag{32}$$

$$I_{c2}=\int_0^\infty(\alpha-\gamma)J_2(\alpha t)H_1^{(2)}(\alpha r)\,d\alpha$$

$$+\int_\infty^P(-i\alpha+i\nu')J_2(-i\alpha t)H_1^{(2)}(-i\alpha r)(-i)\,d\alpha$$

$$+\int_P^0(-i\alpha-i\nu)J_2(-i\alpha t)H_1^{(2)}(-i\alpha r)\,(-i)\,d\alpha \tag{33}$$

where

$$\nu=(P^2-\alpha^2)^{1/2},\quad \nu'=(\alpha^2-P^2)^{1/2} \tag{34}$$

Because of $I_{c1}+I_{c2}=0$, $R_1(r,t)$ for $t<r$ can be finally written as

$$R_1(r,t)=\frac{2}{\pi}P^2\left\{\int_0^1\alpha I_2(\alpha Pt)K_1(\alpha Pr)\,d\alpha\right.$$

$$\left.+\int_1^\infty[\alpha-(\alpha^2-1)^{1/2}]I_2(\alpha Pt)K_1(\alpha Pr)\,d\alpha\right\},\quad t<r \tag{35}$$

$R_1(r,t)$ for $t>r$ can be also found as follows:

$$R_1(r,t)=-\frac{2}{\pi}P^2\left\{\int_0^1\alpha K_2(\alpha Pt)I_1(\alpha Pr)\,d\alpha\right.$$

$$\left.+\int_1^\infty[\alpha-(\alpha^2-1)^{1/2}]K_2(\alpha Pt)I_1(\alpha Pr)\,d\alpha\right\}$$

$$+\frac{1}{2}(I_{1\epsilon}+I_{2\epsilon}),\quad t>r \tag{36}$$

where the integrands have the pole of first-order, so that $I_{1\epsilon}$ and $I_{2\epsilon}$ expressed by the following forms are to be necessary. That is,

$$I_{1\epsilon}\equiv\lim_{\epsilon\to0}\int_{\pi/2}^0L(\gamma,\epsilon e^{i\theta})H_2^{(1)}(t\epsilon e^{i\theta})J_1(r\epsilon e^{i\theta})i\epsilon e^{i\theta}d\theta=Pr/t^2 \tag{37}$$

$$I_{2\epsilon}\equiv\lim_{\epsilon\to0}\int_{-\pi/2}^0L(\gamma,\epsilon e^{i\theta})H_2^{(2)}(t\epsilon e^{i\theta})J_1(r\epsilon e^{i\theta})i\epsilon e^{i\theta}d\theta=Pr/t^2 \tag{38}$$

The kernels given in the form of equations (35) and (36) will allow their numerical evaluation with good accuracy.

Successively, for the sake of convenience of the numerical calculation, we rewrite equation (20) in the form

$$R_2(r,t) = -\frac{2}{\pi}\int_0^\infty \left[\frac{\alpha^2}{\gamma I_2(\gamma)} I_2(\gamma t) K_2(\gamma) I_1(\gamma r) - A^*(\alpha,r,t)\right] d\alpha - \frac{2}{\pi}\int_0^\infty A^*(\alpha,r,t)\, d\alpha \tag{39}$$

where

$$A^*(\alpha,r,t) = a_1 e^{-(2-r-t)\alpha} + \frac{a_2}{\alpha}\left[e^{-(2-r-t)\alpha} - e^{-\delta\alpha}\right] \tag{40}$$

$$\int_0^\infty A^*(\alpha,r,t)\, d\alpha = \frac{a_1}{2-r-t} + a_2 ln[\delta/(2-r-t)] \tag{41}$$

The forms of a_1 and a_2 come from the leading terms in the asymptotic ($\alpha \to \infty$) expansion of $\alpha^2 I_2(\gamma t) K_2(\gamma) I_1(\gamma r)/\gamma I_2(\gamma)$, and are given, respectively, as:

$$a_1 = \frac{1}{2(rt)^{1/2}}, \quad a_2 = \left[\frac{3}{8}\left(10 - \frac{1}{r} - \frac{5}{t}\right) - \frac{(2-r-t)P^2}{2}\right] a_1 \tag{42}$$

Besides, to use the a_2/α term without causing divergence of the associated integral term, it is necessary to artificially include $e^{-\delta\alpha}$. We merely choose δ so that it has little effect on the integrand values for large α; We actually use $\delta = 2$.

Now, to solve equation (27), we assume the unknown density $\Phi^*(\tau)$ in the form [3]

$$\Phi^*(\tau) = \sum_{n=0}^\infty B_n P_n^{(1/2,-1/2)}(\tau) \tag{43}$$

where $P_n^{(1/2,-1/2)}(\tau)$ denotes the Jacobi polynomials. Substituting equation (43) into equation (27), we obtain the equation

$$\sum_{n=0}^\infty B_n\left[-P_n^{(-1/2,1/2)}(s) + w_n(s) + p_n(s)\right] = -1 + \frac{1}{2}(1-a) B_0 \pi P \tag{44}$$

where

$$w_n(s) \equiv -\frac{3(1-a)}{4\pi r}\int_{-1}^1 \log|\tau - s| P_n^{(1/2,-1/2)}(\tau)\left(\frac{1-\tau}{1+\tau}\right)^{1/2} d\tau$$

$$= -\frac{3(1-a)}{4r}(s - \log 2), \quad n = 0$$

$$= \frac{3(1-a)(2n)!}{4r(n!)^2 2^{2n}}\left[\frac{1}{n} T_n(s) - \frac{1}{n+1} T_{n+1}(s)\right], \quad n = 1,2,\ldots \tag{45}$$

$$p_n(s) = \frac{1}{\pi}\int_{-1}^1 K(s,\tau) P_n^{(1/2,-1/2)}(\tau)\left(\frac{1-\tau}{1+\tau}\right)^{1/2} d\tau \tag{46}$$

$T_n(s)$ in equation (45) denotes the n-order Chebyshev polynomials of the first kind. Considering the orthogonality relations of the Jacobi polynomials, the following equation is given from equation (44):

$$\theta_k^{(-1/2,1/2)} B_k - \sum_{n=0}^\infty [\gamma_{kn} + C_{kn}] B_n = d_k\left[1 - \frac{1}{2}(1-a) B_0 \pi P\right], \quad k = 0,1,2,\ldots \tag{47}$$

where

$$\theta_0^{(-1/2,1/2)} = \pi \tag{48}$$

$$\theta_k^{(-1/2,1/2)} = \frac{2(2k)!(2k+2)!\pi}{(1+2k)(k!)^3(k+1)! 2^{2(2k+1)}} \tag{49}$$

$$\gamma_{kn} = \int_{-1}^1 P_k^{(-1/2,1/2)}(s) w_n(s)\left(\frac{1+s}{1-s}\right)^{1/2} ds \tag{50}$$

$$C_{kn} = \int_{-1}^1 P_k^{(-1/2,1/2)}(s) p_n(s)\left(\frac{1+s}{1-s}\right)^{1/2} ds \tag{51}$$

$$d_k = \pi\delta_{k0} \tag{52}$$

δ_{k0} in equation (52) denotes the Kronecker delta.

The evaluation of integrals in equation (50) and (51) can be easily performed by using the following Gauss-Jacobi quadrature formula [3], i.e.,

$$\int_{-1}^1 \left(\frac{1+s}{1-s}\right)^{1/2} f(s)\, ds \fallingdotseq \frac{2\pi}{2N+1}\sum_{i=1}^N (1+s_i) f(s_i), \quad s_i = \cos\left(\frac{2i-1}{2N+1}\pi\right) \tag{53}$$

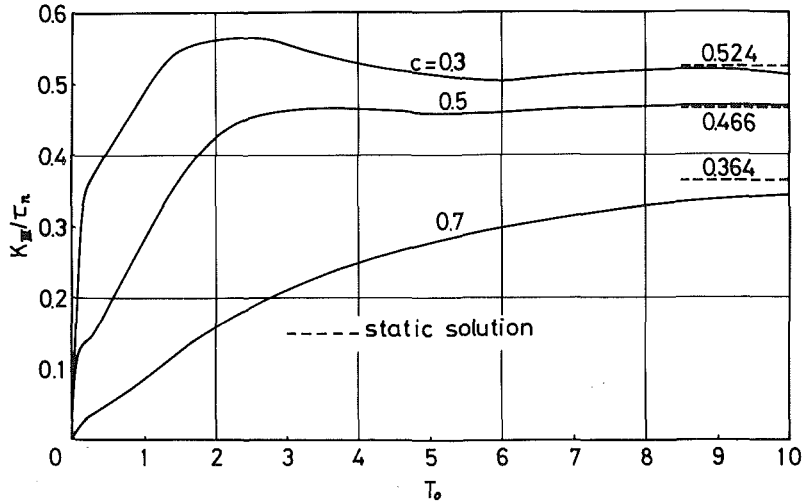

Fig. 3 Variation of dynamic stress-intensity factor with time

$$\int_{-1}^{1}\left(\frac{1-\tau}{1+\tau}\right)^{1/2} f(\tau)\,d\tau \doteq \frac{2\pi}{2N+1}\sum_{j=1}^{N}(1-\tau_j)f(\tau_j),$$

$$\tau_j = \cos\left(\frac{2j\pi}{2N+1}\right) \tag{54}$$

Dynamic Singular Stresses Near the Crack Tip

To find the local dynamic stress field, the inverse Laplace transform of the expressions $\tau^*_{r\theta}(r,z,p)$ and $\tau^*_{\theta z}(r,z,p)$, which are obtained by substituting equation (10) into equations (2) and (3), must be applied. The singular stresses are obtained by expanding the integrands in the stress integrals of $\tau^*_{r\theta}(r,z,p)$ and $\tau^*_{\theta z}(r,z,p)$ for large α. Considering the theorem [6] on the behavior of Cauchy integral near the ends of the path of integration and performing the Laplace transform inversion of the singular stresses, dynamic singular stresses near the crack tip are obtained as

$$\tau_{r\theta}(r,z,T) \sim \frac{K_{III}(T)}{(2\pi\rho_1)^{1/2}}\cos(\theta_1/2) \tag{55}$$

$$\tau_{\theta z}(r,z,T) \sim \frac{K_{III}(T)}{(2\pi\rho_1)^{1/2}}\sin(\theta_1/2) \tag{56}$$

where $K_{III}(T)$ is a so-called dynamic stress-intensity factor defined as the following expression

$$K_{III}(T) \equiv \lim_{r\to a^-}[2\pi(a-r)]^{1/2}\tau_{\theta z}(r,0,T)$$

$$= \tau_0(2c)^{1/2}a\frac{1}{2\sqrt{\pi i}}\int_{Br}\frac{1}{P}\Phi^*(-1,P)e^{Pc_2T}dP \tag{57}$$

In equations (55) and (56), ρ_1, θ_1 denotes the following polar coordinates, that is,

$$\rho_1 = [(r-a)^2+z^2]^{1/2}, \quad \theta_1 = \tan^{-1}\left(\frac{z}{r-a}\right) \tag{58}$$

The Laplace transform inversion of equation (57) is carried out numerically by using the formula [4]:

$$F^*(P/\beta) \equiv \int_0^\infty F(T')e^{-(P/\beta)T'}dT'$$

$$= \beta\sum_{j=1}^{N} w_j x_j^{P-1}F(-\beta\log x_j) \tag{59}$$

where β is a variable that regulates time scale, x_j $(j=1,\cdots,N)$ are the roots of the equation $P_N(1-2x)=0$ in which $P_N(\ )$ denotes the Legendre polynomials of order n, and w_j denotes weight functions given by the relation

$$w_j = -\frac{1}{2}\int_0^1 \frac{P_N(1-2x)}{(x-x_j)[P'_N(1-2x)]_{x=x_j}}dx \tag{60}$$

In equation (60), $P'_N(1-2x)$ denotes the differentiation $dP_N(1-2x)/d(1-2x)$.

Numerical Results and Considerations

Solving the infinite system of linear algebraic equation (47) and performing the Laplace transform inversion numerically, we have determined dynamic stress-intensity factors of an infinite cylinder with a circumferential edge crack under sudden twisting. The dimensionless values of K_{III}/τ_n versus T_0 are shown in Fig. 3 for the cases of $c = 0.3$, 0.5, and 0.7. τ_n denotes nominal stress $2M_0/\pi a^3$, and T_0 denotes dimensionless time c_2T/c, and the results shown by the dotted lines are those of the related statical solution for the case of $P=0$ in equation (47), and are in good agreement with the results in reference [5]. Generally, the values of the dynamic stress-intensity factor become larger and reach the maximum values close to those of statical one through the point of inflection as the time increases.

We note that the term of rigid displacement given in the present solution is important for solving such problems of dynamic stress-intensity factor.

Acknowledgment

It should be acknowledged that the expense for this study has been appropriated from the Scientific Research Fund of the Ministry of Education for the fiscal year 1980.

References

1 Sih, G. C., and Embley, G. T., "Sudden Twisting of a Penny-Shaped Crack," ASME JOURNAL OF APPLIED MECHANICS, Vol. 39, 1972, pp. 395–400.

2 Chen, E. P., "Sudden Twisting of a Penny-Shaped Crack in a Finite Elastic Cylinder," *Proc. 4th Int. Conf. on Fracture 3*, Taplin, D. M. R., ed., 1977, pp. 71–78.

3 Erdogan, F., Gupta, G. D., and Cook, T. S., "Numerical Solution of Singular Integral Equations," *Methods of Analysis and Solutions of Crack Problems*, Noordhoff, Leyden, 1973, pp. 368–425.

4 Bellman, R., Kalaba, R., and Lockett, J., *Numerical Inversion of the Laplace Transform*, Elsevier, Amsterdam, 1966.

5 Shibuya, T., Koizumi, T., and Okuya, T., "The Axisymmetric Stress Field in an Infinite Solid Cylinder With a Circumferential Crack Under Torsion," (in Japanese), *Trans. JSME*, Series A, Vol. 44, 1978, 4052–4056.

6 Muskhelishvili, N. I., *Singular Integral Equations*, Noordhoff, Groningen, 1946.

Y. Takao[2]
Research Associate.

T. W. Chou
Professor.

M. Taya
Assistant Professor.
Assoc. Mem. ASME

Department of Mechanical and Aerospace Engineering,
107 Evans Hall,
University of Delaware,
Newark, Del. 19711

Effective Longitudinal Young's Modulus of Misoriented Short Fiber Composites[1]

This paper examines the effective longitudinal Young's modulus of composites containing misoriented short fibers. The analysis is based on the Eshelby's equivalent inclusion method and the average induced strain approach of Taya, Mura, and Chou. The present approach is unique in that it takes into account the interactions among fibers at different orientations. Numerical results are presented to demonstrate the effects of fiber elastic property, aspect ratio, volume fraction, and orientation distribution function on composite Young's modulus. Fiber orientation distribution has a more significant effect on composite longitudinal Young's modulus than fiber volume friction, within the range examined.

1 Introduction

Discontinuous-fiber reinforced plastics are attractive in their versatility in properties and relatively low fabrication costs. They consist of relatively short, variable length, and imperfectly aligned fibers distributed in a continuous matrix material. The orientation of the short fibers depends on the processing conditions employed and may vary from random to nearly aligned. Thus, it is imperative to take into consideration the effects of the bias in fiber orientation and variation in fiber aspect ratio on composite elastic properties.

The stiffness properties of two-dimensional random fiber composites were analyzed by Halpin and Pagano [1] for instance, under the assumption that such materials can be modeled as laminated systems composed of layers of unidirectional short-fiber composites oriented at specific angles with respect to the reference axes. The case of three-dimensional misaligned fiber composites has been analyzed in [2, 3]. Christensen [2] obtained the results by summing up the contributions to stiffness for all the fiber orientations. The stiffness value of each orientation was obtained by the tensor transformation of stiffness of the system with aligned fibers parallel to the loading direction. Chou and Nomura [3] used the results from both the bound and self-consistent [4] approaches for the values for each orientation. In the analyses of [2] and [3] the interactions between fibers at different orientation are not considered.

In this paper we consider the effect of the distribution in fiber orientation on the effective Young's modulus. The interaction among fibers at different orientations is included in the analysis by adopting the average induced strain approach [5, 6] and the modified Eshelby's equivalent inclusion method [7].

In the formulation, the general approach is described first and it is shown that the average induced strain has only two unknown components. Then we describe the approach in detail by the use of this result. Numerical results of effective Young's modulus are presented for two types of fiber distribution patterns (uniform and cosine-type) with the parameter of distribution limit α as a function of fiber orientation angles. The effect of the volume fraction is also presented.

2 Formulation

The infinite elastic body containing misoriented short fibers and subjected to the applied stress σ_0 is shown in Fig. 1(*a*). The fibers are modeled as ellipsoidal inclusions of the same size. Let the domains of the infinite body and the fibers (inhomogeneity) be denoted by D and Ω, respectively. Hence the domain of the matrix becomes $D-\Omega$. The elastic stiffness tensors of the matrix and fiber are denoted by $\mathbf{C}_0$ and $\mathbf{C}_f$, respectively. The bold-face letter stands for tensorial quantity.

Under the applied stress σ_0, the average of the total stress in the matrix can be given by $\sigma_0 + <\sigma>$, where

$$<\sigma> = \mathbf{C}_0 \bar{\mathbf{e}} \tag{1}$$

Here, $<>$ denotes the volume average of a quantity and $\bar{\mathbf{e}}$ stands for the average disturbance in strain of the matrix due to the presence of all fibers.

Following Mori and Tanaka [8], a single fiber is introduced into the composite D. The orientation of this fiber is defined by the angles θ and ϕ as shown in Fig. 1(*b*). To apply the Eshelby's equivalent inclusion method [7] to this single fiber

[1]This work is supported by the National Science Foundation (Grant No. CME-7918249).

[2]On leave from Research Institute for Applied Mechanics, Kyushu University, Higashi-ku, Fukuoka, Japan.

Contributed by the Applied Mechanics Division for presentation at the Winter Annual Meeting, Phoenix, Ariz., November 14-19, 1982, of THE AMERICAN SOCIETY OF MECHANICAL ENGINEERS.

Discussion on this paper should be addressed to the Editorial Department, ASME, United Engineering Center, 345 East 47th Street, New York, N.Y. 10017, and will be accepted until two months after final publication of the paper itself in the JOURNAL OF APPLIED MECHANICS. Manuscript received by ASME Applied Mechanics Division, September, 1981; final revision, February, 1982. Paper No. 82-WA/APM-7.

Copies will be available until July, 1983.

the local coordinate system $x_1'\ x_2'\ x_3'$ is also adopted, where the x_3' axis coincides with the fiber axis. Then

$$\sigma_0' + \sigma' = \mathbf{C}_0\,(\mathbf{e}_0' + \bar{\mathbf{e}}' + \mathbf{e}' - \mathbf{e}^{*\prime})$$
$$= \mathbf{C}_f\,(\mathbf{e}_0' + \bar{\mathbf{e}}' + \mathbf{e}') \tag{2}$$

and

$$\mathbf{e}' = \mathbf{S}\,\mathbf{e}^{*\prime} \tag{3}$$

where σ' is the disturbances of stress due to this single fiber, $\mathbf{e}'$ is that of strain due to only this single fiber, S is the Eshelby tensor for Ω (see [9] for details), and $\mathbf{e}^{*\prime}$ is the eigenstrain (or transformation strain), which has nonvanishing components in Ω, but becomes zero outside Ω. The prime indicates tensorial quantities referred to the local coordinate system $x_1'\ x_2'\ x_3'$. The stress disturbance σ' in Ω can be obtained from equation (2).

$$\sigma' = \mathbf{C}_0\,(\bar{\mathbf{e}}' + \mathbf{S}\,\mathbf{e}^{*\prime} - \mathbf{e}^{*\prime}) \tag{4}$$

Also,

$$\sigma_0' = \mathbf{C}_0\,\mathbf{e}_0' \quad (\text{or } \sigma_0 = \mathbf{C}_0\,\mathbf{e}_0) \tag{5}$$

Since the added single fiber can be regarded as any fiber in the composite, equations (2) and (4) hold for any inclusion in the matrix. From equation (2)

$$\mathbf{e}^{*\prime} = -((\mathbf{C}_f - \mathbf{C}_0)\mathbf{S} + \mathbf{C}_0)^{-1} \cdot (\mathbf{C}_f - \mathbf{C}_0)(\mathbf{e}_0' + \bar{\mathbf{e}}') \tag{6}$$

and

$$\mathbf{e}' - \mathbf{e}^{*\prime} = -(\mathbf{S} - \mathbf{I})((\mathbf{C}_f - \mathbf{C}_0)\mathbf{S} + \mathbf{C}_0)^{-1} \cdot (\mathbf{C}_f - \mathbf{C}_0)(\mathbf{e}_0' + \bar{\mathbf{e}}') \tag{7}$$

The results of $\mathbf{e}^{*\prime}$ and $\mathbf{e}'$ from equations (6) and (7), after being transformed to the global coordinate system of $x_1\ x_2\ x_3$, are applied to the following relation

$$\bar{\mathbf{e}} + 1/V_D \int_\Omega (\mathbf{e} - \mathbf{e}^*)\,dV = 0 \tag{8}$$

where V_D denotes the volume of domain D. It is shown in Appendix A that equation (8) is equivalent to the requirement that the integration of the stress distrubance over the whole domain vanishes [5, 6, 9] namely, $\int_D \sigma\,dV = 0$. Equation (8) represents, in general, six linear algebraic equations with the six unknown components of $\bar{\mathbf{e}}$. The subsitution of $\bar{\mathbf{e}}$ into equation (6) yields $\mathbf{e}^{*\prime}$.

Furthermore, the equivalency of the strain energies of the composite system [5] can be expressed by

$$1/2\ \sigma_0 \cdot \mathbf{C}_c^{-1}\ \sigma_0 = 1/2\ \sigma_0 \cdot \mathbf{e}_0 + 1/2\quad 1/V_D \int_\Omega \sigma_0 \cdot \mathbf{e}^* dV \tag{9}$$

where $\mathbf{C}_c$ is the effective stiffness tensor of the composite to be computed. We consider here the uniaxially applied stress σ_0 along the x_3-axis as shown in Fig. 1(*a*). Then the effective longitudinal Young's modulus E_L of the composite can be obtained by inserting $\mathbf{e}^{*\prime}$ into equation (9).

$$\frac{\mathrm{E}_L}{\mathrm{E}_0} = \frac{1}{1 + \dfrac{\mathrm{E}_0}{\sigma_0} \cdot \dfrac{1}{V_D} \displaystyle\int_\Omega e_{33}^*\,dV} \tag{10}$$

where E_0 is the Young's modulus of the matrix and e_{33}^* is the normal eigenstrain along the x_3-axis.

The volume integrals of equations (8) and (10) are performed by the use of the density function ρ [Appendix B], which is a function of θ only, and also by the use of the relations between $\mathbf{e}^*$ (θ, ϕ) and $\mathbf{e}^*$ $(\theta, 0)$, and between $\mathbf{e}(\theta, \phi)$ and $\mathbf{e}(\theta, 0)$ [Appendix C].

By taking into account the fact that $\bar{\mathbf{e}}$ has only two unknown components, $\bar{e}_{11}$ $(\equiv \bar{e}_{22})$ and $\bar{e}_{33}$ [Appendix D] and using the results of Appendices B, C, and D the following results are obtained from equation (8)

$$\bar{e}_{11} + f\int_0^\alpha g(\theta)\ 1/2\ \{e_{11}(\theta,0) + e_{22}(\theta,0) - e_{11}^*(\theta,0) - e_{22}^*(\theta,0)\}\,d\theta = 0 \tag{11}$$

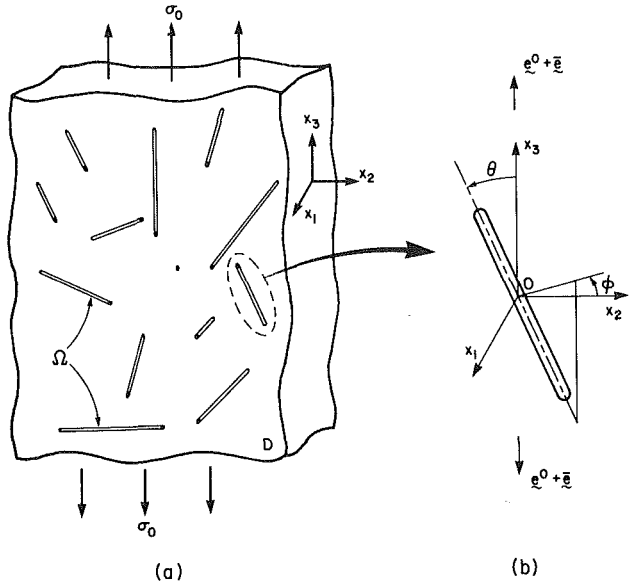

Fig. 1 Calculation model

$$\bar{e}_{33} + f\int_0^\alpha g(\theta) \cdot \{e_{33}(\theta,0) - e_{33}^*(\theta,0)\}\,d\theta = 0 \tag{12}$$

where f is the volume fraction of fiber and

$$g(\theta) = \begin{cases} \dfrac{\sin\theta}{1-\cos\alpha} & \text{for} \quad \rho = \rho_0 \qquad (13) \\[2ex] \dfrac{\cos a\,\theta \sin\theta}{\dfrac{1-\cos(1+a)\alpha}{2(1+a)} + \dfrac{1-\cos(1-a)\alpha}{2(1-a)}} & \text{for } \rho = \rho_0 \cos a\,\theta \qquad (14) \end{cases}$$

Here, the fibers are assumed to be distributed in $0 \leqq \theta \leqq \alpha$. Also, $e_{ij}(\theta, 0)$ and $e_{ij}^*(\theta, 0)$ are, respectively, components of the induced strain and eigenstrain for a fiber in the global coordinate system. For convenience of calculation, this fiber is assumed to lie in the $x_2 - x_3$ plane at an angle θ with the x_3-axis.

By using the vector notation,

$$\mathbf{e}_0'(\theta,0) = (-\nu,\ \sin^2\theta - \nu\cos^2\theta,\ -\nu\sin^2\theta + \cos^2\theta,$$
$$0,\ 0,\ (1+\nu)\sin\theta\cos\theta)^t\,\frac{\sigma_0}{\mathrm{E}_0}$$
$$\bar{\mathbf{e}}'(\theta,0) = (\bar{e}_{11},\ \bar{e}_{33}\sin^2\theta + \bar{e}_{11}\cos^2\theta,\ \bar{e}_{11}\sin^2\theta + \bar{e}_{33}\cos^2\theta,\ 0,\ 0,\ (\bar{e}_{33} - \bar{e}_{11})\sin\theta\cos\theta)^t \tag{15}$$

where t denotes the transpose.

Then, from equations (15) and (6) and the tensor transformation it can be shown that the integrals in equations (11) and (12) are functions of the linear combinations of the unknowns $\bar{e}_{11}$ and $\bar{e}_{33}$

$$\bar{e}_{11} + f(a_{11}\,\bar{e}_{11} + a_{13}\,\bar{e}_{33} + a_{10}) = 0$$
$$\bar{e}_{33} + f(a_{31}\,\bar{e}_{11} + a_{33}\,\bar{e}_{33} + a_{30}) = 0 \tag{16}$$

where a_{ij} are constants.

Inputting solutions of $\bar{e}_{11}$ and $\bar{e}_{33}$ into equations (15) and (7), and replacing unit matrix $\mathbf{I}$ by zero matrix $\mathbf{0}$ in equation (7) leads to the result that the left-hand side of equation (7) becomes $1/V_D \int_\Omega \mathbf{e}^* dV$. This result is substituted into equation (10) to obtain the solution of E_L.

3 Results

Results of this analysis are first compared with existing solutions of composite elastic moduli where the fibers are completely random in their orientations. Figure 2(*a*) shows the comparisons of the effective Young's modulus E_L for the short fiber case where the elastic properties, following those of [3], are $E_f/E_0 = 20$, $\nu_f = 0.3$, and $\nu_0 = 0.4$, and $L/r = 2$. E_f is the fiber Young's modulus, ν_0 and ν_f are, respectively, matrix and fiber Poisson's ratios. Also, fiber length is $2L$ and diameter is $2r$. The dotted lines are the upper and lower-bound predictions of Chou and Nomura [3]. Figure 2(*b*) is for the case of continuous fibers and the elastic properties [3] are $E_f/E_0 = 32.4$, $\nu_f = 0.25$ and $\nu_0 = 0.4$. $L/_r = 10{,}000$ is actually used in the present calculations. The present theory again lies within the bound predictions of [3] and is lower than that of a self-consistent approach by Chou, Nomura, and Taya [4].

Figures 3 and 4 demonstrate the effect of fiber density distribution on the effective Young's modulus E_L. The case of short carbon fiber-reinforced polyamide 66 is considered and the material elastic properties are $E_f/E_0 = 100$, $\nu_0 = 0.42$ and $\nu_f = 0.17$. Two fiber density distributions, uniform and cosine types, are examined (see equations (*B*-4) and (*B*-5) for details). The angle α denotes the range of fiber orientation distribution relative to the x_3-axis or the loading direction. Figure 3 shows that, for a fixed fiber volume function f, E_L is higher for the cosine-type orientation distribution than the uniform-type as expected. The case of uniform fiber orientation distribution and $\alpha = 90$ deg gives rise to an isotropic material and thus the lowest effective Young's modulus.

Figure 4 demonstrates E_L as a function of α for both types of fiber orientation distributions. The effective moduli in Fig. 4 are normalized by E_*, the composite effective moduli when the fibers are aligned with the x_3-axis. E_* naturally is a function of fiber volume fraction and its values are, for instance, 8.50 E_0, 16.41 E_0, 24.77 E_0 and 33.62 E_0 for $f = 0.1$, 0.2, 0.3, and 0.4 respectively. The values of E_L/E_* drops rapidly in the range of $\alpha = 30$ and 60 deg. It is also interesting to note that E_L/E_* is more sensitive to fiber orientation distribution than fiber volume content.

4 Conclusions and Discussions

1 The present analysis is based on the Eshelby's equivalent inclusion method [7] and the average induced strain approach of Taya and Chou [5], and Taya and Mura [6].

2 Previous theories [2-3] of effective Young's modulus of misoriented short fiber composites are performed by first evaluating the modulus of the aligned short fiber composite at

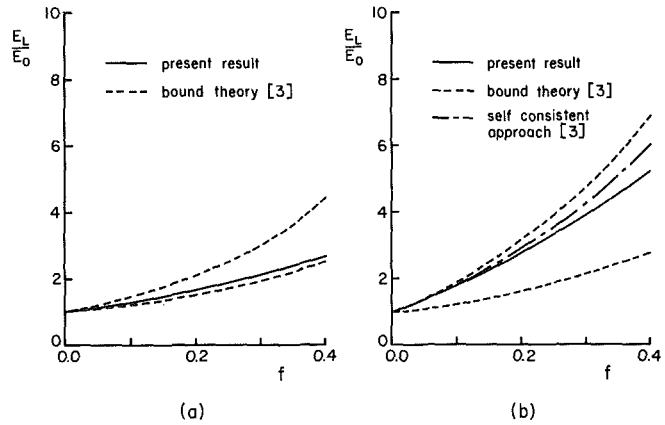

Fig. 2 The effective Young's modulus E_L for the cases of: (*a*) $E_f/E_0 = 20.0$, $\nu_f = 0.3$, $\nu_0 = 0.4$, $L/r = 2.0$; and (*b*) $E_f/E_0 = 32.4$, $\nu_f = 0.25$, $\nu_0 = 0.4$, $L/r \to \infty$

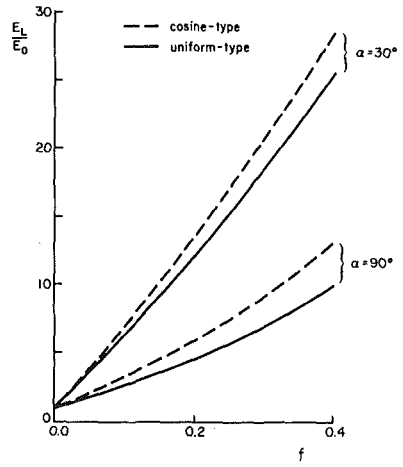

Fig. 3 The variation of effective Young's modulus E_L with fiber volume fraction f

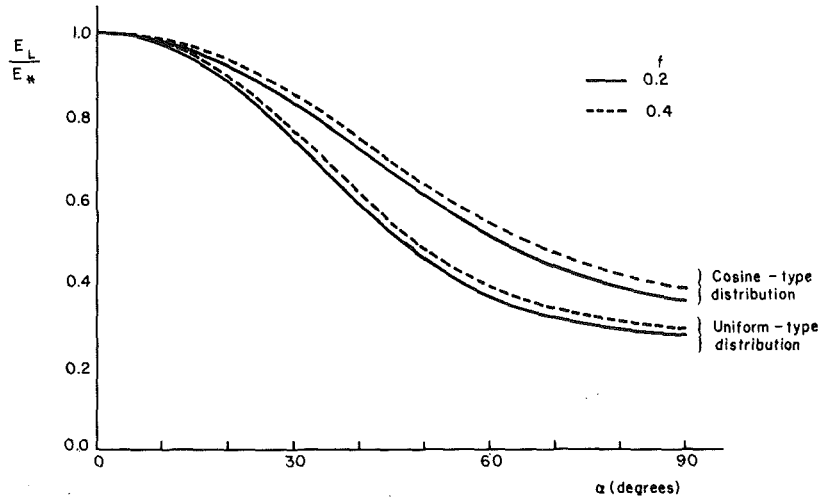

Fig. 4 The variation of effective Young's modulus ratio E_L/E_* with fiber distribution limit angle α

the same fiber volume content. The modulus value at a specific fiber orientation is obtained by tensor transformation of the aligned fiber case. Then the effective Young's modulus is derived by integrating the modulus values within the range of fiber orientation distributions and using the fiber orientation distribution function as the weighting function in the integration. The linear superposition of elastic moduli of different orientations neglects the interaction of the fibers, which is included in the present analysis.

3 The effective Young's modulus of a short fiber composite is more sensitive to fiber orientation distribution than fiber volume content.

5 Acknowledgment

We thank Mr. Y. Mikata for his help in some of the computations.

References

1 Halpin, J. C., and Pagano, N. J., "A Laminate Approximation for Randomly Oriented Fibrous Composites," *Journal of Composite Materials*, Vol. 3, 1969, pp. 720-724.

2 Christensen, R. M., *Mechanics of Composite Materials*, Wiley-Interscience, New York, 1979.

3 Chou, T. W., and Nomura, S., "Fiber Orientation Effects on the Thermoelastic Properties of Short-Fiber Composites," *Fiber Science and Technology*, Vol. 14, 1980-1981, pp. 279-291.

4 Chou, T. W., Nomura, S., and Taya, M., "A Self-Consistent Approach to the Elastic Stiffness of a Short-Fiber Composite," *Journal of Composite Materials*, Vol. 14, 1980, pp. 178-188.

5 Taya, M., and Chou, T. W., "On Two Kinds of Ellipsoidal Inhomogeneities in an Infinite Elastic Body: An Application to a Hybrid Composite," *International Journal of Solids and Structures*, Vol. 17, 1981, pp. 553-563.

6 Taya, M., and Mura, T., "On Stiffness and Strength of an Aligned Short-Fiber Reinforced Composite Containing Fiber-End Cracks Under Uniaxial Applied Stress," ASME JOURNAL OF APPLIED MECHANICS, Vol. 48, 1981, pp. 361-367.

7 Eshelby, J. D., "The Determination of the Elastic Field of an Ellipsoidal Inclusion, and Related Problems," *Proceedings, Royal Society of London*, Vol. A241, 1957, pp. 376-396.

8 Mori, T., and Tanaka, K., "Average Stress in Matrix and Average Elastic Energy of Materials With Misfitting Inclusions," *Acta Mettallurgica*, Vol. 21, 1973, pp. 571-574.

9 Mura, T., "Micromechanics of Defects in Solids," Noordhoof International Publishing, in press.

APPENDIX

Appendix A (Derivation of equation (8))

The equation (2) is rewritten as follows by using the global coordinate system $x_1\ x_2\ x_3$

$$\boldsymbol{\sigma}_0+\boldsymbol{\sigma}=\mathbf{C}_0\,(\mathbf{e}_0+\bar{\mathbf{e}}+\mathbf{e}-\mathbf{e}^*) \tag{A-1}$$

Applying equation (A-1) to $\int_D \boldsymbol{\sigma}\,dV = 0$ along with the use of $\boldsymbol{\sigma}_0 = \mathbf{C}_0\,\mathbf{e}_0$ we obtain

$$\int_{D-\Omega}\mathbf{C}_0\,(\bar{\mathbf{e}}+\mathbf{e})\,dV+\int_\Omega \mathbf{C}_0\,(\bar{\mathbf{e}}+\mathbf{e}-\mathbf{e}^*)dV=0 \tag{A-2}$$

The first integral in (A-2) of the matrix region $D-\Omega$ is defined in equation (1) as $\mathbf{C}_0\,\bar{\mathbf{e}}\cdot V_{D-\Omega}$, where $V_{D-\Omega}$ is the volume of the matrix region. Then

$$\int_{D-\Omega}\mathbf{C}_0\,\mathbf{e}\,dV=0 \tag{A-3}$$

and

$$\int_D \mathbf{C}_0\bar{\mathbf{e}}\,dV+\int_\Omega \mathbf{C}_0\,(\mathbf{e}-\mathbf{e}^*)dV=0 \tag{A-4}$$

Premultiplying equation (A-4) by $\mathbf{C}_0^{-1}$ and dividing by the total volume V_D, we obtain

$$\bar{\mathbf{e}}+1/V_D\int_\Omega(\mathbf{e}-\mathbf{e}^*)dV=0 \qquad (6)\text{ and }(A\text{-}5)$$

Appendix B (Volume Integrals in equations (8) and (10))

We consider the case of $\mathbf{e}^*$. When the direction of the fiber *OP* in Fig. 5 is determined, $\mathbf{e}^*$ has the unique value and the reason is as follows. We consider fibers of the same size, that

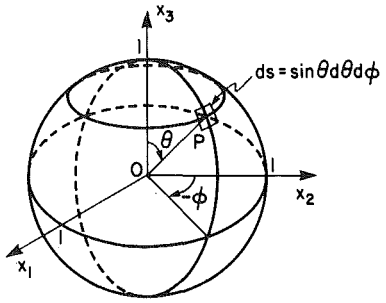

Fig. 5 Fiber orientation space

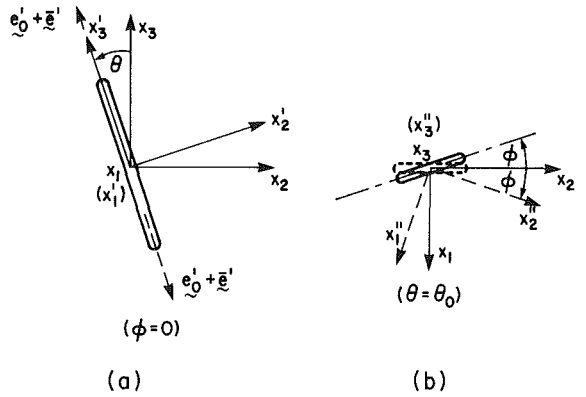

Fig. 6 The relation of strain tensors for e and e^* between $\theta = \theta, \phi = \phi$ and $\theta = 0, \phi = 0$

is, the Eshelby tensor $\mathbf{S}$ is the same for every fiber. Then, the stiffness $\mathbf{C}_f$ and $\mathbf{C}_0$ are constant, and e_0' and $\mathbf{e}'$ are functions of θ and ϕ only because $\mathbf{e}_0$ and $\bar{\mathbf{e}}$ are constant. Thus from equation (6), $\mathbf{e}^{*\prime}$ or $\mathbf{e}^*$ is also a function of θ and ϕ only, $\mathbf{e}^* = \mathbf{e}^*(\theta,\phi)$.

Then, the volume integral of $\mathbf{e}^*$ is

$$1/V_D\int_\Omega e^*\,dV=1/V_D\int_0^\alpha\int_0^{2\pi}\mathbf{e}^*(\theta,\phi)\cdot\rho(\theta,\phi)\cdot V\,dS \tag{B-1}$$

where $\rho(\theta,\phi)$ is the number of fibers intersecting a unit area of the surface of the unit sphere in Fig. 5, V is the volume of a single fiber, and the infinitesimal surface area of the sphere $dS = \sin\theta d\theta d\phi$. The distribution of fibers is in the region defined by $0 \le \phi \le 2\pi$ and $0 \le \theta \le \alpha$. The volume fraction of fiber f is defined by the following equation.

$$f=1/V_D\int_\Omega\rho(\theta,\phi)\,VdS \tag{B-2}$$

By inserting equation (B-2) into equation (B-1), we obtain

$$1/V_D\int_\Omega\mathbf{e}^*dV=f\cdot\frac{\int_0^\alpha\int_0^{2\pi}\mathbf{e}^*(\theta,\phi)\cdot\rho(\theta,\phi)\cdot\sin\theta d\theta d\phi}{\int_0^\alpha\int_0^{2\pi}\rho(\theta,\phi)\sin\theta d\theta d\phi} \tag{B-3}$$

We consider two types of orientation distribution function: ρ_0 and $\rho_0\cos a\theta$, where a and ρ_0 are the constants. When $\rho(\theta,\phi) = \rho_0$,

$$1/V_D\int_\Omega\mathbf{e}^*\,D_V=f\int_0^\alpha\frac{\sin\theta}{1-\cos\alpha}d\theta\cdot1/2\pi\int_0^{2\pi}\mathbf{e}^*(\theta,\phi)\,d\phi \tag{B-4}$$

When $\rho(\theta,\phi) = \rho_0\cos\theta$,

$$1/V_D\int_\Omega\mathbf{e}^*\,dV$$

$$=f\int_0^\alpha\frac{\cos a\theta\cdot\sin\theta}{\frac{1}{2(1+a)}(1-\cos(1+a)\alpha)+\frac{1}{2(1-a)}(1-\cos(1-a)\alpha)}\cdot$$

$$1/2\pi\int_0^{2\pi} \mathbf{e}^*(\theta,\phi)\,d\phi \qquad (B\text{-}5)$$

Appendix C (Derivation of Eigenstrain $\mathbf{e}^*(\theta,\phi)$)

We apply equation (6) to the case of Fig. 6(*a*), where $\phi = 0$. After the transformation from the local to the global system we get $e^*_{11}(\theta,0)$, $e^*_{22}(\theta,0)$, $e^*_{33}(\theta,0)$, $e^*_{12}(\theta,0)$, $e^*_{13}(\theta,0)$, and $e^*_{23}(\theta,0)$, which are components of the eigenstrain $\mathbf{e}^*$. The general case, that is, a fiber indicated by the solid line (Fig. 6(*b*)) has the same components of the eigenstrain as those of a fiber indicated by the dotted line and represented by the local coordinate system $x_1'' \; x_2'' \; x_3''$. Then

$$e^*_{11}(\theta,\phi) = e^*_{11}(\theta,0)\cos^2\phi + e^*_{12}(\theta,0)(-2\sin\phi\cos\phi) + e^*_{22}(\theta,0)\sin^2\phi$$

$$e^*_{22}(\theta,\phi) = e^*_{11}(\theta,0)\sin^2\phi + e^*_{12}(\theta,0)(2\sin\phi\cos\phi) + e^*_{22}(\theta,0)\cos^2\phi$$

$$e^*_{33}(\theta,\phi) = e^*_{33}(\theta,0)$$

$$e^*_{12}(\theta,\phi) = (e^*_{11}(\theta,0) - e^*_{22}(\theta,0))\sin\phi\cos\phi + e^*_{12}(\theta,0)(\cos^2\phi - \sin^2\phi)$$

$$e^*_{13}(\theta,\phi) = e^*_{13}(\theta,0)\cos\phi - e^*_{23}(\theta,0)\sin\phi$$

$$e^*_{23}(\theta,\phi) = e^*_{13}(\theta,0)\sin\phi + e^*_{23}(\theta,0)\cos\phi \qquad (C\text{-}1)$$

Appendix D (Unknowns in equation (8))

By the use of equation (*C*-1) we get the integral $1/2\pi\int_0^{2\pi} e^*_{ij}(\theta,\phi)\,d\phi$ in equations (*B*-4) and (*B*-5) as follows,

$$\begin{array}{ll} 1/2\,(e^*_{11}(\theta,0)+e^*_{22}(\theta,0)) & \text{for } (i,j)=(1,1) \text{ or } (2,2) \\ e^*_{33}(\theta,0) & \text{for } (i,j)=(3,3) \\ 0 & \text{for } (i,j)=(1,2),(1,3), \text{ or } (2,3) \end{array} \qquad (D\text{-}1)$$

Thus the volume integral of e^*_{ij} gives

$$1/V_D\int_\Omega e^*_{11}\,dV = 1/V_D\int_\Omega e^*_{22}\,dV$$

$$1/V_D\int_\Omega e^*_{12}\,dV = 1/V_D\int_\Omega e^*_{13}\,dV = 1/V_D\int_\Omega e^*_{23}\,dV = 0 \qquad (D\text{-}2)$$

The same discussions are applicable to the volume integral of $\mathbf{e} - \mathbf{e}^*$ in equation (8). We can conclude that a normal component of $\bar{\mathbf{e}}$ along the x_1 axis is the same as the one along the x_2 axis, and that shear components are zero. Then equation (6) has only two unknowns.

Boundary-Layer Effects in Composite Laminates:

Part 1—Free-Edge Stress Singularities

S. S. Wang
Associate Professor.
Assoc. Mem. ASME

I. Choi
Research Associate.

Department of Theoretical and Applied Mechanics,
University of Illinois,
Urbana, Ill. 61801

A study of boundary-layer stress singularities in multilayered fiber-reinforced composite laminates is presented. Based on Lekhnitskii's stress potentials and the theory of anisotropic elasticity, formulation of the problem leads to a pair of coupled governing partial differential equations (P.D.E.'s). An eigenfunction expansion method is developed to obtain the homogeneous solution for the governing P.D.E.'s. The order or strength of boundary-layer stress singularity is determined by solving the transcendental characteristic equation obtained from the homogeneous solution for the problem. Numerical examples of the singular strength (or singular eigenvalues) of boundary-layer stresses are given for angle-ply and cross-ply composites as well as the cases of more general composite lamination.

1 Introduction

The response of a multilayered fiber-reinforced composite laminate near its geometric boundaries has been a subject of intensive investigation during the last decade. Both experimental studies and approximate analytical solutions have indicated that complex stress states with a rapid change of gradients occur along the edges of composite laminates; see, for example, references [1-15]. This phenomenon is considered to result from the presence and interactions of geometric discontinuities of the composite and material discontinuities through the laminate thickness. The anomaly has been found to occur only within a very local region near the geometric boundaries of a composite laminate, and is, therefore, frequently referred to as a "boundary-layer effect" or "free-edge effect"—a problem unique to composite laminates and not observed in homogeneous solids in general. It has been shown further that the boundary-layer effect is three dimensional in nature and not predictable by classical lamination theory (C.L.T.) [16, 17]. The boundary-layer effect is apparently one of the most fundamental and important problems in the mechanics and mechanical behavior of composite laminates. The high stresses developed in the boundary-layer region coupled with the low interlaminar strength are certainly of critical significance in aggravating the failure of composite materials and structures. For example, boundary-layer stresses have been observed to be responsible for the initiation and growth of local heterogeneous damage in the forms of interlaminar (delamination) and intralaminar (transverse cracking) fracture in composite laminates under static loading [3, 18]. They are considered to have even greater effects on the long-term strength of composite laminates under cyclic fatigue loading [19, 20].

While the significance of boundary-layer effects has long been recognized, research progress on this subject has been relatively slow. The situation is apparently caused by the inherent complexities involved in the problem: the strong anisotropy of mechanical properties of each individual ply, the abrupt change of material properties through the laminate thickness direction, the geometric discontinuity along laminate boundaries, and the coupling between in-plane and transverse deformations and stresses near the edges of a composite laminate. According to Pagano [14], analytical studies of this problem to date may be roughly classified into two general categories: approximate theories and numerical solutions. The first approximate solution for finite-width composite laminates was proposed by Puppo, et al. [4] based on a laminate model containing anisotropic laminae and isotropic shear layers with interlaminar normal stress being neglected throughout the laminate. Other approximate theories were also attempted to examine the problem such as the extension of the higher-order plate theory [21] by Pagano [10], the perturbation method by Hsu, et al. [12], and a boundary-layer theory by Tang, et al. [11]. Recently, Pagano [14, 15] has developed an approximate theory based on assumed in-plane stresses and the use of Reissner's variational principle. Even though there is no singularity involved in the formulation, the approach has certain features significantly important in objectively determining detailed laminate stress fields. The study of edge stresses in composites by using a numerical (finite difference) method was apparently first made by Pipes, et al. [5]. Isakson and Levy [6] developed a finite-element scheme containing membrane elements, which closely resemble the laminate model of Puppo et al. [4]. Later finite element studies on this subject by Wang, et al. [13] and Herakovich, et al. [18] led to numerical solutions similar to

Contributed by the Applied Mechanics Division for publication in the JOURNAL OF APPLIED MECHANICS.

Discussion on this paper should be addressed to the Editorial Department, ASME, United Engineering Center, 345 East 47th Street, New York, N.Y. 10017, and will be accepted until two months after final publication of the paper itself in the JOURNAL OF APPLIED MECHANICS. Manuscript received by ASME Applied Mechanics Division, October, 1981; final revision, April, 1982.

that given by Pipes [5]. Due to the singular nature of the problem, a large number of elements, especially through the thickness direction, are required in conjunction with a lengthy extrapolation procedure in order to achieve satisfactory solutions even for a simple two or three-layer laminate. Improved finite-element methods by using a more complex element stiffness formulation based on Maxwell stress functions [7] and by hybrid-stress elements [22] have been able to achieve an expeditious computation with significantly less elements. Unfortunately, the refinements do not guarantee [23] the convergence and accuracy of the numerical solutions because of the singular nature of the boundary-layer stress field. That is, with each more refined analysis, numerical values of the maximum interlaminar stresses are shown to rise with continuously decreasing element size. The quest, apparently, is to show that a stress singularity exists at the edge of a composite laminate.

From a linear elasticity point of view, it is well known that stress singularities generally occur at the corners of geometric boundaries joining dissimilar materials (see, for example, [24-26]). Unfortunately, the search for the order of stress singularity in the boundary-layer region of a composite laminate containing anisotropic plies has not been successful to date, to the authors' knowledge. Since the singular boundary-layer stresses are observed to be very localized, the precise nature of the boundary-layer effect will not be fully understood until the exact order of the stress singularity is determined. In this paper, the first in succession, a theoretical investigation of the free-edge stress singularity in composite laminates is presented.

In the next section, a mathematical model and basic equations for each lamina of the composite are presented. Based on the theory of anisotropic elasticity and Lekhnitskii's stress potentials [27], a pair of linear governing partial differential equations is derived. Associated near-field boundary conditions, interface continuity, and end loading conditions are also given. The homogeneous solution for the problem is obtained in Section 3 by an eigenfunction expansion method. A solution procedure used to evaluate the exact order of the boundary-layer stress singularity is presented. Commonly used cross-ply and general angle-ply composite laminates are examined in detail. Numerical examples of edge stress singularities for graphite-epoxy composites with various fiber orientations are given in Section 4. As will be shown later, the free-edge stress singularity in a composite laminate is determined explicitly in this paper. It settles, once and for all, the previous conjecture of boundary-layer stress singularities in composite materials, and provides a rigorous mathematical method for determining the exact order of the edge stress singularity. This gives a fundamental basis for the development of boundary-layer theory in composites. Some of the results have been reported earlier in [28].

2 Formulation

2.1 Basic Equations. Consider a composite laminate composed of fiber-reinforced plies with constitutive equations described by generalized Hooke's law in contracted notation as

$$\epsilon_i = S_{ij}\sigma_j \quad (i,j=1,2,3,4,5,6), \tag{1}$$

where the repeated subscript indicates summation and S_{ij} is the compliance tensor. The engineering strains, ϵ_i, in (1) are defined in a Cartesian coordinate system by

$$\epsilon_1 = \epsilon_x = \frac{\partial u}{\partial x}, \quad \epsilon_2 = \epsilon_y = \frac{\partial v}{\partial y}, \quad \epsilon_3 = \epsilon_z = \frac{\partial w}{\partial z},$$

$$\epsilon_4 = \gamma_{yz} = \frac{\partial w}{\partial y} + \frac{\partial v}{\partial z}, \quad \epsilon_5 = \gamma_{xz} = \frac{\partial w}{\partial x} + \frac{\partial u}{\partial z},$$

$$\epsilon_6 = \gamma_{xy} = \frac{\partial u}{\partial y} + \frac{\partial v}{\partial x}, \tag{2}$$

where u, v, and w are the components of displacements. The stresses, σ_i, are defined in an analogous manner in the Cartesian coordinate system.

The composite laminate considered here has a finite width and is subjected to surface tractions acting in planes normal to the generator of the lateral surface and not varying along the generator, i.e., the z-axis (Fig. 1). The composite is assumed to be sufficiently long that, in the region far from the ends, the end effect is neglected by virtue of Saint Venant's principle. Consequently, the stresses in the laminate are independent of the z-coordinate. The case of a finite-width composite laminate subjected to a uniform axial strain, $\epsilon_z = e$, along the z-axis has been intensively studied by many researchers [5-13]. The special case in which stresses and displacements are independent of z and $\epsilon_z = 0$ corresponds to the well-known generalized plane deformation [27]. Under these assumptions, the equations of equilibrium without body force read

$$\frac{\partial \sigma_x}{\partial x} + \frac{\partial \tau_{xy}}{\partial y} = 0, \quad \frac{\partial \tau_{xy}}{\partial x} + \frac{\partial \sigma_y}{\partial y} = 0, \quad \frac{\partial \tau_{xz}}{\partial x} + \frac{\partial \tau_{yz}}{\partial y} = 0. \tag{3}$$

Following the procedure in [27], it can be shown after some mathematical manipulation that the general expressions for displacements and the stress component σ_z have the following forms:

$$u = -\frac{1}{2}A_1 S_{33} z^2 - A_4 yz + U(x,y) + \omega_2 z - \omega_3 y + u_0, \tag{4a}$$

$$v = -\frac{1}{2}A_2 S_{33} z^2 + A_4 xz + V(x,y) + \omega_3 x - \omega_1 z + v_0, \tag{4b}$$

$$w = (A_1 x + A_2 y + A_3) S_{33} z + W(x,y) + \omega_1 y - \omega_2 x + w_0, \tag{4c}$$

$$\sigma_z = A_1 x + A_2 y + A_3 - S_{3j}\sigma_j / S_{33}, \quad (j = 1,2,4,5,6,). \tag{4d}$$

The unknown functions, U, V, and W depend on x and y only, and can be shown easily to obey the following relations:

$$\frac{\partial U}{\partial x} = \tilde{S}_{1j}\sigma_j + S_{13}(A_1 x + A_2 y + A_3), \tag{5a}$$

$$\frac{\partial V}{\partial y} = \tilde{S}_{2j}\sigma_j + S_{23}(A_1 x + A_2 y + A_3), \tag{5b}$$

$$\frac{\partial W}{\partial x} = \tilde{S}_{5j}\sigma_j + S_{53}(A_1 x + A_2 y + A_3) + A_4 y, \tag{5c}$$

$$\frac{\partial W}{\partial y} = \tilde{S}_{4j}\sigma_j + S_{43}(A_1 x + A_2 y + A_3) - A_4 x, \tag{5d}$$

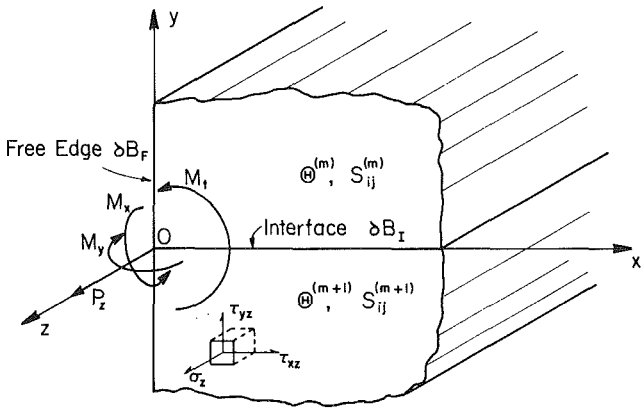

Fig. 1 Geometry and coordinates of a free edge in a composite laminate

$$\frac{\partial U}{\partial y}+\frac{\partial V}{\partial x}=\tilde{S}_{6j}\sigma_j+S_{63}(A_1x+A_2y+A_3), \tag{5e}$$

where

$$\tilde{S}_{ij}=S_{ij}-S_{i3}S_{j3}/S_{33}, \quad (i,j=1,2,4,5,6). \tag{5f}$$

It is obvious that the constants, u_0, v_0, w_0, and ω_i ($i=1,2,3$) in equations (4a–4d) characterize the rigid-body translation and rotation of the solid. A_1 and A_2 represent the bending of the laminate in the x-z and y-z planes. A_3 characterizes the uniform axial extension of the composite laminate, and A_4, the relative angle of rotation about the z-axis.

2.2 Governing Partial Differential Equations. Introducing Lekhnitskii's stress potentials, $F(x,y)$ and $\psi(x,y)$ [27], such that

$$\sigma_x=\frac{\partial^2 F}{\partial y^2}, \quad \sigma_y=\frac{\partial^2 F}{\partial x^2}, \quad \tau_{xy}=-\frac{\partial^2 F}{\partial x\partial y},$$
$$\tau_{xz}=\frac{\partial \psi}{\partial y}, \quad \tau_{yz}=-\frac{\partial \psi}{\partial x}, \tag{6}$$

one can show that the equations of equilibrium are satisfied identically. Eliminating U and V from equations (5a), (5b), and (5e) and W from equations (5c) and (5d) by differentiation, we obtain the following system of governing partial differential equations for the problem:

$$\begin{cases} L_3F+L_2\psi=-2A_4+A_1S_{34}-A_2S_{35}, & (7a)\\ L_4F+L_3\psi=0, & (7b)\end{cases}$$

where L_2, L_3, and L_4 are linear differential operators defined as

$$L_2=\tilde{S}_{44}\frac{\partial^2}{\partial x^2}-2\tilde{S}_{45}\frac{\partial^2}{\partial x\partial y}+\tilde{S}_{55}\frac{\partial^2}{\partial y^2}, \tag{7c}$$

$$L_3=-\tilde{S}_{24}\frac{\partial^3}{\partial x^3}+(\tilde{S}_{25}+\tilde{S}_{46})\frac{\partial^3}{\partial x^2\partial y}-(\tilde{S}_{14}+\tilde{S}_{56})\frac{\partial^3}{\partial x\partial y^2}+\tilde{S}_{15}\frac{\partial^3}{\partial y^3}, \tag{7d}$$

$$L_4=\tilde{S}_{22}\frac{\partial^4}{\partial x^4}-2\tilde{S}_{26}\frac{\partial^4}{\partial x^3\partial y}+(2\tilde{S}_{12}+\tilde{S}_{66})\frac{\partial^4}{\partial x^2\partial y^2}-2\tilde{S}_{16}\frac{\partial^4}{\partial x\partial y^3}+\tilde{S}_{11}\frac{\partial^4}{\partial y^4}. \tag{7e}$$

2.3 Boundary and End Conditions. Assuming that the edges of a composite laminate, ∂B_F, are traction free and that the interface of the mth and $(m+1)$th plies is a straight line meeting the traction-free edge at a right angle (Fig. 1), we can obtain the following boundary conditions along ∂B_F:

$$\sigma_x=\tau_{xy}=\tau_{xz}=0. \tag{8}$$

The conditions at the ends of the composite laminate may have the forms from the statically equivalent loads as

$$\iint_B \tau_{xz}dx\,dy=0, \quad \iint_B \tau_{yz}dx\,dy=0, \quad \iint_B \sigma_z dx\,dy=P_z,$$
$$\iint_B \sigma_z y\,dx\,dy=M_x, \quad \iint_B \sigma_z x\,dx\,dy=M_y,$$
$$\iint_B (\tau_{yz}x-\tau_{xz}y)\,dx\,dy=M_t, \tag{9}$$

where the integrals are taken over the entire area B of the cross section, and P_z, M_x, M_y, and M_t are the applied force, bending moments, and twisting moment acting on the ends of the composite, respectively.

2.4 Interface Continuity Conditions. Consider a portion of the laminate cross section composed of the mth and $(m+1)$th fiber-reinforced laminae, as shown in Fig. 1. Assuming that the plies are perfectly bonded along the interface ∂B_I, one can immediately establish the continuity conditions of the stresses and displacements along the interface as the following:

$$\sigma_x^{(m)}n_x^{(m)}+\tau_{xy}^{(m)}n_y^{(m)}=-\sigma_x^{(m+1)}n_x^{(m+1)}-\tau_{xy}^{(m+1)}n_y^{(m+1)}, \tag{10a}$$
$$\tau_{xy}^{(m)}n_x^{(m)}+\sigma_y^{(m)}n_y^{(m)}=-\tau_{xy}^{(m+1)}n_x^{(m+1)}-\sigma_y^{(m+1)}n_y^{(m+1)}, \tag{10b}$$
$$\tau_{xz}^{(m)}n_x^{(m)}+\tau_{yz}^{(m)}n_y^{(m)}=-\tau_{xz}^{(m+1)}n_x^{(m+1)}-\tau_{yz}^{(m+1)}n_y^{(m+1)}, \tag{10c}$$

and

$$u^{(m)}=u^{(m+1)}, \quad v^{(m)}=v^{(m+1)}, \quad w^{(m)}=w^{(m+1)}, \tag{10d–f}$$

where the superscripts denote the mth and $(m+1)$th plies in a composite laminate, and n_x and n_y are components of unit outward normal to the interface.

3 Homogeneous Solution and Free-Edge Stress Singularity

The governing equations, (7a) and (7b), are coupled linear partial differential equations with constant coefficients related to the anisotropic elastic constants of each individual lamina. With the aid of aforementioned near-field boundary conditions and interface continuity conditions, the structure of the homogeneous solution for the governing P.D.E.'s can be determined easily. The homogeneous boundary conditions and interface continuity conditions also provide important information for determining the strength or the order of the free-edge stress singularity in a composite laminate, which is the major concern in this paper.

According to Lekhnitskii [27], the homogeneous solution for the governing partial differential equations has the general form as

$$F(x,y)=\sum_{k=1}^{6}F_k(x+\mu_k y), \quad \psi(x,y)=\sum_{k=1}^{6}\eta_k F_k'(x+\mu_k y), \tag{11a,b}$$

where the prime (′) in equation (11b) denotes differentiation of the function $F_k(x+\mu_k y)$ with respect to its argument, and the coefficients μ_k are the roots of the following algebraic characteristic equation:

$$l_4(\mu)l_2(\mu)-l_3^2(\mu)=0, \tag{12a}$$

and

$$\eta_k=-l_3(\mu_k)/l_2(\mu_k)=-l_4(\mu_k)/l_3(\mu_k), \tag{12b}$$

where

$$l_2(\mu)=\tilde{S}_{55}\mu^2-2\tilde{S}_{45}\mu+\tilde{S}_{44}, \tag{12c}$$
$$l_3(\mu)=\tilde{S}_{15}\mu^3-(\tilde{S}_{14}+\tilde{S}_{56})\mu^2+(\tilde{S}_{25}+\tilde{S}_{46})\mu-\tilde{S}_{24}, \tag{12d}$$
$$l_4(\mu)=\tilde{S}_{11}\mu^4-2\tilde{S}_{16}\mu^3+(2\tilde{S}_{12}+\tilde{S}_{66})\mu^2-2\tilde{S}_{26}\mu+\tilde{S}_{22}. \tag{12e}$$

It can be shown that equation (12a) cannot have a real root (thus, μ_k have to appear as complex conjugates) and that F_k are analytic functions of the complex variables $Z_k=x+\mu_k y=r(e^{i\theta}+\lambda_k e^{-i\theta})/(1+\lambda_k)$ with $\lambda_k=(1+i\mu_k)/(1-i\mu_k)$ and r and θ being components of polar coordinates. Substituting the expressions of $F(x,y)$ and $\psi(x,y)$, equations (11a) and (11b), into equations (6a–e), the homogeneous solution for stresses σ_i may be expressed in terms of $F_k(Z_k)$ as

$$\sigma_x^{(h)}=\sum_{k=1}^{6}\mu_k^2F_k''(Z_k), \tag{13a}$$

$$\sigma_y^{(h)} = \sum_{k=1}^{6} F_k''(Z_k), \tag{13b}$$

$$\tau_{yz}^{(h)} = -\sum_{k=1}^{6} \eta_k F_k''(Z_k), \tag{13c}$$

$$\tau_{xz}^{(h)} = \sum_{k=1}^{6} \mu_k \eta_k F_k''(Z_k), \tag{13d}$$

$$\tau_{xy}^{(h)} = -\sum_{k=1}^{6} \mu_k F_k''(Z_k). \tag{13e}$$

The expressions for displacement components may be obtained directly from equations (5), (7), and (13) with omission of the terms that are to be included in the particular solution,

$$u^{(h)} = \sum_{k=1}^{6} p_k F_k'(Z_k), \tag{14a}$$

$$v^{(h)} = \sum_{k=1}^{6} q_k F_k'(Z_k), \tag{14b}$$

$$w^{(h)} = \sum_{k=1}^{6} t_k F_k'(Z_k), \tag{14c}$$

where

$$p_k = \tilde{S}_{11}\mu_k^2 + \tilde{S}_{12} - \tilde{S}_{14}\eta_k + \tilde{S}_{15}\eta_k\mu_k - \tilde{S}_{16}\mu_k, \tag{14d}$$

$$q_k = \tilde{S}_{12}\mu_k + \tilde{S}_{22}/\mu_k - \tilde{S}_{24}\eta_k/\mu_k + \tilde{S}_{25}\eta_k - \tilde{S}_{26}, \tag{14e}$$

$$t_k = \tilde{S}_{14}\mu_k + \tilde{S}_{24}/\mu_k - \tilde{S}_{44}\eta_k/\mu_k + \tilde{S}_{45}\eta_k - \tilde{S}_{46}. \tag{14f}$$

We now choose the form of $F_k(Z_k)$ as

$$F_k(Z_k) = C_k Z_k^{\delta+2}/[(\delta+1)(\delta+2)], \tag{15}$$

where C_k and δ are arbitrary complex constants to be determined later. Substituting equation (15) into equations (13) and (14) gives

$$\sigma_x^{(h)} = \sum_{k=1}^{3} [C_k\mu_k^2 Z_k^\delta + C_{k+3}\bar{\mu}_k^2 \bar{Z}_k^\delta], \tag{16a}$$

$$\sigma_y^{(h)} = \sum_{k=1}^{3} [C_k Z_k^\delta + C_{k+3}\bar{Z}_k^\delta], \tag{16b}$$

$$\tau_{yz}^{(h)} = -\sum_{k=1}^{3} [C_k\eta_k Z_k^\delta + C_{k+3}\bar{\eta}_k \bar{Z}_k^\delta], \tag{16c}$$

$$\tau_{xz}^{(h)} = \sum_{k=1}^{3} [C_k\eta_k\mu_k Z_k^\delta + C_{k+3}\bar{\eta}_k\bar{\mu}_k \bar{Z}_k^\delta], \tag{16d}$$

$$\tau_{xy}^{(h)} = -\sum_{k=1}^{3} [C_k\mu_k Z_k^\delta + C_{k+3}\bar{\mu}_k \bar{Z}_k^\delta], \tag{16e}$$

and

$$u^{(h)} = \sum_{k=1}^{3} [C_k p_k Z_k^{\delta+1} + C_{k+3}\bar{p}_k\bar{Z}_k^{\delta+1}]/(\delta+1), \tag{17a}$$

$$v^{(h)} = \sum_{k=1}^{3} [C_k q_k Z_k^{\delta+1} + C_{k+3}\bar{q}_k\bar{Z}_k^{\delta+1}]/(\delta+1), \tag{17b}$$

$$w^{(h)} = \sum_{k=1}^{3} [C_k t_k Z_k^{\delta+1} + C_{k+3}\bar{t}_k\bar{Z}_k^{\delta+1}]/(\delta+1), \tag{17c}$$

where the overbar denotes the complex conjugate of the associated quantity. For convenience, we drop the superscript h associated withthe aforementioned homogeneous solutions for stresses and displacements in this paper.

The homogeneous solutions are required to satisfy the homogeneous boundary conditions and interface continuity conditions. This leads to a standard eigenvalue problem for determining the values of δ. It is noted that δ generally appears as a set of complex conjugates, which enable us to make equations (16) and (17) real functions by superposition. Furthermore, the value of δ is required to satisfy the condition

$$Re[\delta] > -1 \tag{18}$$

to ensure the finiteness of displacement components at the origin, where Re represents the real part of δ.

To expedite further developments, we transform the stress and displacement components from Cartesian coordinates to polar coordinates. Thus, we have

$$\sigma_{\theta\theta} = \sum_{k=1}^{3} (C_k H_{1k} Z_k^\delta + C_{k+3}\bar{H}_{1k}\bar{Z}_k^\delta), \tag{19a}$$

$$\tau_{\theta z} = \sum_{k=1}^{3} (C_k H_{2k} Z_k^\delta + C_{k+3}\bar{H}_{2k}\bar{Z}_k^\delta), \tag{19b}$$

$$\tau_{\theta r} = \sum_{k=1}^{3} (C_k H_{3k} Z_k^\delta + C_{k+3}\bar{H}_{3k}\bar{Z}_k^\delta), \tag{19c}$$

$$\sigma_{rr} = \sum_{k=1}^{3} (C_k H_{4k} Z_k^\delta + C_{k+3}\bar{H}_{4k}\bar{Z}_k^\delta), \tag{19d}$$

$$\tau_{rz} = \sum_{k=1}^{3} (C_k H_{5k} Z_k^\delta + C_{k+3}\bar{H}_{5k}\bar{Z}_k^\delta), \tag{19e}$$

and

$$u_r = \sum_{k=1}^{3} [C_k H_{6k} Z_k^{\delta+1}/(\delta+1) + C_{k+3}\bar{H}_{6k}\bar{Z}_k^{\delta+1}/(\delta+1)], \tag{20a}$$

$$u_\theta = \sum_{k=1}^{3} [C_k H_{7k} Z_k^{\delta+1}/(\delta+1) + C_{k+3}\bar{H}_{7k}\bar{Z}_k^{\delta+1}/(\delta+1)], \tag{20b}$$

$$u_z = \sum_{k=1}^{3} [C_k H_{8k} Z_k^{\delta+1}/(\delta+1) + C_{k+3}\bar{H}_{8k}\bar{Z}_k^{\delta+1}/(\delta+1)], \tag{20c}$$

where Z_k are defined in polar coordinates, and H_{jk} ($j = 1,2, \ldots 8$) are functions of η_k, μ_k, p_k, q_k, t_k, and θ given in Appendix 1.

The traction-free boundary conditions, equations (8a–c), along the free edges of the mth and $(m+1)$th plies in polar coordinates read

$$\sigma_{\theta\theta}^{(m)} = \tau_{\theta z}^{(m)} = \tau_{r\theta}^{(m)} = 0 \quad \text{on} \quad \theta = \frac{\pi}{2}, \tag{21a}$$

$$\sigma_{\theta\theta}^{(m+1)} = \tau_{\theta z}^{(m+1)} = \tau_{r\theta}^{(m+1)} = 0 \quad \text{on} \quad \theta = -\frac{\pi}{2}. \tag{21b}$$

The continuity conditions, equations (10a–f), along the ply interface give

$$\{\sigma_{\theta\theta}^{(m)}, \tau_{\theta z}^{(m)}, \tau_{r\theta}^{(m)}, u_r^{(m)}, u_\theta^{(m)}, u_z^{(m)}\} = \{\sigma_{\theta\theta}^{(m+1)}, \tau_{\theta z}^{(m+1)}, \tau_{r\theta}^{(m+1)}, u_r^{(m+1)}, u_\theta^{(m+1)}, u_z^{(m+1)}\} \quad \text{on} \quad \theta = 0. \tag{21c}$$

More explicitly, the homogeneous boundary conditions, equations (21a,b), and the continuity conditions, equation (21c), provides

$$\sum_{k=1}^{3} \left\{ C_k^{(m)} H_{jk}^{(m)}\left(\frac{\pi}{2}\right)\left[\Omega_k^{(m)}\left(\frac{\pi}{2}\right)\right]^\delta + C_{k+3}^{(m)}\overline{H_{jk}^{(m)}\left(\frac{\pi}{2}\right)}\left[\overline{\Omega_k^{(m)}\left(\frac{\pi}{2}\right)}\right]^\delta \right\} = 0, \tag{22a}$$

$$\sum_{k=1}^{3} \left\{ C_k^{(m+1)} H_{jk}^{(m+1)}\left(\frac{-\pi}{2}\right)\left[\Omega_k^{(m+1)}\left(\frac{-\pi}{2}\right)\right]^\delta \right.$$

$$+C_{k+3}^{(m+1)}\overline{H_{jk}^{(m+1)}\left(\frac{-\pi}{2}\right)}\overline{\left[\Omega_k^{(m+1)}\left(\frac{-\pi}{2}\right)\right]^{\delta}}\Bigg\}=0, \quad (22b)$$

$$\sum_{k=1}^{3}\{[C_k^{(m)}\Gamma_{rk}^{(m)}+C_{k+3}^{(m)}\bar{\Gamma}_{rk}^{(m)}]-[C_k^{(m+1)}\Gamma_{rk}^{(m+1)}$$

$$+C_{k+3}^{(m+1)}\bar{\Gamma}_{rk}^{(m+1)}]\}=0, \quad (j=1,2,3;\ r=1,2,3,4,5,6), \quad (22c)$$

where $H_{jk}(\pi/2)$ and $H_{jk}(-\pi/2)$ are values of H_{ij} evaluated at $\theta=\pi/2$ and $\theta=-\pi/2$, respectively; $\Omega_k(\theta)$ are defined as

$$\Omega_k(\theta)=(e^{i\theta}+\lambda_k e^{-i\theta})/(1+\lambda_k), \quad (23)$$

and

$$\Gamma_{1k}=1,\Gamma_{2k}=\eta_k,\Gamma_{3k}=\mu_k,\Gamma_{4k}=p_k,\Gamma_{5k}=q_k,\Gamma_{6k}=t_k. \quad (24)$$

Solving for $C_k^{(m)}$ from equation (22c) in terms of $C_k^{(m+1)}$, one finds

$$C_k^{(m)}=a_{ks}C_s^{(m+1)} \quad (k,s=1,2,\ldots 6). \quad (25)$$

Substituting equation (25) into equation (22a) gives

$$\sum_{s=1}^{6}\left(C_s^{(m+1)}\sum_{k=1}^{3}\left\{H_{jk}^{(m)}\left(\frac{\pi}{2}\right)a_{ks}\left[\Omega_k^{(m)}\left(\frac{\pi}{2}\right)\right]^{\delta}\right.\right.$$

$$\left.\left.+\overline{H_{jk}^{(m)}\left(\frac{\pi}{2}\right)}a_{(k+3)s}\overline{\left[\Omega_k^{(m)}\left(\frac{\pi}{2}\right)\right]^{\delta}}\right\}\right)=0. \quad (26)$$

Equations (22b) and (26) constitute a system of homogeneous linear algebraic equations in $C_k^{(m+1)}$. The existence of a nontrival solution for $C_k^{(m+1)}$ requires vanishing of the coefficient determinant

$$|\Delta(\delta)|=0, \quad (27)$$

where $\Delta(\delta)$ is a 6×6 matrix involving δ in a transcendental form. Thus, equation (27) is a transcendental characteristic equation for the standard eigenvalue problem. It has a very complicated structure as can be seen from the coefficients of $C_k^{(m+1)}$ in equations (22) and (26), and the detailed expression for $\Delta(\delta)$ is not given here. To obtain solutions for the characteristic equation requires the employment of standard numerical techniques such as Muller's method [29] with the aid of a digital computer. The eigenvalues obtained from the numerical solution of equation (27) give important information concerning the behavior of the edge stress and displacement. Due to positive definiteness of strain energy of the elastic body and the argument given in equation (18), the eigenvalues, δ_n, bounded by

$$-1<Re[\delta_n]<0, \quad (28)$$

characterize the order of stress singularity in the boundary layer. Thus, for small values of r, the asymptotic stresses are proportional to $r^{Re[\delta_n]}$, provided that δ_n satisfy equation (28).

4 Degenerated Cases—Cross-Ply Composite Laminates

In the case of a cross-ply composite laminate, i.e., laminae with 0 and 90 deg fiber orientations only, the stresses σ_x, σ_y, τ_{xy} are uncoupled with τ_{xz} and τ_{yz} by virtue of the material symmetry in each lamina. For illustrative purposes, we restrict our attention to the problem of composite laminates under stretching and/or bending; thus, we shall concentrate our study on the four stress components, σ_x, σ_y, τ_{xy}, σ_z. The general expressions for displacements and σ_z may be simplified as

$$u=-\frac{1}{2}A_1S_{33}z^2+U(x,y)+\omega_2 z-\omega_3 y+u_0, \quad (29a)$$

$$v=-\frac{1}{2}A_2S_{33}z^2+V(x,y)+\omega_3 x-\omega_1 z+v_0, \quad (29b)$$

$$w=(A_1x+A_2y+A_3)S_{33}z+\omega_1 y-\omega_2 x+w_0, \quad (29c)$$

$$\sigma_z=A_1x+A_2y+A_3-(S_{31}\sigma_x+S_{32}\sigma_y)/S_{33}. \quad (29d)$$

Following the same procedure shown in the preceding section, the governing partial differential equations are uncoupled and may be written as

$$L_4F(x,y)=0, \quad (30a)$$

where L_4 is defined as before

$$L_4=\tilde{S}_{22}\frac{\partial^4}{\partial x^4}+(2\tilde{S}_{12}+\tilde{S}_{66})\frac{\partial^4}{\partial x^2\partial y^2}+\tilde{S}_{11}\frac{\partial^4}{\partial y^4}. \quad (30b)$$

The homogeneous solution for equation (30a) may be obtained in a simplier form as

$$F(x,y)=\sum_{k=1}^{4}F_k(x+\mu_k y), \quad (31)$$

where μ_k are the roots of the following algebraic equation:

$$l_4(\mu)=\tilde{S}_{11}\mu^4+(2\tilde{S}_{12}+\tilde{S}_{66})\mu^2+\tilde{S}_{22}=0. \quad (32)$$

The homogeneous stress and displacement solutions are then given as

$$\sigma_x=\sum_{k=1}^{4}\mu_k^2F_k''(x+\mu_k y), \quad \sigma_y=\sum_{k=1}^{4}F_k''(x+\mu_k y),$$

$$\tau_{xy}=-\sum_{k=1}^{4}\mu_k F_k''(x+\mu_k y), \quad (33)$$

$$U(x,y)=\sum_{k=1}^{4}p_k F_k'(x+\mu_k y),$$

$$V(x,y)=\sum_{k=1}^{4}q_k F_k'(x+\mu_k y), \quad (34)$$

where

$$p_k=\tilde{S}_{11}\mu_k^2+\tilde{S}_{12}, \quad q_k=\tilde{S}_{21}\mu_k+\tilde{S}_{22}/\mu_k. \quad (35)$$

We shall choose the form of $F_k(x,y)$ as

$$F_k(Z_k)=\sum_{k=1}^{4}C_k Z_k^{\delta+2}/[(\delta+1)(\delta+2)], \quad (36)$$

where C_k and δ are, as before, arbitrary complex constants to be determined later. Imposing the homogeneous traction-free boundary conditions along the free edges and the continuity condition along the ply interface, one can proceed with the same procedure outlined in the preceding section. Then, the eigenvalues and eigenfunctions can be determined in a manner similar to those in the previous cases.

5 Numerical Examples

From the structure of the governing partial differential equations and the homogeneous solution for the problem, it is clearly seen that the asymptotic stress and strain fields in the vicinity of the edge are governed by the singular terms with the strength of stress singularity δ_n determined from the eigenvalue analysis. Examining the structure of equations (22b) and (26), we easily find that the eigenvalue solution and, therefore, the edge stress singularity is related to laminar constitutive properties and fiber orientations of adjacent plies only.

Consider a composite laminate with ply properties typical of a high-modulus graphite-epoxy system [5]:

$$E_L=20\times 10^6 \text{ psi}, \quad E_T=E_z=2.1\times 10^6 \text{ psi},$$

$$G_{LT}=G_{Lz}=G_{Tz}=0.85\times 10^6 \text{ psi}, \quad (37)$$

$$\nu_{LT}=\nu_{Tz}=\nu_{Lz}=0.21,$$

Table 1 Roots μ_K of characteristic equations for graphite-epoxy composite system with fiber orientation Θ*

±Θ	$\mu_{1,2}$	$\mu_{3,4}$	$\mu_{5,6}$
15°	±0.88782 i	±1.10301 i	±1.56776 i
30°	±0.86222 i	±1.06956 i	±2.53630 i
45°	±0.80902 i	±1.03503 i	±3.44438 i
60°	±0.73316 i	±1.01323 i	±4.15870 i
75°	±0.66324 i	±1.00294 i	±4.61201 i

*Θ is the angle measured counterclockwise from the positive z-axis to the fiber direction

Table 2 First 12 noninteger eigenvalues* for free-edge stress solutions in [± 45 deg] graphite-epoxy composite

-2.5575658 E-2
8.8147184 E-1 ± i 2.3400497 E-1
1.5115263 E 0 ± i 7.9281732 E-1
2.3389433 E 0 ± i 1.1158402 E 0
3.0913532 E 0 ± i 1.7360464 E 0
3.9520023 E 0 ± i 2.0287146 E 0
4.7440929 E 0 ± i 2.5683871 E 0
5.6021457 E 0 ± i 2.8588510 E 0
6.3962635 E 0 ± i 3.3652707 E 0
7.2565174 E 0 ± i 3.6575937 E 0
8.0497237 E 0 ± i 4.1479983 E 0
8.9120567 E 0 ± i 4.4407609 E 0

*Integers (0,1,2,...n) are always eigenvalues obtained from Eq 27

where the subscripts, L, T, and z refer to the fiber, transverse, and thickness directions of an individual ply, respectively. The influence of material properties of composite plies on the boundary-layer stresses may be related to the roots μ_k of the characteristic equation, equation (12*a*). With the lamina properties given in the foregoing, the roots of the characteristic equation for the graphite-epoxy laminae of different fiber orientations Θ are shown in Table 1. It appears that all the six roots μ_k are purely imaginary by virtue of the material properties in equation (37). Furthermore, the μ_k for the $+\Theta$ ply are the same as those for the $-\Theta$ ply due to the in-plane rotation of fiber directions.

Based on the material constants, μ_k, p_k, q_k, and t_k obtained for the graphite-epoxy, the transcendental characteristic equation, equation (27), can be solved numerically to provide eigenvalues for the homogeneous solution. For illustration, the first 12 noninteger eigenvalues associated with the stress solution for the free edge of a [±45 deg] graphite-epoxy composite are shown in Table 2. Eigenvalues δ_n smaller than -1 are excluded for the reasons given in the preceding section. It is seen that there exists one and only one eigenvalue, i.e., $\delta_1 = -0.02557$, which satisfies the required constraint condition of equation (28) for the [±45 deg] laminate. The eigenvalue δ_1 is the strength (or the order) of free-edge or boundary-layer stress singularity, which is of major concern in this study. In fact, only one δ_n which meets equation (28) is observed in each case of all of the composites with various fiber orientations studied in the present research. Higher-order eigenvalues, occurring as integers (including zero) and complex conjugates, always exist and should be included in determining the complete solution when remote boundary and end conditions are matched by an appropriate method.

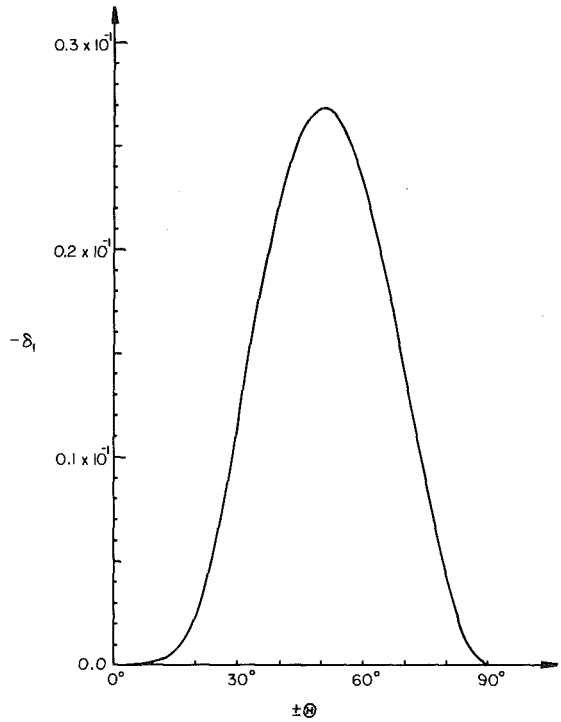

Fig. 2 Strength of boundary-layer stress singularity in [±Θ] graphite-epoxy composites

For the commonly used [±Θ] angle-ply graphite-epoxy composite, as anticipated, the order of boundary-layer stress singularity is a function of the fiber orientation Θ. Numerical results of δ_1 for each of the [±Θ] fiber composites are calculated and shown in a graphic form in Fig. 2. It is clearly seen from the figure that the free edge of a composite laminate having approximately [±51 deg] fiber orientations possesses the strongest boundary-layer stress singularity. As the Θ changes to either direction, the order of the stress singularity δ_1 decreases rapidly. Its value converges to zero for the cases of Θ = 0 and 90 deg, since the two adjacent plies become identical with orthotropic elastic properties.

In the case of a composite edge associated with plies of more general fiber orientations instead of the symmetric [+Θ/−Θ] configuration, solutions for the eigenvalues δ_n are also obtained. To illustrate the nature of the eigenvalues for this situation, free-edge stress singularities associated with [30 deg/Θ] fiber orientations in graphite-epoxy composites are determined, where Θ varies from 7.5 to 82.5 deg. The first few noninteger eigenvalues for various Θ's are given in Table 3. The integers (including zero) are also eigenvalues, but not included in the Table. The [30 deg/30 deg] graphite-epoxy composite is not included either since the two plies are identical. Again, for each of the [30 deg/Θ] composite laminates there exist only one δ_n which meets the requirement of equation (28) and gives the dominant edge stress singularity.

The degenerated cases of cross-ply composite laminates discussed in the preceding section are also investigated. The eigenvalues for the boundary-layer stresses in a graphite-epoxy composite with [0/90 deg] lamination are given in Table 4. The dominant stress singularity in the present [0/90 deg] case has an order of magnitude similar to those in [±Θ] angle-ply composites and in more general [Θ_1/Θ_2] laminates. It is noted that the orders of the boundary-layer stress singularity for both angle-ply and cross-ply composites are generally much weaker than those associated with other

Table 3 First five noninteger eigenvalues* for free-edge stresses associated with [30 deg/Θ] graphite-epoxy composites

Θ	δ_1	δ_2	δ_3	δ_4	δ_5
7.5°	-2.792991 E-3	9.887419 E-1 ±i 8.435637 E-2	1.930568 E 0 ±i 3.319540 E-1	3.095930 E 0 ±i 8.103959 E-2	3.862698 E 0 ±i 7.204410 E-1
15°	-1.986115 E-3	9.943591 E-1 ±i 6.113543 E-2	1.949288 E 0 ±i 2.882098 E-1	2.726071 E 0	3.441129 E 0 ±i 5.183480 E-1
22.5°	-6.725306 E-4	9.989196 E-1 ±i 2.920556 E-2	1.989893 E 0 ±i 1.661871 E-1	2.649382 E 0	3.342300 E 0 ±i 5.276117 E-1
30°	—	—	—	—	—
37.5°	-9.077774 E-4	1.001306 E 0 ±i 5.180632 E-3	1.984327 E 0	2.182540 E 0 ±i 1.910473 E-1	3.204760 ±i 8.009168 E-1
45°	-3.771122 E-3	9.624687 E-1	1.061916 E 0	1.821684 E 0	2.021985 ±i 4.926242 E-1
52.5°	-8.292252 E-3	9.291682 E-1	1.168571 E 0	1.621302 E 0	1.906136 E 0 ±i 6.212519 E-1
60°	-1.367358 E-2	9.010723 E-1	1.354059 E 0 ±i 1.864060 E-1	1.825695 E 0 ±i 6.942274 E-1	3.518516 E 0 ±i 1.413627 E 0
67.5°	-1.897304 E-2	8.810614 E-1	1.321793 E 0 ±i 3.224246 E-1	1.773577 E 0 ±i 7.358765 E-1	3.488780 E 0 ±i 1.428440 E 0
75°	-2.343868 E-2	8.719040 E-1	1.303673 E 0 ±i 3.820090 E-1	1.743059 E 0 ±i 7.550141 E-1	3.485411 E 0 ±i 1.425960 E 0
82.5°	-2.668523 E-2	8.778236 E-1	1.310388 E 0 ±i 3.866969 E-1	1.725286 E 0 ±i 7.501905 E-1	3.513604 E 0 ±i 1.387356 E 0

*Integers, 0,1,2,....n, are also eigenvalues.

Table 4 First 12 noninteger eigenvalues for free-edge stresses in cross-ply graphite-epoxy composite*

-3.33888 E-2
8.80268 E-1
1.41674 E 0 ± i 3.93303 E-1
1.65345 E 0 ± i 6.85523 E-1
2.83449 E 0 ± i 1.76219 E 0
3.75294 E 0 ± i 1.1853E E 0
4.29235 E 0 ± i 2.66884 E 0
5.70726 E 0 ± i 3.57190 E 0
5.79010 E 0 ± i 1.52461 E 0
7.12293 E 0 ± i 4.48145 E 0
7.81068 E 0 ± i 1.76401 E 0

*Integers, 0,1,2,3..., are also eigenvalues

typical singular elastostatic problems such as the elastic crack problem. The relatively weak singularity for the laminate edge stresses introduces several unique features as well as difficulties for the evaluation of boundary-layer effects in composites, which are discussed in [30].

6 Summary and Conclusions

A study of boundary-layer stress singularities in both angle-ply and cross-ply composite laminates has been presented. Formulation of the problem is based on Lekhnitskii's complex-variable stress functions and basic relationships in the anisotropic elasticity theory. An eigenfunction expansion method has been developed to obtain the homogeneous solution for the coupled governing partial differential equations for the problem. Angle-ply and cross-ply composites as well as more general laminates have been studied. The strength of boundary-layer stress singularity for each case has been determined to illustrate the fundamental nature of the edge effects in composite materials.

Based on the information obtained, the following conclusions may be reached:

1. Boundary-layer or free-edge stresses in a composite laminate are generally singular in nature due to the geometric and material discontinuities.
2. The order of boundary-layer stress singularity can be determined by solving the transcendental characteristic equation obtained from the homogeneous solution for the governing partial differential equations.
3. The boundary-layer stress singularity depends only on material elastic constants and fiber orientations of adjacent plies in a composite laminate.
4. For angle-ply and cross-ply composites as well as more general laminates the order of boundary-layer stress singularity is very weak in general. In a graphite-epoxy system, for example, δ_1 is much smaller than other kinds of singular stress problems in elastostatics such as the elastic crack problem.

7 Acknowledgment

The work described in this paper was supported in part by the National Aeronautics and Space Administration-Lewis Research Center (NASA-LRC), Cleveland, Ohio under Grant NSG 3044. The authors are grateful to Dr. C. C. Chamis of NASA-LRC, Dr. G. P. Sendeckyj of the Air Force Flight Dynamic Laboratory, Professor R. B. Pipes of the University of Delaware, Professor A. S. D. Wang of Drexel University, and Professor H. T. Corten of the University of Illinois at Urbana-Champaign for the valuable discussion and encouragement during the course of this study.

8 References

1 Pipes, R. B., and Daniel, I. M., "Moiré Analysis of the Interlaminar Shear Edge Effect in Laminated Composites," *Journal of Composite Materials*, Vol. 5, Apr. 1971, pp. 255-259.

2 Whitney, J. M., "Free-Edge Effects in the Characterization of Composite Materials," *Analysis of the Test Methods for High Modulus Fibers and Composites, ASTM STP 521*, American Society for Testing and Materials, 1973, pp. 167-180.

3 Pipes, R. B., Kaminski, B. E., and Pagano, N. J., "Influence of the Free Edge Upon the Strength of Angle-Ply Laminates," *Analysis of the Test Methods for High Modulus Fibers and Composites, ASTM STP 521*, American Society for Testing and Materials, 1973, pp. 218-228.

4 Puppo, A. H., and Evensen, H. A., "Interlaminar Shear in Laminated Composites Under Generalized Plane Stresses," *Journal of Composite Materials*, Vol. 4, 1970, pp. 204-220.

5 Pipes, R. B., and Pagano, N. J., "Interlaminar Stresses in Composite Laminates Under Uniform Axial Extension," *Journal of Composite Materials*, Vol. 4, 1970, pp. 538-548.

6 Isakson, G., and Levy, A., "Finite Element Analysis of Interlaminar Shear in Fiberous Composites," *Journal of Composite Materials*, Vol. 5, Apr. 1971, pp. 273-276.

7 Rybicki, E. F., "Approximate Three-Dimensional Solutions for Symmetric Laminates Under In-Plane Loading," *Journal of Composite Materials*, Vol. 5, July 1971, pp. 354-360.

8 Pagano, N. J., and Pipes, R. B., "Influence of Stacking Sequence on Laminate Strength," *Journal of Composite Materials*, Vol. 5, 1971, pp. 51-57.

9 Pipes, R. B., and Pagano, N. J., "Interlaminar Stresses in Composite Laminates—An Approximate Elasticity Solution," ASME JOURNAL OF APPLIED MECHANICS, Vol. 41, No. 3, 1974, pp. 668-672.

10 Pagano, N. J., "On the Calculation of Interlaminar Normal Stress in Composite Laminate," *Journal of Composite Materials*, Vol. 8, Jan. 1974, pp. 65-82.

11 Tang, S., and Levy, A., "A Boundary Layer Theory—Part II: Extension of Laminated Finite Strip," *Journal of Composite Materials*, Vol. 9, Jan. 1975, pp. 42-45.

12 Hsu, P. W., and Herakovich, C. T., "Edge Effects in Angle-Ply Composite Laminates," *Journal of Composite Materials*, Vol. 11, Oct. 1977, pp. 422-428.

13 Wang, A. S. D., and Crossman, F. W., "Some New Results on Edge Effects in Symmetric Composite Laminates," *Journal of Composite Materials*, Vol. 11, Jan. 1977, pp. 92-106.

14 Pagano, N. J., "Stress Fields in Composite Laminates," *International Journal of Solids and Structures*, Vol. 14, 1978, pp. 385-400.

15 Pagano, N. J., "Free-Edge Stress Fields in Composite Laminates," *International Journal of Solids and Structures*, Vol. 14, 1978, pp. 401-406.

16 Reissner, E., and Stavsky, Y., "Bending and Stretching of Certain Types of Heterogeneous Aeolotropic Elastic Plates," ASME JOURNAL OF APPLIED MECHANICS, Vol. 28, 1961, pp. 402-408.

17 Dong, S. B., Pister, K. S., and Taylor, R. L, "On the Theory of Laminated Anisotropic Shells and Plates," *Journal of the Aerospace Science*, Vol. 28, 1962, pp. 966-972.

18 Herakovich, C. T., Nagarkar, A., and O'Brien, D. A., "Failure Analysis of Composite Laminates with Free Edges," in *Modern Developments in Composite Materials and Structures*, Vinson, J. R., Ed., ASME, 1979, pp. 53-66.

19 Christensen, R. M., *Mechanics of Composite Materials*, Wiley, New York, 1979.

20 Wilkins, D. J., Eisenmann, J. R., Camin, R. A., Margolis, W. W., and Benson, R. A., "Characterizing Delamination Growth in Graphite-Epoxy," *Damage in Composite Materials: Basic Mechanisms, Accumulation, Tolerance and Characterization, ASTM STP 775*, American Society for Testing and Materials, 1982, pp. 168—183.

21 Whitney, J. M., and Sun, C. T., "A Higher Order Theory for Extensional Motion of Laminated Composites," *Journal of Sound and Vibrations*, Vol. 30, 1973, pp. 85-97.

22 Spilker, R. L., and Chou, S. C., "Edge Effects in Symmetric Composite Laminates: Importance of Satisfying the Traction-Free Edge Condition," *Journal of Composite Materials*, Vol. 14, Jan. 1980, pp. 2-20.

23 Tong, P., and Pian, T. H. H., "On the Convergence of the Finite Element Methods for Problems with Singularity," *International Journal of Solids and Structures*, Vol. 9, 1973, pp. 313-321.

24 Hein, V. L., and Erdogan, F., "Stress Singularities in a Two-Material Wedge," *International Journal of Fracture Mechanics*, Vol. 7, 1971, pp. 317-330.

25 Bogy, D. B., "Edge-Bonded Dissimilar Orthogonal Elastic Wedges Under Normal and Shear Loading," ASME JOURNAL OF APPLIED MECHANICS, Vol. 35, 1968, pp. 460-466.

26 Kuo, M. C., and Bogy, D. B., "Plane Solutions for Traction Problems on Orthotropic Unsymmetrical Wedges and Symmetrically Twinned Wedges," ASME JOURNAL OF APPLIED MECHANICS, Vol. 41, 1974, pp. 203-208.

27 Lekhnitskii, S. G., *Theory of Elasticity of an Anisotropic Body*, Holden-Day, San Francisco, 1963.

28 Wang, S. S., and Choi, I., "Boundary-Layer Thermal Stresses in Angle-Ply Composite Laminates," in *Modern Developments in Composite Materials and Structures*, Vinson, J. R., Ed., ASME, 1979, pp. 315-341.

29 Muller, D. E., "A Method for Solving Algebraic Equations Using an Automatic Computer," *Mathematical Tables and Computations*, Vol. 10, Oct. 1956, pp. 208-215.

30 Wang, S. S., and Choi, I., "Boundary-Layer Effects in Composite Laminates: Part 2—Free-Edge Stress Solutions and Basic Characteristics," ASME JOURNAL OF APPLIED MECHANICS, Vol. 49, 1982, pp. 549-560.

APPENDIX I

Expressions for $H_{ij}(\theta)$ in equations (19) and (20)

$$H_{1k} = (\mu_k \sin\theta + \cos\theta)^2$$

$$H_{2k} = -\eta_k (\mu_k \sin\theta + \cos\theta)$$

$$H_{3k} = -(\mu_k \sin\theta + \cos\theta)(\mu_k \cos\theta - \sin\theta)$$

$$H_{4k} = (\mu_k \cos\theta - \sin\theta)^2$$

$$H_{5k} = \eta_k (\mu_k \cos\theta - \sin\theta)$$

$$H_{6k} = p_k \cos\theta + q_k \sin\theta$$

$$H_{7k} = -p_k \sin\theta + q_k \cos\theta$$

$$H_{8k} = t_k$$

Boundary-Layer Effects in Composite Laminates:

Part 2—Free-Edge Stress Solutions and Basic Characteristics

S. S. Wang
Associate Professor.
Assoc. Mem. ASME

I. Choi
Research Associate.

Department of Theoretical and Applied Mechanics,
University of Illinois,
Urbana, Ill. 61801

Boundary-layer effects in composite laminates are considered. Based on the theory of anisotropic elasticity and Lekhnitskii's complex-variable stress function formulation, the exact laminate elasticity solution is derived for the problem. The solution contains the exact boundary-layer stress singularity and higher-order terms in eigenfunction series. Convergence and accuracy of the solution are studied, and present results are compared with existing approximate numerical solutions. For illustrative purposes, the complete solution for a symmetric [45/−45/−45/45] graphite-epoxy composite is presented to elucidate fundamental characteristics of the boundary-layer effects. Detailed stress distributions in the boundary-layer region are determined. Boundary-layer stress intensity factors are introduced to characterize the singular edge-stress field. Physical significance of the parameters is discussed in the realm of fracture initiation and failure modes in the laminate boundary region.

1 Introduction

In the absence of complete and accurate information on the boundary-layer field, some of the most fundamental problems involved in simple mechanical testing and characterization of basic material properties and behavior of composite laminates still remain controversial and unresolved [1–7]. More complex problems such as fracture initiation, failure modes, and strength and stiffness degradations under static and cyclic fatigue loading conditions would not be tractable without a thorough knowledge of the complex state of stress and deformation in the composite laminate, especially in the boundary-layer region. Thus it is imperative to establish a rigorous, accurate, and complete solution for the boundary-layer problem in the current development of the composite material technology and in advancing more reliable design and analyses of composite structures.

In an associated paper [8], a study of the fundamental nature of the boundary-layer effect in composite laminates has been formulated on the basis of the theory of anisotropic elasticity. The basic structure of the boundary-layer field solution has been obtained by using Lekhnitskii's complex-variable stress potentials [9]. The boundary-layer stress field has been found to be singular at composite laminate edges, and the exact order or strength of the boundary-layer stress singularity has been determined by the use of an eigenfunction expansion method. The formulation and the homogeneous solution given in reference [8] deal only with the local geometry and lamination variables at the free edge. Complete solutions for the boundary-layer stress and deformation require a full consideration of the overall composite laminate geometry, lamination and material variables, remote boundary conditions, and end loading conditions. In this paper, the second in succession, the complete solution for the boundary-layer problem is presented, and fundamental characteristics associated with the boundary-layer stress field are studied in detail.

Specific objectives of this paper are directed to (1) determine the particular solution for a composite laminate with given lamination variables and loading conditions, (2) present complete solutions for symmetric composite laminates to illustrate fundamental characteristics of the boundary-layer stress field, and (3) introduce basic physical parameters, e.g., the boundary-layer stress intensity factors, which provide a practical measure of the severity of the singular stress field and its influence on failure modes and mechanics in composite materials.

In the next section, general solutions for boundary-layer stress and deformation fields in composite laminates are constructed from the homogeneous solution in the form of eigenfunction series and a properly selected particular solution in polynomials. A collocation method is used to determine free constants in the truncated series solution. To illustrate the solution method, commonly used symmetric composite systems are considered in Section 3. Further

Contributed by the Applied Mechanics Division for publication in the JOURNAL OF APPLIED MECHANICS.

Discussion on this paper should be addressed to the Editorial Department, ASME, United Engineering Center, 345 East 47th Street, New York, N.Y. 10017, and will be accepted until two months after final publication of the paper itself in the JOURNAL OF APPLIED MECHANICS. Manuscript received by ASME Applied Mechanics Division, October, 1981; final revision, February, 1982.

simplifications and the detailed solution scheme are presented for both symmetric angle-ply and cross-ply composites. Based on the complete solution obtained, the asymptotic solution structure of the boundary-layer stress field is identified, and important physical parameters are introduced in Section 4. Due to space limitation, only the complete solution for a [45/−45/−45/45] graphite-epoxy composite under uniform axial strain is presented in Section 5 for illustration and comparison. A study of solution accuracy and convergence is also given. Characteristics of the boundary-layer stress field in composite laminates are determined. A more appropriate definition of boundary-layer width is introduced on the basis of strain energy density consideration. Influences of geometric and lamination variables, environmental conditions, and loading modes on the boundary-layer stress field are reported in future papers.

2 General Solution

2.1 Homogeneous Solution. Once the eigenvalues δ_n are determined, the relationships among C_n's can be established from equations (19)–(20) in reference [8]. Thus homogeneous solutions for the stress and displacement fields have the following expressions:

$$\sigma_i^{(h)} = \sum_{n=1}^{\infty} c_{1n}\, Re\Big\{\sum_{k=1}^{3}[b_{kn}\Lambda_{ik}Z_k^{\delta_n} + b_{(k+3)n}\bar{\Lambda}_{ik}\bar{Z}_k^{\delta_n}]\Big\} + \sum_{n=1}^{\infty} c_{2n}\, Im\Big\{\sum_{k=1}^{3}[b_{kn}\Lambda_{ik}Z_k^{\delta_n} + b_{(k+3)n}\bar{\Lambda}_{ik}\bar{Z}_k^{\delta_n}]\Big\}, \quad (1a)$$

$$u_j^{(h)} = \sum_{n=1}^{\infty} c_{1n} Re\Big\{\sum_{k=1}^{3}[b_{kn}\Gamma_{(j+3)k}Z_k^{(\delta_n+1)} + b_{(k+3)n}\bar{\Gamma}_{(j+3)k}\bar{Z}_k^{(\delta_n+1)}]/(\delta_n+1)\Big\} + \sum_{n=1}^{\infty} c_{2n} Im\Big\{\sum_{k=1}^{3}[b_{kn}\Gamma_{(j+3)k}Z_k^{(\delta_n+1)} + b_{(k+3)n}\bar{\Gamma}_{(j+3)k}\bar{Z}_k^{(\delta_n+1)}]/(\delta_n+1)\Big\}, \quad (i=1,2,4,5,6;\ j=1,2,3), \quad (1b)$$

where b_{kn} are known constants related to the eigenvectors; c_{in} are real constants to be determined, and $\Lambda_{1k} = \mu_k^2$, $\Lambda_{2k} = 1$, $\Lambda_{4k} = -\eta_k$, $\Lambda_{5k} = \mu_k\eta_k$, $\Lambda_{6k} = -\mu_k$, $\Gamma_{4k} = p_k$, $\Gamma_{5k} = q_k$, and $\Gamma_{6k} = t_k$ with the constants μ_k, η_k, p_k, q_k, t_k being defined in reference [8]. For the convenience of the later development, the homogeneous solutions, equations (1*a*, *b*), are expressed in simpler forms as

$$\sigma_i^{(h)} = \sum_n d_n f_{in}(x,y;\delta_n) \quad (i=1,2,4,5,6), \quad (2a)$$

$$u_j^{(h)} = \sum_n d_n g_{jn}(x,y;\delta_n) \quad (j=1,2,3), \quad (2b)$$

where f_{in} and g_{jn} denote the known eigenfunctions corresponding to the nth eigenvalue δ_n; the unknowns d_n are real constants to be determined in conjunction with a particular solution through remote boundary and end conditions. Generally, there are infinite number of eigenvalues δ_n so that the number of unknown constants d_n is infinite. Proper truncation of the infinite eigenfunction series is needed to approximate the edge-field solution.

2.2 Particular Solution. The particular solution for the governing partial differential equations in [8] may be sought in the form of polynomials,

$$F^{(p)}(x,y) = a_1x^3 + a_2x^2y + a_3xy^2 + a_4y^3 + a_5x^2 + a_6xy + a_7y^2, \quad (3a)$$

$$\psi^{(p)}(x,y) = a_8x^2 + a_9xy + a_{10}y^2 + a_{11}x + a_{12}y, \quad (3b)$$

where a_i are arbitrary constants to be determined later. The particular solutions for stress and displacement in each ply can be shown to have the general forms as follows:

$$\sigma_x^{(p)} = 2a_3x + 6a_4y + 2a_7, \quad (4a)$$

$$\sigma_y^{(p)} = 6a_1x + 2a_2y + 2a_5, \quad (4b)$$

$$\tau_{yz}^{(p)} = -2a_8x - a_9y - a_{11}, \quad (4c)$$

$$\tau_{xz}^{(p)} = a_9x + 2a_{10}y + a_{12}, \quad (4d)$$

$$\tau_{xy}^{(p)} = -2a_2x - 2a_3y - a_6, \quad (4e)$$

$$u^{(p)} = -\frac{1}{2}A_1S_{33}z^2 - A_4yz + U^{(p)}(x,y) + \omega_2z - \omega_3y + u_0, \quad (5a)$$

$$v^{(p)} = -\frac{1}{2}A_2S_{33}z^2 + A_4xz + V^{(p)}(x,y) + \omega_3x - \omega_1z + v_0, \quad (5b)$$

$$w^{(p)} = (A_1x + A_2y + A_3)S_{33}z + W^{(p)}(x,y) + \omega_1y - \omega_2x + w_0, \quad (5c)$$

where

$$U^{(p)} = \frac{1}{2}G_{11}x^2 + G_{12}xy + G_{13}x + \frac{1}{2}(G_{62} - G_{21})y^2 + \frac{1}{2}G_{63}y, \quad (6a)$$

$$V^{(p)} = G_{21}xy + \frac{1}{2}G_{22}y^2 + G_{23}y + \frac{1}{2}(G_{61} - G_{12})x^2 + \frac{1}{2}G_{63}x, \quad (6b)$$

$$W^{(p)} = \frac{1}{2}G_{51}x^2 + (G_{52} + A_4)xy + G_{53}x + \frac{1}{2}G_{42}y^2 + G_{43}y, \quad (6c)$$

in which G_{ij} are related to the lamina stiffness matrix S_{ij} and the constants a_i and A_i by

$$G_{j1} = 2\tilde{S}_{j1}a_3 + 6\tilde{S}_{j2}a_1 - 2\tilde{S}_{j4}a_8 + \tilde{S}_{j5}a_9 - 2\tilde{S}_{j6}a_2 + S_{j3}A_1, \quad (7a)$$

$$G_{j2} = 6\tilde{S}_{j1}a_4 + 2\tilde{S}_{j2}a_2 - \tilde{S}_{j4}a_9 + 2\tilde{S}_{j5}a_{10} - 2\tilde{S}_{j6}a_3 + S_{j3}A_2, \quad (7b)$$

$$G_{j3} = 2\tilde{S}_{j1}a_7 + 2\tilde{S}_{j2}a_5 - \tilde{S}_{j4}a_{11} + \tilde{S}_{j5}a_{12} - \tilde{S}_{j6}a_6 + S_{j3}A_3, \quad (7c)$$

$$(j=1,2,4,5,6).$$

The particular solutions $\sigma_i^{(p)}$ and $u_i^{(p)}$ given by equations (4) and (5) are required to satisfy the governing partial differential equations for the problem. It is clearly seen that equation (7*b*) in [8] is satisfied identically and that equation (7*a*) in [8] leads to the following relationship for each ply:

$$-6\tilde{S}_{24}a_1 + 2(\tilde{S}_{25} + \tilde{S}_{46})a_2 - 2(\tilde{S}_{14} + \tilde{S}_{56})a_3 + 6\tilde{S}_{15}a_4 + 2\tilde{S}_{44}a_8 - 2\tilde{S}_{45}a_9 + 2\tilde{S}_{55}a_{10} = -2A_4 + A_1S_{34} - A_2S_{35}. \quad (8)$$

Furthermore, equations (4) and (5) are also required to satisfy near-field traction-free boundary conditions and interface continuity conditions of the adjacent kth and $(k+1)$th plies. These lead to the establishment of the following relationships:

$$a_i^{(m)} = 0, \quad (i=3,4,6,7,10,12;\ m=k,k+1), \quad (9)$$

$$a_j^{(k)} = a_j^{(k+1)}, \quad (j=1,2,5,8,11); \tag{10}$$

$$A_i^{(k)} S_{33}^{(k)} = A_i^{(k+1)} S_{33}^{(k+1)}, \quad (i=1,2,3); \quad A_4^{(k)} = A_4^{(k+1)}, \tag{11}$$

$$G_{11}^{(k)} = G_{11}^{(k+1)}, \; G_{13}^{(k)} = G_{13}^{(k+1)}, \; G_{61}^{(k)} - G_{12}^{(k)} = G_{61}^{(k+1)} - G_{12}^{(k+1)}, \tag{12}$$

$$\frac{1}{2} G_{63}^{(k)} + \omega_3^{(k)} = \frac{1}{2} G_{63}^{(k+1)} + \omega_3^{(k+1)}, \quad G_{51}^{(k)} = G_{51}^{(k+1)},$$

$$G_{53}^{(k)} = G_{53}^{(k+1)}, \tag{13}$$

$$u_0^{(k)} = u_0^{(k+1)}, \quad v_0^{(k)} = v_0^{(k+1)}, \quad w_0^{(k)} = w_0^{(k+1)}, \tag{14}$$

$$\omega_1^{(k)} = \omega_1^{(k+1)}, \quad \omega_2^{(k)} = \omega_2^{(k+1)}. \tag{15}$$

Examining equations (4), (5), and (8)–(15), we observe that for the kth and $(k+1)$th plies, there exist 44 unknowns (including rigid-body translation and rotation) related by 34 linear algebraic equations. After solving these algebraic equations, there remain 10 unknowns which may be determined in conjunction with the homogeneous solution by using the end conditions and remaining remote boundary conditions other than those along the traction-free edges.

The sum of the homogenous and particular solutions satisfies identically the boundary conditions at free-edge surfaces. However, along lateral surfaces ($\partial B - \partial B_F$) other than the free edges, there appear residual tractions. The free constants in the homogeneous solution permit matching the complete stress solution ($\sigma_i^{(h)} + \sigma_i^{(p)}$) with the boundary conditions along these surfaces through the following relationships:

$$\sigma_x^{(h)} n_x + \tau_{xy}^{(h)} n_y = -\sigma_x^{(p)} n_x - \tau_{xy}^{(p)} n_y, \tag{16a}$$

$$\tau_{xy}^{(h)} n_x + \sigma_y^{(h)} n_y = -\tau_{xy}^{(p)} n_x - \sigma_y^{(p)} n_y, \tag{16b}$$

$$\tau_{xz}^{(h)} n_x + \tau_{yz}^{(h)} n_y = -\tau_{xz}^{(p)} n_x - \tau_{yz}^{(p)} n_y. \tag{16c}$$

As the eigenfunctions are nonorthogonal, equations (16a–c) may be satisfied in the least-square sense by truncating the infinite series of the eigenfunctions through a boundary collocation method, which is discussed in Section 5.

2.3 Complete Solution. Now the complete elasticity solutions for the boundary-layer field in a composite laminate can be written as

$$\sigma_i = \sigma_i^{(h)} + \sigma_i^{(p)} \quad (i=1,2,3,4,5,6), \tag{17a}$$

$$u_j = u_j^{(h)} + u_j^{(p)} \quad (j=1,2,3), \tag{17b}$$

where expressions for $\sigma_z^{(h)}$ and $\sigma_z^{(p)}$ may be obtained as

$$\sigma_z^{(h)} = -S_{3j}\, \sigma_j^{(h)} / S_{33}, \tag{17c}$$

$$\sigma_z^{(p)} = (A_1 x + A_2 y + A_3) - S_{3j}\, \sigma_j^{(p)} / S_{33} \quad (j=1,2,4,5,6). \tag{17d}$$

3 Simplifications and Solutions for Symmetric Composite Laminates Under Uniform Axial Extension

The formulation and solution method outlined previously are for composite laminates with arbitrary lamination under general loading conditions as described in [8]. In practical engineering structures and components, composite laminates are usually constructed with certain material, geometric, and structural symmetries. Significant simplifications of the formulation and solutions can be achieved due to the lamination symmetry conditions. To illustrate these simplifications and the basic nature of the solutions, symmetric angle-ply and cross-ply composite laminates subjected to uniform axial extension along the z-axis, $\epsilon_z = e$, are considered in this section.

3.1 Symmetric Angle-Ply $[\pm\Theta]_{ns}$ Composite Laminates. Consider an angle-ply composite laminate consisting of unidirectional fiber-reinforced laminae with symmetric Θ and $-\Theta$ fiber orientations and geometry; i.e., for each ply above the midplane, $y = 0$, of the laminate there always exists a ply at the corresponding position below $y = 0$ with the same ply orientation and thickness. It can be easily shown that the reduced stiffness matrix $\tilde{S}_{ij}$ of each ply in laminate structural axes has the following properties:

$$\tilde{S}_{1j} = \tilde{S}_{2j} = \tilde{S}_{3j} = \tilde{S}_{5j} = 0 \quad (j=4,6). \tag{18a}$$

The Θ and $-\Theta$ fiber orientations in the laminate lead to the relationships of $\tilde{S}_{ij}$ in the adjacent plies as

$$\tilde{S}_{ij}^{(k)} = \tilde{S}_{ij}^{(k+1)}, \; (i,j=1,2,3); \quad \tilde{S}_{ii}^{(k)} = \tilde{S}_{ii}^{(k+1)}, \; (i=4,5,6); \tag{18b}$$

$$\tilde{S}_{5j}^{(k)} = -\tilde{S}_{5j}^{(k+1)}, \; (j=1,2,3), \tag{18c}$$

where the superscripts refer to the quantities associated with the kth and $(k+1)$th plies, respectively.

Under the uniform axial strain, the composite laminate possesses the following symmetry and antisymmetry conditions of deformation:

$$u(x,y,z) = u(x,-y,z), \quad v(x,y,z) = -v(x,-y,z),$$
$$w(x,y,z) = w(x,-y,z). \tag{19a}$$

$$u(x,y,z) = -u(-x,y,z), \quad v(x,y,z) = v(-x,y,z),$$
$$w(x,y,z) = -w(-x,y,z). \tag{19b}$$

Equations (19a,b) may be written in equivalent forms leading to the boundary conditions as follows:

$$u_{,y}(x,0,z) = v_{,x}(x,0,z) = w_{,y}(x,0,z) = 0, \tag{20a}$$

$$u_{,y}(0,y,z) = v_{,x}(0,y,z) = w_{,y}(0,y,z) = 0. \tag{20b}$$

The relationships given by equations (18) and (20) together with the imposed end conditons $\epsilon_z = e$ lead to

$$A_1^{(\alpha)} = A_2^{(\alpha)} = A_4^{(\alpha)} = 0, \tag{21a}$$

$$A_3^{(\alpha)} = e / S_{33}^{(\alpha)}, \quad (\alpha = k, k+1). \tag{21b}$$

Also, by using equations (9)–(13) and equations (18a–c), it can be easily shown that

$$\omega_3^{(k)} = \omega_3^{(k+1)}, \tag{22a}$$

$$a_5^{(k)} = a_5^{(k+1)} = -eS_{53}^{(k)} / [2S_{33}^{(k)} \tilde{S}_{52}^{(k)}], \tag{22b}$$

and that all other unknowns are equal to zero.

Thus, the particular solution for the symmetric angle-ply laminate under the loading condition takes the following forms:

$$\sigma_x^{(p)} = \tau_{yz}^{(p)} = \tau_{zx}^{(p)} = \tau_{xy}^{(p)} = 0, \tag{23a}$$

$$\sigma_y^{(p)} = -eS_{53} / (S_{33}\, \tilde{S}_{52}), \tag{23b}$$

$$\sigma_z^{(p)} = \left(1 + \frac{S_{32}\, S_{53}}{S_{33}\, \tilde{S}_{52}}\right) \frac{e}{S_{33}}, \tag{23c}$$

and

$$U^{(p)} = \left(S_{13} - \frac{S_{53}\, \tilde{S}_{12}}{\tilde{S}_{52}}\right) \frac{ex}{S_{33}}, \tag{23d}$$

$$V^{(p)} = \left(S_{23} - \frac{S_{53}\, \tilde{S}_{22}}{\tilde{S}_{52}}\right) \frac{ey}{S_{33}} \tag{23e}$$

$$W^{(p)} = 0, \tag{23f}$$

where the superscript α ($\alpha = k, k+1$) in $\sigma_i^{(p)}$, $U^{(p)}$, $V^{(p)}$, $W^{(p)}$, and the k in $S_{ij}^{(k)}$ and $\tilde{S}_{ij}^{(k)}$ are dropped in proceding equations for convenience.

Thus the complete solutions for stresses and displacements in a symmetric angle-ply composite laminate can be written in explicit forms as

$$\sigma_x = \sum_n d_n f_{1n}(x,y;\delta_n), \tag{24a}$$

$$\sigma_y = \sum_n d_n f_{2n}(x,y;\delta_n) - \frac{eS_{53}}{S_{33}\tilde{S}_{52}}, \tag{24b}$$

$$\tau_{yz} = \sum_n d_n f_{4n}(x,y;\delta_n), \tag{24c}$$

$$\tau_{zx} = \sum_n d_n f_{5n}(x,y;\delta_n), \tag{24d}$$

$$\tau_{xy} = \sum_n d_n f_{6n}(x,y;\delta_n), \tag{24e}$$

$$\sigma_z = \frac{e}{S_{33}} - \frac{S_{3j}\sigma_j}{S_{33}}, \quad (j=1,2,4,5,6), \tag{24f}$$

and

$$u = \sum_n d_n g_{1n}(x,y;\delta_n) + \left(S_{13} - \frac{S_{53}\tilde{S}_{12}}{\tilde{S}_{52}}\right)\frac{ex}{S_{33}}, \tag{25a}$$

$$v = \sum_n d_n g_{2n}(x,y;\delta_n) + \left(S_{23} - \frac{S_{53}\tilde{S}_{22}}{\tilde{S}_{52}}\right)\frac{ey}{S_{33}}, \tag{25b}$$

$$w = \sum_n d_n g_{3n}(x,y;\delta_n) + ez, \tag{25c}$$

where the unknown constants d_n are to be determined by matching the preceding solutions with remote boundary conditions.

3.2 Symmetric Cross-Ply Composite Laminates. In the case of a symmetric cross-ply composite laminate, the formulation and solution procedure for the boundary-layer stress problem can be simplified further. By virtue of the material and lamination symmetry, the interlaminar and in-plane shear stresses, τ_{yz} and τ_{xz}, are uncoupled with other stress components in the formulation. Following the same procedure given in the preceding section, we can determine in a similar manner the constants in the particular solution. It can be shown easily that the following relationships hold for the cross-ply case:

$$a_5^{(k)} = a_5^{(k+1)} = \left[\frac{S_{13}^{(k+1)}}{S_{33}^{(k+1)}} - \frac{S_{13}^{(k)}}{S_{33}^{(k)}}\right]\frac{e}{2[\tilde{S}_{12}^{(k)} - \tilde{S}_{12}^{(k+1)}]}, \tag{26a}$$

$$A_1^{(\alpha)} = A_2^{(\alpha)} = A_4^{(\alpha)} = 0, \quad (\alpha = k, k+1), \tag{26b}$$

$$A_3^{(k)} S_{33}^{(k)} = A_3^{(k+1)} S_{33}^{(k+1)} = e, \tag{26c}$$

with all other constants a_i being zero.

The particular solutions for stress and displacement in the symmetric cross-ply composite may be shown in a manner similar to those in Section 3.1 as

$$\sigma_x^{(p)} = \tau_{xy}^{(p)} = \tau_{xz}^{(p)} = \tau_{yz}^{(p)} = 0, \tag{27a}$$

$$\sigma_y^{(p)} = \left[\frac{S_{13}^{(k+1)}}{S_{33}^{(k+1)}} - \frac{S_{13}^{(k)}}{S_{33}^{(k)}}\right]\frac{e}{[\tilde{S}_{12}^{(k)} - \tilde{S}_{12}^{(k+1)}]}, \tag{27b}$$

$$\sigma_z^{(p)} = \frac{e}{S_{33}}\left(1 - \frac{S_{32}}{[\tilde{S}_{12}^{(k)} - \tilde{S}_{12}^{(k+1)}]}\left[\frac{S_{13}^{(k+1)}}{S_{33}^{(k+1)}} - \frac{S_{13}^{(k)}}{S_{33}^{(k)}}\right]\right), \tag{27c}$$

and

$$U^{(p)} = \left(\frac{\tilde{S}_{12}}{[\tilde{S}_{12}^{(k)} - \tilde{S}_{12}^{(k+1)}]}\left[\frac{S_{13}^{(k+1)}}{S_{33}^{(k+1)}} - \frac{S_{13}^{(k)}}{S_{33}^{(k)}}\right] + \frac{S_{13}}{S_{33}}\right)ex, \tag{27d}$$

$$V^{(p)} = \left(\frac{\tilde{S}_{22}}{[\tilde{S}_{12}^{(k)} - \tilde{S}_{12}^{(k+1)}]}\left[\frac{S_{13}^{(k+1)}}{S_{33}^{(k+1)}} - \frac{S_{13}^{(k)}}{S_{33}^{(k)}}\right] + \frac{S_{23}}{S_{33}}\right)ey, \tag{27e}$$

$$W^{(p)} = 0, \tag{27f}$$

where the superscript α ($\alpha = k, k+1$) in $\sigma_i^{(p)}$, $U^{(p)}$, $V^{(p)}$, $W^{(p)}$, S_{ij}, and $\tilde{S}_{ij}$ is dropped in the preceding equations for convenience. The complete solution for the symmetric cross-ply composite laminate can be established in a manner similar to equations (24) and (25).

4 Boundary-Layer Stress Intensity Factors

The complete solutions for the stress and displacement

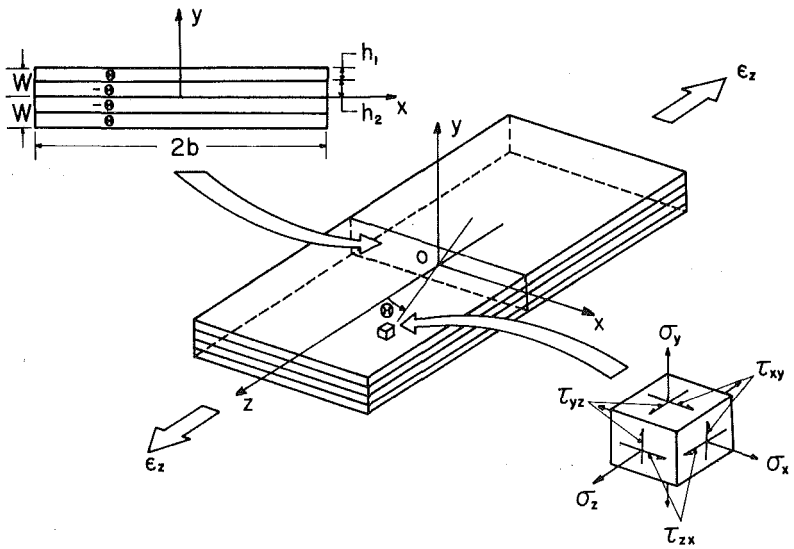

Fig. 1 Coordinates and geometry of asymmetric [θ/−θ/−θ/θ] composite laminate under uniform axial strain ϵ_z

fields given in the previous sections are shown to possess the forms of equations (24) and (25) with the constants d_n to be determined by a proper method through matching remote boundary conditions. Since the boundary-layer stress field in a composite laminate is singular in nature, the near-field stresses may be written in a general form as

$$\sigma_i = \sum_{k=1}^{3} [D_{ik} Z_k^{\delta_1} + D_{i(k+3)} \bar{Z}_k^{\delta_1}] + 0(\text{higher-order, nonsingular terms}), \quad (i=1,2,3, \ldots . 6), \tag{28}$$

where Z_k and $\bar{Z}_k$ have the origin located at the intersection of the free edge and the interface of the composite laminate (Fig. 2). The coefficients D_{ik} and $D_{i(k+3)}$ are associated with the eigenvalue δ_1 and dependent on loading geometric and lamination variables of a given composite laminate. The exponent δ_1 in equation (28) is the order of the boundary-layer stress singularity defined in reference [8].

In the context of elasticity problems with singularities, the singular terms in the solution dominate local response of the solid. Thus the singular terms in equations (24) and (28) govern the boundary-layer stress field and are of major concern in this study. Coefficients of the $Z_k^{\delta_1}$ and $\bar{Z}_k^{\delta_1}$ terms depict the intensification of the edge stresses in the boundary-layer region. Since the interlaminar stresses are most crucial along the ply interface due to the discontinuities in geometry and material properties and become singular at the interface/edge intersection, it is possible to characterize the amplitudes of the asymptotic boundary-layer stresses by introducing the near-field parameters, K_i, as

$$K_i = \lim_{x \to 0} x^{-\delta_1} \sigma_i(x,0;\delta_1) \quad (i=1,2,3, \ldots . 6). \tag{29}$$

The K_i are dependent on geometric variables (e.g., laminar thickness, number of plies, etc.), lamination parameters (e.g., fiber orientation, ply stacking sequence, etc.), loading modes, and environmental conditions (e.g., temperature, moisture, etc.).

It is noted that the fundamental structure of the boundary-layer stress solution shown in equation [28] resembles that of an elastic crack problem except that the order of stress singularity δ_1 and higher-order eigenvalues are different between the two cases. (In fact, it has been shown [10] that a degenerated case of the present boundary-layer stress problem can lead to the well-known edge-delamination problem in composite laminates.) The nature of the K_i defined in equation (29) is similar to that of the so-called crack-tip stress intensity factors in linear-elastic fracture mechanics. Thus, in this context, it may be appropriate to denote the K_i as the "boundary-layer stress intensity factors" or "free-edge stress intensity factors" in composite laminates. The sign and magnitude of the boundary-layer stress intensity factors are of significant physical importance, since they may control the near-field response, i.e., fracture initiation and failure modes, along boundaries of composite laminates.

5 Numerical Results and Discussion

To illustrate the solution scheme and the fundamental nature of boundary-layer stresses, commonly used symmetric angle-ply and cross-ply graphite-epoxy composites under uniform axial extension $\epsilon_z = e$ are examined. Ply elastic properties of each graphite-epoxy lamina and geometric variables of the composite laminates used in references [1-8] are employed here (i.e., $E_L = 20 \times 10^6$ psi, $E_T = E_z = 2.1 \times 10^6$ psi, $G_{LT} = G_{Tz} = G_{Lz} = 0.85 \times 10^6$ psi, $\nu_{LT} = \nu_{Tz} = \nu_{Lz} = 0.21$, $h_1 = h_2 = h = 0.25$ in., $b = 8h$). These particular material and geometric constants are selected, because they have been used extensively in previous approximate

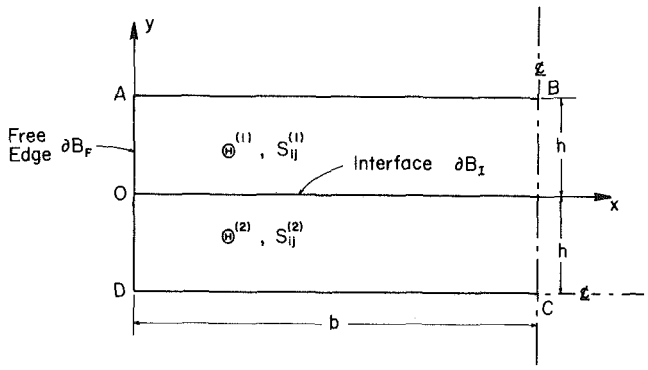

Fig. 2 Free-edge geometry and the interface between $\theta^{(1)}$ and $\theta^{(2)}$ plies

studies of the bondary-layer problem [1-7]. Thus solutions obtained in this study can be readily compared with existing approximate numerical solutions available in the literature. Due to space limitation, only the results for the symmetric [45/−45/−45/45] graphite-epoxy composite are given in this paper. Solutions for symmetric cross-ply laminates and for composites with other ply orientations, geometric, and lamination variables will be reported later.

In what follows, accuracy and convergence of the present solutions are established first. Comparisons with existing approximate solutions are made to ensure the validity of the current method of approach. Fundamental characteristics of the boundary-layer stress field are studied. Boundary-layer stress intensity factors and distributions of in-plane and interlaminar stresses are examined in detail. The boundary-layer width in a composite laminate is defined on the basis of strain-energy density consideration.

5.1 Accuracy and Convergence of the Present Solution. Since the complete solutions are required to satisfy the remote boundary conditions and laminate symmetry conditions, it can be easily shown that the following relationships must be held along the surfaces of $y = \pm h$ and of $x = b$ (Fig. 2) in the symmetric angle-ply laminate:

$$\begin{cases} \sum_n d_n f_{2n}^{(1)}(x,h;\delta_n) = eS_{53}^{(1)}/[\bar{S}_{52}^{(1)} S_{33}^{(1)}], & (30a) \\ \sum_n d_n f_{4n}^{(1)}(x,h;\delta_n) = 0, & (30b) \\ \sum_n d_n f_{6n}^{(1)}(x,h;\delta_n) = 0, & (30c) \end{cases}$$

$$\begin{cases} \sum_n d_n f_{1n}^{(2)}(x,-h;\delta_n) = 0, & (31a) \\ \sum_n d_n f_{2n}^{(2)}(x,-h;\delta_n) = 0, & (31b) \\ \sum_n d_n f_{3n}^{(2)}(x,-h;\delta_n) = 0, & (31c) \end{cases}$$

$$\begin{cases} \sum_n d_n f_{1n}^{(\alpha)}(b,y;\delta_n) = 0, & (32a) \\ \sum_n d_n f_{2n}^{(\alpha)}(b,y;\delta_n) = 0, \quad (\alpha=1,2) & (32b) \\ \sum_n d_n f_{3n}^{(\alpha)}(b,y;\delta_n) = 0, & (32c) \end{cases}$$

where f_{in} denotes differentiation of g_{in} according to equations (20a,b), respectively. The constants d_n are then evaluated by a

Table 1 Maximum mismatch* in boundary collocation for [45/−45/−45/45] graphite-epoxy under uniform axial strain

No. of Collocation Stations	No. of Terms	Prescribed Traction† $-\sigma_y^{(p)}$ (psi)	$\sigma_y^{(h)}$ (psi)† from Eigenfunction Expansion	Relative Mismatch†† $\Delta\sigma_y/\sigma_y^{(p)}$
	25		−8.158280	0.010201
	35		−8.177839	0.007828
38	45	−8.242364	−8.187168	0.006696
	55		−8.201219	0.004992
	65		−8.209751	0.003956
	25		−8.159152	0.010095
	35		−8.174614	0.008219
54	45	−8.242364	−8.184179	0.007059
	55		−8.199372	0.005215
	65		−8.209355	0.004004
	25		−8.159168	0.010093
	35		−8.174698	0.008209
70	45	−8.242364	−8.183901	0.007092
	55		−8.199213	0.005235
	65		−8.208830	0.004068
	25		−8.159152	0.010095
	35		−8.174781	0.008199
86	45	−8.242364	−8.184185	0.007058
	55		−8.199273	0.005227
	65		−8.208373	0.004123

*At point A (i.e., x = 0, y = h) in Figure 2,

†Stress scaled by $\epsilon_z \times 10^6$,

††$\Delta\sigma_y = \max|\sigma_y^{(p)} + \sigma_h^{(h)}|$.

boundary collocation method. Truncated forms of the eigenfunction series solution are used to satisfy the foregoing boundary conditions in the least square sense at a given number of selected collocation stations.

Using equations (30), (31), and (32) and following a standard boundary collocation procedure, the following system of M linear equations for the unknowns d_n can be established:

$$\sum_{n=1}^{M} d_n \left[\int_{AB} (f_{2m}^{(1)} f_{2n}^{(1)} + f_{4m}^{(1)} f_{4n}^{(1)} + f_{6m}^{(1)} f_{6n}^{(1)})\, ds + \int_{CD} (l_{1m}^{(2)} l_{1n}^{(2)} + l_{2m}^{(2)} l_{2n}^{(2)} + l_{3m}^{(2)} l_{3n}^{(2)})\, ds + \int_{BC} (l_{1m}^{(\alpha)} l_{1n}^{(\alpha)} + l_{2m}^{(\alpha)} l_{2n}^{(\alpha)} + l_{3m}^{(\alpha)} l_{3n}^{(\alpha)})\, ds \right] = \left[\frac{eS_{53}^{(1)}}{\bar{S}_{52}^{(1)} S_{33}^{(1)}} \right] \int_{AB} f_{2m}^{(1)}\, ds, \qquad (m = 1,2, \ldots, M;\ \alpha = 1 \text{ for } y > 0, \text{ and } \alpha = 2 \text{ for } y < 0) \tag{33}$$

where the integrals in equation (33) are evaluated numerically by standard Gaussian quadrature. Once the constants d_n are obtained, the stress and displacement fields can be determined explicitly from equations (24) and (25). It is clear here that accuracy and convergence of the solutions for stresses and displacements are related to truncation of the eigenfunction series and the number of collocation stations. The term "convergence" refers to the condition in which relatively constant solutions are ensured when proper numbers of terms in the eigenfunction series and collocation points are used.

The accuracy and convergence study of the solution is carried out by examining the mismatch between the truncated eigenfunction series solution and the remote traction boundary conditions and by comparing the present boundary-layer stresses with existing approximate solutions for the finite-dimensional composite. In the [45/−45/−45/45] graphite-epoxy laminate, the maximum mismatch appears always to be the transverse normal stress σ_y at the intersection of the free edge and the upper lateral surface (i.e., at point A in Fig. 2). The interlaminar normal stress $\sigma_y^{(p)}$ (equations (23*b*) and (24*b*)) resulting from the uniform-axial-strain end condition has the value $\sigma_y^{(p)} = 8.242364 \times 10^6\, \epsilon_z$ (psi) along $y = h$, and is required to be cancelled by the homogeneous solution. The resulting $\sigma_y^{(h)}$ at point A (i.e., $x = 0, y = h$) by using different numbers of terms in the eigenfunction series and different numbers of stations in the boundary collocation procedure is given in Table 1. Also shown in the Table is the maximum relative mismatch of the transverse normal stress $\Delta\sigma_y/\sigma_y^{(p)}$, which provides a measure of accuracy and convergence of the present approach. It is clearly seen from Table 1 that the maximum mismatch in the current solution is very small. The numerical results seem to be insensitive to the number of collocation stations used due to the relatively simple geometry and boundary conditions. The homogeneous solutions apparently converge to the prescribed boundary stress $-\sigma_y^{(p)}$ within 1 percent as the number of terms used in the eigenfunction series exceeds 30.

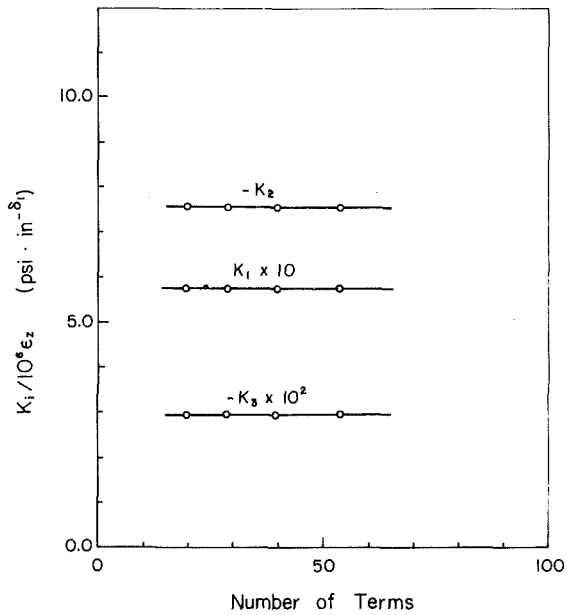

Fig. 3 Boundary-layer stress intensity factors K_i (i = 1, 2, 3) as a function of number of the terms used in eigenfunction series (86 collocation stations)

The solution convergence is further studied by examining the near-field edge stresses and associated boundary-layer stress intensity factors for the composite laminate. The solutions for boundary-layer stresses and stress intensity factors are found to be insensitive also to the increase in numbers of terms in eigenfunction series and collocation stations. For illustrative purposes, typical solution convergence of the first three boundary-layer stress intensity factors, K_1, K_2, and K_3, as a function of the number of terms and collocation stations is shown in Figs. 3 and 4 for the [45/−45/−45/45] graphite-epoxy composite. It is clearly seen from Fig. 3 that all of the K_i remain virtually the same when different numbers of terms of the eigenfunctions are used in numerical calculation (in this case, the number of collocation stations is 86). The influence of the number of collocation stations on the values of K_i is found to be similarly negligible (Fig. 4); all the K_i remain unchanged as the number of collocation stations increases from 40 to 86 (here 56 terms are used). The excellent solution convergence and stability provide a solid foundation for further studying the detailed nature of the complex singular boundary-layer stresses.

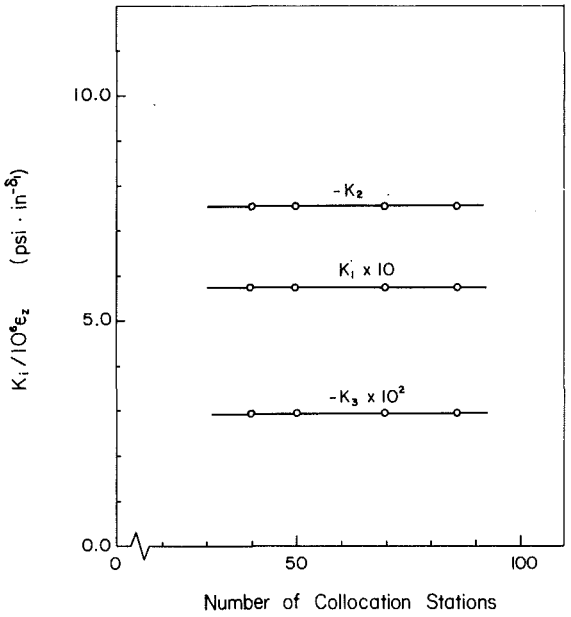

Fig. 4 Boundary-layer stress intensity factors K_i (i = 1, 2, 3) as a function of the number of collocation stations in boundary collocation (56 terms)

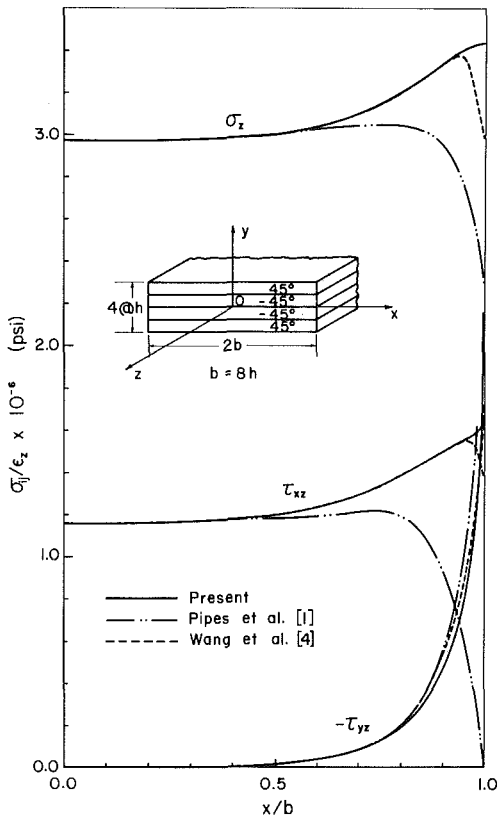

Fig. 5 Comparison of the present laminate elasticity solution for interface stresses σ_z, τ_{xz}, and τ_{yz} (along $y = h^+$) with approximate numerical solutions

5.2 Comparison With Existing Approximate Solutions. Boundary-layer stresses in a composite laminate determined by the present eigenfunction expansion approach are compared with existing approximate numerical solutions available in the literature. In Figs. 5 and 6, distributions of in-plane and interlaminar stresses along the ply interface $y = h$ of the [45/−45/−45/45] graphite-epoxy under uniform axial strain ϵ_z are shown by solid lines. Approximate solutions obtained

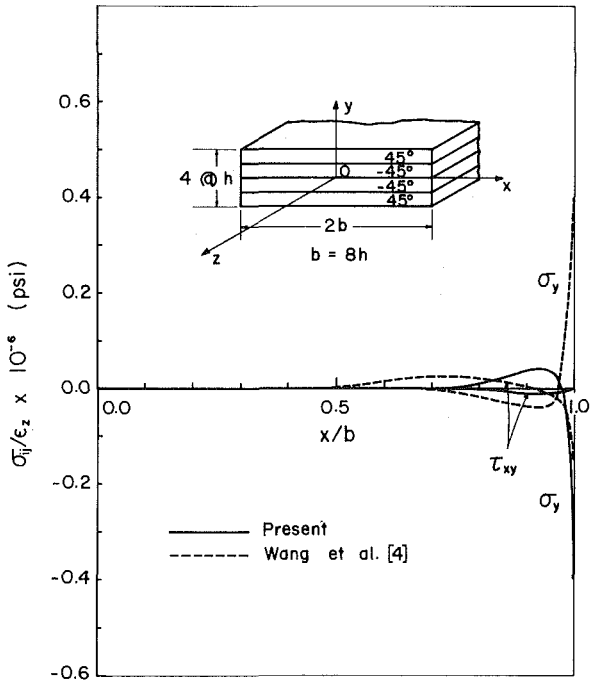

Fig. 6 Comparison of present laminate elasticity solutions for interface stresses σ_y and τ_{xy} with approximate numerical solutions

by Pipes, et al. [1] using a finite-difference analysis and by Wang, et al. [4] a constant-strain-using triangle finite element approach are shown also by dotted lines in the figures. These solutions are in good agreement in the region away from laminate edges, and converge to what is predicted with classical lamination theory (C.L.T.) [11]. As the laminate boundary is approached, discrepancies among the solutions become very significant due to the presence of the boundary-layer stress singularity, which the previous approximate numerical solutions fail to include. (The accuracy of the current solution is further supported by an independent study based on a singular hybrid finite element approach [12]). Thus, near the laminate edge, the stress field is completely governed by the singular terms $K_i x^{\delta_i}$ in the solution. Numerical approximate solutions for the problem such as the finite-difference solution [1] and the conventional finite element results [4] approximate the singular stress field in a piecewise manner. As pointed out by Tong, et al. in [13], solution convergence in elasticity problems with singularities by conventional finite elements is independent of refinement of the mesh and increase in the order of element formulation. The comparison between the present laminate elasticity solution and the finite-element approximation shown in Figs. 5 and 6 and elsewhere [12] tends to support this thesis.

It is noted further that in the evaluation of interlaminar stresses along the ply interface the conventional finite element approximation generally requires tedious and elaborate extrapolation schemes, which by themselves may introduce numerical errors in the final results. On the contrast, the present laminate elasticity theory provides, in addition to the inclusion of the correct stress singularity, exact analytical solutions for all stress components along the ply interface without the need of any extrapolation.

Comparison of through-thickness distributions of the boundary-layer stresses with the approximate solutions is also made. For example, distributions of the most dominant interlaminar shear stress τ_{yz} along the y-direction are shown in Fig. 7, as calculated by different approaches. The current solution for τ_{yz} is observed in good agreement with the finite element results [4] away from the interface in the far field,

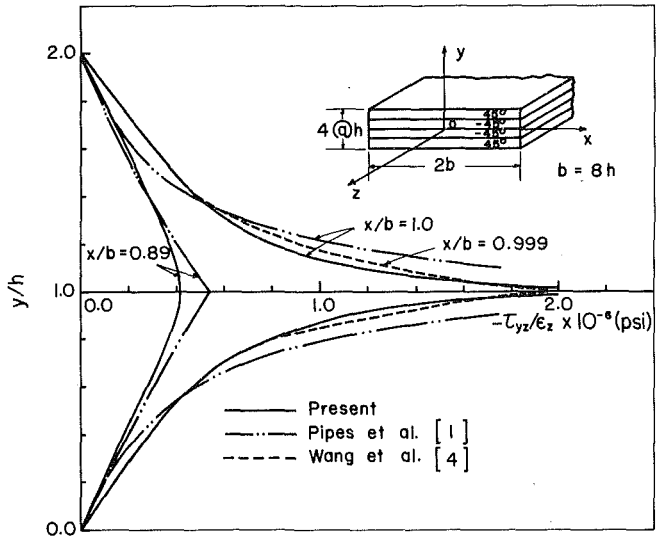

Fig. 7 Comparison of the present elasticity solution for interlaminar stress τ_{yz} through laminate thickness with approximate numerical solutions

say, at $x/b = 0.89$; however, they differ appreciably as the interface is approached. At the free edge, $x/b = 1.0$, the difference between the present results and that of Pipes, et al. [1] becomes significant. The finite difference and finite element approximations yield finite values for τ_{yz} at the laminate edge, but the current eigenfunction solution becomes unbounded as $x \to b$ and $y \to h$, due to the presence of the stress singularity. The discrepancies apparently result from the aforementioned approximations involved in the previous solutions. That is, the stresses along the ply interface are obtained by approximate averaging and extrapolation schemes without the consideration of the singular terms, whereas the present solution includes the stress singularity and satisfies exactly the interface continuity and traction boundary conditions, which give an exact elasticity solution for the boundary-layer problem.

5.3 Fundamental Characteristics of the Boundary-Layer Field. Basic characteristics of the boundary-layer response in a composite laminate may be best elucidated by the overall distributions of the edge stresses in a laminate cross section. The overall distributions of in-plane stresses, σ_x, σ_z, and τ_{xz}, over the $x-y$ plane are shown in Figs. 8, 9, and 10, and distributions of interlaminar stress components σ_y, τ_{xz}, and τ_{yz} are given in Figs. 12, 13, and 14 for the [45/−45/−45/45] graphite-epoxy system under uniform axial strain ϵ_z. These

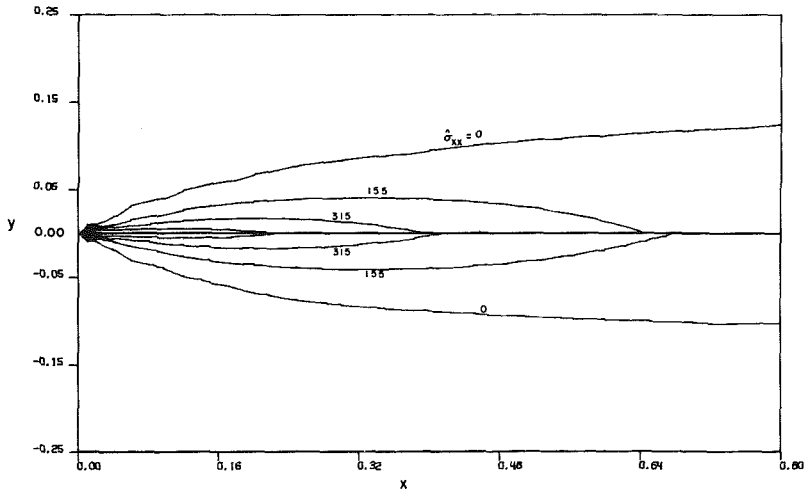

Fig. 8 Distribution of in-plane normal stress $\hat{\sigma}_x(\sigma_x/\epsilon_z \times 10^{-3}$ psi) in the upper left quadrant of a cross section in [45/−45/−45/45] graphite-epoxy composite laminate

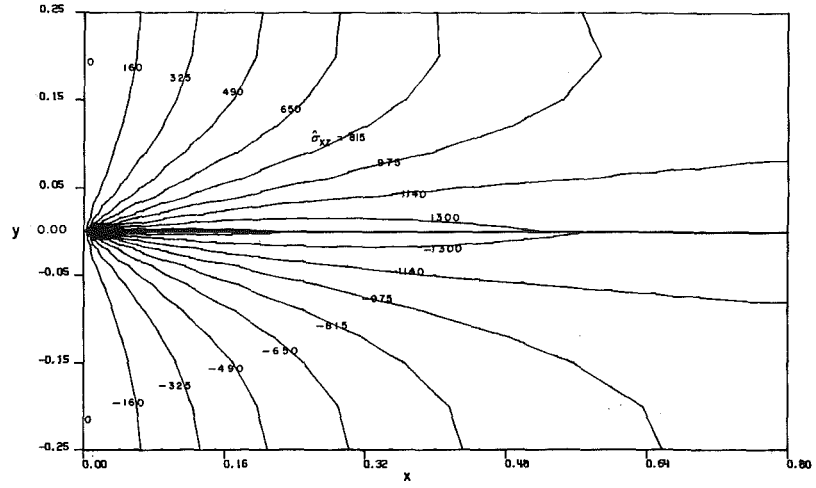

Fig. 9 Distribution of in-plane shear stress $\hat{\tau}_{xz}(\tau_{xz}/\epsilon_z \times 10^{-3}$ psi) in the upper left quadrant of a cross section in [45/−45/−45/45] graphite-epoxy composite laminate

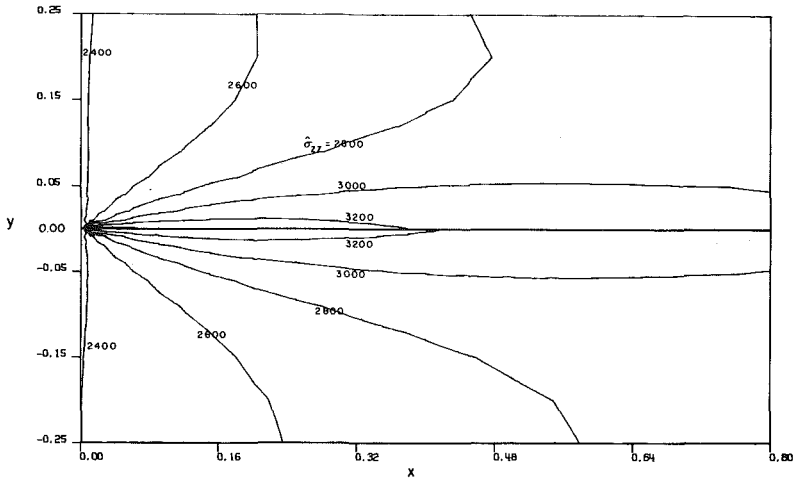

Fig. 10 Distribution of in-plane normal stress $\hat{\sigma}_z(\sigma_z/\epsilon_z \times 10^{-3}$ psi) in the upper left quadrant of a cross section in [45/ – 45/ – 45/45] graphite-epoxy composite laminate

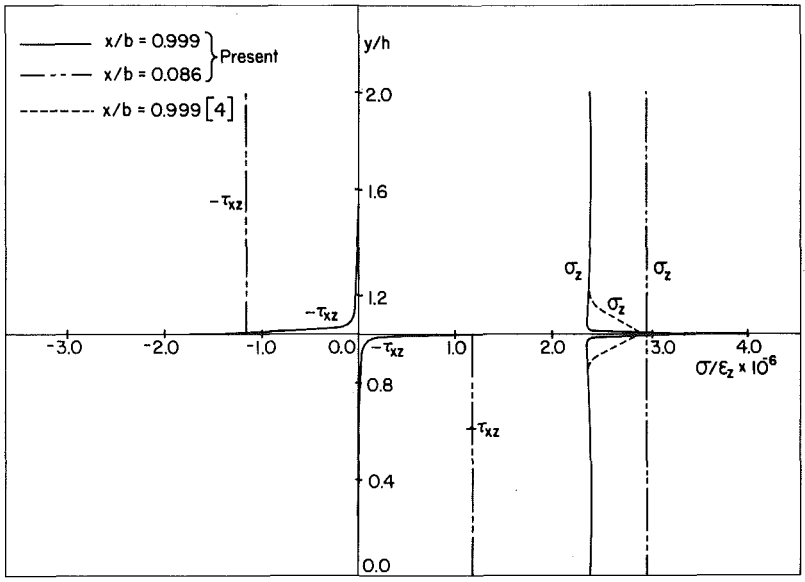

Fig. 11 Through-thickness distributions of in-plane stresses τ_{xz} and σ_z in [45/ – 45/ – 45/45] graphite-epoxy composite laminate

figures cover a portion of the upper left quadrant of the laminate cross section. Each contour line in the figures, i.e., the isostress contour, represents the stress component σ_i of a constant magnitude normalized by a scaling factor $10^3\ \epsilon_z$. The y-axis in the figures is the laminate free-edge boundary, and the x-axis is actually the interface between the 45 and -45 deg layers. The nonuniform distributions of the in-plane stresses shown in Figs. 8, 9, and 10 clearly reveal significant perturbation of the C.L.T. stress field in the neighborhood of a ply interface near the laminate boundary. More precise description of the variation of the in-plane stresses through the laminate thickness is given, for example, in Fig. 11, in which uniform distributions of in-plane stresses along the y-direction are severely altered near the laminate boundary as the ply interface is approached. Complicated distributions and high magnitudes of intensification of interlaminar stresses in the boundary-layer region are clearly shown in Figs. 12, 13, and 14. Detailed information on the through-thickness distribution of interlaminar stresses is obtained; for example, the interlaminar shear stress τ_{yz} is given in Fig. 7.

Near the composite laminate edge, the singular boundary-layer stress field may be characterized by the presently introduced parameters K_i. For the composite laminate under consideration, the boundary-layer or free-edge stress intensity factors are found to have the following values:

$$K_1 = \ \ 0.57298\,E0, \qquad K_4 = -0.16443\,E2,$$
$$K_2 = -0.75345\,E1, \qquad K_5 = \ \ 0.14440\,E1,$$
$$K_3 = -0.29523\,E-1, \qquad K_6 = \ \ 0.0,$$

where the K_i have the dimension [psi-$in^{-\delta_1}$] in accordance with the definition given in equation (29). The correctness of the boundary-layer stress intensity factors has recently been verified by an independent study [12] using a singular hybrid finite-element approach. The high negative value of K_2 indicates the development of significant compressive interlaminar normal stress σ_y along the 45 and -45 deg ply interface. This is evidenced in Fig. 6, where the compressive interlaminar normal stress σ_y is clearly shown by the solid line and is noted to be opposite in sign to the results obtained from the previous finite-element approximation [4].

In general, the K_i associated with interlaminar stresses are found to be much larger than those with in-plane stresses in

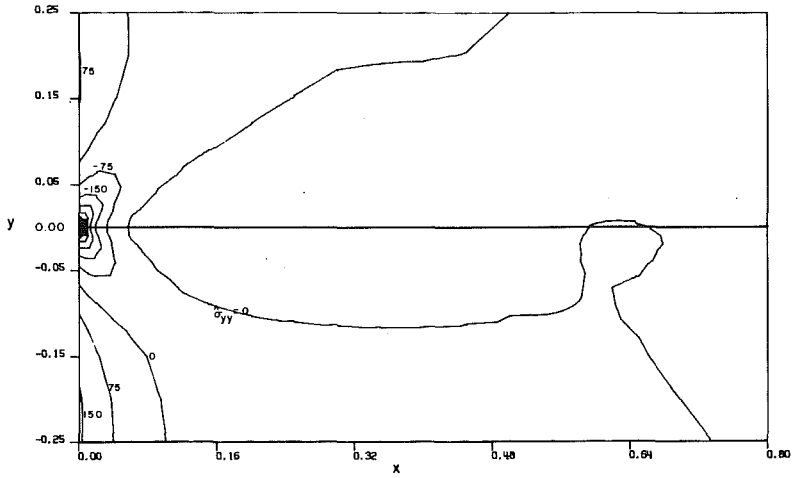

Fig. 12 Distribution of interlaminar normal stress $\hat{\sigma}_y(\sigma_y/\epsilon_z \times 10^{-3}$ psi) in the upper left quadrant of a cross section in [45/−45/−45/45] graphite-epoxy composite laminate

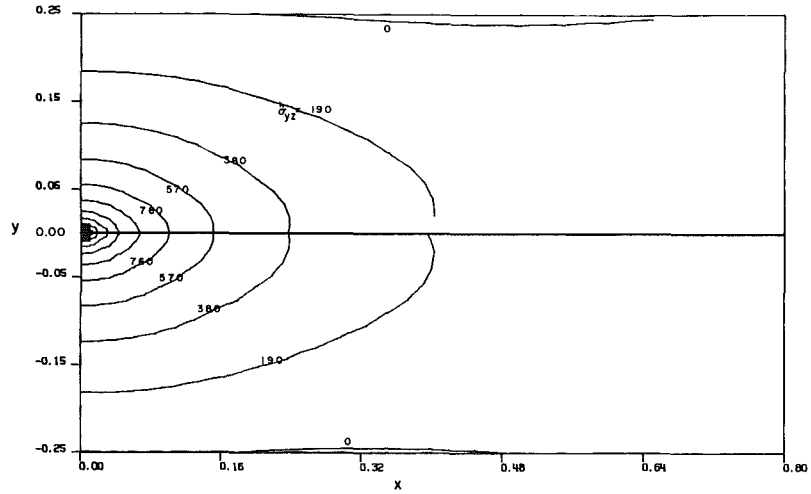

Fig. 13 Distribution of interlaminar shear stress $\hat{\tau}_{yz}(\tau_{yz}/\epsilon_z \times 10^{-3}$ psi) in the upper left quadrant of a cross section in [45/−45/−45/45] graphite-epoxy composite laminate

symmetric angle-ply composite laminates. This indicates the significance and dominance of the interlaminar stresses in controlling the local response and fracture initiation in the vicinity of laminate edges. In symmetric $[\Theta/-\Theta/-\Theta/\Theta]$ composite laminates K_6 is found to vanish for all fiber orientations, whereas in symmetric cross-ply laminates such as the [0/90/90/0] and [90/0/0/90] systems, K_4 and K_5 are identically zero due to the material and lamination symmetry conditions. Details of the influences of fiber orientations, stacking sequence, geometric variables, and other lamination parameters on the magnitude and sign of K_i will be reported later.

Careful examination of the results obtained in the study leads to the establishment of the following fundamental characteristics of the boundary-layer stress field in a composite laminate:

1. The state of stress in the boundary-layer region is generally singular and inherently three-dimensional. The strength of the boundary-layer stress singularity δ_1 depends on elastic properties and fiber orientations of adjacent plies, as discussed in reference [8].

2. The intensification of boundary-layer stresses near laminate edges is governed by the boundary-layer or free-edge stress intensity factors. The K_i depend on ply elastic constants, lamination parameters, geometric variables, loading, and environmental conditions.

3. The stress field recovers almost completely to what classical lamination theory (C.L.T.) predicts in the far field. Near the laminate edge, in-plane stress components in the neighborhood of a ply interface differ significantly from those predicted by C.L.T. inside individual lamina, due to the presence of the free edge.

4. The interlaminar normal and shear stresses cannot be obtained by classical lamination theory, but can be determined exactly by the present laminate elasticity solution. The development of the interlaminar stresses is very localized near laminate boundaries, and the stresses become singular at composite edges.

5. Failure modes and mechanics in the commonly encountered edge delamination or transverse cracking problems may be controlled by the sign and magnitude of the boundary-layer stress intensity factors. A composite with a high magnitude of positive K_2 may be more prone to fail in a delamination mode, whereas a composite with a negative K_2 may fail either in an interlaminar mode or in intralaminar (or transverse) cracking depending on the relative magnitudes of K_4, K_5 and K_1, K_3.

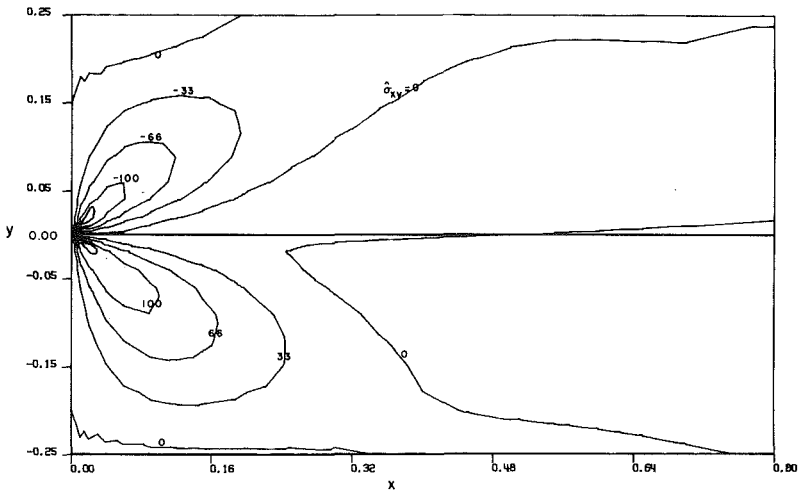

Fig. 14 Distribution of interlaminar shear stress $\hat{\tau}_{xy}(\tau_{xy}/\epsilon_z \times 10^{-3}$ psi) in the upper left quadrant of a cross section in [45/−45/−45/45] graphite-epoxy composite laminate

5.4 Strain Energy Density Distribution and Boundary-Layer Width. The rapid development of interlaminar stresses is found, as discussed in the previous sections, to be restricted to the neighborhood of laminate edges. The region in which severe perturbation of classical lamination theory occurs is often referred to in the literature as the "boundary-layer width (or thickness)." The complex state of high stresses in the boundary layer is inherently three-dimensional and cannot be determined by C.L.T. Since the size and nature of the boundary-layer stress perturbation are of vital importance in controlling fracture initiation and strength degradation of composite laminates, it is necessary to define the boundary-layer width on a rigorous basis.

Pipes, et al. [1] previously defined the boundary-layer width as the distance from a laminate edge at which the interlaminar stress τ_{yz} is about 3 percent of the value calculated at the intersection of the ply interface and the free edge by an approximate finite-difference procedure. Since the theoretical value of τ_{yz} at the intersection is unbounded due to the presence of edge stress singularity, the validity of this definition is somewhat questionable. Furthermore, if the value of τ_{yz} is used to define the boundary-layer width, it would lead to a significant problem in the cases of symmetric cross-ply laminates because both τ_{yz} and τ_{xz} are identically zero everywhere in the composites. Thus, in this study, an alternative definition of the boundary-layer width is introduced on the basis of strain-energy density consideration.

Examining the strain energy-density distribution $E(x,y)$ along the interface $y = h^+$ in the [45/−45/−45/45] graphite-epoxy laminate (Fig. 15), one immediately observes that the $E(x,h^+)$ remains relatively constant in the far field and has a nominal value E obtainable from C.L.T. and that its value increases drastically, in fact, by an order of magnitude in the present case, as the free edge is approached. The nominal value of $E(x,h^+)$, i.e., E_0, is used as a reference here for defining the boundary-layer width. In this paper, the boundary-layer width, B, is defined as the distance away from the edge, where the strain energy density along the ply interface is 3 percent higher than the value of E_0 obtained in the far field. Generally, $E(x,h^+)$ differs slightly from $E(x,h^-)$ in a symmetric angle-ply composite laminate due to the discontinuous in-plane stresses at $y = h^+$ and h^-; thus, an average value of B is designated as the width of the boundary-layer region. Based on this definition, the boundary-layer width for the [45/−45/−45/45] grahite-epoxy under uniform axial strain is found to be approximately 2.2 ply thickness. It is noted that the boundary-layer width depends on geometric variables, lamination parameters, loading modes, and environmental conditions [14]. The boundary-layer widths for composite laminates with other stacking sequences, fiber orientations, and ply thickness will be reported in future papers.

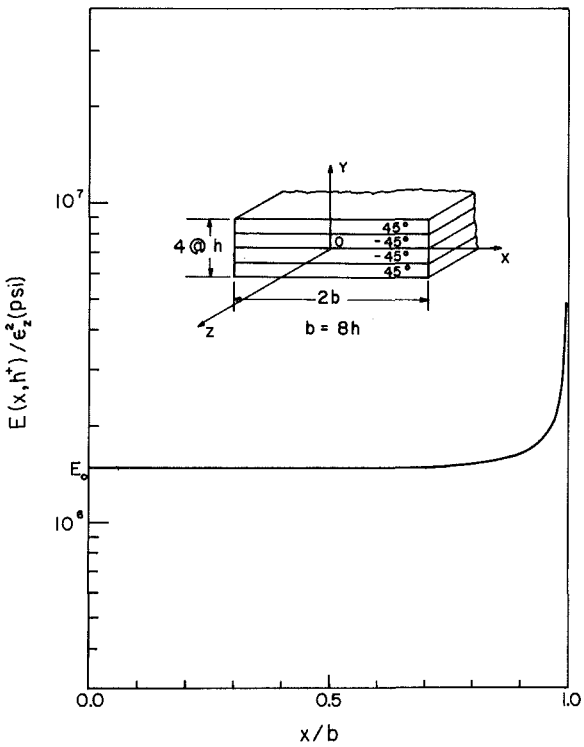

Fig. 15 Strain energy density distribution $E(x,h^+)$ along 45/−45 deg ply interface in [45/−45/−45/45] graphite-epoxy composite laminate

6 Summary and Conclusions

The complete laminate elasticity solution for the boundary-layer problem in a finite-dimensional composite has been obtained. The homogeneous solution in an eigenfunction series and the particular solution in a polynomial form have been fully determined for a given composite laminate system. The solution procedure has been outlined for composites with general lamination variables. Detailed solutions for the boundary-layer field have been presented for commonly used

symmetric angle-ply and cross-ply composites. Accuracy and convergence study has been conducted to ensure the validity of the results and the efficiency of the current approach. To illustrate the solution method and to elucidate fundamental characteristics of the boundary-layer stress and deformation, detailed information on a $[45/-45/-45/45]$ graphite-epoxy lamiante under uniform axial strain has been presented. Based on the results obtained, the following conclusions may be reached:

1. The states of stress and deformation in the boundary-layer region are inherently three-dimensional. They cannot be determined accurately by classical lamination theory nor by any approximate method without including the edge stress singularity. The current laminate elasticity solution provides accurate information on the singular nature and exact distributions of the boundary-layer stresses.

2. Comparing the current elasticity solution with previous approximate numerical solutions, we find that all solutions are in good agreement in the far field but significant discrepancies occur in the boundary-layer region, due to the fact that near the laminate edge the stress field is completely governed by the singular terms, which the previous approximate solutions fail to include.

3. The singular boundary-layer stress field may be characterized by the presently introduced "boundary-layer stress intensity factors" or "free-edge stress intensity factors." The K_i are functions of lamination variables, geometric parameters, and loading conditions. The boundary-layer stress intensity factors may be used to evaluate the criticality of various geometric and lamination variables in a composite and their influences on interlaminar (delamination) and intralaminar (transverse cracking) fracture at laminate edges.

4. The boundary-layer width which characterizes the size of the domain where classical lamination theory does not hold is defined by considering the strain energy density distribution along the ply interface. The boundary-layer width depends on all of the lamination and geometric variables, loading modes and environmental conditions. In the $[\Theta/-\Theta/-\Theta/\Theta]$ graphite-epoxy composites, the case of $\Theta = 45$ deg possesses the maximum boundary-layer width, $B/h \simeq 2.2$.

5. The present formulation and the method of solution are also valid for asymmetric composite laminates under other loading conditions, since bending, twisting, and rotational components of deformation are included. The results of these more complex situations will be reported in future papers.

7 Acknowledgment

The work described in this paper was supported in part by the National Aeronautics and Space Administration-Lewis Research Center (NASA-LRC), Cleveland, Ohio under Grant NSG 3044. The authors are grateful to Dr. C. C. Chamis of NASA-LRC, Dr. G. P. Sendeckyj of the Air Force Flight Dynamics Laboratory, Professor R. B. Pipes of the University of Delaware, Professor A. S. D. Wang of Drexel University, and Professor H. T. Corten of the University of Illinois at Urbana-Champaign for the valuable discussion and encouragement during the course of this study.

References

1 Pipes, R. B., and Pagano, N. J., "Interlaminar Stresses in Composite Laminates Under Uniform Axial Extension," *Journal of Composite Materials*, Vol. 4, 1970, pp. 538–548.

2 Pagano, N. J., "On the Calculation of Interlaminar Normal Stress in Composite Laminates," *Journal of Composite Materials*, Vol. 8, 1974, pp. 65–81.

3 Tang, S., and Levy, A., "A Boundary Layer Theory—Part II: Extension of Laminated Finite Strip," *Journal of Composite Materials*, Vol. 9, 1975, pp. 42–45.

4 Wang, A. S. D., and Crossman, F. W., "Some New Results on Edge Effect in Symmetric Composite Laminates," *Journal of Composite Materials*, Vol. 11, 1977, pp. 92–106.

5 Hsu, P. W., and Herakovich, C. T., "Edge Effects in Angle-Ply Composite Laminates," *Journal of Composite Materials*, Vol. 11, 1977, pp. 422–438.

6 Pagano, N. J., "Free-Edge Stress Fields in Composite Laminates," *International Journal of Solids and Structures*, Vol. 14, 1978, pp. 401–406.

7 Spilker, R. L., and Chou, S. C., "Edge Effects in Symmetric Composite Laminates," *Journal of Composite Materials*, Vol. 14, 1980, pp. 2–20.

8 Wang, S. S., and Choi, I., "Boundary-Layer Effects in Composite Laminates: Part 1—Free Stress Singularity," ASME JOURNAL OF APPLIED MECHANICS, Vol. 49, 1982, pp. 541–548.

9 Lekhnitskii, S. G., *Theory of Elasticity of an Anisotropic Body*, Holden-Day, San Francisco, 1963.

10 Wang, S. S., and Choi, I., "Mechanics of Delamination Fracture Problems in Composite Laminates," Technical Report, Contract No. N00014-79-C-0579, Office of Naval Research, Arlington, Va., 1982.

11 Jones, R. M., *Mechanics of Composite Materials*, McGraw-Hill, New York, 1975.

12 Wang, S. S., and Yuan, F.-K., "A Singular Hybrid Finite Element Analysis of Boundary-Layer Stresses in Composite Laminates," to appear in *International Journal of Solids and Structures*, 1982.

13 Tong, P., and Pian, T. H. H., "On the Convergence of the Finite Element Methods for Problems with Singularity," *International Journal of Solids and Structures*, Vol. 9, 1973, pp. 313–321.

14 Wang, S. S., and Choi, I., "Boundary-Layer Thermal Stresses in Angle-Ply Composite Laminates," in *Modern Developments in Composite Materials and Structures*, Vinson, J. R., Ed., ASME, New York, 1979, pp. 315–341.

On the Logarithmic Singularity of Free-Edge Stress in Laminated Composites Under Uniform Extension

R. I. Zwiers[1]
Graduate Student.

T. C. T. Ting
Professor.
Mem. ASME

R. L. Spilker
Associate Professor.
Assoc. Mem. ASME

Department of Materials Engineering,
University of Illinois at
Chicago Circle,
Chicago, Ill. 60680

The stress singularities at the free edge of an interface between adjacent layers in a laminated composite are studied. Each layer of the composite is assumed to be of the same orthotropic material with one of the principal axes being the fiber direction. The angle θ, however, which is the fiber orientation, varies from layer to layer. The composite is subjected to uniform extension in the plane of the layers. At the interface between adjacent layers having fiber angles $(0/90)$, $(\theta/-\theta)$, and a family of special combinations of (θ/θ') shown in the paper, the singularity of the type k^*r^δ $(\delta<0)$, seems to be the only possibility. For an interface with other combinations of fiber orientations in the the adjacent layers, it is shown that an additional singularity of the form $k(\ln r)$ exists. Since the constant k^* depends on the stacking sequence of the layers and the complete boundary conditions, and may vanish in some cases, the existence of a k^*r^δ singularity at a free edge is not certain until a complete problem is solved. In contrast, the constant k, which is called the logarithmic stress-intensity factor, is independent of the stacking sequence of the layers and the complete boundary conditions. Its value is determined once the fiber orientations on both sides of the interface are known. Therefore, at the interface between adjacent layers for which $k\neq 0$, the free-edge stress is inherently singular. Moreover, the singularity is logarithmic.

1 Introduction

A free edge in a composite is the intersection of an interface plane (between any two layers) and the free surface of the composite. The unusually large and possibly infinite stress at the free edges is one of the factors responsible for delamination when the composite is subjected to external loading. Many investigators have analyzed the stress near the free edge [1–9]. An analytical solution which is valid for the whole composite is practically impossible to obtain. Several approximate numerical solutions are available which show good agreement between them for points away from the free edge. For points near the free edge, numerical solutions are not capable of predicting an infinite stress when it exists, and this is where the discrepancies between various approximate solutions occur. Wang and Choi [8] used an eigenfunction expansion technique to determine the stress at the interface. However, the completeness of the eigenfunction expansion is an open question [10]. In fact, the existence of the logarithmic singularity discussed in this paper implies that the eigenfunction expansion in terms of r^δ powers may not be complete. It is doubtful that the addition of $(\ln r)$ terms would make the eigenfunction expansion complete. As pointed out in [10, 11], singular terms of $(\ln r)^2$ and $(\ln r)^3$ etc., may also exist.

While the nature of the singularity, be it k^*r^δ or $k(\ln r)$, at a free edge is independent of the stacking sequence of the layers in the composite and the complete boundary conditions, the unknown constant in the singular solution is not. This unknown constant is k^* in the case of the r^δ singularity and an arbitrary constant α_1 (not k) in the case of the $(\ln r)$ singularity. This suggests that one might use a special finite element at the free edge (with regular finite elements elsewhere) so that the exact nature of the singularity is prescribed in the special element while the unknown constants associated with the special element at each free edge are determined by solving the complete boundary-value problem. If k^* so obtained happens to be zero at a particular free edge.

For composites whose layers are isotropic elastic materials, use of the biharmonic function, or the Airy stress function, seems to be the universal approach in the analysis of the stress singularities. (See [10, 12, 13], for example.) There appears to

[1] Now employed by Portland Cement Association, Skokie, Ill. 60077.

Contributed by the Applied Mechanics Division for publication in the JOURNAL OF APPLIED MECHANICS.

Discussion on this paper should be addressed to the Editorial Department, ASME, United Engineering Center, 345 East 47th Street, New York, N.Y. 10017, and will be accepted until two months after final publication of the paper itself in the JOURNAL OF APPLIED MECHANICS. Manuscript received by ASME Applied Mechanics Division, December, 1981; final revision, April, 1982.

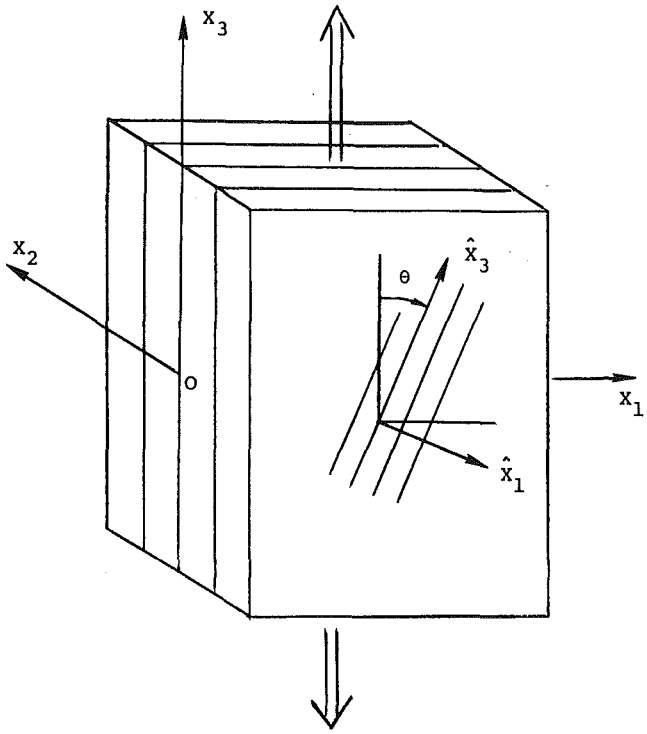

Fig. 1 Geometry of an angle-ply laminated composite

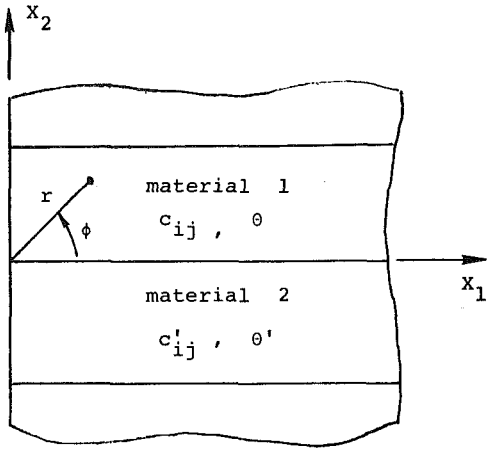

Fig. 2 A free edge between two adjacent layers (θ/θ')

be no universal approach in analyzing the stress singularities in anisotropic elastic materials. Lekhnitskii [14] introduced two stress functions to analyze general anisotropic materials. His approach was used by Wang and Choi [8] to study the thermal stresses at the interface in a layered composite. Green and Zerna [15] employed a complex function representation for the general solution. Their approach was used by Bogy [16] and Kuo and Bogy [17] in conjunction with a generalized Mellin transform to analyze stress singularities in an anisotropic wedge. In this paper we use the approach that was originated by Stroh [18] and further developed by Barnett and others [19–21] for studying the surface waves in anisotropic elastic materials.

2 Formulation of the Problem

Consider a laminated composite that consists of a finite number of anisotropic elastic layers perfectly bonded at the interface, Fig. 1. Each layer of the composite lies in a plane parallel to the (x_1, x_3) plane and is a fiber-reinforced composite material in which the fiber direction makes an angle θ with the x_3-axis. The composite is subjected to an extensional strain ϵ_3 in the x_3-direction. We assume that the composite is sufficiently long so that, at least in the region near the $x_3 = 0$ plane, the displacement u_i (except that u_3 has an additional term $\epsilon_3 x_3$) and hence the strain ϵ_{ij} and the stress σ_{ij} are independent of x_3. The strain-displacement, stress-strain, and equilibrium equations of each layer are

$$\epsilon_{ij} = (\partial u_i/\partial x_j + \partial u_j/\partial x_i)/2 \tag{1}$$

$$\sigma_{ij} = c_{ijkp}\epsilon_{kp} \tag{2}$$

$$\partial\sigma_{i1}/\partial x_1 + \partial\sigma_{i2}/\partial x_2 = 0 \tag{3}$$

where repeated indices imply summation, and

$$c_{ijkp} = c_{kpij} = c_{jikp} \tag{4}$$

are the elasticity constants.

For the purpose of numerical calculations later on, we may also use c_{ij} instead of c_{ijkp} and write equations (2) and (4) as

$$\sigma_i = c_{ij}\epsilon_j, \quad c_{ij} = c_{ji} \tag{5}$$

where

$$\left.\begin{aligned} &\sigma_{11} = \sigma_1, \quad \sigma_2 = \sigma_{22}, \quad \sigma_3 = \sigma_{33} \\ &\sigma_4 = \sigma_{23}, \quad \sigma_5 = \sigma_{13}, \quad \sigma_6 = \sigma_{12} \end{aligned}\right\} \tag{6a}$$

$$\left.\begin{aligned} &\epsilon_1 = \epsilon_{11}, \quad \epsilon_2 = \epsilon_{22}, \quad \epsilon_3 = \epsilon_{33} \\ &\epsilon_4 = 2\epsilon_{23}, \quad \epsilon_5 = 2\epsilon_{13}, \quad \epsilon_6 = 2\epsilon_{12} \end{aligned}\right\} \tag{6b}$$

We will also write the inverse of equation (5) as

$$\epsilon_i = s_{ij}\sigma_j, \quad s_{ij} = s_{ji} \tag{7}$$

where s_{ij} are the elastic compliances.

When the extensional strain ϵ_3 is applied in the x_3-direction a general solution for equations (1)–(3) can be obtained by letting

$$u_i = v_i f(Z) + \delta_{i3}\epsilon_3 x_3 \tag{8}$$

$$Z = x_1 + px_2 \tag{9}$$

where δ_{ij} is the Kronecker delta, p and v_i are constants, and f is an arbitrary function of Z. Substituting into equations (1)–(3) we have

$$\sigma_{ij} = \tau_{ij} df(Z)/dZ + c_{ij33}\epsilon_3 \tag{10}$$

$$D_{ik}v_k = 0 \tag{11}$$

where

$$\tau_{ij} = (c_{ijk1} + pc_{ijk2})v_k \tag{12}$$

$$D_{ik} = c_{i1k1} + p(c_{i1k2} + c_{i2k1}) + p^2 c_{i2k2} \tag{13a}$$

For a nontrivial solution of v_i, it follows from equation (11) that the determinant of D_{ik} must vanish. That is

$$\|D_{ik}\| = 0 \tag{13b}$$

This results in a sextic equation for p. Since the eigenvalues p are all nonreal [14, 18], there are three pairs of complex conjugates for p and three pairs of associated eigenvectors v_i.

To analyze the singular nature of the stress at a free edge, the origin of the (x_1, x_2) coordinates is placed at one of the free edges, Fig. 2. The function $f(Z)$ in equation (8) is chosen to be [8, 11]

$$f(Z) = Z^{1+\delta}/(1+\delta) \tag{14}$$

where δ is a constant. Equations (8) and (10) for displacement and stress can then be written as

$$u_i = \Sigma\{A_L v_{i,L} Z_L^{1+\delta} + B_L \bar{v}_{i,L} \bar{Z}_L^{1+\delta}\}/(1+\delta) + \delta_{i3}\epsilon_3 x_3 \tag{15}$$

$$\sigma_{ij} = \Sigma\{A_L \tau_{ij,L} Z_L{}^{\delta} + B_L \bar{\tau}_{ij,L} \bar{Z}_L{}^{\delta}\} + c_{ij33}\epsilon_3 \tag{16}$$

where an overbar denotes the complex conjugate; A_L and B_L are complex constants, and the subscript L identifies the three pairs of eigenvalues. Unless otherwise indicated, Σ in equations (15) and (16) and subsequently stands for summation over L from $L=1$-3. Using the polar coordinates (r, ϕ), Fig. 2, Z may be written as [11, 22]

$$Z = x_1 + px_2 = r\zeta \tag{17}$$

where

$$\zeta = \cos\phi + p\sin\phi \tag{18}$$

Equations (15) and (16) can then be written as

$$u_i = r^{1+\delta}\Sigma\{A_L v_{i,L} \zeta_L{}^{1+\delta} + B_L \bar{v}_{i,L} \bar{\zeta}_L{}^{1+\delta}\}/(1+\delta) + \delta_{i3}\epsilon_3 x_3 \tag{19}$$

$$\sigma_{ij} = r^{\delta}\Sigma\{A_L \tau_{ij,L} \zeta_L{}^{\delta} + B_L \bar{\tau}_{ij,L} \bar{\zeta}_L{}^{\delta}\} + c_{ij33}\epsilon_3 \tag{20}$$

Similar equations may be written for the material with elasticity constants $c_{ij}{}'$ be adding a prime to all quantities except r, ϕ, and δ. We see from equation (20) that if the real part of δ is negative σ_{ij} is singular at $r-0$.

By applying the stress-free boundary conditions

$$\sigma_{11} = \sigma_{12} = \sigma_{13} = 0 \tag{21}$$

at $\phi = \pm\pi/2$ and the interface continuity conditions at $\phi = 0$

$$[u_1] = [u_2] = [u_3] = 0 \tag{22}$$

$$[\sigma_{21}] = [\sigma_{22}] = [\sigma_{23}] = 0 \tag{23}$$

where $[f] = f - f'$ represents the difference in f values across the interface, we obtain 12 linear equations for A_L, B_L, $A_L{}'$, $B_L{}'$ which can be written as

$$r^{\delta}\mathbf{K}_c(\delta)\mathbf{q} = \epsilon_3\mathbf{b} \tag{24}$$

where $\mathbf{K}_c$ is a complex valued square matrix whose elements depend on δ, $\mathbf{b}$ is a constant column matrix whose elements are c_{ij33} and $c_{ij33}{}'$, and $\mathbf{q}$ is a column matrix whose elements are A_L, B_L, $A_L{}'$, $B_L{}'$ ($L=1$, 2, 3). The right-hand side of equation (24) is constant while the left-hand side depends on r. Therefore, to satisfy equation (24) we let $\delta = 0$:

$$\mathbf{K}_c(0)\mathbf{q} = \epsilon_3\mathbf{b} \tag{25}$$

and obtain a particular solution for $\mathbf{q}$. However, this is not the only solution for $\mathbf{q}$ in equation (24). If δ is a root of the determinant

$$\|\mathbf{K}_c(\delta)\| = 0 \tag{26}$$

we see that $\mathbf{q}$ has the following arbitrary additional solution

$$\mathbf{K}_c(\delta)\mathbf{q} = \mathbf{0} \tag{27}$$

Since the problem is linear, a linear superposition of solutions associated with different $\mathbf{q}$'s is also a solution.

Notice that the elements of $\mathbf{K}_c(\delta)$ are the coefficients of A_L, B_L in equations (19) and (20). Therefore, if δ is a complex root of equation (26), so is the conjugate $\bar{\delta}$. To obtain a real value for u_i and σ_{ij} from equations (19) and (20), we simply superimpose the solutions associated with δ and $\bar{\delta}$. However, when the root of equation (26) is real we may choose

$$B_L = \bar{A}_L = (a_L + i\tilde{a}_L)/2 \tag{28}$$

where a_L and $\tilde{a}_L$ are real. Equations (19) and (20) then have the real expressions

$$u_i = r^{1+\delta}\Sigma\{a_L Re(v_{i,L}\zeta_L{}^{1+\delta}) + \tilde{a}_L Im(v_{i,L}\zeta_L{}^{1+\delta})\}/(1+\delta) + \delta_{i3}\epsilon_3 x_3 \tag{29}$$

$$\sigma_{ij} = r^{\delta}\Sigma\{a_L Re(\tau_{ij,L}\zeta_L{}^{\delta}) + \tilde{a}_L Im(\tau_{ij,L}\zeta_L{}^{\delta})\} + c_{ij33}\epsilon_3 \tag{30}$$

where Re and Im stand for real imaginary, respectively. Equations (25) and (27) are then replaced by

$$\mathbf{K}(0)\mathbf{a} = \epsilon_3\mathbf{b} \tag{31}$$

$$\mathbf{K}(\delta)\mathbf{a} = \mathbf{0} \tag{32}$$

where $\mathbf{K}$ is now a real valued square matrix and $\mathbf{a}$ is a real column matrix whose elements are a_L, $\tilde{a}_L$, $a_L{}'$, and $\tilde{a}_L{}'$ ($L=1$, 2, 3). The real root δ is then obtained from

$$\|\mathbf{K}(\delta)\| = 0 \tag{33}$$

We will next discusss equation (26) or (33) and equation (31) separately. Notice that equation (26) or (33) has nothing to do with ϵ_3. Indeed, if $\epsilon_3 = 0$ the formulation here reduces to that of the plane strain problems considered in [22], and equation (26) or (33) is identical to the one obtained in [22]. As we will see in this paper, the seemingly innocent appearance of the ϵ_3 terms in the preceding formulation makes the stress at the free edge inherently singular for certain composites. Moreover, the singularity is logarithmic.

It should be pointed out that the formulation here tacitly assumed that the eigenvalues p_L of the elasticity constants, equation (13b), are distinct. For degenerate cases in which p_L is a multiple root, equations (15) and (16) have different expressions. The correct expressions for equations (15) and (16) when p_L is a multiple root were given in [11] when $f(Z)$ assumes the special form of equation (14) and in [23] when $f(Z)$ is arbitrary.

3 The Roots δ

Two different illustrative composite materials are used for the numerical calculations. Each layer of the composite[2] is assumed to be made of the same orthotropic material.[3] The orientation of the axes of symmetry ($\hat{x}_1$, x_2, $\hat{x}_3$), however, differs from layer to layer. Referring to the ($\hat{x}_1$, x_2, $\hat{x}_3$) axes, the following engineering constants for the layers in the two composites are taken from [6] and [24], respectively.

Composite W

(Typical high modulus graphite/epoxy, [6])

$$\left.\begin{aligned} &E_1 = E_2 = 14.48 \times 10^6 \text{ kPa } (2.1 \times 10^6 \text{ psi}) \\ &E_3 = 137.9 \times 10^6 \text{ kPa } (20 \times 10^6 \text{ psi}) \\ &G_{12} = G_{23} = G_{31} = 4.98 \times 10^6 \text{ kPa } (.85 \times 10^6 \text{ psi}) \\ &\nu_{21} = \nu_{31} = \nu_{32} = .21 \end{aligned}\right\} \tag{34}$$

Composite T

(T300/5208 graphite/epoxy, [24])

$$\left.\begin{aligned} &E_1 = E_2 = 10.62 \times 10^6 \text{ kPa } (1.54 \times 10^6 \text{ psi}) \\ &E_3 = 151.7 \times 10^6 \text{ kPa } (22 \times 10^6 \text{ psi}) \\ &G_{12} = G_{23} = G_{31} = 5.58 \times 10^6 \text{ kPa } (.81 \times 10^6 \text{ psi}) \\ &\nu_{21} = \nu_{31} = \nu_{32} = .28 \end{aligned}\right\} \tag{35}$$

In equations (34) and (35), E_i are the Young's moduli, G_{ij} the shear moduli, and ν_{ij} are the Poisson's ratios [25]. Using

[2] The present analysis is concerned with the interface between any two adjacent layers in a laminated composite. For simplicity, the terminology "laminated composite," "composite," etc., is used in this paper to refer to these adjacent layers.

[3] The theory presented here applies to composites in which each layer is an anisotropic material. For numerical examples, however, we assume the layers to be of the same orthotropic material.

Table 1 Roots[a] δ for r^δ terms in composite W

(θ/θ')	δ_1	δ_2	δ_3	δ_4	δ_5
15/−15	−.001	.997 + .042 i	1.974 + .187 i	2.961 + .261 i	
0/15	−.000	.999 + .023 i	1.995 + .085 i	2.991 + .134 i	
90/15	−.033	1.411 + .387 i	1.660 + .688 i	2.835 + 1.758 i	
60/−60	−.023	.831 + .271 i	1.482 + .773 i	2.149 + 1.246 i	2.942 + 1.755 i
0/60	−.020	1.009 + .108 i	1.747 + .659 i		
90/60	−.011	.942 + .201 i	1.917 + .681 i	2.769 + 1.243 i	

[a]zero and positive integers are also roots for δ

Table 2 Roots[a] δ for r^δ terms in composite T

(θ/θ')	δ_1	δ_2	δ_3	δ_4	δ_5
15/−15	−.003	.990 + .079 i	1.944 + .294 i	2.933 + .382 i	
0/15	−.001	.997 + .044 i	1.989 + .135 i	2.984 + .194 i	
90/15	−.052	.853	1.405 + .572 i	1.650 + .665 i	2.846 + 1.819 i
60/−60	−.031	.787 + .314 i	1.450 + .817 i	2.093 + 1.336 i	2.940 + 1.806 i
0/60	−.034	1.023	1.716 + .703 i		
90/60	−.015	1.781	.921 + .243 i	1.940 + .738 i	2.728 + 1.243 i

[a]zero and positive integers are also roots for δ

equation (34) or (35), the elastic compliance $\hat{s}_{ij}$ referred to the $(\hat{x}_1, x_2, \hat{x}_3)$ axes can be computed [25, 26]. Its inverse, $\hat{c}_{ij}$ is obtained by using the relations derived in [25]. s_{ij}, c_{ij}, s_{ij}', and c_{ij}' associated with various θ and θ' are then determined from equations derived in [22, 27]. Equations (13b) and (11) provide the eigenvalues p_L, $(L=1, 2, 3)$ and the associated eigenvectors $v_{i,L}$. For Composite W all three eigenvalues p_L are purely imaginary for any ply angle θ [22], while for Composite T two of the three eigenvalues are complex for $|\theta|$ less than 71.5377 deg. The roots of equation (26) for some (θ/θ') combinations are listed in Table 1 for composite W given by equation (34) and in Table 2 for composite T given by equation (35). Double precision was used in the calculations but we have rounded the roots in Tables 1 and 2 to four digits. Both complex and real roots were found. Since complex conjugates of these values are also roots of $\|\mathbf{K}_c\|$, we list only complex roots with positive imaginary parts in Tables 1 and 2. Detailed information on locating the complex roots can be found in [27].

Most interesting of these roots are the positive integer values of δ, which seem to consistently appear for all (θ/θ') combinations for both composites. There appears to be a negative real root for δ, but there are no other complex roots with a negative real part. Since the negative δ is the one contributing to the singular stress, we present in Figs. 3 and 4 the negative δ for all possible combinations of (θ/θ') angles. Curves of constant δ are given only in one quarter of the (θ/θ') plane since the curves in the remaining three quarters are a repetition of the curves shown. We see that the (0/90) composite, which has the same δ value as the (90/0) composite, has the largest negative value of δ. The negative δ values appear to be simple roots of equation (33), and hence **a** of equation (32) is unique up to a multiplicative constant, say k^*. By substituting **a** of (32) into (30), we may write equation (30) as

$$\sigma_{ij} = k^* r^\delta \sigma_{ij}^*(\phi) \tag{36}$$

where σ_{ij}^* depends on ϕ. The analysis presented here provides the order of singularity δ and σ_{ij}^*. k^*, which may be identified with the stress-intensity factor if elements of σ_{ij}^* are normalized, can be determined only by solving the global boundary-value problem. For instance, one may use a finite element scheme in which a special element, whose stress is given by equation (36), is introduced at the free edge. If k^* associated with a free-edge point happens to be zero after solving the global boundary-value problem, there is no singularity of r^δ at that particular free-edge point. Therefore, *a singularity of the form given by equation (36) at a free edge is not certain until the global problem is solved.*

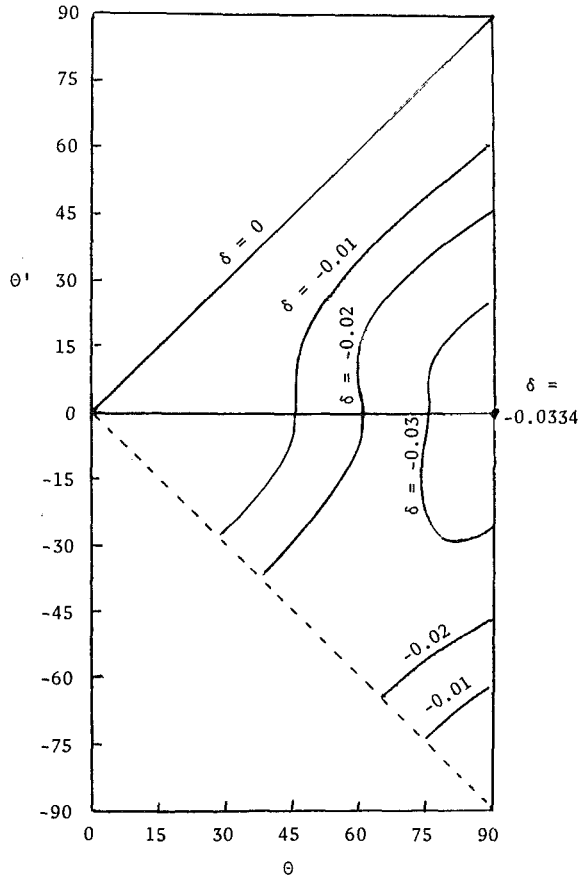

Fig. 3 δ of the r^δ singularity for composite W

4 Uniform Stress Solution ($\epsilon_3 \neq 0$)

The solution of equation (31) for **a** would have been straightforward were it not for the fact that $\delta = 0$ is a root of equation (33), and hence $\mathbf{K}(0)$ is singular. Therefore, a solution for **a** in equation (31) exists if and only if [28]

$$\mathbf{l}^T\mathbf{b} = 0 \tag{37}$$

where T denotes the transpose and **l** is a left eigenvector of $\mathbf{K}(0)$:

$$\mathbf{l}^T\mathbf{K}(0) = \mathbf{0} \tag{38}$$

It turns out that there are two left eigenvectors of $\mathbf{K}(0)$. Equation (37) then must be satisfied for both **l**. For (0/90),

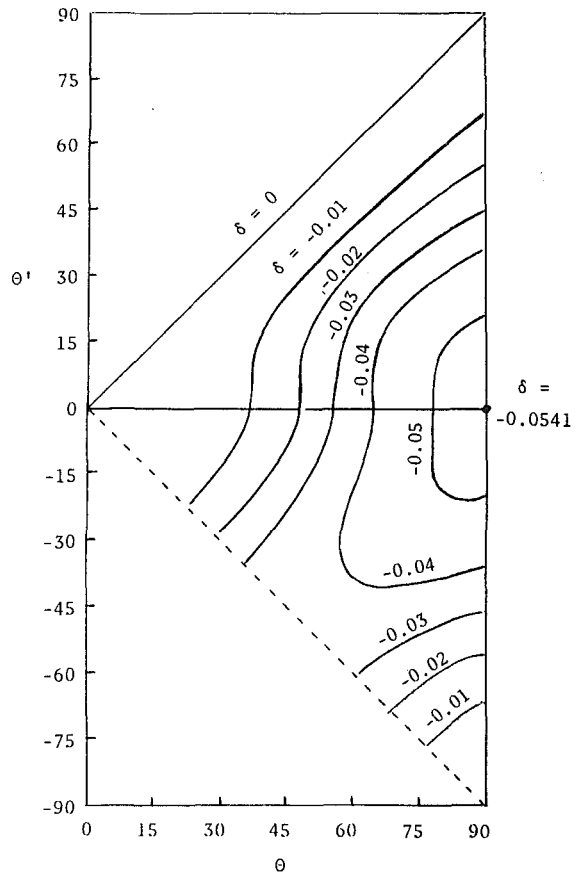

Fig. 4 δ of the r^{δ} singularity for composite T

$(\theta/-\theta)$, and a special family of (θ/θ')[4] composites, numerical solutions indicate that equation (37) holds, and equation (31) has a particular solution $\epsilon_3 \mathbf{a}^{(p)}$ and two arbitrary solutions $\mathbf{a}^{(1)}$ and $\mathbf{a}^{(2)}$:

$$\mathbf{a} = \epsilon_3 \mathbf{a}^{(p)} + \alpha_1 \mathbf{a}^{(1)} + \alpha_2 \mathbf{a}^{(2)} \tag{39}$$

where α_1 and α_2 are arbitrary constants. Substitution of equation (39) into equations (29) and (30) with $\delta = 0$ yields

$$u_i = \epsilon_3 u_i^{(p)} + \alpha_1 u_i^{(1)} + \alpha_2 u_i^{(2)} \tag{40}$$

$$\sigma_{ij} = \epsilon_3 \sigma_{ij}^{(p)} + \alpha_1 \sigma_{ij}^{(1)} \tag{41}$$

where

$$u_i^{(p)} = \Sigma\{a_L^{(p)} Re(v_{i,L} Z_L) + \tilde{a}_L^{(p)} Im(v_{i,L} Z_L)\} + \delta_{i3} x_3 \tag{42a}$$

$$u_i^{(n)} = \Sigma\{a_L^{(n)} Re(v_{i,L} Z_L) + \tilde{a}_L^{(n)} Im(v_{i,L} Z_L)\}, \quad (n = 1,2) \tag{42b}$$

$$\sigma_{ij}^{(p)} = \Sigma\{a_L^{(p)} Re(\tau_{ij,L}) + \tilde{a}_L^{(p)} Im(\tau_{ij,L})\} + c_{ij33} \tag{42c}$$

$$\sigma_{ij}^{(1)} = \Sigma\{a_L^{(1)} Re(\tau_{ij,L}) + \tilde{a}_L^{(1)} Im(\tau_{ij,L})\} \tag{42d}$$

Equation (17) has been used in reducing equations (42*a*, 42*b*). The reason $\sigma_{ij}^{(2)}$ is absent in equation (41) is because we have chosen $\mathbf{a}^{(1)}$ and $\mathbf{a}^{(2)}$ such that $u_i^{(2)}$ is a rigid body rotation and hence $\sigma_{ij}^{(2)}$ associated with $u_i^{(2)}$ vanishes. Notice that $\sigma_{ij}^{(1)}$ and $\sigma_{ij}^{(p)}$ are constants. By equation (41), σ_{ij} is constant and we have a uniform stress solution. For composites other than (0/90), $(\theta/-\theta)$, and the special family of (θ/θ'), which has already been mentioned, it was found that equation (37) does not hold and hence no uniform stress solutions exist.

Numerical calculations for the composites given by (34) and (35) for (0/90), $(\theta/-\theta)$, and the special family of (θ/θ') show that $\sigma_{ij}^{(1)}$ of equation (42*d*) have the expression

$$\sigma_{ij}^{(1)} = \begin{bmatrix} 0 & 0 & 0 \\ 0 & 0 & 1 \\ 0 & 1 & 0 \end{bmatrix} \tag{43}$$

when $\mathbf{a}^{(1)}$ of equation (39) is properly normalized while $\sigma_{ij}^{(p)}$ has the form

$$\sigma_{ij}^{(p)} = \begin{bmatrix} 0 & 0 & 0 \\ 0 & \tilde{\sigma}_{22} & 0 \\ 0 & 0 & \tilde{\sigma}_{33} \end{bmatrix} \tag{44}$$

The values of $\tilde{\sigma}_{22}$ $(=\tilde{\sigma}_{22}')$ and $\tilde{\sigma}_{33}$ $(=\tilde{\sigma}_{33}')$ for $(\theta/-\theta)$ composites are given in Table 3. It is interesting to notice that for $(15/-15)$ of composite W, $\tilde{\sigma}_{22}$ is more than five times the value of $\tilde{\sigma}_{33}$. In other words, the interlaminar normal stress at the free edge of the interface is more than five times the applied extensional stress. This interpretation, of course, is based on the assumption that no singularity of r^{δ} is present.

We also calculate $\tilde{\sigma}_{22}$ and $\tilde{\sigma}_{33}$ for (0/90) composites. However, the results will be presented in a later section when we discuss the solution for composites other than (0/90), $(\theta/-\theta)$, and the special family of (θ/θ').

5 Uniform Stress Solution ($\epsilon_3 \neq 0$) – Alternate Method

In this section we reconsider the uniform stress solution obtained in the preceding section by using an alternate approach. With this approach, we not only obtain explicit expressions for $\tilde{\sigma}_{22}$ and $\tilde{\sigma}_{33}$ of equation (44), but we also see clearly why a uniform stress solution fails to exist for composites other than (0/90), $(\theta/-\theta)$, and the special family of (θ/θ').

For the composites considered here, the material in each layer is symmetric with respect to the (x_1, x_3) plane and hence [25, 26],

$$s_{14} = s_{16} = s_{24} = s_{26} = s_{34} = s_{36} = s_{54} = s_{56} = 0 \tag{45}$$

By applying these material symmetry properties along with the stress-free boundary conditions, equation (21), equation (7) can be written for $i = 1, 3, 5$ as

$$\epsilon_1 = s_{12}\sigma_2 + s_{13}\sigma_3 \tag{46}$$

$$\epsilon_3 = s_{32}\sigma_2 + s_{33}\sigma_3 \tag{47}$$

$$\epsilon_5 = s_{52}\sigma_2 + s_{53}\sigma_3 \tag{48}$$

Solving for σ_3 from equation (47), and eliminating σ_3 in (46) and (48) we have

$$\sigma_3 = \epsilon_3/s_{33} - (s_{32}/s_{33})\sigma_2 \tag{49}$$

$$\epsilon_1 = R_1\epsilon_3 + R_{12}\sigma_2 \tag{50}$$

$$\epsilon_5 = R_5\epsilon_3 + R_{52}\sigma_2 \tag{51}$$

where

$$\left.\begin{aligned} R_1 &= s_{13}/s_{33} \\ R_{12} &= s_{12} - s_{13}s_{32}/s_{33} \\ R_5 &= s_{53}/s_{33} \\ R_{52} &= s_{52} - s_{53}s_{32}/s_{33} \end{aligned}\right\} \tag{52}$$

The interface continuity conditions of equation (22) are equivalent to

[4] This special family of (θ/θ') composites is shown in Figs. 5 and 6 by the curve $k = 0$ which begins at (0/0) and ends at (90/0).

Table 3 $\tilde{\sigma}_{22}$ and $\tilde{\sigma}_{33}$ of equation (44) for $(\theta/-\theta)$ composites

	θ	15 deg	30 deg	45 deg	60 deg	75 deg
Composite	$\tilde{\sigma}_{22}=\tilde{\sigma}_{22}'$	191.14	29.887	8.2424	1.4187	−1.2079
W	$\tilde{\sigma}_{33}=\tilde{\sigma}_{33}'$	35.231	7.2214	3.4618	2.2766	1.8203
Composite	$\tilde{\sigma}_{22}=\tilde{\sigma}_{22}'$	71.464	16.660	5.9075	2.2697	0.8352
T	$\tilde{\sigma}_{33}=\tilde{\sigma}_{33}'$	23.032	6.5434	3.3082	2.2137	1.7821

The unit for σ_{ij} is 6.894757×10^6 kPa (10^6 psi)

$$[\epsilon_1]=[\epsilon_3]=[\epsilon_5]=0 \tag{53}$$

Applying equations (23) and (53) to equations (50) and (51), we obtain,

$$[R_{12}]\sigma_2+[R_1]\epsilon_3=0 \tag{54}$$

$$[R_{52}]\sigma_2+[R_5]\epsilon_3=0 \tag{55}$$

For cross ply composites, i.e., (0/90) composites, $R_5=R_5'=R_{52}=R_{52}'=0$. Hence equations (55) is automatically satisfied and equation (54) yields

$$\sigma_2=-\epsilon_3[R_1]/[R_{12}] \tag{56}$$

For $(\theta/-\theta)$ composites, $R_{12}=R_{12}'$ and $R_1=R_1'$. Equation (54) is automatically satisfied and equation (55) provides σ_2:

$$\sigma_2=-\epsilon_3[R_5]/[R_{52}] \tag{57}$$

Equations (54) and (55) are also compatible if they are linearly dependent. This, as we will determine later, occurs for the previously mentioned special family of (θ/θ'). For other (θ/θ') combinations, equations (54) and (55) contradict each other. This indicates that a uniform stress solution due to the prescribed ϵ_3 extension does not exist. It also explains why equation (37) does not hold for composites other than (0/90), $(\theta/-\theta)$, and the special family of (θ/θ').

When a uniform stress solution exists, σ_2 is obtained from equation (56) or (57), σ_3 is obtained from equation (49), while σ_4 is arbitrary. Thus the stress can be expressed in the form of equation (41) with $\sigma_{ij}^{(1)}$ and $\sigma_{ij}^{(p)}$ given by equations (43) and (44). $\tilde{\sigma}_{22}$ in equation (44) is the coefficient of ϵ_3 in equation (56) or (57). With $\tilde{\sigma}_{22}$ so obtained, $\tilde{\sigma}_{33}$ is determined from equation (49).

6 Logarithmic Singularity

If equation (37) does not hold, a uniform stress due to a uniform extension ϵ_3 does not exist. In such a case, instead of using equations (15) and (16) we use the following solution:

$$u_i=\frac{\partial}{\partial\delta}\left\{\sum\left(A_L v_{i,L} Z_L{}^{1+\delta}+B_L \bar{v}_{i,L}\bar{Z}_L{}^{1+\delta}\right)/(1+\delta)\right\}+\epsilon_3\delta_{i3}x_3 \tag{58}$$

$$\sigma_{ij}=\frac{\partial}{\partial\delta}\left\{\sum\left(A_L\tau_{ij,L}Z_L{}^{\delta}+B_L\bar{\tau}_{ij,L}\bar{Z}_L{}^{\delta}\right)\right\}+c_{ij33}\epsilon_3 \tag{59}$$

where A_L, B_L are now functions of δ. It can be shown that equations (58) and (59) satisfy equations (1)–(3) with p, v_i, and τ_{ij} given by equations (13b), (11), and (12). If δ is real, then using equation (28), we may write equations (58) and (59) as,

$$u_i=\frac{\partial}{\partial\delta}\left\{r^{1+\delta}\sum\left(a_L Re\left(v_{i,L}\zeta_L{}^{1+\delta}\right)+\tilde{a}_L Im\left(v_{i,L}\zeta_L{}^{1+\delta}\right)\right)/(1+\delta)\right\}+\epsilon_3\delta_{i3}x_3 \tag{60}$$

$$\sigma_{ij}=\frac{\partial}{\partial\delta}\left\{r^{\delta}\sum\left(a_L Re(\tau_{ij,L}\zeta_L{}^{\delta})+\tilde{a}_L Im\left(\tau_{ij,L}\zeta_L{}^{\delta}\right)\right)\right\}+c_{ij33}\epsilon_3 \tag{61}$$

where a_L, $\tilde{a}_L$ are real functions of δ. Performing the differentiation, we obtain

$$u_i=r^{1+\delta}(ln\,r+\partial/\partial\delta)\sum\left\{a_L Re\left(v_{i,L}\zeta_L{}^{1+\delta}\right)+\tilde{a}_L Im\left(v_{i,L}\zeta_L{}^{1+\delta}\right)\right\}/(1+\delta)+\epsilon_3\delta_{i3}x_3 \tag{62}$$

$$\sigma_{ij}=r^{\delta}(ln\,r+\partial/\partial\delta)\sum\left\{a_L Re\left(\tau_{ij,L}\zeta_L{}^{\delta}\right)+\tilde{a}_L Im\left(\tau_{ij,L}\zeta_L{}^{\delta}\right)\right\}+c_{ij33}\epsilon_3 \tag{63}$$

Equations (62) and (63) differ from equations (29) and (30) by a factor of $(ln\,r+\partial/\partial\delta)$. If we substitute equations (62) and (63) into the free-surface conditions, equation (21), and the interface continuity conditions, equations (22) and (23), we obtain 12 equations which can be written as (cf. equation (24))

$$r^{\delta}(ln\,r+\partial/\partial\delta)\mathbf{K}(\delta)\mathbf{a}(\delta)=\epsilon_3\mathbf{b} \tag{64}$$

where $\mathbf{a}$, whose components are a_L,$\tilde{a}_L$, a_L', $\tilde{a}_L'$, is now a function of δ. This equation holds for arbitrary r if we let $\delta=0$, and

$$\mathbf{K}(0)\mathbf{a}(0)=\mathbf{0} \tag{65}$$

$$\frac{\partial}{\partial\delta}\{\mathbf{K}(\delta)\mathbf{a}(\delta)\}\,|_{\delta=0}=\epsilon_3\mathbf{b} \tag{66}$$

For simplicity, we write equations (65) and (66) as

$$\mathbf{K}\mathbf{a}=\mathbf{0} \tag{67}$$

$$(d\mathbf{K}/d\delta)\mathbf{a}+\mathbf{K}(d\mathbf{a}/d\delta)=\epsilon_3\mathbf{b} \tag{68}$$

where it is understood that all quantities on the left-hand side of (67) and (68) are evaluated at $\delta=0$. Equations (67) and (68) consist of 24 equations for $\mathbf{a}$ and $d\mathbf{a}/d\delta$. If a solution exists, substitution of $\mathbf{a}$ and $d\mathbf{a}/d\delta$ back into equations (62) and (63) with $\delta=0$ provides the desired solution.

Before we discuss the solution of (67) and (68) in the next section, we write equations (62) and (63) in full with $\delta=0$:

$$u_i=(ln\,r)\Sigma\{a_L Re(v_{i,L}Z_L)+\tilde{a}_L Im(v_{i,L}Z_L)\}+\Sigma\{a_L Re(v_{i,L}Z_L(ln\zeta_L-1))+\tilde{a}_L Im(\tilde{v}_{i,L}Z_L(ln\zeta_L-1))+(da_L/d\delta)Re(v_{i,L}Z_L)+(d\tilde{a}_L/d\delta)Im(v_{i,L}Z_L)\}+\epsilon_3\delta_{i3}x_3 \tag{69}$$

$$\sigma_{ij}=(ln\,r)\Sigma\{a_L Re(\tau_{ij,L})+\tilde{a}_L Im(\tau_{ij,L})\}+\Sigma\{a_L Re(\tau_{ij,L})ln\zeta_L)+\tilde{a}_L Im(\tau_{ij,L}ln\zeta_L)+(da_L/d\delta)Re(\tau_{ij,L})+(d\tilde{a}_L/d\delta)Im(\tau_{ij,L})\}+c_{ij33}\epsilon_3 \tag{70}$$

We see that σ_{ij} has a logarithmic singularity. Again, equation (17) has been used in deducing equation (69).

7 The Logarithmic Stress-Intensity Factor

The system of equations, equations (67) and (68), has a unique solution for $\mathbf{a}$ if (see [10])

$$d^N\|\mathbf{K}\|/d\delta^N\neq 0, \quad N=n-m, \tag{71}$$

where n and m are, respectively, the order and rank of $\mathbf{K}$. For the composites considered here $N=2$. However, it is rather difficult to prove or disprove equation (71) analytically or numerically in view of the fact that $\mathbf{K}$ is a 12 × 12 matrix.

Table 4 $\tilde{\sigma}_{ij}$ of equation (79) for composite W, $(0/\theta')$

θ'	15 deg	30 deg	45 deg	60 deg	75 deg	90 deg
k	0.0022	0.0033	0.0042	0.0040	0.0025	0
$\tilde{\sigma}_{11}(0)$	0.0221	0.0145	0.0102	0.0056	0.0016	0
$\tilde{\sigma}_{11}'(0)$	−0.0222	−0.0149	−0.0112	−0.0067	−0.0021	0
$\tilde{\sigma}_{22}(90)$	190.43	29.599	8.0106	1.2162	−1.3911	−2.1000
$\tilde{\sigma}_{22}(0)$	190.45	29.613	8.0208	1.2218	−1.3895	−2.1000
$\tilde{\sigma}_{22}'(-90)$	190.47	29.628	8.0310	1.2274	−1.3880	−2.1000
$\tilde{\sigma}_{33}(90)$	59.990	26.216	21.682	20.256	19.708	19.559
$\tilde{\sigma}_{33}(0)$	60.000	26.222	21.687	20.258	19.708	19.559
$\tilde{\sigma}_{33}'(0)$	35.132	7.1872	3.4312	2.2440	1.7848	1.6590
$\tilde{\sigma}_{33}'(-90)$	35.137	7.1903	3.4340	2.2461	1.7856	1.6590
$\tilde{\sigma}_{23}(90)$	0	0	0	0	0	0
$\tilde{\sigma}_{23}(0)$	0	0	0	0	0	0
$\tilde{\sigma}_{23}'(-90)$	0.0003	0.0006	0.0007	0.0004	0	0
$\tilde{\sigma}_{13}(0)$	−0.0035	−0.0052	−0.0065	−0.0063	−0.0040	0
$\tilde{\sigma}_{13}'(0)$	0.0034	0.0048	0.0059	0.0059	0.0039	0
$\tilde{\sigma}_{12}(0)$	0.0140	0.0092	0.0065	0.0035	0.0010	0

The unit for k and σ_{ij} is 6.894757×10^6 kPa (10^6 psi)

Table 5 $\tilde{\sigma}_{ij}$ of equation (79) for composite T, $(0/\theta')$

θ'	15 deg	30 deg	45 deg	60 deg	75 deg	90 deg
k	0.0349	0.0610	0.0729	0.0658	0.0394	0
$\tilde{\sigma}_{11}(0)$	0.2203	0.1919	0.1335	0.0695	0.0192	0
$\tilde{\sigma}_{11}'(0)$	−0.2218	−0.1990	−0.1467	−0.0817	−0.0238	0
$\tilde{\sigma}_{22}(90)$	62.232	13.729	3.3929	0.0314	−1.2148	−1.5400
$\tilde{\sigma}_{22}(0)$	67.452	13.921	3.5264	0.1009	−1.1956	−1.5400
$\tilde{\sigma}_{22}'(-90)$	67.672	14.115	3.6623	0.1729	−1.1753	−1.5400
$\tilde{\sigma}_{33}(90)$	40.825	25.844	22.950	22.009	21.660	21.569
$\tilde{\sigma}_{33}(0)$	40.948	25.952	23.025	22.048	21.671	21.569
$\tilde{\sigma}_{33}'(0)$	22.241	6.0686	2.8463	1.7151	1.2441	1.1088
$\tilde{\sigma}_{33}'(-90)$	22.260	6.0653	2.8494	1.7218	1.2474	1.1088
$\tilde{\sigma}_{23}(90)$	0	0	0	0	0	0
$\tilde{\sigma}_{23}(0)$	0	0	0	0	0	0
$\tilde{\sigma}_{23}'(-90)$	0.0036	0.0115	0.0118	0.0062	0.0011	0
$\tilde{\sigma}_{13}(0)$	−0.0549	−0.0959	−0.1145	−0.1034	−0.0619	0
$\tilde{\sigma}_{13}'(0)$	0.0498	0.0893	0.1076	0.0997	0.0612	0
$\tilde{\sigma}_{12}(0)$	0.1444	0.1258	0.0875	0.0455	0.0126	0

The unit for k and σ_{ij} is 6.894757×10^6 kPa (10^6 psi)

Instead, we regard equations (67) and (68) as a system of 24 equations for $\mathbf{a}$ and $d\mathbf{a}/d\delta$, and solve the system numerically. We find that $\mathbf{a}$ is unique while $d\mathbf{a}/d\delta$ has a particular solution and two arbitrary solutions.

Noting that $N=2$, one can see that $\mathbf{K}$ has two right eigenvectors $\mathbf{a}^{(1)}$ and $\mathbf{a}^{(2)}$ such that

$$\mathbf{K}\mathbf{a}^{(n)} = \mathbf{0}, \quad (n=1, 2) \tag{72}$$

If $\mathbf{a}$ is the unique solution of equations (67) and (68), it must also be a solution of equation (67), and hence $\mathbf{a}$ is proportional to a right eigenvector. Without loss of generality, let $\mathbf{a}^{(1)}$ be the eigenvector to which $\mathbf{a}$ is proportional, i.e.,

$$\mathbf{a} = k\epsilon_3 \mathbf{a}^{(1)} \tag{73}$$

Since $\mathbf{a}$ is unique, k is uniquely determined if $\mathbf{a}^{(1)}$ is properly normalized. The fact that $d\mathbf{a}/d\delta$ has two arbitrary solutions is obvious from equation (68) because the coefficient of $d\mathbf{a}/d\delta$ is $\mathbf{K}$ which is singular of order two. If $\epsilon_3(d\mathbf{a}/d\delta)^{(p)}$ is a particular solution of $d\mathbf{a}/d\delta$, we have

$$d\mathbf{a}/d\delta = \epsilon_3(d\mathbf{a}/d\delta)^{(p)} + \alpha_1 \mathbf{a}^{(1)} + \alpha_2 \mathbf{a}^{(2)} \tag{74}$$

where α_1, α_2 are arbitrary constants. With equations (73) and (74), equations (69) and (70) can be rewritten as

$$u_i = k\epsilon_3 \{(ln\, r)u_i^{(1)} + u_i^{(\phi)}\} + \epsilon_3 u_i^{(p)} + \alpha_1 u_i^{(1)} + \alpha_2 u_i^{(2)} \tag{75}$$

$$\sigma_{ij} = k\epsilon_3 \{(ln\, r)\sigma_{ij}^{(1)} + \sigma_{ij}^{(\phi)}\} + \epsilon_3 \sigma_{ij}^{(p)} + \alpha_1 \sigma_{ij}^{(1)} \tag{76}$$

where $u_i^{(1)}$, $u_i^{(2)}$, and $\sigma_{ij}^{(1)}$ are defined in equations (42*b*) and (42*d*), while

$$u_i^{(p)} = \Sigma\{(da_L/d\delta)^{(p)} Re(v_{i,L} Z_L) + (da_L/d\delta)^{(p)} Im(v_{i,L} Z_L)\} + \delta_{i3} x_3 \tag{77a}$$

$$u_i^{(\phi)} = \Sigma\{a_L^{(1)} Re(v_{i,L} Z_L (ln\zeta_L - 1)) + \tilde{a}_L^{(1)} Im(v_{i,L} Z_L (ln\zeta_L - 1))\} \tag{77b}$$

$$\sigma_{ij}^{(p)} = \Sigma\{da_L/d\delta)^{(p)} Re(\tau_{ij,L}) + (d\tilde{a}_L/d\delta)^{(p)} Im(\tau_{ij,L})\} + c_{ij33} \tag{77c}$$

$$\sigma_{ij}^{(\phi)} = \Sigma\{a_L^{(1)} Re(\tau_{ij,L} ln\zeta_L) + \tilde{a}_L^{(1)} Im(\tau_{ij,L} ln\zeta_L)\} \tag{77d}$$

Again the reason $\sigma_{ij}^{(2)}$ is missing in equation (76) is due to the fact that $u_i^{(2)}$ is a rigid body rotation.

Although the solution obtained here is for composites other than (0/90), $(\theta/-\theta)$, and the special family of (θ/θ'), application of the present solution to these three cases yields $k=0$. Hence $\mathbf{a}=\mathbf{0}$ by equation (73), and the solution for $d\mathbf{a}/d\delta$ from equation (68) is identical to the solution for $\mathbf{a}$ in equation (31). It follows that $(d\mathbf{a}/d\delta)^{(p)}$ of equation (74) is identical to $\mathbf{a}^{(p)}$ of equation (39), and that $u_i^{(p)}$, $\sigma_{ij}^{(p)}$ in equations (77*a*) and (77*c*) and equations (42*a*) and (42*c*) are also identical. Thus, the solution obtained in equations (75) and (76) reduces to that given in equations (40) and (41) when the composite is (0/90), $(\theta/-\theta)$, or the special family of (θ/θ').

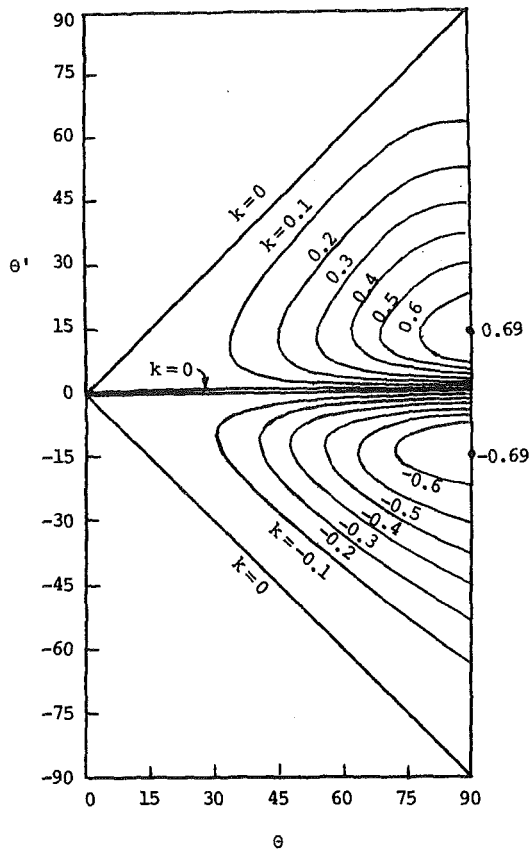

Fig. 5 k of the $k(\ln r)$ singularity for composite W. The unit for k is 6.89457×10^6 kPa (10^6 psi).

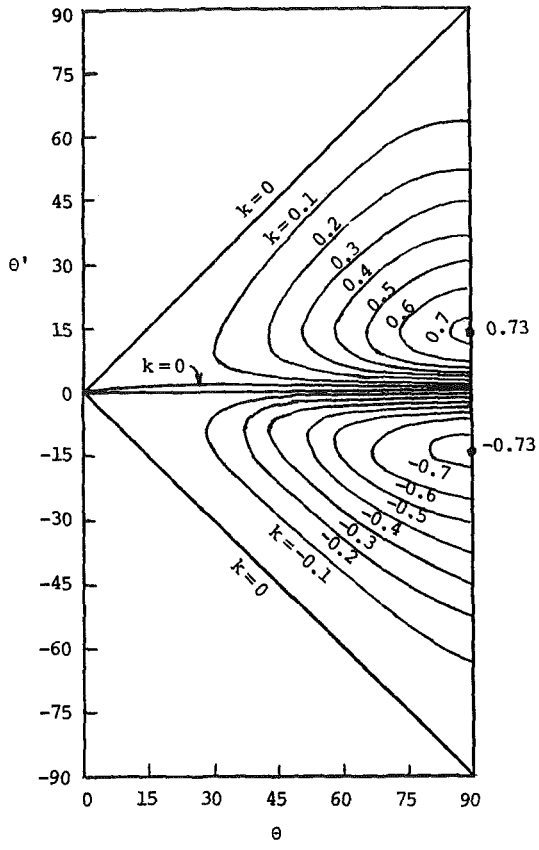

Fig. 6 k of the $k(\ln r)$ singularity for composite T. The unit for k is 6.894757×10^6 kPa (10^6 psi).

When $k \neq 0$, we see from equation (76) that σ_{ij} has a logarithmic singularity unless $\epsilon_3 = 0$. Therefore, unless $\epsilon_3 = 0$, the stress is inherently singular for composites for which $k \neq 0$. Moreover, the singularity is logarithmic. Since the larger the value of k the stronger the logarithmic singularity, k may be regarded as the "logarithmic stress-intensity factor." It should be pointed out that the singularity of $k^* r^\delta$, $(\delta < 0)$, as analyzed in Section 3, may still exist for all composites. However, the determination of the intensity factor k^* requires a global solution while k in equation (76) does not.

For the purpose of presenting numerical results, we write equation (76) as

$$\sigma_{ij} = \{k\epsilon_3 (\ln r) + \alpha_1\} \sigma_{ij}^{(1)} + \epsilon_3 \tilde{\sigma}_{ij}(\phi) \tag{78}$$

where

$$\tilde{\sigma}_{ij}(\phi) = k\sigma_{ij}^{(\phi)} + \sigma_{ij}^{(p)} \tag{79}$$

For the composites considered here, $\sigma_{ij}^{(1)}$ has the form given in equation (43) if $\mathbf{a}^{(1)}$ of equation (73) is properly normalized. Although $\sigma_{ij}^{(p)}$ is constant, $\sigma_{ij}^{(\phi)}$ is not. Hence $\tilde{\sigma}_{ij}(\phi)$ and $\tilde{\sigma}_{ij}'(\phi)$ depend on ϕ. In Tables 4 and 5 we list the value k and $\tilde{\sigma}_{ij}(\phi)$ and $\tilde{\sigma}_{ij}'(\phi)$ on the interface ($\phi = 0$) and on the free-edge surface ($\phi = \pm 90$ deg) for the $(0/\theta')$ composites. Notice that $\tilde{\sigma}_{11} = \tilde{\sigma}_{12} = \tilde{\sigma}_{13} = 0$ at $\phi = 90$ deg. Similarly $\tilde{\sigma}_{11}' = \tilde{\sigma}_{12}' = \tilde{\sigma}_{13}' = 0$ at $\phi = -90$ deg. Hence these components are not listed in the tables. Also, since $\tilde{\sigma}_{22}' = \tilde{\sigma}_{22}$, $\tilde{\sigma}_{21}' = \tilde{\sigma}_{21}$, and $\tilde{\sigma}_{23}' = \tilde{\sigma}_{23} =$ at $\phi = 0$, only $\tilde{\sigma}_{22}(0)$, $\tilde{\sigma}_{21}(0)$, $\sigma_{23}(0)$ are listed. Similar tables for other (θ/θ') combinations can be found in [27].

For (0/90), $(\theta/-\theta)$, or the special family of (θ/θ') composites, $k = 0$, and equations (78) and (79) reduce to

$$\sigma_{ij} = \alpha_1 \sigma_{ij}^{(1)} + \epsilon_3 \tilde{\sigma}_{ij} \tag{80}$$

$$\tilde{\sigma}_{ij} = \sigma_{ij}^{(p)} \tag{81}$$

$\tilde{\sigma}_{ij}$ is now independent of ϕ. This agrees with the result obtained in equation (41). The numerical calculations of $\tilde{\sigma}_{ij}$ for (0/90) composites are included in Tables 4 and 5, while those for $(\theta/-\theta)$ composites were given in Table 3.

Again notice that $\tilde{\sigma}_{22}$ for the (0/15) composite in Table 4 is many times larger than $\tilde{\sigma}_{33}$ and $\tilde{\sigma}_{33}'$. In other words, the interlaminar normal stress at the interface is many times larger than the applied axial extensional stress. This may not be important here since the logarithmic singularity is present for σ_{23}.

Finally, the values of k for all possible combinations of (θ/θ') are presented in Figs. 5 and 6. Again, curves of constant k are given only in one quarter of the (θ/θ') plane because the curves in the rest of the plane are a repetition of the curves shown. We see that there are three contour lines along which $k = 0$. The first line is along $\theta' = \theta$. This is a trivial case because $\theta' = \theta$ implies that the layer on both sides of the interface have the same fiber orientation, and hence there exists no real interface and no logarithmic singularity. The second line is along $\theta' = -\theta$. This is the $(\theta/-\theta)$ composite and the analysis presented earlier predicted that $k = 0$ for this composite. The third line along which $k = 0$ starts at (0/0), runs slightly above the horizontal line $\theta' = 0$, and ends at (90/0). This is the special family of (θ/θ') composites referred to earlier. For this family of composites, equation (37) holds and equations (54) and (55) are compatible. Notice that (0/90) is a member of this family because the singularity of (0/90) and (90/0) are identical. Figures 5 and 6 show that the largest absolute value of k occurs at $(90/\theta')$ where θ' is near ± 15 deg. Thus for the composites considered here, the logarithmic stress singularity is the strongest for the (90/15) and (90/−15) composites.

8 Concluding Remarks

The analysis presented here shows that the stress near the

free edge of the interface in a (θ/θ') composite subjected to an extensional strain of ϵ_3 is given by

$$\sigma_{ij} = k^* r^\delta \sigma_{ij}^* + \{ k\epsilon_3 (ln\, r) + \alpha_1 \} \sigma_{ij}^{(1)} + \epsilon_3 \tilde{\sigma}_{ij} \tag{82}$$

where $\delta < 0$, k^*, k, α_1 and $\sigma_{ij}^{(1)}$ are constants while σ_{ij}^* and $\tilde{\sigma}_{ij}$ depend on ϕ. Knowing the fiber orientations θ and θ', the analysis presented here provides all quantities in equation (82) except k^* and α_1 which have to be determined by solving the complete boundary-value probelm. Therefore, the existence of the r^δ singularity depends on the stacking sequence and the complete boundary conditions while the existence of the $(ln\, r)$ singularity does not. For composites other than (0/90), $(\theta/-\theta)$, and the special family of (θ/θ') shown in the paper, it was shown that $k \neq 0$, and hence the free-edge stress is inherently singular.

It should be pointed out that if $\delta < 0$ is a double root of equation (33) one would have, besides the r^δ singularity, a singularity of the form r^δ (lnr), [11]. For the composites considered here, $\delta < 0$ appears to be a simple root of equation (33). It should also be noted that even though the layers are assumed to be of the same orthotropic material for the numerical illustrations, the theory presented here applies to any anisotropic layered composite.

Acknowledgments

The work presented here is supported by the Army Materials and Mechanics Research Center, Watertown, Mass., through contract DAAG 46-80-C-0081. Special thanks are due to Dr. S. C. Chou, the technical monitor, for his encouragement and valuable discussions.

References

1 Pipes, R. B., and Pagano, N. J., "Interlaminar Stresses in Composite Laminates Under Uniform Axial Extension," *J. Composite Materials*, Vol. 4, 1970, pp. 538–548.

2 Pipes, R. B., and Pagano, N. J., "Interlaminar Stresses in Composite Laminates—An Approximate Elasticity Solution," ASME JOURNAL OF APPLIED MECHANICS, Vol. 41, 1974, pp. 668–672.

3 Tang, S., and Levy, A., "A Boundary Layer Theory—Part II: Extension of Laminated Finite Strip," *J. Composite Materials*, Vol. 9, 1975, pp. 42–45.

4 Herakovich, C. T., "On Thermal Edge Effects in Composite Laminates," *Int. J. Mech. Sciences*, Vol. 18, 1976, pp. 129–134.

5 Hsu, P. W., and Herakovich, C. T., "Edge Effects in Angle-Ply Composite Laminates," *J. Composite Materials*, Vol. 11, 1977, pp. 422–428.

6 Wang, A. S. D., and Crossman, F. W., "Some New Results on Edge Effects in Symmetric Composite Laminates," *J. Composite Materials*, Vol. 11, 1977, pp. 92–106.

7 Pagano, N. J., "Free-Edge Stress Fields in Composite Laminates," *Int. J. Solids and Structures*, Vol. 14, 1978, pp. 385–400.

8 Wang, S. S., and Choi, I., "Boundary Layer Thermal Stresses in Angle-Ply Composite Laminates," *Modern Developments in Composite Materials and Structures*, J. L. Vinson, Ed., ASME, 1979, pp. 315–341.

9 Spilker, R. L., and Chou, S. C., "Edge-Effects in Symmetric Composite Laminates: Importance of Satisfying the Traction-Free Edge Condition," *J. Composite Materials*, Vol. 14, 1980, pp. 2–20.

10 Dempsey, J. P., and Sinclair, G. B., "On the Stress Singularities in the Plane Elasticity of the Composite Wedge," *J. Elasticity*, Vol. 9, 1979, pp. 373–391.

11 Ting, T. C. T., and Chou, S. C., "Edge Singularities in Anisotropic Composites,," *Int. J. Solids and Structures*, Vol. 17, 1981, pp. 1057–1068.

12 Bogy, D. B., "On the Problem of Edge-Bonded Elastic Quarter Planes Loaded at the Boundary," *Int. J. Solids and Structures*, Vol. 6, 1970, pp. 1287–1313.

13 Dempsey, J. P., and Sinclair, G. B., "On the Singular Behavior at the Vertex of a Bi-Material Wedge," *J. Elasticity*, Vol. 11, 1981, pp. 317–327.

14 Lekhnitskii, S. G., *Theory of Elasticity on an Anisotropic Elastic Body*, (translated by P. Fern), Holden-Day, San Francisco, 1963.

15 Green, A. E., and Zerna, W., *Theoretical Elasticity*, The Clarendon Press, Oxford, 1954, Chapter 6.

16 Bogy, D. B., "The Plane Solution for Anistropic Elastic Wedges Under Normal and Shear Loading," ASME JOURNAL OF APPLIED MECHANICS, Vol. 39, 1972, pp. 1103–1109.

17 Kuo, M. C., and Bogy, D. B., "Plane Solutions for the Displacement and Traction-Displacement Problems for Anistropic Elastic Wedges," ASME JOURNAL OF APPLIED MECHANICS, Vol. 41, 1974, pp. 197–203.

18 Stroh, A. N., "Steady State Problems in Anistropic Elasticity," *J. Math. Phys.*, Vol. 41, 1962, pp. 77–103.

19 Barnett, D. M., and Lothe, J., "Synthesis of the Sextic and the Integral Formalism for Dislocation, Greens Functions and Surface Waves in Anisotropic Elastic Solids," *Phys. Norv.*, Vol. 7, 1973, pp. 13–19.

20 Barnett, D. M., and Lothe, J., "Line Force Loadings on Anisotropic Half-Space and Wedges," *Phys. Norv.*, Vol. 8, 1975, pp. 13–22.

21 Chadwick, P., and Smith, G. D., "Foundations of the Theory of Surface Waves in Anistropic Elastic Materials," *Adv. Appl. Mech.*, Vol. 17, 1977, pp. 303–376.

22 Ting, T. C. T., and Chou, S. C., "Stress Singularities in Laminated Composites," *Proc. Second USA-USSR Symposium on Fracture of Composite Materials*, Sih, G., and Tamuzs, V., Eds., Noordhoff, 1981, pp. 249–261.

23 Ting, T. C. T., "Effects of Change of Reference Coordinates on the Stress Analyses of Anistropic Elastic Materials," *Int. J. Solids and Structures*, Vol. 18, 1982, pp. 139–152.

24 Chou, S. C., "Delamination of T300/5208 Graphite/Epoxy Laminates," *Proc. Second USA-USSR Symposium on Fracture of Composite Materials*, Sih, G., and Tamuzs, V., Eds., Noordhoff, 1981, pp. 231–248.

25 Jones, R. M., *Mechanics of Composite Materials*, McGraw-Hill, New York, 1975.

26 Christensen, R. M., "Mechanics of Composite Materials," Wiley-Interscience, New York, 1979.

27 Zwiers, R. I., and Ting, T. C. T., "Free-Edge and Contact-Edge Singularities in Laminated Composites," AMMRC TR 82-21, Department of Materials Engineering, University of Illinois at Chicago Circle, Apr. 1982.

28 Hilderbrand, F. B., *Method of Applied Mathematics*, Prentice-Hall, Englewood Cliffs N.J., 1954.

On the Stability of Waves in a Thin Orthotropic Spinning Disk

J. L. Nowinski
Professor Emeritus,
Department of Mechanical and Aerospace Engineering,
University of Delaware,
Newark, Del. 19711

A system of two ordinary coupled differential equations with periodic coefficients of the Mathieu type for two temporal perturbation parameters is derived. A closed-form solution of the system in terms of elementary functions is found and discussed. A condition for the wave stability involving the coefficients of anisotropy is established. Illustration involves a specific range of these coefficients.

Introduction

The last two decades have seen a revived interest in the nonlinear phenomenon involving transverse vibrations and circumferential waves occurring in thin membrane-like spinning disks [1–5]. Most of the earlier work concerned the isotropic materials, but the development of composites endowed with certain types of anisotropic structure made it useful to reconsider the problem in a more general, i.e., anisotropic, setting. The conclusion of the studies was rather encouraging: it appeared that the anisotropy of the material, through an appropriate choice of elastic moduli, influences strongly the induced motions and stresses in the spinning disk. This involves, in particular, the circumferential transverse waves whose stability with respect to a specific perturbation is the topic of the present paper.

As is well known, the waves induced by the rotation of the disk propagate both forward, in the direction of rotation, and backward. The latter are primarily responsible for failures of the disks, and their sustenance is chiefly attributed to the presence of the atmosphere, thus far ignored in theoretical studies.

In [6], we discussed the stability of circumferential waves in a disk of orthotropic material with respect to a temporal perturbation of motion. We arrived at a system of two ordinary differential equations for two perturbation parameters. The equations were of the second order, coupled, with periodic coefficients, and were examined in two of their simpler alternatives. In the present paper, we wish to discuss the solution of the equations in a complete form. It turns out that, despite the complexity of the equations, their solution can be put into a closed form in terms of elementary, principally trigonometric and hyperbolic functions.

We first record the main equations governing motions of an anisotropic membrane-like spinning disk free from external tractions. By confining the investigation to the mode with two nodal diameters and no nodal circles, we impose small perturbations on the time functions appearing in the expression for the deflection. An analysis of the solution of the so-called "variational" equations for the perturbation parameters, gained by an appropriate trigonometric transformation, leads to a condition for the stability of motions dependent on the coefficients of anisotropy of the material of the disk.

General Equations

To make this study relatively self-contained, it is helpful to recall that the transverse deflections of a spinning orthotropic disk are governed by two equations [2], one of which is the equation of motion and the other one of compatibility of deformations. The equations are:

$$\left(\frac{1}{r}\frac{\partial\phi}{\partial r}+\frac{1}{r^2}\frac{\partial^2\phi}{\partial\theta^2}\right)\frac{\partial^2 w}{\partial r^2}+\left(\frac{1}{r}\frac{\partial w}{\partial r}+\frac{1}{r^2}\frac{\partial^2 w}{\partial\theta^2}\right)\frac{\partial^2\phi}{\partial r^2}$$
$$-2\frac{\partial}{\partial r}\left(\frac{1}{r}\frac{\partial w}{\partial\theta}\right)\cdot\frac{\partial}{\partial r}\left(\frac{1}{r}\frac{\partial\phi}{\partial\theta}\right)-\frac{1}{2}\rho\Omega^2 r^2\nabla^2 w$$
$$-\rho\Omega^2 r\frac{\partial w}{\partial r}-\rho\frac{\partial^2 w}{\partial t^2}=0, \tag{1}$$

and

$$\frac{\partial^4\phi}{\partial r^4}+\frac{p^2}{r^2}\frac{\partial^4\phi}{\partial r^2\partial\theta^2}+\frac{k^2}{r^4}\frac{\partial^4\phi}{\partial\theta^4}+\frac{2}{r}\frac{\partial^3\phi}{\partial r^3}-\frac{p^2}{r^3}\frac{\partial^3\phi}{\partial r\partial\theta^2}$$
$$-\frac{k^2}{r^2}\frac{\partial^2\phi}{\partial r^2}+\frac{p+2k^2}{r^4}\frac{\partial^4\phi}{\partial\theta^4}+\frac{k^2}{r^3}\frac{\partial\phi}{\partial r}$$
$$=E_\theta\left[-\frac{1}{r}\left(\frac{\partial w}{\partial r}+\frac{1}{r}\frac{\partial^2 w}{\partial\theta^2}\right)\frac{\partial^2 w}{\partial r^2}+\frac{1}{r^2}\left(\frac{\partial^2 w}{\partial r\partial\theta}\right)^2\right. \tag{2}$$
$$\left.-\frac{2}{r^3}\frac{\partial w}{\partial\theta}\frac{\partial^2 w}{\partial r\partial\theta}+\frac{1}{r^4}\left(\frac{\partial w}{\partial\theta}\right)^2\right]-s\rho\Omega^2,$$

respectively, where $w = w(r,\theta;t)$ is the transverse deflection of the membrane-like disk, ∇^2 is the plane Laplacian, $k^2 = E_\theta/E_r$, $p^2 = (E_\theta/G_{r\theta})-2\nu_\theta$, and $s = k^2+2\nu_\theta-3$. Furthermore, E_r and E_θ designate Young's moduli in the radial and hoop directions, respectively, $G_{r\theta}$ is the shear modulus, ρ is the mass density of the material of the disk, and ν_θ is Poisson's ratio associated with the radial tension. Ω and ϕ are the constant angular velocity of the disk and the stress function, respectively. Finally, we have the known relation, $E_r\nu_\theta = E_\theta\nu_r$.

Contributed by the Applied Mechanics Division for publication in the JOURNAL OF APPLIED MECHANICS.

Discussion on this paper should be addressed to the Editorial Department, ASME, United Engineering Center, 345 East 47th Street, New York, N.Y. 10017, and will be accepted until two months after final publication of the paper itself in the JOURNAL OF APPLIED MECHANICS. Manuscript received by ASME Applied Mechanics Division, November, 1981; final revision, March, 1982.

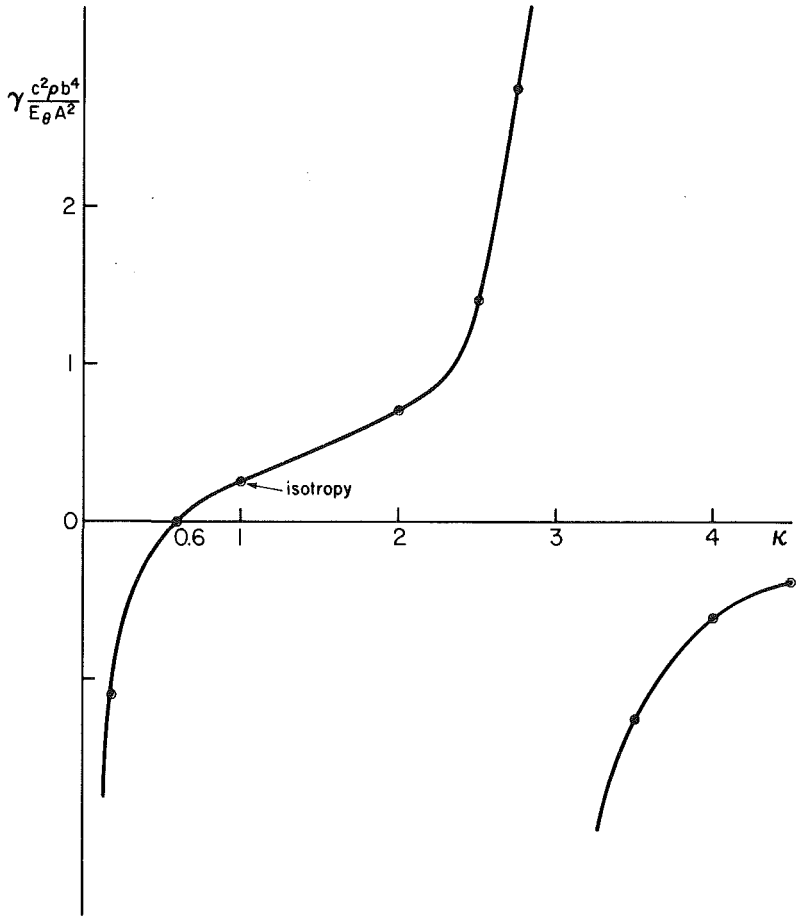

Fig. 1 Parameter γ versus the coefficient of orthotropy k

As the boundary conditions, we take

$$\tau_{rr}(b,\theta;t)=0, \quad \tau_{r\theta}(b,\theta;t)=0, \tag{3}$$

which express the absence of external radial and hoop tractions at the edge $r = b$ of the disk. Our investigation involves the mode of propagation of circumferential waves with no nodal circles and two nodal diameters. This mode is of special importance, inasmuch as it corresponds to the gravest mode of vibration in the linear case; it is represented in the expanded form by

$$w(r,\theta;t)=A\left(\frac{r}{b}\right)^2 [\cos 2\theta \cos 2\mathrm{ct} \mp \sin 2\theta \sin 2\mathrm{ct}], \tag{4}$$

where the upper (lower) sign refers to the backward (forward) traveling wave, and A denotes the amplitude of the wave. Following [5], we impose on the deflection $w(r,\theta;t)$ of the disk two slight temporal perturbations, $\delta_1(t)$ and $\delta_2(t)$, of the time functions cos 2ct and sin 2ct obtaining

$$\begin{aligned} w(r,\theta;t,\delta)=A\left(\frac{r}{b}\right)^2 \{&\cos 2\theta\,[\cos 2\mathrm{ct}+\delta_1(t)] \\ &+\sin 2\theta[\mp \sin 2\mathrm{ct}+\delta_2(t)]\}. \end{aligned} \tag{5}$$

We say that the wave motion is *stable* with respect to the given perturbations if the solutions of the "variational" equations satisfied by the perturbations $\delta_1(t)$ and $\delta_2(t)$ are bounded functions of time. On the contrary, we say that the motion is *unstable* if the solutions of the equations are unbounded functions of time[1]. We restate that in equation (5), as well as everywhere throughout this text, the upper (lower) sign is associated with a backward (forward) traveling wave.

A lengthy computation using an orthogonalization procedure (see [6]) results in the following equations, central to our subsequent discussion, and obtained from equation (1):

$$\begin{aligned} &\delta_1''+[d+\gamma(1+\cos 2\tau)]\delta_1 = \mp\gamma \sin 2\tau\cdot\delta_2+(1-d)\cos\tau, \\ &\delta_2''+[d+\gamma(1-\cos 2\tau)]\delta_2 = \mp\gamma \sin 2\tau\cdot\delta_1 \mp(1-d)\sin\tau. \end{aligned} \tag{6}$$

Here,

$$\gamma=\frac{E_\theta A^2(5k-3)}{c^2(9-k^2)\rho b^4 k}, \quad d=\gamma+\frac{(5-\nu_\theta)\Omega^2}{8c^2}, \quad \tau=2\mathrm{ct}, \tag{6a}$$

and the prime superscripts denote differentiation with respect to τ.

We note that in the isotropic case in which $k = 1$, there is $d = 1$ and

$$c^2=\frac{EA^2}{4\rho b^4}+\frac{5-\nu}{8}\Omega^2 \tag{6b}$$

(see [6], equation (20)).

The left-hand members of equations (6) are clearly of the Mathieu type. Although linear, they exhibit two unwelcome features: variable coefficients and coupling. For those who recall the intricacies involved in the analysis of the seemingly innocent looking standard Mathieu equation (cf., e.g., [7]), it comes rather as a surprise that the system (6) admits a closed-form solution in terms of elementary functions. To demonstrate this, it is more convenient to discuss the system (6) in its homogeneous form. This follows from the observation that the particular integrals of the system are

$$\delta_1^0=\beta\cos\tau, \quad \delta_2^0=\mp\beta\sin\tau, \tag{7}$$

[1] More precisely, it is required that the perturbations remain small at all times. This guarantees smallness of the deviations of the perturbed deflections from the original ones, and roughly corresponds to the Liapounov criterion of stability (cf., e.g., [8], p. 133).

where $\beta = (1-d)/(d+2\gamma-1)$. Inasmuch as the foregoing expressions constitute bounded functions of τ, they do not influence the stability of the solution of the system (6), and may, therefore, be put out of mind. We are thus left with the system, or more exactly with two systems:

$$\delta_1'' + (a+\gamma\cos 2\tau)\,\delta_1 = \pm\gamma\sin 2\tau\cdot\delta_2,$$
$$\delta_2'' + (a-\gamma\cos 2\tau)\,\delta_2 = \pm\gamma\sin 2\tau\cdot\delta_1, \qquad (8\pm)$$

where $a = d+\gamma$. Now, it is easy to see that if the solution of $(8+)$ is δ_1^+ and δ_2^+, say, then the solution of $(8-)$ is $\delta_1^- = \delta_1^+$ and $\delta_2^- = -\delta_2^+$. In terms of stability, it therefore suffices to consider but one of the two systems, say $(8+)$, associated with the backward traveling wave. Thus, all conclusions reached with regard to the stability of the last named wave also characterize the behavior of the forward traveling wave (with accuracy to the appropriate sign).

Since this result holds for the orthotropic materials, all the more it holds for the isotropic one. Consequently, the isotropic case solution, in the otherwise brilliant paper [5], implying simultaneous stability of the backward traveling wave and instability of the forward traveling wave cannot be correct. Actually, the equations (19) in [5] for δ_1^+ and δ_2^- (denoted there be ϵ_1 and ϵ_2) are free from error, while the equations (23) for δ_1^- and δ_2^- (denoted there by ϵ_3 and ϵ_4) are not. This may be verified by observing that expressions (23) in [5] do not satisfy the governing equations (22) in [5] (at least the present author was unsuccessful in demonstrating such satisfaction). Likewise incorrect becomes, based on the incorrect result in [5], that portion of the sentence in [6] (following equations (32*b*) in [6]) that concerns the stability of the forward traveling wave.

We now apply the "rotational" transformation

$$u = \delta_1\sin\tau + \delta_2\cos\tau, \quad v = \delta_1\cos\tau - \delta_2\sin\tau, \qquad (9)$$

and by simple manipulations cast equations $(8+)$ in the form

$$u^{IV} + 2(a+1)u'' + [(a-1)^2 - \gamma^2]u = 0, \qquad (10)$$

$$v^{IV} + 2(a+1)v'' + [(a-1)^2 - \gamma^2]v = 0, \qquad (11)$$

in which the functions involved become separated and the coefficients constant. In the isotropic case, we have $a = 1+\gamma$, and one recovers the solution (19) derived in [5].

For the sake of argument and to avoid too many technicalities, let us confine our discussion to the case in which the orthotropy of the material is not too excessive. We thus assume that the coefficient of orthotropy $k^2 = E_\theta/E_r$ is contained in the half-open interval [0.36, 9], say. This includes such materials of rather different mechanical properties as plywood ($k^2 = 0.5$ or $k^2 = 2$, respectively) and borsic-aluminum composite ($k^2 = 0.4$ or $k^2 = 2.5$, respectively).

As seen in Fig. 1, in the corresponding interval, in which $0.6 \le k < 3$, the coefficient γ is positive. Consequently, $a > 0$, and the discriminant Δ of the characteristic equation associated with equations (10) and (11) is positive, $\Delta = 4a+\gamma^2 > 0$. With these data in mind, the roots of the characteristic equation become

$$\alpha_1 = -\alpha_2 \equiv \beta_1 \equiv [-(a+1) + (4a+\gamma^2)^{1/2}]^{1/2}, \qquad (12)$$

$$\alpha_3 = -\alpha_4 \equiv i\beta_2 \equiv i[(a+1) + (4a+\gamma^2)^{1/2}]^{1/2}. \qquad (13)$$

As a consequence, one arrives at three alternatives of the solution characterized in Table 1.

It is immediately seen (without recourse to the explicit solution) that the alternative (I) represents an unstable motion, as follows from the existence of the real positive root α_1. The same concerns the isotropic case (alternative (II)) on account of the presence of the double root $\alpha_1 = \alpha_2 = 0$ that implies a term proportional to τ. On the contrary, alternative (III) characterizes a motion that is stable. Alternative (I) being the most diversified, it is of interest to record the associated solution explicitly as follows:

Table 1 Three alternatives of the solution

Roots	(I) $\gamma^2 > (a-1)^2$	(II) $\gamma^2 = (a-1)^2$	(III) $\gamma^2 < (a-1)^2$
α_1	real pos.	0	imag. pos.
α_2	real neg.	0	imag. neg.
α_3	imag. pos.	imag. pos.	imag. pos.
α_4	imag. neg.	imag. neg.	imag. neg.

$$\begin{aligned}\delta_1 = {} & C_1[\sinh\beta_1\tau\cdot\sin\tau + \lambda_1\cosh\beta_1\tau\cdot\cos\tau] \\ & + C_2[\cosh\beta_1\tau\cdot\sin\tau + \lambda_1\sinh\beta_1\tau\cdot\cos\tau] \\ & + C_3[\sin\beta_2\tau\cdot\sin\tau + \lambda_2\cos\beta_2\tau\cdot\cos\tau] \\ & + C_4[\cos\beta_2\tau\cdot\sin\tau - \lambda_2\sin\beta_2\tau\cdot\cos\tau],\end{aligned} \qquad (14)$$

$$\begin{aligned}\delta_2 = {} & C_1[\sinh\beta_1\tau\cdot\cos\tau - \lambda_1\cosh\beta_1\tau\cdot\sin\tau] \\ & + C_2[\cosh\beta_1\tau\cdot\cos\tau - \lambda_1\sinh\beta_1\tau\cdot\sin\tau] \\ & + C_3[\sin\beta_2\tau\cdot\cos\tau - \lambda_2\cos\beta_2\tau\cdot\sin\tau] \\ & + C_4[\cos\beta_2\tau\cdot\cos\tau + \lambda_2\sin\beta_2\tau\cdot\sin\tau])\end{aligned} \qquad (15)$$

where

$$\lambda_1 = \frac{\beta_1^2 + a - \gamma - 1}{2\beta_1} = \frac{2\beta_1}{-\beta_1^2 - a - \gamma + 1},$$
$$\lambda_2 = \frac{\beta_2^2 - a + \gamma + 1}{2\beta_2} = \frac{2\beta_2}{\beta_2^2 - a - \gamma + 1}. \qquad (16)$$

Conclusions

It is shown that, in the orthotropic case, the stability conditions for forward and backward traveling waves are the same. Consequently, the isotropic case solution derived in [5], and implying the opposite, is partially incorrect. Also incorrect is the respective inference in [6] based on [5]. Illustration given involves limited values of the elastic parameters, but the study may be extended to a more exhaustive analysis of the related characteristic equations.

References

1 Nowinski, J. L., "Nonlinear Transverse Vibrations of a Spinning Disk," ASME JOURNAL OF APPLIED MECHANICS, Vol. 31, 1964, pp. 72–78.

2 Nowinski, J. L., and Woodall, S. R., "Finite Vibrations of a Free Rotating Anisotropic Membrane," *Journal of the Acoustical Society of America*, Vol. 36, 1964, pp. 2113–2118.

3 Advani, S. H., "Stationary Waves in a Spinning Disc," *International Journal of Mechanical Sciences*, Vol. 9, 1967, pp. 307–313.

4 Advani, S. H., and Bulkeley, P. Z., "Non-linear Transverse Vibrations and Waves in Spinning Membrane Discs," *International Journal for Nonlinear Mechanics*, Vol. 4, 1969, pp. 123–127.

5 Bulkeley, P. Z., "Stability of Transverse Waves in a Spinning Membrane Disk," ASME JOURNAL OF APPLIED MECHANICS, Vol. 40, 1973, pp. 133–136.

6 Nowinski, J. L., "Propagation and Stability of Non-Linear Waves in Spinning Anisotropic Membrane-Like Disks," *International Journal of Non-Linear Mechanics*, Vol. 16, 1981, pp. 427–437.

7 McLachlan, N. W., *Theory and Applications of Mathieu Functions*, Dover, New York, 1964.

8 Knops, R. J., and Wilkes, E. W., "Theory of Elastic Stability," in *Encyclopedia of Physics*, Fluegge, S., ed., Vol. VI*a*/3 (ed., C. Truesdell), Springer, Berlin, 1973, pp. 125–302.

Efficient Pulse Shapes to Deform Beams With Axial Constraints

W. J. Stronge[1]
Michelson Laboratory,
Naval Weapons Center,
China Lake, Calif. 93555

The transient motion of a simply supported, rigid-plastic beam in response to a uniformly distributed pressure pulse of arbitrary shape is determined. The beam is subject to an axial force in addition to the transverse pressure. This axial force is a parameter that can approximate constraint forces resulting from deformation of beams with fixed or elastically restrained ends. The pulse shape that maximizes deflection at the center of the beam is determined for a specified applied impulse. When a transverse pressure applies a limited amount of impulse to the beam, an impulsive load causes the largest deformation. Axial force decreases the deformation but has no effect on the most efficient pulse shape.

Introduction

In some dynamic loading systems, the pressure applied to a workpiece can be a controllable function of time although the total impulse applied is fixed. In these systems, what pressure pulse shape, $p(t)$, results in the largest central deflection of plastically deforming beams?

For small deformation of rigid-plastic beams, an impulsive pressure has been shown to be most effective in causing deflection [1, 2]. This same pulse shape will be shown to be most effective also when the beam is subjected to constant axial force in addition to the transverse pressure. By setting the axial force equal to the yield force, this analysis can approximate the deformation-dependent constraint force resulting from ends fixed against axial displacement. This approximation is consistent with approximating the hyperbolic yield condition of a rigid-plastic beam by a rectangular yield condition. The technique used to determine the most effective pulse shape is based on the calculus of variations and is more direct and generally useful than an earlier proof [1].

The effect of pulse shape on the response of rigid-plastic structures was previously investigated by Symonds [3] and Youngdahl [2, 4]. Youngdahl showed that two variables, impulse and an effective pressure are sufficient to determine the dynamic plastic deformation of four structural elements subjected to time-dependent pressures. Krajcinovic [5] proved this correlation to be exact for time-independent deformation modes and a good approximation for higher pressure loadings where time-dependent deformation modes exist. Hence, when a specified impulse is applied, deformation is a monotonically increasing function of effective pressure. This is only true with axial forces if appropriate parameterization of the axial force is used.

The beam with an axial force is significantly different from Youngdahl's examples in having an internal-energy dissipation rate term that depends on deflection. The element stiffens with increasing deflection. This term becomes increasingly important with larger deformations, irrespective of whether the axial force is imposed or develops from fixed-end conditions.

This investigation does not address the coupling between axial force and bending moments in plastically deforming sections. Those interactions are eliminated by an approximation to the yield condition that is used for analytic simplification.

Analytical Model

The simply supported beam shown in Fig. 1 is subject to a suddenly applied, uniformly distributed pressure, $p(t)$. This beam is of unit width and has a mass, ρ, per unit length. It is initially straight and at rest.

Consider a beam composed of a rigid perfectly-plastic

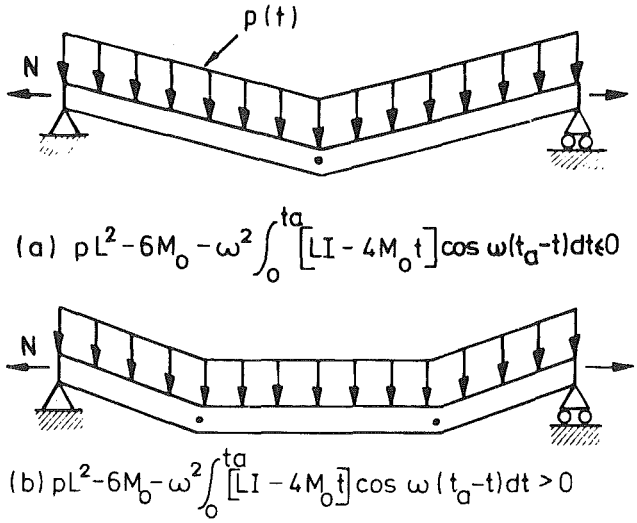

Fig. 1 Low and high pressure deformation modes

[1] Present address: University of Cambridge, Department of Engineering, Cambridge CB2 1Pz, England.

Contributed by the Applied Mechanics Division for presentation at the Winter Annual Meeting, Phoenix, Ariz., November 14-19, 1982, of THE AMERICAN SOCIETY OF MECHANICAL ENGINEERS.

Discussion on this paper should be addressed to the Editorial Department ASME, United Engineering Center, 345 East 47th Street, New York, N.Y. 10017, and will be accepted until two months after final publication of the paper itself in the JOURNAL OF APPLIED MECHANICS. Manuscript received by ASME Applied Mechanics Division, October, 1981; final revision, February, 1982. Paper No. 82-WA/APM-6.

Copies will be available until July, 1983.

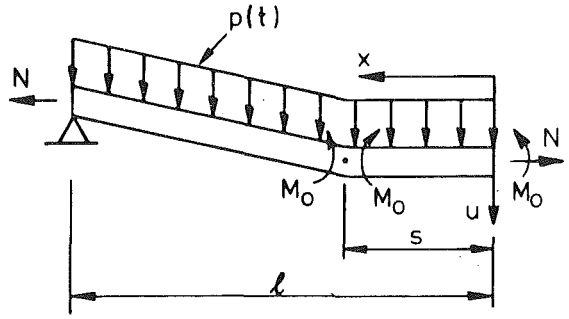

Fig. 2 Beam segment being analyzed

material so that the moment curvature relation is a step located at the origin.[2] The static collapse mode for this rigid-plastic beam with uniform loading is a single "plastic hinge" located at the center of the beam. The hinge separates two rigid segments that rotate about the end supports.

Let the yield moment be M_y[3]. As long as the pressure is less than the static collapse pressure, $p_y = 2M_y/L^2$, the bending moment throughout the beam is less than yield and no motion occurs. When $p > p_y$, motion begins. For convenience, time is measured from the instant this inequality is first satisfied. At $t = 0$, depending on the pressure, either one or two plastic hinges are formed. If the initial pressure $1 < p(0)/p_y \leqq 3$ there will be a hinge at the center of the beam as shown in Fig. 1(*a*). If $p(0)/p_y > 3$ the single hinge deformation mode results in a moment $M(x) > M_y$ for some $0 < x < L$. Consequently, to satisfy the moment-curvature relation, two symmetrically located hinges shown in Fig. 1(*b*) will occur. Between the hinges, $M(x)$ is constant. The double hinges move along the beam as a function of both applied impulse and time. As deformation proceeds, the axial force, N, remains constant along the length. (It is assumed there is only transverse motion of the beam.) Toward the end of the loading pulse, as pressure and beam momentum decrease, the hinges move toward the center and coalesce. When the motion remains flexural, the final stage is always the single hinge mode.

To analyze the motion of the beam, assume a kinematically admissible velocity field.

$$\begin{aligned} \dot{u}(x,t) &= \dot{U}(t) && x<s \\ \dot{u}(x,t) &= \dot{U}(t)\,[(L-x)/(L-s)] && x>s \end{aligned} \tag{1}$$

where $\dot{u}$ is the transverse velocity and $\dot{U}(t) = \dot{u}(0,t)$ is the center velocity. Symonds [3] has shown this velocity field is exact for monotonically decreasing pressures but only approximate otherwise. (With increasing pressures and outward moving hinges, $\dot{u}$ varies for $x < s$ although $\ddot{u}$ is constant in this region.) Using the assumed velocity field, the law of momentum for half the beam about the end results in

$$\rho\dot{U}[L^2-(L-s)^2/3] = LI/2 - 2\int_0^t (M+NU)\,dt \tag{2}$$

where $I = \int_0^t 2Lp(\tau)\,d\tau$ is the total impulse applied since $t = 0$, M is the bending moment at a plastic hinge, and N is the axial force.

For an axially loaded beam, hinge moment and axial force are related through the yield function. In a rigid-plastic beam with rectangular cross section, the yield condition is

$$1 = |M|/M_0 + (N/N_0)^2 \tag{3}$$

[2] Conditions for real structures wherein the rigid-plastic material idealization is useful have been discussed by Symonds [6].

[3] In a rigid-plastic beam, the axial force, N, reduces the yield moment, $My = Mo(1 - f(N/No))$ where Mo is yield moment (with no axial force), No is yield force (with no moment), and f is a function of cross-section shape.

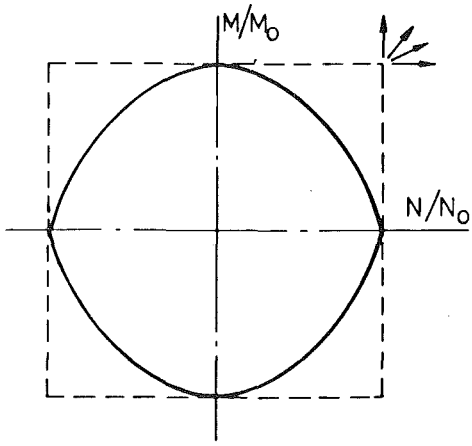

Fig. 3 Yield surface of rigid-plastic beam

The fully plastic hinge moment or axial force in a beam of rectangular cross section and unit width would be

$$M_0 = \sigma_0 H^2/4, \quad N_0 = \sigma_0 H \tag{4}$$

where σ_0 is the yield stress and H is the beam depth.

Hence, the yield condition is the pair of parabolas shown in Fig. 3. Axial force reduces the moment at a plastic hinge. This model of beam response is limited by the yield condition and "flow rule" to displacements $U/H \leqq \frac{1}{2}$ for a fixed-end constraint. For larger displacements with this boundary condition, the hinge moment is zero and a "plastic string" deformation mode prevails [7].

The hyperbolic yield condition is shown as a solid line in Fig. 3. Jones has shown that a square approximation to this yield condition (the dashed line) results in considerable analytic simplification [8]. This approximation generally has the effect of decoupling bending and axial forces in the yielding segments and makes these forces independent of deformation. With the prescribed loads, forces at a plastic hinge will be

$$M = M_o, \quad N \leqq N_o \tag{5}$$

The associated axial strain rate field will have $\dot{\epsilon} = 0$ for $N < N_o$ corresponding to an imposed axial force at beam ends that can move axially. When $N = N_o$, $\dot{\epsilon} > 0$ for $-L < x < L$ corresponding to beam ends fixed against axial displacement. In the case of $N = N_o$, Jones has demonstrated that circumscribing squares overestimate the forces and result in smaller beam displacements than the parabolic yield condition predicts. Likewise, inscribing squares underestimate the forces and result in larger beam displacements than the parabolic yield condition predicts. The difference between these bounds on the solution would be less for $N < N_o$. The square yield condition approximation has been used throughout the following analysis.

Evolution of Deformation

A solution for the initial low pressure, single hinge mode of deformation will be

$$U(t) = \int_0^t \phi \cos\omega(t-\tau)\,d\tau \tag{6a}$$

$$\dot{U}(t) = \phi - \omega\int_0^t \phi \sin\omega(t-\tau)\,d\tau, \quad t \leqq t_a \tag{6b}$$

where $\phi(t) = 3(LI(t) - 4M_o t)/4\rho L^2$ is the velocity resulting from impulse in excess of the minimum required to maintain static collapse with $N = 0$ and $\omega^2 = 3N/\rho L^2$ is a measure of the axial force. This single hinge mode of deformation continues until the applied pressure increases to an extent that the condition for a rigid segment $M(x) < M_o$

can only be satisfied with hinges located outward from the center. The time, t_a that double hinges first occur with any pressure pulse can be calculated from the condition $d^2M(0,t)/dx^2 = 0$ while $M(0,t) = M_o$,

$$0 = L^2 p(t_a) - 6M_0 - \frac{3\omega^2}{2}\int_0^{t_a} [LI(\tau) - 4M_0\tau]\cos\omega(t_a - \tau)\,d\tau \tag{7}$$

At the end of this initial, single hinge deformation mode, for $U_a = U(t_a)$, $P_a = p(t_a)$, the transition conditions are

$$U_a = (p_a L^2 - 6M_o)/6N \quad \text{for} \quad N > 0 \tag{8a}$$

$$\dot{U}_a = \phi_a - \omega\int_0^{t_a} \phi\sin\omega(t_a - \tau)\,d\tau \tag{8b}$$

For $t > t_a$, motion proceeds in the double hinge mode until a time, t_b, after the pressure has dropped when the hinges coalesce. During the double hinge phase of motion

$$U(t) = U_a + \dot{U}_a(t - t_a) + \int_{t_a}^{t} (I - I_a)/2\rho L\,d\tau \tag{9a}$$

$$\dot{U}(t) = \dot{U}_a + (I - I_a)/2\rho L, \quad t_a \leqq t \leqq t_b \tag{9b}$$

With the rigid-plastic material and the assumed velocity field, all deformation occurs at the plastic hinges although $M(x) = M_o$, $N(x) = N$ for $x < s$ [7]. The hinge position during $t_a < t < t_b$ can be calculated from equation (2).

$$s/L = 1 - [(3\dot{U} - 2(\dot{U}_a - \phi + \phi_a + \omega^2\int_{t_a}^{t} U\,d\tau))/\dot{U}]^{1/2} \tag{10}$$

By setting $s = 0$, the time, t_b, of hinge coalescence at the center is determined.

$$0 = (\dot{U}_b - \dot{U}_a) - (\phi_b - \phi_a) + \omega^2\int_{t_a}^{t_b} U\,d\tau \tag{11}$$

The final stage of deformation, $t_b \leqq t \leqq t_f$ is again in the single hinge deformation mode. Center velocity will be

$$\dot{U} = -\omega^2\int_0^{t} U\,d\tau + \phi - \gamma, \quad t_b \leqq t \leqq t_f \tag{12a}$$

$$\gamma = -\omega^2\int_0^{t_b} U\,d\tau + \phi_b - \dot{U}_b \tag{12b}$$

Recalling the expression for $\dot{U}_a$,

$$\gamma = \dot{U}_b - \dot{U}_a$$

is the change in central velocity during the double hinge deformation mode. Solving for the center displacement,

$$U = \int_0^{t} (\phi - \gamma)\cos\omega(t - \tau)\,d\tau, \quad t_b \leqq t \leqq t_f \tag{13}$$

The time when motion stops, t_f, is obtained from the condition that beam velocity goes to zero.

$$0 = \phi - \gamma - \omega\int_0^{t_f} (\phi - \gamma)\sin\omega(t_f - \tau)\,d\tau \tag{14}$$

This final time depends on the entire history of loading whereas, without an axial force, it is only dependent on the total applied impulse.

The final center displacement given by equation (13) with $t = t_f$ applies to general pulse shapes resulting from positive applied pressures. The only restriction on shape is to pulses that result in only a single period of time in the double hinge deformation mode. Pulse shapes that maximize this center displacement when a specified impulse is imparted to the beam can now be found.

Best Pulse Shape for Specified Impulse

An impulsive pressure causes the largest deformation of rigid-plastic beams from a specified applied impulse.

This statement follows from determining the impulse function that results in an extremal for the final center displacement $U(t_f) = \delta$.

$$\delta = \int_0^{t_f} (\phi - \gamma)\cos\omega(t_f - t)\,dt \tag{15}$$

Since the pressure applied to the beam is restricted to positive values, the applied impulse is a monotonically increasing function of time.

$$0 \leqq I(t) \leqq I_f \tag{16}$$

This inequality constraint augments the relation for the final beam center displacement. A technique for solving constrained optimization problems of this type, called the slack-variable method, was suggested by Valentine [9]. Defining a new constraint variable, V, where

$$V^2 = I(I_f - I) \geqq 0 \tag{17}$$

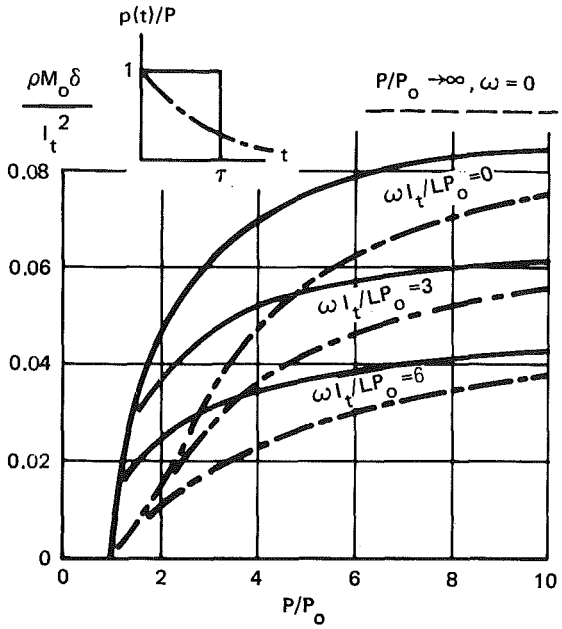

Fig. 4 Maximum beam deflection from rectangular and exponentially decaying pulses

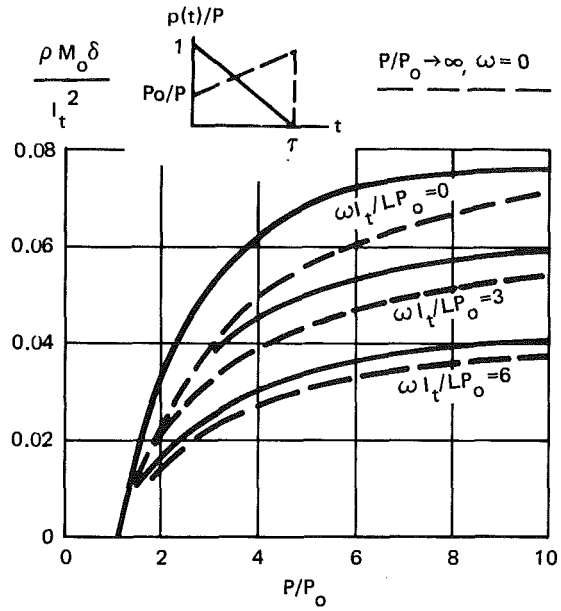

Fig. 5 Maximum beam deflection from triangular pressure pulses

an augmented functional can be formed from (15) and (17). The integrand of this functional is

$$F=(LI-4M_0t-4\rho L^2\gamma/3)\cos\omega(t_f-t)+\lambda[I(I_f-I)-V^2] \tag{18}$$

where $\lambda(t)$ is a Lagrange multiplier. In this formulation, dependence of the limit of integration, t_f, on the control function, $I(t)$, can be eliminated by a transformation on time, $t=\beta t_f$, so that the time variable has values in a fixed range $0 \leqq \beta \leqq 1$ [10]. After this transformation, the range, t_f, can be regarded as a parameter with the result

$$\delta=\int_0^1 F(I(\beta), V)\,d\beta \tag{19}$$

where

$$F=[LI-4M_0t_f\beta-4\rho L^2\gamma/3]t_f\cos[\omega t_f(1-\beta)] + \lambda(\beta)[I(I_f-I)-V^2] \tag{20}$$

Euler equations for variables I and V (which are necessary conditions for an extremal) are

$$0=Lt_f\cos\omega t_f(1-\beta)+\lambda(I_f-2I) \tag{21}$$

$$0=2\lambda V \tag{22}$$

To satisfy the second equation, either λ or V is zero. Since $\lambda = 0$ results in no admissible solutions for equation (21), these equations imply that the optimal solution is the equality constraint associated with equation (17); $I(t) = I_f$ for $t > 0$. Hence, a pressure applied to a Dirac delta function in time results in the largest deformation for a specified impulse.

Beam Response to Specific Pulse Shapes

To illustrate dependence of final deformation on pulse shape, beam response to rectangular, triangular, and exponentially decaying pressures pulses has been obtained. In these pulses, both maximum pressure, P, and characteristic pulse duration, τ, are variable. (Since the impulse is specified, higher pressure corresponds to shorter pulse duration.) Figures 4 and 5 show the final displacement nondimensionalized by total applied impulse, $I_t = \int_0^\infty 2Lp dt$, to be a monotonically increasing function of maximum pressure [4,5]. Thus, in agreement with the preceding proof, short high-pressure pulses are more effective than longer low-pressure pulses.

Pulses of equal duration and maximum pressure but differing shape still result in differing final deformation. Between two triangular pulses shown in Fig. 5, the more compact around $t = 0$ results in more permanent deformation. (In the terms of Youngdahl, the effective pressure $p_e = I^2/(2\int_0^t tp dt)$ is larger.) The difference in effect between the two pulse shapes is greatest for low pressures because then, most deformation occurs while the pulse is acting whereas with higher pressures, sufficient beam momentum is developed so deformation continues after pressure is removed.

The effect of axial force on the deformation enters through the parameter ω. Since deformation with axial force dissipates more energy than without, axial force reduces the deformation from a specified impulse.

Conclusions

An optimization technique based on the calculus of variations has been used to determine most effective pressure pulse shapes for deforming beams. Results from small deformation theory for optimal pulse shape to plastically deform a rigid-plastic beam have been extended to include axial forces that can arise from end restraint. Addition of a linear function of displacement to the energy dissipation during deformation represents addition of a constant axial force acting on the beam. This additional load does not change the pulse shape that maximizes deformation. With a specified impulse, an impulsive pressure causes the largest deformation.

The effect of the axial force is to initiate a double hinge deformation mode at a lower pressure and, for any pressure, to locate yield hinges closer to the ends than would occur without the axial force. The cumulative effect is to decrease both the total time of deformation and the final beam displacement in comparison with an unrestrained beam.

Acknowledgment

The results shown for particular pulses were calculated by Ross Heimdahl. His assistance was quite helpful. The reviewers comments were greatly appreciated.

References

1 Stronge, W. J., "Efficient Pulse Shapes to Plastically Deform Beams," ASME JOURNAL OF APPLIED MECHANICS, Vol. 41, 1974, pp. 604–608.

2 Youngdahl, C. K., "Correlation Parameters for Eliminating the Effect of Pulse Shape on Dynamic Plastic Deformation," ASME JOURNAL OF APPLIED MECHANICS, Vol. 37, 1970, pp. 744–753.

3 Symonds, P. S., "Dynamic Load Characteristics in Plastic Bending of Beams," ASME JOURNAL OF APPLIED MECHANICS, Vol. 20, 1953, pp. 505–515.

4 Youngdahl, C. K., "Influence of Pulse Shape on the Final Plastic Deformation of a Circular Plate," *International J. of Solids and Structures*, Vol. 7, No. 9, pp. 1127–1142.

5 Krajcinovic, D., "On Approximate Solutions for Rigid-Plastic Structures Subjected to Dynamic Loading," *International Journal of Nonlinear Mechanics*, Vol. 7, 1972, pp. 571–575.

6 Symonds, P. S., "Survey of Methods of Analysis for Plastic Deformation Under Dynamic Loading," Brown University Report, 1967.

7 Symonds, P. S., and Jones, N., "Impulsive Loading of Fully Clamped Beams With Finite Plastic Deformations and Strain-Rate Sensitivity," *International Journal of Mechanical Sciences*, Vol. 14, 1972, pp. 49–69.

8 Jones, N., "A Theoretical Study of the Dynamic Plastic Behaviour of Beams and Plates With Finite-Deflections," *International Journal of Solids and Structures*, Vol. 7, 1971, pp. 1007–1029.

9 Valentine, F. A., "The Problems of Lagrange With Differential Inequalities as Added Side Conditions," in: *Contributions to the Calculus of Variations, 1933–1937*, Dept. of Mathematics, University of Chicago, University of Chicago Press, 1937.

10 Hestenes, M. R., *Calculus of Variations and Optimal Control Theory*, Wiley, New York, 1966.

[4] This nondimensionalized displacement is not a monotonic function of pressure for all load parameters, e.g., $\omega\tau$.

[5] P is the maximum transverse pressure and $P_o = 2M_o/L^2$ is the static collapse pressure.

The Compressible Elastica on an Elastic Foundation

A. M. Nicolau
Steinman Boynton
Gronquist & Birdsall
50 Broad Street
New York, N.Y. 10004

J. V. Huddleston
Professor of Engineering and
Applied Sciences,
State University of New York
at Buffalo,
Buffalo, N.Y. 14260
Mem. ASME

The nonlinear two-point boundary-value problem describing the compressible elastica on an elastic foundation is formulated exactly within the context of the technical theory of bending as a set of eight first-order differential equations plus appropriate initial-point conditions and terminal-point conditions. The problem is then solved by a shooting method that determines two missing quantities. Graphs of load versus displacements and load versus the missing quantities are presented for various combinations of the system parameters. These results show that the presence of the elastic foundation enables the member to sustain unsymmetric (as opposed to antisymmetric) shapes in its postbuckled state, and that bifurcations from the straight configuration to symmetric buckled modes and bifurcations from symmetric buckled modes to unsymmetric ones depend on two system parameters—a compressibility measure and the foundation modulus. For a given compressibility and foundation stiffness, equilibrium paths are plotted globally, enabling unsymmetric paths to be extended from one bifurcation point to another, with the result that the complete postbuckling process can be traced. Finally, a discussion of path shapes as a function of foundation stiffness is given.

Introduction

The classical theory of buckling of a bar on an elastic foundation assumes small rotations of the cross sections and neglects axial strain (compressibility) at the axis of centroids (also called the "center line") of the bar. For a prismatic bar, it consists of a linear fourth-order differential equation, the eigenvalues of which are the buckling loads corresponding to the number of half waves into which the bar buckles. An energy solution of the problem with this same level of approximation is given by Timoshenko and Gere [1]. A recent paper by Kuznetsov and Johns [2] utilizes the classical fourth-order differential equation to study the initial postbuckling behavior of an incompressible beam-column on an elastic foundation.

Although the linear theory is adequate in many practical problems, it is incapable of dealing with the postbuckling range, where interesting events such as bifurcations can occur. In certain geophysical applications, where plates constrained by a surrounding matrix are subjected to large compressive forces, the compressibility may have a significant effect, and the postbuckling behavior may determine the final outcome of events.

A study of the effect of compressibility on the elastica without any transverse forces acting was published by Huddleston [3]. Two related papers by the same author followed—one on an incompressible prebuckled arch with transverse (vertical) loads acting [4], and one on a compressible prebuckled arch also with transverse loads acting [5]. The present paper, an extension of those investigations, contains a formulation of the theory for a compressible elastica with transverse forces acting, and deals specifically with the problem of the elastic foundation. The theory imposes no restrictions on the size of the displacements and hence makes possible an analysis of the entire postbuckling range. It combines a corrected moment-curvature relation with unrestricted equilibrium equations and furthermore accounts for the effect of center line stretching on distributed force intensities.

Contributed by the Applied Mechanics Division for presentation at the Winter Annual Meeting, Phoenix, Ariz., November 14–19, 1982, of THE AMERICAN SOCIETY OF MECHANICAL ENGINEERS.

Discussion on this paper should be addressed to the Editorial Department, ASME, United Engineering Center, 345 East 47th Street, New York, N.Y. 10017, and will be accepted until two months after final publication of the paper itself in the JOURNAL OF APPLIED MECHANICS. Manuscript received by ASME Applied Mechanics Division, March 1981; final revision, January, 1982. Paper No. 82-WA/APM-1.

Copies will be available until July, 1983.

The Boundary-Value Problem

Figure 1(*a*) shows a highly buckled member that is assumed to be constrained by a reactive foundation (symbolized by a spring). The x-axis is taken along the undeformed center line (axis of centroids) of the member, the coordinate x being used to locate a generic cross section at D that displaces to D' (with coordinate ξ) during the deformation. In some applications, the force P is an applied force producing a displacement δ. In others, δ is an impressed displacement causing a reactive P. The displacements at D' are u_x and u_y, the inclination is θ, and the distance along the center line is s. Figure 1(*b*) shows an elemental length ds (originally dx) located at D'. It carries a normal force N, a transverse shear Q, and a bending couple M, as well as distributed forces p_x and p_y per unit of original length.

The exact differential equations (exact within the technical theory of bending) are obtained by modifying the classical Bernoulli-Euler formula for axial strain, expressing the exact geometric relationships for the displaced element, and utilizing the differential equations of equilibrium derived for the deformed and displaced element, as was done in [4]. The complete system of equations is as follows:

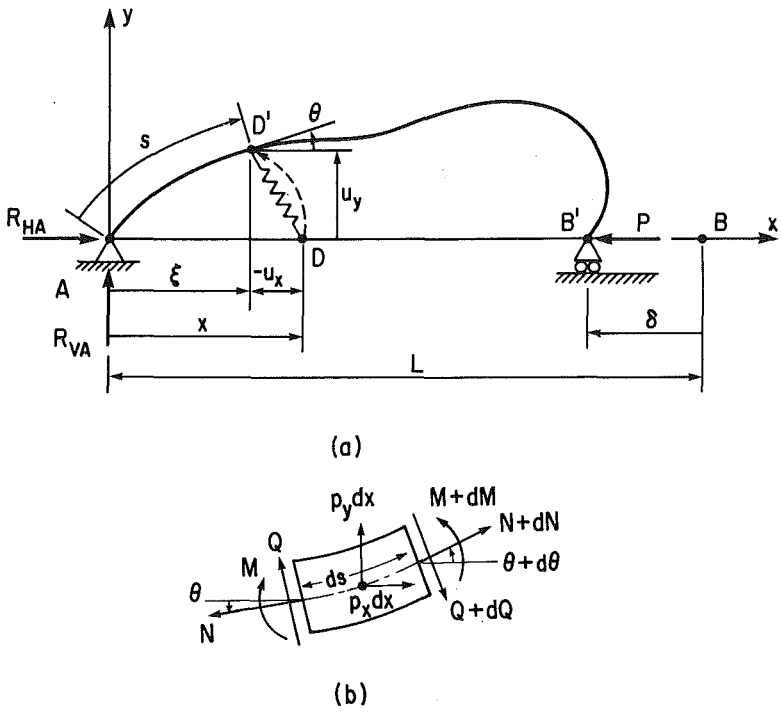

Fig. 1 The compressible elastica constrained by a reactive foundation. (*a*) Entire strut. (*b*) Elemental length *ds* at point *D'*.

$$
\left.
\begin{aligned}
&(1)\quad \frac{d\theta}{dx} = \frac{M}{EI} \quad , \\
&(2)\quad \frac{du_y}{dx} = \left(1+\frac{N}{EA}\right)\sin\theta \quad , \\
&(3)\quad \frac{d\xi}{dx} = \left(1+\frac{N}{EA}\right)\cos\theta \quad , \\
&(4)\quad \frac{ds}{dx} = 1+\frac{N}{EA} \quad , \\
&(5)\quad \frac{du_x}{dx} = \frac{d\xi}{dx} - 1 \quad , \\
&(6)\quad \frac{dN}{dx} = -Q\frac{d\theta}{dx} - p_x\cos\theta - p_y\sin\theta \quad , \\
&(7)\quad \frac{dQ}{dx} = N\frac{d\theta}{dx} - p_x\sin\theta + p_y\cos\theta \quad , \\
&(8)\quad \frac{dM}{dx} = Q\left(1+\frac{N}{EA}\right) \quad ,
\end{aligned}
\right\} \qquad (A)
$$

where E is Young's modulus, A is the cross-sectional area, and I is the moment of inertia (all three of these parameters may vary with x).

The foregoing is a general formulation which includes distributed forces with both x and y-components and allows for any type of foundation medium. In the problem considered in this paper, however, it is assumed that during deformation the foundation springs shift freely in the x-direction so as to remain vertical and exert only y-forces, but that they remain attached to the member at fixed points along the center line. In symbols,

$$
\left.
\begin{aligned}
p_x &= 0 \quad , \\
p_y &= -k_y u_y \quad , \\
R_{HA} &= P \quad ,
\end{aligned}
\right\} \qquad (B)
$$

where k_y is the foundation modulus in units of force per unit of displacement per unit of original length (k_y may still vary with x). It is obvious from equations (B) that the foundation is now assumed to be of continuously reacting type and not like a set of discrete springs. It is also assumed to be a linear foundation, although any other type of elastic response could be easily incorporated into the solution procedure. Finally, the foundation is assumed to be of the Winkler type (i.e., the reactive forces at adjacent points are not coupled as in a continuous medium).

The boundary conditions at A and B' can be stated as follows:

$$
\left.
\begin{aligned}
&(1)\quad \theta(0) = \theta_A && \theta(L) = ? \\
&(2)\quad u_y(0) = 0 && u_y(L) = 0 \\
&(3)\quad \xi(0) = 0 && \xi(L) = ? \\
&(4)\quad s(0) = 0 && s(L) = ? \\
&(5)\quad u_x(0) = 0 && u_x(L) = ? \\
&(6)\quad N(0) = -P\cos\theta_A - R_{VA}\sin\theta_A && N(L) = ? \\
&(7)\quad Q(0) = -P\sin\theta_A + R_{VA}\cos\theta_A && Q(L) = ? \\
&(8)\quad M(0) = 0 && M(L) = 0
\end{aligned}
\right\} \qquad (C)
$$

Method of Solution

The boundary-value problem formulated in the preceding section can be solved using a shooting method by noting that

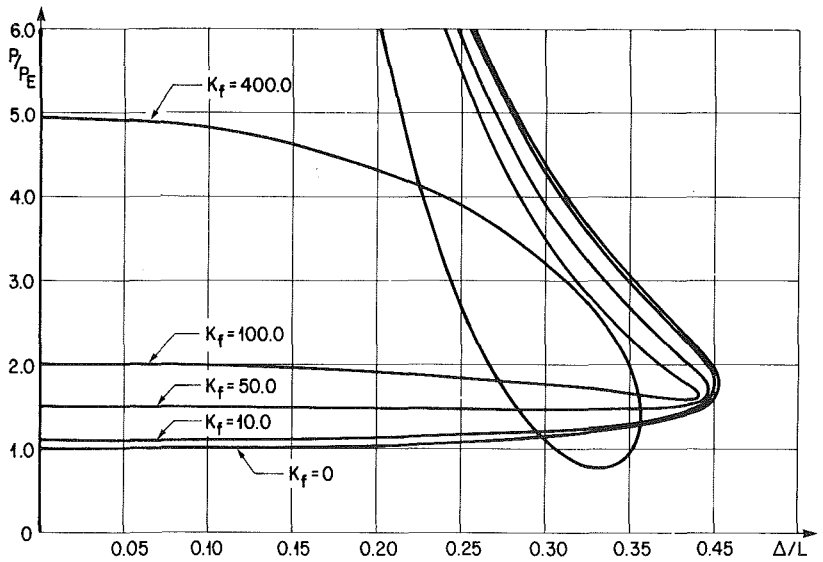

Fig. 2 P-Δ curves for $C = 0.001$ and various values of K_f

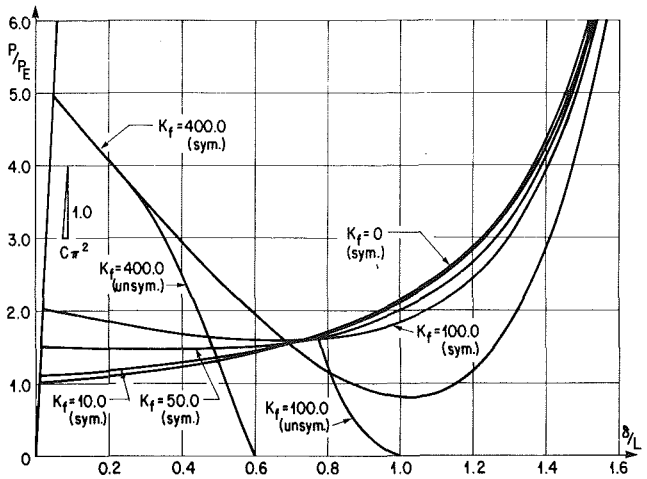

Fig. 3 P-δ curves for $C = 0.001$ and various values of K_f

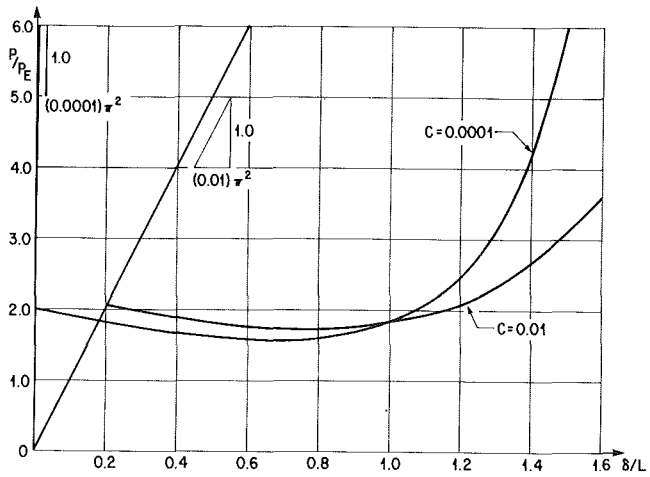

Fig. 4 P-δ curves for $K_f = 100.0$ and two values of C

there are two missing input quantities, θ_A and R_{VA} needed to create a complete set of initial conditions, and that there are two terminal conditions, on $u_y(L)$ and $M(L)$, which supply target values. All solutions in this paper have been obtained by using a two-level regula falsi to systematically adjust the two input quantities until the two output quantities are within prescribed tolerances of their target values, and the errors in the computed points have been made so small as to be totally indiscernible on the resulting graphs.

Results

The example chosen in this paper takes I, A, and k_y as constants in x (say I_0, A_0, and k_f, respectively). All variables are nondimensionalized in appropriate ways, and, in the process, two-dimensionless system parameters emerge: a compressibility measure defined by

$$C = \frac{I_0}{A_0 L^2} \quad , \qquad (D)$$

and a foundation modulus defined by

$$K_f = \frac{k_f L^4}{\mathrm{E} I_0} \quad . \qquad (E)$$

To nondimensionalize the load P, the Euler load defined by

$$P_E = \frac{\pi^2 \mathrm{E} I_0}{L^2} \quad , \qquad (F)$$

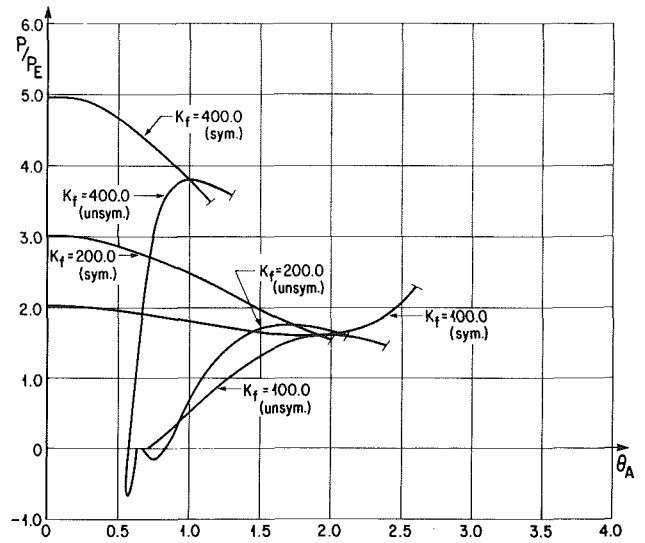

Fig. 5 P-θ_A curves for $C = 0.001$ and three values of K_f

is used. Finally, all displacement quantities with dimensions of length, such as the y-deflection Δ of the midpoint of the strut, are nondimensionalized by dividing by the original length L.

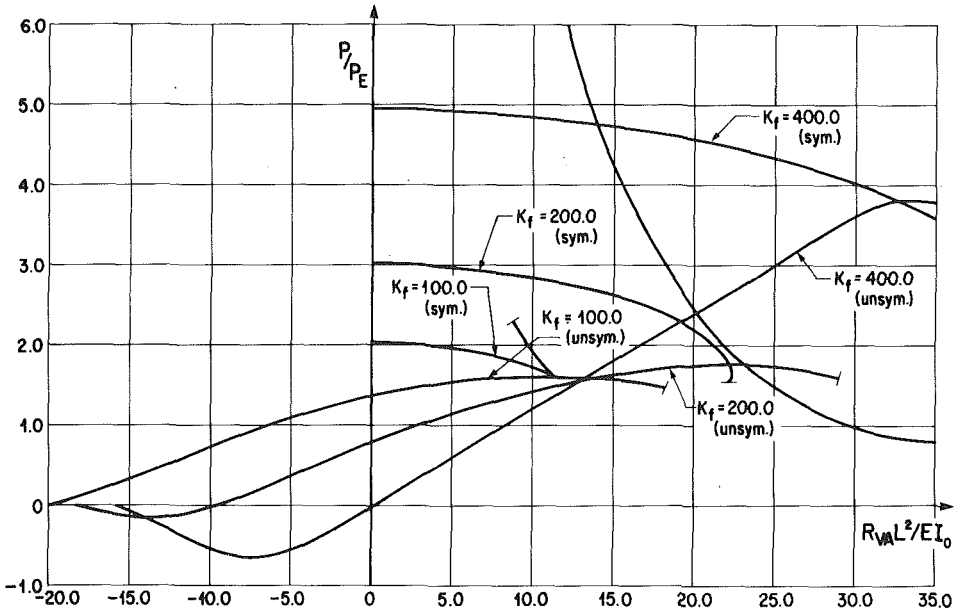

Fig. 6 P-R_{VA} curves for $C = 0.001$ and three values of K_f

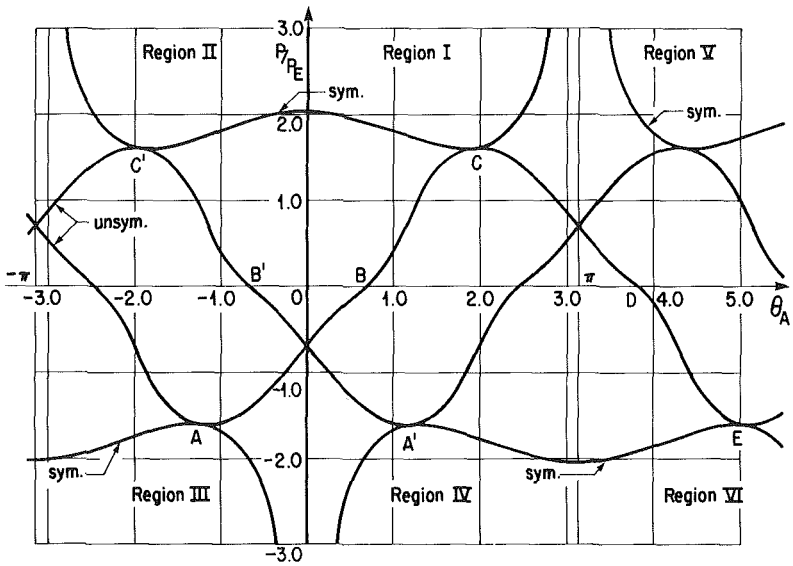

Fig. 7 Global P-θ_A curves for $C = 0.001$ and $K_f = 100.0$

Figure 2 shows curves of load versus midpoint displacement for $C = 0.001$ and various values of K_f. All of these curves represent buckled shapes with symmetry about the midspan. Figure 3 shows curves of load versus axial displacement for the same cases as Fig. 2. On it appear the bifurcation points where the deflected position leaves the straight position and where unsymmetric modes branch off from the symmetric modes for the cases $K_f = 100.0$ and $K_f = 400.0$.

The stability or instability of the various equilibrium states can be determined from Fig. 3, which shows the applied force plotted against its own displacement. Thus, the area under the curves represents the total energy added to and stored in the system (consisting of strut and foundation springs). The system will follow the path that minimizes this energy unless prevented from doing so by external constraints.

For example, under "testing machine" conditions, in which δ is impressed and P is measured, the straight member (identified by the straight line in Fig. 3) is a stable equilibrium state until the first bifurcation is reached, after which the straight configuration (corresponding to the continuation of the straight line) becomes unstable. Similarly, the symmetric deflected shape is a stable state until the next bifurcation point is reached, after which it also becomes unstable and the unsymmetric shape becomes the stable configuration.

Figure 4 shows curves of load versus axial displacement in the case of symmetric configurations for $K_f = 100.0$ and two values of C.

Figure 5 shows curves of load versus end rotation for $C = 0.001$ and three values of K_f, while Fig. 6 shows curves of load versus dimensionless end reaction for the same three cases. Values of θ_A and R_{VA} determined from these figures allow one to assemble a full set of initial conditions for an initial-value problem, which, when solved, produces a complete description of the member in its deformed state. From this solution, all quantities of interest can be determined.

The bifurcations mentioned previously appear again in Figs. 5 and 6, first from the straight configuration (vertical

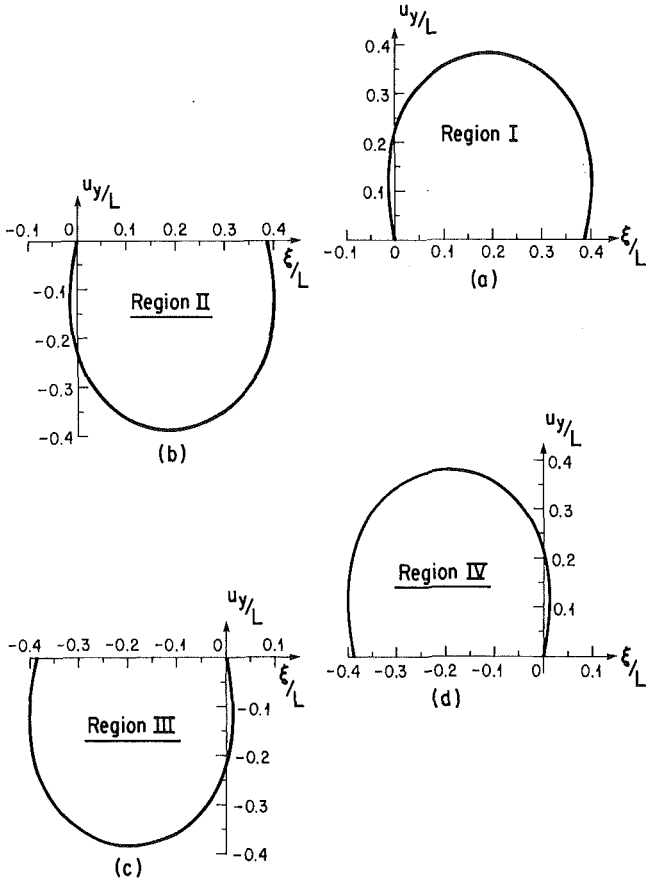

Fig. 8 Symmetrical deflection curves near postbuckling bifurcations for $C = 0.001$ and $K_f = 100.0$

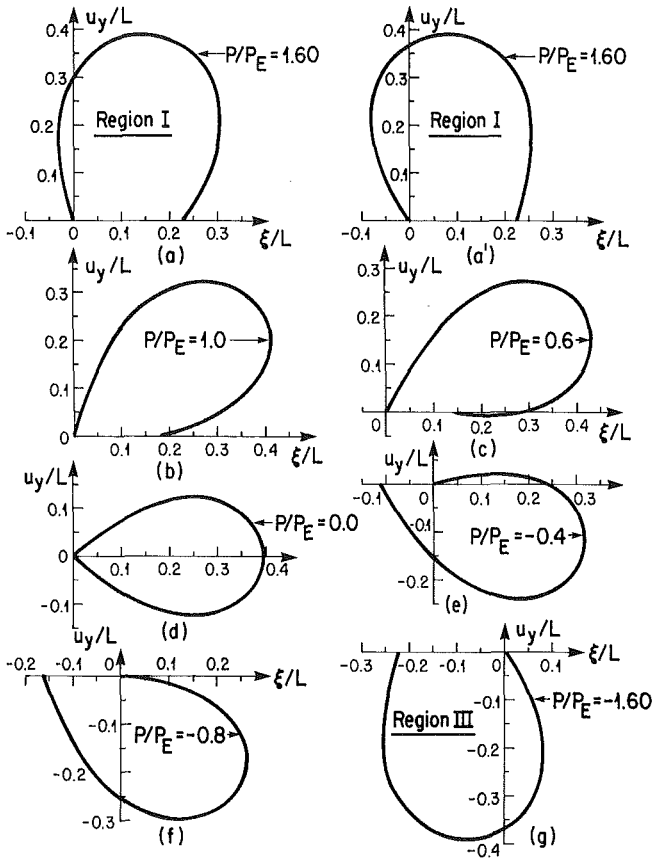

Fig. 9 Sequence of unsymmetrical deflection curves for $C = 0.001$ and $K_f = 100.0$

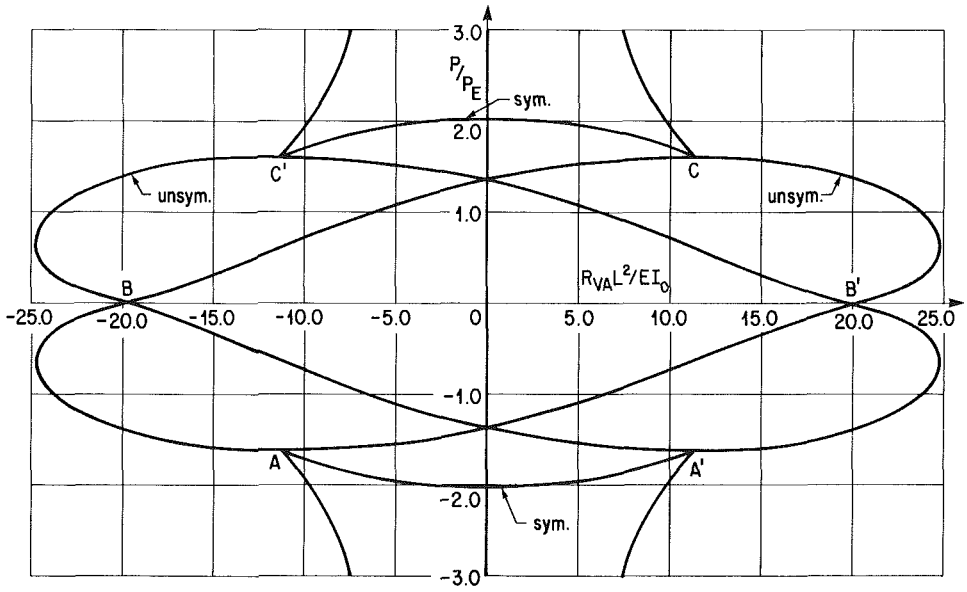

Fig. 10 Global P-R_{VA} curves for $C = 0.001$ and $K_f = 100.0$

axis) to a symmetric deflected shape (curves intersecting the vertical axis) and then from the path of symmetric shapes to a path of unsymmetric shapes. The curves for the unsymmetric mode are plotted to the point where the strut reaches a self-equilibrating configuration (force P zero) that is symmetric with respect to the x-axis in Fig. 1.

To understand how the member arrives at that state, and what happens subsequently, it is necessary to recognize that at each bifurcation point there are two alternative branches on the bifurcated curve that the system may follow. Furthermore, there are many possible configurations corresponding to reflections and inversions of the buckled strut about the horizontal and vertical axes, as well as to multiple values of θ_A obtained by adding and subtracting multiples of 2π. All of this is best illustrated by plotting the P-θ_A curves in a global fashion, as is done for the case of $C = 0.001$ and K_f

= 100.0 in Fig. 7. First consider a symmetric shape produced by a force P/P_E with absolute value 1.61 just before the system bifurcates to an unsymmetric path. Figure 8 shows four possible configurations corresponding to four regions correspondingly labeled in Fig. 7. Now suppose that the system is in Region I of Fig. 7 and reaches the bifurcation point *C*. Figures 9(*a*) and (*a'*) show two possible shapes after bifurcation, when the force has decreased to 1.60 along either of the unsymmetric paths *CBA* and *CDE* in Fig. 7. Thus, if the system follows path *CBA*, it will successively achieve the shapes illustrated in Figs. 9(*b*)-(*g*), all occurring while the force P is decreasing. The case in Fig. 9(*d*) is the self-equilibrating, symmetric configuration mentioned previously. After that, the force required for equilibrium becomes negative (i.e., acts toward the right on the moving end). If the force decreases still further, while the moving end continues toward the left, the system will achieve the shape of Fig. 8(*c*)

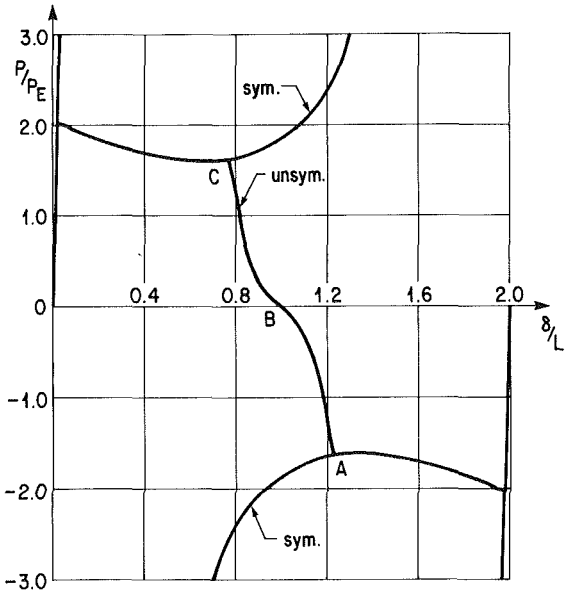

Fig. 11 Global P-δ curves for C = 0.001 and K_f = 100.0

when P/P_E is at -1.61. As in the classical treatment of the elastica, it is assumed here that the moving end of the member can pass the fixed end.

Figure 10 shows global curves for load versus end reaction for the same combination of parameters as the previous three figures, with the unsymmetric path discussed before again labeled *CBA*. Figure 11 shows global curves for P/P_E versus δ/L, where δ is the displacement of the moving end. Path *CBA* is also labeled in this figure. Under testing-machine conditions, in which δ is impressed and P measured, one can trace the entire buckling process from Fig. 11. The system starts at the origin. From there, the force builds up to just over 2.0 while the member remains straight, and then drops back to about 1.61 as the member buckles into a symmetric shape. It drops still further to zero and then becomes negative after the member has bifurcated to an unsymmetric shape. At about -1.61, the member again becomes symmetric and remains so while the force drops to just under -2.0. At that point, the member becomes straight again as the force increases rapidly to zero, leaving the member unstressed and with δ/L at exactly 2.0. The path segments followed in this sequence represent stable equilibrium states.

It is apparent from Figs. 5 and 6 that the curves for K_f = 100.0 cross the horizontal axis only once, while the curves for the other two cases cross it twice. This means that the other two experience a self-equilibrating configuration that is not symmeric about the x-axis before going through a negative-force phase and returning to zero force with a shape that is symmetric about the x-axis. Subsequently, they go through a positive loop before continuing on to the bifurcation point in the negative-force region.

To illuminate the differences in behavior, Figs. 12 and 13 show graphs of end angle and end reaction, respectively, plotted against K_f, for the condition $P = 0$ (C again = 0.001). For K_f below about 136, there is only one intersection with the zero-force axis. At about 136, there is a "bifurcation" to two intersections. At K_f = 349.80, the two intersection points with the θ_A-axis coincide.

A final comment about Figs. 12 and 13 is that at $K_f = 0$ there is no reactive foundation at all. In that case the self-equilibrating shape is the same as the closed-loop elastica without foundation rotated 90 deg.

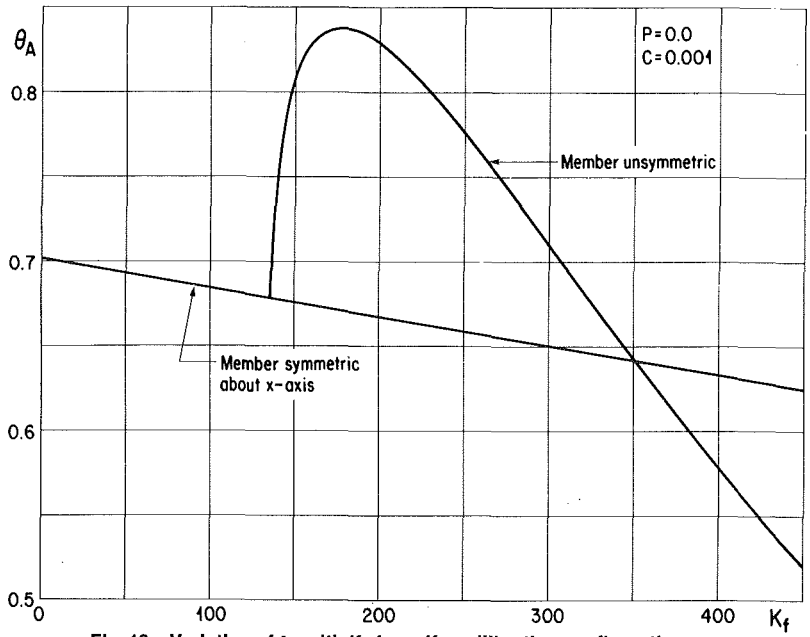

Fig. 12 Variation of θ_A with K_f for self-equilibrating configurations

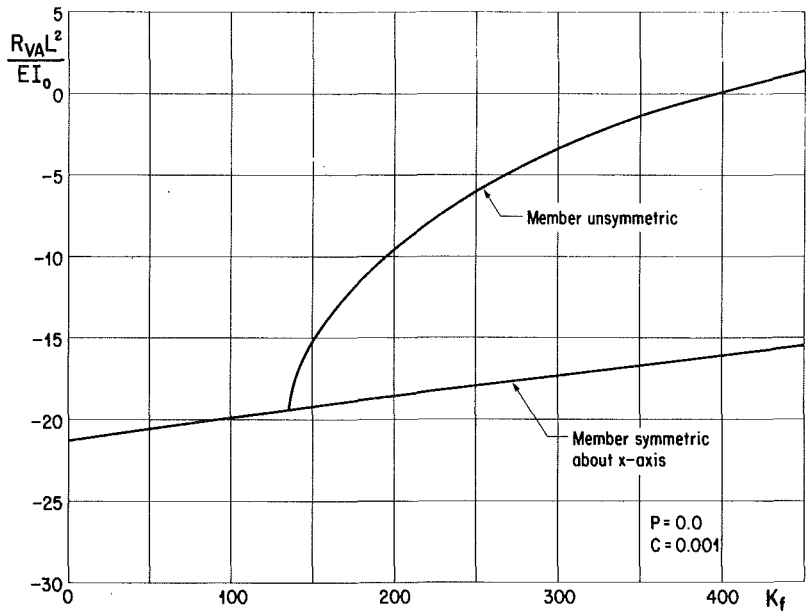

Fig. 13 Variation of R_{VA} with K_f for self-equilibrating configurations

References

1 Timoshenko, S. P., and Gere, J. M., *Theory of Elastic Stability*, second ed., Engineering Societies Monographs, 1961.

2 Kuznetsov, E. N., and Johns, T. G., "Post-Buckling Behavior of a Beam-Column on a Nonlinear Elastic Foundation with a Gap," *Proceedings of the Symposium on Computational Methods in Nonlinear Structural and Solid Mechanics*, Washington, D.C., Oct. 1980, pp. 165–173.

3 Huddleston, J. V., "Effect of Axial Strain on Buckling and Postbuckling Behavior of Elastic Columns," *Developments in Theoretical and Applied Mechanics*, Vol. 4, Proceedings of the Fourth Southeastern Conference on Theoretical and Applied Mechanics, New Orleans, La., Feb. 1968, pp. 263–273.

4 Huddleston, J. V., "Dead-Load Effects on a Proposed Very-Large-Size Dome," *Shell Structures and Climatic Influences*, Proceedings of the Symposium held by I.A.S.S. in Calgary, Alberta, Canada, July 1972, pp. 395–404.

5 Huddleston, J. V., "Effect of Axial Compressibility on the Snap-Through Buckling of Prestressed Arches," *Teknologi* (Engineering Journal of University of Technology of Malaysia), Vol. 1, No. 1, April 1977, pp. 75–85.

T. Yabuta
Staff Engineer.

N. Yoshizawa
Engineer.

N. Kojima
Deputy Director.

Outside Plant Development Division,
Ibaraki Electrical Communication Laboratory,
Nippon Telegraph and Telephone Public Corporation,
Tokai, Ibaraki-ken, 319-11, Japan

Cable Kink Analysis: Cable Loop Stability Under Tension

Submarine cable kinking is a continuing design problem. Cable kink occurs when a cable loop forms due to torsion and tension action, and then tightens under subsequent tension increase. This paper describes cable loop stability under the subsequent tension and clarifies the kinking mechanism. Results show that kinking occurrence mainly depends on residual twist in the cable loop.

1 Introduction

Cable kinking is well recognized as a significant problem in the use of cables for oceanic applications. In oceanic applications, a cable loop occurs because of torsional stress due to the helical strength member when tension on the cable is temporarily reduced. When the cable is retensioned, the loop will decrease in diameter, will kink, and may cause the cable to be damaged.

Little investigation has been reported on this cable kinking phenomenon, and the relation between cable mechanical properties and cable kinking has never been clarified completely. Previous analyses [1-4] using force equilibrium were reported from a viewpoint that the cable loop would kink or reopen. These results only show the tendency that cable kinking seldom occurs when the cable is easy to twist and hard to bend. However, these analyses could not clarify the unstable phenomenon of cable kinking completely. Ross [5] investigated cable loop formation due to torsional stress from the energy transfer viewpoint and clarifies the condition of cable loop formation.

The present paper shows that the cable loop formed due to torsional stress could then tighten or reopen under the subsequent energy transfer. Results are obtained by a principle of minimum potential energy to determine cable loop stability. Results show that kinking occurrence mainly depends on residual twist in the cable loop.

2 Cable Kinking Phenomenon

Figure 1 shows a kinking phenomenon diagram. As the submarine cable strength member employs helical stranded wires, torsional strain is induced under tension. Then, if the tensile load is decreased, perhaps due to wave motion, a reversed torsional load is induced which also can cause a loop,

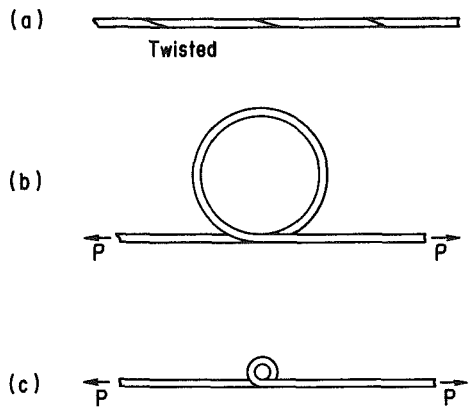

Fig. 1 Kinking phenomenon diagram

as shown in Fig. 1(*b*). This phenomenon is instability from transfer of torsional strain energy to bending strain energy, because a cable loop absorbs one twist of the torsion during formation. After cable loop formation, as shown in Fig. 1(*b*), the loop will decrease in diameter and kink, shown in Fig. 1(*c*), if the loop is a stable loop when the cable is retensioned. However, when bending strain energy increase and the cable loop becomes unstable in the process of decreasing in diameter, the cable loop will reopen and strain energy transfers back from bending strain energy to torsional strain energy.

This paper investigates cable loop stability in the process of decreasing in diameter, going from Fig. 1(*b*) to Fig. 1(*c*), and clarifies the cable reopening condition that the cable loop is unstable in the process of decreasing in diameter.

3 Cable Kink Analysis

To simplify the problem, cable kink analysis uses the following assumptions:

(1) Cable weight is neglected.

(2) Cable elongation under tension is neglected.

Contributed by the Applied Mechanics Division for publication in the JOURNAL OF APPLIED MECHANICS.

Discussion on this paper should be addressed to the Editorial Department, ASME, United Engineering Center, 345 East 47th Street, New York, N.Y. 10017, and will be accepted until two months after final publication of the paper itself in the JOURNAL OF APPLIED MECHANICS. Manuscript received by ASME Applied Mechanics Division, June, 1981; final revision, January, 1982.

(3) Cable deformation is exactly elastic.

The coordinates used for the analysis are shown in Fig. 2. Tension P applies parallel to the x axis ($\theta=0$). The cable loop crossing point is at $x=0$, $\theta=-\pi/2$. It is assumed that the cable loop transfers from the condition, shown in Fig. 2(a), which only stores bending strain energy to the condition, shown in Fig. 2(b), whose part of bending strain energy transfers to torsional strain energy when the crossing point of the cable loop shifts a little in the z direction.

Cable loop shape is assumed to be as follows.

$$X=(x,y,z)=(r\cos\theta, r\sin\theta, z) \tag{1}$$

Curvature κ and torsion ϕ are obtained using (1) as follows [6].

$$\kappa^2=[\{r^2+(r')^2+(z')^2\}\{(r'')^2+4(r')^2+r^2 -2rr''+(z'')^2\}-(r'r''+rr'+z'z'')^2]\cdot\{r^2+(r')^2+(z')^2\}^{-3} \tag{2}$$

$$\phi=[z'\{r^2-4rr''+3(r'')^2-2r'r''+6(r')^2\}+z''(4rr'+rr'''-3rr'')+z'''\{r^2+rr''+2(r')^2\}]\cdot[r^4+4r^2(r')^2-2r^3r''+r^2(r')^2+r^2\{(z'')^2+(z')^2\}]^{-1} \tag{3}$$

where $(\,)'$ and $(\,)''$ indicate $d/d\theta\,(\,)$ and $d^2/d\theta^2(\,)$, respectively. Twist of the cable loop is obtained as follows [7].

$$\tau=\tau_0+\phi \tag{4}$$

where τ_0 indicates residual twist which the cable loop cannot absorb when it forms from the twisted cable straight condition shown in Fig. 1(a) in the fixed end condition.

Strain energy in the cable loop can be calculated using equations (2) and (4). Banding strain energy V_B and torsional strain energy V_T in the cable loop are defined as follows.

$$V_B=\int_0^L \frac{1}{2}EI\kappa^2\,ds \tag{5}$$

$$V_T=\int_0^L \frac{1}{2}GJ\tau^2\,ds \tag{6}$$

where EI is bending rigidity and GJ is torsion rigidity.

Displacement ΔL of the cable end from the condition shown in Fig. 1(a) to the condition shown in Fig. 1(b) is defined as follows, if ds_x is the x-direction vector of the segment vector ds of the line:

$$\Delta L=L_0-L,\quad L_0=\left|\int_0^L ds_x\right|. \tag{7}$$

Work W done by the external force P is obtained as follows, assuming cable tension P is constant during the loop formation:

$$W=P\Delta L \tag{8}$$

Potential energy E of the cable loop, shown in Fig. 2(b), due to general deformation by both bending and torsion, is given by

$$E=V_B+V_T-W \tag{9}$$

Cable loop stability is investigated using this potential energy E.

Cable loop curves are assumed to have the following forms:

$$r=\sum_{i=1}^{n} a_i f_i(\theta),\quad Z=\sum_{j=1}^{m} b_j g_j(\theta) \tag{10}$$

where $f_i(\theta)$, $g_j(\theta)$ are functions to be specified. Cable loop equilibrium is obtained by the following simultaneous equations using (9).

$$\frac{\partial E}{\partial a_i}=0,\quad \frac{\partial E}{\partial b_j}=0 \tag{11}$$

where $i=1,2,\ldots,n$ $j=1,1,\ldots,m$.

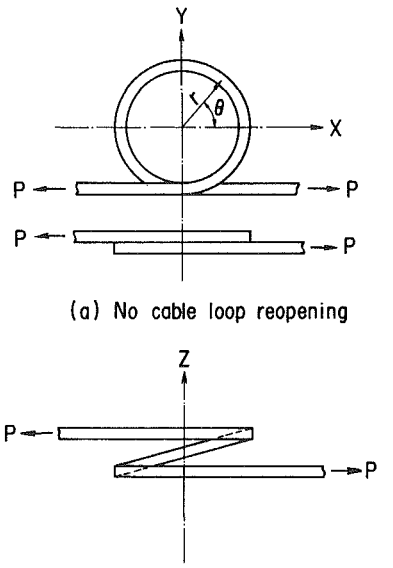

Fig. 2 Analysis model

Equilibrium stability ($X=X_0$) determined from (11) is investigated by second differential calculus for potential energy under the criterion

i $X=X_0$ is in stable equilibrium, if $F_{X=X_0}>0$
ii $X=X_0$ is in neutral equilibrium, if $F_{X=X_0}=0$
iii $X=X_0$ is in unstable equilibrium, if $F_{X=X_0}<0$

where F is the determinant

$$F=\left|\frac{\partial^2 E}{\partial a_i \partial b_j}\right| \tag{12}$$

4 Approximate Numerical Results Using Helix Assumption

Although equation (10) is considered as the general deformation of the cable loop, only the first term in (10) is considered in order to simplify the problem for the cable shape shown in Fig. 2. Therefore, the following displacement is assumed:

$$r=R\begin{cases} z=R\delta\theta, & 0\le\theta\le\pi \\ z=0, & -\dfrac{\pi}{2}\le\theta\le 0 \\ z=R\delta\pi, & \pi\le\theta\le\dfrac{3}{2}\pi \end{cases} \tag{13}$$

where displacement in the z direction is assumed to be very small for simplicity, which is $0\le\delta\ll 1$. This assumption applies just when the cable loop begins to reopen. Outside this cable loop region, the cable shape is assumed to be straight for simplicity.

The curvature κ is obtained from equations (2) and (13) as

$$\kappa^2=\frac{1}{R^2}\,\frac{1}{(1+\delta^2)^2},\quad 0<\theta<\pi$$

$$\kappa^2=\frac{1}{R^2},\quad -\frac{\pi}{2}\le\theta<0,\ \pi<\theta\le\frac{3}{2}\pi \tag{14}$$

The torsion ϕ, which is induced by cable loop reopening, is obtained from (3) and (13) as

$$\phi=\frac{1}{R}\cdot\frac{\delta}{1+\delta^2},\quad 0\le\theta\le\pi$$

$$\phi=0,\quad \theta<0,\quad \pi<\theta \tag{15}$$

The differential is length ds, obtained as follows:

$$ds = d\theta\left[R^2 + \left(\frac{dz}{d\theta}\right)^2\right]^{1/2} = \begin{cases} R(1+\delta^2)^{1/2}\,d\theta, & 0 \le \theta \le \pi \\ Rd\theta, & \theta < 0, \pi < \theta \end{cases} \quad (16)$$

Using equations (5), (6), and (14)–(16) the bending strain energy V_B and torsional strain energy V_T are obtained as follows, considering that curvature in the straight cable ($\theta < -\pi/2$, $3/2\pi < \theta$) is zero and that cable torsion of the region ($\theta < 0$, $\pi < \theta$) is only τ_0:

$$V_B = \frac{1}{2}\frac{\pi EI}{R}(1+\delta^2)^{-3/2} + \frac{1}{2}\frac{\pi EI}{R} \quad (17)$$

$$V_T = \frac{1}{2}\pi GJR\left(\frac{1}{R}\frac{\delta}{1+\delta^2} + \tau_0\right)^2 (1+\delta^2)^{1/2} + \frac{1}{2}GJ\tau_0{}^2 L_1 \quad (18)$$

where

$$L_1 = L - \int_0^{\pi}(1+\delta^2)^{1/2} R\,d\theta$$

The work W is considered to be divided into W_1 and W_2. W_1 indicates the work during cable loop formation from the condition shown in Fig. 1(*a*) to the condition shown in Fig. 1(*b*). W_2 indicates the work during a small cable reopening from the condition shown in Fig. 2(*a*) to the condition shown in Fig. 2(*b*). W_1 is obtained as follows:

$$W_1 = P\left(-\int_0^{2\pi} R\,d\theta\right) = -2\Pi RP \quad (19)$$

The angle β of segment motion in the z direction during a small loop reopening is given as follows, assuming β to be very small:

$$\beta = \frac{dz}{rd\theta} \quad (20)$$

W_2 is obtained as follows from (20), considering segment displacement in the x direction:

$$W_2 = P\int_0^{\pi}(\cos\beta - 1)\cos\left(\frac{\pi}{2} + \theta\right) ds$$

$$= P\int_0^{\pi}\frac{1}{2}\left(\frac{dz}{rd\theta}\right)^2 \sin\theta\, ds = PR\delta^2(1+\delta^2)^{1/2} \quad (21)$$

The potential energy E is defined as follows, using (17)–(19) and (21), and considering small terms up to the third order:

$$E = \frac{\pi EI}{R}\left(1 - \frac{3}{4}\delta^2\right) + \frac{\pi GJ}{2R}\delta^2 + \frac{1}{2}\pi GJ\tau_0\delta(1-\delta^2)$$

$$+ \frac{1}{2}GJ\tau_0{}^2 L + 2\pi PR - PR\delta^2 \quad (22)$$

From (19), equilibrium of the cable loop is obtained from the following simultaneous equation:

$$\frac{\partial E}{\partial \delta} = -\frac{3\pi EI}{2R}\delta + \frac{\pi GJ\tau_0}{R}\delta + \frac{\pi GJ\tau_0}{2}\left(1 - \frac{3}{2}\delta^2\right) - 2PR\delta = 0 \quad (23)$$

$$\frac{\partial E}{\partial R} = -\frac{\pi EI}{R^2}\left(1 - \frac{3}{4}\delta^2\right) - \frac{\pi GJ}{2R^2}\delta^2 + 2\pi P = 0 \quad (24)$$

Stability of the equilibrium determined by (23) and (24) is investigated using (12).

$$F = \begin{vmatrix} \dfrac{\partial^2 E}{\partial \delta^2} & \dfrac{\partial^2 E}{\partial \delta \partial R} \\ \dfrac{\partial^2 E}{\partial R \partial \delta} & \dfrac{\partial^2 E}{\partial R^2} \end{vmatrix} \quad (25)$$

Equilibrium stability depends on the sign of F as noted at (12).

4.1 Results When $\tau_0 = 0$. In this case, the cable loop does not have residual twist. Equilibrium is determined as follows, using (23) and (24).

$$\delta = 0 \quad R = \sqrt{EI/2P} \quad (26)$$

Then, at equilibrium, F is given by

$$F = \frac{\pi^2 GJR^2}{2EI}\left\{1 - \left(\frac{3}{2} + \frac{1}{\pi}\right)\frac{EI}{GJ}\right\} \quad (27)$$

and we have the following cases:

i if $F > 0$, that is $\dfrac{EI}{GJ} < \dfrac{2\pi}{3\pi+2}$

then $\delta = 0$ is a stable equilibrium. Therefore, the cable loop shown in Fig. 2(*a*) is stable and a kink will occur.

ii if $F = 0$, that is $\dfrac{EI}{GJ} = \dfrac{2\pi}{3\pi+2}$

then $\delta = 0$ is a neutral equilibrium.

iii if $F < 0$, that is $\dfrac{EI}{GJ} > \dfrac{2\pi}{3\pi+2}$

then $\delta = 0$ is an unstable equilibrium and the cable loop is not stable. The cable loop deformation transfers to another stable equilibrium, which is determined by solving the problem exactly without the assumptions of equation (22). In this case, the loop will not kink and reopen, since the stable equilibrium may be $\delta > 0$, because equilibrium does not exist ($\delta < 0$).

Equation (27) indicates that kinking is difficult when bending rigidity (EI) is large and torsion rigidity (GJ) is small. This result agrees with results in references [1–4].

The following relation is obtained [8] when the cable is a homogeneous elastic body:

$$G = \frac{E}{2(1+\nu)} \quad (28)$$

For a circular cable of diameter d, I and J are defined as:

$$I = \pi d^4/64 \quad J = \pi d^4/32 \quad (29)$$

Introducing (28) and (29) into (27), $F < 0$ is obtained when Poisson's ratio ν is assumed to be 0.3. This result indicates that a homogeneous elastic cable will not kink without initial twist.

4.2 Results When $\tau_0 > 0$. In this case, the cable loop has residual twist τ_0. Equilibrium is determined by solving the simultaneous equations defined by (23) and (24). However, if the second small terms (δ^2) is neglected in (23) and (24) to simplify the problem, then

$$R_0 = \sqrt{EI/2P}\ ,\delta_0 = \frac{-\dfrac{\pi}{2}GJ\tau_0}{\left(\dfrac{\pi GJ}{R_0} - \dfrac{3\pi EI}{2R_0} - 2PR_0\right)} \quad (30)$$

Using (28) and (29), the following relation is obtained is cable is a homogeneous elastic body:

$$\frac{\pi GJ}{R_0} - \frac{3\pi EI}{2R_0} - 2PR_0 < 0 \quad (31)$$

Equation (31) indicates that the equilibrium $\delta = \delta_0$ determined by (30) has δ_0 positive. Equilibrium stability at $\delta = \delta_0$ is investigated using (25) rewritten as follows, considering (30) and neglecting the second small term (δ_0^2):

$$(F)\ \delta = \delta_0 = \frac{2\pi EI}{R^3{}_0}\left(-\frac{3\pi EI}{2R_0} + \frac{\pi GJ}{R_0} - \frac{3}{2}\pi GJ\tau_0\delta_0 - 2PR_0\right)$$
$$R = R_0$$
$$< 0 \quad (32)$$

This result indicates that equilibrium at $\delta = \delta_0$ is unstable. Therefore, there is no stable equilibrium in $\delta > 0$ in the

neighborhood of $\delta=0$, when the cable loop has residual twist. However, experiments show that a cable loop has stable equilibrium in the neighborhood of $\delta=0$ when accompanied by cable loop rotation as shown in Fig. 3.

Cable loop rotation is investigated using potential energy. When the rotation is Φ, work W_2 done by external force is defined by

$$W_2 = -Pd\Phi \tag{33}$$

It is assumed that cable torsion ϕ caused by rotation angle Φ occurs equally throughout the cable loop, i.e.,

$$\phi = \frac{\Phi}{2\pi R} \tag{34}$$

Using (34), torsional strain energy V_T is obtained as follows.

$$V_T = \int_0^{2\pi} \frac{1}{2} GJ(\tau_0 - \phi)^2 R d\theta + \frac{1}{2} GJ\tau_0^2 L_2 \tag{35}$$

where

$$L_2 = L - \int_0^{2\pi} R d\theta$$

Bending strain energy V_B is defined by equation (14) as

$$V_B = \frac{\pi EI}{R} \tag{36}$$

Potential energy E is determined as follows, using (19), (33), (35), and (36):

$$E = V_B + V_T - W_1 - W_2$$
$$= \frac{\pi EI}{R} + \frac{GJ\Phi^2}{4\pi R} - GJ\Phi\tau_0 + \frac{1}{2} GJ\tau_0^2 L + 2\pi RP + Pd\Phi \tag{37}$$

Equilibrium is obtained as follows, using equations (11) and (37):

$$\Phi_0 = \frac{2\pi R_0}{GJ}(GJ\tau_0 - Pd) \tag{38}$$

$$R_0 = \left[\frac{EI}{2P - (GJ\tau_0 - Pd)^2/GJ}\right]^{1/2} \tag{39}$$

Stability of this equilibrium was investigated, using (12)

$$F_{\Phi=\Phi_0, R=R_0} = \frac{GJ \cdot EI}{R_0^4} > 0 \tag{40}$$

Equation (40) indicates that the equilibrium determined by equations (38) and (39) is stable. Figure 4 shows an outline of the potential energy change when $GJ\tau_0 > Pd$. In this case, when the cable loop has initial twist, Fig. 4 shows that stable equilibrium exists where the cable loop rotates at angle Φ_0. Figure 4 also shows that the equilibrium at $\delta=\delta_0>0$ is unstable and the cable loop would not reopen from $\delta=0$. Equation (38) indicates that the rotation Φ_0 decreases with increasing external force P. As a result, the sign of rotation Φ becomes minus, when $GT\tau_0 < Pd$. In this case, the potential energy change outline is shown in Fig. 5. This figure shows that stable equilibrium exists at $\delta=0$ between the cable loop rotating region and the cable loop reopening region. These results indicate that cable loop would kink when the cable loop has residual twist since there is no stable equilibrium for $\delta>0$ in the neighborhood of $\delta=0$.

4.3 Initial Displacement Effect. Numerical results show that the cable loop reopens and would not kink if the cable loop completely absorbs the cable twist, which indicates that the cable loop has no residual twist, if the cable is a homogeneous elastic body. However, if the cable loop cannot absorb the cable twist completely, which indicates that cable loop has residual twist, then the equilibrium shown in Fig. 3(*a*) is stable and the cable would kink. However, some experiments, which are shown in Fig. 7, show that cable loop

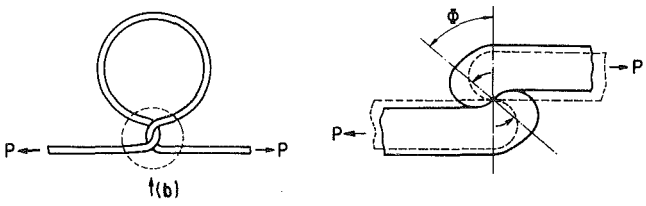

(a) Rotating phenomenon (b) Rotating phenomenon magnification from the bottom side

Fig. 3 Cable loop rotation

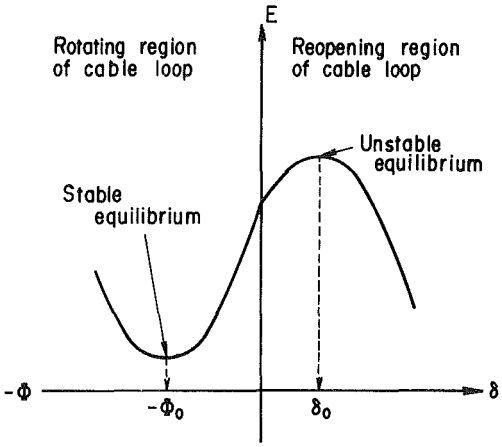

Fig. 4 Schematic figure of potential energy change

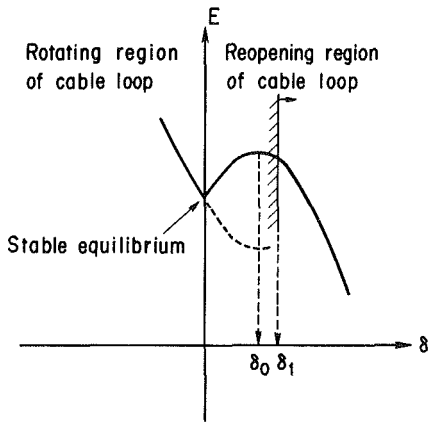

Fig. 5 Schematic figure of potential energy change

reopens, even if cable loop has residual twist, when the cable loop diameter decreases due to external force. This is opposed to numerical results. The reason can be explained by the following analysis.

Even if cable loop does not reopen, initial displacement in the z direction exists due to cable diameter d. This initial deformation δ_1 is determined by (13) as

$$\delta_1 = d/\pi R \tag{41}$$

Therefore, when the cable loop forms as shown in Fig. 1(*b*), there exists a δ value, determined by (41), which is not actually $\delta=0$. Equation (41) shows that δ_1 increases and approaches unstable equilibrium at $\delta=\delta_0$, when the cable loop radius decreases due to external force. When δ_1 becomes larger than δ_0, the equilibrium transfers to another equilibrium state, which exists in the $\delta>\delta_0$ region, and the cable loop would reopen, which is shown in Fig. 5. The condition that the cable loop reopens is obtained by the condition $\delta_0 < \delta_1$.

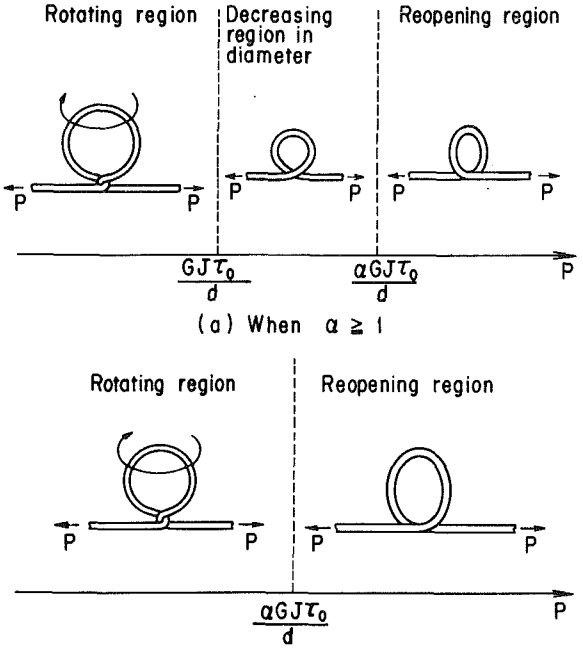

Fig. 6 Cable loop displacement modes

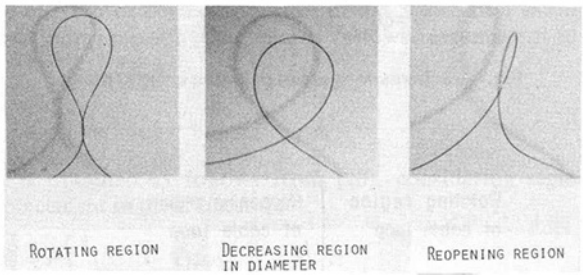

Fig. 7 Experimental results for displacement modes

$$\frac{d}{\pi R_0} \geq \frac{-\frac{\pi}{2} GJ\tau_0}{\left(\frac{\pi GJ}{R_0} - \frac{3\pi EI}{2R_0} - 2PR_0\right)} \tag{42}$$

Equation (42) is rewritten, using (30), as follows.

$$R_0 < \left[\frac{2}{\pi}\left\{\left(\frac{1}{\pi}+\frac{3}{2}\right)\frac{EI}{GJ} - 1\right\}\frac{d}{\tau_0}\right]^{1/2} \tag{43}$$

These result shows that the cable loop reopens when the cable loop radius satisfies the condition determined by (43) under the tension if the cable loop has residual twist.

New parameters are defined by the following equation:

$$\alpha = \frac{\frac{\pi}{4}}{\left(\frac{1}{\pi}+\frac{3}{2}\right) - \frac{GJ}{EI}}, \quad P_0 = GJ\tau_0/d \tag{44}$$

Then cable loop stability is divided into three regions, when $\alpha \geqq 1$.

a When $P < P_0$, the cable loop rotating deformation, as shown in Fig. 3(*a*), is stable. In this case, the rotation angle Φ decreases, according to the increase in external force.

b When $P_0 < P < \alpha P_0$, the condition ($\Phi = 0$), shown in Fig. 1(*a*), is stable. The cable loop diameter decreases according to the increase in external force.

c When $P > \alpha P_0$, the cable loop reopens.

These displacement modes are shown in Fig. 6(*a*).

Cable loop stability is divided into two regions, when $\alpha < 1$.

a When $P < \alpha P_0$, cable loop rotating deformation is stable.

b When $P > \alpha P_0$, cable loop reopens.

These displacement modes are shown in Fig. 6(*b*). If the cable is a homogeneous elastic body, then $\alpha < 1$ is obtained by (28) and (29) and results in the second case apply.

This investigation shows that the cable loop reopens if it has residual twist. However, this result does not mean that the cable loop will not kink. Kinking depends on the cable loop reopening radius determined by (43). The cable receives damage because of kinking only when the cable reopening radius decreases and the cable loop deformation falls into the plastic range. Then, bending rigidity (*EI*) decreases suddenly and it becomes more difficult to reopen the cable loop.

5 Discussion and Conclusion

Figure 7 shows experimental results for cable reopening displacement modes. Test samples were jacketed optical fibers of very small diameter which are easy to investigate. Experimental reopening modes agree with calculated displacements shown in Fig. 6. In these displacements, the cable loop reopening radius is an important factor in cable kink phenomenon. When the cable loop reopens in elastic deformation, the cable loop does not receive damage. However, when the cable loop reopening phenomenon gives rise to plastic deformation, the cable is easy to kink and receives damage. Here the bending rigidity (*EI*) of the cable decreases suddenly and cable kink occurs easily. Calculated results show that the cable reopening radius decreases according to the increase of residual twist. This result means that cable kink occurs easily when cable has residual twist.

Since this paper reports investigations on kinking mechanism using several assumptions to simplify the problem, it is necessary to compare the theoretical results with experimental results in detail and to correct the kinking model in order to clarify the kinking mechanism completely. It is also necessary to investigate cable loop formation, because residual twist on the cable loop is related to cable loop formation, which is the most important factor in cable kink occurrence.

Acknowledgment

The authors thank Dr. Fukatomi, Dr. Kato, and Mr. Negishi for their encouragement and their effective suggestions during this work.

References

1 Yoshida, S., "Research on Kink of Cables (I)," *The Sumitomo Electrical Review*, No. 35, 1949, pp. 17-21 (in Japanese).
2 Yoshida, S., "Research on Kink of Cables (II)," *The Sumitomo Electrical Review*, No. 38, 1949, pp. 21-26 (in Japanese).
3 Yoshida, S., "Research on Kink of Cables (III)," *The Sumitomo Electrical Review*, No. 40, 1950, pp. 28-33 (in Japanese).
4 Yoshimura, M., "Cable Kink," *Fujikuradensen-giho*, No. 1, 1949, pp. 21-28, (in Japanese).
5 Ross, A. L., "Cable Kinking Analysis and Prevention," ASME *Journal of Engineering for Industry*, Vol. 99, No. 1, 1977, pp. 112-115.
6 Eisenhart, L. P., *A Treatise on the Differential Geometry of Curves and Surfaces*, Dover Publications, New York, 1909.
7 Love, A. E. H., *Mathematical Theory of Elasticity*, Dover Publications, New York, 1944.
8 Timoshenko, S., *Elasticity*, McGraw-Hill, New York, 1951.

K. C. Park
Staff Scientist,
Applied Mechanics Laboratory,
LOCKHEED PALO ALTO RESEARCH LABORATORY,
3251 Hanover Street,
Palo Alto, Calif., 94304
Mem. ASME

An Improved Semi-Implicit Method for Structural Dynamics Analysis[1]

A semi-implicit algorithm is presented for direct time integration of the structural dynamics equations. The algorithm avoids the factoring of the implicit difference solution matrix and mitigates the unacceptable accuracy losses which plagued previous semi-implicit algorithms. This substantial accuracy improvement is achieved by augmenting the solution matrix with two simple diagonal matrices of the order of the integration truncation error.

1 Introduction

The direct time integration of large structural dynamics equations is a challenging problem because the task requires the extensive use of both computer resources and engineering manpower. There are basically three approaches: implicit, explicit, and semi-implicit methods. In implicit methods, the new state vector is obtained by solving the coupled difference equations, which involves the factoring of the solution matrix and back and forward substitutions. It is hoped that the price paid for such extensive calculations per each time increment is unconditional stability without the restriction of the time increments. In explicit methods, the new state vector is computed by using the known state vector sets plus the forcing function vector. Hence, the calculation sequence is considerably simpler than for the case of implicit methods. However, the maximum time increment for all the explicit methods is restricted due to the inherent stability limits.

Recently, implicit-explicit methods have been proposed by several investigators [1-7], to exploit the different spatial distributions of low and high-frequency response patterns in the structure. Here the high-frequency domains (elements, degrees of freedom) are treated by implicit methods while the dominant low-frequency domains are treated by explicit methods. Implicit-explicit methods have thus significantly reduced computations especially for large-scale structural dynamics problems. However, the attendant solution matrix pertaining to the implicitly partitioned domains still has to be assembled and factored whenever a new step size is chosen or a new stiffness matrix is required in nonlinear analysis.

In semi-implicit methods, the new state vector is obtained by invoking a Jacobi-like solution procedure, thus avoiding the matrix factoring. In that sense the semi-implicit methods can be likened to explicit methods. The idea is then to maintain the unconditional stability of implicit methods while simplifying calculations as in explicit methods.

It was shown by Trujillo [8] that his semi-implicit algorithm is unconditionally stable provided the stiffness matrix is split symmetrically into the lower and the upper triangular matrices for the Jacobi-like approximation. However, the symmetrically split semi-implicit algorithm showed an unacceptable accuracy for practical time-increment ranges. He then tried to split the stiffness matrix unsymmetrically, which improved the accuracy but with the loss of unconditional stability of the symmetrical splitting. Park and Housner presented an alternative semi-implicit algorithm [9], which shed light on why unsymmetrical splittings give rise to restricted stability limits and why the accuracy can be improved by unsymmetrical splittings. They identified the cause of accuracy degradation of the symmetrical splitting due to the violation of rigid-body preservation requirements and proposed a guideline on how to split the stiffness matrix in order to preserve key rigid-body motions by unsymmetrical splittings.

In this paper an improved semi-implicit method is presented, which adopts symmetrical splittings of stiffness matrix by adding two diagonal matrices which are in the order of the truncation error of the integration algorithm. The essential feature of the proposed algorithm hinges on the approximate factorization utilizing the concept of penalty matrix. Suppose one wants to solve the coupled difference equation which is dependent on parameter δ, viz.,

$$(\mathbf{I}+\delta^2\mathbf{A})u=g \tag{1.1}$$

A Jacobi-like solution for (1.1) can be devised as

$$(\mathbf{I}+\delta^2\mathbf{L})(I+\delta^2\mathbf{U})u\simeq g \tag{1.2}$$

where $\mathbf{L}$ and $\mathbf{U}$ are lower and upper triangular matrices, respectively. Equation (1.2) can be rearranged in the form

$$(\mathbf{I}+\delta^2\mathbf{A}+\delta^4\mathbf{C})u\simeq g \tag{1.3}$$

Hence, the factored difference equation (1.2) gives

$$u\to 0 \text{ as } \delta\to\infty \tag{1.4}$$

unless $\mathbf{C}$ is singular. On the other hand if $\mathbf{L}$ and $\mathbf{U}$ are chosen such that

$$\mathbf{C}u=0 \text{ for all } \delta \tag{1.5}$$

then one obtains

$$u\simeq(\mathbf{I}+\delta^2\mathbf{A})^{-1}g \tag{1.6}$$

for considerably wider ranges of the parameter δ. This is the

[1] Supported by NASA Langley Research Center, Hampton, Va.
Contributed by the Applied Mechanics Division for presentation at the Winter Annual Meeting, Phoenix, Ariz., November 14-19, 1982, of THE AMERICAN SOCIETY OF MECHANICAL ENGINEERS.
Discussion on this paper should be addressed to the Editorial Department, ASME, United Engineering Center, 345 East 47th Street, New York, N.Y. 10017, and will be accepted until two months after final publication of the paper itself in the JOURNAL OF APPLIED MECHANICS. Manuscript received by ASME Applied Mechanics Division, July, 1981; final revision, January, 1982. Paper No. 82-WA/APM-2.
Copies will be available until July, 1983.

essence of the proposed algorithm. In this paper this is accomplished by augmenting the solution matrix by two simple diagonal matrices, which are easy to construct.

2 Precursors of the Proposed Semi-Implicit Method

The linear undamped structural dynamic equations can be written in the form

$$\mathbf{M}\,\ddot{\mathbf{u}}_n + \mathbf{K}\,\mathbf{u}_n = \mathbf{f}_n \tag{2.1}$$

where $\mathbf{M}$ and $\mathbf{K}$ are the diagonal mass, and stiffness matrices, $\mathbf{f}$ is the applied force vector, $\mathbf{u}_n$ is displacement vector, and the superscript dot (˙) denotes time differentiation. Equation (2.1) can be integrated by a pair of one-step formulas

$$\mathbf{u}_{n+1} = \mathbf{u}_n + h(\alpha\dot{\mathbf{u}}_{n+1} + (1-\alpha)\dot{\mathbf{u}}_n) \tag{2.2}$$

$$\dot{\mathbf{u}}_{n+1} = \dot{\mathbf{u}}_n + h(\beta\ddot{\mathbf{u}}_{n+1} + (1-\beta)\ddot{\mathbf{u}}_n) \tag{2.3}$$

where α and β are real coefficients, and h is the time step size. Time discretizing (2.1) by (2.2) and (2.3) yields

$$\mathbf{E}\,\mathbf{u}_{n+1} = \mathbf{g}_{n+1} \tag{2.4}$$

where

$$\mathbf{E} = \mathbf{M} + \delta^2\mathbf{k} \quad \delta^2 = \alpha\beta h^2 \tag{2.5}$$

$$\mathbf{g}_{n+1} = (\mathbf{M} - h^2\alpha(1-\beta)\mathbf{K})u_n + h\mathbf{M}\dot{u}_n + \alpha h^2(\beta\mathbf{f}_{n+1} + (1-\beta)\mathbf{f}_n) \tag{2.6}$$

In general, the solution matrix $\mathbf{E}$ as given by (2.4) is fully coupled and consequently the implicit solution ($\beta \neq 0$) of the difference equation (2.4) require the factoring of $\mathbf{E}$. To alleviate the effort required for factoring the solution matrix $\mathbf{E}$ and at the same time to preserve the unconditional stability of the implicit integration formula, Jacobi-like solution procedures have been proposed [8, 9]. The essence of these procedures may perhaps be best explained from the viewpoint of approximate factoring of the solution matrix $\mathbf{E}$ as illustrated in the following.

Let us split $\mathbf{E}$ as

$$\mathbf{E} = \mathbf{M} + \delta^2\mathbf{K}^L + \delta^2\mathbf{K}^U \tag{2.7}$$

and rearrange (2.4) as

$$(\mathbf{M} + \delta^2\mathbf{K}^L)\mathbf{u}_n = \mathbf{g}_n - \delta^2\mathbf{K}^U\mathbf{u}_n^p \tag{2.8}$$

where $\mathbf{K}^L$ and $\mathbf{K}^U$ are lower and upper triangular matrices so that

$$\mathbf{K} = \mathbf{K}^L + \mathbf{K}^U \tag{2.9}$$

Note that if $\mathbf{K}^U\,\mathbf{u}_n^p$ term in the right-hand side of (2.8) is predicted, the solution for $\mathbf{u}_n$ by (2.8) requires no factorization. At this point Trujillo's method and the Park and Housner method diverge in that the former [8] updates the velocity and the right-hand side vectors, and alternates the next step solution

$$(\mathbf{M} + \delta^2\mathbf{K}^U)\mathbf{u}_{n+1} = \mathbf{g}_{n+1} - \delta^2\mathbf{K}^L\mathbf{u}_{n+1}^p \tag{2.10}$$

In the Park and Housner method [2], instead, an additional iteration is performed for $\mathbf{u}_n$, viz.,

$$(\mathbf{M} + \delta^2\mathbf{K}^U)\mathbf{u}_n{}^{(1)} = \mathbf{g}_n - \delta^2\mathbf{K}^L\mathbf{u}_n \tag{2.11}$$

then the velocity $\dot{\mathbf{u}}_n$ is updated. For comparison of the two methods, the Park and Housner method should use twice the step size of the Trujillo method.

It can be shown that the Park and Housner method can be rearranged as

$$[\mathbf{M} + \delta^2\mathbf{K} + \delta^4\mathbf{K}^L\mathbf{M}^{-1}\mathbf{K}^U]\mathbf{u}_n{}^{(1)} = \mathbf{g}_n + \delta^4\mathbf{K}^L\mathbf{M}^{-1}\mathbf{K}^U\mathbf{u}_n^p \tag{2.12}$$

where the velocity is updated by (2.2) and

$$\mathbf{u}_n^p = \mathbf{u}_{n-1} \tag{2.13}$$

and a similar expression can be derived for the Trujillo method.

From the viewpoint of approximate factorization (2.12) can be written in the form

$$(\mathbf{E} + \delta^4\mathbf{C})u_n = \mathbf{g}_n + \delta^4\mathbf{C}\,\mathbf{u}_n^p \tag{2.14}$$

where

$$\mathbf{C} = \mathbf{K}^L\mathbf{M}^{-1}\mathbf{K}^U \tag{2.15}$$

Note that unless $\mathbf{C}$ is singular one obtains from (2.15)

$$\mathbf{u}_n \to \mathbf{u}_n^p \text{ as } \delta \to \infty \tag{2.16}$$

since $\delta^4\,\mathbf{C}$ dominates over $\mathbf{E}$. Experience has shown that even for intermediate stepsize ranges, $\delta^4\mathbf{C}$ often dominates over or becomes of the same order of magnitude as $\mathbf{E}$ and consequently unacceptable error makes the solution meaningless. This dominance can be abated by employing a penalty concept:

$$\mathbf{C}\mathbf{u} = \mathbf{0} \tag{2.17}$$

This is the essense of the proposed semi-implicit method.

3 New Semi-Implicit Method

Let us rearrange (2.14) using (2.13) and modify it to the form with $\alpha = \beta = \frac{1}{2}$

$$[\mathbf{E} + \delta^4\hat{\mathbf{C}}_n]\Delta\mathbf{u}_n = \hat{\mathbf{g}}_n \tag{3.1}$$

where

$$\hat{\mathbf{g}}_n = \delta\mathbf{M}\dot{\mathbf{u}}_{n-1} - \delta^2\mathbf{K}\mathbf{u}_{n-1} + \frac{\delta^2}{2}(\mathbf{f}_n + \mathbf{f}_{n-1}) \tag{3.2}$$

$$\Delta\mathbf{u}_n = \frac{1}{2}(\mathbf{u}_n - \mathbf{u}_{n-1}) \tag{3.3}$$

and the velocity is updated by (2.3). In the selection of $\hat{\mathbf{C}}_n$ the following three conditions are imposed for stability, accuracy, and simplicity. They are:

1 $\hat{\mathbf{C}}_n$ is symmetric.

2 The singularity requirement of $\hat{\mathbf{C}}_n$ is compromised for computational simplicity by

$$\hat{\mathbf{C}}_n\,\mathbf{u}_{n-1} = \mathbf{O} \tag{3.4}$$

3 $\hat{\mathbf{C}}_n$ is obtained from $\mathbf{C}_n$ by adding two diagonal matrices in the order of $\mathbf{C}_n$.

The first condition implies

$$\mathbf{K}^L = (\mathbf{K}^U)^t \tag{3.5}$$

The second and the third conditions are realized by introducing two diagonal matrices $\mathbf{m}$ and $\mathbf{k}$ to yield

$$\hat{\mathbf{C}}_n\,\mathbf{u}_{n-1} = \Big[\mathbf{m} + \mathbf{k} + (\mathbf{K}^L + \frac{\delta^2}{2}\mathbf{k})(\mathbf{M} + \delta^4\mathbf{m})^{-1}(\mathbf{K}^U + \frac{\delta^2}{2}\mathbf{k})\Big]\mathbf{u}_{n-1} = \mathbf{O} \tag{3.6}$$

Equation (3.1) can now be expressed in factored form

$$(\mathbf{I} + \delta^2\hat{\mathbf{K}}^L)\hat{\mathbf{M}}(\mathbf{I} + \delta^2\hat{\mathbf{K}}^u)\Delta\mathbf{u}_n = \hat{\mathbf{g}}_n \tag{3.7}$$

where

$$\hat{\mathbf{M}} = \mathbf{M} + \delta^4\mathbf{m} \tag{3.8}$$

$$\hat{\mathbf{K}}^L = (\mathbf{K}^L + \frac{\delta^2}{2}\mathbf{k})\hat{\mathbf{M}}^{-1} \tag{3.9}$$

$$\hat{\mathbf{K}}^u = \hat{\mathbf{M}}^{-1}(\mathbf{K}^u + \frac{\delta^2}{2}\mathbf{k})$$

It is noted that the symmetricity of $\hat{\mathbf{C}}_n$ is necessary for stability as detailed in Section 4. The second condition $\hat{\mathbf{C}}_n\,\mathbf{u}_{n-1} = \mathbf{O}$ achieves a similar effect on the accuracy of the semi-implicit solution as the singularity of $\hat{\mathbf{C}}_n$ with simplicity.

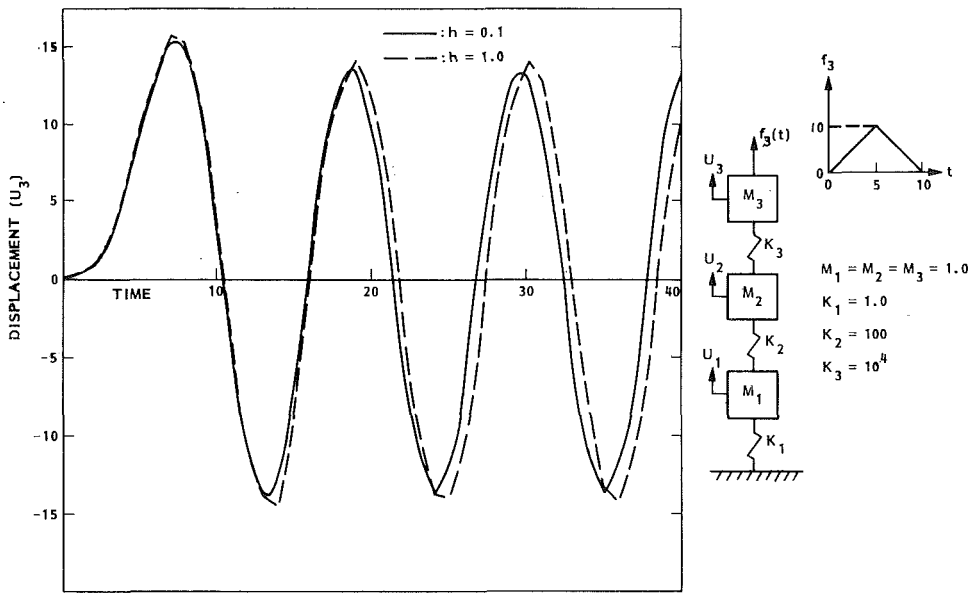

Fig. 1

The addition of two diagonal matrices $\mathbf{m}$ and $\mathbf{k}$ is the simplest modification to ensure that $\hat{\mathbf{C}}_n \mathbf{u}_{n-1} = \mathbf{O}$ holds (see Appendix A for details). This completes the description of the proposed semi-implicit method.

4 Stability Analysis

The stability of the new semi-implicit method (3.1–3.9) can be examined by seeking a nontrivial solution in the form

$$\mathbf{u}_{n+k} = \left(\frac{1+z}{1-z}\right)^k \mathbf{u}_n \tag{4.1}$$

where Re $(z) \leq 0$ for stability. To this end let us rewrite (3.7) in an expanded form with $\mathbf{f} = \mathbf{O}$

$$(\mathbf{M} + \delta^2\mathbf{K} + \delta^4\mathbf{C}_{n-1})(\mathbf{u}_n - \mathbf{u}_{n-1}) = 2\delta\mathbf{M}\dot{\mathbf{u}}_{n-1} - 2\delta\mathbf{K}\,\mathbf{u}_{n-1} \tag{4.2}$$

The appropriate formula for updating $\dot{\mathbf{u}}_n$ is:

$$\dot{\mathbf{u}}_n = \dot{\mathbf{u}}_{n-1} + \delta(\ddot{u}_n + \ddot{u}_{n-1}) \tag{4.3}$$

or,

$$\dot{\mathbf{u}}_n = \dot{\mathbf{u}}_{n-1} - \delta\mathbf{M}^{-1}\mathbf{K}(\mathbf{u}_n + \mathbf{u}_{n-1}) \tag{4.4}$$

by substituting the accelerations from the equations of motion (2.1). The velocity term $\dot{\mathbf{u}}_{n-1}$ from (4.2) can be eliminated by using (4.4) so that one obtains

$$\mathbf{M}(\mathbf{u}_{n+1} - 2\mathbf{u}_n + u_{n-1}) + \delta^2\mathbf{K}(\mathbf{u}_{n+1} + 2\mathbf{u}_n + \mathbf{u}_{n-1}) + \delta^4\hat{\mathbf{C}}_n(\mathbf{u}_{n+1} - \mathbf{u}_n) - \delta^4\hat{\mathbf{C}}_n(\mathbf{u}_n - \mathbf{u}_{n-1}) = \mathbf{O} \tag{4.5}$$

Now, it is noted that by virtue of (3.6) one can express

$$\hat{\mathbf{C}}_n\mathbf{u}_n = \hat{\mathbf{C}}_{n-1}\mathbf{u}_{n-1} = \mathbf{O} \tag{4.6}$$

Furthermore, the third and fourth terms in (4.5), when combined with (4.1) become, respectively,

$$\hat{\mathbf{C}}_n(\mathbf{u}_{n+1} - \mathbf{u}_n) = \left(\frac{1+z}{1-z} - 1\right)\hat{\mathbf{C}}_n\mathbf{u}_n \tag{4.7}$$

and

$$\hat{\mathbf{C}}_{n-1}(\mathbf{u}_n - \mathbf{u}_{n-1}) = \left(\frac{1+z}{1-z} - 1\right)\hat{\mathbf{C}}_{n-1}u_{n-1} \tag{4.8}$$

both of which become zero vectors from (4.6). This implies that the effect of introducing the penalty matrix $\hat{\mathbf{C}}$ does not propagate to the subsequent integration steps. By invoking (4.6–4.8) in (4.5) and introducing (4.1) one finally obtains

$$\mathbf{J}(z)\mathbf{u}_{n-1} = \mathbf{O} \tag{4.9}$$

where

$$\mathbf{J}(z) = \mathbf{M}z^2 + \delta^2\mathbf{K} \tag{4.10}$$

since the stiffness matrix $\mathbf{K}$ is semi-positive definite for stable structures and the diagonal mass matrix $\mathbf{M}$ is positive matrix, $\mathbf{J}(z)$ is a positive polynomial. Therefore, the algorithm is unconditionally stable for linear (or linearized) structural dynamics systems. It is also important to point out that the conditions (3.4) not only enhances the accuracy but also guarantees unconditional stability.

5 Implementation and Numerical Experiments

Even though the determination of the fictitious diagonal matrices $\mathbf{m}$ and $\mathbf{k}$ appears to be a horrendous task, it is relatively simple requiring about one matrix-vector multiplication. For each ith row of (3.6) one has (see Appendix A for details)

$$a\,m_i^2 + bm_i + c + (d + am_i)k_i + \frac{a}{4}k_i^2 = 0 \tag{5.1}$$

It is a simple exercise to show that there exist real m_i and k_i that satisfy (5.1). In practice, three simple sets of (m_i, k_i) have been considered:

$$\text{if} \quad c = 0 \quad \text{then} \quad m_i = k_i = 0 \tag{5.2}$$

$$\text{if} \quad a = 0 \quad \text{then} \quad bm_i + dk_i + c = 0 \tag{5.3}$$

and

$$\text{if} \quad a \neq c \neq 0 \quad \text{then} \quad m_i + k_i = 0 \tag{5.4}$$

$$\text{or} \quad m_i + \frac{1}{2}k_i = 0 \tag{5.5}$$

with constraints

$$M_i + \delta^4 m_i > 0, \quad M_i + \delta^2[K_{ii}/2 + \delta^2(m_i + k_i/2)] > 0 \tag{5.6}$$

The present semi-implicit method was applied to solve the two example problems in [8] and they are shown in Figs. 1 and 2, respectively.

For the first example problem the time increment up to $h = 0.20$ gives almost no discernible error to the converged solution. Also, the time increment $h = 1.0$ gives an identical result as could be obtained by a fully implicit method, which turns out to give about 8 percent phase error after three periods. In addition, a normalized cantilever beam with three equal beam elements was tested by the present algorithm. The

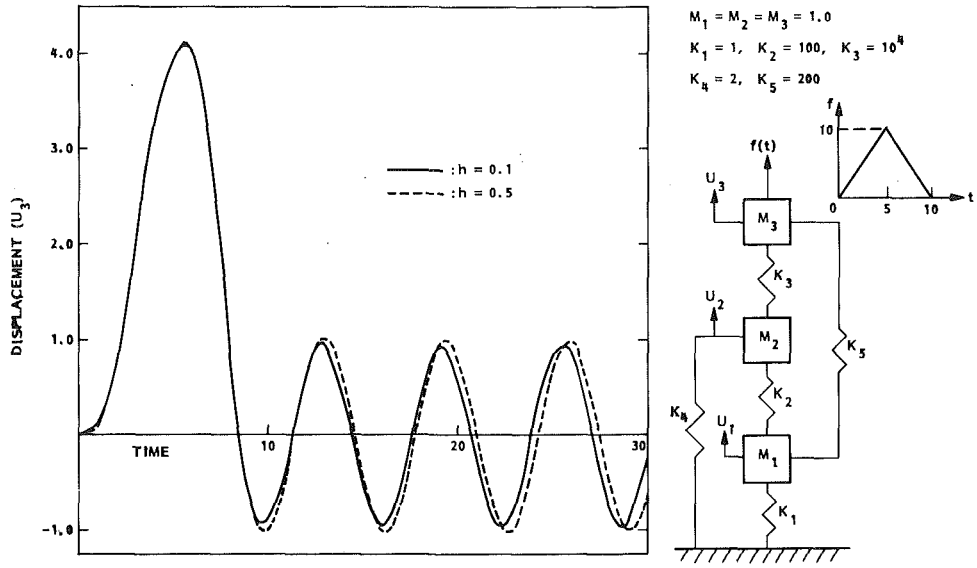

Fig. 2

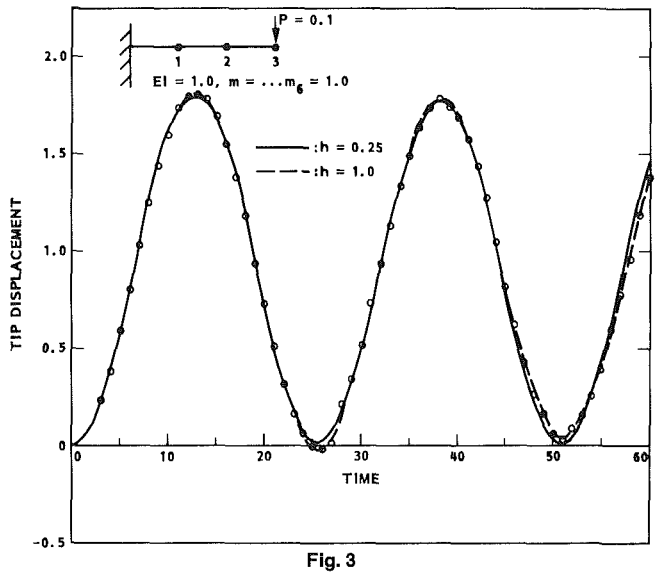

Fig. 3

maximum time increment by the central difference method is 0.32 and Fig. 3 shows two solutions for $h = 0.25$ and $h = 1.0$. Both of the results are quite satisfactory and it is expected that the time increment margin between the explicit and the semi-implicit methods will become wider if more elements are used.

6 Applications to Static Equilibrium Problems

The present method can be easily modified to solve the static equilibrium equation

$$r(p,u) = f - \mathbf{S}(\mathbf{u}) \tag{6.1}$$

by augmenting appropriate α damping matrix in the form

$$\mathbf{D} = \alpha\mathbf{M} + \beta\mathbf{K} \tag{6.2}$$

where $\mathbf{S}(\mathbf{u})$ is the internal force vector.

A preliminary benchmark experiment indicates that the method has potential as an effective dynamic relaxation method since the iteration steps sizes are easy to change and the only factor for stepsize restriction is its overshoot possibility due to large relaxation step sizes.

7 Concluding Remarks

An improved semi-implicit method is presented for the solution of both the dynamic and static equilibrium equations. The method does not require matrix factorization and hence the adjustment of the time-step increments can be made at any step-advancing and/or iteration cycle. This is not the case with fully implicit or implicit-explicit methods without reforming the solution matrix and refactoring.

The unacceptable poor accuracy associated with previous semi-implicit methods has been successfully abated without loss of stability and without regard to matrix profile variations. This is accomplished by augmenting the solution matrix by two simple diagonal matrices, which are easy to compute and are in the order of the truncation error. The net effect is analogous to introducing singular penalty matrix in other physics and engineering problems such as constrained optimization, incompressibility effect in solid, under integration in finite-element formulation.

So far the results from the simple problems are promising and the applications of the method to nonlinear static and dynamic problems are presently being carried out. It is hoped that a stand-alone module based on the present method will lead to programming simplicity and the desired reliability in that one method is used to solve both static and dynamic structural mechanics problems.

One potential area of the applications of the method is in the finite element-based fluid mechanics problems. Here, the widely known alternating direction methods are not applicable because it is not possible, in finite-element formulations of fluid mechanics problems, to partition the matrix in terms of the usual direction-sensitive derivatives. It appears, therefore, that the present method may provide potential computational pay-off by providing simple triangular splittings. This and other possibilities are now under active considerations.

Acknowledgments

The author wishes to thank Dr. Jerrold M. Housner for his enthusiasm and encouragement throughout the development of the present method. The support for the present study was made possible through a research contract from the Structures and Dynamics Division, NASA Langley Research Center.

References

1 Belytschko, T., and Mullen, R., "Mesh Partitions of Explicit-Implicit Time Integration," in: Bathe, K. J., Oden, J. T., and Wunderlich, W., eds., *Formulations and Computational Algorithms in Finite Analysis*, MIT Press, Cambridge, Mass., 1976, pp. 673-690.

2 Belytschko, T., and Mullen, R., "Stability of Explicit-Implicit Mesh

Partitions in Time Integration, *Int. J. Numer. Meths. Eng.* Vol. 12, 1978, pp. 1575-1586.

3 Hughes, T. J. R., and Liu, W. K., "Implicit-Explicit Finite Elements in Transient Analysis: Stability Theory," ASME JOURNAL OF APPLIED MECHANICS, Vol. 45, 1978, pp. 371-374.

4 Hughes, T. J. R., and Liu, W. K., "Implicit-Explicit Finite Elements in Transient Analysis: Implementation and Numerical Examples," ASME JOURNAL OF APPLIED MECHANICS, Vol. 45, 1978, pp. 375-378.

5 Belyschko, T., Yen, H. J., and Mullen, R., "Mixed Methods for Time Integration," *Comp. Meths. Appl. Mech. Eng.* Vol.17/18, 1979, pp. 259-275.

6 Park, K. C., "Partitioned Transient Analysis Procedures for Coupled-Field Problems: Stability Analysis," ASME JOURNAL OF APPLIED MECHANICS, Vol. 47, 1980, pp. 370-376.

7 Park, K. C., and Felippa, C. A., "Partitioned Transient Analysis Procedures for Coupled-Field Problems: Accuracy Analysis," ASME JOURNAL OF APPLIED MECHANICS, Vol. 47, 1980, pp.919-926.

8 Trujillo, D. M., "An Unconditionally Stable Explicit Algorithm for Structural Dynamics," *Int. J. Num. Meth. Eng.*, Vol. II, 1977, pp.1579-1592.

9 Park, K. C., and Housner, J. M., "Semi-Implicit Transient Analysis Procedures for Structural Dynamics Analysis," Presented at NASA/GWU Nonlinear Mechanics Conference, Oct. 6-8 1980, Washington, D. C.; submitted to *Int. J. Num. Meth. Eng.* for publication.

APPENDIX A

Proof of the Existence of Real Matrices m and k

The ith row of (3.6) can be written as

$$m_i u_i + k_i u_i + \sum_{j=1}^{i-1} K_{ij}\left(\sum_{l=j}^{N} K_{jl}u_l\right)/\hat{M}_j + \frac{K_{ii}}{2}\left(\sum_{l=i}^{N} K_{il}u_l\right)\hat{M}_i + \frac{\delta^2}{2}\sum_{j=1}^{i-1}(K_{ij}k_j u_j/\hat{M}_j) + \frac{\delta^2}{4}K_{ii}u_i k_i/\hat{M}_i + \frac{\delta^2}{2}\sum_{l=i}^{N} K_{il}u_l k_i/\hat{M}_i + \frac{\delta^4}{4}k_j u_i/\hat{M}_i = 0 \qquad (A.1)$$

Equation (A.1) can be simplified as

$$a\,m_i^2 + bm_i + c + (d + am_i)k_i + \frac{a}{4}k_i^2 = 0 \qquad (A.2)$$

where

$$a = \delta^4 u_i \qquad (A.3)$$

$$b = M_i(u_i + \delta^4 b\phi) \qquad (A.4)$$

$$c = c\phi + M_i b\phi \qquad (A.5)$$

$$d = M_i u_i + \frac{\delta^2}{2}K_{ii}u_i + \frac{\delta^2}{2}\sum_{l=i+1}^{N} K_{il}u_l \qquad (A.6)$$

$$b\phi = \sum_{j=1}^{i-1}\left(K_{ij}\cdot\left(\sum_{l=j}^{N} K_{jl}u_l/\hat{M}_j + \frac{\delta^2}{2}K_j u_j/\hat{M}_j\right)\right) \qquad (A.7)$$

$$c\phi = \frac{K_{ii}}{2}\cdot\sum_{1=i}^{N} K_{il}u_l \qquad (A.8)$$

There are three cases for which the existence of real m_i and k_i must be examined.

Case 1 $c = 0$.

For this case (A.2) reduces to

$$(am_i + b)m_i + \left(\frac{a}{4}k_i + am_i + d\right)k_i = 0 \qquad (A.9)$$

Certainly, $m_i = d_i = 0$, which is the simplest, satisfies (3.6).

Case 2 $a = 0$.

This case reduces (A.2) to linear for both m_i and k_i.

$$bm_i + c + dk_i = 0$$

As long as b and d are not concurrently zero (A.10) has a solution. $b = d = 0$ can occur when $\{u_i = 0, i\text{-}1, \ldots, N\}$. For this particular case one finds from (A.5), $c = 0$. Otherwise, either b or d can be made nonzero by adjusting δ. In practice, this situation has rarely occurred.

Case 3 $a \neq 0$ and $c \neq 0$.

For this case there exist real m_i and k_i if

$$Q = (d + am_i)^2 - (am_i^2 + bm_i + c) \qquad (A.11)$$

is non-negative. This requirement is simplified to

$$(2ad - b)m_i + (d^2 - c) \geq 0 \qquad (A.12)$$

which can always be satisfied unless

$$(2ad - b) = 0 \text{ and } d^2 - c \leq 0 \qquad (A.13)$$

Again this indefinite case can be avoided by varying parameters if necessary. This proves the existence or real augmenting matrices **m** and **k**.

K. Miya
Associate Professor of
Nuclear Engineering Research Laboratory.
Mem. ASME

M. Uesaka
Graduate Student of
Nuclear Engineering Research Laboratory.

University of Tokyo,
Tokai-Mura, Ibaraki-Prefecture,
319-11, Japan

F. C. Moon
Professor of
Theoretical and Applied Mechanics,
Cornell University,
Ithaca, N.Y. 14850
Mem. ASME

Finite Element Analysis of Vibration of Toroidal Field Coils Coupled With Laplace Transform

A numerical analysis of a vibration of toroidal field coils in a magnetic fusion reactor is shown here on the basis of the finite element method coupled with Laplace transform. Lagrangian consisting of kinetic, elastic strain, and magnetic energies was utilized to deduce equations of motion of the coils. The equations were solved numerically by applying the Laplace transform to a formulation with respect to time and the finite element method to one with respect to space. The Fast Fourier Transform algorithm was utilized for a calculation of the inverse Laplace transform to obtain a nodal vector of the coil's displacement in the original domain. Numerical results reasonably explain a dependency of the coil current on a frequency of the coil.

Introduction

The Laplace transform is well known as an effective way to obtain a solution of ordinary or partial differential equations by converting them into algebraic equations. Tables may be available for the inverse Laplace transform when analytic computations are applied to comparatively easy differential equations. However, cases may occur where this procedure is no longer applicable because of the difficulty of calculating residues. In other words, the inverse Laplace transform cannot often be solved analytically even when a solution of the ordinary differential equation resulting from the Laplace transform of a partial differential can be found. For this case a numerical calculation of the inverse Laplace transform must be applied. As far as the authors know, examples of numerical analysis with the Laplace transform have been very few. Krings and Waller [1] gave a numerical solution of linear partial differential equations with two independent variables x and t applying the method of Laplace transform coupled with an algorithm of the Fast Fourier Transform (FFT) developed in 1965 by Cooley and Tukey [2]. Manolis and Beskos [3] applied the Laplace transform to a solution of dynamic stress concentration around holes. Their method consists of applying the Laplace transform with respect to time to the equation of motion and solving the formulated equation numerically in the transformed domain by the boundary integral equation method.

On the other hand, the authors have been deeply concerned with an instability of toroidal field coils for Tokamak-type fusion reactors [4]. The magnetoelastic buckling of the toroidal field coils was first proved by Moon [5] to be closely related to a vibration characteristics of the coils in a magnetic field. Miya and Uesaka [6] first showed a finite element analysis of a harmonic vibration of the toroidal field coils that have lateral supports. The vibration of the toroidal field coils in a strong magnetic field is too complicated in geometry and boundary conditions to solve analytically, which suggests application of the finite element method. The analysis of the harmonic vibration of the toroidal field coil gives us only a series of natural frequency from a solution of an eigenvalue equation. An extension of the work requires us to develop the numerical method to solve a forced vibration of the coils. To obtain the solution, the Laplace transform was applied for the discretization of the partial differential equation with respect to time, while the finite element method was applied for the discretization with respect to space. One reason for the application of the Laplace transform is the fact that time-savings in the computation of the vibration can be expected with use of the Fast Fourier Transform algorithm. Also the Fourier transform cannot be successfully applied to the equation of motion with no damping because of singularities at natural frequencies of the vibration.

A necessity for the dynamic analysis of toroidal field coils arises from the fact that the toroidal field coils experience transient electromagnetic forces due to the transient poloidal magnetic field generated by the Ohmic heating coils and a rapid change of plasma current. In addition, the structural response of the coils to an earthquake must be known for the structural design of the toroidal field coils.

Theory of Coupled Vibration of Toroidal Field Coils With Toroidal Magnetic Field

Basic Equations. Each of the toroidal field coils experiences attractive forces from the rest of the coils when the coil currents flow in the same direction. The attractive forces that are common in actual toroidal field coils of a magnetic

Contributed by the Applied Mechanics Division for publication in the JOURNAL OF APPLIED MECHANICS.

Discussion on this paper should be addressed to the Editorial Department, ASME, United Engineering Center, 345 East 47th Street, New York, N.Y. 10017, and will be accepted until two months after final publication of the paper itself in the JOURNAL OF APPLIED MECHANICS. Manuscript received by ASME Applied Mechanics Division, June, 1981; final revision, February, 1982.

fusion reactor are balanced since the coils are symmetrically arrayed in a torus. However, the balance of the forces could be broken when an external force such as an earthquake or electromagnetic force induced by a transient poloidal magnetic field acts on the coils. If a coil current exists, the motion of the coil is strongly affected by the coil current itself as experimentally shown by Moon [5]. The experimental result showed that the squared frequency decreases linearly with the squared coil current. The same relation was proved for a harmonic vibration of the toroidal coils by Miya and Uesaka [6] on the basis of the finite element analysis. Thus our concern in this paper is placed on showing a numerical solution of a forced vibration of the toroidal field coils. A characteristic feature of the numerical solution is such that the Laplace transform is applied for a discretization of equation of motion with regard to time while the finite element method is applied for the discretization with regard to space.

The energy method is easier for the finite element formulation of the motion of the toroidal field coils than the method of force balance. For that purpose Lagrange's equation can be used. To construct the Lagrangian, kinetic and elastic energies as well as a magnetic energy should be taken into consideration. The kinetic energy T is given by

$$T=\frac{1}{2}\sum_i\iint\rho\left(\frac{\partial w}{\partial t}\right)^2 h\ dxdy \tag{1}$$

where w is a small deflection normal to the coil plane. ρ and h are the density and the thickness of the coil, respectively. The elastic strain energy U is stored in the coil when the coil deflects and is expressed as follows in terms of generalized strain $\{\epsilon\}$ and stress $\{\sigma\}$ as,

$$U=\frac{1}{2}\sum_i\iint\{\epsilon\}^T\{\sigma\}\ dxdy \tag{2}$$

where

$$\{\epsilon\}^T = \left\{-\frac{\partial^2 w}{\partial x^2}, -\frac{\partial^2 w}{\partial y^2}, -2\frac{\partial^2 w}{\partial x\partial y}\right\} \tag{3}$$

$$\{\sigma\}^T = \{M_x, M_y, M_{xy}\} \tag{4}$$

M_x, for example, is a bending moment around the y-axis as usually defined in the theory of plate bending. The magnetic energy is expressed with a vector potential $\mathbf{A}$ and current density $\mathbf{J}$ as,

$$W=\frac{1}{2}\sum_i\iint\mathbf{A}\cdot\mathbf{J}\ h\ dxdy \tag{5}$$

A summation in equations (1), (2), and (5) is carried over all the toroidal field coils.

The Lagrangian L is given by

$$L=T-U+W \tag{6}$$

Thus the equation of motion is derived by the Lagrange's equation which is generally defined by

$$\frac{d}{dt}\left(\frac{\partial L}{\partial \dot{w}}\right)-\frac{\partial L}{\partial w}=F \tag{7}$$

where $\dot{w}=\partial w/\partial t$ and F is an external force acting on the coil. A substitution of equations (1), (2), and (5) in equation (7) yields

$$\sum_i\iint\rho\ddot{w}h\ dxdy+\sum_i\frac{\partial}{\partial w}\left[\frac{1}{2}\iint\{\epsilon\}^T\{\sigma\}\ dxdy\right]$$

$$-\sum_i\frac{\partial}{\partial w}\left[\frac{1}{2}\iint\mathbf{A}\cdot\mathbf{J}h\ dxdy\right]=\sum_i F_i \tag{8}$$

This is the equation of motion of the toroidal field coils which we aimed to obtain. The third term in the left-hand side of equation (8) is coupled with movements of the rest of the coils while the first and second terms are independent of the relative displacements between coils. Thus if the vector potential $\mathbf{A}$ of the third term is calculated with consideration of other coil's movement, we can omit the summation Σ_i in equation (8). Of all the toroidal modes, the pairing mode is the easiest to occur as stated in reference [5], and is supposed to occur for the present analysis. Finite element formulation of equation (8) is too lengthy to show here since it is shown in detail in reference [6]. And the detailed calculation of the third term of equation (8), which is a perturbation of the magnetic energy stored in the coil system, is given in references [6], [7]. The result deduced in the paper is given by,

$$[M]\{\ddot{q}\}+\{[K_e]-[K_m]\}\{q\}=\{F\} \tag{9}$$

where

$$[M]=\iint\lfloor N\rfloor^T\rho[N]h\ dxdy \tag{10}$$

$$[K_e]=\iint([H]^{-1})^T[P]^T[D][P][H]^{-1}\ dxdy \tag{11}$$

$$[K_m]=\iint\left[J_{x0}\cdot A_{x0}\frac{\partial[N]^T}{\partial x}\frac{\partial[N]}{\partial x}+J_{y0}\cdot A_{y0}\frac{\partial[N]^T}{\partial y}\right.$$

$$\left.\frac{\partial[N]}{\partial y}+(J_{x0}\cdot A_{x2}+J_{y0}\cdot A_{y2})[N]^T[N]\right]h\ dxdy \tag{12}$$

where $\{q\}$ is a nodal deflection vector and $[N]$ is a shape function which is given by

$$w=[N]\{q\}=[R][H]^{-1}\{q\} \tag{13}$$

$$[R]=[1,x,y,x^2,xy,y^2,x^3,xy(x+y),y^3] \tag{14}$$

$$[P] = -\begin{Bmatrix}\dfrac{\partial^2}{\partial x^2}\\ \dfrac{\partial^2}{\partial y^2}\\ 2\dfrac{\partial^2}{\partial x\partial y}\end{Bmatrix}[R] \tag{15}$$

$[D]$ is an elastic matrix, J_{x0} and J_{y0} are x and y-components of the current density, and A_{x0} and A_{y0} are x and y-components of the vector potential. A_{x2} and A_{y2} are coefficients of the squared term w^2 in Taylor's expansion of the vector potential. The matrices $[M]$, $[K_e]$, and $[K_m]$ are called the mass matrix, the stiffness matrix, and the magnetic stiffness matrix, respectively.

Numerical Solution of Vibration of Toroidal Field Coil With Laplace Transform

Application of Laplace Transform. The magnetically coupled free vibration of a set of toroidal field coils can be modeled by a linear chain of masses coupled by negative springs and with periodic boundary conditions. Such a harmonic motion is well known and is discussed in reference [8].

According to the statement, the general motion of the set of the toroidal field coils can be represented by N modes as,

$$\{q\}_i=\sum_{\alpha=0}^{N-1}\{Q\}_\alpha e^{j\omega\alpha t}e^{j2\pi\alpha/N} \tag{16}$$

where $j=\sqrt{-1}$, $\{Q\}_\alpha$ is independent of time, and ω_α is a frequency of the αth mode. A substitution of equation (16) in equation (9) gives,

$$[-\omega^2{}_\alpha[M]+([K_e]-[K_m])]\{Q\}_\alpha=\{F\}_\alpha \tag{17}$$

The external force $\{F\}$ is zero for the harmonic vibration. This case leads to an eigenvalue problem. The frequency of the αth toroidal mode, ω_α, is obtained as an eigenvalue of the following equation,

$$|([K_e]-[K_m])-\omega^2{}_\alpha[M]|=0 \tag{18}$$

The effect of the toroidal mode on the value ω_α does not appear explicitly in equation (18). However, the mode must be considered when one calculates the perturbed vector potential generated on a coil. Since the smallest frequency ω_α is obtained for $\alpha=(N-1)/2$ for N odd or $\alpha=N/2$ for N even, numerical analyses following this section were done for this toroidal case. This case corresponds to a motion such that any two neighboring coils approaches and departs in pairs.

The Laplace transform may be applicable to equation (9) as follows

$$[s^2[M]+\{[K_e]-[K_m]\}]\{Q_s\} = \{F_s\}+s[M]\{q_0\}+[M]\{\dot{q}_0\} \tag{19}$$

where

$$s=\beta-j\omega \tag{20}$$

Let L be an operator of Laplace transform, and thus

$$L\{q\}=\{Q_s\}$$
$$L\{F\}=\{F_s\}$$

and $\{q_0\}$, $\{\dot{q}_0\}$ are initial deflection and velocity of the nodal vector. A solution of equation (19) is

$$\{Q_s\}=[s^2[M]+\{[K_e]-[K_m]\}]^{-1}[\{F_s\}+s[M]\{q_0\}+[M]\{\dot{q}_0\}] \tag{21}$$

The solution $\{Q_s\}$ is obtained for discrete values of frequency ranging $-k$ to k which gives significant value of $\{Q_s\}$.

Application of the Fast Fourier Transform. The nodal deflection $\{q\}$ is obtained by the inverse Laplace transform of $\{Q_s\}$ as follows,

$$\{q(t)\}=\frac{1}{2\pi j}\int_{\beta-j\infty}^{\beta+j\infty}\{Q_s(s)\}e^{st}\,ds \tag{22}$$

Introduction of equation (20) in equation (22) results in

$$\{q(t)\}=\frac{e^{\beta t}}{2\pi}\int_{-\infty}^{\infty}\{Q_s(\beta-j\omega)\}e^{-j\omega t}\,d\omega \tag{23}$$

If nontrivial change in $Q_s(s)$ does not occur beyond a distance greater than k, then the largest wave number of interest is defined by,

$$\lambda=2\pi/k \tag{24}$$

Thus the $\{q(t)\}$ can be approximately calculated by the next equation

$$\{q(t)\}=\frac{e^{\beta t}}{2\pi}\int_{-k}^{k}\{Q_s(\beta-j\omega)\}e^{-j\omega t}\,d\omega \tag{25}$$

or shifting the frequency from ω to $\omega+k$

$$\{q(t)\}=\frac{e^{\beta t}}{2\pi}\int_{0}^{2k}\{Q_s(\beta-j\omega+jk)\}e^{-j(\omega-k)t}\,d\omega \tag{26}$$

This integral may further be approximated by the summation, as

$$\{q(t)\}=\frac{1}{2\pi}\cdot\frac{2k}{N}e^{\beta t}e^{jkt}\sum_{I=1}^{N}\{Q_s(\beta+jk-j\omega_I)\}e^{-j\omega It} \tag{27}$$

where

$$\omega_I=\frac{2k}{N}\left\{\left(I-1+\frac{1}{2}\right)\right\} \tag{28}$$

Equation (27) can be simply rewritten as follows

$$\{q(t)\}=\frac{k}{\pi N}e^{\beta t}e^{j\{k-(k/N)\}t}\sum_{I=1}^{N}\{Q_s(\beta+jk-j\omega_I)\}e^{-j(2k/N)(I-1)t} \tag{29}$$

while time t is defined as

$$t=\frac{\lambda}{2}(J-1)=\frac{\pi}{k}(J-1)(J=1,2\ldots) \tag{30}$$

By substitution of equation (30) into equation (29) the following equation is obtained

$$\{q(t)\}=\frac{k}{N}e^{\beta(\pi/k)(J-1)}e^{j(1/N)\pi(J-1)}\cdot\sum_{I=1}^{N}\{Q_s(\beta+jk-j\omega_I)\}e^{-j2(\pi/N)(I-1)(J-1)} \tag{31}$$

Equation (31) can be calculated using the algorithm of the Fast Fourier Transform (FFT) which makes computing time remarkably shorter compared with that of the direct integration method since the FFT makes use of special properties of harmonic functions for the evaluation of equation (31). The amount of computation is proportional to $(N)^2$ for the conventional calculation, while that of the FFT is proportional to $2N\log_2 N$.

Results of Numerical Analysis and Discussions

Verification of the Computer Code. For a verification of a validity of the computer code made on the basis of equations (19)-(31) the following one-dimensional dynamic problem was solved.

$$m_0\ddot{x}(t)+C_0\dot{x}(t)+k_0\,x(t) = f_0\,\sin(\omega_0\,t)\;(u(t)-u(t-T_s)) \tag{32}$$

where $u(t)$ is called the Heaviside's unit step function and, $m_0=1.16\times10^{-3}$, $C_0=0.08$, $k_0=4.49\times10^2$, $f_0=1.39$, $\omega_0=50$, and $T_s=10$ msec.

A solution of equation (32) is given by,

$$x(t)=A_1\,e^{\alpha t}\,\sin(A_2t+A_3)+A_4\sin(A_5t+A_6)\quad(0\le t\le T_s)$$
$$x(t)=B_1\,e^{\alpha t}\,\sin(A_2t+B_2)\quad(T_s\le t) \tag{33}$$

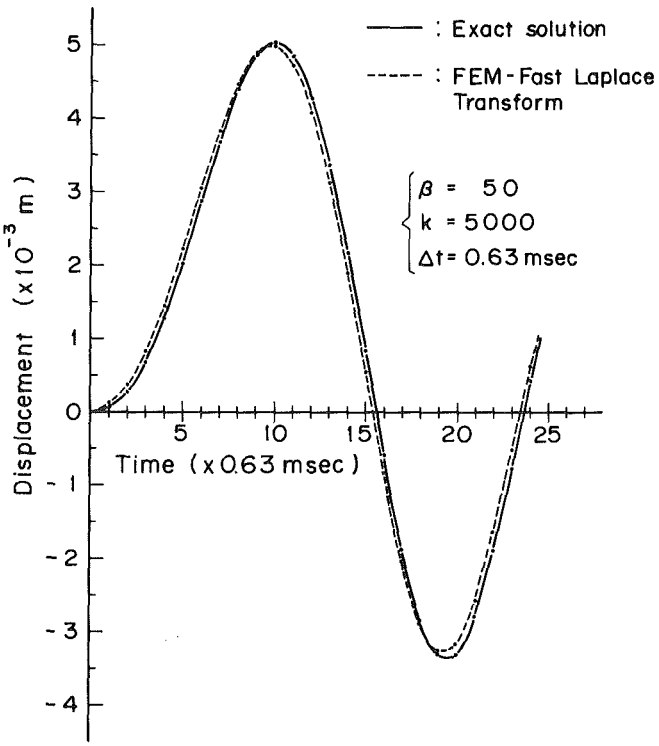

Fig. 1 Comparison of results by finite element method-fast Laplace transform with exact solution (one-dimensional problem)

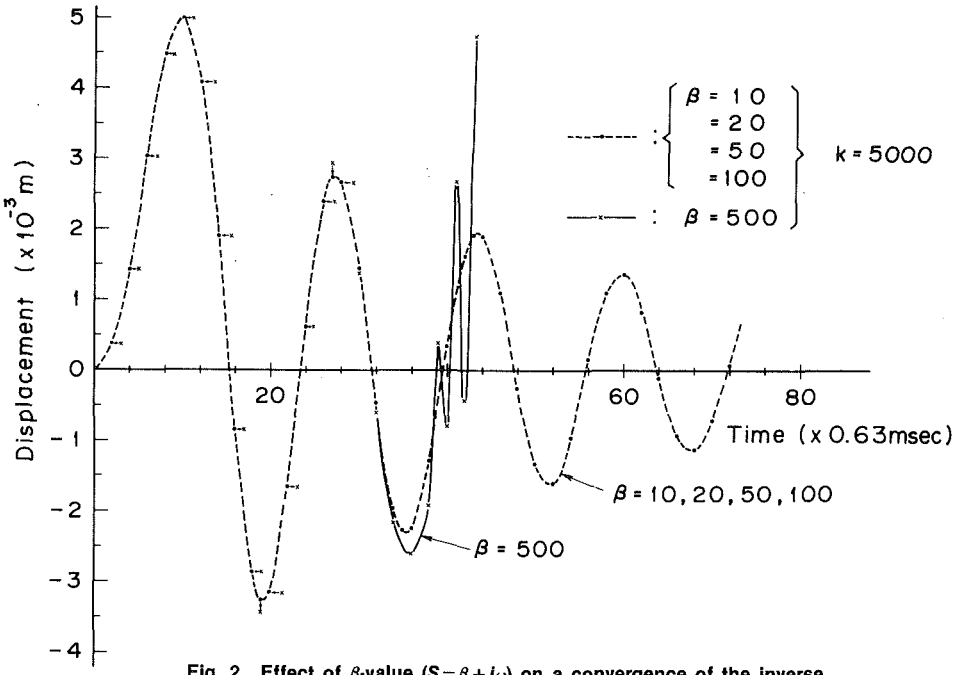

Fig. 2 Effect of β-value ($S=\beta+i\omega$) on a convergence of the inverse Laplace transform

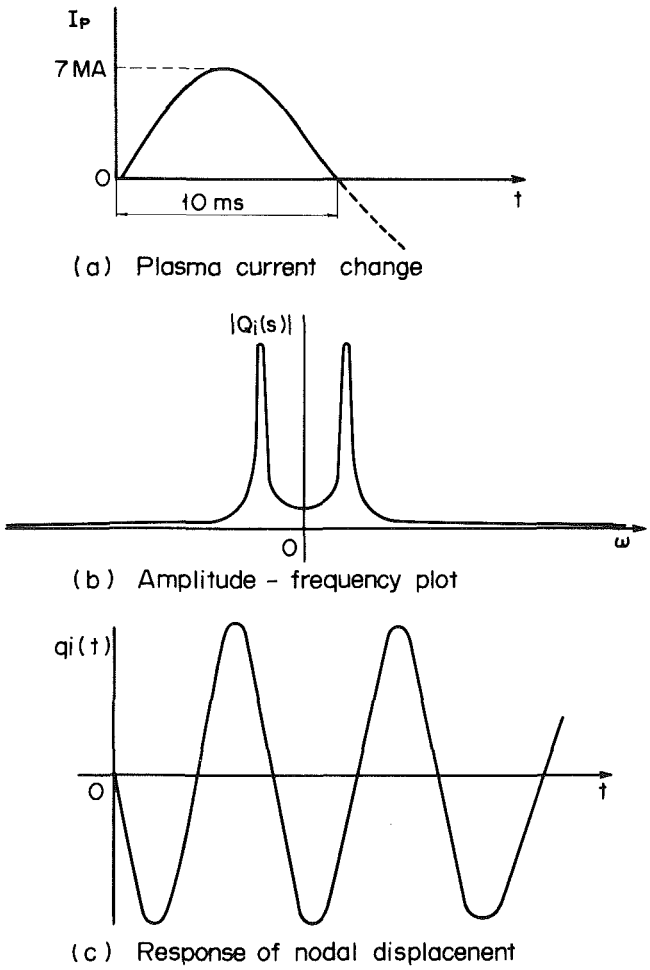

Fig. 3 Forced vibration of *TF* coil

where $A_1=-2.139$, $A_2=0.620$, $A_3=1.46\times10^{-4}$, $A_4=4.154$, $A_5=0.31416$, $A_6=7.52\times10^{-5}$, $\alpha=-34.37$, $B_1=-5.15$, and $B_2=1.95\times10^{-4}$.

Numerical solutions were obtained with a parameter of β and k values in equation (31). A comparison between numerical result from the FEM-FLT (Fast Laplace Transform) method and the exact solution is shown in Fig. 1, where $\beta=50$ and $k=5000$ were used. Since a time mesh is given by $\Delta t=\pi/k$, $\Delta t=0.63$ msec. Amplitudes of two oscillations shown in the figure agree with each other within a few percent of error while their periods agree almost completely.

In the application of the Laplace transform a proper choice of the β and k values is crucial for obtaining a reasonable result when computing the inverse Laplace transform. A rough choice of the value is recommended by Krings and Waller [1] as $3k/\pi N\le\beta\le10k/\pi N$. For values of $N=2^8$ and $k=500$ the criteria is $18.7\le\beta\le62.2$. An examination of convergence is shown in Fig. 2, where a convergent oscillation is depicted with a dotted line for $\beta=10$, 20, 50, 100 and an oscillation with a solid line is divergent for $\beta=500$. Although cases with $\beta=10$ and 100 do not satisfy the criteria given by Krings and Waller [1], the dynamic displacements obtained for the β of 10–100 agree completely with each other. The β of 500 is too far away from the criteria to obtain a convergent solution. Thus the criteria given by Krings and Waller [1] may be a sufficient condition for a convergent solution of the inverse Laplace transform.

Vibration of Toroidal Field Coils. A plasma current change would be one of two sources that could cause the vibration of the toroidal field coils. The other is a change of Ohmic heating coil current. In the present paper the change of the plasma current is utilized. The plasma current is charged slowly by the Ohmic heating coil current and may occasionally disrupt very quickly. The major disruption could more rigorously cause a forced vibration of the toroidal coils than the Ohmic heating coil. The plasma current was assumed to disrupt like a sine function as shown in Fig. 3(*a*). It is zero after 10 msec. For this case the term $\{F\}$ in equation (17) is expressed as

$$\{F\}=\{F_i\}\sin(\pi t/2\tau_0) \tag{34}$$

and the Laplace transform of equation (34) is

$$\{F_s\}=\{F_i\}\frac{\pi/2\tau_0}{s^2+(\pi/2\tau_0)^2}(1+e^{-s\pi/2\tau0}) \tag{35}$$

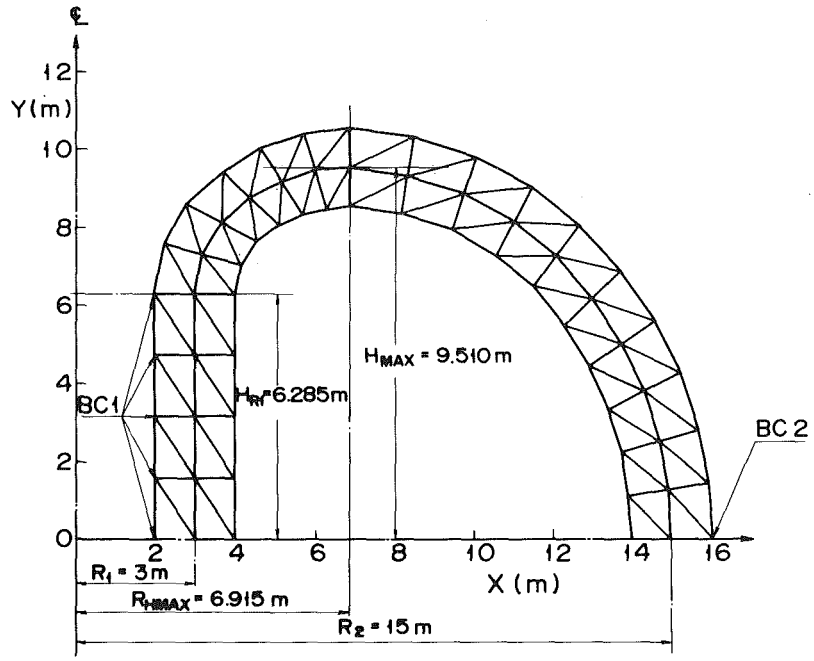

Fig. 4 A half of a coil divided into triangular meshes

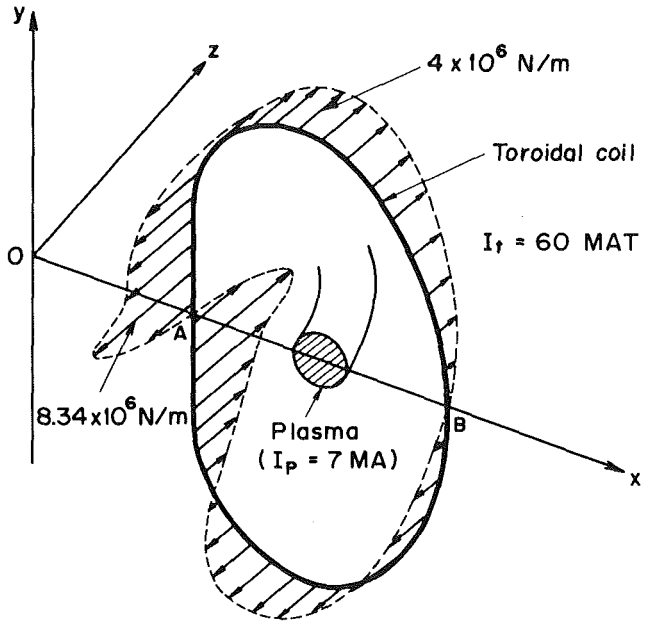

Fig. 5 Electromagnetic force acting on toroidal field coil

The Laplace transform $\{Q_s\}$ of the nodal vector $\{q\}$ is obtained from equation (19) for a constant β and variable frequencies ω. An example of a frequency dependence of $|Q_{is}|$ at a nodal point "i" is shown in Fig. 3(b). Since the following properties of symmetry are valid,

$$R_e(Q_{is}) = R_e(Q_{-is})$$
$$I_m(Q_{is}) = -I_m(Q_{-is}) \quad (36)$$

$|Q_{is}|$ is symmetric with regard to an ordinate in Fig. 3(b). To obtain the nodal displacement $\{q\}$, $\{Q_s\}$ must be inversely transformed based on equation (31). A schematic example of the results is shown in Fig. 3(c).

It should be noted here that the Fourier transform cannot be applied to the vibration problem with no damping while the problem with the damping such as shown in equation (32) can be solved by its application. The reason is that the left-hand side of equation (19) has singularities at the frequencies obtained from $|-\omega^2[M]+\{[K_e]-[K_m]\}|=0$. For the Laplace transform the term is not zero for nonzero $\beta(s=\beta-i\omega)$. Thus the harmonic vibration shown schematically in Fig. 3(c) cannot be solved by the Fourier transform.

A half of the toroidal field coil that is divided into triangular finite element meshes is shown in Fig. 4. Its bore is about 17m × 10m. Shape and dimension of the coil were determined to be free of bending moment using Young-Moses's method [9]. The numbers of node and element are 66 and 80, respectively. Symbols denoted with BC1 and BC2 in Fig. 4 mean that a straight portion of the coil marked with an arrow of BC1 is completely constrained to a bucking post for the case of BC1 and a lateral support is set at a nodal point marked with BC2 as well as the straight portion for the case of BC2. At the boundary conditions, both the deflection and the rotation were constrained at those nodal points.

In Fig. 5 a distribution of electromagnetic force acting on the toroidal field coil is shown, which is caused by an interaction between the toroidal coil current of 60 MAT and a poloidal magnetic field generated by a plasma current of 7 MA. The force acts normal to the coil surface resulting in a huge overturning torque since the force distribution is antisymmetric with respect to the x-axis. A vibration of the toroidal field coils may be caused by a major plasma disruption which is at the present stage thought to occur occasionally. The maximum force per unit length of 8.34×10^6 N/m appears at a point of the straight portion near x-axis.

The electromagnetic forces at two intersecting points (A and B) should be zero because of antisymmetry as indicated in Fig. 5. The plasma current was dealt with as a line current when computing the magnetic flux density at portions of the toroidal field coil.

Figure 6 shows some examples of the vibration of toroidal field coils with a parameter of a sound speed $\sqrt{E/\rho}$ where E and ρ are equivalent Young's modulus and density of the coil, respectively. The coil consists of structural support, superconducting material, and insulation. It is very difficult to take into consideration a complicated detail of the coil section even for a numerical analysis. For brevity, a concept of equivalent Young's modulus and density was applied in this paper. The

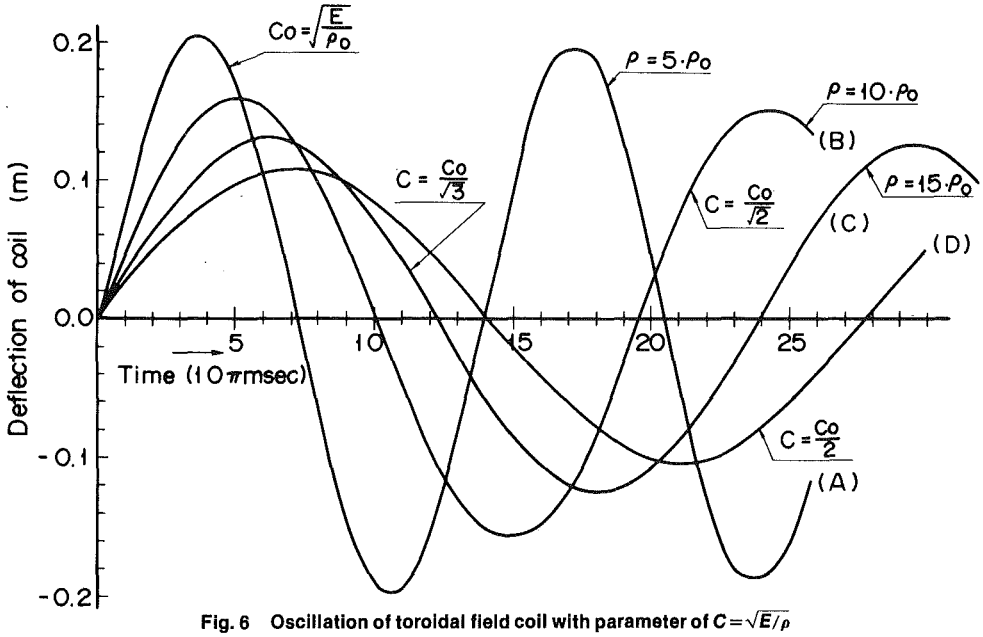

Fig. 6 Oscillation of toroidal field coil with parameter of $C=\sqrt{E/\rho}$

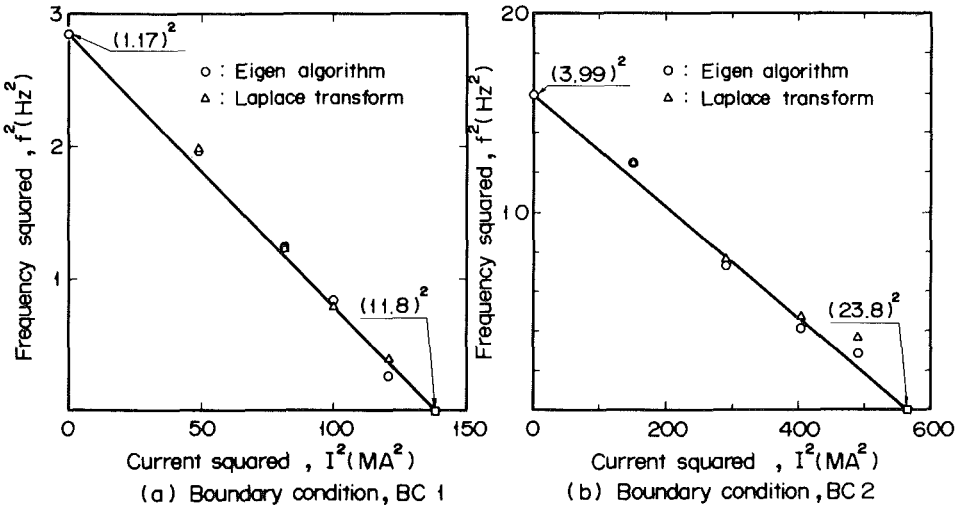

Fig. 7 Frequency-current dispersion curves for an eight-coil full torus

deflection plotted as an ordinate in the figure is one at a point marked with BC2 in Fig. 4. In this case the boundary condition denoted with BC1 was applied and thus the point marked with BC2 is free of any mechanical constraint. Input values as the equivalent Young's modulus and the density were given as those of copper as $E=6.89\times10^4$ MPa and $\rho_0=8.9\times10^3$ Kg/m^3. It is shown in the figure that a period of the oscillation increases with a decrease of the sound speed while an amplitude decreases with a decrease in sound speed. This characteristic feature is understandable from a free oscillation of an undamped mass-spring system.

Figure 7 shows frequency-current dispersion curves for an eight-coil full torus. The left figure is for the boundary condition denoted with BC1 and the right one is for the BC2 boundary condition. Blank circles show results from the lowest of eigenvalues of equation (18) and blank triangles show results from the FEM-FLT method which has been developed in this paper. Both results seem to agree very well in the figure. The frequency corresponding to zero current is a natural one which is not affected by the toroidal field and they are 1.17 Hz and 3.99 Hz for BC1 and BC2 boundary conditions, respectively. The natural frequency increases by its very nature with the number of mechanical constraint. It is also clear that the current corresponding to the zero frequency in Fig. 7 is the same as the critical current which causes the buckling of the toroidal field coil, as discussed in reference [5]. They are 11.8 MA and 23.8 MA for BC1 and BC2 boundary conditions, respectively. As is the case for the natural frequency, the buckling current also increases with the number of mechanical constraint. The figure shows an important fact that the linear relation between a frequency squared and a current squared exists.

In Fig. 8 the lowest natural frequency calculated from solutions of equation (18) and equation (31), which are expressed with the eigenvalue algorithm and the Laplace transform, respectively, in the figure, is plotted versus density and Young's modulus of the coil. Two linear relations between the frequency squared and the inverse of density, and the frequency squared and Young's modulus, are implied to be valid from the following equation,

$$f^2=f_0{}^2-4L_1I^2/V\rho$$

or

$$f^2=(\lambda E-4L_1I^2/V)/\rho \tag{37}$$

where f_0 is a natural frequency when the coil current I is zero

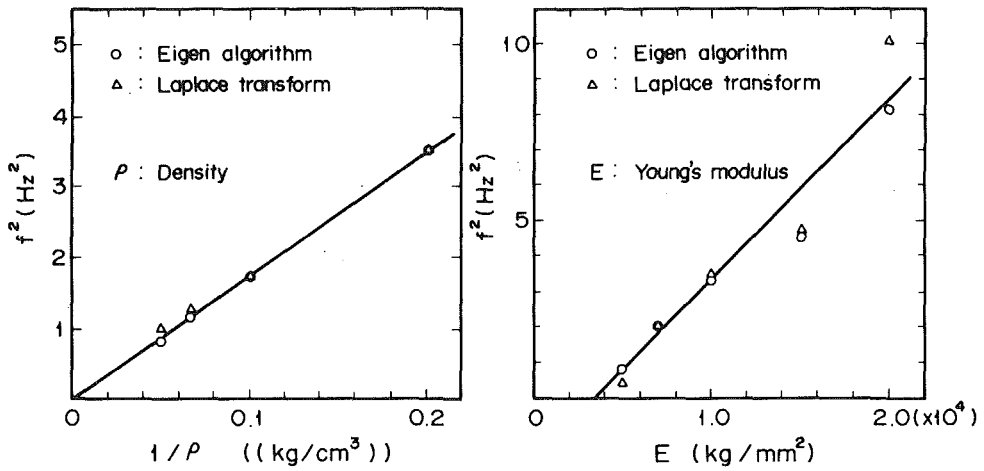

Fig. 8 Relation between frequency squared (f^2) and equivalent density (ρ), Young's modulus

and its square is proportional to a ratio of E/ρ, V is a volume of the coil, and L_1 is a coefficient of a deflection squared in a Taylor series of a mutual inductance between the coils. Equation (37) was deduced by Moon applying a modal analysis to the toroidal field coils. Thus it could be expected that the frequency squared of the coil shown in Fig. 4 is proportional to the inverse of density and Young's modulus. Results shown in Fig. 8 prove the conjecture. These relations are very useful for a rough estimation of the natural frequency, which is needed for a structural design of a toroidal field coil.

Acknowledgment

This work was performed partially at Cornell University through a grant from the United States Office of Naval Research and was completed at the Nuclear Engineering Research Laboratory, University of Tokyo. The authors would like to express their sincere appreciation for discussions with Prof. J. Abel of Cornell University. They would also like to thank Prof. R. Kiyose (Chairman of the Steering Committee on CTR Blanket Engineering Research Facilities) and Prof. Y. Tabata of the University of Tokyo, for their encouragements on this work.

References

1 Krings, W., and Waller, H., "Contribution to the Numerical Treatment of Partial Differential Equations With the Laplace Transformation—an Application of the Algorithm of the Fast Fourier Transformation," *Int. J. for Numerical Methods in Engineering*, Vol. 14, 1979, pp. 1183–1196.

2 Cooley, J. W., and Tukey, J. W., "An Algorithm for the Machine Calculation of Complex Fourier Series," *Math. Comp.*, Vol. 19, 1965, pp. 297–301.

3 Manolis, G. D., and Beskos, D. E., "Dynamic Stress Concentration Studies by Boundary Integrals and Laplace Transform," *Int. J. for Numerical Methods in Engineering*, Vol. 17, 1981, pp. 573–599.

4 Baker, C. C., et al., "STARFIRE-Commercial Tokamak Fusion Power Plant Study," ANL/FPP-80-1, Argonne National Laboratory, 1980.

5 Moon, F. C., and Swanson, C., "Experiments on Buckling and Vibration of Superconducting Coils," ASME Journal of Applied Mechanics, Vol. 44, 1977, pp. 707–713.

6 Miya, K., Uesaka, M., and An, S., "Structural Dynamics of Toroidal Field Coil in Magnetic Fusion Reactor," *Proceedings of the 4th American Nuc. Soc. Topical Meeting on the Technology of Controlled Nuclear Fusion*, King of Prussia, Philadelphia, Penn, Oct. 1980.

7 Miya, K., Takagi, T., and Uesaka, M., "Finite Element Analysis of Magnetoelastic Buckling and Experiments on a Three-Coil Superconducting Partial Torus," Mechanics of Superconducting Structures, ASME *Journal of Mechanical Design*, Vol. 41, 1980, pp. 91–107.

8 Brillouin, L., *Wave Propagation in Periodic Structures*, Dover, New York, 1953.

9 Moses, R. W., and Young, W. C., "Analytic Expressions for Magnetic Forces on Sectored Toroidal Coils," *6th Symp. on Engineering Problems of Fusion Research*, San Diego, Calif., 1975, pp. 917–921.

The Dynamics of a Gyroscope Supported by a Flexible Circular Plate

J. S. Burdess
Lecturer,
Department of Mechanical Engineering,
University of Newcastle upon Tyne,
Newcastle upon Tyne, NE1 7RU, England

The dynamics of a rigid rotor supported on a flexible circular plate is investigated and it is shown that the arrangement is capable of operating as a tuned free rotor gyroscope. The performance characteristics of the gyroscope are evaluated and the analysis shows that the steady displacment of the rotor may be used to measure either the angular velocity or angular displacement of the supporting casing. For both modes of operation the free motion and the response to a constant rate and a vibratory input is determined.

1 Introduction

During recent years elastically supported gyroscopes such as the Oscillogyro and the Hooke's Joint Gyroscope have been developed with the aim of replacing the more expensive floated gyroscope. Offering simplicity of construction and therefore lower manufacturing costs it is felt that the next generation of high accuracy gyroscopes will be found amongst instruments of this type. The Oscillogryo, originally developed by Philpot and Mitchell at R.A.E. and later investigated by Walley and Maunder [1] has been the forerunner of this class. Its construction [1] is simply a sensing element usually in the form of a flat bar, elastically connected to a drive shaft by means of a torsional hinge. By matching the inertia coefficients of the sensing element with the suspension stiffness the oscillo-bar may be tuned at its running frequency to provide a direct measure of casing rotation. The Hooke's Joint Gyroscope [2] is a two-axis version of the Oscillogyro and exhibits similar characteristics.

Despite the simplicity of these devices their performance as inertial instruments has been limited because of their poor response to harmonic inputs at twice the tuning frequency. Much recent research has therefore considered instruments that exhibit the tuning characteristic but are free from the drifts associated with 2ω vibration.

A suspension system based on heavy elastic beams has recently been proposed by Maunder and Bulman [3] and this has been shown in [4] to have tuning characteristics and 2ω immunity. The purpose of this paper is to show that other elastic suspensions are possible by considering the case of a rotor supported on a heavy circular plate.

2 Description of System and Analysis

Figure 1 shows the form of the elastically supported gyroscope considered in this paper. The sensing element, in this case a symmetric rotor, is connected to the drive shaft by means of a heavy circular plate. The inner and outer edges of the plate are assumed to be rigidly clamped to the drive shaft and the rotor, respectively.

Consider the set of case-fixed axes $OXYZ$ shown in Fig. 2. The origin 0 is fixed at the mass center of the rotor and axes OX, OY, and OZ are aligned with the initial directions of the rotor's principle axes at O. In this datum state the plate is arranged to lie in the OXY plane with its normal through its center coincident with OZ. It will be assumed that the rotor moves in rotation only and that its center of mass G always remains fixed at O. In practice it is necessary to prevent axial translation. This constraint is often achieved by connecting the rotor to the drive shaft using a light axial strut. In the analysis that follows, the stiffness of this strut will be

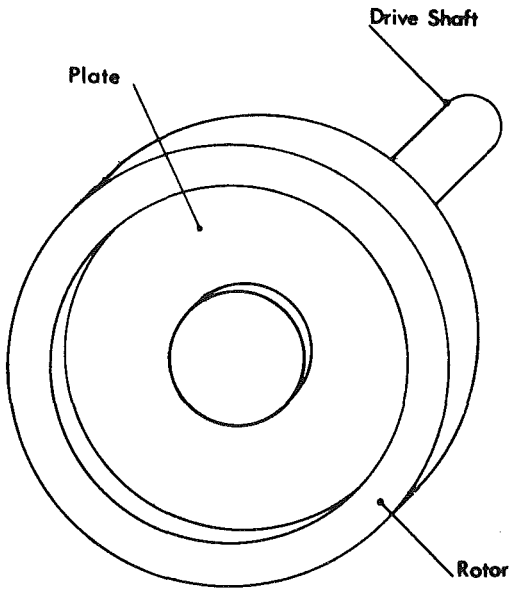

Fig. 1 Gyroscope assembly

Contributed by the Applied Mechanics Division for publication in the JOURNAL OF APPLIED MECHANICS.
Discussion on this paper should be addressed to the Editorial Department, ASME, United Engineering Center, 345 East 47th St., New York, N.Y. 10017, and will be accepted until two months after final publication of the paper itself in the JOURNAL OF APPLIED MECHANICS. Manuscript received by ASME Applied Mechanics Division, July, 1981; final revision, November, 1981.

neglected. This omission does not affect the results of the investigation. Rotor motion relative to $OXYZ$ is given by a rotation nt about the spin axis OZ, to take $OXYZ$ to $OX_1Y_1Z_1$, followed by small rotations ϕ_x about OX_1, to take $OX_1Y_1Z_1$ to $OX_2Y_2Z_2$ and ϕ_y about OY_2, and to take $OX_2Y_2Z_2$ to $Oxyz$. The axes $Oxyz$ remain fixed to the rotor's principal axes. The input to the rotor is specified by an angular velocity Ω about the case-fixed axis OX.

3 Dynamics

To accommodate the displacements ϕ_x and ϕ_y the plate deflects. To describe this deflection it is convenient to consider the motion of the plate with respect to axes $OX_1Y_1Z_1$. Figure 3 shows the deflection W along OZ_1 of a typical point P situated on the midplane of the plate and specified by polar coordinates r and θ. Because the plate is assumed clamped at its inner edge, the deflection must satisfy boundary conditions

$$W(r_i)=0 \quad \text{and} \quad \frac{\partial W}{\partial r}(r_i)=0 \quad \text{at} \quad r=r_i \tag{1}$$

Likewise, because of the rigid attachment to the rotor it follows that the deflection and radial slope of the plate at $r=r_0$ are constrained by the motion of the rotor to be of the form

$$W(r_0)=r_0(\phi_x\sin\theta-\phi_y\cos\theta)$$
$$r_0\frac{\partial W}{\partial r}(r_0)=W(r_0) \tag{2}$$

Since the plate is assumed to have significant mass, the general behavior of the rotor and plate assembly will be determined by the modes that characterize the way the plate can vibrate. However, because the plate's outer edges are kinematically constrained by the motion of the rotor, only asymmetric modes with *one* modal diameter are permissible. It can be further assumed that the fundamental of this set will determine the behavior of the gyroscope.

The governing equations of motion will now be established via Lagrange's equations by assuming a plate deflection compatible with the shape of this fundamental.

Since the deflected form of the plate must satisfy the geometric constraints (1) and (2) an approximate solution may be constructed by assuming W to be given by

$$W=\psi(r).\{\phi_x\sin\theta-\phi_y\cos\theta\} \tag{3}$$

where $\psi(r)$ is chosen to satisfy boundary conditions

$$\psi=0 \quad \text{and} \quad \frac{\partial\psi}{\partial r}=0 \quad \text{at} \quad r=r_i$$

and

$$\psi=r_0 \quad \text{and} \quad \frac{\partial\psi}{\partial r}=1 \quad \text{at} \quad r=r_o. \tag{4}$$

Clearly there is more than one function $\psi(r)$ that can be chosen to satisfy (4). For the purpose of the present analysis we shall select $\psi(r)$ to be the function that describes the static deflection of the nonrotating plate when the rotor is given a unit rotation about OX_1. For this situation $\psi(r)$ can be shown to be given by

$$\psi(r)=\frac{2(r_o^2+r_i^2)r\,ln\left(\frac{r}{r_i}\right)-\frac{1}{r}(r^2+r_o^2)(r^2-r_i^2)}{2\left[r_i^2\left(1+ln\left(\frac{r_o}{r_i}\right)\right)+r_0^2\left(ln\left(\frac{r_o}{r_i}\right)-1\right)\right]} \tag{5}$$

If the kinetic energy T and potential energy V of the gyro assembly are now determined using (5), then the equations determining the rotor motion may be derived from Lagrange's equations. The total kinetic energy of the assembly is determined by adding the kinetic energies of the

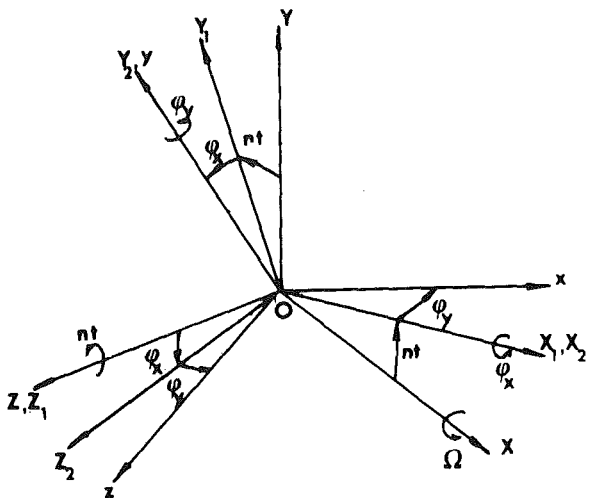

Fig. 2 System axes

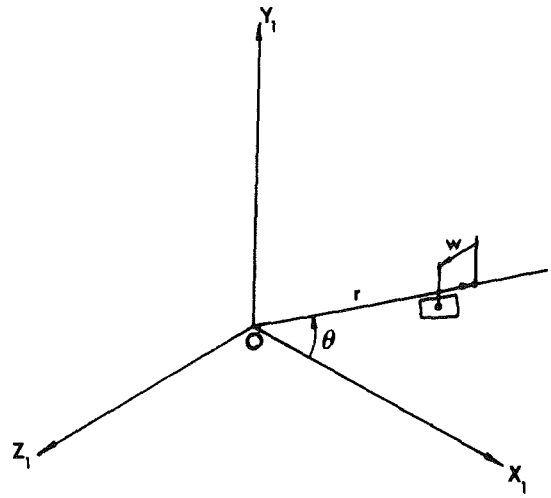

Fig. 3 Plate deflection

Nomenclature

A,A,C = rotor inertias about principal axes
E = Youngs modulus
ν = Poisson's ratio
$D=\frac{Eh^3}{12(1-\nu^2)}$ = plate flexural stiffness
h = plate thickness
ρ = density of plate material
α = coefficient of thermal expansion
T = temperature
n = rotor spin rate
ω = tuning speed
W = plate deflection
ϕ_x = rotor deflection about OX_1
ϕ_y = rotor deflection about OY_2
β_x = rotor deflection about OX
β_y = rotor deflection about OY
Φ = vibration amplitude
s = frequency
η_j = phase angle
$p_{1,2}$ = natural frequency
Ω = casing input about OX

rotor and the plate. For small ϕ_x and ϕ_y the kinetic energy of the rotor, T_R, is given by

$$T_R = \frac{1}{2}[A(\dot{\phi}_x - n\phi_y + \omega_x)^2 + A(\dot{\phi}_y + n\phi_x + \omega_y)^2 + C(n^2 - n^2\phi_x{}^2 - n^2\phi_y^2 - 2n\phi_x\omega_y + 2n\dot{\phi}_y\phi_x + 2n\phi_y\omega_x)] \quad (6)$$

where $\omega_x = \Omega\cos nt$ and $\omega_y = -\Omega\sin nt$.
Likewise the kinetic energy of the plate, T_p, is

$$T_p = \frac{1}{2}\rho h\int_{r=r_i}^{r=r_o}\int_{\theta=0}^{2\pi}[(W\omega_y - rn\sin\theta)^2 + (W\omega_x - rn\cos\theta)^2 + \left(\frac{\partial W}{\partial t} + \omega_x r\sin\theta - \omega_y r\cos\theta\right)^2]r\,dr\,d\theta \quad (7)$$

The potential energy of the assembly is associated with the strain energy stored in the plate and using the results given in [6] is given by

$$V = \frac{D}{2}\int_{r=r_o}^{r_o}\int_{\theta=0}^{2\pi}\left[\left(\frac{\partial^2 W}{\partial r^2}\right)^2 + \left(\frac{1}{r^2}\frac{\partial^2 W}{\partial\theta^2} + \frac{1}{r}\frac{\partial W}{\partial r}\right)^2 + 2\nu\frac{\partial^2 W}{\partial r^2}\cdot\left(\frac{1}{r^2}\frac{\partial^2 W}{\partial\theta^2} + \frac{1}{r}\frac{\partial W}{\partial r}\right) + 2(1-\nu)\left(\frac{1}{r}\frac{\partial^2 W}{\partial r\partial\theta} - \frac{1}{r^2}\frac{\partial W}{\partial\theta}\right)^2\right]r\,dr\,d\theta \quad (8)$$

$$+ \frac{h}{2}\int_{r=r_i}^{r_o}\int_{\theta=0}^{2\pi}\left[\sigma_{rr}\left(\frac{\partial W}{\partial r}\right)^2 + \sigma_{\theta\theta}\left(\frac{1}{r}\frac{\partial W}{\partial\theta}\right)^2\right]r\,dr\,d\theta$$

The quantities σ_{rr} and $\sigma_{\theta\theta}$ represent the inplane radial and circumferential stress fields due to centrifugal loading and any thermal prestress introduced during assembly. The relationships determining σ_{rr} and $\sigma_{\theta\theta}$ are well known [5], and for a thin disk rotating with angular velocity n are

$$\sigma_{rr} = \frac{\alpha E T}{1-\nu} + C_0 + \frac{C_1}{r^2} - \frac{(3+\nu)}{8}\rho n^2 r^2$$

$$\sigma_{\theta\theta} = \frac{\alpha E T}{1-\nu} + C_0 - \frac{C_1}{r^2} - \frac{(1+3\nu)}{8}\rho n^2 r^2 \quad (9)$$

The constants C_0 and C_1 are determined by the fixing of the plate at the drive shaft and rotor connections. If, for example, the drive shaft and rotor are assumed radially rigid these constants follow from the conditions that the inplane deflections at $r = r_i$ and at $r = r_o$ are zero.
For this situation C and C_1 are given by

$$C_0 = \frac{1+\nu}{8}\rho n^2(r_i^2 + r_o^2)$$

and

$$C_1 = \frac{1-\nu}{8}\rho n^2 r_i{}^2 r_o{}^2. \quad (10)$$

Although it has been convenient to derive the kinetic and potential energies with respect to axes fixed to the rotor, interpretation of the system dynamics is greatly simplified if the rotor displacements are rewritten in terms of displacements β_x and β_y about the case fixed axes $OXYZ$. This transformation can be achieved by resolving ϕ_x and ϕ_y along $OXYZ$ to give

$$\beta_x = \phi_x\cos nt - \phi_y\sin nt$$
$$\beta_y = \phi_x\sin nt + \phi_y\cos nt \quad (11)$$

If equations (5) and (11) are now substituted into (6)–(8) the linearized equations defining β_x and β_y follow from Lagrange's equation in the form

$$\frac{d}{dt}\left(\frac{\partial T}{\partial\dot{\beta}_i}\right) - \frac{\partial T}{\partial\beta_i} + \frac{\partial V}{\partial\beta_i} = 0 \quad (12)$$

and may be written

$$(A+a)\ddot{\beta}_x + n(C+2a)\dot{\beta}_y + [K_o - n^2(a+k_1)]\beta_x = -(A+b)\dot{\Omega}$$
$$(A+a)\ddot{\beta}_y - n(C+2a)\dot{\beta}_x + [K_o - n^2(a+k_1)]\beta_y = n(C+2b)\Omega, \quad (13)$$

where

$$a = \rho h\pi\int_{r_i}^{r_o} r\psi^2(r)dr$$

$$b = \rho h\pi\int_{r_i}^{r_o} r^2\psi(r)dr$$

$$K_o = \pi D\int_{r_i}^{r_o}\left[r\left(\frac{d^2\psi}{dr^2}\right)^2 + \frac{1}{r}\left(\frac{d\psi}{dr} - \frac{1}{r}\psi\right)^2 + 2\nu\frac{d^2\psi}{dr^2}\cdot\left(\frac{d\psi}{dr} - \frac{1}{r}\psi\right) + \frac{2(1-\nu)}{r}\left(\frac{d\psi}{dr} - \frac{\psi}{r}\right)^2\right]dr + \pi\cdot\frac{\alpha E T}{1-\nu}h\int_{r_i}^{r_o}\left[r\left(\frac{d^2\psi}{dr^2}\right)^2 + \frac{1}{r}\psi^2\right]dr$$

$$k_1 = -\frac{\pi h}{2}\int_{r_i}^{r_o}\left[\sigma_{rr}\left(\frac{d\psi}{dr}\right)^2 + \sigma_{\theta\theta}\left(\frac{\psi}{r}\right)^2\right]dr \quad (14)$$

Equations (13) allow the rotor and the suspension to be treated as a single rigid body having two degrees of freedom connected to the drive shaft by a massless suspension.

The parameter a represents the equivalent inertia of the plate about the rotor's principal axes Ox and Oy, and b is an inertia factor that determines the portion of the plate loading due to Ω which is transmitted to the rotor. The quantity $(K_o - n^2k_1)$ represents the stiffness of the equivalent suspension where K_o is the stiffness of the nonrotating plate and is a function of preload and plate flexibility and k_1 represents the reduction in stiffness due to centrifugal loading. It should be appreciated that the magnitude of k_1 is determined by the inplane fixing between the drive shaft, plate, and rotor. For example, if the rotor and the drive shaft are assumed rigid, k_1 is positive. When rotor elasticity is considered its value decreases and in the limiting case – unconstrained radial displacement – k_1 is negative. It will be shown that the values of K_o and k_1 are important and have a considerable influence on the value of the gyro's running speed.

The response of the gyroscope will depend on the input Ω. To obtain an understanding of the characteristics of the instrument it is necessary to evaluate the behavior of the rotor due to standard test inputs. The free response and responses to a constant rate and a vibratory input will therefore be determined.

3.1 Free Motion. If $\Omega = 0$ the equations describing the free motion of the gyroscope follow from (13) as

$$\beta_x = \sum_{j=1}^{2}\beta_{oj}\sin(p_j t + \eta_j)$$

$$\beta_y = \sum_{j=1}^{2}\lambda_j\beta_{oj}\cos(p_j t + \eta_j), \quad (15)$$

where p_j is a natural frequency of free vibration and is given by the roots of

$$[np_j(C+2a)]^2 - [(K_o - n^2(a+k_1)) - p_j^2(A+a)]^2 = 0$$

and

$$\lambda_j = .[K_o - n^2(a+k_1) - p_j^2(A+a)]/np_j(C+2a). \quad (16)$$

The solutions of (16) yields two roots which are functions of rotor speed n.

$$p_j = \frac{n(C+2a)}{2(A+a)}\left[1 \pm \left[1 + \frac{4(A+a)(K_o - n^2(a+k_1)}{n^2(C+2a)^2}\right]^{1/2}\right] \quad (17)$$

When $n = 0$ the roots of (17) coincide at $p_{1,2} \approx \sqrt{K_o/A+a}$. As n is increased the roots separate. The highest natural frequency p_2 increases steadily with n and at high speeds approaches the nutational frequency Cn/A of the free rotor. The lower frequency p_1 decreases with increasing n and for large values of n approaches a value $(K_o - n^2(a+k_1))/nC$. It is of some importance to note that p_1 is zero when $n = \omega = [K_o/(a+k_1)]^{1/2}$. This indicates the existence of a tuning condition and since the natural frequencies of the tuned gyro correspond to those of an ideal free disk, i.e., $p_1 = 0$ and $p_2 = Cn/A$, it may be implied that tuning produces a zero stiffness suspension. When run tuned, the rotor tend to behave as a free body decoupled from the motion of the drive shaft and supporting casing.

It is shown that the tuning condition is only a function of the plate parameter K_o, k_1 and a. Since the value of k_1 is influenced by the radial expansion of the rotor due to centrifugal loading it can be appreciated that any preload introduced by thermal stressing must be carefully calculated so as to ensure tuning at the correct speed. Furthermore it is also desirable to make $(a+k_1)$ as large as possible so that the tuning equation $K_o - n^2(a+k_1) = 0$ is not ill conditioned. Interpretation of k_1 indicates that this can only be achieved if the radial stiffness of the plate is less then that of the rotor. The greater the difference in radial stiffness the more well defined is the tuning speed.

$$\beta_x = \Theta$$
$$\beta_y = 0 \quad (20)$$

The rotor spin axis maintains it initial offset without drift and a *stationary* nodal diameter is produced in the disk.

3.2 Response to Constant Rate Input. When a constant rate input Ω is applied about the case-fixed axis OX, the steady-state solution of (15) shows that the rotor takes up a steady position about OY given by

$$\beta_y = \frac{n(C+2b)\Omega}{K_o - n^2(a+k_1)} \quad (21)$$

The magnitude of β_y is directly proportional to the applied rate and (21) indicates that the untuned gyroscope is capable of functioning as a rate measuring device.

If the gyro is tuned, the character of the steady-state response changes and can be shown to be given by

$$\beta_x = -\left(\frac{C+2b}{C+2a}\right).\Omega t \approx -\Omega t$$

$$\beta_y = 0 \quad (22)$$

In this instance a rate input produces a steady rotation of the rotor about OX and in a direction that tends to maintain the spin axis fixed in space. Thus if the rotor inertia C is selected such that $C >> 2a$ and $2b$, then (22) indicates that the tuned gyro will provide a true measure of the casing displacement, and thereby an inertial reference.

3.3 Response to Vibratory Input. Let the vibratory input to the casing be represented by

$$\Omega = s\Phi\cos(st+\eta) \quad (23)$$

where it will be assumed that $n >> s\Phi$.

The steady-state response of the rotor is

$$\beta_x = \Phi s^2.\ \frac{[(A+b)[[K_o - n^2(a+k_1)] - s^2(A+a)] + n^2(C+2a)(C+2b)]\sin(st+\eta)}{[(K_o - n^2(a+k_1) - s^2(A+a))^2 - (C+2a)^2n^2s^2]}$$

$$\beta_x = \Phi\frac{[(C+2a)(C+2b)n^2 - (A+a)(A+b)s^2]}{[(A+a)^2s^2 - (C+2a)^2n^2]}\sin(st+\eta) \quad (24)$$

If the factors λ_1 and λ_2 are calculated, the shape traced by the extremity of the rotor spin axis may be determined for each mode of vibration. From (16) these ratios are given by $\lambda_1 \doteqdot 1$ and $\lambda_2 \doteqdot -1$. For the first mode and for rotor speeds $n < \omega$ the tip of the rotor axis traces approximately a circle in the opposite direction to that of rotor spin. When $n > \omega$ the direction of the orbit changes and the tip of the rotor spin axis moves in the same direction to that of rotor spin. In the limiting case, when $n = \omega$ the rotor spin axis remains stationary. The motion of the rotor axis associated with the second mode is again approximately a circle but this time the displacement occurs in the same direction to that of rotor spin for all values of n.

If the gyro is now tuned the solution of equation (13) takes the form

$$\beta_x = \beta_{01} + \beta_{02}\sin(p_2t+\eta_2)$$
$$\beta_y = \beta_{01} - \beta_{02}\frac{p_2(A+a)}{\omega(C+2a)}\cos(p_2t+\eta_2) \quad (19)$$

For example, if at $t=0$ the rotor is displaced Θ about OX and then released from rest it follows from (19) that the resulting motion is simply

The foregoing analysis shows that the rotor responds about both OX and OY and that the tip of the spin axis traces out an elliptical orbit with frequency s. For the untuned gyro it follows that resonance occurs when s coincides with a natural frequency p_i.

When the gyro is tuned the expressions for the β_x and β_y simplify and are given by

$$\beta_x = \Phi\frac{[(C+2a)(C+2b)n^2 - (A+a)(A+b)s^2]}{[(A+a)^2s^2 - (C+2a)^2n^2]}\sin(st+\eta)$$
$$\beta_y = .\Phi ns.\ \frac{(2A-C)(a-b)}{[(A+a)^2s^2 - (C+2a)^2n^2]}\cos(st+\eta). \quad (25)$$

These expressions show that the tuned rotor will only resonate when s is equal to the highest natural frequency,

$$p_2 = n\left(\frac{(C+2a)}{A+a}\right)$$

and that the resonant motion occurs about OX and OY with equal amplitude.

At this point it is useful to contrast the performance of this type of gyroscope with that of other tunable instruments – the Oscillogyro and the Hooke's Joint Gyroscope – particularly

in the case where the excitation frequency s is at twice rotor frequency.

It is well known, [1], that if either the Oscillogyro or the Hooke's Joint Gyroscope are subjected to vibratory inputs at frequency $s = 2\omega$ a steady drift of the rotor spin axis occurs at a rate proportional to the amplitude and phase of the vibration. This phenomenon, referred to as 2ω drift, limits their performance. If we set $s = 2\omega$ in equation (25) the response of the gyro described in this paper becomes

$$\beta_x = -\Phi\frac{(2A+C+2(a+b))}{(2A+C+4a)}.\sin(2nt+\eta)$$

$$\beta_y = 2\Phi\frac{(a-b)}{(2A+C+4a)}.\cos(2nt+\eta) \tag{26}$$

It is seen that this design of gyroscope is insensitive to 2ω vibrations insofar as no resultant drift of the rotor spin axis occurs. This result can readily by appreciated by examining equations (13). Because of the assumed symmetry of the rotor and its suspension, the forcing term associated with the input excitation is not modulated at twice running frequency – this modulation occurs in the case of the single gimbal Hooke's Joint gyroscope and the Oscillogyro – and therefore does not give rise to a steady torque that will be interpreted as a constant rate input.

4 Conclusions

The dynamics of an elastically supported gyroscope consisting of a rotor mounted on a heavy circular plate has been considered, and approximate equations of motion have been established using a mode shape consistent with the first mode of vibration of the stationery plate. Using these equations it has been shown that the gyroscope possesses two natural frequencies, p_1 and p_2 which are functions of rotor speed n. The highest natural frequency p_2 increases, almost linearly with n, whereas p_1 decreases. It has also been shown that it is possible to tune the gyroscope by making $p_1 = 0$. This condition is achieved by matching the dynamical characteristics of the plate suspension with the rotor speed and enables the rotor to behave approximately as a free spinning body.

When an externally applied rate of turn is applied to the supporting casing the steady-state displacement of the untuned rotor is proportional to the applied rate and occurs about an axis perpendicular to the input axis. The untuned gyroscope therefore acts as a two-axis rate sensor. If the gyroscope is tuned, the displacement of the rotor is proportional to the applied displacement and occurs about an axis so as to maintain the rotor in a fixed position with respect to inertial space.

The response of the rotor to harmonic inputs has been evaluated and it has been shown that the performance of the gyroscope as a rate or displacement sensor is not seriously affected by vibrations at twice rotor speed.

References

1 Walley, R., Holgate, M. J., and Maunder, L., "The Oscillogyro," *JMES*, Vol. 9, No. 1, 1967, pp. 55–61.

2 Howe, E. H., and Savet, P. H., "The Dynamically Tuned Free Rotor Gyro," *Control Engineering*, June 1964, pp. 67–72.

3 Bulman, D. N., and Maunder, L., "Dynamics of a Dynatune Gyroscope," *JMES*, Vol. 22, No. 3, 1980, pp. 137–141.

4 Fox, C. H. J., and Burdess, J. S., "The Dynamic Characteristics of a Gyroscope With a Tuned Elastic Suspension," ASME JOURNAL OF APPLIED MECHANICS, Vol. 47, 1980, pp. 161–167.

5 Timoshenko, *Theory of Elasticity*, McGraw Hill, New York.

6 Timoshenko, and Woinowsky-Kreiger, *Theory of Plates and Shells*, McGraw Hill, New York,

7 Red, W. E., "Examination of the Response of a Flexible Circular Rotor Subjected to Specified Gyroscopic Rates," ASME *Journal of Engineering for Industry*, Nov. 1974, pp. 1297–1306.

Bifurcations in Three-Dimensional Motions of Articulated Tubes,

Part 1: Linear Systems and Symmetry[1]

A. K. Bajaj
Assistant Professor,
School of Mechanical Engineering,
Purdue University,
West Lafayette, Ind. 47907

P. R. Sethna
Professor and Head,
Department of Aerospace Engineering
and Mechanics,
University of Minnesota,
Minneapolis, Minn. 55455
Mem. ASME

Three-dimensional motions of a two-segment articulated tube system carrying a fluid and having rotational symmetry about the vertical axis are examined for bifurcating periodic solutions. As the flow rate through the tubes is increased past a critical value, the downward vertical position of equilibrium gets unstable and bifurcates into two qualitatively different kinds of periodic motions. The mathematical problem is more general than that occurring in the Hopf bifurcations and the method of analysis used is the method of Alternate Problems. Since physical systems invariably have some asymmetry, the analysis takes into account these symmetry-breaking perturbations. In Part 1 of this two-part paper, symmetry properties of the system and the linear stability are discussed.

1 Introduction

Recent developments in the study of flow-induced motions of tubes carrying a fluid started with the work of Benjamin [1,2] on articulated tubes. Much of the early work is concerned with linear analysis of the stability of initially straight tubes for motions in a plane. Among the references, the works of Gregory and Paidoussis [3,4], Paidoussis and Issid [5], and Herrmann and Nemat-Nasser [6] may be mentioned. For linear analysis of three-dimensional motions of continuous tubes there is the work of Lundgren, Sethna, and Bajaj [7]. Nonlinear analysis for linearly unstable planar motions has been done by Holmes [8], Rousselet and Herrmann [9], and Bajaj, Sethna, and Lundgren [10].

In this paper we study three-dimensional nonlinear motions of articulated tubes. The analysis is made as simple as possible by treating the case of only two tubes. Furthermore, we restrict the study to only those cases where the static solution breaks up into periodic motions. Even under these restrictions the system exhibits a wide variety of behavior.

The mathematical problem is a problem in bifurcation theory in systems with rotational symmetry. It will be shown that as the flow velocity is increased beyond a critical value, the straight position of the tube becomes unstable and depending on the remaining system parameters, develops into two qualitatively different types of nonlinear periodic motions. The equilibrium position loses stability because a *double* pair of complex eigenvalues of the linearized system crosses the pure imaginary axis from the left to the right half of the complex plane. The nonlinear phenomena exhibited are more complicated than those associated with Hopf bifurcations [11]. For example supercritical bifurcations [11] may not be stable in contrast to the case of Hopf bifurcations.

This problem in addition to its intrinsic physical and mathematical interest has the potential for secondary and higher order bifurcations, perhaps, eventually leading to chaotic motions reminiscent of the Bernard problem. Furthermore, we here have the advantage of having to treat a mathematical problem that is only finite dimensional. In this context the present work can be viewed as a study of the simplest bifurcation in this system.

The mathematical analysis given here is based on the work of Bajaj [12, 13] on general discrete dynamical systems with rotational symmetry. In the interest of brevity we give only a few of the mathematical details and rely heavily on these references.

In this first part of this work, the equations of motion of the articulated tubes system are presented along with a discussion of their symmetry properties. We also discuss the stability of the downward vertical equilibrium position of the tubes system. The nonlinear analysis for bifurcating solutions is carried out in the second part of this paper.

2 Equations of Motion

In the following, we derive the equations of motion for three-dimensional motions of a two-segment articulated tube system. The system consists of a vertically hanging articulated tube made of two segments. The fluid enters the tube at the top and after its passage through the tube, it is discharged, tangentially to the end of the tube, to the atmosphere. A Cartesian coordinate system is fixed at the top of the tube where the fluid enters with the Z-axis coinciding with the downward vertical position. X and Y-axes then define the position coordinates in the plane normal to the Z-axis.

The basic assumptions are as follows:

[1]This work was supported by funds from the National Science Foundation under Grant NSF-CME-7921351.

Contributed by the Applied Mechanics Division for publication in the JOURNAL OF APPLIED MECHANICS.

Discussion on this paper should be addressed to the Editorial Department, ASME, United Engineering Center, 345 East 47th Street, New York, N.Y. 10017, and will be accepted until two months after final publication of the paper itself in the JOURNAL OF APPLIED MECHANICS. Manuscript received by ASME Applied Mechanics Division, August 1981; final revision, March, 1982.

1. The fluid is incompressible. The velocity profile of the fluid at any cross section is uniform and the velocity of fluid relative to the tubes is constant.

2. Both tubes have the same circular cross section and the diameters of the tubes is small compared to their lengths.

3. The bending stiffnesses of the joints have radial symmetry and the elastic restoring forces are linearly dependent on the angles between the center lines of adjacent tubes.

4. The joints have no torsional stiffness.

Following Benjamin [1], the equations of motion of the articulated tubes system are given by

$$\frac{d}{dt}\left(\frac{\partial \mathcal{L}}{\partial \dot{q}_i}\right) - \frac{\partial \mathcal{L}}{\partial q_i} = -MU(\dot{\mathbf{R}} + U\tau)\cdot\frac{\partial \mathbf{R}}{\partial q_i}, \quad i=1,2,3,4 \tag{1}$$

where q_i, $i=1,2,3,4$ are the generalized coordinates, $\mathcal{L} = T_1 + T_2 - V_1 - V_2$, T_1 and V_1 are, respectively, kinetic and potential energies associated with the tube system itself, T_2 and V_2 are the corresponding quantities for the contained fluid, $\mathbf{R}$ and $\dot{\mathbf{R}}$ are, respectively, the position and velocity vectors of the free end, τ is the unit vector tangent to the free end, and M and U are, respectively, the mass per unit length and the velocity of the fluid relative to the tubes.

As mentioned in the Introduction, we will see that motions of the system are of two qualitatively different kinds. One kind occurs in a vertical plane passing through the Z-axis and the other can be viewed as circular motion around the vertical axis. These motions cannot be analyzed in a unified manner with any form of polar coordinates since equations in these coordinates become singular for motions passing through the vertical axis. Therefore, a reference frame consisting of two orthogonal vertical planes OXZ and OYZ has been used. If, however, the motions passing through the vertical axis are excluded, an alternate simpler procedure utilizing polar coordinates can be used.

For the two-segment system, let us choose u_{11}, u_{12}, u_{21}, and u_{22} as the generalized coordinates. Here u_{11} and $u_{11} + u_{12}$ are, respectively, the position coordinates along the X-axis of the end points of the upper and lower tube segments. Similarly u_{21} and $u_{21} + u_{22}$ are, respectively, the position coordinates along the Y-axis. The system kinetic and potential energies can then be shown to be

$$\begin{aligned} T_1 + T_2 = {} & \frac{1}{6}(m+M)(l_1+3l_2)(\dot{u}_{11}^2 + \dot{u}_{21}^2 + \dot{z}_1^2) \\ & + \frac{1}{6}(m+M)l_2(\dot{u}_{12}^2 + \dot{u}_{22}^2 + \dot{z}_2^2) + \frac{1}{2}MU^2(l_1+l_2) \\ & + \frac{1}{2}(m+M)l_2(\dot{u}_{11}\dot{u}_{12} + \dot{u}_{21}\dot{u}_{22} + \dot{z}_1\dot{z}_2) \\ & + MU(\dot{u}_{11}u_{12} + \dot{u}_{21}u_{22} + \dot{z}_1 z_2) \end{aligned} \tag{2}$$

and

$$\begin{aligned} V_1 + V_2 = {} & (m+M)g\left[\left(\frac{1}{2}l_1 + l_2\right)(l_1 - z_1) + \frac{1}{2}l_2(l_2 - z_2)\right] \\ & + \frac{1}{2}(k_1\phi_1^2 + k_2\phi_2^2) \end{aligned} \tag{3}$$

where

$$z_1^2 = l_1^2 - (u_{11}^2 + u_{21}^2) \quad \text{and} \quad z_2^2 = l_2^2 - (u_{12}^2 + u_{22}^2)$$

In (2) and (3), l_1 and l_2 are the lengths of the upper and lower segments, m is the mass per unit length for each tube, k_1 and k_2 are the bending stiffnesses of the upper and lower joints, ϕ_1 is the acute angle between the upper tube and the Z-axis, and ϕ_2 is the acute angle between the two tube segments.

The position vector $\mathbf{R}$ and the unit tangent vector τ defining the generalized forces in (1) are

$$\mathbf{R} = (u_{11}+u_{12})\mathbf{i} + (u_{21}+u_{22})\mathbf{j} + (z_1+z_2)\mathbf{k} \tag{4}$$

and

$$\tau = \frac{1}{l_2}(u_{12}\mathbf{i} + u_{22}\mathbf{j} + z_2\mathbf{k})$$

where $\mathbf{i}$, $\mathbf{j}$, and $\mathbf{k}$ are the unit vectors along the three coordinate axes.

We study small nonlinear motions of the system close to its vertical equilibrium position; that is, when u_{11}, u_{12}, u_{21}, and u_{22} are small and therefore retain only linear and cubic terms in the equations of motion. We now introduce nondimensional variables and parameters:

$$\begin{aligned} & x_{11} = \frac{u_{11}}{l_1}, \quad x_{21} = \frac{u_{21}}{l_1}, \quad x_{12} = \frac{u_{12}}{l_2}, \quad x_{22} = \frac{u_{22}}{l_2}, \\ & a = \frac{l_1}{l_2}, \ \kappa = \frac{k_1}{k_2}, \quad \beta = \frac{3M}{m+M}, \quad \rho = U\left[\frac{(m+M)l_2}{3k_2}\right]^{1/2}. \\ & G = \frac{(m+M)}{2k_2}gl_2^2 \quad \text{and} \quad \bar{t} = t\left[\frac{3k_2}{(m+M)l_2^3}\right]^{1/2}. \end{aligned} \tag{5}$$

Taking into account (2)–(4), the equations of motion (1) then take the form:

$$\begin{aligned} & a^2(a+3)\ddot{x}_{11} + \frac{3}{2}a\ddot{x}_{12} + a^2\beta\rho\dot{x}_{11} + 2a\beta\rho\dot{x}_{12} + a\beta\rho^2(x_{12}-x_{11}) \\ & + a(a+2)Gx_{11} + \kappa x_{11} + (x_{11}-x_{12}) = -a^2(a+3)x_{11}(\dot{x}_{11}^2 + \dot{x}_{21}^2 \\ & + x_{11}\ddot{x}_{11} + x_{21}\ddot{x}_{21}) - \frac{3}{2}ax_{11}(\dot{x}_{12}^2 + \dot{x}_{22}^2 + x_{12}\ddot{x}_{12} + x_{22}\ddot{x}_{22}) \\ & - 2a\beta\rho x_{11}(x_{21}\dot{x}_{21} + x_{22}\dot{x}_{22}) + x_{11}(x_{11}^2 + x_{21}^2)\left\{-\frac{1}{2}a(a+2)G \right. \\ & \left. - \frac{2}{3}\kappa - \frac{1}{2} + \frac{a\beta\rho^2}{2}\right\} + x_{11}(x_{12}^2 + x_{22}^2)\left\{\frac{1}{2} - \frac{\beta a\rho^2}{2}\right\} \\ & - \frac{1}{6}(x_{11}-x_{12})\{(x_{11}-x_{12})^2 + (x_{21}-x_{22})^2\} - \beta\rho a^2 x_{11}(x_{11}\dot{x}_{11} \\ & + x_{21}\dot{x}_{21}) + 0(|\mathbf{x}|^5 + |\dot{\mathbf{x}}|^5), \end{aligned} \tag{6}$$

$$\begin{aligned} & a^2(a+3)\ddot{x}_{21} + \frac{3}{2}a\ddot{x}_{22} + \beta\rho a^2\dot{x}_{21} + 2a\beta\dot{x}_{22} + a\beta\rho^2(x_{22}-x_{21}) \\ & + a(a+2)Gx_{21} + \kappa x_{21} + (x_{21}-x_{22}) = -a^2(a+3)x_{21}(\dot{x}_{11}^2 + \dot{x}_{21}^2 \\ & + x_{11}\ddot{x}_{11} + x_{21}\ddot{x}_{21}) - \frac{3}{2}ax_{21}(\dot{x}_{12}^2 + \dot{x}_{22}^2 + x_{12}\ddot{x}_{12} + x_{22}\ddot{x}_{22}) \\ & - 2a\beta\rho x_{21}(x_{12}\dot{x}_{12} + x_{22}\dot{x}_{22}) + x_{21}(x_{11}^2 + x_{21}^2)\left\{-\frac{1}{2}a(a+2)G \right. \\ & \left. - \frac{2}{3}\kappa - \frac{1}{2} + \frac{a\beta\rho^2}{2}\right\} + x_{21}(x_{12}^2 + x_{22}^2)\left\{\frac{1}{2} - \frac{\beta a\rho^2}{2}\right\} \\ & - \frac{1}{6}(x_{21}-x_{22})\{(x_{11}-x_{12})^2 + (x_{21}-x_{22})^2\} - \beta\rho a^2 x_{21}(x_{11}\dot{x}_{11} \\ & + x_{21}\dot{x}_{21}) + 0(|\mathbf{x}|^5 + |\dot{\mathbf{x}}|^5), \end{aligned} \tag{7}$$

$$\begin{aligned} & \frac{3}{2}a\ddot{x}_{11} + \ddot{x}_{12} + \beta\rho\dot{x}_{12} + Gx_{12} + (x_{12}-x_{11}) = -x_{12}[(\dot{x}_{12}^2 + \dot{x}_{22}^2 \\ & + x_{12}\ddot{x}_{12} + x_{22}\ddot{x}_{22}) + \frac{3}{2}a(\dot{x}_{11}^2 + \dot{x}_{21}^2 + x_{11}\ddot{x}_{11} + x_{21}\ddot{x}_{21})] \\ & - \frac{1}{2}(1+G)x_{12}(x_{12}^2 + x_{22}^2) + \frac{1}{2}x_{12}(x_{11}^2 + x_{21}^2) + \frac{1}{6}(x_{11}-x_{12}) \\ & \{(x_{11}-x_{12})^2 + (x_{21}-x_{22})^2\} - \beta\rho x_{12}(x_{12}\dot{x}_{12} + x_{22}\dot{x}_{22}) \\ & + 0(|\mathbf{x}|^5 + |\dot{\mathbf{x}}|^5), \end{aligned} \tag{8}$$

and

$$\frac{3}{2}a\ddot{x}_{21} + \ddot{x}_{22} + \beta\rho\dot{x}_{22} + Gx_{22} + (x_{22}-x_{21}) = -x_{22}[(\dot{x}_{12}^2 + \dot{x}_{22}^2$$

$$+x_{12}\ddot{x}_{12}+x_{22}\ddot{x}_{22})+\frac{3}{2}a(\dot{x}_{11}{}^2+\dot{x}_{21}{}^2+x_{11}\ddot{x}_{11}+x_{21}\ddot{x}_{21})]$$

$$-x_{22}(x_{12}{}^2+x_{22}{}^2)\frac{1}{2}(1+G)+\frac{1}{2}x_{22}(x_{11}{}^2+x_{21}{}^2)+\frac{1}{6}(x_{21}-x_{22})$$

$$\{(x_{11}-x_{12})^2+(x_{21}-x_{22})^2\}-\beta\rho x_{22}(x_{12}\dot{x}_{12}+x_{22}\dot{x}_{22})$$

$$+0(|\mathbf{x}|^5+|\dot{\mathbf{x}}|^5), \tag{9}$$

Here x_{11} and x_{12} are the nondimensional coordinates along the X-axis, x_{21} and x_{22} are the coordinates along the Y-axis, $\tilde{t}$ is the nondimensional time, and $\mathbf{x} = (x_{11}, x_{12}, x_{21}, x_{22})^T$.

The system depends on five dimensionless parameters, a, κ, β, ρ, and G. The parameter "a" is the "length ratio" and "κ" is the "stiffness ratio." It is the ratio of stiffness of the upper joint to the lower joint. The "mass ratio" β is zero for the solid tube and takes the maximum value three when the tube thickness is zero. The "flow velocity" in dimensionless form is denoted by ρ, and G is the dimensionless gravitation parameter.

We now convert equations (6)–(9) into a first-order vector form.

Let,

$$\mathbf{z} \equiv (\mathbf{z}_1,\mathbf{z}_2)^T = (x_{11}, x_{12}, \dot{x}_{11}, \dot{x}_{12}, x_{21}, x_{22}, \dot{x}_{21}, \dot{x}_{22})^T \tag{10}$$

with $\mathbf{z}_i \in \mathbb{R}^4$, $i=1,2$. The system equations then take the form

$$\dot{\mathbf{z}} = \mathbf{A}(\rho)\mathbf{z} + \mathbf{h}(\mathbf{z},\rho), \tag{11}$$

where

$$\mathbf{A} = \begin{bmatrix} \hat{\mathbf{A}} & 0 \\ 0 & \hat{\mathbf{A}} \end{bmatrix} \tag{12}$$

is a 8×8 constant matrix dependent on the parameters with

$$\hat{\mathbf{A}} \equiv \begin{bmatrix} 0 & 0 & 1 & 0 \\ 0 & 0 & 0 & 1 \\ -\frac{A}{(4a+3)} & -\frac{B}{(4a+3)} & -\frac{4\beta\rho}{(4a+3)} & -\frac{2\beta\rho}{a(4a+3)} \\ -\frac{C}{(4a+3)} & -\frac{D}{(4a+3)} & \frac{6a\beta\rho}{(4a+3)} & -\frac{4a\beta\rho}{(4a+3)} \end{bmatrix} \tag{13}$$

and where

$$A = \frac{4(1+\kappa)}{a^2} + \frac{1}{a}(6-4\beta\rho^2) + \frac{4}{a}(a+2)G,$$

$$B = \frac{1}{a}(4\beta\rho^2-6) - \frac{4}{a^2} - \frac{6G}{a},$$

$$C = 6\beta\rho^2 - 4(a+3) - \frac{6(1+\kappa)}{a} - 6G(a+2)$$

and

$$D = \frac{6}{a} + (4a+12-6\beta\rho^2) + 4G(a+3).$$

For the nonlinear function $\mathbf{h}$ in (11), we note that its components h_1, h_2, h_5, and h_6 are zero. The remaining and nonzero components are given in Appendix A.

Equations (6)–(9) have some symmetry properties that play a crucial role in the analysis.

3 Symmetry Properties of the System

From the assumptions 2 and 3 it is clear that the system is invariant to rotations about the Z-axis. This is exhibited mathematically by the following conditions, which are satisfied by the matrix $\mathbf{A}$ and the vector $\mathbf{h}$.

$$\tilde{\tilde{\mathbf{S}}}(\theta)\,\mathbf{A}(\rho) = \mathbf{A}(\rho)\,\tilde{\tilde{\mathbf{S}}}(\theta),$$

and

$$\tilde{\tilde{\mathbf{S}}}(\theta)\,\mathbf{h}(\mathbf{z},\rho) = \mathbf{h}(\tilde{\tilde{\mathbf{S}}}(\theta)\mathbf{z},\rho) \tag{14}$$

where $\tilde{\tilde{\mathbf{S}}}(\theta)$ is the one-parameter rotation matrix defined by

$$\tilde{\tilde{\mathbf{S}}}(\theta) \equiv \begin{bmatrix} \cos\theta\,\mathbf{I}_4 & \sin\theta\,\mathbf{I}_4 \\ -\sin\mathbf{I}_4 & \cos\mathbf{I}_4 \end{bmatrix}, \quad \theta \in [0,2\pi) \tag{15}$$

and where $\mathbf{I}_4$ is the 4×4 identity matrix.

Equations (14) express the fact that the system equations remain invariant if the OXY system is rotated by angle θ about the Z-axis.

There is an additional symmetry in the equations which can be expressed mathematically as follows.

Let

$$\mathbf{g}(\mathbf{z},\rho) \equiv \mathbf{A}(\rho)\mathbf{z} + \mathbf{h}(\mathbf{z},\rho),$$

and

$$\mathbf{g}(\mathbf{z},\rho) \equiv \hat{\mathbf{g}}(\mathbf{z}_1,\mathbf{z}_2,\rho) = (\mathbf{g}_1,\mathbf{g}_2)^T$$

where $\hat{\mathbf{g}}_1$ and $\hat{\mathbf{g}}_2$ are four-vector functions. Then, from equations (6)–(9) and the definition of vector $\mathbf{z}$ in (10), it is evident that

$$\hat{\mathbf{g}}_1(\mathbf{z}_1,\mathbf{z}_2,\rho) = \hat{\mathbf{g}}_1(\mathbf{z}_1,-\mathbf{z}_2,\rho)$$

and

$$\hat{\mathbf{g}}_2(\mathbf{z}_1,\mathbf{z}_2,\rho) = \hat{\mathbf{g}}_2(-\mathbf{z}_1,\mathbf{z}_2,\rho) \tag{16}$$

and therefore $\hat{\mathbf{g}}_1(\mathbf{0},\mathbf{z}_2,\rho) = \hat{\mathbf{g}}_2(\mathbf{z}_1,\mathbf{0},\rho) = 0$ for all ρ.

The conditions (16) can be interpreted physically if we observe that the components $\mathbf{z}_1$ and $\mathbf{z}_2$ of the vector $\mathbf{z}$ represent motions in two orthogonal planes, the two planes intersecting at the axis of rotational symmetry. These conditions then express the fact that the motion in one plane is coupled to the motion in the orthogonal plane only through even terms.

We are interested in bifurcation phenomena. A bifurcation is said to occur when a system exhibits more than one, and usually qualitatively different states as some system parameter goes through a critical value. For most values of the system parameters the system eigenvalues are away from the pure imaginary axis and the linearized equations determine the system behavior. Bifurcation phenomena therefore usually occur when some eigenvalue(s) of the linearized system cross the pure imaginary axis. In view of this we study the behavior of the linearized system as a function of the system parameters. It will be seen that because of the system symmetry the eigenvalue behavior is more complicated than that for a simple divergence or flutter instability.

4 Analysis of the Linear System

The linearized system is given by

$$\dot{\mathbf{z}} = \mathbf{A}(\rho)\mathbf{z}. \tag{17}$$

Because of the structure of $\mathbf{A}$ it is important to observe that each *eigenvalue of* $\mathbf{A}$ *has multiplicity of at least two* and, in fact, one need only study the system

$$\dot{\tilde{\mathbf{y}}} = \hat{\mathbf{A}}\tilde{\mathbf{y}} \tag{18}$$

where $\hat{\mathbf{A}}$ is the 4×4 matrix given in (13). This system has been studied in great detail by Benjamin [1] and most of the discussion in this section follows his work closely.

The stability of the zero solution $\tilde{\mathbf{y}} = \mathbf{0}$ is determined by the eigenvalues of the matrix $\hat{\mathbf{A}}$ which are the roots of the characteristic equation

$$a^2\left(a+\frac{3}{4}\right)\lambda^4+a^2(a+1)\beta\rho\lambda^3+[(a+1)^3+\kappa+(a^3+4a^2+2a)G$$
$$-\left(\frac{3}{2}a^2+a-a^2\beta\right)\beta\rho^2\Big]\lambda^2+[(a+1)^2+\kappa+2(a^2+a)G$$
$$-a\beta\rho^2]\beta\rho\lambda+\kappa+\{(a+1)^2+\kappa+(a^2+2a)G-a\beta\rho^2\}G=0. \quad (19)$$

In this equation it is reasonable to consider a, β, κ, and G as fixed parameters that characterize a particular physical system. The stability problem may be regarded as a study of the changes in character of the four roots of (19) as the flow rate ρ is varied.

For small values of ρ, all the four roots of (19) are in the left half of the complex plane and therefore the vertical equilibrium position is stable. As ρ is increased, it reaches a value, $\rho = \rho_{cr}$, where some eigenvalue(s) of (19) cross the imaginary axis from left to right rendering the equilibrium position unstable. Depending on the other system parameters, a single real eigenvalue of (19) can become positive or a complex conjugate pair can cross the imaginary axis, which in turn means that the solution $\mathbf{z} = \mathbf{0}$ becomes unstable when a double eigenvalue goes through zero or a double pair of complex eigenvalues crosses the imaginary axis.

As already indicated in the Introduction, we are only intrested in those cases in which the loss of stability generates periodic motions. This is when complex conjugate pairs of eigenvalues cross the imaginary axis. By using Routh-Hurwitz criterion and arguments in [1] and [12] it can be shown that the minimum value of the flow rate required to produce this type of instability is given by the smaller of the roots of the following quadratic equation in $(a\beta\rho^2)$:

$$[6a^2+6a+1-4a\beta(1+a)](a\beta\rho^2)^2-2[(a+1)^2\{5a^2+5a+1$$
$$-2a(a+1)\beta\}+\kappa\{3a^2+3a+1-2a(a+1)\beta\}+2a(a+1)^2$$
$$\cdot\{3a+1-2a\beta\}G](a\beta\rho^2)+[(a+1)^2(2a+1)$$
$$+\kappa+2a(a+1)^2G]^2=0 \quad (20)$$

Let ρ_{cr} denote the least of the real positive roots of this equation. Then $\mathbf{z} = \mathbf{0}$ is stable for $\rho < \rho_{cr}$. At this critical flow rate, if the pure-imaginary pair of eigenvalues of (19) is $\pm i\omega_0$, it is readily obtained by substituting $\lambda = i\omega_0$ in (19) to give

$$\omega_0{}^2=\frac{[(a+1)^2+\kappa+2(a+1)aG-a\beta\rho^2]}{a^2(a+1)} \quad (21)$$

We are now interested in finding the nonlinear bifurcating periodic solutions of the system (11) for flow rates near ρ_{cr}. At $\rho = \rho_{cr}$, two coincident pairs of complex conjugate eigenvalues of the matrix $\mathbf{A}$ are on the imaginary axis while the rest of the eigenvalues are in the left half of the complex plane. This is precisely the situation treated in [12, 13] where bifurcations in general, discrete, dynamical systems with symmetries of the type defined in (14) and (16) have been discussed.

Let us next introduce Jordan canonical variables corresponding to the linearized system.

5 System in Jordan Canonical Variables

As is very well known, there exists a transformation $\mathbf{z} = \mathbf{C}\mathbf{y}$ such that the system (11) transforms into a form in which the matrix $\mathbf{A}$ is in Jordan canonical form. The 8×8 real matrix $\mathbf{C}$ is given by

$$\mathbf{C}=[2\mathbf{c}^1,2\mathbf{d}^1,2\mathbf{c}^2,2\mathbf{d}^2,\ldots.],$$

and it consists of column vectors that are the real and imaginary parts of the eigenvectors $\mathbf{a}^i$, $i = 1, 2, \ldots, 8$ of the eigenvalue problem

$$\mathbf{A}\mathbf{a}^i=\lambda_i\mathbf{a}^i \quad (22)$$

for the matrix $\mathbf{A}$. We assume, for convenience, that the eigenvalues have been ordered such that the first four eigenvalues correspond to the critical eigenvalues. These eigenvalues at critically ($\rho = \rho_{cr}$) are given by the coincident pairs $\pm i\omega_0$, $\pm i\omega_0$.

The system adjoint to the eigenvalue problem (22) is given by

$$\mathbf{A}^T\mathbf{b}^i=\lambda_i\mathbf{b}^i \quad (23)$$

for any eigenvalues λ_i of $\mathbf{A}$. Let $\mathbf{b}^j = \mathbf{e}^j + i\mathbf{f}^j$, $j = 1, 2, \ldots, 8$ and define the matrix $\mathbf{D}$ as

$$\mathbf{D}\equiv[\mathbf{e}^1,-\mathbf{f}^1,\mathbf{e}^2,-\mathbf{f}^2,\ldots.]$$

$\mathbf{b}^i$ have been normalized so that $\mathbf{a}^i\cdot\mathbf{b}^j = \delta_{ij}$; here $i,j=1,2,\ldots,8$. Then, using $\mathbf{z} = \mathbf{C}\mathbf{y}$, the system (11) is transformed into the form

$$\dot{\mathbf{y}}=\bar{\mathbf{A}}(\rho)\mathbf{y}+\mathbf{k}(\mathbf{y},\rho) \quad (24)$$

where

$$\bar{\mathbf{A}}(\rho)\equiv\mathbf{D}^T\mathbf{A}(\rho)\mathbf{C} \quad \text{and} \quad \mathbf{k}(\mathbf{y},\rho)\equiv\mathbf{D}^T\mathbf{h}(\mathbf{C}\mathbf{y},\rho)$$

Consider the system (24). At $\rho = \rho_{cr}$, $\bar{\mathbf{A}}(\rho_{cr})$ has two pairs of coincident pure imaginary eigenvalues $\pm i\omega_0$. To study the nonlinear behavior for small deviations from ρ_{cr}, let

$$\rho=\rho_{cr}+\mu$$

so that the system (24) can now be written as

$$\dot{\mathbf{y}}=\bar{\mathbf{A}}_0\mathbf{y}+\mu\bar{\mathbf{A}}_1(\mu)\mathbf{y}+\bar{\mathbf{k}}(\mathbf{y},\mu) \quad (25)$$

where

$$\bar{\mathbf{A}}_0=\bar{\mathbf{A}}(\rho_{cr}), \quad \mu\bar{\mathbf{A}}_1(\mu)=\bar{\mathbf{A}}(\rho_{cr}+\mu)-\bar{\mathbf{A}}_0$$

and

$$\bar{\mathbf{k}}(\mathbf{y},\mu)=\mathbf{k}(\mathbf{y},\rho_{cr}+\mu).$$

In (25) $\bar{\mathbf{A}}_0$ has the structure

$$\bar{\mathbf{A}}_0=\text{diag}(\mathbf{D}_{10},\mathbf{D}_{20}),$$

$$\mathbf{D}_{10}=\left[\begin{array}{cc:cc} 0 & \omega_0 & & \\ -\omega_0 & 0 & & 0 \\ \hdashline & & 0 & \omega_0 \\ & 0 & -\omega_0 & 0 \end{array}\right] \quad (26)$$

and $\mathbf{D}_{20}$ is the 4×4 matrix with all four eigenvalues in the left half of the complex plane.

The matrix $\bar{\mathbf{A}}_1(\mu)$ is also in block diagonal form with two blocks of 4×4 matrices each. In the limit as $\mu \to 0$ the upper nonzero block determines the rate of change of critical eigenvalues and is given by

$$\tilde{\mathbf{D}}_{110}=\left[\begin{array}{cc:cc} \xi & \tilde{\omega} & & \\ \tilde{\omega} & \xi & & 0 \\ \hdashline & & \xi & \tilde{\omega} \\ & 0 & \omega & 0 \end{array}\right] \quad (27)$$

where

$$\xi=\frac{d}{d\rho}(\text{Re}\lambda_1)\Big|_{\rho=\rho_{cr}} \quad \text{and} \quad \tilde{\omega}=\frac{d}{d\rho}(\text{Im}\lambda_1)\Big|_{\rho=\rho_{cr}}.$$

The rates ξ and $\tilde{\omega}$ can be easily shown to be determined by the relations [12],

$$\xi=\text{Re}\left\{\mathbf{b}^{1T}\frac{d\mathbf{A}(\rho)}{d\rho}\mathbf{a}^1\right\}_{\rho=\rho_{cr}}$$

and $$\tilde{\omega} = \mathrm{Im}\left\{\mathbf{b}^{1T}\frac{d\mathbf{A}(\rho)}{d\rho}\mathbf{a}^{1}\right\}_{\rho=\rho_{cr}} \tag{28}$$

which are arrived at by differentiating (22) and (23) with respect to ρ and then using the biorthogonality conditions.

The nonlinear function $\bar{\mathbf{k}}(\mathbf{y},\mu)$ in (25) can be obtained with some lengthy calculations from the nonlinear function $\mathbf{h}$ whose components are given in Appendix A. Since these expressions are very long, they shall not be presented here explicitly.

Now, for a real system any kind of symmetry is a mathematical idealization. For example, the stiffnesses k_1 and k_2 of the joints will, in general, not be radially symmetric. We thus wish to account for small asymmetries in the articulated tube system and therefore we will analyze the more general system

$$\dot{\mathbf{y}} = \bar{\bar{\mathbf{A}}}_0\mathbf{y} + \mu\bar{\bar{\mathbf{A}}}_1(\mu)\mathbf{y} + \alpha\bar{\bar{\mathbf{A}}}_2\mathbf{y} + \bar{\mathbf{k}}(\mathbf{y},\mu). \tag{29}$$

The parameter α is an additional parameter that determines the size of the asymmetry in the system whereas the structure of matrix $\bar{\bar{\mathbf{A}}}_2$ determines the manner in which the rotational symmetry of the system is destroyed. Since the latter can take many forms, we shall not specify $\bar{\bar{\mathbf{A}}}_2$ at present. In the second part of this work, we shall study some particular cases for their effect on the nature of the bifurcating periodic solutions of the symmetric system.

The system (25) or the more general system (29) with $\alpha = 0$ satisfies conditions similar to (14) with respect to a new matrix $\mathbf{S}^*(\theta)$ defined by $\mathbf{S}^*(\theta) \equiv \mathbf{D}^T\,\bar{\bar{\mathbf{S}}}(\theta)\mathbf{C}$ which can be shown to be of the form

$$\mathbf{S}^*(\theta) = \mathrm{diag}(\mathbf{S}_1{}^*(\theta), \mathbf{S}_2{}^*(\theta)), \quad \theta\epsilon[0,2\pi)$$

where

$$\mathbf{S}_1{}^*(\theta) = \cos\theta\mathbf{I}_4 + \sin\theta\mathbf{J}_4,$$

and where

$\mathbf{J}_4$ is the 4×4 matrix given by $\mathbf{J}_4 = \begin{bmatrix} \mathbf{0} & \mathbf{I}_2 \\ -\mathbf{I}_2 & \mathbf{0} \end{bmatrix}$.

The nonlinear function $\bar{\mathbf{k}}$ in (29) is not completely arbitrary and its form is determined by its invariance with respect to the matrix $\mathbf{S}^*(\theta)$. It is clearly odd in $\mathbf{y}$. As will be seen in the bifurcation analysis, the first approximation to periodic solutions is determined by the cubic terms in $\bar{k}_i$, $i=1,2,3,4$ in the critical variables y_i, $i=1,2,3,4$. Using symmetry arguments it can be shown [13] that there are at most 12 arbitrary constants B_i, $i=1,2,\ldots,12$ in these cubic terms. These arguments, along with the resulting general form of the functions $\bar{k}_i$, $i=1,2,3,4$, are given in Appendix B. Clearly, the constants B_i are functions of the critical eigenfunctions of the matrix $\mathbf{A}$ as well as the coefficients of the cubic terms in the nonlinear function $\mathbf{h}$.

We are now ready to analyze the nonlinear system (29) for bifurcating periodic solutions for small values of parameters μ and α. This analysis is carried out in the second part of this work.

References

1 Benjamin, T. B., "Dynamics of a System of Articulated Pipes Conveying Fluid. I. Theory," *Proc. Roy. Soc. London*, Series A. Vol. 261, 1961, pp 457–486.

2 Benjamin, T. B., "Dynamics of a System of Articulated Pipes Conveying Fluid. II. Experiments," *Proc. Roy. Soc. London*, Vol. 261, 1961, pp. 487–499.

3 Gregory, R. W., and Paidoussis, M. P., "Unstable Oscillation of Tubular Cantilevers Conveying Fluid, I. Theory," *Proc. Roy. Soc. London*, Series A, Vol. 293, 1966, pp. 512–527.

4 Gregory, R. W., and Paidoussis, M. P., "Unstable Oscillation of Tubular Cantilevers Conveying Fluid. II. Experiments," *Proc. Roy. Soc. London*, Series A, Vol. 293, 1966, pp. 528–542.

5 Paidoussis, M. P., and Issid, T. N., "Dynamic Stability of Pipes Conveying Fluid," *J. Sound and Vibrations*, Vol. 33, 1974, pp. 267–294.

6 Herrmann, G., and Namat-Nasser, S., "Instability Modes of Cantilevered Bars Induced by Fluid Flow Through Attached Pipes," *Int. J. of Sol. and Struct.*, Vol. 3, 1967, pp. 39–52.

7 Lundgren, T. S., Sethna, P. R., and Bajaj, A. K., "Stability Boundaries for Flow Induced Motions of Tubes With an Inclined Terminal Nozzle," *J. Sound and Vibrations*, Vol. 64, 1979, pp. 553–571.

8 Holmes, P. J., "Bifurcations to Divergence and Flutter in Flow Induced Oscillations: a Finite Dimensional Analysis," *J. Sound and Vibrations*, Vol. 53, 1977, pp. 471–503.

9 Rousselet, J., and Herrmann, G., "Flutter of Articulated Pipes at Finite Amplitude," ASME JOURNAL OF APPLIED MECHANICS, Vol. 44, 1977, pp. 154–158.

10 Bajaj, A. K., Sethna, P. R., and Lundgren, T. S., "Hopf Bifurcation Phenomena in Tubes Carrying a Fluid," *SIAM J. Appl. Math.*, Vol. 39, 1980, pp. 213–230.

11 Iooss, G., and Joseph, D. D., *Elementary Stability and Bifurcation Theory*, Springer-Verlag, New York, 1980.

12 Bajaj, A. K., "Bifurcation to Periodic Solutions in Rotationally Symmetric Discrete Mechanical Systems," Ph.D Thesis, University of Minnesota, 1981.

13 Bajaj, A. K., "Bifurcating Periodic Solutions in Rotationally Symmetric Systems," *SIAM J. Appl. Math.*, Vol. 42, Oct. 1982.

14 Sattinger, D. H., "Group Theoretic Methods in Bifurcation Theory," *Lecture Notes in Math.*, No. 762, Springer-Verlag, 1979.

APPENDIX A

The nonzero components of the nonlinear function $\mathbf{h}$ in (11) up to the cubic terms are as follows:

$$\begin{aligned}
h_3 &= [z_1(z_1^2+z_5^2)\{4A(a+3)/(4a+3) - 8(\kappa+1)/3a^2 \\
&\quad + (2\beta\rho^2-1)/a\} + z_1(z_2^2+z_6^2)\{6D/a(4a+3) + 4/3a^2 \\
&\quad - (2\beta\rho^2+1)/a\} + z_1(z_1z_2+z_5z_6)\{4B(a+3)/(4a+3) \\
&\quad + 6C/a(4a+3) + 4/3a^2 + 2/a\} - 4(a+3)z_1(z_3^2+z_7^2) \\
&\quad - 6z_1(z_4^2+z_8^2)/a + z_1(z_1z_3+z_5z_7)\{16\beta\rho(a+3)/(4a+3) \\
&\quad - 4\beta\rho\} + 8\beta\rho(a+3)z_1(z_1z_4+z_5z_8)/a(4a+3) \\
&\quad - 36\beta\rho z_1(z_2z_3+z_6z_7)/(4a+3) + \{24\beta\rho/(4a+3) \\
&\quad - 8\beta\rho/a\}z_1(z_2z_4+z_6z_8) + z_2(z_1^2+z_5^2)\{2/3a^2 - 9A/ \\
&\quad (4a+3) - 2/a\} + z_2(z_2^2+z_6^2)\{2/3a^2 - 6D/a(4a+3) \\
&\quad + 4/a\} + z_2(z_1z_2+z_5z_6)\{-4/3a^2 - 6C/a(4a+3) \\
&\quad - 9B/(4a+3) - 2/a\} + 6z_2(z_4^2+z_8^2)/a + 36\beta\rho z_2(z_2z_3 \\
&\quad + z_6z_7)/(4a+3) + z_2(z_2z_4+z_6z_8)\{6\beta\rho/a \\
&\quad - 24\beta\rho/(4a+4)\} + 9z_2(z_3^2+z_7^2) - 36\beta\rho z_2(z_1z_3 \\
&\quad + z_5z_7)/(4a+3) - 18\beta\rho z_2(z_1z_4+z_5z_8)/ \\
&\quad a(3a+3)]/(4a+3),
\end{aligned} \tag{A1}$$

$$\begin{aligned}
h_4 &= [z_1(z_1^2+z_5^2)\{4(\kappa+1)/a - 3\beta\rho^2 - 6Aa(a+3)/(4a+3) \\
&\quad + 2(a+3)/3\} + z_1(z_2^2+z_6^2)\{-9D/(4a+3) - 2/a + 3\beta\rho^2 \\
&\quad + 2(a+3)/3\} + z_1(z_1z_2+z_5z_6)\{-6Ba(a+3)/(4a+3) \\
&\quad - 9C/(4a+3) - 2/a - 4(a+3)/3\} + 6a(a+3)z_1(z_3^2+z_7^2) \\
&\quad 9z_1(z_4^2+z_8^2) + z_1(z_1z_3+z_5z_7)\{6a\beta\rho - 24a\beta\rho(a+3)/ \\
&\quad (4a+3)\} - 12\beta\rho(a+3)z_1(z_1z_4+z_5z_8)/(4a+3) \\
&\quad + 54a\beta\rho z_1(z_2z_3+z_6z_7)/(4a+3) + z_1(z_2z_4 \\
&\quad + z_6z_8)\{12\beta\rho - 36a\beta\rho/(4a+3)\} + z_2(z_1^2+z_5^2)\{6aA(a+3)/ \\
&\quad (4a+3) - 1/a + 4(a+3)/3\} + z_2(z_2^2+z_6^2)\{4D(a+3)/ \\
&\quad (4a+3) - 1/a - 8(a+3)/3\} + z_2(z_1z_2+z_5z_6)\{2/a \\
&\quad + 4C(a+3)/(4a+3) + 6aB(a+3)/(4a+3) + 4(a+3)/3\} \\
&\quad - 4(a+3)z_2(z_4^2+z_8^2) - 24\beta\rho a(a+3)z_2(z_2z_3+z_6z_7)/
\end{aligned}$$

$$(4a+3)+z_2(z_2z_4+z_6z_8)\{16a\beta\rho(a+3)/(4a+3)$$
$$-(4a+3)\beta\rho\}-6a(a+3)z_2(z_3^2+z_7^2+24\alpha\beta\rho(a+3)z_2(z_1z_3$$
$$+z_5z_7)/(4a+3)+12\beta\rho(a+3)z_2(z_1z_4+z_5z_8)/$$
$$(4a+3)]/(4a+3). \quad (A2)$$

The remaining components h_7, and h_8 are obtained, respectively, from h_3 and h_4 by replacing z_i, $i=1,2,3,4$ by z_{i+4} and z_j, $j=5,6,7,8$ by z_{j-4}. Also, the constants A, B, C, and D in the preceding expressions are as defined in (13).

APPENDIX B

The components $\tilde{k}_i$, $i=1,2,3,4$ of the nonlinear function $\tilde{\mathbf{k}}$ satisfy the condition

$$\mathbf{S}_1{}^*(\theta)\tilde{\mathbf{k}}(\tilde{\mathbf{y}},\mu)=\tilde{\mathbf{k}}(\mathbf{S}^*(\theta)\tilde{\mathbf{y}},\mu),\ \theta\epsilon[0,2\pi) \quad (B1)$$

where

$$\tilde{\mathbf{y}}\equiv(y_1,y_2,y_3,y_4)^T,\quad \tilde{k}_i(\tilde{\mathbf{y}},\mu)\equiv\tilde{k}_i(\mathbf{y},\mu),\quad i=1,2,3,4,$$
$$\mathbf{y}=(\tilde{\mathbf{y}},\mathbf{0})^T$$

and where $\mathbf{S}_1{}^*(\theta)$ is the symmetry matrix defined by

$$\mathbf{S}_1{}^*(\theta)=\cos\theta\mathbf{I}_4+\sin\theta\mathbf{J}_4,\quad \theta\epsilon[0,2\pi). \quad (B2)$$

Given (B1), our objective is to determine the most general form of $\tilde{\mathbf{k}}(\tilde{\mathbf{y}},\mu)$. This is accomplished in the following using ideas from Sattinger [14].

To find the most general form of $\tilde{\mathbf{k}}$ satisfying (B1), it is more convenient to work with the complex forms of $\tilde{\mathbf{k}}$ and $\mathbf{S}_1{}^*(\theta)$. Therefore, we first transform (B1) into a complex form.

We first note that $\mathbf{S}_1{}^*(\theta)$ can be written as $\mathbf{S}_1{}^*(\theta)=e^{\mathbf{J}_4\theta}$. Also, the matrix $\mathbf{J}_4$ can be diagonalized by the similarity transformation $\mathbf{P}^{-1}\mathbf{J}_4\mathbf{P}=\mathbf{\Lambda}$ where $\mathbf{\Lambda}=\mathrm{diag}(i,-i,i,-i)$ and $\mathbf{P}$ is composed of the eigenvectors of $\mathbf{J}_4$. Thus, $\mathbf{S}_1{}^*(\theta)=e^{\mathbf{J}_4\theta}=e^{\mathbf{P}\mathbf{\Lambda}\mathbf{P}^{-1}\theta}=\mathbf{P}e^{\mathbf{\Lambda}\theta}\mathbf{P}^{-1}$ and (B1) takes the form

$$\mathbf{e}^{\mathbf{\Lambda}\theta}\mathbf{G}(\mathbf{w},\mu)=\mathbf{G}(e^{\mathbf{\Lambda}\theta}w,\mu) \quad (B3)$$

where $\mathbf{w}\equiv\mathbf{P}^{-1}\tilde{\mathbf{y}}$ and $\mathbf{G}(\cdot,\mu)\equiv\mathbf{P}^{-1}\tilde{\mathbf{k}}(\mathbf{P}(\cdot),\mu)$. Here $\mathbf{w}$ and $\mathbf{G}$ are complex four-vectors.

Since Λ and, therefore, $e^{\Lambda\theta}$ are diagonal, it is easy to express the conditions (B3). Let

$$G_1(\mathbf{w},\mu)=\sum_{r+s+p+q=3}^{\infty}A_{rspq}\,w_1^r\bar{w}_1^s w_2^p\bar{w}_h^q \quad (B4)$$

where A_{rspq} are complex coefficients dependent on μ, where p, q, r, and s are non-negative integers, and were we have set $\mathbf{w}=(\bar{w}_1,w_1,\bar{w}_2,w_2)^T$. With this form of G_1, the first of the equations (B3) gives that r, s, p, and q must satisfy

$$r-s+p-q+1=0,\quad \forall\quad r,s,p,q\geq 0,\quad r+s+p+q\geq 3. \quad (B5)$$

Therefore, at the lowest order, the functions $\tilde{k}_1$ and $\tilde{k}_3$ are given by

$$\tilde{k}_1(\tilde{\mathbf{y}},\mu)=(y_1^2+y_3^2)\Big(\sum_{i=1}^{4}C_iy_i\Big)+(y_1y_2+y_3y_4)\Big(\sum_{i=1}^{4}D_iy_i\Big)$$
$$+(y_2^2+y_4^2)\Big(\sum_{i=1}^{4}E_iy_i\Big), \quad (B6)$$

and

$$\tilde{k}_3(\tilde{\mathbf{y}},\mu)=(y_1^2+y_3^2)\Big(\sum_{i=1}^{2}(C_iy_{i+2}-C_{i+2}y_i)\Big)$$
$$+(y_1y_2+y_3y_4)\Big(\sum_{i=1}^{2}(D_iy_{i+2}-D_{i+2}y_i)\Big)$$
$$+(y_2^2+y_4^2)\Big(\sum_{i=1}^{2}(E_iy_{i+2}-E_{i+2}y_i)\Big) \quad (B7)$$

where the real coefficients C_i, D_i, and E_i, $i=1,2,3,4$ depend on μ.

Expressions similar to (B6) and (B7) are obtained for $\tilde{k}_2$ and $\tilde{k}_4$ with C_i, D_i, and E_i replaced by F_i, G_i, and H_i, respectively, when the second of equations (B3) is considered. Thus, at the lowest order there are 24 arbitrary constants in $\tilde{\mathbf{k}}(\mathbf{y},\mu)$. We have, however, not yet accounted for the additional conditions (16). Taking these into account and noting that the two linearly independent eigenvectors corresponding to any coincident eigenvalues of $\mathbf{A}$ can be taken of the form $\mathbf{a}^1=(\mathbf{a}_1,\mathbf{0})^T$ and $\mathbf{a}^2=(\mathbf{0},\mathbf{a}_1)^T$, it can be easily shown that coefficients C_i, D_i, E_i, F_i, G_i, and H_i, $i=3,4$ are zero. The nonlinear functions $\tilde{k}_i$, $i=1,2,3,4$ are, therefore, given by

$$\tilde{k}_1(\tilde{\mathbf{y}},\mu)=(y_1^2+y_3^2)(B_1y_1+B_2y_2)+(y_1y_2+y_3y_4)(B_3y_1$$
$$+B_4y_2)+(y_2^2+y_4^2)(B_5y_1+B_6y_2),$$
$$\tilde{k}_2(\tilde{\mathbf{y}},\mu)=(y_1^2+y_3^2)(B_7y_1+B_8y_2)+(y_1y_2+y_3y_4)(B_9y_1$$
$$+B_{10}y_2)+(y_2^2+y_4^2)(B_{11}y_1+B_{12}y_2),$$
$$\tilde{k}_3(\tilde{\mathbf{y}},\mu)=(y_1^2+y_3^2)(B_1y_3+B_2y_4)+(y_1y_2+y_3y_4)(B_3y_3$$
$$+B_4y_4)+(y_2^2+y_4^2)(B_5y_3+B_6y_4),$$

and

$$\tilde{k}_4(\tilde{\mathbf{y}},\mu)=(y_1^2+y_3^2)(B_7y_3+B_8y_4)+(y_1y_2+y_3y_4)(B_9y_3$$
$$+B_{10}y_4)+(y_2^2+y_4^2)(B_{11}y_3+B_{12}y_4) \quad (B8)$$

where we have redefined all the coefficients. Clearly, there are only 12 real arbitrary constants.

A. K. Bajaj
Assistant Professor,
School of Mechanical Engineering,
Purdue University,
West Lafayette, Ind. 47907

P. R. Sethna
Professor and Head,
Department of Aerospace Engineering
and Mechanics,
University of Minnesota,
Minneapolis, Minn. 55455
Mem. ASME

Bifurcations in Three-Dimensional Motions of Articulated Tubes,

Part 2: Nonlinear Analysis[1]

The equations of motion of the two-segment articulated tube system, discussed in Part 1, are analyzed for bifurcating periodic solutions near critical flow velocities. In addition to the flow parameter, the system depends on four other parameters. Depending on the values of these parameters the system exhibits a wide variety of behavior. This behavior is studied in detail in several specific cases.

6 Determination of Periodic Solutions

In Part 1 of this paper it was shown that the downward vertical position of equilibrium of the two-segment articulated tube system becomes unstable when the flow velocity, ρ, reaches a critical value ρ_{cr}. This loss of stability is associated with two coincident pairs of complex conjugate eigenvalues crossing the imaginary axis. In this part of the paper, the nonlinear equations of motion of the system, which in standard form are given in (29), are analyzed for bifurcating periodic solutions.

There are many methods available for finding small periodic solutions of a weakly nonlinear system. For multiparameter systems, which is the case here, and especially when the scaling relationship between the small parameters and the amplitude of nonlinear oscillations is, apriori, unknown, either the method of Liapunov-Schmidt or the method of Alternate Problems is appropriate. The scaling that relates the amplitude of periodic solutions to the small parameters in the problem is ultimately suggested by the "bifurcation equations." Here we follow the latter method. We will present the basic ideas of the method of Alternate Problems. For the mathematical details the reader should consult references [1, 2].

Consider the system (29). At $\mu=\alpha=0$, the linearized system

$$\dot{\mathbf{y}}=\bar{\bar{\mathbf{A}}}_0\mathbf{y}$$

has two pairs of pure imaginary eigenvalues $\pm i\omega_0$, $\omega_0>0$. Thus, the linearized system at criticality has two pairs of periodic solutions of period $2\pi/\omega_0$. We are interested in finding periodic solutions of the complete system (29) when μ and α are nonzero but small. Although we do not know the period of the solutions of the nonlinear system, it is known that in the limit as parameters μ and α go to zero, it converges to the period of the periodic solutions of the linearized system at criticality. Let us assume that the unknown period is $T=2\pi/\omega$ and let $\tau=\omega t$. We introduce a new small parameter χ so that $\omega=\omega_0/(1+\chi)$. Then (29) becomes

$$\omega_0\dot{\mathbf{y}}=\bar{\bar{\mathbf{A}}}_0\mathbf{y}+\mathbf{F}(\mathbf{y},\mu,\alpha,\chi) \tag{30}$$

where

$$\mathbf{F}(\mathbf{y},\mu,\alpha,\chi)\equiv\chi\bar{\bar{\mathbf{A}}}_0\mathbf{y}+(1+\chi)\{\mu\bar{\bar{\mathbf{A}}}_1\mathbf{y}+\alpha\bar{\bar{\mathbf{A}}}_2\mathbf{y}+\bar{\mathbf{k}}(\mathbf{y},\mu)\} \tag{31}$$

and where $(\dot{\ })$ now denotes differentiation with respect to τ. We now obtain 2π-periodic solutions of the system (31).

We first define some operators in the context of the nonhomogeneous linear system

$$\omega_0\dot{\mathbf{y}}=\bar{\bar{\mathbf{A}}}_0\mathbf{y}+\mathbf{f}(t). \tag{32}$$

Let $P_2\pi$ be the space of continuous 2π-periodic $2n$-vector functions defined by

$$P_{2\pi}=\{\mathbf{g}:\ \mathbf{R}\rightarrow\ \mathbf{R}^{2n},\ \ \mathbf{g}\text{ continuous and }2\pi\text{-periodic, with norm }\|\mathbf{g}\|=\sup|\mathbf{g}(\tau)|\}$$
$$0\le\tau<2\pi$$

where $|\cdot|$ denotes the Eucledean norm in $\mathbf{R}^{2n}$. The $(2n\times 4)$-matrix functions $\Phi(\tau)$ and $\Psi(\tau)$ defined by

$$\Phi(\tau)=\exp\left(\frac{1}{\omega_0}\bar{\bar{\mathbf{A}}}_0\tau\right)(\mathbf{e}_1,\mathbf{e}_2,\mathbf{e}_3,\mathbf{e}_4), \tag{33}$$

$$\Psi(\tau)=\exp\left(-\frac{1}{\omega_0}\bar{\bar{\mathbf{A}}}_0{}^T\tau\right)(\mathbf{e}_1,\mathbf{e}_2,\mathbf{e}_3,\mathbf{e}_4) \tag{34}$$

are, respectively, a basis for the 2π-periodic solutions of the homogeneous part of the linear system (32) and its adjoint

$$\omega_0\dot{\mathbf{y}}=-\bar{\bar{\mathbf{A}}}_0{}^T\mathbf{y}. \tag{35}$$

Here $\mathbf{e}_i$, $i=1, 2, 3, 4$ denote $2n$-vectors with 1 in the ith entry and zero elsewhere.

Following Hale [2], we also define projection operators on $P_{2\pi}$ by

$$\mathbf{Uf}=\Phi(\cdot)\mathbf{P}^{-1}\int_0^{2\pi}\Phi^T(s)\mathbf{f}(s)\,ds$$

and

[1]This work was supported by funds from the National Science Foundation under Grant NSF-CME-7921351.

Contributed by the Applied Mechanics Division for publication in the JOURNAL OF APPLIED MECHANICS.

Discussion on this paper should be addressed to the Editorial Department, ASME, United Engineering Center, 345 East 47th Street, New York, N.Y. 10017, and will be accepted until two months after final publication of the paper itself in the JOURNAL OF APPLIED MECHANICS. Manuscript received by ASME Applied Mechanics Division, August, 1981; final revision, March, 1982.

$$\mathbf{Vf} = \mathbf{\Psi}(\cdot)\mathbf{Q}^{-1}\int_0^{2\pi} \mathbf{\Psi}^T(s)\mathbf{f}(s)\ ds \tag{36}$$

for any $\mathbf{f} \in P_2\pi$, where $\mathbf{P}$ and $\mathbf{Q}$ are 4×4 nonsingular constant matrices given by

$$\mathbf{P} = \int_0^{2\pi} \Phi^T(s)\Phi(s)\ ds, \quad \mathbf{Q} = \int_0^{2\pi} \mathbf{\Psi}^T(s)\mathbf{\Psi}(s)\ ds.$$

Note that $\mathbf{U}$ takes $P_{2\pi}$ onto the subspace of $P_{2\pi}$ spanned by the 2π-periodic solutions of $\omega_0\dot{\mathbf{y}} = \bar{\mathbf{A}}_0\mathbf{y}$. Similarly, $\mathbf{V}$ takes $P_{2\pi}$ onto the subspace of $P_{2\pi}$ spanned by the 2π-periodic solutions of (35). Also, let $\mathbf{E} = (\mathbf{I} - \mathbf{V})$ where $\mathbf{I}$ is the identity operator on $P_{2\pi}$.

We define one more operator K. If $\mathbf{f}(s) \in P_{2\pi}$ in (32), then $K\mathbf{Ef}$ is the particular integral of (32) with $\mathbf{Vf} = 0$ and $\mathbf{U}K\mathbf{Ef} = 0$. K is defined on the range of $\mathbf{E}$ and has a range that is contained in the range of the projection $(\mathbf{I} - \mathbf{U})$; furthermore, $K\mathbf{E}$ is a bounded linear operator on $P_{2\pi}$.

With these definitions, the problem of finding 2π-periodic solutions of the system (30) can be shown to be equivalent to finding solution $\mathbf{y}, \mathbf{y} \in P_{2\pi}$, of the alternate problem

$$\mathbf{y} = \mathbf{Uy} + K(\mathbf{I} - \mathbf{V})\mathbf{F}(\mathbf{y}, \mu, \alpha, \chi) \tag{37}$$

and

$$\mathbf{Vf}(\mathbf{y}, \mu, \alpha, \chi) = 0. \tag{38}$$

In terms of the familar perturbation procedure, equation (38) is equivalent to the usual solvability condition used to remove secular terms. The second term on the right-hand side of equation (37) then determines the unique solutions of the sequence of linear nonhomogeneous problems that arise after removing the secular terms while the first term $\mathbf{Uy}$ gives the solutions of the homogeneous linear systems.

In the spirit of the method of Alternate Problems, if we let $\mathbf{y} = \mathbf{y}_1 + \mathbf{y}_2$, the component $\mathbf{y}_1 = \mathbf{Uy}$ of the periodic solution $\mathbf{y}$ of (30) is composed of the solutions of the homogeneous part of equation (32) whereas the component $\mathbf{y}_2 = (\mathbf{I} - \mathbf{U})\mathbf{y}$ contains the higher harmonics. In view of this decomposition of $\mathbf{y}$ we have

$$\mathbf{y}_2 = K(\mathbf{I} - \mathbf{V})\mathbf{F}(\mathbf{y}_1 + \mathbf{y}_2, \mu, \alpha, \chi)$$

which can, using the implicit function theorem, be solved uniquely for $\mathbf{y}_2$ in terms of $\mathbf{y}_1, \mu, \alpha$, and χ for small enough $\mathbf{y}_1$, μ, α, and χ. The function $\mathbf{y}_2 = \mathbf{y}_2(\mathbf{y}_1, \mu, \alpha, \chi)$ is smooth in its arguments. Substituting $\mathbf{y} = \mathbf{y}_1 + \mathbf{y}_2\ (\mathbf{y}_1, \mu, \alpha, \chi)$ in (38) gives the bifurcation equations in $\mathbf{y}_1$, μ, α, and χ and to every solution of the bifurcation equations there corresponds a periodic solution of (30). The operator bifurcation equations $\mathbf{VF}(\mathbf{y}_1 + \mathbf{y}_2(\mathbf{y}_1, \mu, \alpha, \chi), \mu, \alpha, \chi) = 0$ thus obtained reduce to four algebraic nonlinear bifurcation equations if we note that every $\mathbf{y}_1$ is given by $\mathbf{y}_1 = \mathbf{\Phi}(\tau)\mathbf{d}$ where $\mathbf{d}$ is some constant vector in $\mathbb{R}^4$.

To obtain the bifurcation equations explicitly, we write

$$\bar{\mathbf{A}}_1(\mu) = \bar{\mathbf{A}}_{10} + \mu\bar{\mathbf{A}}_{11} + 0(\mu^2),$$

and

$$\bar{\mathbf{k}}(\mathbf{y}, \mu) = \bar{\mathbf{k}}_c(\mathbf{y}) + 0(|\mathbf{y}|^5) + 0(|\mu| \cdot |\mathbf{y}|^3)$$

where $\bar{\mathbf{k}}_c(\mathbf{y})$ is a homogeneous cubic in $\mathbf{y}$. Then substituting the preceding expressions in (37) and (38) and expanding the resulting expressions in Taylor series, we get the algebraic bifurcation equations

$$\begin{aligned}\mathbf{G}(\mathbf{d}, \mu, \alpha, \chi) \equiv\ & \chi\mathbf{M}_\chi\mathbf{d} + \mu\mathbf{M}_\mu\mathbf{d} + \alpha\mathbf{M}_\alpha\mathbf{d} + C_k(\mathbf{d}) \\ & + 0(|(\mu, \chi)|^2 \cdot |\mathbf{d}|) \\ & + 0(|(\mu, \chi)| \cdot |\mathbf{d}|^3) + 0(|\mathbf{d}|^5) = 0\end{aligned} \tag{39}$$

where

$$\mathbf{M}_\chi \equiv \int_0^{2\pi} \mathbf{\Psi}^T(s)\bar{\mathbf{A}}_0\mathbf{\Phi}(s)\ ds, \quad \mathbf{M}_\mu \equiv \int_0^{2\pi} \mathbf{\Psi}^T(s)\bar{\mathbf{A}}_{10}\mathbf{\Phi}(s)\ ds,$$

$$\mathbf{M}_\alpha \equiv \int_0^{2\pi} \mathbf{\Psi}^T(s)\bar{\mathbf{A}}_2\mathbf{\Phi}(s)\ ds$$

and $\mathbf{C}_k(\mathbf{d}) \equiv \int_0^{2\pi} \mathbf{\Psi}^T(s)\bar{\mathbf{k}}_c(\mathbf{\Phi}(s)\mathbf{d})\ ds.$ (40)

Note that in these equations we have set $\mathbf{y}_1 = \mathbf{\Phi}(\tau)\mathbf{d}$ for some $\mathbf{d} \in \mathbf{R}^4$.

Equations (39) are a system of four nonlinear algebraic equations dependent on two small parameters μ and α which can be varied independently. A general analysis of these equations, to determine all the possible small solutions $(\mathbf{d}, \chi)$ for μ and α varying over the whole neighborhood of the origin $(0,0)$ in (μ, α) plane, is quite difficult in general. Equations of this kind have been analyzed in detail by Chow, Hale, and Mallet-Paret [3, 4].

The proper scaling for the system (39) can now be determined. Assume that $\mathbf{C}_k(\mathbf{d})$ implies $\mathbf{d} = 0$. Then it can be shown [3] that every small solution of (39) satisfies the inequality

$$|\mathbf{d}| \le \hat{\eta}(|\mu|^{1/2} + |\chi|^{1/2} + |\alpha|^{1/2}) \tag{41}$$

for some constant $\hat{\eta} \neq 0$. This inequality suggests the scaling

$$\mathbf{d} = \epsilon\hat{\mathbf{d}}, \quad \chi = \epsilon^2\chi_2, \ \mu = \epsilon^2\mu_2 \quad \text{and} \quad \alpha = \epsilon^2\alpha_2 \tag{42}$$

which reduces the system (39) to

$$\chi_2\mathbf{M}_\chi\hat{\mathbf{d}} + \mu_2\mathbf{M}_\mu\hat{\mathbf{d}} + \alpha_2\mathbf{M}_\alpha\hat{\mathbf{d}} + \mathbf{C}_k(\hat{\mathbf{d}}) + 0(|\epsilon|^2) = 0. \tag{43}$$

The parameter ϵ can be fixed by normalizing the vector $\hat{\mathbf{d}}$ using the condition

$$|\hat{\mathbf{d}}| = 1. \tag{44}$$

Then ϵ is a measure of the amplitude of the periodic solution. The reduced bifurcation equations are obtained by taking the limit $\epsilon \to 0$ to give

$$\begin{aligned}\chi_{20}\mathbf{M}_\chi\hat{\mathbf{d}}_0 + \mu_{20}\mathbf{M}_\mu\hat{\mathbf{d}}_0 + \alpha_{20}\mathbf{M}_\alpha\hat{\mathbf{d}}_0 + \mathbf{C}_k(\hat{\mathbf{d}}_0) = 0, \\ |\hat{\mathbf{d}}| = 1.\end{aligned} \tag{45}$$

The solutions to these equations determine the first approximation to the periodic solutions of (30). Note that, since μ and α are independent and small in (39), α_{20} in (45) is independent, finite, and real. We are looking for solutions $(\hat{\mathbf{d}}_0, \mu_{20}, \chi_{20})$ of (45) for given values of α_{20}. The case of symmetric systems corresponds to $\alpha_{20} = 0$. These equations have been studied in complete generality for the rotationally invariant systems in [1]. In the remaining of this section we quickly summarize the analysis in [1] and then present results for $\alpha_{20} = 0$. The effects of symmetry-breaking perturbations $(\alpha_{20} \neq 0)$ will be discussed in a later section.

The bifurcation equations (45), taking the equations (27), (33), (34), and (40) into account, are given by

$$\begin{aligned}&-\chi_{20}\omega_0 a_1 \sin\phi + \mu_{20}a_1(\xi\cos\phi - \tilde{\omega}\sin\phi) \\ &\quad + \frac{a_1}{8}[a_1^2\{H_1\cos\phi + H_2\sin\phi\} \\ &\quad + a_2^2\{H_1\cos\phi + (2H_8 + H_{10})\sin\phi\}] = 0, \\ &\chi_{20}\omega_0 a_1\cos\phi + \mu_{20}a_1(\tilde{\omega}\cos\phi + \xi\sin\phi) + \\ &\quad \frac{a_1}{8}[a_1^2\{H_1\sin\phi - H_2\cos\phi\} \\ &\quad + a_2^2\{-H_2\cos\phi + (2H_7 - H_9)\sin\phi\}] = 0, \\ &\mu_{20}a_2\xi + \frac{a_2}{8}[a_1^2\{2H_7 + H_9\cos 2\phi \\ &\quad - H_{10}\sin 2\phi\} + H_1 a_2^2] = 0, \\ &\chi_{20}\omega_0 a_2 + \mu_{20}a_2\tilde{\omega} + \frac{a_2}{8} \\ &\quad [a_1^2\{-2H_8 + H_{10}\cos 2\phi + H_9\sin 2\phi\} - H_2 a_2^2] = 0,\end{aligned}$$

and

$$a_1^2 + a_2^2 = 1. \tag{46}$$

Here we have replaced $\hat{\mathbf{d}}_0$ by the polar variables

$$\hat{d}_{01} = a_1\cos\phi_1, \quad \hat{d}_{02} = a_1\sin\phi_1,$$
$$\hat{d}_{03} = a_2\cos\phi_2, \quad \hat{d}_{04} = a_2\sin\phi_2,$$

and then set $\phi_1 = \phi$ and $\phi_2 = 0$ because the system (30) is autonomous and, therefore, its phase is arbitrary.

The coefficients H_1, H_2, H_7, H_8, H_9, and H_{10} in (46) are formed by combinations of the 12 coefficients B_i of the cubic nonlinear terms given in Appendix B of Part 1 and are given by

$$\begin{aligned} H_1 &= 3B_1 + B_4 + B_5 + B_8 + B_9 + 3B_{12}, \\ H_2 &= -B_2 - B_3 - 3B_6 + 3B_7 + B_{10} + B_{11}, \\ H_7 &= B_1 + B_5 + B_8 + B_{12}, \\ H_8 &= -B_2 - B_6 + B_7 + B_{11}, \\ H_9 &= B_1 + B_4 - B_5 - B_8 + B_9 + B_{12}, \end{aligned}$$

and

$$H_{10} = -B_2 + B_3 + B_6 - B_7 - B_{10} + B_{11}.$$

Note that these coefficients are not completely independent but satisfy the relations

$$H_1 = 2H_7 + H_9 \text{ and } 2H_8 = H_2 + H_{10}.$$

If we define $a_1 = r\cos\hat{\psi}$, $a_2 = r\sin\hat{\psi}$, and eliminate μ_{20} and χ_{20} from equations (46), we get a system of two equations which, in matrix form, can be written as[2]

$$\begin{bmatrix} 4H_{10}\sin\phi\sin2\hat{\psi} & 4H_9\sin\phi\sin2\hat{\psi} \\ 4H_9\sin\phi\sin2\hat{\psi} & -4H_{10}\sin\phi\sin2\hat{\psi} \end{bmatrix} \begin{bmatrix} \cos\phi \\ \sin\phi\cos2\hat{\psi} \end{bmatrix} = 0$$

We are seeking real solutions to these equations. Note that the two vectors forming the rows of the matrix are orthogonal to each other and their inner product with the same vector $(\cos\phi, \sin\phi\cos2\hat{\psi})^T$ is zero. Thus, there are only three possible solutions which in terms of the original vector $\hat{\mathbf{d}}_0$ are given by

$$(a)\ \hat{\mathbf{d}}_{01} = \frac{1}{\sqrt{2}}(-\sin\psi, \cos\psi, \cos\psi, \sin\psi)^T, \quad 0 \le \psi < 2\pi,$$

$$\mu_{20} = -\frac{H_7}{4\xi}, \quad \chi_{20} = \frac{H_8}{4\omega_0} + \frac{\tilde{\omega}H_7}{4\xi\omega_0}, \tag{47a}$$

$$(b)\ \hat{\mathbf{d}}_{02} = \frac{1}{\sqrt{2}}(\sin\psi, -\cos\psi, \cos\psi, \sin\psi)^T, \quad 0 \le \psi < 2\pi,$$

$$\mu_{20} = -\frac{H_7}{4\xi}, \quad \chi_{20} = \frac{H_8}{4\omega_0} + \frac{\tilde{\omega}H_7}{4\xi\omega_0}, \tag{47b}$$

and

$$(c)\ \hat{\mathbf{d}}_{03} = (\cos\theta\cos\psi, \cos\theta\sin\psi, -\sin\theta\cos\psi, -\sin\theta\sin\psi)^T,$$
$$0 \le \theta, \psi < 2\pi,$$
$$\mu_{20} = -\frac{H_1}{8\xi}, \quad \chi_{20} = \frac{H_2}{8\omega_0} + \frac{\tilde{\omega}H_1}{8\xi\omega_0} \tag{48}$$

where ψ accounts for the arbitrary phase.

Let us interpret these solutions in terms of the original coordinates $\mathbf{z} = (\mathbf{z}_1, \mathbf{z}_2)^T$ where $\mathbf{z}_1$ and $\mathbf{z}_2$ represent motions in two orthogonal planes in the physical space, the two planes intersecting in the axis of rotational symmetry. We recall that

$$\mathbf{z} = \begin{bmatrix} \mathbf{z}_1 \\ \mathbf{z}_2 \end{bmatrix} = \epsilon\mathbf{C}\Phi(\tau)\hat{\mathbf{b}}_0 + 0(\epsilon^2)$$

[2] This procedure was suggested by Dr. George Sell.

where

$$\Phi(\tau) = \left[\begin{array}{cc|cc} \sin\tau & \cos\tau & \multicolumn{2}{c}{\multirow{2}{*}{0}} \\ \cos\tau & -\sin\tau & & \\ \hline \multicolumn{2}{c|}{\multirow{2}{*}{0}} & \sin\tau & \cos\tau \\ \multicolumn{2}{c|}{} & \cos\tau & -\sin\tau \\ \hline 0 & & 0 & \end{array}\right]$$

Thus the periodic solution that corresponds to (47*a*) is given by

$$\begin{aligned} \mathbf{z}_1(\tau) &= \sqrt{2}\epsilon[\mathbf{c}_1{}^1\cos(\tau - \psi) - \mathbf{d}_1{}^1\sin(\tau - \psi)] + 0(\epsilon^2), \\ \mathbf{z}_2(\tau) &= \sqrt{2}\epsilon[\mathbf{d}_1{}^1\cos(\tau - \psi) + \mathbf{c}_1{}^1\sin(\tau - \psi)] + 0(\epsilon^2) \\ &\psi \in [0, 2\pi). \end{aligned} \tag{49}$$

From these two expressions we see that $\mathbf{z}_1 = \mathbf{z}_2$ $(\tau + \pi/2)$ and, therefore, the motion, when viewed along the axis of symmetry, will appear to be a circle with the axis of symmetry as the center and the motion along the circle will be counterclockwise. A similar conclusion holds for the solution (47*b*) except that the motion in this case is clockwise. Because of these features of the solutions (47), we call these solutions "circular" solutions.

The amplitudes of the periodic solutions (47*a*) and (47*b*) are the same, and in the first-order theory, they are determined in terms of the external parameter μ by $\mu = \mu_{20}\epsilon^2 + 0(\epsilon^3)$. Thus, using the expression for μ_{20} from (47) we get

$$\epsilon \simeq \sqrt{-\frac{4\mu\xi}{H_7}}. \tag{50}$$

If $H_7 > 0$, $\mu_{20} < 0$ and for ϵ to be positive, we have to take $\mu < 0$. Thus, for $H_7 > 0$ the circular solutions are subcritical. If $H_7 < 0$, we have to take $\mu > 0$ and the circular solutions are supercritical.

We now consider the solution (48). Without much difficulty we can see that the corresponding periodic solution is given by

$$\begin{aligned} \mathbf{z}_1 &= 2\epsilon[\mathbf{c}_1{}^1\sin(\tau + \psi) + \mathbf{d}_1{}^1\cos(\tau + \psi)]\cos\theta + 0(\epsilon^2), \\ \mathbf{z}_2 &= 2\epsilon[-\mathbf{c}_1{}^1\sin(\tau + \psi) - \mathbf{d}_1{}^1\cos(\tau + \psi)]\sin\theta + 0(\epsilon^2), \\ &0 \le \psi, \theta < 2\pi \end{aligned} \tag{51}$$

Equations (51) represent motion in a plane that passes through the axis of symmetry. The plane of motion is determined by the angle θ. For example, for $\theta = 0$, the motion is in the plane $\mathbf{z}_2 = \mathbf{0}$. We call this family "planar" motion.

The amplitude ϵ of these planar motions is given by

$$\epsilon \simeq \sqrt{-\frac{8\xi\mu}{H_1}} \tag{52}$$

The solution is supercritical if $H_1 < 0$ and subcritical if $H_1 > 0$.

The frequency of the preceding motions is, of course, amplitude dependent. The quantity χ_{20} determines the correction, from ω_0, to the frequency of the corresponding solutions. The frequency of each of the foregoing solutions is given by

$$\omega = \omega_0/\{1 + \epsilon^2\chi_{20} + 0(\epsilon^3)\} \tag{53}$$

with appropriate ϵ and χ_{20} as given in the foregoing.

We now discuss the stability of the periodic motions.

7 Stability of the Bifurcating Solutions

The stability of the periodic solutions is determined by the Floquet exponents [2] of the variational equation

$$\omega_0 \dot{\psi} = \bar{\bar{\mathbf{A}}}_0 \psi + \epsilon^2 \mathbf{K}(\tau, \alpha_2, \epsilon)\psi \tag{54}$$

for the system (30) where

$$\mathbf{K}(\tau,\alpha_2,\epsilon) \equiv \chi_2(\epsilon)\bar{\bar{\mathbf{A}}}_0 + (1+\epsilon^2\chi_2(\epsilon))\{\mu_2(\epsilon)\bar{\bar{\mathbf{A}}}_1 + \alpha_2\bar{\bar{\mathbf{A}}}_2 + \bar{\mathbf{k}}_{\mathbf{y}}(\hat{\mathbf{y}}(\tau,\epsilon),\epsilon^2\mu_2(\epsilon))\},$$

$$\bar{\mathbf{k}}_{\mathbf{y}}(\mathbf{y},\mu) \equiv \frac{\partial \bar{\mathbf{k}}}{\partial \mathbf{y}}(\mathbf{y},\mu)$$

and where

$$(\epsilon\hat{\mathbf{y}}(\tau,\epsilon),\epsilon^2\chi_2(\epsilon),\epsilon^2\mu_2(\epsilon),\epsilon^2\alpha_2)$$

is a periodic solution of (30) whose stability is being studied. Equation (54) is a linear 2π-periodic differential system which depends smoothly on ϵ for small enough ϵ uniformly in τ. It can be easily shown that the four noncritical Floquet exponents of (54) are given by

$$\hat{\beta}_j(\epsilon) = \lambda_j{}^0 + 0(\epsilon), \quad j = 5,6,7,8$$

where $\lambda_j{}^0$ are the noncritical eigenvalues of the matrix $\bar{\bar{\mathbf{A}}}_0$.

The stability of the periodic solutions is, therefore, basically determined by the remaining four Floquet exponents $\hat{\beta}_j(\epsilon)$, $j=1$, 2, 3, 4 for small ϵ. These exponents can be determined using any of the standard perturbation techniques. Using the method of Alternate Problems, explained in the preceding section, we can show that these exponents $\hat{\beta} \equiv \epsilon^2\hat{\beta}_2$ are the solutions of

$$[\chi_2\mathbf{M}_\chi + \mu_2\mathbf{M}_\mu + \alpha_2\mathbf{M}_\alpha + \mathbf{C}_{kd}(\hat{\mathbf{d}}) - \hat{\beta}_2\omega_0\mathbf{I} + 0(\epsilon^2)]\mathbf{d} = 0 \tag{55}$$

which is just the eigenvalue problem for the variational equation of the bifurcation equations (39). In the limit as $\epsilon \to 0$, the Floquent exponents $\hat{\beta}_{20}$ are the roots of the characteristic equation

$$\det[\chi_{20}\mathbf{M}_\chi + \mu_{20}\mathbf{M}_\mu + \alpha_{20}\mathbf{M}_\alpha + \mathbf{C}_{kd}(\hat{\mathbf{d}}_0) - \hat{\beta}_{20}\omega_0\mathbf{I}] = 0 \tag{56}$$

which is a quartic in $\omega_0\hat{\beta}_{20}$. We consider here the cases of the three periodic solutions discussed in Section 6 for $\alpha_2 = 0$. The case with $\alpha_2 \neq 0$ will be considered in a later section.

The characteristic equations (56) for the two circular periodic solutions corresponding to solutions (47*a*) and (47*b*) reduce to a single equation given by

$$\sigma^4 - \frac{1}{4}(H_1+H_9)\sigma^3 + \frac{1}{16}(H_9{}^2 + H_{10}{}^2 + 2H_7H_9)\sigma^2 - \frac{H_7}{32}(H_9{}^2 + H_{10}{}^2)\sigma = 0 \tag{57}$$

where $\sigma = \omega_0\hat{\beta}_{20}$. Thus both the solutions have the same stability properties and the physical system in the stable case, and will perform either of the two circular motions depending on the initial conditions for the system (30).

Considering equation (57), it is clear that one root is zero which is a consequence of the fact that system (30) is autonomous and therefore for any periodic solution $\mathbf{y}$, $\partial\mathbf{y}/\partial\psi$ is a 2π-periodic solution of (54) for all ϵ. By the theorem of "orbital stability" of a periodic solution (Hale [2]), the bifurcating circular periodic solution is asymptotically orbitally stable with asymptotic phase if the three nonzero roots σ_i, $i=2,3,4$ of the equation (57) lie in the left half of the complex plane. Stability of these solutions for a variety of cases, as determined by specific values of system parameters, is discussed in the next section.

The stability of the two-parameter family of periodic solutions (51), called the planar solutions, cannot be deduced directly from the discussion for the circular solutions although the general analysis remains valid. The four critical Floquet exponents still are the roots of the quartic (56). One can easily verify that equation (56), for this case, when evaluated at the solution (49) of the reduced bifurcation equations, reduces to

$$\sigma^4 - \frac{1}{4}(H_1 - H_9)\sigma^3 - \frac{H_1H_9}{16}\sigma^2 = 0. \tag{58}$$

Clearly, two roots of (58) are identically zero which is because the solution is a two-parameter family and both $\partial\mathbf{y}/\partial\psi$ and $\partial\mathbf{y}/\partial\theta$ are linearly independent 2π-periodic solutions of the variational equation (54). In fact, the independence of $\partial\mathbf{y}/\partial\psi$ and $\partial\mathbf{y}/\partial\theta$ implies that two Floquet exponents are identically zero for all ϵ. Equation (58) determines first approximation to the remaining two nonzero Floquet exponents. These two nonzero roots of (58) are

$$\sigma_1 = H_1/4 \quad \text{and} \quad \sigma_2 = -H_9/4$$

and therefore the critical characteristic exponents for the planar solution in terms of the external parameter μ are given by

$$0, 0, -\frac{2\xi\mu}{\omega_0} + 0(|\mu|^{3/2}) \quad \text{and} \quad \frac{2H_9}{\omega_0 H_1}\mu + 0(|\mu|^{3/2}). \tag{59}$$

It then follows, from a theorem by Hale and Stokes [5] on the stability of k-parameter family of periodic solutions, that if the two nonzero critical exponents given in (59) are in the left half of the complex plane, the two-parameter family of periodic solutions (51) is asymptotically stable with asymptotic phase ψ and asymptotic angle θ. This concept of stability is a natural generalization of the concept of orbital stability of a periodic solution and precise definitions can be found in Hale and Stokes [5]. In the context of the planar solution (51) this concept of stability can be explained as follows: consider any periodic solution $\mathbf{z}(\tau,\psi;\theta_1)$ for a fixed value of θ, say $\theta = \theta_1$. This motion is in the plane defined by the angle θ_1. Let I_{θ_1} be a small interval around θ_1. Let M be the solution manifold in $\mathbf{R}^{2n+1}$ which is defined by $\mathbf{x} = \mathbf{z}(\tau,\psi;\theta)$, $\theta \in I_{\theta_1}$, $\psi \in [0, 2\pi)$. If this solution manifold is stable in this sense, given a small disturbance to this family, the solution of (30) with $\alpha = 0$ tends to the foregoing manifold. However, the parameter θ determining the plane of the motion goes to some value $\bar{\theta}_1$ as $\tau \to \infty$. The asymptotic angle $\bar{\theta}_1$ depends on the initial conditions. The smaller the disturbance, the smaller is the angle difference $|\bar{\theta}_1 - \theta_1|$. Therefore, if we disturb a stable planar motion, the plane of the motion drifts into another nearby plane.

Consider now the planar solution. Since $\xi > 0$ and $\mu = \mu_{20}\epsilon^2 + 0(\epsilon^3) = -H_1/8\xi\,\epsilon^2 + 0(\epsilon^3)$, it bifurcates for $\mu > 0$ (supercritically) if $H_1 < 0$ and for $\mu < 0$ (subcritically) if $H_1 > 0$. From the Floquet exponents (59), we can distinguish three distinct possibilities which are in contrast to the problem of Hopf bifurcations where there are only two cases. For subcritical solutions, $H_1 > 0$ and $\mu < 0$; therefore, one of the Floquet exponents is always positive. Thus, the subcritical planar solution is always unstable. For the supercritical case, there are *two* possibilities depending on the sign of H_9. If $H_9 > 0$, the supercritical solution is stable while if $H_9 < 0$, it is unstable.

The preceding conclusions regarding stability depend on the values of the constants H_i. As shown earlier, these constants depend in a very complicated manner on the system parameters and the eigenvectors of the matrix $\mathbf{A}$. Detailed specific results are therefore best obtained by computing these quantities numerically. We discuss these results for specific ranges of parameters in the next section.

8 Results and Discussion for the Symmetric System

In the following we present results and numerical calculations over a range of system parameters ρ, β, κ, a, and G. As noted in Section 2, β lies between 0–3 while a, G, and κ are all positive. To study the whole parameter space is a very difficult task. Therefore our calculations are restricted to within realistic limits. We consider five values 0.25, 0.5, 1.0, 2.0, and 4.0 for each of the parameters a and κ. For each fixed

pair (κ,a), the parameter β was varied over the whole interval (0,3). Since the parameter μ only determines the size of the periodic motions, the significant quantity is $(1/|\mu_{20}|)^{1/2}$ and it is the one that is presented in the results.

The situation with respect to the gravitation parameter G is much more involved. This is because the effect of G on the problem is fundamental in that it can change the character of the instability. We can see from (19) that for $G = 0$, the the articulated pipes system gets unstable only by complex eigenvalues crossing the imaginary axis. On the other hand, if G is very large, it can be shown that for $\beta > 0.5$, the vertical position gets unstable with real eigenvalues crossing the imaginary axis through the origin. For small enough G, below some critical value $G = G^*$, we still get the oscillatory instability over the whole β range and it is of primary interest here. This number G^* is determined by other system parameters. We have therefore treated cases in which the gravitational forces are much smaller compared to the elastic restoring forces. Specifically, we present results for $G = 0.0$ and $G = 0.25$. There are, however, cases (when κ is small) when G has to be as low as 0.1 for all instabilities to be of oscillatory nature. We should mention here that cases, when one pair of complex eigenvalues and one real eigenvalue cross the imaginary axis simultaneously, have been studied by Holmes [6].

Since it is not possible to present results for all the parameter values considered, we describe in detail a few typical cases and then summarize the major conclusions of numerical calculations.

The results are simplest to describe in the case when the length ratio $a = 2.0$. Representative behavior is shown in Figs. 1(a) and (b) for a = 2.0, $\kappa = 1.0$, and for $G = 0.0$ and 0.25, respectively. It may be noted that the system parameters in this case, to some extent, approximate the case of a continuous cantilever tube. In these figures, as well as in all the others discussed later, the solid lines denote supercritical circular solutions while the dotted lines denote supercritical planar solutions.

Let us first consider Fig. 1(a) corresponding to $G = 0.0$. The curves here are typical for all stiffness values considered. It is found that both planar and circular periodic motions are supercritical. Their amplitude increases monotonically with the mass ratio β, being smallest near $\beta = 0.0$ and largest at $\beta = 3.0$. For small values of β, the planar solution is of larger amplitude and is stable while for larger values of β the circular solutions are of larger amplitude and are stable. The two kinds of solutions exchange stability at the value of β where they cross. It is also observed that for a given β, the amplitude of periodic motions, whether planar or circular, goes down as the stiffness ratio κ is increased. It is to be noted that, in contrast to Hopf bifurcations, it is possible to have unstable supercritical bifurcations in systems of the kind discussed here.

We now consider Fig. 1(b) which is for $G = 0.25$ with other parameters being as for Fig. 1(a). For $\beta < 1.19$ the nature of solutions here is the same as in Fig. 1(a). For $\beta > 1.19$, there also exist subcritical solutions that are not present in Figure 1(a). These subcritical solutions are all unstable. The planar and circular subcritical solutions are denoted, respectively, by single chain and double chain lines. Thus, even very small gravity effects have profound influence on the periodic solutions for this parameter range. Based on these and other numerical calculations it is observed that for a fixed β, the amplitudes of the supercritical planar and circular solutions increase as G is increased from zero until a value of G is reached when the circular solution first becomes subcritical. If G is increased further, another value of G is reached where planar supercritical solution also becomes subcritical. For every value of G there are values of the mass ratio β above which all circular and planar solutions are subcritical. It is

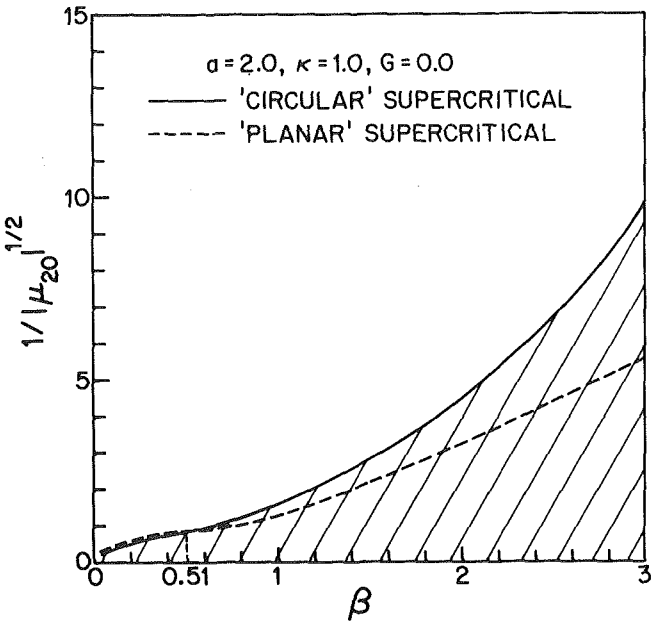

Fig. 1(a) Amplitudes of periodic solutions for $a = 2.0$, $\kappa = 1.0$, $G = 0.0$

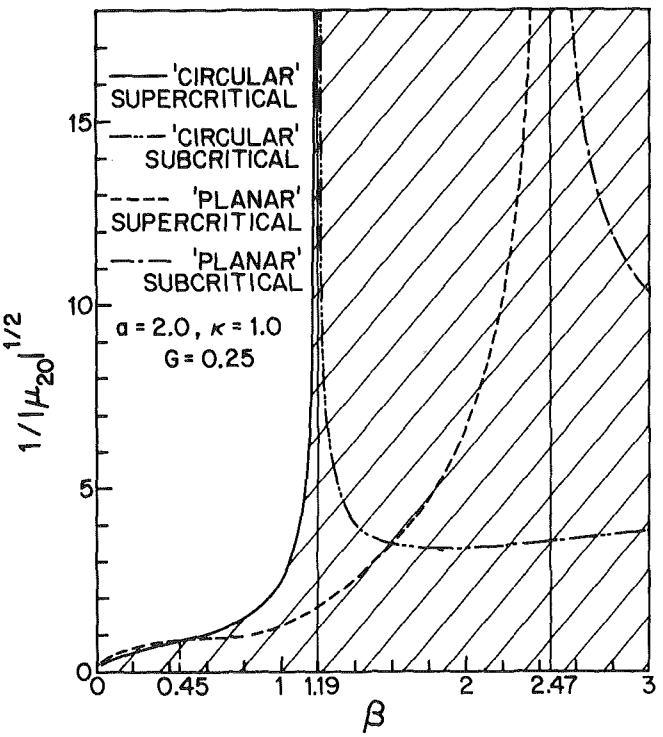

Fig. 1(b) Amplitudes of periodic solutions for $a = 2.0$, $\kappa = 1.0$, $G = 0.25$

Fig. 1

also observed from Fig. 1(b) that if for a given β at least one of the solutions is subcritical, both solutions are unstable. This is found to be the case for all parameter values considered. This does not imply that there are no stable periodic solutions for such values of β. The present conclusions are valid only for the first approximation.

In the graphs discussed in the foregoing there was only one intersection (and exchange of stability) of supercritical planar and circular solutions. This is not the case for all parameter values. In Fig. 2 results are given for $a = 0.25$, $\kappa = 4.0$, and $G = 0.0$. Both the solutions are supercritical for $\beta > 0.72$ whereas for $\beta < 0.72$ the planar solution is subcritical and the

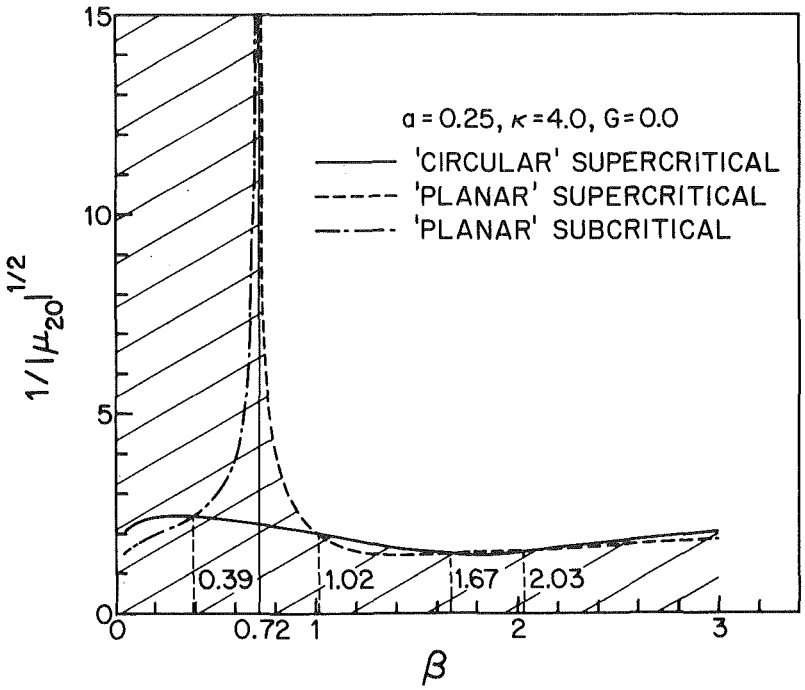

Fig. 2 Amplitudes of periodic solutions for $a = 0.25$, $\kappa = 4.0$, $G = 0.0$

circular solution is supercritical. The two supercritical solutions intersect at $\beta = 1.02$, 1.67, and 2.03 and exchange their stability. For example, as β is increased through 1.67, the stable circular solution becomes unstable and the unstable planar solution gains stability. The planar subcritical and the supercritical circular solutions for small values of β are both unstable. It is also observed from calculations that the gravitation effects are small in this and other cases, where the length ratio is smaller and the stiffness ratio is greater than one. This insensitivity of the solutions to G for small a can be explained by the fact that G appears in nonlinear terms multipled with factors quadratic in a.

We now summarize the main conclusions from numerical results described in the foregoing and those that were obtained for other values of system parameters discussed earlier.

1. Both supercritical and subcritical planar as well as circular solutions can exist over the interval $0 \leq \beta \leq 3.0$ for the range of parameters a, G, and κ studied.

2. For a fixed value of β, if either of the solutions (planar or circular) is subcritical, both the solutions are unstable based on the first-order theory.

3. If planar as well as circular solutions are supercritical, the solution with the larger amplitude is stable and whenever the two amplitude curves intersect, there is an exchange of stability. For a fixed value of parameters a, κ, and G, there can be many intervals in β of alternating stability and instability.

4. For small values of β, the circular solution is always supercritical and unstable while the planar solution can be supercritical and stable or subcritical and unstable.

5. For large values of β, the circular solution is in most cases stable if supercritical and always unstable if subcritical. On the other hand, the planar solution is in most cases unstable if supercritical and always unstable if subcritical.

6. For length ratio less than unity, the influence of gravity G on the qualitative and quantitative nature of periodic solutions is small. This influence is, however, very pronounced for $a > 1.0$ especially for larger values of β.

7. The intervals in β over which subcritical solutions exist is very much influenced by the stiffness ratio κ and the gravity parameter G.

8. Over the whole range of parameters considered, subcritical circular solutions were never found to exist for small β.

9 Periodic Solutions With Symmetry-Breaking Perturbations

In Section 6 it was shown that reduced bifurcation equations for perturbed symmetric systems are given by

$$\chi_{20}\mathbf{M}_\chi \hat{\mathbf{d}}_0 + \mu_{20}\mathbf{M}_\mu \hat{\mathbf{d}}_0 + \alpha_{20}\mathbf{M}_\alpha \hat{\mathbf{d}}_0 + \mathbf{C}_k(\hat{\mathbf{d}}_0) = 0$$

and (60)

$$|\hat{\mathbf{d}}_0| = 1.$$

The solution of these equations clearly depends on the nature of the matrix $\mathbf{M}_\alpha$ which in turn is determined by the choice of the matrix $\bar{\bar{\mathbf{A}}}_{20}$ that represents the asymmetry in the linear part of the system.

Without loss in generality we can introduce asymmetry through only one of the two linear modes in the Jordan form. The dynamical system in Jordan coordinates will then be in the form.

$$\dot{\mathbf{y}} = \bar{\bar{\mathbf{A}}}_0\mathbf{y} + \mu\bar{\bar{\mathbf{A}}}_1(\mu)\mathbf{y} + \alpha\bar{\bar{\mathbf{A}}}_{20}\mathbf{y} + \bar{\mathbf{k}}(\mathbf{y},\mu) \tag{61}$$

where the general form of the symmetry-breaking matrix is assumed to be

$$\bar{\bar{\mathbf{A}}}_{20} = \left[\begin{array}{cc:c} p_1 & p_2 & \\ -p_2 & p_1 & 0 \\ \hdashline & & \\ 0 & & 0 \end{array}\right] \tag{62}$$

and where p_1 and p_2 are real arbitrary constants. For $\alpha = 0$ the behavior of eigenvalues of the system as a function of ρ for both modes is the same. In case $p_1 = 0$, $p_2 \neq 0$, only the periods of the two linear modes are different and the

eigenvalues cross the pure imaginary axis at the same value of the flow rate. This possibility can arise when the stiffness of any of the joints does not have polar symmetry and stiffness in one plane is slightly greater than in the other. Similarly, if $p_1 \neq 0$, $p_2 = 0$, the two linear modes have the same period but they cross the pure imaginary axis at slightly different values of the flow rate. Such a situation may arise if the damping in one plane is a little more than in the other.

With this form of the matrix $\bar{\bar{\mathbf{A}}}_{20}$, we intend to solve the reduced bifurcation equations (60). The solutions of (60) for $\alpha_{20} = 0$ have already been discussed in the preceding section. It is clear from equation (43) in Section 6 that for $\alpha_2 \sim 0(\epsilon)$ (i.e., $\alpha \sim 0(\mu)$), the circular solutions of (60) with $\alpha_{20} = 0$ give first approximation to solutions of the perturbed system. Here we are interested in solutions of the perturbed system when μ and α are of the same order. Because $\mu = \mu_2\epsilon^2$ and $\alpha = \alpha_2\epsilon^2$, we would therefore like to find solutions of (60) for given α_{20} such that μ_{20} and α_{20} are of the same order of magnitude.

For any solution $(\hat{\mathbf{d}}_0, \mu_{20}, \chi_{20})$ of (60) with a given α_{20}, the stability is determined by the roots of the characteristic equation (56):

$$\det[\chi_{20}\mathbf{M}_\chi + \mu_{20}\mathbf{M}_\mu + \alpha_{20}\mathbf{M}_\alpha + \mathbf{C}_{kd}(\hat{\mathbf{d}}_0) - \sigma\mathbf{I}_4] = 0 \qquad (63)$$

The system of equations (60) is nonlinear and very difficult to solve in the general case. We take advantage of the known solution for $\alpha_{20} = 0$ and solve them numerically. In the numerical solution, α_{20} is increased in steps and the solution of the preceding step is taken as the initial guess for the solution corresponding to the new value of α_{20}. Once the solution is known, its stability is determined by finding roots of (63).

The main purpose of introducing asymmetry is to have the assurance that the solutions obtained for the perfectly symmetric system will persist in slightly modified form in the presence of small asymmetry. Therefore, we checked the influence of asymmetry in only a few cases.

The numerical solutions of (60) were obtained for $\beta = 1.5$, $a = \kappa = 1.0$, and $G = 0.0$ starting with the circular solution for $\alpha_{20} = 0$ which is supercritical and stable. The cases ($p_1 \neq 0$, $p_2 = 0$) and ($p_1 = 0$, $p_2 \neq 0$) were studied separately by finding solutions with $(p_1, p_2) = (1.0, 0.0)$ and $(0.0, 1.0)$. For the range of α_{20} (0.0–0.1) considered, all solutions were found to be supercritical and stable. Some of the interesting observations that can be made from these results are as follows:

1. $(p_1, p_2) = (1.0, 0.0)$: This is the case when, for $\alpha_{20} > 0$, the first mode crosses the pure imaginary axis before the second one. As one would expect, the amplitude of this mode is the larger of the two and the resulting motion is elliptic in nature. The average amplitude also increases with α_{20}, $\alpha_{20} > 0$.

2. $(p_1, p_2) = (0.0, 1.0)$: In this case, for $\alpha_{20} > 0$, the frequency of the first mode is larger than that of the second. Again, the amplitude of the first mode is greater than that of second and the periodic motion in physical three-space is elliptic in nature. In this case, however, the average amplitude does not change much with increasing α_{20}. Also, the eccentricity of the ellipse in this case is much greater. The difference in amplitudes of the two modes here can be attributed to a different physical phenomenon: the linear part of system has different frequencies in the two modes. On the other hand, for periodic nonlinear motions the frequency in either mode has to be the same. Since, in general, the period of nonlinear motions depends on the amplitude, the system adjusts the amplitudes of the two modes to different values in such a way as to attain the same frequency in each mode.

Thus, we see that the difference in the rate of growth of the linear modes has more pronounced influence on the amplitude while the difference in periods of linear modes gives rise to larger eccentricity of elliptic motions. In a given physical situation, the actual behavior of the system will be determined by the factor that dominates.

We would like to finally mention that no effort was made to study the effect of asymmetry on the plane periodic motions.

Acknowledgment

We would like to thank one of the reviewers for very constructive suggestions, which have improved this work.

References

1 Bajaj, A. K., "Bifurcating Periodic Solutions in Rotationally Symmetric Systems," *SIAM J. Appl. Math.*, Vol. 42, Oct. 1982.
2 Hale, J. K., *Ordinary Differential Equations*, Wiley-Interscience, New York, 1969.
3 Chow, S. N., Hale, J. K., and Mallet-Paret, J., "Applications of Generic Bifurcations, I," *Arch. Rat. Mech. Anal.*, Vol. 59, 1975, pp. 159–188.
4 Chow, S. N., Hale, J. K., and Mallet-Paret, J., "Applications of Generic Bifurcations, II," *Arch. Rat. Mech. Anal.*, Vol. 62, 1976, pp. 209–235.
5 Hale, J. K., and Stokes, A. P., "Behavior of Solutions Near Integral Manifolds," *Arch. Rat. Mech. Anal.*, Vol. 6, 1960, pp. 133–170.
6 Holmes, P. J., "Center Manifolds, Normal Forms and Bifurcations of Vector Fields With Application to Coupling Between Periodic and Steady Motions," *Physica 2D*, Vol. 2, 1981, pp. 449–481.

S. F. Masri
Professor.
Mem. ASME

H. Sassi
Graduate Student.

Civil Engineering Department,
School of Engineering,
University of Southern California,
Los Angeles, Calif. 90007

T. K. Caughey
Professor,
Division of Engineering and
Applied Science,
California Institute of Technology,
Pasadena, Calif. 91109

Nonparametric Identification of Nearly Arbitrary Nonlinear Systems

A nonparametric identification technique is presented for use with discrete multidegree-of-freedom nonlinear dynamic systems. The method requires information regarding the system response and estimates of its pertinent "mode shapes" to determine, by means of regression techniques involving the use of two-dimensional orthogonal functions, an approximate expression for the system generalized restoring forces in terms of the corresponding generalized system state variables. The technique is applied to several example systems. The method can be used with deterministic or random excitation to identify dynamic systems with arbitrary nonlinearities, incuding those with hysteretic characteristics. It is also shown that the method is easy to implement and needs much less computer time and storage requirements compared to the Wiener-kernel approach.

1 Introduction

The identification and modeling of nonlinear multidegree-of-freedom dynamic systems through the use of experimental data is a problem of considerable importance in the applied mechanics area. A recent survey article by Ibañez [1], containing over 130 references related to system and parameter identification, is indicative of the wide range of applicability of this subject in the structural dynamics field.

Since the model structure in many practical dynamic problems is by no means clear, the use of parametric identification methods, which assume that the structure is known and only parameter values need to be identified, may not be appropriate. As a result, an increasing amount of attention has recently been devoted to nonparametric identification methods such as the ones that use the Volterra-series or Wiener-kernel approach [2–5].

However, the traditional nonparametric identification techniques have their own problems. Some include restrictions on the nature of dynamic systems to be identified (nonhysteretic, stationary) and on the input signal that can be used (white noise). Furthermore, when dealing with systems that incorporate commonly encountered nonlinearities, such as polynomial nonlinearities, the evaluation of higher-order terms requires a prohibitive amount of computational effort, coupled with very demanding (and usually unrealistic) storage requirements.

A recent paper by the authors [6] presented a relatively simple and straightforward approach to the identification of a broad class of nonlinear single-degree-of-freedom (SDOF) dynamic models. The method is based on the use of regression techniques in conjunction with orthogonal polynomials and alleviates most of the aforementioned problems associated with the traditional nonparametric identification techniques. The procedure has the following specific attributes: (*a*) it was shown to be applicable to systems with practically arbitrary nonlinearities (including hysteretic types); (*b*) it has virtually no restriction on the wave form of the probing signal used for identification purposes, so long as the signal adequately excites the system; (*c*) both computer execution time and storage requirements are relatively minimal; and (*d*) the convergence rate is rapid, even for nonpolynomial types of nonlinearities.

The method in [6] was extended to handle the special case of chain-like multidegree-of-freedom (MDOF) nonlinear

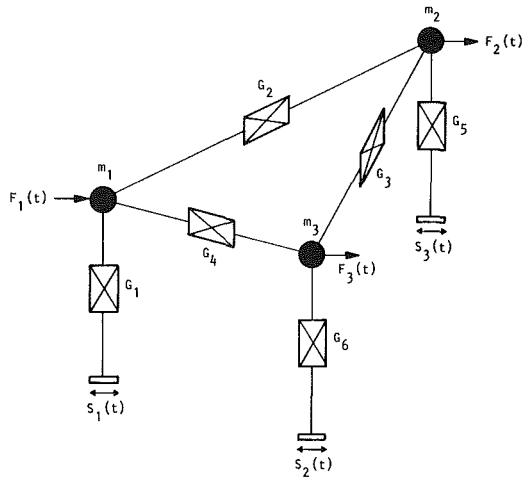

Fig. 1 Simplified model of nonlinear multidegree-of-freedom system

Contributed by the Applied Mechanics Division for publication in the JOURNAL OF APPLIED MECHANICS.

Discussion on this paper should be addressed to the Editorial Department, ASME, United Engineering Center, 345 East 47th Street, New York, N.Y. 10017, and will be accepted until two months after final publication of the paper itself in the JOURNAL OF APPLIED MECHANICS. Manuscript received by ASME Applied Mechanics Division, December, 1981; final revision, February, 1982.

$$G_i(z, \dot{z}) = p_1^{(i)} z + p_2^{(i)} \dot{z} + p_3^{(i)} z^3$$

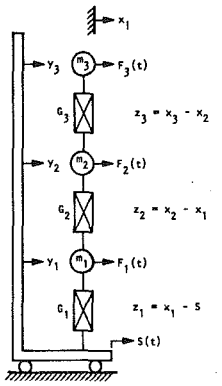

ELEMENT NO. i / PARAMETER	ELEMENT TYPE	m_i	$p_1^{(i)}$	$p_2^{(i)}$	$p_3^{(i)}$
3	SOFTENING	12	14900	60	-223
2	HYSTERETIC	12	$k_1 = 14900$	$\frac{k_2}{k_1} = 0.414$	$z_{yield} = 2.5$
1	HARDENING	12	7241	21	72.14

(a) System Model (b) Characteristics of Hysteretic Model UCB-3

Fig. 2 Example nonlinear 3 DOF system

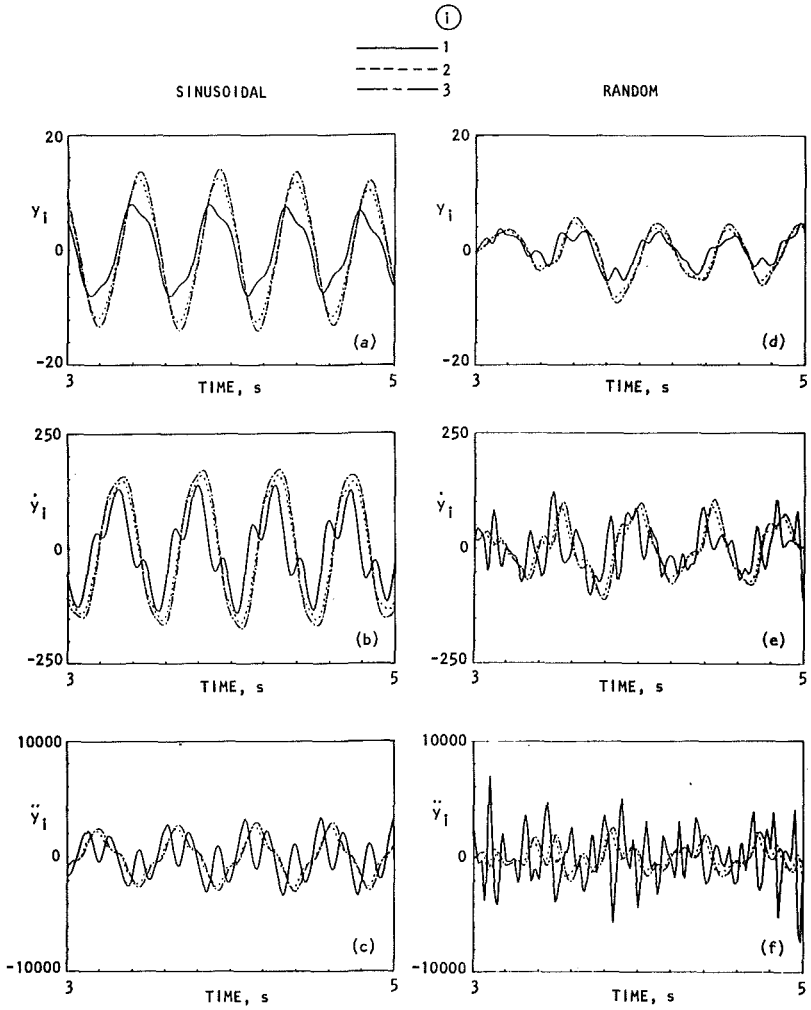

Fig. 3 Response time history of the hysteretic system UCB-3 under sinusoidal and random excitation

dynamic systems whose components are interconnected by a single nonlinear element [7]. These structures have the property that the nonlinearities in the various links of the chain are independent of each other. Thus, with a suitable transformation of variables, the method just described for SDOF systems can be applied directly to each link separately.

The present paper further extends the work in [6] by generalizing the approach to handle, approximately, the case of arbitrary nonlinear MDOF dynamic systems with multiple inputs and outputs. Section 2 of this paper presents the identification procedure, including problem formulation, generation of needed experimental data, information processing to extract the generalized system state variables, and final determination, by the use of orthogonal functions,

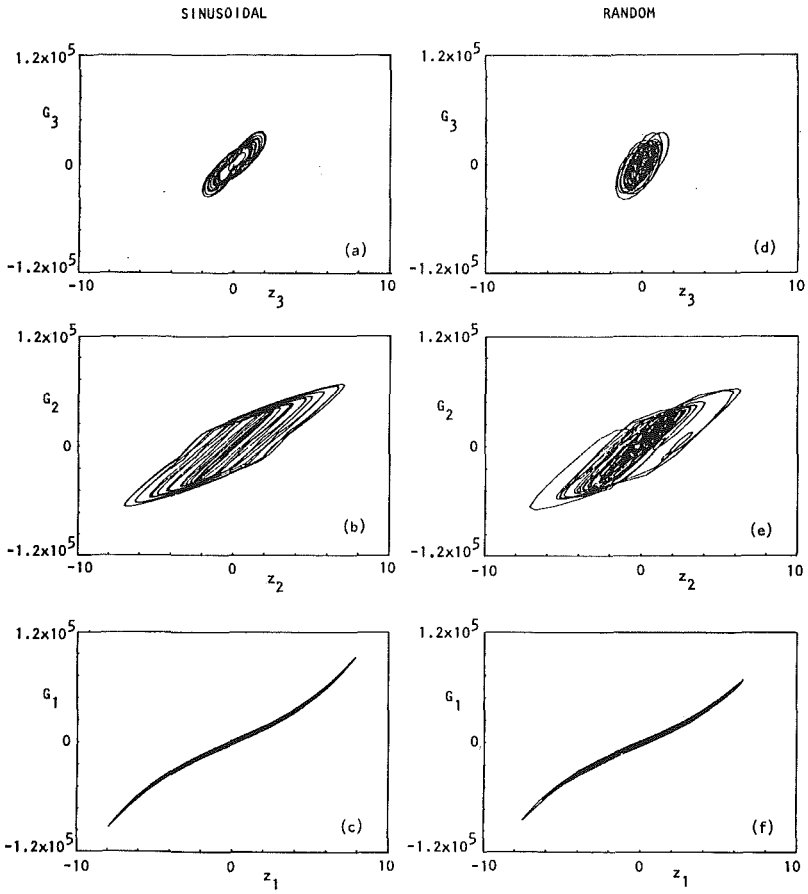

Fig. 4 Variation of restoring functions G_i with the corresponding state variable z_i in the hysteretic system UCB-3

of the best estimate of the system "restoring forces." In Section 3, the method is applied to a model of a three-story building that has been extensively analyzed, both analytically and experimentally, at the University of California at Berkeley (UCB). It is shown via numerical "experiments" that the approximate method under discussion is very efficient and can be utilized under realistic conditions to accurately identify general MDOF dynamic systems with arbitrary types of nonlinear components, even those possessing hysteretic characteristics and undergoing large nonlinear deformations—situations that pose serious problems to conventional identification methods.

2 Identification Procedure

Consider a discrete nonlinear MDOF system that consists of a collection of lumped masses, each of magnitude m_i, which are interconnected by means of discrete elements G_k with arbitrary nonlinear characteristics. To clarify the presentation, a simplified version of such a system with three masses and six nonlinear elements is shown in Fig. 1.

The structure may be subjected to nonuniform base excitation and/or directly applied forces. The displacement of m_i is measured by $y_i(t)$. It is assumed that the excitation and response of the system are available from measurements and that the masses m_i are known or easily estimated.

2.1 Formulation. Consider a nonlinear dynamic system whose motion is governed by

$$m\ddot{\mathbf{y}} + \mathbf{f}(\mathbf{y},\dot{\mathbf{y}}) = \mathbf{p}(t), \tag{1}$$

where m = diagonal mass matrix of order n
$\mathbf{y}$ = displacement vector = col. $\{y_1, y_2, \ldots, y_n\}$
$\mathbf{f}$ = function that represents nonconservative nonlinear forces
$\mathbf{p}(t)$ = excitation vector

The transformation matrix ϕ of order $n \times r$ is introduced:

$$\mathbf{y} = \phi\mathbf{u}, \tag{2}$$

where the r columns of ϕ represent estimates of the r "modes" of interest pertaining to the nonlinear system of equation (1).

Substituting (2) into (1) and premultiplying by ϕ^T,

$$M\ddot{\mathbf{u}} + h(\mathbf{u},\dot{\mathbf{u}}) = \mathbf{Q}(t), \tag{3}$$

where M = diagonal mass matrix = $\phi^T m \phi$
$\mathbf{h} = \phi^T \mathbf{f}$
$\mathbf{Q}(t) = \phi^T \mathbf{p}(t)$

For a linear system with classical normal-modes [8], function $\mathbf{f}$ is of the form

$$\mathbf{f}(\mathbf{y},\dot{\mathbf{y}}) = c\dot{\mathbf{y}} + k\mathbf{y}, \tag{4}$$

where c and k are constant matrices.

If matrix ϕ appearing in the transformation of equation (2) is the eigenvector matrix associated with $m^{-1}k$, then for the linear system

$$\mathbf{h}(\mathbf{u},\dot{\mathbf{u}}) = C\dot{\mathbf{u}} + K\mathbf{u} \tag{5}$$

where C = diagonal damping matrix = $\phi^T c \phi$
K = diagonal stiffness matrix = $\phi^T k \phi$

Due to the orthogonality condition, equation (3) simplifies in the cases of linear systems to a set of uncoupled equations

$$M_i\ddot{u}_i + h_i(u_i,\dot{u}_i) = Q_i(t), \quad i = 1,2, \ldots, r \tag{6}$$

in which each function h_i depends only on the corresponding generalized coordinate u_i and its time derivative $\dot{u}_i$.

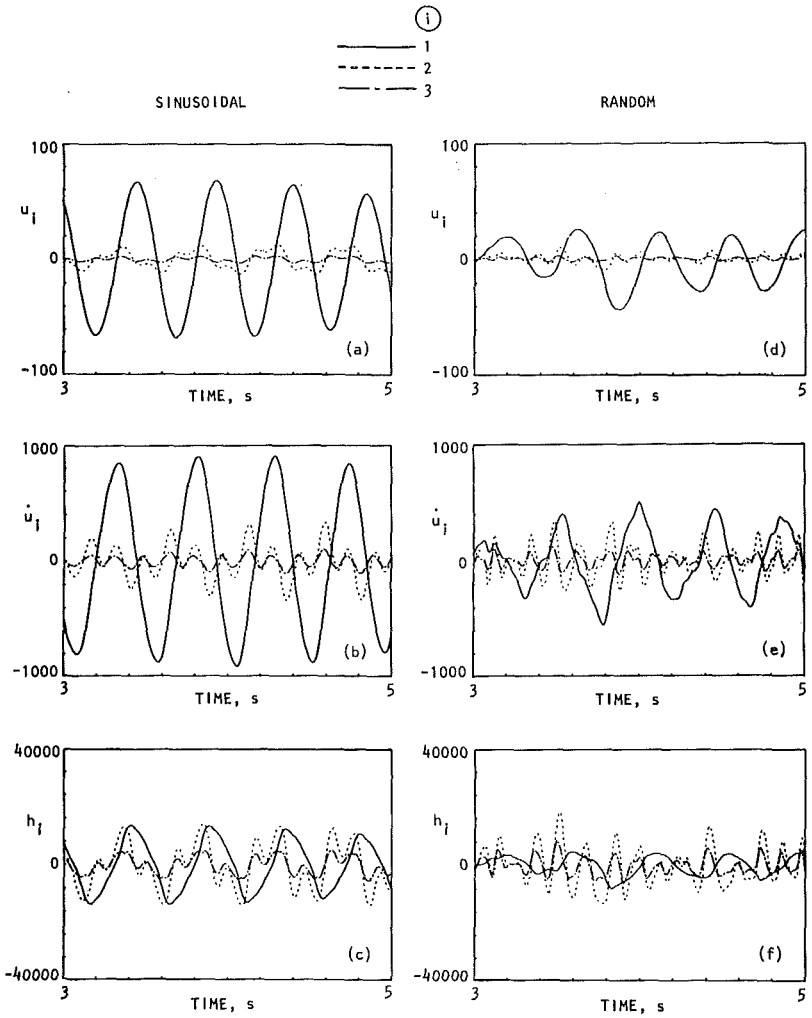

Fig. 5 Time history of modal state variables u_i and $\dot{u}_i$ and modal restoring forces h_i in hysteretic model UCB-3 under sinusoidal and random excitation

Returning to the more general problem represented by equation (3), the "generalized restoring force" $\mathbf{h}$ can be expressed as

$$\mathbf{h}(\mathbf{u},\dot{\mathbf{u}}) = \mathbf{Q}(t) - M\ddot{\mathbf{u}}. \tag{7}$$

Consider the ith component of equation (7);

$$h_i(\mathbf{u},\dot{\mathbf{u}}) = Q_i(t) - M_i\ddot{u}_i, \quad i = 1,2, \ldots, r \tag{8}$$

Thus, if m, $\ddot{\mathbf{y}}$, and $\mathbf{p}(t)$ are known, $h_i(\mathbf{u}, \dot{\mathbf{u}})$ can be determined from (8).

Let an estimate of $h_i(\mathbf{u}, \dot{\mathbf{u}})$ be given by $\hat{h}_i^{(1)}$, where $\hat{h}_i^{(1)}$ is expressed as a double series involving Chebyshev orthogonal polynomials:

$$\hat{h}_i(\mathbf{u},\dot{\mathbf{u}}) \approx \hat{h}_i^{(1)}(u_i,\dot{u}_i) = \sum_k \sum_l C1_{kl}^{(i)} T_k(u_i) T_l(\dot{u}_i). \tag{9}$$

Note from (9) that $\hat{h}_i^{(1)}$ considers only the contribution of terms of the type $u_i^k \dot{u}_i^l$ (i.e., only the ith "mode" is involved).

In order to better approximate h_i $(\mathbf{u}, \dot{\mathbf{u}})$ let the deviation between h_i and its first estimate $\hat{h}_i^{(1)}$ be given by

$$h_i^{(1)}(\mathbf{u},\dot{\mathbf{u}}) = h_i(\mathbf{u},\dot{\mathbf{u}}) - \hat{h}_i^{(1)}(u_i,\dot{u}_i) \tag{10}$$

The contribution of "modal interaction" to h_i can be accounted for by determining a new Chebyshev double series fit involving mode i and $j \neq i$:

$$h_i^{(1)}(\mathbf{u},\dot{\mathbf{u}}) \approx \hat{h}_i^{(2)}(u_i,u_j) = \sum_k \sum_l C2_{kl}^{(i)} T_k(u_i) T_l(u_j) \tag{11}$$

Similarly, the contribution of terms involving products of various powers of $\dot{u}_i$ and $\dot{u}_j$ can be found from

$$h_i^{(2)}(\mathbf{u},\dot{\mathbf{u}}) = h_i^{(1)}(\mathbf{u},\dot{\mathbf{u}}) - \hat{h}_i^{(2)}(u_i,u_j) \tag{12}$$

and

$$h_i^{(2)}(\mathbf{u},\dot{\mathbf{u}}) \approx \hat{h}_i^{(3)}(\dot{u}_i,\dot{u}_j) = \sum_k \sum_l C3_{kl}^{(i)} T_k(\dot{u}_i) T_l(\dot{u}_j) \tag{13}$$

Obviously, this procedure can be extended to account for all "modes" that have significant interaction with "mode" i. When this is done, h_i will be approximated by

$$h_i(\mathbf{u},\dot{\mathbf{u}}) \approx \hat{h}_i^{(1)}(u_i,\dot{u}_i) + \hat{h}_i^{(2)}(u_i,u_j) + \hat{h}_i^{(3)}(\dot{u}_i,\dot{u}_j) + \ldots \tag{14}$$

where the choice of j would usually be $(i - 1)$ and $(i + 1)$.

2.2 Processing of Experimental Data. To identify a particular system, perform the following steps:

(1) Measure $\mathbf{y}$, $\dot{\mathbf{y}}$, $\ddot{\mathbf{y}}$, and $\mathbf{p}(t)$ at a given sampling rate.

(2) Compute or estimate the diagonal mass matrix of order $n \times n$ and matrix ϕ of order $n \times r$.

(3) Determine sampled values of $\mathbf{u}(t)$, $\dot{\mathbf{u}}(t)$, and $\mathbf{h}(t)$ from the following relationships:

(a) If the order of ϕ is such that $n = r$,

$$\mathbf{u}(t) = M^{-1}\phi^T m\mathbf{y}(t), \quad \dot{\mathbf{u}}^{(t)} = M^{-1}\phi^T m\dot{\mathbf{y}}(t) \tag{15}$$

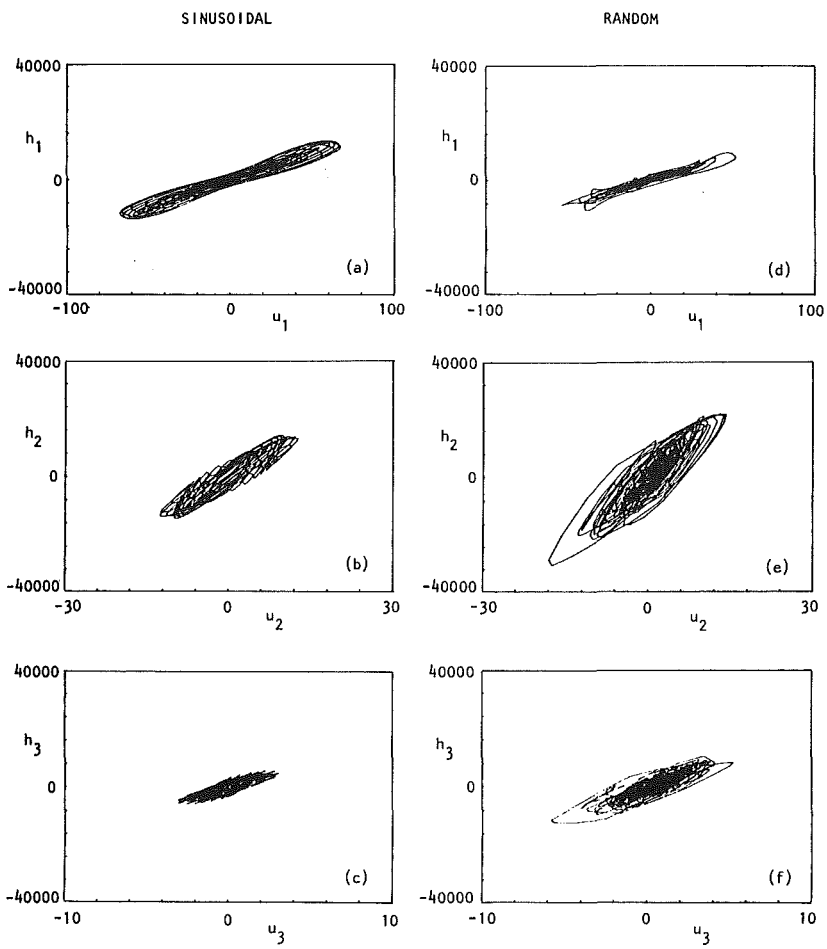

Fig. 6 Variation of modal restoring forces h_l with the corresponding state variables u_l in hysteretic model UCB-3 under sinusoidal and random excitation

(*b*) If $r < n$, then $\mathbf{u}$ and $\dot{\mathbf{u}}$ can be found from

$$\mathbf{u}(t) = A\mathbf{y}_r(t), \quad \dot{\mathbf{u}}(t) = A\dot{\mathbf{y}}_r(t) \tag{16}$$

where matrix $A = \phi_r^{-1}$ is the inverse of the submatrix ϕ_r consisting of the first r rows of ϕ, and $\mathbf{y}_r$ is a vector of the first r components of $\mathbf{y}$. Next compute the time history of the "modal restoring force" from

$$\mathbf{h}(t) = \phi^T \mathbf{f}(t) = \phi^T(\mathbf{p}(t) - m\ddot{\mathbf{y}}(t)) \tag{17}$$

(4) For each mode i, determine the two-dimensional Chebyshev series coefficients $C1^{(i)}$ for $h_i(\mathbf{u}, \dot{\mathbf{u}})$,

$$\hat{h}_i^{(1)}(u_i,\dot{u}_i) = \sum_k \sum_l C1_{kl}^{(i)} T_k(u_i) T_l(\dot{u}_i) \tag{18}$$

(5) Compute the residual error in the fit for all digitized values of $h_i(t)$,

$$h_i^{(1)}(t) = h_i(t) - \hat{h}_i^{(1)}(t) \tag{19}$$

(6) Determine a two-dimensional Chebyshev fit for $h_i^{(1)}(t)$ in terms of u_i and u_j, where j is any arbitrary "mode" that significantly interacts with mode i,

$$\hat{h}_i^{(2)}(u_i,u_j) = \sum_k \sum_l C2_{kl}^{(i)} T_k(u_i) T_l(u_j) \tag{20}$$

(7) Compute the residual error in the fit for the digitized values of $h_i^{(1)}(t)$,

$$h_i^{(2)}(t) = h_i^{(1)}(t) - \hat{h}_i^{(2)}(t) \tag{21}$$

(8) Determine a two-dimensional fit for $h_i^{(2)}(t)$ in terms of $\dot{u}_i$ and $\dot{u}_j$,

$$\hat{h}_i^{(3)}(\dot{u}_i,\dot{u}_j) = \sum_k \sum_l C3_{kl}^{(i)} T_k(\dot{u}_i) T_l(\dot{u}_j) \tag{22}$$

(9) Repeat steps 6–8 for different values of mode index j, until the norm of the residual error after s approximations is within an acceptable limit,

$$\| h_i^{(s)}(t) \| \le \delta \tag{23}$$

where δ is a small positive constant.

(10) Repeat steps 4–9 for each mode $i = 1, 2, \ldots, r$.

This step concludes the identification task. To use the results for predicting the response to an excitation other than the probing signal used for identification, the governing nonlinear equations of motions can be evaluated numerically. At a given time t_0 with values of $\mathbf{u}$ and $\dot{\mathbf{u}}$ known, the magnitude of each $h_i(t)$ can be estimated from

$$h_i(t) \approx \hat{h}_i(\mathbf{u},\dot{\mathbf{u}}) = \hat{h}_i^{(1)}(u_i,\dot{u}_i) + \hat{h}_i^{(2)}(u_i,u_j) + \hat{h}_i^{(3)}(\dot{u}_i,\dot{u}_j) + \ldots + \hat{h}_i^{(s)}(u_i,u_k) \tag{24}$$

Once $h_i(t)$ is determined, the governing equations of motion can be solved numerically to compute the response u_i at $(t + \Delta t)$:

$$M_i\ddot{u}_i(t) + h_i(t) = Q_i(t), \quad i = 1,2, \ldots, r \tag{25}$$

At any time t, $\mathbf{y}$ and $\mathbf{f}(\mathbf{y}, \dot{\mathbf{y}})$ can be found from

$$\mathbf{y}(t) = \phi\mathbf{u}(t) \tag{26}$$

$$\mathbf{f}(\mathbf{y},\dot{\mathbf{y}}) = \mathbf{p}(t) - m\ddot{\mathbf{y}}(t) \tag{27}$$

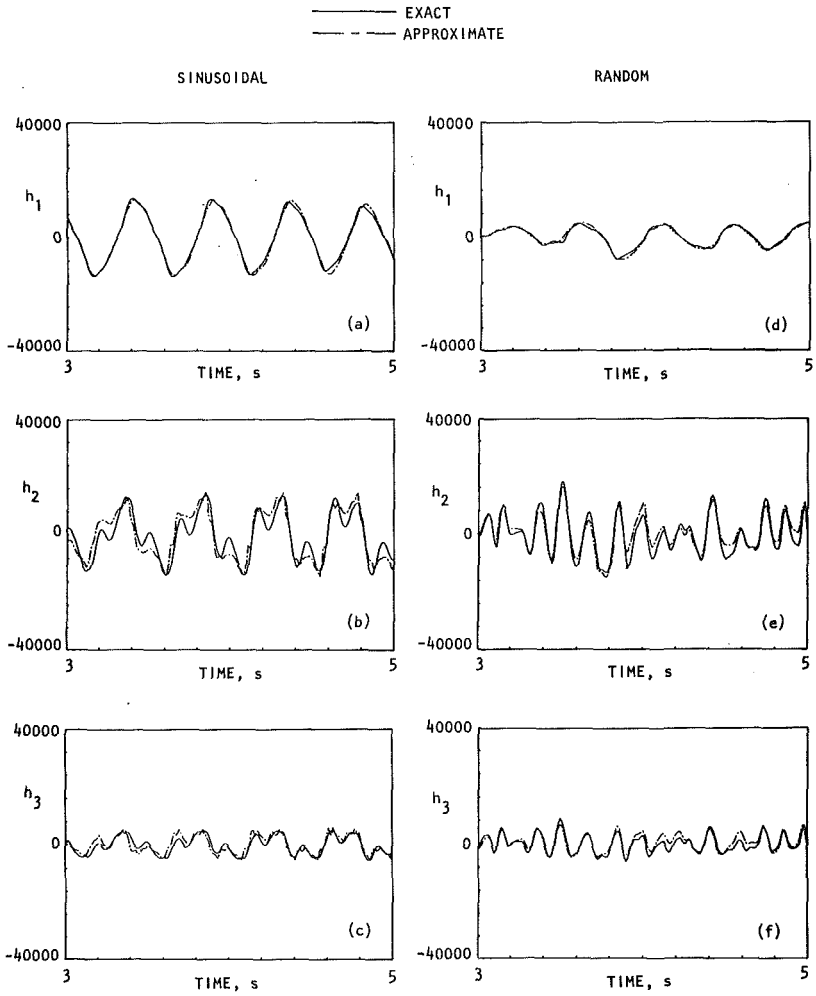

Fig. 7 Comparison between the exact and approximate modal restoring forces in hysteretic system UCB-3 under sinusoidal and random excitation

3 Applications

To illustrate the application of the method under discussion, consider the UCB frame that has been the subject of extensive analytical and experimental studies [9, 10]. A simplified three-degree-of-freedom stick model of this frame is shown in Fig. 2.

The chain-like structure of this model makes it ideally suited for treatment by the procedure in [7]. However, a major feature of the present identification method is that it is not restricted to any particular structure or class of discrete nonlinear systems. Consequently, the close-coupled nature of the example system in Fig. 2 will not be invoked and it will in no way modify the identification procedure from what it would otherwise be for systems that are not chain-like.

3.1 Polynomial Nonlinearities. The arbitrary nonlinear elements G_i interposed between the masses are dependent on the relative displacement z and velocity $\dot{z}$ across the terminals of each element. In the case of elements with polynomial nonlinearities, the elements assume the form

$$G_i(z,\dot{z}) = p_1^{(i)} z + p_2^{(i)} \dot{z} + p_3^{(i)} z^3 \tag{28}$$

where $p_1^{(i)}$ is the linear stiffness component, $p_2^{(i)}$ is the linear viscous damping term, and $p_3^{(i)}$ corresponds to the coefficient of the nonlinear cubic displacement term. Thus, depending on the sign of $p_3^{(i)}$, the form of G_i given in equation (28) can be made to represent restoring forces with hardening or softening nonlinearities—a commonly encountered type of nonlinearity in physical systems.

3.2 Hysteretic Nonlinearities. The form of the nonlinearity discussed so far involved polynomial-type without cross-product terms. To illustrate the wide applicability of the present method, a hysteretic-type restoring force will be considered. Such a nonlinearity not only involves cross-product terms of displacement and velocity, but is of course not even expressible in polynomial form. Hysteretic systems, widely encountered in all areas of applied mechanics (particularly building and equipment systems), are among the more difficult types of nonlinear properties to investigate and identify [11-21].

Consider the nonlinear model shown in Fig. 2 in which the first element G_1 has a hardening nonlinearity of the polynomial type, element G_2 is of a hysteretic type, and element G_3 has a softening nonlinearity of the polynomial type. Element G_2 is of the bilinear hysteretic form in which

$$\begin{aligned} z_y &\equiv \text{yield displacement level} = 2.5 \\ k_1 &\equiv \text{stiffness in the elastic range} = 14{,}900 \\ \alpha &\equiv k_2/k_1 = \text{stiffness ratio} = 0.414 \end{aligned} \tag{29}$$

This model will henceforth be referred to as model UCB-3.

As pointed out earlier, the nonparametric identification technique under discussion allows great freedom in the choice of the probing signal used for identification as long as the signal is persistently exciting and large enough to drive the system beyond the elastic region. To illustrate this, two simulated "experiments" will be considered: one case in

Table 1 Coefficients of $C1_{kl}^{(i)}$ of two-dimensional Chebyshev series for the identification of modal restoring functions for model UCB-3

TYPE OF EXCITATION : Random
LEVEL OF EXCITATION: σ = 30.000
LOCATION : At Mass 1
MODE : All 3

$$\hat{h}_i(u_i,\dot{u}_i) = \sum_k \sum_\ell C1_{k\ell}^{(i)}\, T_k(u_i)\, T_\ell(\dot{u}_i)$$

i = 1

k \ ℓ	$T_0(\dot{u})$	$T_1(\dot{u})$	$T_2(\dot{u})$	$T_3(\dot{u})$	$T_4(\dot{u})$	$T_5(\dot{u})$	$T_6(\dot{u})$	$T_7(\dot{u})$
$T_0(u)$	-123.20	1767.00	-90.45	723.50	-190.50	633.00	-126.40	83.93
$T_1(u)$	8801.00	-54.30	-16.18	-142.20	-130.30	84.99	-78.13	-60.90
$T_2(u)$	-127.50	198.80	-14.89	381.20	-4.96	310.30	126.10	-129.90
$T_3(u)$	-254.10	210.50	177.50	8.72	216.90	112.70	152.40	-73.49
$T_4(u)$	-20.31	-147.90	-60.59	100.60	-15.24	-92.25	128.50	-9.75
$T_5(u)$	-364.50	-84.94	-203.90	-0.21	-220.70	-43.66	-75.76	-3.14
$T_6(u)$	54.73	-89.86	16.90	-111.80	84.68	-125.40	-171.40	-66.21
$T_7(u)$	13.07	-132.40	77.50	39.17	105.60	-56.43	79.06	-6.58

ϵ^* = 0.2109

i = 2

k \ ℓ	$T_0(\dot{u})$	$T_1(\dot{u})$	$T_2(\dot{u})$	$T_3(\dot{u})$	$T_4(\dot{u})$	$T_5(\dot{u})$	$T_6(\dot{u})$	$T_7(\dot{u})$
$T_0(u)$	-6610.00	8761.00	-522.10	-1124.00	779.30	116.00	-534.80	-503.30
$T_1(u)$	24890.00	-16.60	-733.50	-106.60	-71.10	-223.60	19.57	49.79
$T_2(u)$	-756.00	-657.50	301.70	-205.30	82.25	61.68	-289.80	-263.50
$T_3(u)$	-291.70	148.00	766.30	-80.39	545.60	604.40	-84.13	-99.12
$T_4(u)$	173.30	170.00	321.70	146.80	-136.30	-463.70	-21.20	13.84
$T_5(u)$	582.60	-110.30	335.40	65.00	-640.40	-14.30	-130.00	-339.60
$T_6(u)$	38.75	-122.60	9.62	167.50	220.80	89.88	-11.13	230.10
$T_7(u)$	-228.80	66.81	-373.40	-131.00	49.18	-110.10	34.55	91.50

ϵ^* = 0.3416

i = 3

k \ ℓ	$T_0(\dot{u})$	$T_1(\dot{u})$	$T_2(\dot{u})$	$T_3(\dot{u})$	$T_4(\dot{u})$	$T_5(\dot{u})$	$T_6(\dot{u})$	$T_7(\dot{u})$
$T_0(u)$	-1826.00	4534.00	135.00	-106.30	176.80	-385.60	123.70	-15.28
$T_1(u)$	9890.00	-12.38	-226.60	-1.44	135.00	11.66	-55.16	-38.65
$T_2(u)$	-868.40	30.13	310.30	-207.00	-163.10	39.56	5.29	-19.67
$T_3(u)$	-287.30	68.38	176.60	-32.52	-108.30	10.83	-8.67	70.84
$T_4(u)$	-374.50	1.33	59.97	159.20	29.92	-70.58	110.90	59.49
$T_5(u)$	415.40	-94.95	170.50	-9.70	-60.93	-24.29	15.96	-55.51
$T_6(u)$	472.60	1.09	-169.00	-44.59	-35.93	-45.23	-92.88	30.12
$T_7(u)$	-228.90	78.80	-172.50	67.63	130.10	60.35	50.78	-17.98

ϵ^* = 0.4288

which a swept-sine excitation is used, and another case in which a broad-band random excitation is applied.

Following the identification procedure outlined in the foregoing and using mode-shape estimates based on the average stiffness of the system result in the measurements shown in Figs. 3 and 4. From Fig. 4(*b*) the example structure is clearly undergoing a large nonlinear deformation of the bilinear hysteretic type with a ductility ratio $\mu \equiv$ (peak displacement)/(yield displacement) of about $\mu = 2$.

The representative measurements, shown in Figs. 5(*a*) and (*d*) for the estimated modal displacements u_i and in Figs. 5(*b*) and (*e*) for the estimated modal velocities $\dot{u}_i$ (under swept-sine and random excitation, respectively), clearly indicate the predominant component of the response corresponds to the first mode in both excitation cases. Howevere, the estimated modal restoring forces shown in Figs. 5(*c*) and (*f*) show that contributions of higher modes are quite significant, particularly under broad-band excitation.

The plots of the estimated modal restoring forces versus their corresponding modal displacement in Fig. 6 clearly indicate the presence of hysteretic components in the system.

Using Chebyshev polynomials in accordance with equations (9)–(14) to obtain two-dimensional fits for the surfaces of the modal restoring functions will yield the typical identification results shown in Table 1 and Fig. 7.

Although the fits for the various modal restoring forces over the total record length are not as good as in the case of polynomial nonlinearities [24] as evidenced by the residual error, the representative time-history segments exhibited in Fig. 7 clearly show that the quality of the Chebyshev fit, under both swept-sine and random excitation, is good for the frequency content as well as amplitude of each of the three modal restoring forces.

The identification process yields a nonparametric model for an equivalent memoryless nonlinear system. The area enclosed by the loop is the mechanical energy dissipated per cycle of motion. Using energy approaches, the work done by the hysteretic element per cycle can be equated to that done by an equivalent viscous damper [22, 23] to estimate the value of c_{eq}, the equivalent coefficient of viscous damping for the hysteretic element. The C_{01} coefficients in Table 1 corresponding to h_i are close estimates of the generalized equivalent viscous damping c_{eq_i} for each mode.

It should be emphasized that the identification does not find the parameters of the hysteretic loop. Rather, it produces the Chebyshev coefficients of a model whose response matches the measured system response in a least-squares sense for the given excitation. The fact that the hysteretic loop is not an analytic function is immaterial, since the Chebyshev expansion treats all nonlinearities equally. When the nonlinearity is not a function, the procedure fits an equivalent memoryless nonlinear restoring force in a least-squares sense.

It is clear from Table 1 that determining the optimum least-squares fit for the data associated with the hysteretic system does involve many cross-product terms in displacement and velocity. It also requires a relatively larger number of terms in the series (eight used in the present example) for a good estimate.

The preceeding is a good illustration of the need to use two-dimensional surface fits rather than uncoupled one-dimensional series to estimate the system properties. Whether cross-coupling is significant or not is a decision that need not

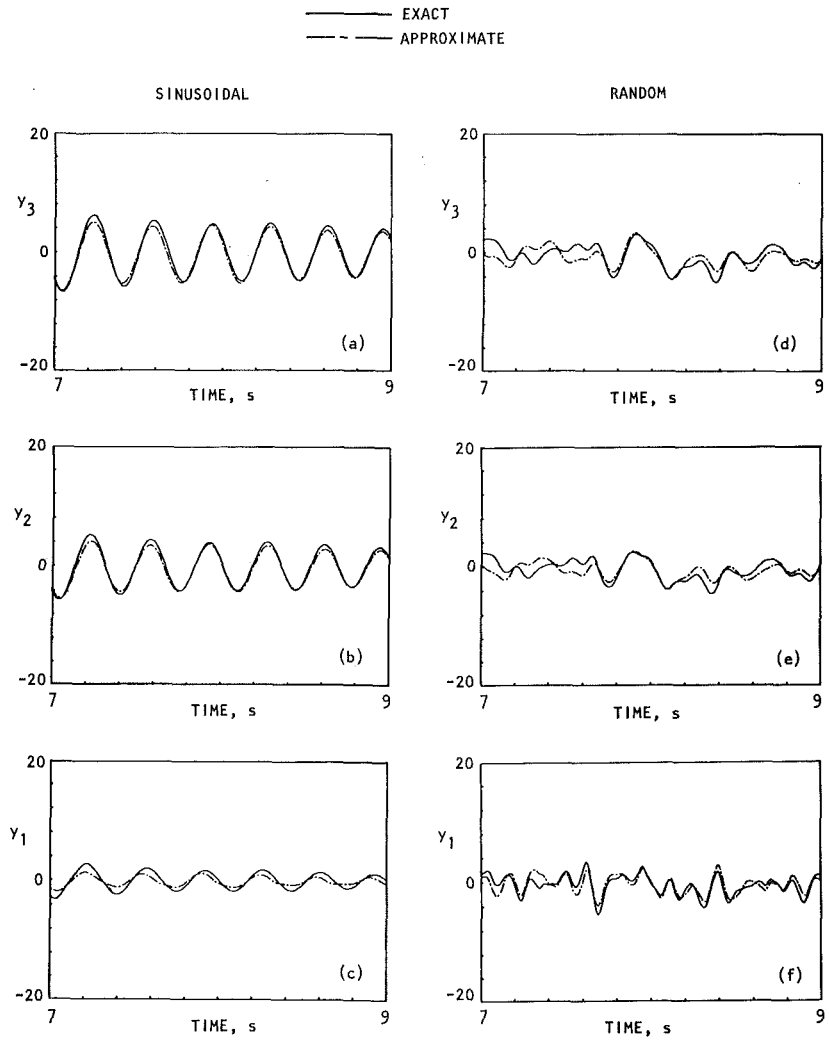

Fig. 8 Comparison between the measured and predicted displacement of hysteretic system UCB-3 under sinusoidal and random excitation by using in both cases the approximate model identified with *random* excitation

be made a priori when following the method presented here—the system will effectively "decide" by its own response (signature) the extent and relative dominance or contribution arising from various powers of $T_i(u)\,T_j(\dot{u})$.

The adequacy of the approximate (identified) nonlinear model to predict the response of the exact (hysteretic) nonlinear system UCB-3 under deterministic and random excitation is clearly illustrated by the results shown in Figs. 8–10, in which the "exact" displacement, velocity, and acceleration of each mass location of the system UCB-3 is compared to its corresponding value as computed on the basis of the approximate nonlinear model. A further demonstration of the validity of the present identification method is that the estimated response of the system under *sinusoidal* excitation shown in Figs. 8–10 was predicted by means of the approximate nonlinear model identified by means of a *random* probing signal.

Additional details and examples that are useful in evaluating the identification method under discussion are available in [24].

4 Summary and Conclusions

A relatively simple and approximate nonparametric identification technique has been presented that is suitable for use with discrete multidegree-of-freedom nonlinear dynamic systems. The method requires information regarding the system response and estimates of its pertinent "mode shapes" to determine, by means of regression techniques involving the use of two-dimensional orthogonal functions, an approximate expression for the surface of each of the system generalized restoring forces in terms of the corresponding generalized system state variables.

The main features of this method are:

(1) Practically any type of nonlinear system characteristics can be accurately identified. Hysteretic systems, which pose problems for conventional nonparametric identification techniques, can be easily handled and reasonably estimated by the present method since they are not treated any differently from other arbitrary nonlinearities.

(2) Virtually any type of probing signal can be used for identification; i.e., random signals (stationary or nonstationary) and swept-sine signals are equally suitable.

(3) Very modest amounts of computer time are needed to implement the method.

(4) Computer storage requirements are extremely compact for the characterization of arbitrarily nonlinear systems.

(5) Fast convergence can be achieved with very few terms in the series expansion even in the case of hysteretic systems.

(6) Noise pollution of the data has a minimal effect on the identification results obtained by this technique.

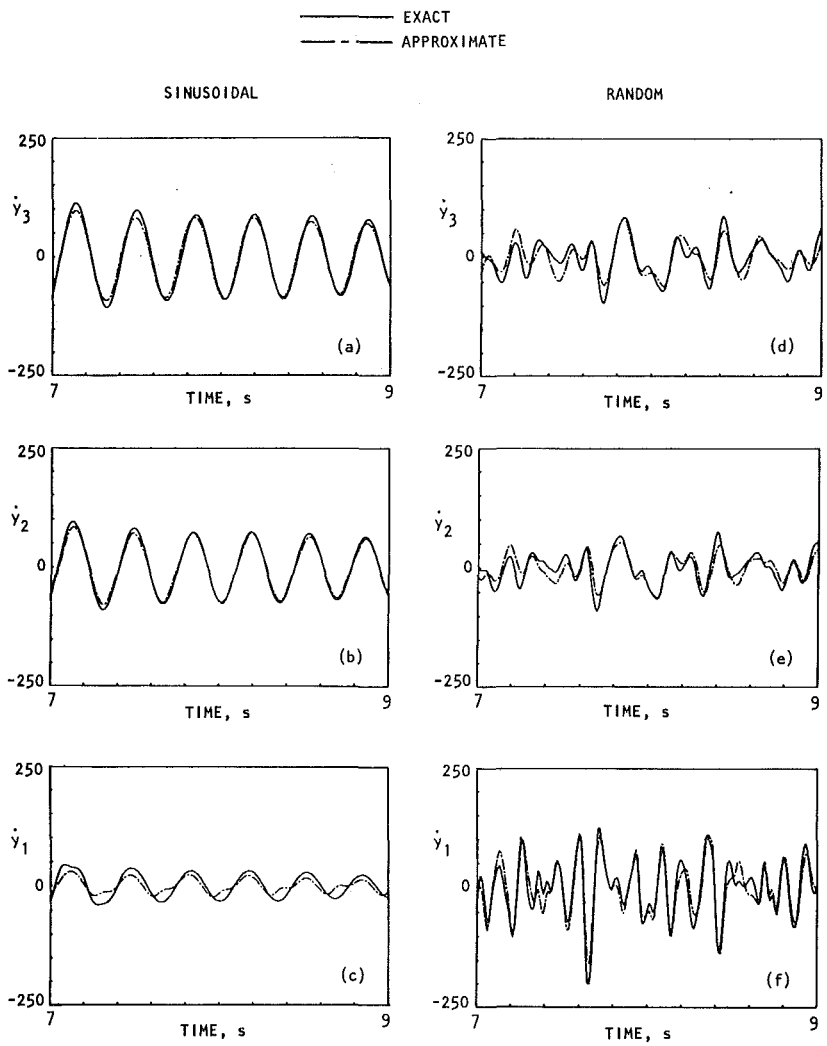

Fig. 9 Comparison between the measured and predicted velocity of hysteretic system UCB-3 under sinusoidal and random excitation by using in both cases the approximate model identified with random excitation

Acknowledgments

This study was supported in part by a grant from the National Science Foundation. The comments of G. A. Bekey and the assistance of D. Oba in the preparation of the manuscript are appreciated.

References

1 Ibanez, P., "Review of Analytical and Experimental Techniques for Improving Structural Dynamic Models," *Welding Research Council Bulletin*, No. 249, June 1979.

2 Volterra, V., *Theory of Functionals and of Integral and Integro-Differential Equations*, Dover, New York, 1959.

3 Wiener, N., *Nonlinear Problems in Random Theory*, M.I.T. Press, Cambridge, Mass., 1958.

4 Lee, Y. W., and Schetzen, M., "Measurement of the Wiener Kernels of a Nonlinear System by Cross Correlation," *International Journal of Control*, Vol. 2, 1965, pp. 237-254.

5 Caughey, T. K., "Nonlinear Analysis, Synthesis and Identification Theory," *Proc. Symposium on Testing and Identification of Nonlinear Systems*, California Institute of Technology, Mar. 1975, pp. 1-14.

6 Masri, S. F., and Caughey, T. K., "A Nonparametric Identification Technique for Nonlinear Dynamic Problems," ASME JOURNAL OF APPLIED MECHANICS, Vol. 46, June 1979, pp. 433-447.

7 Masri, S. F., Bekey, G. A., Sassi, H., and Caughey, T. K., "Non-parametric Identification of a Class of Nonlinear Multidegree Dynamic Systems," *Journal of Earthquake Engineering and Structural Dynamics*, Vol. 10, 1982, pp. 1-30.

8 Caughey, T. K., and O'Kelley, M. E. J., "Classical Normal Modes in Damped Linear Dynamic Systems," ASME JOURNAL OF APPLIED MECHANICS, Vol. 32, 1965, p. 583.

9 Clough, R. W., and Tang, D. T., "Earthquake Simulated Study of a Steel Frame Structure, Vol. I: Experimental Results," University of California, Berkeley, Report No. EERC 75-6, Apr. 1975.

10 Tang, D. T., "Earthquake Simulated Study of a Steel Frame Structure, Vol. II: Analytical Results," University of California, Berkeley, Report No. EERC 75-36, Oct. 1975.

11 Andronikou, A. M., and Bekey, G. A., "Identification of Hysteretic Systems," *Proc. of the 18th IEEE Conf. on Decision and Control*, Dec. 1979, pp. 1072-1073.

12 Distefano, N., and Todeschini, R., "Modeling Identification and Prediction of a Class of Nonlinear Viscoelastic Materials," *International Journal of Solids and Structures*, Part I, Vol. 9, 1974, pp. 805-818.

13 Distefano, N., and Todeschini, R., "Modeling, Identification and Prediction of a Class of Nonlinear Viscoelastic Materials," *International Journal of Solids and Structures*, Part II, 1973, pp. 1431-1438.

14 Caughey, T. K., "Random Excitation of a System with Bilinear Hysteresis," ASME JOURNAL OF APPLIED MECHANICS, Vol. 27, Dec. 1960, pp. 649-652.

15 Caughey, T. K., "On the Response of a Class of Nonlinear Oscillators to Stochastic Excitation," *Proc. Colloq. International de Centre National de la Rocherche Scientifique*, Marseille, France, No. 148, 1964, pp. 393-402.

16 Clough, R. W., and Benuska, K. L., "Nonlinear Earthquake Behavior of Tall Buildings," *Journal of Engineering Mechanics Division*, Proc. ASCE, Vol. 93, No. EM3, June 1967, pp. 129-146.

17 Iwan, W. D., "The Steady-State Response of the Double Bilinear Hysterestic System," ASME JOURNAL OF APPLIED MECHANICS, Vol. 32, Dec. 1965, pp. 921-925.

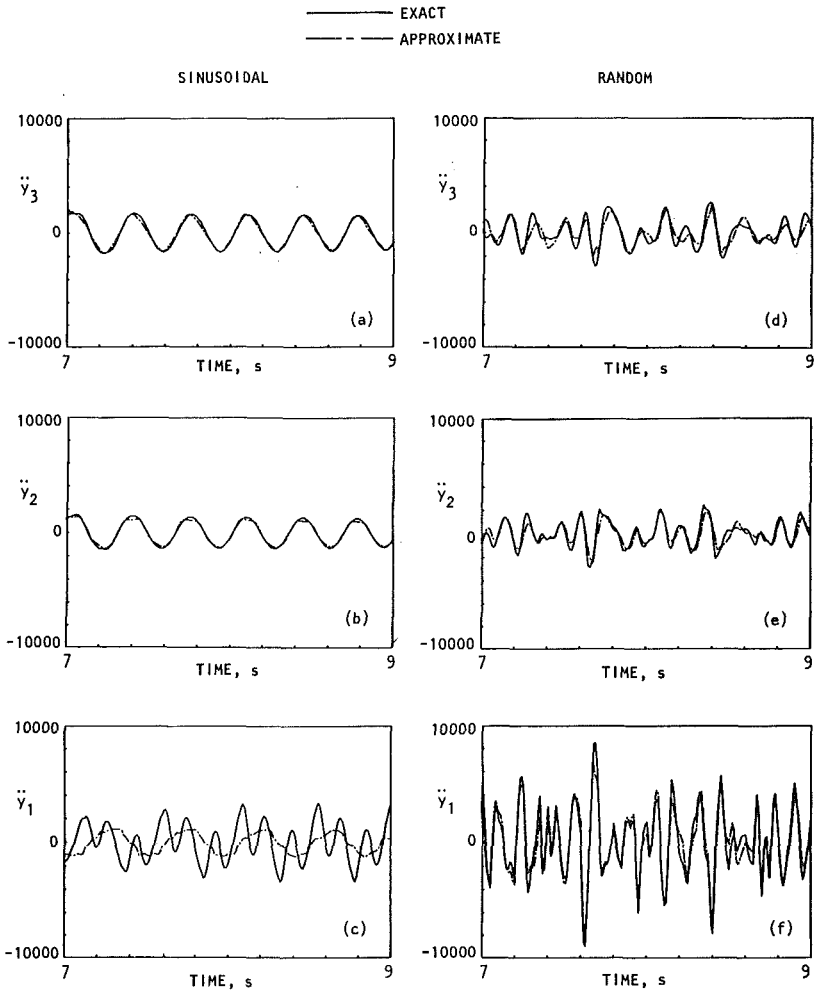

Fig. 10 Comparison between the measured and predicted acceleration of hysteretic system UCB-3 under sinusoidal and random excitation by using in both cases the approximate model identified with random excitation

18 Iwan, W. D., "A Distributed-Element Model for Hysteresis and Its Steady-State Dynamic Response," ASME JOURNAL OF APPLIED MECHANICS, Vol. 33, No. 4, Dec. 1966, pp. 893–900.

19 Iwan, W. D., and Lutes, L. D., "Response of the Bilinear Hysteretic System to Stationary Random Excitation," *Journal of the Acoustical Society of America*, Vol. 43, No. 3, Mar. 1968, pp. 545–552.

20 Jennings, P. C., "Periodic Response of a General Yielding Structure," *Journal of Engineering Mechanics Division*, Proc. ASCE, Vol. 90, No. EM2, 1964, pp. 131–166.

21 Lutes, L. D., and Takemiya, H., "Random Vibration of Yielding Oscillator," *Journal of the Engineering Mechanics Division*, Proc. ASCE, Vol. 100, No. EM2, pp. 343–358.

22 Hudson, D. E., "Equivalent Viscous Friction for Hysteretic Systems With Earthquake-Like Excitation," *Proc. 3WCEE*, New Zealand, 1965.

23 Jennings, P. C., "Equivalent Viscous Damping for Yielding Structures," *Journal of Engineering Mechanics*, ASCE, Feb. 1968.

24 Masri, S. F., Sassi, H., and Caughey, T. K., "Nonparametric Identification of Nonlinear Systems," University of Southern California, Department of Civil Engineering, Report No. CE-82-01, Los Angeles, Calif., Jan. 1982.

T. K. Caughey
Professor of Applied Mechanics.

F. -Ma
Graduate Student in Applied Mathematics.

California Institute of Technology,
Pasadena, Calif. 91125

The Steady-State Response of a Class of Dynamical Systems to Stochastic Excitation

In this paper a class of coupled nonlinear dynamical systems subjected to stochastic excitation is considered. It is shown how the exact steady-state probability density function for this class of systems can be constructed. The result is then applied to some classical oscillator problems.

1 Introduction

In the last 20 years the response of nonlinear dynamical systems to stochastic excitation has been extensively studied. The diffusion processes approach to this problem leads to the Kolmogorov equations, which have, until now, been explicitly solved only in a few simple cases. For linear systems the transition probability density function can be obtained by a variety of methods [1, 2], whereas in the nonlinear case only some specific one-dimensional systems have been exactly solved so far [3]. An honest survey of the developments in this area can be found in [3, 4]. In recent years the use of approximate techniques in the treatment of random vibrations has become increasingly popular [5–7]. It is expected that in the next decade this trend will continue as computing costs decrease.

Our present knowledge of the steady-state response of nonlinear systems to white noise excitation is also far from a state of maturity [3]. The exact steady-state probability density for any one-dimensional nonlinear system, if it exists, has been found. Some specific nonlinear dynamical systems of higher dimensions have been considered [3], but in general very little is known. If the steady-state probability density of a dynamical system exists and can be found, then it may be possible to obtain the approximate nonstationary response by perturbation analysis [8]; the exact procedures to be used are dependent on the system under consideration. The purpose of this paper is to construct the exact steady-state probability density of a class of nonlinear dynamical systems subjected to stochastic excitation. It will also be shown that some previously published results [3] are particular cases of our present investigation.

2 Construction of Steady-State Solution

Consider the autonomous dynamical system in R^{2n} whose behavior when subjected to white noise excitation is described by the following equation

$$\left.\begin{aligned}\begin{pmatrix}\dot{x}_{2i-1}\\ \dot{x}_{2i}\end{pmatrix} &= \begin{pmatrix} h_i(x_{2i}) \\ -f(H)h_i(x_{2i}) - g_i(x_1, x_3, \ldots, x_{2n-1})\end{pmatrix} + \begin{pmatrix}0\\ w_i(t)\end{pmatrix}\\ x_i(0) &= y_i.\end{aligned}\right\} \tag{1}$$

for $1 = 1, 2, \ldots, n$, where $w_i(t)$ are independent Wiener processes with zero means and $E(dw_i(t)dw_j(t)) = 2D\delta_{ij}dt$. The functions $g_i(x_1, x_3, \ldots, x_{2n-1})$ assumed to arise from a potential function $V(x_1, x_3, \ldots, x_{2n-1})$:

$$g_i(x_1, x_3, \ldots, x_{2n-1}) = \frac{\partial}{\partial x_{2i-1}} V(x_1, x_3, \ldots, x_{2n-1}) \qquad i = 1, 2, \ldots, n \tag{2}$$

and H *is* defined by

$$H(\mathbf{x}) = \sum_{i=1}^{n} \int_0^{x_{2i}} h_i(\zeta)\, d\zeta + V(x_1, x_3, \ldots, x_{2n-1}) \tag{3}$$

where

$$\mathbf{x} = \begin{pmatrix} x_1 \\ x_2 \\ \cdot \\ \cdot \\ \cdot \\ x_{2n} \end{pmatrix}$$

At the present stage we further assume that

(*i*) f, H, V have continuous second-order derivatives, $H \geq 0$ and there exists an $H_0 > 0$ such that $f(H) \geq 0$ if $H > H_0$. In addition,

$$f^{-2}\frac{df}{dH} \to 0 \text{ as } H \to \infty$$

(*ii*) There exists a constant L such that

$$\sum_{i=1}^{n} |h_i|^2 + \sum_{i=1}^{n} |f(H)h_i + g_i|^2 \leq L(1 + |\mathbf{x}|^2) \tag{5}$$

Contributed by the Applied Mechanics Division for publication in the JOURNAL OF APPLIED MECHANICS.

Discussion on this paper should be addressed to the Editorial Department, ASME, United Engineering Center, 345 East 47th Street, New York, N.Y. 10017, and will be accepted until two months after final publication of the paper itself in the JOURNAL OF APPLIED MECHANICS. Manuscript received by ASME Applied Mechanics Division, July, 1981.

where the vector $\mathbf{x}$ is defined by (4) and the arguments of the functions on the left-hand side are those components of $\mathbf{x}$ previously indicated.

These restrictions will be relaxed later on. The preceding assumptions are such that the Lipschitz conditions for system (1) are satisfied. A little manipulation with L and the Lipschitz constants reveals that assumptions (*i*) and (*ii*) are sufficient to guarantee the following result of Ito [3, 9]: there exists an almost everywhere continuous solution of system (1) which is a homogeneous Markov process, the solution being unique up to a stochastic equivalence. Moreover, when an invariant distribution exists, the unique steady-state probability density $p(\mathbf{x})$ may be obtained from the stationary form of the Fokker-Planck equation where $\partial p/\partial t = 0$. The previous statement expresses the equivalence under very mild restrictions of the stochastic differential equations approach and the diffusion processes approach [10], a topic that has been rigorously examined by mathematicians. Hence we will have constructed the only steady-state probability density from the stationary Fokker-Planck equation subsequently, under assumptions (*i*) and (*ii*).

We have been interpreting the dynamical system (1) using Ito calculus [10]. It is immaterial whether system (1) is regarded in the sense of Ito or in the sense of Stratonovich [11, 12] since in this particular case the so-called Wong and Zakai [13] corrections terms to the drift vector are identically zero. It is for this reason that assumption (1) need only hold on every finite domain. (Suppose S is a system where conditions (*i*) only hold on every finite region. Define a sequence of systems S_n in the following way: S_n is the restriction of S on the closed ball $B(0, n)$, and f, H, V are assigned suitable constant values outside $B(0, n)$. As $n \to \infty$, S_n tends to S and, for the type of systems considered in this paper [13, 14], the solution of S_n converges to the solution of S. (We have not discussed condition (*ii*) because it will later be removed.) Let $p(\mathbf{x}, t \mid \mathbf{y})d\mathbf{x}$ be the probability of the system (1) in the range $(x, x+\mathbf{dx})$ at time t given that it is initially at $\mathbf{y}$. The associated system of Fokker-Planck equations has the form

$$\left.\begin{aligned}\frac{\partial p}{\partial t} = &-\frac{\partial}{\partial x_{2i-1}}\left[h_i(x_{2i})p\right] + \frac{\partial}{\partial x_{2i}}\Big[(f(H)h_i(x_{2i}) + \\ &g_i(x_1, x_3, \ldots, x_{2n-1}))p\Big] + D\frac{\partial^2 p}{\partial x_{2i}^2} \\ &i = 1,2, \ldots, n\end{aligned}\right\} \quad (6)$$

As previously explained, the steady-state density is governed by the following system of linear partial differential equations

$$g_i\frac{\partial p}{\partial x_{2i}} - h_i(x_{2i})\frac{\partial p}{\partial x_{2i-1}} + \frac{\partial}{\partial x_{2i}}\left[f(H)h_i(x_{2i})p + D\frac{\partial p}{\partial x_{2i}}\right] = 0 \quad (7)$$

$$i = 1, 2, \ldots, n$$

First we observe that if $p(\mathbf{x})$ satisfies the following conditions it will certainly be a solution of (7)

$$g_i\frac{\partial p}{\partial x_{2i}} - h_i(x_{2i})\frac{\partial p}{\partial x_{2i-1}} = 0 \quad (8)$$

$$\frac{\partial}{\partial x_{2i}}\left[f(H)h_i(x_{2i})p + D\frac{\partial p}{\partial x_{2i}}\right] = 0 \quad (9)$$

$$i = 1, 2, \ldots, n$$

Since (8) constitutes a linear first-order system of partial differential equations, we may solve them by the method of characteristics [15]. The subsidiary equations are

$$-\frac{dx_{2i-1}}{h_i(x_{2i})} = \frac{dx_{2i}}{g_i} = \frac{dp}{0} \quad i = 1, 2, \ldots, n$$

for which two independent integrals are

$$p = \text{constant} \quad (10)$$

and

$$V(x_1, x_3, \ldots, x_{2n-1}) + \int_0^{x_{2i}} h_i(\zeta)d\zeta = k_i \quad (11)$$

$$i = 1,2, \ldots, n$$

where k_i is a constant depending on x_{2j}, $j = 1, 2, \ldots, n$, $j \neq i$. The system of equations (11) is equivalent to

$$H = V(x_1, x_3, \ldots, x_{2n-1}) + \sum_{i=1}^{n}\int_0^{x_{2i}} h(\zeta)d\zeta = \text{constant} \quad (12)$$

Thus the general solution for (8) is of the form

$$p = \phi(H) \quad (13)$$

where ϕ is an arbitrary function. Since p and its first partial derivatives vanish as $|\mathbf{x}| \to \infty$, equations (9) imply

$$f(H)h_i(x_{2i})p + D\frac{\partial p}{\partial x_{2i}} = 0 \quad i = 1,2, \ldots, n \quad (14)$$

Substituting (13) into (14), we have

$$h_i(x_{2i})\left[D\frac{d\phi}{dH} + f(H)\phi\right] + 0 \quad i = 1,2, \ldots, n \quad (15)$$

Assuming that none of h_i is identically zero, it follows that

$$\phi = A\exp\left(-\frac{1}{D}\int_0^H f(\zeta)d\zeta\right)$$

where A is a normalizing constant. Hence the steady state density is given by

$$p(\mathbf{x}) = \frac{\exp\left(-\frac{1}{D}\int_0^H f(\zeta)d\zeta\right)}{\int_{-\infty}^{\infty}\exp\left(-\frac{1}{D}\int_0^H f(\zeta)d\zeta\right)d\mathbf{x}} \quad (16)$$

where the denominator is a $2n$-fold integral. It can be easily checked that the expression defined in (16) satisfies all the requirements for a probability density function and therefore it represents the unique steady-state density of the coupled nonlinear dynamical system (1), under the assumptions (*i*) and (*ii*).

The assumption (*ii*) is a rather severe growth restriction on the class of systems under consideration. It should be removed if our results are to be of practical use. To this end we recall the concept of well-behaved solutions (see Appendix). Now it can be shown that under assumption (*i*) the solution (16) is a well-behaved solution of the stationary Fokker-Planck equation (7). Since it has been shown that a well-behaved solution of the stationary Fokker-Planck equation is unique [8, 16], we have the following result.

Theorem. The solution (16) is the unique steady-state solution of the dynamical system (1) subjected only to conditions (*i*).

It should be noted that the last theorem can also be established by using only the diffusion processes approach (i.e., a direct interpretation of the solution of the stochastic differential equation (1); using Ito calculus is not required). In this case (see the Appendix) some caution is needed to furnish a rigorous argument because the hard machinery needed comes from the theory of partial differential equations [8]. It is clear that assumption (*i*) is sufficient but not necessary and thus can be relaxed. In order to keep physically interpretable conditions, this will not be done in this paper.

3 Applications and Further Discussion

We shall apply the theorem established in the previous section to some classical oscillator problems, mentioning possible extensions when appropriate.

Example 1. The motion of a Brownian particle in a constant force field with dissipation of Rayleigh type [1, 17] may be described by

$$\ddot{x}+\beta\dot{x}+g=\dot{w}(t) \tag{17}$$

where $E(\dot{w}(S)\dot{w}(t))=2D\delta(t-s)$. The associated Fokker-Planck equation is

$$\frac{\partial p}{\partial t}=-\dot{x}\frac{\partial p}{\partial x}+g\frac{\partial p}{\partial \dot{x}}+\frac{\partial}{\partial \dot{x}}\left[\beta\dot{x}p+D\frac{\partial p}{\partial \dot{x}}\right] \tag{18}$$

We assume that there is a reflecting barrier at $x=0$, so that the particle does not disappear toward $x=-\infty$. We may consider the present system as a particular case of (1) and make the following identifications:

$$n=1$$
$$x_1=x$$
$$x_2=\dot{x}=h_1$$
$$f=\beta$$
$$g_1=g$$

Then $H=1/2\dot{x}^2+gx$ and the unique steady-state density as given by (16) is

$$p(x,\dot{x})=\frac{1}{g}\sqrt{\frac{2\pi D}{\beta}}\exp\left(-\frac{\beta}{D}\left(\frac{1}{2}\dot{x}^2+gx\right)\right) \tag{19}$$

for $x\geq 0$, $-\infty<\dot{x}<\infty$. This is the well-known barometric distribution [1].

Example 2. Consider the following self-excited oscillator corrupted by white noise

$$\ddot{x}-\epsilon(1-\dot{x}^2-x^2)\dot{x}+x=w(t) \tag{20}$$

where $\epsilon>0$. This can be written in the equivalent form

$$\begin{bmatrix}\dot{x}_1\\ \dot{x}_2\end{bmatrix}=\begin{bmatrix}x_2\\ \epsilon(1-x_1^2-x_2^2)x_2-x_1\end{bmatrix}+\begin{bmatrix}0\\ \dot{w}(t)\end{bmatrix} \tag{21}$$

Hence by taking $h_1=x_2$, $g_1=x_1$, we have $H=1/2\,{x_1}^2+1/2{x_2}^2$, $f=-\epsilon(1-2H)$, and the steady-state density is given by

$$p(x_1,x_2)=C\exp\left(\frac{\epsilon}{D}H(1-H)\right) \tag{22}$$

where $C=\int_{-\infty}^{\infty}\int_{-\infty}^{\infty}\exp(\epsilon/DH(1-H))\,dx_1dx_2$. It is easy to check that the function (22) is a well-behaved solution of the associated Fokker-Planck equation. It is also easy to see that all circles on the x_1x_2 plane with centers at the origin are loci of constant probability for the steady-state distribution. Moreover the steady-state density attains a maximum when $H=1/2$ corresponding to ${x_1}^2+{x_2}^2=1$, and decreases exponentially on either side of the unit circle. If we now examine the deterministic oscillator obtained by omitting the last term on the right-hand side of (21), we will find by a standard analysis using the Poincaré-Bendixson theorem [18] that the unit circle is the unique limit cycle for the deterministic oscillator.

The information given in the last paragraph suggests that the nonstationary response of the system (21) in the neighborhood of the limit cycle may be obtained by perturbation techniques. This has been done by one of us for the case of weak damping and weak excitation [8], when $\epsilon, D<<1$. The approximate spectral density has also been obtained by the same means.

Example 3. A class of generalized Van der Pol-Rayleigh oscillators subjected to white noise excitation is described by the equation [3]

$$\ddot{x}+f(H)\dot{x}+g(x)=\dot{w}(t)\quad x(0)=y,\dot{x}(0)=\dot{y} \tag{23}$$

where $E((dw(t))^2)=2D\,dt$. The equivalent first-order system is

$$\begin{bmatrix}\dot{x}_1\\ \dot{x}_2\end{bmatrix}=\begin{bmatrix}x_2\\ -f(H)x_2-g(x_1)\end{bmatrix}+\begin{bmatrix}0\\ \dot{w}(t)\end{bmatrix} \tag{24}$$

where $H=1/2x_2{}^2+\int_0^{x_1}g(\zeta)d\zeta$ is a measure of the system energy. In this case the associated Fokker-Planck equation is

$$\left.\begin{aligned}\frac{\partial p}{\partial t}&=-x_2\frac{\partial p}{\partial x_1}+\frac{\partial p}{\partial x_2}(f(H)x_2+g(x_1))p+D\frac{\partial^2 p}{\partial {x_2}^2}\\ \lim_{t\to 0}\ p(x_1,x_2,t\,|y,\dot{y})&=\delta(x_1-y)\,\delta(x_2-\dot{y})\end{aligned}\right\} \tag{25}$$

The steady-state solution as given by (16) is

$$p(x_1,x_2)=C\exp\left(-\frac{1}{D}\int_0^H f(\zeta)d\zeta\right) \tag{26}$$

where $C^{-1}=\int_{-\infty}^{\infty}\int_{-\infty}^{\infty}\exp\ (-1/D\int_0^H f(\zeta)d\zeta)dx_1dx_2$. If the system (24) possesses limit cycles, then the steady-state density (26) will have relative peaks on these limit cycles, with exponential decay away from the limit cycles. The nonstationary response in the neighborhood of a limit cycle may be obtained by perturbation techniques, the particular methods used are dependent on the form of $f(H)$. Moreover, asymptotic matching on regions enclosed by two adjacent limit cycles may be used in some cases to determine a uniform approximation. This is the subject of a subsequent paper.

4 Conclusion

In this paper the exact steady-state probability density function of a class of stochastic dynamical systems has been constructed. The construction has been justified by two alternative procedures. The result has been tested in some classical oscillator problems. When the steady-state density is known, the possibility of using perturbation techniques to compute the nonstationary response has been pointed out. In fact, a multiple-scale analysis has been used by one of us in an earlier paper [8] to derive the approximate nonstationary response of a specific oscillator. The conditions (*i*) made in this paper are sufficient but not necessary. Some of the smoothness requirements may be relaxed to handle specific problems.

References

1 Wang, M. C., and Uhlenbeck, G. E., "On the Theory of the Brownian Motion II," *Rev. Mod. Phy.*, Vol. 17, 1945, pp. 323-342.

2 Bharucha-Reid, A. T., *Elements of the Theory of Markov Processes and Their Applications*, McGraw-Hill, New York, 1960.

3 Caughey, T. K., "Nonlinear Theory of Random Vibrations," *Adv. Appl. Mech.*, Vol. 11, Academic Press, New York, 1971.

4 Ludwig, D., "Persistence of Dynamical Systems Under Random Perturbations," *SIAM Rev.*, Vol. 17, 1975, pp. 605-640.

5 Spanos, P-T. D., and Iwan, W. D., "On the Existence and Uniqueness of Solutions Generated by Equivalent Linearization," *Int. J. Nonlinear Mech.*, Vol. 13, 1978, pp. 71-78.

6 Johnson, J. P., and Scott, R. A., "Extension of Eigenfunction-Expansion Solutions of a Fokker-Planck Equation I. First Order System," *Int. J. Nonlinear Mech.*, Vol. 14, 1979, pp. 315-324.

7 Johnson, J. P., and Scott, R. A., "Extension of Eigenfunction-Expansion Solutions of a Fokker-Planck Equation II. Second Order System," *Int. J. Nonlinear Mech.*, Vol. 15, 1980, pp. 41-56.

8 Caughey, T. K., and Payne, H. J., "On the Response of a Class of Self-Excited Oscillators in Stochastic Excitation," *Int. J. Nonlinear Mech.*, Vol. 2, 1967, pp. 125-151.

9 Gikhman, I. I., and Skorokhad, A. V., *Introduction to the Theory of Random Processes*, Saunders Company, Philadelphia, 1969.

10 Arnold, L., *Stochastic Differential Equations—Theory and Applications*, Wiley-Interscience, New York, 1974.
11 Stratonovich, R. L., *Topics in the Theory of Random Noise, Vol. I*, Gordon and Breach, New York, 1963.
12 Stratonovich, R. L., *Topics in the Theory of Random Noise, Vol. II*, Gordon and Breach, New York, 1967.
13 Wong, E., and Zakai, M., "On the Relation Between Ordinary and Stochastic Differential Equations," *Int. J. Engrg. Sci.*, Vol. 3, 1965, pp. 213–229.
14 Gray, A. H., Jr. and Caughey, T. K., "A Controversy in Problems Involving Random Parametric Excitation," *J. Math. Phys.*, 1965, pp. 288–296.
15 Garabedian, P. R., *Partial Differential Equations*, Wiley, New York, 1964.
16 Gray, A. H., Jr., "Stability and Related Problems in Randomly Excited Systems," Ph.D. Thesis, California Institute of Technology, 1964.
17 Caughey, T. K., "Derivation and Application of the Fokker-Planck Equation to Discrete Nonlinear Dynamic Systems Subjected to White Random Excitation," *J. Acoust. Soc. Am.*, Vol. 35, 1963, pp. 1683–1692.
18 Meirovitch, L., *Methods of Analytical Dynamics*, McGraw-Hill, New York, 1970.

APPENDIX

Many problems in mechanics and related fields involving the response of dynamical systems to stochastic excitation can be modeled by stochastic differential equations of the form

$$d\mathbf{x}(t) = \mathbf{a}(t,\mathbf{x}(t))\,dt + \sum_{k=1}^{m} \sigma_k(t,\mathbf{x}(t))\,dw_k(t)$$
$$\mathbf{x}(t_0) = \mathbf{y} \tag{27}$$

where $\mathbf{x}$, $\mathbf{a}$, $\sigma_k \epsilon R^m$ for $k=1, 2, \ldots, m$, and the $w_k(t)$ for $k=1, 2, \ldots, m$ are independent Wiener processes, with $E(dw_i(t)\,dw_j(t)) = \delta_{ij}\,dt$. It can be shown that the response in this case is a Markov process. In appropriate circumstances [3, 9], the transition probability density function satisfies the Fokker-Planck equation in a region D

$$\frac{\partial p}{\partial t} = -\sum_{i=1}^{m} \frac{\partial}{\partial x_i}[a_i(t,\mathbf{x})]p + \frac{1}{2}\sum_{i=1}^{m} \frac{\partial}{\partial x_i \partial x_j}$$
$$[b_{ij}(t,\mathbf{x})p] = Lp \tag{28}$$

with initial condition

$$\lim_{t \to s} p(\mathbf{x},t\,|\mathbf{y},s) = \delta(\mathbf{x}-\mathbf{y})$$

The coefficients a_i, b_{ij} are derived in the following way: a_i are the components of $\mathbf{a}(t, \mathbf{x})$ and

$$b_{ij} = \sum_{k=1}^{m} \sigma_{ik}(t,\mathbf{x})\sigma_{jk}(t,\mathbf{x}) \tag{29}$$

where σ_{rs}, $r=1, 2, \ldots, m$, are the components of $\sigma_s(t, \mathbf{x})$ defined in (27). A well-behaved solution of the Fokker-Planck equation (28) is defined in the following way:

(*I*) If p_s is a solution of the stationary Fokker-Planck equation $Lp=0$, then it is well-behaved if

$$\sum_{i=1}^{m}\left[a_i p_s - \frac{1}{2}\sum_{j=1}^{m}\frac{\partial b_{ij}p}{\partial x_j}\right]\cdot n_i = 0 \quad p_s = 0 \tag{30}$$

on the boundary ∂D of the region D, where n_i are the components of the outward normal to ∂D. If D is an infinite domain, then (30) should be taken in a limiting sense.

(*II*) If p is a solution of the time-dependent Fokker-Planck equation, it is well behaved if equations (30) are satisfied with p_s replaced by p, and for all solutions p_s of the stationary equation $Lp=0$,

$$\left.\begin{aligned} &\int_D P_s^{-1} p^2\,d\mathbf{x} < \infty \\ &\int_D p_s^{-1}\left(\frac{\partial p}{\partial t}\right)^2 d\mathbf{x} < \infty \end{aligned}\right\} \tag{31}$$

for all $t>0$, with the convergence being uniform in t if D is an infinite domain.

The following has been established [8, 16].

Theorem

Well-behaved solutions to the Fokker-Planck equation are unique. Under some mild restrictions [8] the well-behaved solution p of the time-dependent Fokker-Planck equation converges in L^1 to a function of p_s as $t \to \infty$ and p_s is exactly a solution obtained by solving that stationary equation $L_p = 0$.

Because of the exponential nature of p defined in (16) and the conditions (*i*), it is easy to check that the solution (16) satisfies (30) and is thus the unique well-behaved steady-state solution. By assuming that the time-dependent solution of (28) is well behaved [8], a self-consistent diffusion processes approach based on the Fokker-Planck equation may be developed to derive the same results as in Section 2. In this case the intermediate use of assumption (*II*) is not needed.

Journal of Applied Mechanics

Design Data and Methods

Natural Frequencies of Thick Annular Plates

T. Irie,[1] G. Yamada,[1] and K. Takagi[1]

The natural frequencies of vibration based on the Mindlin plate theory are tabulated for uniform annular plates under nine combinations of boundary conditions.

The design data present the correct natural frequencies (the dimensionless frequency parameters) of uniform thick annular plates under nine combinations of boundary conditions for the six modes. The natural frequencies of annular plates based on the Mindlin theory have been previously obtained by Rao and Prasad under the same boundary conditions [1]. However, their results are incorrect as indicated by the present authors [2].

Here, a brief explanation is presented for the solution of thick annular plates for convenience of the calculation. The moments and shearing force of annular plates are expressed as [3, 4]

$$M_r = D\left\{\frac{\partial \psi_r}{\partial r} + \frac{\nu}{r}\left(\psi_r + \frac{\partial \psi_\theta}{\partial \theta}\right)\right\}$$

$$M_\theta = D\left\{\frac{1}{r}\left(\psi_r + \frac{\partial \psi_\theta}{\partial \theta}\right) + \nu\frac{\partial \psi_r}{\partial r}\right\}$$

$$M_{r\theta} = \frac{D(1-\nu)}{2}\left\{\frac{1}{r}\left(\frac{\partial \psi_r}{\partial \theta} - \psi_\theta\right) + \frac{\partial \psi_\theta}{\partial r}\right\} \tag{1}$$

and

$$Q_r = K^2 Gh\left(\psi_r + \frac{\partial W}{\partial r}\right)$$

$$Q_\theta = K^2 Gh\left(\psi_\theta + \frac{1}{r}\frac{\partial W}{\partial \theta}\right) \tag{2}$$

in terms of the transverse deflection W and the angular rotations ψ_r and ψ_θ of the normal to the middle surface in radial and circumferential directions, respectively. The quantity D is the flexural rigidity expressed by $D = Eh^3/12(1-\nu^2)$ using Young's modulus E, Poisson's ratio ν, and the plate thickness h. The quantity G is the shear modulus and $K^2 = \pi^2/12$ is the shear coefficient. The deflection and the rotations are written as

$$\psi_r = (\sigma_1 - 1)\frac{\partial W_1}{\partial r} + (\sigma_2 - 1)\frac{\partial W_2}{\partial r} + \frac{1}{r}\frac{\partial W_3}{\partial \theta}$$

$$\psi_\theta = (\sigma_1 - 1)\frac{1}{r}\frac{\partial W_1}{\partial \theta} + (\sigma_2 - 1)\frac{1}{r}\frac{\partial W_2}{\partial \theta} - \frac{\partial W_3}{\partial r}$$

$$W = W_1 + W_2 \tag{3}$$

using the functions

$$W_1 = \left\{C_1 J_n\left(\delta_1 \frac{r}{a}\right) + C_1^* Y_n\left(\delta_1 \frac{r}{a}\right)\right\}\cos n\theta$$

$$W_2 = \left\{C_2 J_n\left(\delta_2 \frac{r}{a}\right) + C_2^* Y_n\left(\delta_2 \frac{r}{a}\right)\right\}\cos n\theta$$

$$W_3 = \left\{C_3 J_n\left(\delta_3 \frac{r}{a}\right) + C_3^* Y_n\left(\delta_3 \frac{r}{a}\right)\right\}\sin n\theta$$

$$(n = 0,1,2, \ldots) \tag{4}$$

where C_i and C_i^* $(i = 1,2,3)$ are arbitrary constants and $J_n(x)$ and $Y_n(x)$ express Bessel functions of the first and second kinds, respectively. For simplicity of the treatment, the following dimensionless parameters have been introduced:

$$\delta_1^2, \delta_2^2 = \frac{1}{2}\lambda^4\{R + S \pm \sqrt{(R-S)^2 + 4/\lambda^4}\}$$

$$\delta_3^2 = 2(R\lambda^4 - 1/S)/(1-\nu)$$

$$\sigma_1, \sigma_2 = (\delta_2^2, \delta_1^2)/(R\lambda^4 - 1/S)$$

$$\mathrm{R} = (\mathrm{h/a})^2/12, \quad S = D/K^2 Ga^2 h = \{2/\pi^2(1-\nu)\}(h/a)^2 \tag{5}$$

The circular frequency is expressed as

$$\omega = \frac{\lambda^2}{a^2}\sqrt{\frac{D}{\rho h}} = \lambda^2\left(\frac{h}{a}\right)^2\sqrt{\frac{E}{12(1-\nu^2)\rho h^2}} \tag{6}$$

using a dimensionless frequency parameter λ^2. The quantity a is the outer radius of annular plates, and ρ is the mass per unit volume.

The boundary conditions at the edges are written as

$M_r = M_{r\theta} = Q_r = 0$ at a free edge

[1] Professor, Associate Professor, and Student, respectively, Department of Mechanical Engineering, Hokkaido University, Kita-13, Nishi-8, Kita-ku, Sapporo, 060 Japan.

Manuscript received by ASME Applied Mechanics Division, January, 1981; final revision, November, 1981.

Table 1 Frequency parameters λ_{ns}^2 of uniform annular plates with free inner edge; $\nu = 0.3$

(*a*) Plates with free outer edge

		$b/a=0.1$				0.2				0.3		
n	s	$h/a=0.1$	0.2	0.3	0.4	0.1	0.2	0.3	0.4	0.1	0.2	0.3
0	1	8.65	8.30	7.83	7.31	8.32	8.00	7.55	7.05	8.23	7.89	7.42
	2	35.95	31.23	26.58	22.69	39.08	33.79	28.71	24.55	46.63	39.57	33.18
1	1	19.56	17.75	15.70	13.77	18.59	16.66	14.57	12.65	17.02	15.13	13.16
	2	52.90	42.93	34.62	28.37	49.57	40.49	33.02	27.43	52.50	43.17	35.42
2	1	5.21	5.03	4.81	4.55	5.04	4.86	4.62	4.37	4.80	4.61	4.38
	2	32.69	28.39	24.12	20.51	32.04	27.86	23.68	20.13	30.77	26.63	22.52

		$b/a=0.4$			0.5			0.6		0.7		0.8
n	s	$h/a=0.1$	0.2	0.3	0.1	0.2	0.3	0.1	0.2	0.1	0.2	0.1
0	1	8.46	8.06	7.51	9.10	8.55	7.84	10.31	9.45	12.46	10.89	16.50
	2	59.60	49.09	40.33	81.03	64.01	51.25	118.14	88.23	188.95	131.06	349.39
1	1	15.92	14.08	12.17	15.76	13.77	11.72	16.71	14.19	19.12	15.27	23.85
	2	63.24	51.21	41.59	83.48	65.32	51.94	119.82	89.01	190.04	131.38	349.96
2	1	4.50	4.33	4.10	4.17	4.00	3.78	3.82	3.66	3.47	3.29	3.11
	2	29.03	24.87	20.80	28.05	23.64	19.42	28.75	23.46	31.83	24.19	38.32

(*b*) Plates with simply supported outer edge

		$b/a=0.1$				0.2				0.3		
n	s	$h/a=0.1$	0.2	0.3	0.4	0.1	0.2	0.3	0.4	0.1	0.2	0.3
0	1	4.81	4.70	4.54	4.34	4.68	4.58	4.43	4.25	4.63	4.53	4.39
	2	28.04	24.94	21.67	18.82	29.86	26.48	22.96	19.93	34.92	30.49	26.08
1	1	13.50	12.61	11.50	10.39	13.07	12.10	10.95	9.83	12.19	11.19	10.09
	2	43.83	36.52	30.05	25.08	40.82	33.99	28.09	23.52	41.45	34.80	28.93
2	1	24.26	21.76	19.04	16.63	23.80	21.38	18.73	16.36	23.07	20.71	18.13
	2	61.94	49.77	39.93	32.80	60.03	48.15	38.57	31.63	57.18	45.73	36.61

		$b/a=0.4$			0.5			0.6		0.7		0.8
n	s	$h/a=0.1$	0.2	0.3	0.1	0.2	0.3	0.1	0.2	0.1	0.2	0.1
0	1	4.73	4.62	4.47	5.03	4.91	4.72	5.65	5.47	6.81	6.49	9.23
	2	44.05	37.43	31.28	59.53	48.56	39.22	86.80	66.65	139.61	97.41	259.52
1	1	11.33	10.37	9.34	10.90	9.95	8.94	11.12	10.08	12.29	10.90	15.28
	2	48.15	40.04	32.96	62.28	50.22	40.24	88.71	67.72	140.90	98.04	260.29
2	1	21.95	19.61	17.10	20.92	18.56	16.11	20.71	18.17	22.01	18.86	26.24
	2	59.24	47.29	37.80	70.09	55.00	43.25	94.26	70.84	144.71	99.90	262.59

(*c*) Plates with clamped outer edge

		$b/a=0.1$				0.2				0.3		
n	s	$h/a=0.1$	0.2	0.3	0.4	0.1	0.2	0.3	0.4	0.1	0.2	0.3
0	1	9.90	9.22	8.37	7.50	10.15	9.48	8.62	7.75	11.12	10.35	9.39
	2	36.33	30.20	24.70	20.53	39.22	32.17	26.04	21.48	46.25	36.77	29.08
1	1	20.04	17.58	15.01	12.82	19.20	16.77	14.32	12.25	18.12	15.87	13.64
	2	52.53	41.05	32.23	26.06	49.21	38.52	30.26	24.40	51.74	40.18	31.32
2	1	31.86	26.72	22.02	18.37	31.21	26.24	21.65	18.08	30.08	25.33	20.96
	2	71.35	53.91	41.64	33.49	68.89	52.04	40.14	32.14	66.24	49.74	38.10

		$b/a=0.4$			0.5			0.6		0.7		0.8
n	s	$h/a=0.1$	0.2	0.3	0.1	0.2	0.3	0.1	0.2	0.1	0.2	0.1
0	1	13.19	12.16	10.91	17.02	15.40	13.55	24.26	21.22	39.37	32.44	77.85
	2	58.13	44.17	33.88	77.24	55.27	40.90	108.92	72.13	165.42	99.31	279.83
1	1	18.19	15.99	13.81	20.48	17.94	15.42	26.58	22.81	40.85	33.35	78.68
	2	61.45	46.19	35.19	79.41	56.57	41.71	110.39	72.98	166.42	99.85	280.47
2	1	28.80	24.24	20.13	29.02	24.33	20.21	32.95	27.28	45.19	36.08	81.18
	2	70.91	52.17	39.32	85.76	60.44	44.29	114.75	75.56	169.38	101.49	282.38

Table 2 Frequency parameters λ_{ns}^2 of uniform annular plates with simply supported inner edge; $\nu = 0.3$

(*a*) Plates with free outer edge

		$b/a=0.1$				0.2				0.3		
n	s	$h/a=0.1$	0.2	0.3	0.4	0.1	0.2	0.3	0.4	0.1	0.2	0.3
0	1	3.40	3.26	3.07	2.85	3.31	3.22	3.10	2.94	3.40	3.33	3.22
	2	19.79	17.35	14.81	12.65	23.56	20.80	17.82	15.21	29.79	25.89	21.87
1	1	2.34	2.18	2.02	1.88	2.84	2.72	2.58	2.43	3.33	3.23	3.09
	2	22.94	20.29	17.55	15.15	26.50	23.26	19.88	16.95	32.29	27.87	23.44
2	1	5.34	5.16	4.94	4.68	5.55	5.35	5.10	4.83	5.96	5.74	5.45
	2	33.43	28.93	24.49	20.74	35.30	30.28	25.44	21.40	39.64	33.52	27.78

		$b/a=0.4$			0.5			0.6		0.7		0.8
n	s	$h/a=0.1$	0.2	0.3	0.1	0.2	0.3	0.1	0.2	0.1	0.2	0.1
0	1	3.65	3.58	3.47	4.09	4.01	3.88	4.83	4.70	6.10	5.86	8.63
	2	39.48	33.36	27.49	55.12	44.64	35.44	82.21	62.51	134.41	92.39	252.71
1	1	3.95	3.84	3.69	4.79	4.65	4.46	6.05	5.82	8.09	7.63	11.96
	2	41.58	34.93	28.66	56.87	45.85	36.30	83.63	63.40	135.50	92.99	253.43
2	1	6.66	6.39	6.04	7.79	7.42	6.97	9.63	9.08	12.79	11.79	18.92
	2	47.73	39.42	31.99	61.99	49.35	38.79	87.81	66.01	138.71	94.78	255.56

(*b*) Plates with simply supported outer edge

		$b/a=0.1$				0.2				0.3		
n	s	$h/a=0.1$	0.2	0.3	0.4	0.1	0.2	0.3	0.4	0.1	0.2	0.3
0	1	13.87	12.45	10.86	9.45	16.16	14.69	12.97	11.38	20.22	18.21	15.96
	2	46.95	38.34	31.08	25.72	56.91	45.87	36.82	30.24	71.71	56.08	44.18
1	1	16.10	14.64	13.04	11.56	18.48	16.74	14.79	12.99	22.30	19.98	17.44
	2	51.07	41.66	33.80	27.98	59.99	48.08	38.48	31.55	73.99	57.60	45.27
2	1	24.76	22.16	19.34	16.85	25.93	23.06	20.01	17.35	28.67	25.22	21.67
	2	63.82	50.96	40.74	33.39	69.25	54.53	43.18	35.19	80.78	62.11	48.47

		$b/a=0.4$			0.5			0.6		0.7		0.8
n	s	$h/a=0.1$	0.2	0.3	0.1	0.2	0.3	0.1	0.2	0.1	0.2	0.1
0	1	26.70	23.56	20.26	37.33	31.87	26.67	56.08	45.52	93.26	70.06	181.93
	2	93.58	70.24	54.06	127.17	90.64	67.90	182.10	121.73	280.58	162.31	486.97
1	1	28.50	25.02	21.44	38.86	33.04	27.56	57.36	46.42	94.27	70.70	182.64
	2	95.29	71.32	54.80	128.46	91.39	68.40	183.04	122.25	281.24	162.70	487.37
2	1	33.93	29.32	24.80	43.45	36.49	30.17	61.17	49.08	97.30	72.60	184.78
	2	100.37	74.50	57.00	132.29	93.64	69.93	185.86	123.79	283.19	163.90	488.55

(*c*) Plates with clamped outer edge

		$b/a=0.1$				0.2				0.3		
n	s	$h/a=0.1$	0.2	0.3	0.4	0.1	0.2	0.3	0.4	0.1	0.2	0.3
0	1	21.20	18.07	15.03	12.59	24.92	21.16	17.54	14.65	31.01	25.68	20.89
	2	56.91	43.43	33.51	26.84	68.64	51.25	39.10	31.09	85.50	61.56	46.16
1	1	23.55	20.11	16.81	14.15	27.13	22.88	18.88	15.74	32.84	27.04	21.90
	2	61.03	46.53	36.01	28.92	71.50	53.20	40.59	32.30	87.52	62.87	47.14
2	1	32.60	27.23	22.38	18.65	34.43	28.46	23.20	19.23	38.64	31.32	25.16
	2	73.60	55.17	42.43	34.01	80.17	58.98	44.87	35.73	93.61	66.81	50.04

		$b/a=0.4$			0.5			0.6		0.7		0.8
n	s	$h/a=0.1$	0.2	0.3	0.1	0.2	0.3	0.1	0.2	0.1	0.2	0.1
0	1	40.36	32.16	25.46	55.09	41.62	31.91	79.75	56.14	124.94	80.34	220.96
	2	109.73	75.53	55.50	145.82	95.27	68.30	202.68	124.84	300.62	171.69	498.71
1	1	41.83	33.20	26.23	56.26	42.41	32.50	80.65	56.73	125.61	80.78	221.43
	2	111.20	76.46	56.18	146.89	95.93	68.80	203.45	125.31	301.17	172.06	499.07
2	1	46.41	36.45	28.67	59.84	44.85	34.33	83.40	58.54	127.64	82.13	222.84
	2	115.59	79.21	58.22	150.10	97.89	70.29	205.77	126.72	302.80	173.17	500.15

Table 3 Frequency parameters λ_{ns}^2 of uniform annular plates with clamped inner edge; $\nu = 0.3$

(*a*) Plates with free outer edge

		$b/a=0.1$				0.2				0.3		
n	s	$h/a=0.1$	0.2	0.3	0.4	0.1	0.2	0.3	0.4	0.1	0.2	0.3
0	1	4.15	3.92	3.60	3.27	5.08	4.81	4.44	4.05	6.52	6.14	5.64
	2	23.12	19.05	15.50	12.88	29.30	23.76	19.02	15.58	37.89	29.76	23.27
1	1	3.22	2.84	2.52	2.28	4.61	4.19	3.76	3.38	6.31	5.79	5.21
	2	25.20	21.31	17.98	15.31	31.19	25.52	20.80	17.25	39.54	31.20	24.63
2	1	5.44	5.22	4.98	4.71	6.15	5.75	5.38	5.04	7.55	6.89	6.28
	2	33.95	29.13	24.58	20.79	37.76	31.32	25.85	21.55	44.83	35.68	28.55

		$b/a=0.4$			0.5			0.6		0.7		0.8
n	s	$h/a=0.1$	0.2	0.3	0.1	0.2	0.3	0.1	0.2	0.1	0.2	0.1
0	1	8.78	8.18	7.41	12.57	11.46	10.16	19.47	17.15	33.87	28.05	71.02
	2	50.41	37.86	28.75	69.58	49.27	36.16	100.91	66.21	156.63	93.37	269.85
1	1	8.78	8.02	7.15	12.71	11.43	10.03	19.72	17.20	34.16	28.13	71.29
	2	51.83	39.05	29.82	70.80	50.25	36.99	101.93	66.99	157.45	93.96	270.46
2	1	9.89	8.86	7.90	13.79	12.14	10.56	20.81	17.80	35.23	28.63	72.17
	2	56.22	42.63	32.90	74.48	53.15	39.40	104.98	69.32	159.91	95.71	272.31

(*b*) Plates with simply supported outer edge

		$b/a=0.1$				0.2				0.3		
n	s	$h/a=0.1$	0.2	0.3	0.4	0.1	0.2	0.3	0.4	0.1	0.2	0.3
0	1	16.57	14.07	11.69	9.84	21.06	17.70	14.57	12.16	27.38	22.44	18.12
	2	52.06	40.06	31.55	25.84	64.89	48.64	37.62	30.41	82.17	59.38	45.04
1	1	17.94	15.60	13.52	11.82	22.41	18.98	15.93	13.56	28.60	23.52	19.19
	2	54.68	42.84	34.18	28.11	66.87	50.39	39.18	31.74	83.71	60.62	46.08
2	1	25.13	22.32	19.43	16.90	27.80	23.95	20.45	17.58	32.89	27.32	22.66
	2	64.95	51.33	40.89	33.46	73.61	55.91	43.64	35.35	88.59	64.42	49.12

		$b/a=0.4$			0.5			0.6		0.7		0.8
n	s	$h/a=0.1$	0.2	0.3	0.1	0.2	0.3	0.1	0.2	0.1	0.2	0.1
0	1	36.70	28.96	22.78	51.22	38.36	29.26	75.46	52.74	119.99	76.76	215.00
	2	106.57	73.70	54.75	142.71	93.78	68.08	199.61	123.86	297.80	172.17	496.99
1	1	37.77	29.87	23.65	52.14	39.12	29.97	76.23	53.36	120.61	77.26	215.48
	2	107.77	74.60	55.47	143.65	94.45	68.60	200.34	124.35	298.34	172.49	497.36
2	1	41.29	32.86	26.36	55.05	41.51	32.12	78.62	55.28	122.15	78.78	216.93
	2	111.48	77.34	57.62	146.51	96.46	70.15	202.53	125.81	299.95	173.45	498.45

(*c*) Plates with clamped outer edge

		$b/a=0.1$				0.2				0.3		
n	s	$h/a=0.1$	0.2	0.3	0.4	0.1	0.2	0.3	0.4	0.1	0.2	0.3
0	1	24.63	19.84	15.86	12.99	30.84	24.35	19.16	15.52	39.40	30.04	23.13
	2	62.14	44.91	33.85	26.89	76.56	53.57	39.64	31.15	95.59	64.23	46.66
1	1	25.90	21.18	17.32	14.43	32.00	25.31	20.08	16.39	40.37	30.77	23.78
	2	64.78	47.59	36.31	29.00	78.44	55.20	41.09	32.38	96.99	65.36	47.63
2	1	33.12	27.44	22.48	18.71	36.94	29.52	23.69	19.50	43.98	33.67	26.27
	2	74.87	55.53	42.56	34.07	84.77	60.25	45.24	35.82	101.43	68.81	50.50

		$b/a=0.4$			0.5			0.6		0.7		0.8
n	s	$h/a=0.1$	0.2	0.3	0.1	0.2	0.3	0.1	0.2	0.1	0.2	0.1
0	1	51.70	37.65	28.27	70.28	48.31	35.32	100.07	64.19	152.15	90.20	257.62
	2	121.88	78.17	55.77	159.78	97.39	68.30	217.65	125.76	314.09	172.31	503.46
1	1	52.49	38.20	28.74	70.90	48.73	35.65	100.55	64.49	152.49	90.41	257.84
	2	122.94	79.00	56.46	160.60	98.02	68.80	218.28	126.24	314.57	172.66	503.82
2	1	55.22	40.25	30.47	72.96	50.18	36.86	102.08	65.51	153.57	91.12	258.54
	2	126.22	81.50	58.52	163.08	99.90	70.31	220.18	127.67	316.03	173.70	504.91

$$M_r = \psi_\theta = W = 0 \quad \text{at a simply supported edge}$$
$$\psi_r = \psi_\theta = W = 0 \quad \text{at a clamped edge} \tag{7}$$

The substitution of (4) into (1)–(3) yields the matrix equation

$$\{Z(r)\} = [U(r)]\{C\} \tag{8}$$

where

$$\{Z(r)\} = \{M_r M_{r\theta} Q_r \psi_r \psi_\theta W\}^T$$
$$\{C\} = \{C_1 C_2 C_3 C_1^* C_2^* C_3^*\}^T$$

The elements of the matrix $[U(r)]$ are given by

$$U_{11}, U_{14} = D(\sigma_1 - 1)\left\{Z_n''\left(\delta_1 \frac{r}{a}\right) + \frac{\nu}{r} Z_n'\left(\delta_1 \frac{r}{a}\right) - \frac{\nu n^2}{r^2} Z_n\left(\delta_1 \frac{r}{a}\right)\right\}$$

$$U_{12}, U_{15} = D(\delta_2 - 1)\left\{Z_n''\left(\delta_2 \frac{r}{a}\right) + \frac{\nu}{r} Z_n'\left(\delta_2 \frac{r}{a}\right) - \frac{\nu n^2}{r^2} Z_n\left(\delta_2 \frac{r}{a}\right)\right\}$$

$$U_{13}, U_{16} = \frac{D(1-\nu)n}{r}\left\{Z_n'\left(\delta_3 \frac{r}{a}\right) - \frac{1}{r} Z_n\left(\delta_3 \frac{r}{a}\right)\right\}$$

$$U_{21}, U_{24} = -\frac{D(1-\nu)n(\sigma_1 - 1)}{r}\left\{Z_n'\left(\delta_1 \frac{r}{a}\right) - \frac{1}{r} Z_n(\delta_1 \frac{r}{a})\right\}$$

$$U_{22}, U_{25} = -\frac{D(1-\nu)n(\sigma_2 - 1)}{r}\left\{Z_n'\left(\delta_2 \frac{r}{a}\right) - \frac{1}{r} Zn\left(\delta_2 \frac{r}{a}\right)\right\}$$

$$U_{23}, U_{26} = -\frac{D(1-\nu)}{2}\left\{Z_n''\left(\delta_3 \frac{r}{a}\right) - \frac{1}{r} Z_n'\left(\delta_3 \frac{r}{a}\right) + \frac{n^2}{r^2} Z_n\left(\delta_3 \frac{r}{a}\right)\right\}$$

$$U_{31}, U_{34} = K^2 Gh\sigma_1 Z_n'\left(\delta_1 \frac{r}{a}\right), U_{32}, U_{35} = K^2 Gh\delta_2 Z_n'\left(\delta_2 \frac{r}{a}\right)$$

$$U_{33}, U_{36} = K^2 Gh \frac{n}{r} Z_n\left(\delta_3 \frac{r}{a}\right)$$

$$U_{41}, U_{44} = (\sigma_1 - 1) Z_n'\left(\delta_1 \frac{r}{a}\right), U_{42}, U_{45} = (\sigma_2 - 1) Z_n' Z\left(\delta_2 \frac{r}{a}\right)$$

$$U_{43}, U_{46} = \frac{n}{r} Z_n\left(\delta_3 \frac{r}{a}\right)$$

$$U_{51}, U_{54} = \frac{n(\sigma_1 - 1)}{r} Z_n\left(\delta_1 \frac{r}{a}\right), U_{52}, U_{55} = \frac{n(\sigma_2 - 1)}{r} Z_n\left(\delta_2 \frac{r}{a}\right)$$

$$U_{53}, U_{56} = Z_n'\left(\delta_3 \frac{r}{a}\right)$$

$$U_{61}, U_{64} = Z_n\left(\delta_1 \frac{r}{a}\right), \quad U_{62}, U_{65} = Z_n\left(\delta_2 \frac{r}{a}\right)$$

$$U_{63}, U_{66} = 0 \tag{9}$$

where the function $Z_n(\delta_j r/a)$ $(j = 1,2,3)$ represents $J_n(\delta_j r/a)$ and $Y_n(\delta_j r/a)$ for the first and second elements, respectively. Upon eliminating the coefficients C_i and C_i^* of (8) from the equation that is obtained by substituting (8) into the boundary conditions (7), one can obtain the frequency equation of annular plates under any combination of boundary conditions.

Although the values of δ_1^2 are always positive in sign, the values of δ_2^2 and δ_3^2 become negative and hence δ_2 and δ_3 have imaginary values for $\lambda^4 < 1/RS$. Within this range of λ, the functions $J_n(x)$ and $Y_n(x)$ in the preceding equations should be replaced with modified Bessel functions $I_n(x)$ and $K_n(x)$ of the first and second kinds, respectively.

Tables 1–3 present the frequency parameters λ_{ns}^2 obtained by the theory for uniform annular plates of Poisson's ratio $\nu = 0.3$ under some combination of the thickness ratio h/a and the radii b/a (b: the inner radius of annular plates). The subscript n attached to λ_{ns} represents the number of nodal diameters appearing on the mode shapes of the vibration. Although the subscript s represents, in the classical plate theory, the number of nodal circles of the mode shapes, it indicates the order of the frequencies for thick plates without always representing the number of nodal circles. The frequency parameters decrease monotonically with an increase of the thickness ratio.

One can quote the natural frequencies of annular plates with given boundary conditions and dimensions from the tables, and can also easily obtain the values by the aforementioned process for annular plates with dimensions not tabulated here. The numerical computations presented here were carried out on a HITAC M-200H computer of the Hokkaido University Computing Center.

References

1 Rao, S. S., and Prasad, A. S., "Vibrations of Annular Plates Including the Effects of Rotatory Inertia and Transverse Shear Deformation," *Journal of Sound and Vibration*, Vol. 42, No. 3, 1975, pp. 305–324.

2 Irie, T., Yamada, G., and Aomura, S., "Free Vibration of a Mindlin Annular Plate of Varying Thickness," *Journal of Sound and Vibration*, Vol. 66, No. 2, 1979, pp. 187–197.

3 Mindlin, R. D., and Deresiewicz, H., "Thickness-Shear and Flexural Vibrations of a Circular Disk," *Journal of Applied Physics*, Vol. 25, No. 10, 1954, pp. 1329–1332.

4 Deresiewicz, H., and Mindlin, R. D., "Axially Symmetric Flexural Vibrations of a Circular Disk," ASME JOURNAL OF APPLIED MECHANICS, Vol. 22, No. 1, 1955, pp. 86–88.

APPENDIX 1

In Table A-1, the frequency parameters λ_{ns}^2 of circular plates are compared with those of annular plates with free small circular holes at the center. Although the parameters of the plates with free outer edge are not affected so much by small holes, those of the plates with simply supported or clamped outer edges slightly change the values.

Table *A*-1 Frequency parameters λ_{ns}^2 of uniform circular plates and annular plates with free small hole; $\nu = 0.3$

(*a*) Plates with free outer edge

		b/*a* = 0				*b*/*a* = 0.01			
n	*s*	*h*/*a* = 0.1	0.2	0.3	0.4	*h*/*a* = 0.1	0.2	0.3	0.4
0	1	8.87	8.51	8.01	7.46	8.87	8.50	8.01	7.46
	2	36.04	31.11	26.28	22.27	36.03	31.11	26.28	22.27
1	1	19.71	17.98	15.98	14.09	19.71	17.98	15.98	14.09
	2	54.26	44.43	35.98	29.38	54.25	44.42	35.97	29.37
2	1	5.28	5.11	4.89	4.64	5.28	5.11	4.89	4.64
	2	33.03	28.67	24.32	20.64	33.03	28.66	24.32	20.64

(*b*) Plates with simply supported outer edge

		b/*a* = 0				*b*/*a* = 0.01			
n	*s*	*h*/*a* = 0.1	0.2	0.3	0.4	*h*/*a* = 0.1	0.2	0.3	0.4
0	1	4.89	4.78	4.60	4.40	4.89	4.78	4.60	4.40
	2	28.24	24.99	21.59	18.66	28.23	24.99	21.59	18.66
1	1	13.52	12.67	11.60	10.51	13.56	12.71	11.63	10.53
	2	44.72	37.59	31.12	26.09	44.73	37.59	31.12	26.09
2	1	24.41	21.92	19.18	16.74	24.50	21.97	19.22	16.76
	2	62.68	50.30	40.32	33.10	62.68	50.30	40.32	33.10

(*c*) Plates with clamped outer edge

		b/*a* = 0				*b*/*a* = 0.01			
n	*s*	*h*/*a* = 0.1	0.2	0.3	0.4	*h*/*a* = 0.1	0.2	0.3	0.4
0	1	9.94	9.24	8.36	7.47	9.94	9.24	8.35	7.47
	2	36.48	30.21	24.64	20.42	36.47	30.20	24.63	20.42
1	1	20.23	17.83	15.26	13.04	20.18	17.76	15.19	12.98
	2	53.89	42.41	33.47	27.21	53.84	42.37	33.44	27.20
2	1	32.41	27.21	22.38	18.64	32.20	26.99	22.22	18.54
	2	72.37	54.56	42.05	33.76	72.20	54.45	42.01	33.75

APPENDIX 2

Table *A*-2 shows the comparison of the frequency parameters obtained here with the results of Rao and Prasad [1]. The numerical values of the present authors have been proved to be correct in comparison with the results obtained by other methods – the transfer matrix method and the spline interpolation technique [2]. However, the results of Rao and Prasad are incorrect, because there are probably some mistakes in analytical and computational process.

Table *A*-3 shows the frequency parameters obtained by Rao and Prasad for clamped, simply supported plates. Although the parameters should become small monotonically with an increase of the thickness ratio *h*/*a*, they change in a wavelike manner.

Table *A*-2 Comparison of frequency parameters λ_{ns}^2 of uniform annular plates; $\nu = 0.3$, $b/a = 0.3$, $h/a = 0.2$

	(*n s*) = (0 1)		(*n s*) = (0 2)		(*n s*) = (1 1)		(*n s*) = (1 2)	
	Present	Rao/ Prasad	Present	Rao/ Prasad	Present	Rao/ Prasad	Present	Rao/ Prasad[1]
F-F	7.89	6.822	39.57	–	15.13	17.61	43.17	–
F-SS	4.53	2.35	30.49	31.90	11.19	4.598	34.80	34.03
F-C	10.35	7.198	36.77	46.83	15.87	15.04	40.18	43.89
SS-F	3.33	3.358	25.89	24.30	3.23	2.61	27.87	28.64
SS-SS	18.21	12.74	56.08	80.59	19.98	22.56	57.60	81.71
SS-C	25.68	32.87	61.56	76.20	27.04	34.54	62.87	77.39
C-F	6.14	6.465	29.76	37.13	5.79	5.721	31.20	42.93
C-SS	22.44	23.22	59.38	75.69	23.52	24.38	60.62	77.39
C-C	30.04	39.77	64.23	97.16	30.77	40.61	65.36	97.78

Table *A*-3 Frequency parameters λ_{ns}^2 of uniform annular plates with clamped inner edge and simply supported outer edge [1]; $\nu = 0.3$, $b/a = 0.3$

			h/*a*			
n	*s*	Classical	1/7	1/5	1/4	1/2
0	1	29.90	26.03	23.22	16.66	25.18
0	2	100.0	85.89	75.69	98.62	97.25
1	1	31.40	30.84	24.38	25.36	28.67
1	2	102.0	97.02	77.39	99.17	101.9

Journal of Applied Mechanics

Brief Notes

A Brief Note is a short paper that presents a specific solution of technical interest in mechanics but which does not necessarily contain new general methods or results. A Brief Note should not exceed 1500 words *or equivalent* (a typical one-column figure or table is equivalent to 250 words; a one line equation to 30 words). Brief Notes will be subject to the usual review procedures prior to publication. After approval such Notes will be published as soon as possible. The Notes should be submitted to the Technical Editor of the JOURNAL OF APPLIED MECHANICS. Discussions on the Brief Notes should be addressed to the Editorial Department, ASME, United Engineering Center, 345 East 47th Street, New York, N. Y. 10017, or to the Technical Editor of the JOURNAL OF APPLIED MECHANICS. Discussions on Brief Notes appearing in this issue will be accepted until two months after publication. Readers who need more time to prepare a Discussion should request an extension of the deadline from the Editorial Department.

Estimation of Buckling Loads and Other Eigenvalues via a Modification of the Rayleigh-Ritz Method

R. Schmidt[1]

The Ritz method commonly makes use of approximating functions of the form [1, 2]

$$y=\sum_m A_m f_m(x_1,x_2,\ldots,x_N) \tag{1}$$

in the case of multiterm approximation, or

$$y=Af(x_1,x_2,\ldots,x_N) \tag{2}$$

in the case of the one-term approximation. In equations (1) and (2), A's denote undetermined constants, f's are the assumed, definite, shape functions, and x's represent the N-independent variables. In this Brief Note, by means of two examples, we shall demonstrate the utility of approximating functions of the general form

$$y=\sum_m A_m f_m(x_1,x_2,\ldots,x_N;\quad n_1,n_2,\ldots,n_M), \tag{3}$$

where n's are the M adjustable parameters. The constants A_m can be determined as originally described by Rayleigh and Ritz [1, 2], while the parameters n_i should be adjusted, in the case of eigenvalue problems, in such a way as to minimize (or nearly minimize) the approximate eigenvalue.

Example 1

Let us consider the axisymmetric buckling of a clamped circular plate of radius a and uniform thickness h, if the plate is uniformly compressed by the distributed force N, per unit length [1, 3]. The expression for the potential energy Π in this case is

$$\Pi=\pi D\int_0^a\left(r\beta'^2+\frac{\beta^2}{r}+2\nu\beta\beta'-\frac{N}{D}r\beta^2\right)dr \tag{4}$$

$$=\pi D\left\{[\nu\beta^2]_{r=0}^a+\int_0^a\left(r\beta'^2+\frac{\beta^2}{r}-\frac{N}{D}r\beta^2\right)dr\right\}, \tag{5}$$

where $D=Eh^3/12(1-\nu^2)$ is the flexural stiffness, ν is Poisson's ratio, E is the modulus of elasticity, r denotes the radial distance, β is the rotation of a radial line element dr, and $\beta'=d\beta/dr$. Except for the constant factor of 2, expression (4) coincides in form with the second variation of potential energy given in [1]. Hence, we may use the condition $\Pi=0$ for the determination of the critical value of N. The exact solution [1, 4] of this problem is given by $\beta=AJ_1(rN^{1/2}D^{-1/2})$, where J_1 denotes Bessel function of first order, and the exact value of the critical load is [1, 4]

$$N_{cr}=14.68\frac{D}{a^2}. \tag{6}$$

A fast estimate of the critical load is usually obtained by some work [5] or energy method [1, 6, 7] (e.g., the Rayleigh-Ritz method, which yields the upper bound) with the aid of an assumed simple deflection function satisfying the imposed boundary conditions ($\beta=0$ at $r=0$ and $r=a$, in this example), such as [5]

$$\beta=A(a^2r-r^3), \tag{7}$$

or still better

$$\beta=A(ar-r^2). \tag{8}$$

Substituting first (7) and then (8) into (4) or (5) and using the condition $\Pi=0$, we easily obtain

$$N_{cr}=16.00\frac{D}{a^2}\quad\text{and}\quad N_{cr}=15.00\frac{D}{a^2}, \tag{9a,b}$$

respectively.

Herein, we propose to deviate from the common approach and, instead of (7) or (8), assume

$$\beta=A(a^{n-1}r-r^n). \tag{10}$$

Substituting (10) in (4) or (5), we obtain

$$4n(n+1)(n+3)\Pi=\pi A^2a^{2n}(n-1)^2[2(n+1)(n+3)D-na^2N], \tag{11}$$

from which, and the condition $\Pi=0$,

$$\frac{a^2N}{D}=\frac{2(n+1)(n+3)}{n}. \tag{12}$$

Since n is an adjustable parameter, and the Rayleigh-Ritz method yields upper bounds for the critical load, we minimize expression (12) by differentiating N with respect to n and setting this derivative equal to zero. Thus, $n^2-3=0$, from which $n=\sqrt{3}=1.73205$, and finally from (12),

[1] Professor of Engineering Mechanics, Department of Mechanical Engineering, University of Detroit, Detroit, Mich. 48221. Mem. ASME.

Manuscript received by ASME Applied Mechanics Division, July 1981.

$$N_{cr} = 14.93 \frac{D}{a^2}, \tag{13}$$

which is a better value than those in (9).

We can also solve this problem in a somewhat different way, using the first variation of the potential energy integral Π. The first variation δΠ can be obtained by adding a small virtual increment $\epsilon\xi(r)$ to β, as explained in [1]. Thus,

$$\delta\Pi = 2\epsilon\pi D\int_0^a \left[r\beta'\xi' + \nu(\beta\xi)' + \left(\frac{1}{r} - \frac{Nr}{D}\right)\beta\xi\right]dr. \tag{14}$$

After an integration of (14) by parts [1], we obtain

$$\delta\Pi = 2\epsilon\pi D\left\{[(r\beta' + \nu\beta)\xi]_{r=0}^{a} - \int_0^a \left(\beta'' + \frac{\beta'}{r} - \frac{\beta}{r^2} + \frac{N}{D}\beta\right)r\xi dr\right\}. \tag{15}$$

The condition δΠ = 0 yields the previously obtained critical values, if $\beta = \xi$, i.e., when the Galerkin method is used. However, if we use (10) for β and (8) for ξ, or (8) for β and (10) for ξ, we obtain

$$\frac{a^2N}{D} = \frac{20(n+3)(n+4)}{(n+2)(n+8)} \tag{16}$$

whose minimum occurs when $n = 0.77485$. Hence,

$$\frac{a^2N_{cr}}{D} = 14.805, \tag{17}$$

which is an even better value.

Example 2

As a somewhat more complicated example, let us next consider the axisymmetric buckling of a simply supported (or free) circular plate compressed by a uniformly distributed radial edge load N. A simple function that satisfies the boundary conditions is

$$\beta = A\left(\frac{n+\nu}{1+\nu}a^{n-1}r - r^n\right), \tag{18}$$

which, in conjunction with (4) or (5) and Π = 0, yields

$$2n[n^4 + 2(2+\nu)n^3 - (5-\nu^2)n^2 - 2(3+3\nu+\nu^2)n + 6 + 4\nu + \nu^2]\frac{a^2N}{D} = 4(1+\nu)(n+1)(n+3)[2n^3 - (3-\nu)n^2 - 2\nu n + 1 + \nu], \tag{19}$$

which is too complicated for differentiation. However, since the method under discussion is an approximate one, we need only to determine a near minimum by assuming different values for n and comparing results. Thus, for $\nu = 0.3$, we calculate, using (19),

n	$\frac{a^2N}{D}$
2.0	4.22
2.2	4.21
2.5	4.20
3.0	4.21

etc. Obviously

$$\frac{a^2N_{cr}}{D} = 4.20. \tag{20}$$

The exact value is given as 4.20 in [1, 3, 4].

The method has also been used for calculating buckling loads and natural frequencies for various struts and beams with similarly gratifying results.

References

1 Langhaar, H. L., *Energy Methods in Applied Mechanics*, Wiley, New York, 1962.

2 Finlayson, B. A., *The Method of Weighted Residuals and Variational Principles*, Academic Press, New York, 1972.

3 Timoshenko, S., and Woinowsky-Krieger, S., *Theory of Plates and Shells*, 2nd ed., McGraw-Hill, New York, 1959.

4 Timoshenko, S. P., and Gere, J. M., *Theory of Elastic Stability*, McGraw-Hill, New York, 1961.

5 Föppl, A., and Föppl, L., *Drang und Zwang*, Vols. 1 and 2, 2nd ed., Verlag von R. Oldenbourg, Munich, 1924 and 1928.

6 Schmidt, R., and DaDeppo, D. A., "Variational Formulation of Nonlinear Equations for Straight Elastic Beams," *Industrial Mathematics, The Journal of the Industrial Mathematics Society*, Vol. 23, Part 2, 1973, pp. 117-136.

7 Schmidt, R., and Wempner, G. A., "The Nonlinear Conical Spring," ASME Journal of Applied Mechanics, Vol. 26, No. 4, Dec. 1959, pp. 681-682.

Laminr Flow in the Entrance Region of Circular Sector Ducts

H. M. Soliman[1], A. A. Munis[1], A. C. Trupp[1]

Introduction

In several engineering devices, particularly compact heat

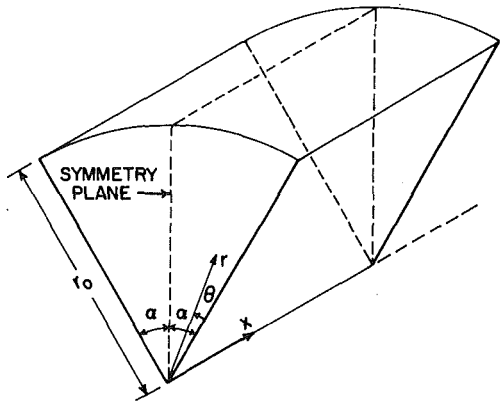

Fig. 1 Geometry and coordinate system

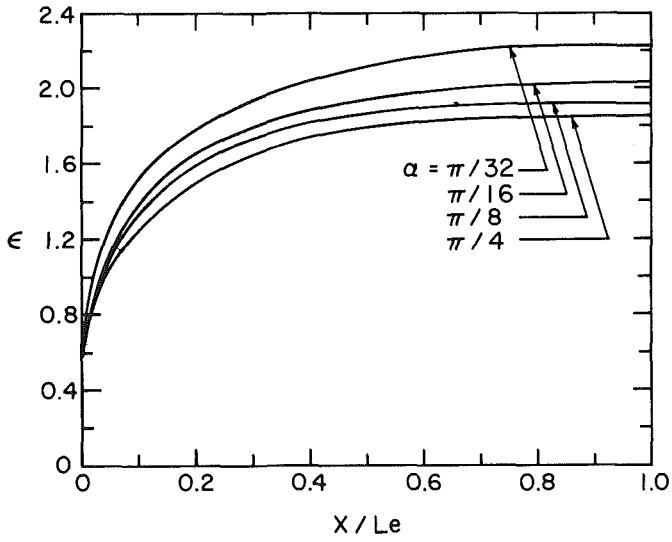

Fig. 2 Development of ϵ along X

[1]Associate Professor and Mem. ASME, Research Assistant, and Associate Professor, respectively, Department of Mechanical Engineering, University of Manitoba, Winnipeg, Canada, R3T2N2.

Manuscript received by ASME Applied Mechanics Division March, 1981; final revision, December, 1981.

$$N_{cr} = 14.93 \frac{D}{a^2}, \tag{13}$$

which is a better value than those in (9).

We can also solve this problem in a somewhat different way, using the first variation of the potential energy integral Π. The first variation δΠ can be obtained by adding a small virtual increment $\epsilon\xi(r)$ to β, as explained in [1]. Thus,

$$\delta\Pi = 2\epsilon\pi D\int_0^a \left[r\beta'\xi' + \nu(\beta\xi)' + \left(\frac{1}{r} - \frac{Nr}{D}\right)\beta\xi\right]dr. \tag{14}$$

After an integration of (14) by parts [1], we obtain

$$\delta\Pi = 2\epsilon\pi D\left\{[(r\beta' + \nu\beta)\xi]_{r=0}^{a} - \int_0^a \left(\beta'' + \frac{\beta'}{r} - \frac{\beta}{r^2} + \frac{N}{D}\beta\right)r\xi dr\right\}. \tag{15}$$

The condition δΠ = 0 yields the previously obtained critical values, if $\beta = \xi$, i.e., when the Galerkin method is used. However, if we use (10) for β and (8) for ξ, or (8) for β and (10) for ξ, we obtain

$$\frac{a^2N}{D} = \frac{20(n+3)(n+4)}{(n+2)(n+8)} \tag{16}$$

whose minimum occurs when $n = 0.77485$. Hence,

$$\frac{a^2N_{cr}}{D} = 14.805, \tag{17}$$

which is an even better value.

Example 2

As a somewhat more complicated example, let us next consider the axisymmetric buckling of a simply supported (or free) circular plate compressed by a uniformly distributed radial edge load N. A simple function that satisfies the boundary conditions is

$$\beta = A\left(\frac{n+\nu}{1+\nu}a^{n-1}r - r^n\right), \tag{18}$$

which, in conjunction with (4) or (5) and Π = 0, yields

$$2n[n^4 + 2(2+\nu)n^3 - (5-\nu^2)n^2 - 2(3+3\nu+\nu^2)n + 6 + 4\nu + \nu^2]\frac{a^2N}{D} = 4(1+\nu)(n+1)(n+3)[2n^3 - (3-\nu)n^2 - 2\nu n + 1 + \nu], \tag{19}$$

which is too complicated for differentiation. However, since the method under discussion is an approximate one, we need only to determine a near minimum by assuming different values for n and comparing results. Thus, for $\nu = 0.3$, we calculate, using (19),

n	$\frac{a^2N}{D}$
2.0	4.22
2.2	4.21
2.5	4.20
3.0	4.21

etc. Obviously

$$\frac{a^2N_{cr}}{D} = 4.20. \tag{20}$$

The exact value is given as 4.20 in [1, 3, 4].

The method has also been used for calculating buckling loads and natural frequencies for various struts and beams with similarly gratifying results.

References

1 Langhaar, H. L., *Energy Methods in Applied Mechanics*, Wiley, New York, 1962.

2 Finlayson, B. A., *The Method of Weighted Residuals and Variational Principles*, Academic Press, New York, 1972.

3 Timoshenko, S., and Woinowsky-Krieger, S., *Theory of Plates and Shells*, 2nd ed., McGraw-Hill, New York, 1959.

4 Timoshenko, S. P., and Gere, J. M., *Theory of Elastic Stability*, McGraw-Hill, New York, 1961.

5 Föppl, A., and Föppl, L., *Drang und Zwang*, Vols. 1 and 2, 2nd ed., Verlag von R. Oldenbourg, Munich, 1924 and 1928.

6 Schmidt, R., and DaDeppo, D. A., "Variational Formulation of Nonlinear Equations for Straight Elastic Beams," *Industrial Mathematics, The Journal of the Industrial Mathematics Society*, Vol. 23, Part 2, 1973, pp. 117-136.

7 Schmidt, R., and Wempner, G. A., "The Nonlinear Conical Spring," ASME Journal of Applied Mechanics, Vol. 26, No. 4, Dec. 1959, pp. 681-682.

Laminr Flow in the Entrance Region of Circular Sector Ducts

H. M. Soliman[1], A. A. Munis[1], A. C. Trupp[1]

Introduction

In several engineering devices, particularly compact heat

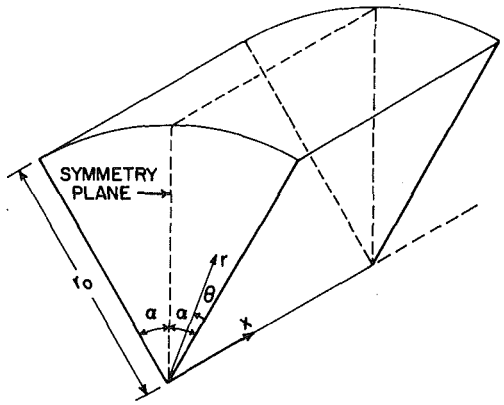

Fig. 1 Geometry and coordinate system

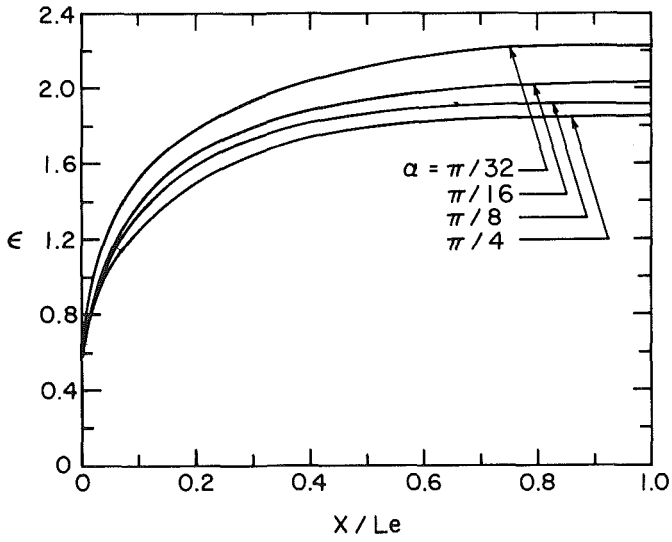

Fig. 2 Development of ϵ along X

[1]Associate Professor and Mem. ASME, Research Assistant, and Associate Professor, respectively, Department of Mechanical Engineering, University of Manitoba, Winnipeg, Canada, R3T2N2.

Manuscript received by ASME Applied Mechanics Division March, 1981; final revision, December, 1981.

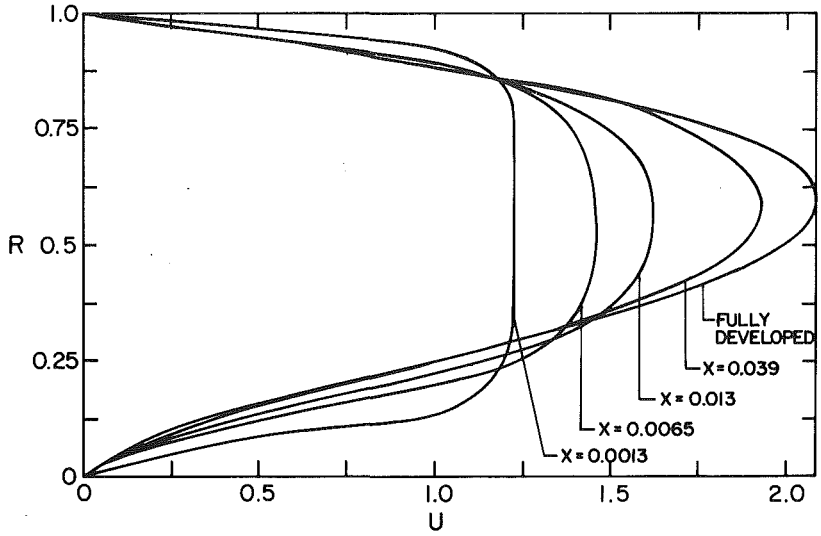

Fig. 3 Velocity distributions at symmetry plane for $\alpha = \pi/4$

Table 1

α	$\pi/32$	$\pi/16$	$\pi/8$	$\pi/4$
Le	0.235	0.144	0.108	0.0786

Table 2

X/Le	$\alpha = \pi/32$		$\alpha = \pi/16$		$\alpha = \pi/8$		$\alpha = \pi/4$	
	fRe	K	fRe	K	fRe	K	fRe	K
0.001	109.3	0.207	147.9	0.177	180.4	0.171	226.0	0.154
0.003	66.09	0.335	81.62	0.281	98.27	0.266	115.7	0.241
0.006	48.27	0.456	60.18	0.377	63.69	0.352	78.29	0.314
0.010	38.52	0.568	48.30	0.469	53.91	0.432	60.26	0.380
0.020	28.93	0.758	35.64	0.628	39.59	0.567	43.93	0.492
0.030	25.09	0.887	30.20	0.739	33.47	0.662	37.37	0.571
0.040	22.70	0.991	27.02	0.830	29.89	0.738	33.50	0.635
0.050	21.18	1.076	24.92	0.901	27.51	0.801	30.88	0.689
0.070	19.90	1.211	22.20	1.019	24.41	0.903	27.44	0.778
0.100	17.34	1.364	19.91	1.153	21.78	1.021	24.40	0.881
0.150	15.82	1.540	17.81	1.313	19.40	1.165	21.58	1.007
0.200	14.95	1.664	16.65	1.429	18.05	1.269	19.95	1.100
0.250	14.47	1.756	15.89	1.517	17.09	1.350	18.87	1.171
0.300	14.07	1.828	15.35	1.588	16.54	1.412	18.07	1.229
0.350	13.83	1.885	14.95	1.646	16.06	1.464	17.51	1.275
0.400	13.59	1.930	14.65	1.695	15.66	1.510	17.05	1.315
0.450	13.51	1.970	14.41	1.735	15.34	1.546	16.70	1.347
0.500	13.35	1.997	14.22	1.770	15.11	1.577	16.41	1.375
0.600	13.19	2.051	13.95	1.825	14.79	1.625	15.96	1.418
0.700	13.03	2.091	13.76	1.868	14.55	1.661	15.67	1.451
0.800	12.95	2.118	13.63	1.902	14.39	1.689	15.46	1.475
0.900	12.90	2.139	13.52	1.930	14.23	1.710	15.31	1.494
1.000	12.87	2.156	13.47	1.951	14.15	1.728	15.19	1.509

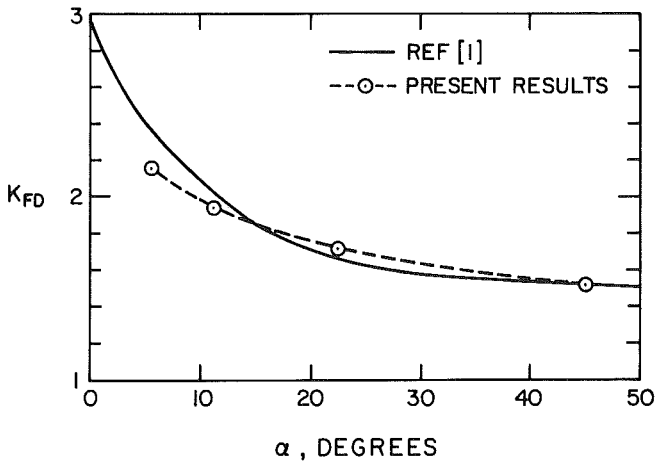

Fig. 4 Comparison with K_{FD}-values reported in [1]

exchangers, the flow over a major part of the channel is in the developing stage. Hence, knowledge of the velocity distribution and pressure gradient during such flows is vital for proper design. One duct geometry, which has received little attention in this regard, is the circular sector [1]. Only one research effort has been reported [2] so far, with numerial results limited to a duct angle $2\alpha = \pi/4$. In addition, it was reported in [1] that the pressure results in [2] are incorrect due to a computational error. The objective of this paper is to fill part of the gap that exits in the literature by providing results for circular section ducts with angles $2\alpha = \pi/16$, $\pi/8$, $\pi/4$, and $\pi/2$. These results are also of interest since they represent the limiting values for developing flow in internally finned tubes as the fins extend to the centerline of the tube.

Exact mathematical models describing developing flows can be formulated by considering the complete set of Navier-stokes equations. However, these models are normally very difficult to solve without the aid of unreaslistic simplifying assumptions. Consequently, other alternative approaches have been developed such as the matching method, the integral method, and several linearization methods. The present solution [3] is based on the linearization method developed by Sparrow et al. [4]. This technique takes into account the effect of transverse flow implicitly, but not rigorously. However, it was found to predict well the axial velocity and pressure drop for many simple geometries (e.g., circular tubes and parallel plate channels [4], concentric annular ducts [5], and rectangular, equilateral, and isosceles triangular ducts [6]). Since the geometry of circular sector ducts is also simple with no strong complications of flow asymmetry, the present linearization technique is expected to provide reasonably accurate results.

Analysis

The geometry of the duct and the coordinate system is shown in Fig. 1. The flow is laminar and steady, the fluid has constant properties, and body forces and viscous dissipation are neglected. The main flow is in the axial x-direction with a local velocity u and a bulk velocity u_b. The pressure p is assumed uniform at any axial cross section. Inlet conditions commonly used in the analysis of hydrodynamically developing flows are: uniform flow, irrotational flow, uniform flow far upstream, and irrotational flow far upstream. The choice among these for any particular application depends on the physical arrangement at entrance, irrespective of the nature of the solution technique employed. However,

the most frequently used assumption is that of uniform flow at inlet, which simulates the actual condition of well-rounded entrance. This assumption was adopted in the present analysis and thus, at $x = 0$, the axial velocity and pressure are uniform with values u_0 and p_0, respectively.

Following the procedure suggested in [4], the nondimensional momentum equation in the axial direction can be written as:

$$\left(\frac{1+\alpha}{2\alpha}\right)^2 \frac{\partial U}{\partial X^*} + \frac{2}{\alpha}\left[\int_0^1 \frac{1}{R}\frac{\partial U}{\partial \theta}\bigg|_{\theta=0} dR - \int_0^\alpha \frac{\partial U}{\partial R}\bigg|_{R=1} d\theta\right] = \frac{\partial^2 U}{\partial R^2} + \frac{1}{R}\frac{\partial U}{\partial R} + \frac{1}{R^2}\frac{\partial^2 U}{\partial \theta^2}, \quad (1)$$

where $R = r/r_0$, $U = u/u_b$, $\epsilon(X) = dX/dX^*$, $X = x/(D_h Re)$, $D_h = 2r_0\alpha/(1+\alpha)$, $Re = D_h u_b/\nu$, and the parameter, ϵ can be formulated as:

$$\epsilon(X) = -\left[\frac{d}{dX^*}\int_A \left(U^2 - \frac{U^3}{2}\right)dA\right] \Big/ \int_A U\frac{\partial U}{\partial X^*}\, dA. \quad (2)$$

The nondimensional pressure gradient is given by:

$$\left(\frac{1+\alpha}{\alpha}\right)^2 \frac{dP}{dX} = \frac{32}{\alpha}\int_A U\frac{\partial U}{\partial X}dA + \frac{16}{\alpha}\left[\int_0^1 \frac{1}{R}\frac{\partial U}{\partial \theta}\bigg|_{\theta=0} dR + \int_0^\alpha \frac{\partial U}{\partial R}\bigg|_{R=1} d\theta\right], \quad (3)$$

where $P = (p_0 - p)/(\frac{1}{2}\rho u_b^2)$. Appropriate boundary and symmetry conditions are:

$$U = 0 \quad \text{at } R = 1, 0 \le \theta \le \alpha, \text{ and } \theta = 0, 0 \le R \le 1, \quad (4a)$$

$$\text{and } \frac{\partial U}{\partial \theta} = 0 \quad \text{at } \theta = \alpha, 0 \le R \le 1. \quad (4b)$$

Due to the symmetry around the plane $\theta = \alpha$, the solution need be carried out only over the region $0 \le \theta \le \alpha$. Details of the derivation of equations (1)–(4) are given in [3].

Solutions were obtained using a finite difference aproach. At any axial location, the solution domain was subdivided by a 33 × 33 mesh, with the subdivisions adjacent to the straight and curved walls further subdivided into six equal parts for more accurate evaluation of wall gradients. The computation was marched from the inlet section to the fully developed region using axial steps with sizes $\Delta X^* = 1 \times 10^{-6}$ near the inlet, increasing to $\Delta X^* = 5 \times 10^{-4}$ as fully developed conditions were approached. Starting from the inlet section $X = X^* = 0$ where the value of U is given, the velocity distribution at $X^* = \Delta X^*$ was obtained by solving (1) interatively at all mesh points, subject to conditions (4). The value of ϵ was then obtained from (2) and the relation $\Delta X = \epsilon \Delta X^*$ was used for the evalution of ΔX. Finally, dP/dX was evaluated from (3) before marching to the next cross section. The solution was progressed until all axial velocities were within 1 percent of the corresponding fully developed value, and the value of X there was taken as the entrance length Le.

Numerical Results

The resulting values of Le are listed in Table 1 for the four duct geometries considered. With simple calculations, we can see from these results that for the same r_0, u_b, and ν, the entrance length increases as α increases. This trend is expected, however, quantitative comparisons are not possible due to lack of similar results. Development of the stretching factor ϵ along the duct is shown in Fig. 2 for different values of α. As shown in [3], the ϵ values for $\alpha = \pi/8$ compared well with those in [2]. The asymptotic value reached here for $\alpha = \pi/8$ is 1.92 as compared to 1.98 in [2]. It is also interesting to note that the present asymptotic values for ϵ (2.22 for $\alpha = \pi/32$, 2.03 for $\alpha = \pi/16$, 1.92 for $\alpha = \pi/8$, and 1.86 for $\alpha = \pi/4$) seem to conform with the asymptotic value of 1.82 obtained in [4] for smooth tubes. A sample of the velocity results illustrating the velocity development at the symmetry plane is shown in Fig. 3. The well-known characteristic of entrance region flow, namely that the fluid is decelerated near the walls and accelerated in the central core is clear from this figure. Again, our velocity results for $\alpha = \pi/8$ compared fairly well [3] with those in [2].

The most commonly used parameters for presenting the pressure results are the product of the friction factor and Reynolds number fRe, and the pressure defect K. In the present analysis, the friction factor was defined as:

$$f = (D_h/2)(-dp/dx)/(\rho u_b^2),$$

and hence

$$fRe = \frac{1}{4}\frac{dP}{dX} \quad (5)$$

The pressure defect is normally defined as:

$$K(X) = [p_0 - p + (dp/dx)_{FD} x]/(\tfrac{1}{2}\rho u_b^2),$$

which reduces to the following nondimensional form:

$$K(X) = P - 4(fRe)_{FD} X. \quad (6)$$

Results based on equations (5) and (6) are listed in Table 2. The values of fRe at $X = Le$ compare to within 3 percent of those reported in [1]. As expected [1], the present pressure results for $\alpha = \pi/8$ are widely different from those in [2]. A comparison between the K-values at $X = Le$ and the fully developed K-values reported in [1] is shown in Fig 4. It must be pointed out that the K_{FD} values reported in [1] are based on an approximate analytical method which utilizes only the fully developed velocity profile. Figure 4 shows a fair agreement with a maximum discrepancy of about 8 percent at $\alpha = \pi/32$.

Acknowledgments

The authors gratefully acknowledge the support provided for this research by the Natural Sciences and Engineering Research Council of Canada.

References

1 Shah, R. K., and London, A. L., *Laminar Flow Forced Convection in Ducts*, Academic Press, 1978.

2 Wendt, R. L., and Wiginton, C. L., "Incompressible Laminar Entrance Flow in a Circular Sector Duct," JOURNAL OF APPLIED MECHANICS, Vol. 98, 1976, pp. 357-359.

3 Munis, A A., "Analysis of Laminar Fluid Flow in the Entrance Region of Circular Sector Ducts," M.Sc. Thesis, University of Manitoba, 1981.

4 Sparrow, E. M., Lin, S. H., and Lundgren, T. S., "Flow Development in the Hydrodynamic Entrance Region of Tubes and Ducts," *Physics of Fluids*, Vol. 7, 1964, pp. 338-347.

5 Sparrow, E. M., and Lin, S. H., "The Developing Laminar Flow and Pressure Drop in the Entrance Region of Annular Ducts," *Journal of Basic Engineering*, Vol. 86, 1964, pp. 827-834.

6 Fleming, D. P., and Sparrow, E. M., "Flow in the Hydrodynamic Entrance Region of Ducts of Arbitrary Cross-Section," ASME *Journal of Heat Transfer*, Vol. 91, 1969, pp. 345-354.

On Stochastic Dynamics of an Embedded Rigid Cylinder

A. Beltzer[1] and R. Parnes[2]

[1] Visiting Professor, School of Aerospace, Mechanical and Nuclear Engineering, University of Oklahoma at Norman, Norman, Okla. 73019. On leave from Holon Technical Institute, Israel. Mem. ASME.

[2] Associate Professor, Department of Solid Mechanics, Materials and Structures, School of Engineering, Tel-Aviv University, Ramat-Aviv, Israel.

Manuscript received by ASME Applied Mechanics Division, July, 1980; final revision, January, 1981.

the most frequently used assumption is that of uniform flow at inlet, which simulates the actual condition of well-rounded entrance. This assumption was adopted in the present analysis and thus, at $x = 0$, the axial velocity and pressure are uniform with values u_0 and p_0, respectively.

Following the procedure suggested in [4], the nondimensional momentum equation in the axial direction can be written as:

$$\left(\frac{1+\alpha}{2\alpha}\right)^2 \frac{\partial U}{\partial X^*} + \frac{2}{\alpha}\left[\int_0^1 \frac{1}{R}\frac{\partial U}{\partial \theta}\bigg|_{\theta=0} dR - \int_0^\alpha \frac{\partial U}{\partial R}\bigg|_{R=1} d\theta\right] = \frac{\partial^2 U}{\partial R^2} + \frac{1}{R}\frac{\partial U}{\partial R} + \frac{1}{R^2}\frac{\partial^2 U}{\partial \theta^2}, \quad (1)$$

where $R = r/r_0$, $U = u/u_b$, $\epsilon(X) = dX/dX^*$, $X = x/(D_h Re)$, $D_h = 2r_0\alpha/(1+\alpha)$, $Re = D_h u_b/\nu$, and the parameter, ϵ can be formulated as:

$$\epsilon(X) = -\left[\frac{d}{dX^*}\int_A \left(U^2 - \frac{U^3}{2}\right)dA\right] \Big/ \int_A U\frac{\partial U}{\partial X^*}\, dA. \quad (2)$$

The nondimensional pressure gradient is given by:

$$\left(\frac{1+\alpha}{\alpha}\right)^2 \frac{dP}{dX} = \frac{32}{\alpha}\int_A U\frac{\partial U}{\partial X}dA + \frac{16}{\alpha}\left[\int_0^1 \frac{1}{R}\frac{\partial U}{\partial \theta}\bigg|_{\theta=0} dR + \int_0^\alpha \frac{\partial U}{\partial R}\bigg|_{R=1} d\theta\right], \quad (3)$$

where $P = (p_0 - p)/(\frac{1}{2}\rho u_b^2)$. Appropriate boundary and symmetry conditions are:

$$U = 0 \quad \text{at } R = 1, 0 \le \theta \le \alpha, \text{ and } \theta = 0, 0 \le R \le 1, \quad (4a)$$

$$\text{and } \frac{\partial U}{\partial \theta} = 0 \quad \text{at } \theta = \alpha, 0 \le R \le 1. \quad (4b)$$

Due to the symmetry around the plane $\theta = \alpha$, the solution need be carried out only over the region $0 \le \theta \le \alpha$. Details of the derivation of equations (1)–(4) are given in [3].

Solutions were obtained using a finite difference aproach. At any axial location, the solution domain was subdivided by a 33 × 33 mesh, with the subdivisions adjacent to the straight and curved walls further subdivided into six equal parts for more accurate evaluation of wall gradients. The computation was marched from the inlet section to the fully developed region using axial steps with sizes $\Delta X^* = 1 \times 10^{-6}$ near the inlet, increasing to $\Delta X^* = 5 \times 10^{-4}$ as fully developed conditions were approached. Starting from the inlet section $X = X^* = 0$ where the value of U is given, the velocity distribution at $X^* = \Delta X^*$ was obtained by solving (1) interatively at all mesh points, subject to conditions (4). The value of ϵ was then obtained from (2) and the relation $\Delta X = \epsilon \Delta X^*$ was used for the evalution of ΔX. Finally, dP/dX was evaluated from (3) before marching to the next cross section. The solution was progressed until all axial velocities were within 1 percent of the corresponding fully developed value, and the value of X there was taken as the entrance length Le.

Numerical Results

The resulting values of Le are listed in Table 1 for the four duct geometries considered. With simple calculations, we can see from these results that for the same r_0, u_b, and ν, the entrance length increases as α increases. This trend is expected, however, quantitative comparisons are not possible due to lack of similar results. Development of the stretching factor ϵ along the duct is shown in Fig. 2 for different values of α. As shown in [3], the ϵ values for $\alpha = \pi/8$ compared well with those in [2]. The asymptotic value reached here for $\alpha = \pi/8$ is 1.92 as compared to 1.98 in [2]. It is also interesting to note that the present asymptotic values for ϵ (2.22 for $\alpha = \pi/32$, 2.03 for $\alpha = \pi/16$, 1.92 for $\alpha = \pi/8$, and 1.86 for $\alpha = \pi/4$) seem to conform with the asymptotic value of 1.82 obtained in [4] for smooth tubes. A sample of the velocity results illustrating the velocity development at the symmetry plane is shown in Fig. 3. The well-known characteristic of entrance region flow, namely that the fluid is decelerated near the walls and accelerated in the central core is clear from this figure. Again, our velocity results for $\alpha = \pi/8$ compared fairly well [3] with those in [2].

The most commonly used parameters for presenting the pressure results are the product of the friction factor and Reynolds number fRe, and the pressure defect K. In the present analysis, the friction factor was defined as:

$$f = (D_h/2)(-dp/dx)/(\rho u_b^2),$$

and hence

$$fRe = \frac{1}{4}\frac{dP}{dX} \quad (5)$$

The pressure defect is normally defined as:

$$K(X) = [p_0 - p + (dp/dx)_{FD} x]/(\tfrac{1}{2}\rho u_b^2),$$

which reduces to the following nondimensional form:

$$K(X) = P - 4(fRe)_{FD} X. \quad (6)$$

Results based on equations (5) and (6) are listed in Table 2. The values of fRe at $X = Le$ compare to within 3 percent of those reported in [1]. As expected [1], the present pressure results for $\alpha = \pi/8$ are widely different from those in [2]. A comparison between the K-values at $X = Le$ and the fully developed K-values reported in [1] is shown in Fig 4. It must be pointed out that the K_{FD} values reported in [1] are based on an approximate analytical method which utilizes only the fully developed velocity profile. Figure 4 shows a fair agreement with a maximum discrepancy of about 8 percent at $\alpha = \pi/32$.

Acknowledgments

The authors gratefully acknowledge the support provided for this research by the Natural Sciences and Engineering Research Council of Canada.

References

1 Shah, R. K., and London, A. L., *Laminar Flow Forced Convection in Ducts*, Academic Press, 1978.

2 Wendt, R. L., and Wiginton, C. L., "Incompressible Laminar Entrance Flow in a Circular Sector Duct," JOURNAL OF APPLIED MECHANICS, Vol. 98, 1976, pp. 357-359.

3 Munis, A A., "Analysis of Laminar Fluid Flow in the Entrance Region of Circular Sector Ducts," M.Sc. Thesis, University of Manitoba, 1981.

4 Sparrow, E. M., Lin, S. H., and Lundgren, T. S., "Flow Development in the Hydrodynamic Entrance Region of Tubes and Ducts," *Physics of Fluids*, Vol. 7, 1964, pp. 338-347.

5 Sparrow, E. M., and Lin, S. H., "The Developing Laminar Flow and Pressure Drop in the Entrance Region of Annular Ducts," *Journal of Basic Engineering*, Vol. 86, 1964, pp. 827-834.

6 Fleming, D. P., and Sparrow, E. M., "Flow in the Hydrodynamic Entrance Region of Ducts of Arbitrary Cross-Section," ASME *Journal of Heat Transfer*, Vol. 91, 1969, pp. 345-354.

On Stochastic Dynamics of an Embedded Rigid Cylinder

A. Beltzer[1] and R. Parnes[2]

[1] Visiting Professor, School of Aerospace, Mechanical and Nuclear Engineering, University of Oklahoma at Norman, Norman, Okla. 73019. On leave from Holon Technical Institute, Israel. Mem. ASME.

[2] Associate Professor, Department of Solid Mechanics, Materials and Structures, School of Engineering, Tel-Aviv University, Ramat-Aviv, Israel.

Manuscript received by ASME Applied Mechanics Division, July, 1980; final revision, January, 1981.

Multidegree-of-freedom vibrations are considered for a rigid cylinder embedded in an isotropic elastic medium that is subjected to random propagating disturbances. The numerical results obtained enable one to select values of parameters of the system which would provide desirable motions of the inclusion.

1 Introduction

The classical linear theory of wave propagation provides a thorough analysis of the phenomenon of wave diffraction. However, this theory is concerned with traveling disturbances that are simple deterministic processes. It is well known that in reality these disturbances are usually random or incompletely defined. Due to this motivation, a number of investigations have been recently carried out on elastic and viscoelastic random waves. A survey of these works was presented by Beltzer [1].

This paper is concerned with random vibrations of an embedded rigid cylinder that are induced by elastic waves. All the stochastic processes used are taken to be stationary with zero mean. In view of the linearity of the system the last restriction does not lead to any loss of generality.

2 Basic Equations

We consider an infinite isotropic elastic medium (defined by its Lamé constants λ and μ and by its mass density ρ) which contains a rigid movable infinite cylinder with arbitrary radius a and mass density ρ_0. The medium is subjected to general plane waves of displacement traveling in the direction x and which impinge on the cylinder (Fig. 1).

The random motion of the cylinder under this impact is characterized by three degrees of freedom: displacements $u(t)$ and $v(t)$ in the directions x and y, respectively, and by a rotation $\phi(t)$ about the direction z. The displacement $u(t)$ is due to the P-component of the incident field only, whereas the SV-component causes both the displacements $v(t)$ and $\phi(t)$.

Let us denote the P or SV-component of the incident field of displacement as W_j $(j = p, s)$, the spectrum of an incident wave as $Q_j(\omega)$, and the spectra of the inclusion motions as $\bar{Q}_k(\omega)$, $k = u, v, \phi$. Taking into account the separability mentioned between P and SV-waves of excitation and the components of the inclusion motion, one can write the following equations governing the steady-state response

$$\begin{Bmatrix} \bar{Q}_u(\omega) \\ \bar{Q}_v(\omega) \\ \bar{Q}_\phi(\omega) \end{Bmatrix} = \begin{bmatrix} |G_u^p(\omega)|^2 & 0 & 0 \\ 0 & |G_v^s(\omega)|^2 & 0 \\ 0 & 0 & |G_\phi^s(\omega)|^2 \end{bmatrix} \begin{Bmatrix} Q_p(\omega) \\ Q_s(\omega) \\ Q_s(\omega) \end{Bmatrix} \tag{1}$$

where $G_k^j(\omega)$, $(j = p, s;\ k = u, v, \phi)$ is the cylinder displacement k due to normalized harmonic j-disturbance.

Making use of the results for the harmonic response of a rigid cylinder [2], we have the following expressions for $G_k^j(\omega)$

$$G_u^p(\omega) = i\eta[8H_1(\beta a) - 4\,\beta a\, H_0(\beta a)](\pi\alpha a\Delta)^{-1} \tag{2}$$

$G_v^s(\omega)$ is given by equation (2) where the replacements

$$\alpha \to \beta \quad \beta \to \alpha \text{ are made} \tag{3}$$

$$G_\phi^s(\omega) = 8\eta[\beta^2 a^2 H_1(\beta a) + 4\eta\beta a\, H_0(\beta a) - 8\eta H_1(\beta a)]^{-1}/(\pi a) \tag{4}$$

where

$$\Delta = 4\eta\, H_1(\alpha a) H_1(\beta a) - (1+\eta)\beta a\, H_0(\beta a)\, H_1(\alpha a)$$

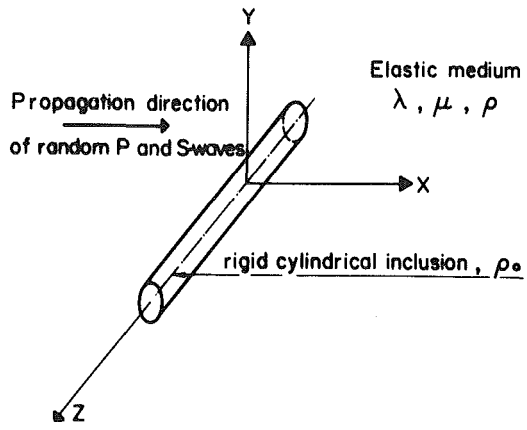

Fig. 1 Geometry of problem

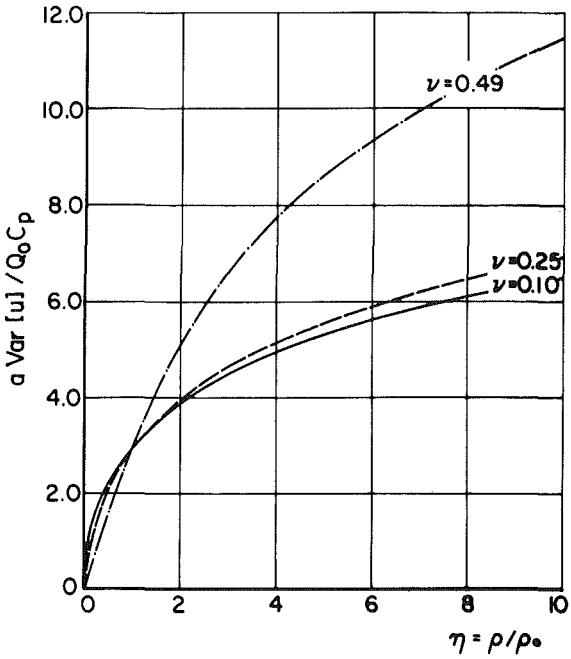

Fig. 2 Mean-square inclusion displacement in the x-direction versus density ratio η

$$-(1+\eta)\alpha a\, H_0(\alpha a)\, H_1(\beta a) + \alpha\beta\, a^2 H_0\,(\alpha a)\, H_0(\beta a) \tag{5}$$

and

$$\alpha = \omega/c_p; \quad \beta = \omega/c_s; \quad \eta = \rho/\rho_0 \tag{6}$$

In the foregoing $H_m(z) \equiv H_m^{(1)}(z)$ stands for the Hankel function of the first kind of the mth order and c_p and c_s are the velocities of dilatational and shear waves in the matrix.

Now we can determine the variances of nth derivatives of each of the stochastic processes of interest, i.e., of $u(t)$, $v(t)$, and $\phi(t)$

$$\mathrm{Var}[k^{(n)}] = \int_{-\infty}^{\infty} \omega^{2n} \bar{Q}_k(\omega)\, d\omega, \quad (k = u, v, \phi;\ n = 0, 1, 2 \ldots) \tag{7}$$

3 Response to White Noise Disturbances

The spectra of the incident field is taken to be

$$Q_j(\omega) = Q_0 = \text{const}; \quad |\omega| < \infty,\ j = p, s \tag{8}$$

Making use of asymptotic expansions for $|G_k^j(\omega)|$ it can be shown that the improper integrals, given by equation 7, exist only for $n = 0$, i.e., for the variance of the displacements. The multivalued character of the Hankel

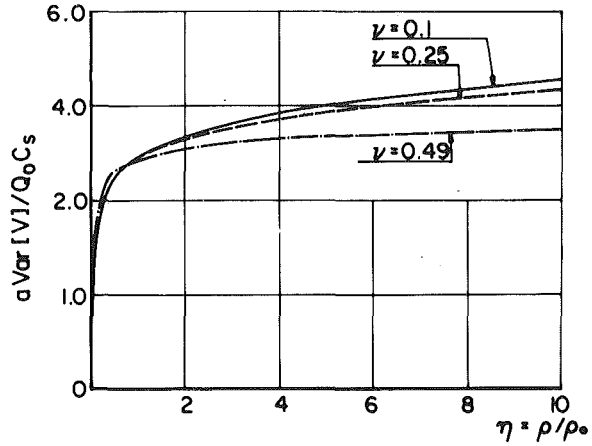

Fig. 3 Mean-square inclusion displacement in the y-direction versus density ratio η

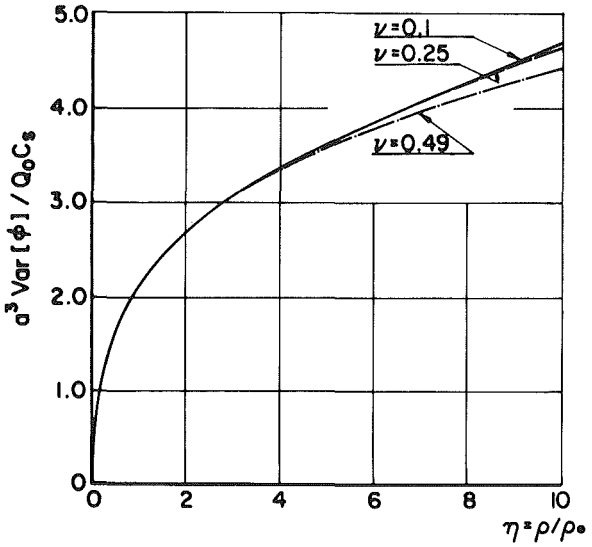

Fig. 4 Mean-square inclusion rotation versus density ratio η

functions necessitates a numerical evaluation of these integrals.

The results computed are presented in Figs. 2–4. As expected, these figures show that the motion of a "heavy" inclusion ($\eta < 1$) is always less random because of its greater inertia. The effect of the Poisson ratio, ν, on the variance of the inclusion motion is shown. For $\eta = 1$ the results are independent of ν for all components of the response. For other values of η, Var[u] and Var[v] are explicitly affected by this parameter whereas the influence on Var[ϕ] is slight. It is of interest to note that greater damping of the motion of a "light" inclusion ($\eta > 1$) in the y-direction occurs for a rubberlike material with $\nu \to 0.5$ as the matrix. On the other hand, for damping of the vibrations in the x-direction values as ν approaches zero are essentially more suitable (Figs. 2 and 3).

4 Conclusion

The results, presented in Figs. 2–4, cover the majority of practically interesting cases. They can be used in the analysis of composite materials to provide minimum (or maximum) damping or better protection of a rigid embedded cylinder. If the inclusion serves as a sensor for monitoring the incoming waves the results obtained can be employed to reduce the distortion due to a random noise.

References

1 Beltzer, A. I., "Random Waves in Solid Media," *The Shock and Vibration Digest*, Vol. 14, No. 3, 1982, pp. 3–6.

2 Pao, Y. H., and Mow, C. C., *Diffraction of Elastic Waves and Dynamic Stress Concentrations*, Crane Russak, New York, 1972.

On the Flow of a Viscoelastic Liquid Past an Infinite Porous Plate due to Fluctuation in the Main Flow

D. N. Mukhopadhyay[1] and T. K. Chaudhury[1]

Introduction

Stuart [1] and Messiha [2] investigated the oscillating flow of viscous liquid over an infinite flat plate with constant suction and variable suction, respectively, at the plate and discussed many interesting features of the flow. Soundalgekar and Puri [3] extended Messiha's problem to the case of non-Newtonian liquid with Walter's liquid B' [4] as the model. However the equations of motion considered by the authors [3] in the approximation of short relaxation time are identical with those of second-order liquid for the same problem and can be solved only by successive approximation. We extend Messiha's problem to the class of viscoelastic liquid known as stress-relaxing liquid of Oldroyd [5] and, as observed in our earlier work [6], we get a more general solution giving the solution [3] as a first approximation for small elastic parameter. Our solution shows some interesting effects of the stress-relaxing property of the liquid on the response of the boundary layer to the fluctuation in the main flow.

Formulation and Solution of the Problem

The constitutive equation for a viscoelastic liquid of Oldroyd [5] has the form

$$P_{ij} = -p\delta_{ij} + T_{ij},$$

$$T_{ij} + \lambda_1 \left(\frac{\partial T_{ij}}{\partial t} + v_K T_{ij,K} - v_{i,K} T_{Kj} - v_{J,K} T_{iK} \right) = 2\eta_0 e_{ij}, \qquad (1)$$

where P_{ij} and e_{ij} are, respectively, stress tensor and rate-of-strain tensor, v_i are velocity components, λ_1, is the relaxation time, and η_0 is the viscosity coefficient. Taking the x'-axis along the plate in the direction of flow and the y'-axis perpendicular to the plate directed into the liquid, the flow field is given by $u' = u'(y', t')$, $v' = v_0'(1 + \epsilon A e^{i\omega' t'})$, $\omega' = 0$ with the free stream velocity $U'(t')$ (cf., Messiha [2]), where v_0' is a nonzero constant mean suction velocity and A and ϵ are small positive constants such that $\epsilon A \leq 1$. The differential equation for u' will be obtained by elimination of stress component $T_{x'y'}$ between (1) and the momentum equation. This elimination is effected by taking the particular solution $T_{y'y'} = 0$, which means vanishing normal stress $T_{y'y'}$ at the line of entry (or exit) of the liquid through pores of the boundary.

Assuming external forces to be absent and introducing nondimensional quantities defined by $y = y' v_0'/\nu$, $t = v_0'^2 t/$

[1] Junior Research Fellow and Reader, respectively, Department of Mathematics, Burdwan University, Burdwan, West Bengal, India.

Manuscript received by ASME Applied Mechanics Division, April, 1981; final revision, December, 1981.

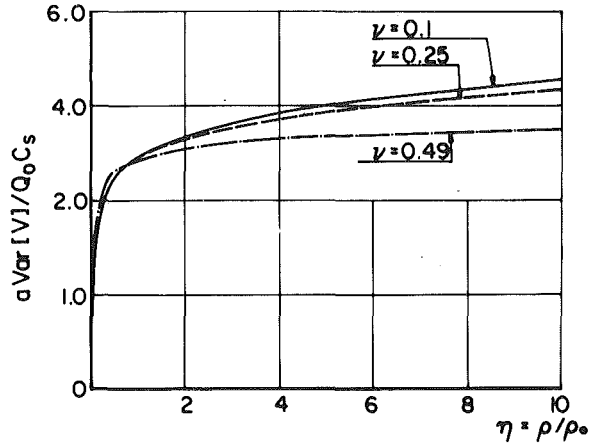

Fig. 3 Mean-square inclusion displacement in the y-direction versus density ratio η

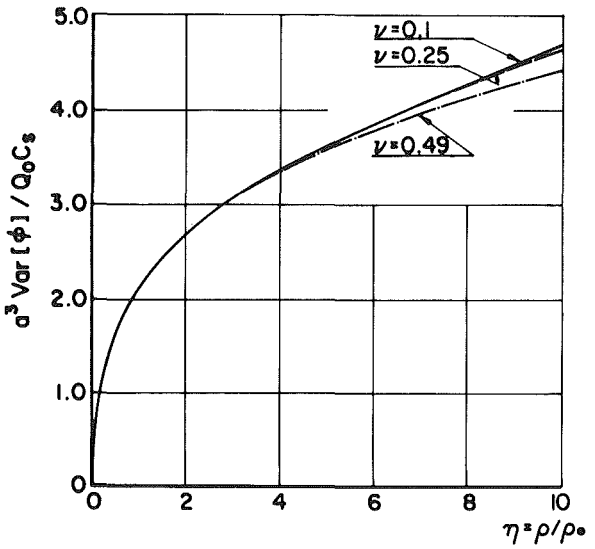

Fig. 4 Mean-square inclusion rotation versus density ratio η

functions necessitates a numerical evaluation of these integrals.

The results computed are presented in Figs. 2–4. As expected, these figures show that the motion of a "heavy" inclusion ($\eta < 1$) is always less random because of its greater inertia. The effect of the Poisson ratio, ν, on the variance of the inclusion motion is shown. For $\eta = 1$ the results are independent of ν for all components of the response. For other values of η, Var[u] and Var[v] are explicitly affected by this parameter whereas the influence on Var[ϕ] is slight. It is of interest to note that greater damping of the motion of a "light" inclusion ($\eta > 1$) in the y-direction occurs for a rubberlike material with $\nu \to 0.5$ as the matrix. On the other hand, for damping of the vibrations in the x-direction values as ν approaches zero are essentially more suitable (Figs. 2 and 3).

4 Conclusion

The results, presented in Figs. 2–4, cover the majority of practically interesting cases. They can be used in the analysis of composite materials to provide minimum (or maximum) damping or better protection of a rigid embedded cylinder. If the inclusion serves as a sensor for monitoring the incoming waves the results obtained can be employed to reduce the distortion due to a random noise.

References

1 Beltzer, A. I., "Random Waves in Solid Media," *The Shock and Vibration Digest*, Vol. 14, No. 3, 1982, pp. 3–6.

2 Pao, Y. H., and Mow, C. C., *Diffraction of Elastic Waves and Dynamic Stress Concentrations*, Crane Russak, New York, 1972.

On the Flow of a Viscoelastic Liquid Past an Infinite Porous Plate due to Fluctuation in the Main Flow

D. N. Mukhopadhyay[1] and T. K. Chaudhury[1]

Introduction

Stuart [1] and Messiha [2] investigated the oscillating flow of viscous liquid over an infinite flat plate with constant suction and variable suction, respectively, at the plate and discussed many interesting features of the flow. Soundalgekar and Puri [3] extended Messiha's problem to the case of non-Newtonian liquid with Walter's liquid B' [4] as the model. However the equations of motion considered by the authors [3] in the approximation of short relaxation time are identical with those of second-order liquid for the same problem and can be solved only by successive approximation. We extend Messiha's problem to the class of viscoelastic liquid known as stress-relaxing liquid of Oldroyd [5] and, as observed in our earlier work [6], we get a more general solution giving the solution [3] as a first approximation for small elastic parameter. Our solution shows some interesting effects of the stress-relaxing property of the liquid on the response of the boundary layer to the fluctuation in the main flow.

Formulation and Solution of the Problem

The constitutive equation for a viscoelastic liquid of Oldroyd [5] has the form

$$P_{ij} = -p\delta_{ij} + T_{ij},$$

$$T_{ij} + \lambda_1 \left(\frac{\partial T_{ij}}{\partial t} + v_K T_{ij,K} - v_{i,K} T_{Kj} - v_{J,K} T_{iK} \right) = 2\eta_0 e_{ij}, \qquad (1)$$

where P_{ij} and e_{ij} are, respectively, stress tensor and rate-of-strain tensor, v_i are velocity components, λ_1, is the relaxation time, and η_0 is the viscosity coefficient. Taking the x'-axis along the plate in the direction of flow and the y'-axis perpendicular to the plate directed into the liquid, the flow field is given by $u' = u'(y', t')$, $v' = v_0'(1 + \epsilon A e^{i\omega' t'})$, $\omega' = 0$ with the free stream velocity $U'(t')$ (cf., Messiha [2]), where v_0' is a nonzero constant mean suction velocity and A and ϵ are small positive constants such that $\epsilon A \leq 1$. The differential equation for u' will be obtained by elimination of stress component $T_{x'y'}$ between (1) and the momentum equation. This elimination is effected by taking the particular solution $T_{y'y'} = 0$, which means vanishing normal stress $T_{y'y'}$ at the line of entry (or exit) of the liquid through pores of the boundary.

Assuming external forces to be absent and introducing nondimensional quantities defined by $y = y' v_0'/\nu$, $t = v_0'^2 t/$

[1] Junior Research Fellow and Reader, respectively, Department of Mathematics, Burdwan University, Burdwan, West Bengal, India.

Manuscript received by ASME Applied Mechanics Division, April, 1981; final revision, December, 1981.

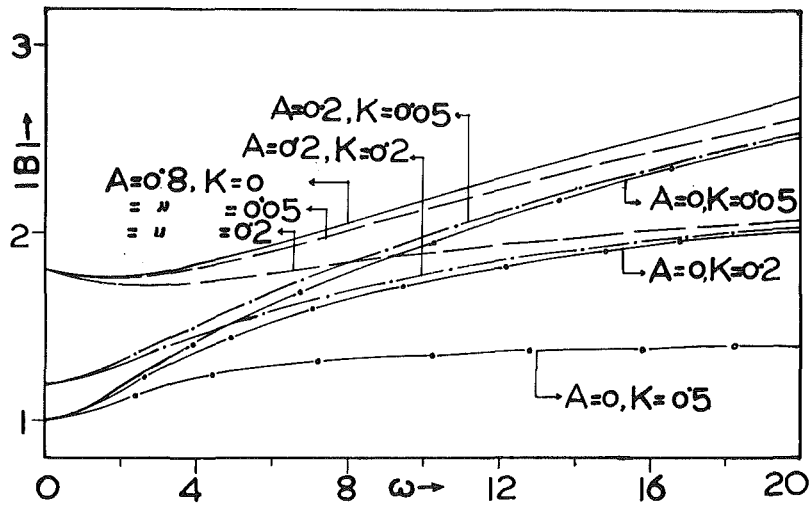

Fig. 1 Amplitude of the skin friction

4ν, $\omega = 4\nu\omega'/v_0'^2$, $u = u'/U_0'$, $U = U'/U_0'$, $K = \lambda_1 v_0'^2/\nu$, where U_0' is a reference velocity, ω' is the frequency of the fluctuation in the main stream, K is the elastic parameter and $\nu = \eta_0/\rho$, we have for u the equation

$$\frac{\partial u}{\partial t} + \frac{K}{4}\frac{\partial^2 u}{\partial t^2} - 2K(1+\epsilon A e^{i\omega t})\frac{\partial^2 u}{\partial y \partial t} - \{4+(4+i\omega K)\epsilon A e^{i\omega t}\}\frac{\partial u}{\partial y} + 4\{K(1+\epsilon A e^{i\omega t})^2 - 1\}\frac{\partial^2 u}{\partial y^2} = \frac{dU}{dt} + \frac{K}{4}\frac{d^2 U}{dt^2} \quad (2)$$

and boundary conditions $u = 0$ at $y = 0$ and $u = U(t)$ as $y \to \infty$. With $U(t) = 1 + \epsilon e^{i\omega t}$ for the free stream, the solution for u in the boundary layer is obtained, if $K < 1$, as $u = 1 - e^{-y/1-KD} + \epsilon e^{i\omega t}(M_r + i M_i)$ up to the first power in ϵ, (3) where

$$M_r = 1 - e^{-m_r y}\left[\cos m_i y - \frac{4A}{\omega(1-K)}\sin m_i y\right],$$

$$M_i = e^{-m_r y}\left[\sin m_i y + \frac{4A}{\omega(1-K)}\cos m_i y\right] - \frac{4A}{\omega(1-K)}e^{-\frac{1}{1-K}y},$$

$$m_r = \frac{2\sqrt{2}+s}{4\sqrt{2}(1-K)}, \quad m_i = \frac{4\omega+\sqrt{2}\omega K s}{4\sqrt{2}s(1-K)},$$

$$s = \sqrt{r+(4-K\omega^2)}, \quad r = \sqrt{(4-K\omega^2)^2+16\omega^2}$$

The transient velocity for $\omega t = \Pi/2$ is $u = 1 - e^{-y/1-KD} - \epsilon M_i$. We assume the nondimensional shear stress as

$$T_{xy} = \frac{T_{x'y'}}{U_0' v_0' \rho} = T_{xy}^{(1)} + \epsilon e^{i\omega t} T_{xy}^{(2)}.$$

Then using the expression for u given in (3) and the free stream velocity $U(t) = 1 + \epsilon e^{i\omega t}$, and utilizing the constitutive equation (1) and momentum equation, we finally obtain

$$T_{xy} = e^{-\frac{1}{1-K}y} + \epsilon e^{i\omega t}\frac{1}{\omega(1-K)}\left[\frac{(\omega-\omega K-4iA)\{4m(1-K)-i\omega K\}}{4+i\omega K}e^{-my} + 4iAe^{-\frac{1}{1-k}y}\right],$$

where $m = m_r + i m_i$

Shear stress at the wall $= T_{xy}|_{y=0} = 1 + \epsilon|B|\cos(\omega t + \alpha)$, (4)

where $B = B_r + i B_i$, $\tan\alpha = \dfrac{B_i}{B_r}$,

and

$$B_r = \frac{4}{16+\omega^2 K^2}\left[4m_r(1-K-AK) + m_i\left(\frac{16A}{\omega}+\omega K-\omega K^2\right) - \frac{\omega^2 K^2}{4} - \frac{4AK}{1-K}\right],$$

$$B_i = \frac{4}{16+\omega^2 K^2}\left[4m_i(1-K-AK) - m_r\left(\frac{16A}{\omega}+\omega K-\omega K^2\right) - \omega K + \frac{16A}{\omega(1-K)} + \frac{2A\omega K^2}{1-K}\right].$$

The results (3) and (4) reduce to those of Messiha [2] when $K = 0$ and to those of Stuart [1] when $K = 0$, $A = 0$. Expanding for small K and retaining only up to the first power in K, (3) and (4) give the results of Soundalgekar and Puri [3].

Discussion

It is found from computations that due to elastic property of the liquid the back flow occurs at the plate at values of ϵ and ω much smaller than those in the case of Newtonian liquids, and this effect of elastic property is seen to be more pronounced in Oldroyd liquid than that in the case of Walter liquid B' or second-order liquid, probably due to the effect of stress-relaxation. It is also found that the velocity near the plate decreases as the elastic parameter K or frequency parameter ω increases while, after a certain distance near the plate an opposite effect is observed.

It is seen from the expression for transient velocity for constant suction that for each K there is a critical ϵ at which the velocity profile is of "separation" type (i.e., with zero skin friction). For ϵ greater than this critical value, the transient velocity profile is transient only on the whole but oscillates with y having reverse flow near the plate. This critical ϵ decreases as k increases and for a given k it is obtained from the relation $\epsilon = 1/(1-k)m_i$. Comparing with Stuart's [1] result it is seen that the elastic parameter k decreases the value of the critical ϵ. Therefore the elastic property of the liquid will carry a high-frequency oscillatory

disturbance of the main stream to the vicinity of the plate more effectively and influence the skin friction even if the amplitude of the disturbance is very small (of the order 10^{-2}). Graphs of the amplitude $|B|$ of the skin friction for different values of A and K are shown in Fig. 1. It can be seen that $|B|$ increases with increasing value of A as observed by Messiha [2]. But for a fixed value of A, $|B|$ decreases with increasing K, this decrease being larger for higher values of ω. Thus the stress-relaxing property of the liqiud decreases the maximum shear stress at the wall and the effect is much more pronounced in Oldroyd liquid considered here than in a second-order liquid (cf., [3]).

References

1 Stuart, J. T., "A Solution of the Navier-Stokes and Energy Equations Illustrating Response of Skin Friction and Temperature of an Infinite Plate Thermometer to Fluctuations in the Stream Velocity," *Proceedings of the Royal Society*, London, Series A, Vol. A 231, 1955, pp. 116–130.

2 Messiha, S. A. S., "Laminar Boundary Layers in Oscillatory Flow Along an Infinite Flat Plate With Variable Suction," *Proceedings of the Cambridge Philosophical Society*, Vol. 62, 1966, p. 329.

3 Soundalgekar, V. M., and Puri, P., "On Fluctuating Flow of an Elastico-Viscous Fluid Past an Infinite Plate With Variable Suction," *Journal of Fluid Mechanics*, Vol. 35, Part 3, 1969, pp. 561–573.

4 Walters, K., *IUTAM International Symposium on Second-Order Effects in Elasticity, Plasticity and Fluid Dynamics*, Reiner, M., and Abir, D., eds., New York, Pergamon, 1964, p. 507.

5 Oldroyd, J. G., "On the Formulation of Rheological Equations of State," *Proceedings of the Royal Society*, London, Vol. A 200, No. 1063, 1950, p. 523.

6 Mukhopadhyay, D. N., and Chaudhury, T. K., "A Note on the Flow of a Viscoelastic Liquid Near an Oscillating Infinite Porous Plate," ASME JOURNAL OF APPLIED MECHANICS, Vol. 47, 1980, pp. 666–667.

Radial Nonuniformity of the Fields Near a Moving Crack Tip in a Material With Linear Strain Hardening

V. Dunayevsky[1] and J. D. Achenbach[1]

1 Introduction

The fields near the tip of a propagating Mode-III crack in an elastic perfectly plastic material have been discussed by Chitaley and McClintock [1]. The results of [1] show bounded stresses, but strains with logarithmic singularities. On the other hand, for a material characterized by J_2-flow theory together with a bilinear effective stress-strain curve, Amazigo and Hutchinson [2] have shown that both stresses and strains contain singularities of the form r^s, where $0<s<-1$. The strengths of the singularities, defined by s, depend significantly on the strain hardening parameter α, which is the ratio of the slopes of the two straight line segments of the effective stress-strain curve. For shear deformations this strain hardening parameter is

$$\alpha=\mu_t/\mu, \quad \alpha\leq 1 \tag{1}$$

where μ is the shear modulus, which defines the slope when the effective stress is less than the yield stress in shear. It was noted in reference [2] that numerical computations suggest $s\to-\alpha^{1/2}$ when $\alpha\to 0$.

It stands to reason that the results for linear strain hardening, as presented in [2], should reduce to those for perfect plasticity, as presented in [1], in the limit $\alpha\to 0$. Since the least amount of strain hardening produces singularities of the type r^s, there appears to be a spatial nonuniformity in the domain of validity of solutions for small α.

In this Note we have attempted to resolve this question by constructing near-tip fields for linear strain hardening with small α. Such fields are of interest on their own accord, but they can also be used to investigate the limit of vanishing α. Our results show the presence of an edge zone (a boundary layer) in which the fields are singular with $s=-\alpha^{1/2}$. The edge zone is defined by $r/r_p=O[\exp(-1/\alpha^{1/2})]$. Outside of the edge zone the solution can be represented by a regular expansion with respect to $\alpha^{1/2}$, the first term being the solution for the elastic perfectly plastic case. In the limit $\alpha\to 0$ the edge zone shrinks on the crack tip, thus eliminating the domain of validity of terms of order r^s. The near-tip fields then reduce to those outside the edge zone, which are the ones for the elastic perfectly plastic material.

2 Governing Equations

Let (x,y,z) define a coordinate system which moves with the crack tip at a constant velocity v, such that the z-axis coincides with the crack edge. Following the notation of reference [2], the stresses and strains for antiplane shear are denoted by $\tau_\beta=\sigma_{z\beta}$ and $\gamma_\beta=2\epsilon_{z\beta}$, where $\beta=x,y$. In the loading region, and relative to the moving coordinate system, the stress-strain relations according to J_2-flow theory with linear strain hardening are [2]:

$$\mu_t\dot{\gamma}_\beta=\alpha\dot{\tau}_\beta+(1-\alpha)\tau^{-1}\tau_\beta\dot{\tau} \tag{2}$$

where α is defined by equation (1), and

$$\tau=(\tau_x^2+\tau_y^2)^{1/2}, \text{ and } \dot{\tau}>0 \tag{3a,b}$$

In (2), $\dot{(\ )}$ denotes material differentiation with respect to any monotonically increasing quantity. In the present paper we set

$$\dot{(\ )}=-v\frac{\partial}{\partial x}=-v\partial_x, \tag{4}$$

consistent with a steady-state situation relative to the moving crack tip. Equations (2)–(4) are supplemented by equations defining equilibrium and strain compatibility:

$$\partial_\beta\tau_\beta=0 \text{ and } \partial_x\gamma_y-\partial_y\gamma_x=0 \tag{5a,b}$$

Let us introduce new variables $\hat{\gamma}_\beta$ and $\hat{\tau}_\beta$ by

$$(\gamma_\beta,\tau_\beta)=(\hat{\gamma}_\beta,\hat{\tau}_\beta)\exp[-\alpha\mu\lambda(x,y)] \tag{6a,b}$$

where

$$\hat{\tau}_x^2+\hat{\tau}_y^2=k^2 \tag{7}$$

Here the constant k defines the yield stress in shear. In terms of the new variables $\hat{\gamma}_\beta,\hat{\tau}_\beta$, and λ the constitutive equations (2) become

$$\partial_x\hat{\gamma}_\beta-\alpha\mu\hat{\gamma}_\beta\partial_x\lambda=\frac{1}{\mu}\partial_x\hat{\tau}_\beta-\hat{\tau}_\beta\partial_x\lambda \tag{8}$$

In the limit $\alpha\to 0$, equation (8) turns into the constitutive equation for an elastic perfectly plastic material.

In the loading region the term $\partial_x\lambda$ should be positive. Indeed, since $\dot{\tau}>0$, we obtain from (3*a*), (4), and (6*b*):

$$\begin{aligned}\dot{\tau}&=-v\partial_x\tau=-v\partial_x[(\hat{\tau}_x^2+\hat{\tau}_y^2)^{1/2}\exp(-\alpha\mu\lambda)]\\&=vk\alpha\mu\exp(-\alpha\mu\lambda)\partial_x\lambda>0\end{aligned} \tag{9}$$

which implies $\partial_x\lambda>0$.

Equation (7) suggests the introduction of the "stress function" $\hat{\omega}$ by the relations

$$\hat{\tau}_x=-k\sin\hat{\omega}, \quad \hat{\tau}_y=k\cos\hat{\omega} \tag{10a,b}$$

It is now convenient to introduce polar coordinates (r,θ).

[1] Department of Civil Engineering, The Technological Institute, Northwestern University, Evanston, Ill. 60201. J. D. Achenbach is a Fellow, ASME.

Manuscript received by ASME Applied Mechanics Division, November, 1981; final revision, January, 1982.

Manuscript received by ASME Applied Mechanics Division, November, 1981; final revision, January, 1982.

disturbance of the main stream to the vicinity of the plate more effectively and influence the skin friction even if the amplitude of the disturbance is very small (of the order 10^{-2}). Graphs of the amplitude $|B|$ of the skin friction for different values of A and K are shown in Fig. 1. It can be seen that $|B|$ increases with increasing value of A as observed by Messiha [2]. But for a fixed value of A, $|B|$ decreases with increasing K, this decrease being larger for higher values of ω. Thus the stress-relaxing property of the liqiud decreases the maximum shear stress at the wall and the effect is much more pronounced in Oldroyd liquid considered here than in a second-order liquid (cf., [3]).

References

1 Stuart, J. T., "A Solution of the Navier-Stokes and Energy Equations Illustrating Response of Skin Friction and Temperature of an Infinite Plate Thermometer to Fluctuations in the Stream Velocity," *Proceedings of the Royal Society*, London, Series A, Vol. A 231, 1955, pp. 116–130.

2 Messiha, S. A. S., "Laminar Boundary Layers in Oscillatory Flow Along an Infinite Flat Plate With Variable Suction," *Proceedings of the Cambridge Philosophical Society*, Vol. 62, 1966, p. 329.

3 Soundalgekar, V. M., and Puri, P., "On Fluctuating Flow of an Elastico-Viscous Fluid Past an Infinite Plate With Variable Suction," *Journal of Fluid Mechanics*, Vol. 35, Part 3, 1969, pp. 561–573.

4 Walters, K., *IUTAM International Symposium on Second-Order Effects in Elasticity, Plasticity and Fluid Dynamics*, Reiner, M., and Abir, D., eds., New York, Pergamon, 1964, p. 507.

5 Oldroyd, J. G., "On the Formulation of Rheological Equations of State," *Proceedings of the Royal Society*, London, Vol. A 200, No. 1063, 1950, p. 523.

6 Mukhopadhyay, D. N., and Chaudhury, T. K., "A Note on the Flow of a Viscoelastic Liquid Near an Oscillating Infinite Porous Plate," ASME JOURNAL OF APPLIED MECHANICS, Vol. 47, 1980, pp. 666–667.

Radial Nonuniformity of the Fields Near a Moving Crack Tip in a Material With Linear Strain Hardening

V. Dunayevsky[1] and J. D. Achenbach[1]

1 Introduction

The fields near the tip of a propagating Mode-III crack in an elastic perfectly plastic material have been discussed by Chitaley and McClintock [1]. The results of [1] show bounded stresses, but strains with logarithmic singularities. On the other hand, for a material characterized by J_2-flow theory together with a bilinear effective stress-strain curve, Amazigo and Hutchinson [2] have shown that both stresses and strains contain singularities of the form r^s, where $0<s<-1$. The strengths of the singularities, defined by s, depend significantly on the strain hardening parameter α, which is the ratio of the slopes of the two straight line segments of the effective stress-strain curve. For shear deformations this strain hardening parameter is

$$\alpha=\mu_t/\mu, \quad \alpha\leq 1 \tag{1}$$

where μ is the shear modulus, which defines the slope when the effective stress is less than the yield stress in shear. It was noted in reference [2] that numerical computations suggest $s\to-\alpha^{1/2}$ when $\alpha\to 0$.

It stands to reason that the results for linear strain hardening, as presented in [2], should reduce to those for perfect plasticity, as presented in [1], in the limit $\alpha\to 0$. Since the least amount of strain hardening produces singularities of the type r^s, there appears to be a spatial nonuniformity in the domain of validity of solutions for small α.

In this Note we have attempted to resolve this question by constructing near-tip fields for linear strain hardening with small α. Such fields are of interest on their own accord, but they can also be used to investigate the limit of vanishing α. Our results show the presence of an edge zone (a boundary layer) in which the fields are singular with $s=-\alpha^{1/2}$. The edge zone is defined by $r/r_p=O[\exp(-1/\alpha^{1/2})]$. Outside of the edge zone the solution can be represented by a regular expansion with respect to $\alpha^{1/2}$, the first term being the solution for the elastic perfectly plastic case. In the limit $\alpha\to 0$ the edge zone shrinks on the crack tip, thus eliminating the domain of validity of terms of order r^s. The near-tip fields then reduce to those outside the edge zone, which are the ones for the elastic perfectly plastic material.

2 Governing Equations

Let (x,y,z) define a coordinate system which moves with the crack tip at a constant velocity v, such that the z-axis coincides with the crack edge. Following the notation of reference [2], the stresses and strains for antiplane shear are denoted by $\tau_\beta=\sigma_{z\beta}$ and $\gamma_\beta=2\epsilon_{z\beta}$, where $\beta=x,y$. In the loading region, and relative to the moving coordinate system, the stress-strain relations according to J_2-flow theory with linear strain hardening are [2]:

$$\mu_t\dot{\gamma}_\beta=\alpha\dot{\tau}_\beta+(1-\alpha)\tau^{-1}\tau_\beta\dot{\tau} \tag{2}$$

where α is defined by equation (1), and

$$\tau=(\tau_x^2+\tau_y^2)^{1/2}, \text{ and } \dot{\tau}>0 \tag{3a,b}$$

In (2), $\dot{(\ )}$ denotes material differentiation with respect to any monotonically increasing quantity. In the present paper we set

$$\dot{(\ )}=-v\frac{\partial}{\partial x}=-v\partial_x, \tag{4}$$

consistent with a steady-state situation relative to the moving crack tip. Equations (2)–(4) are supplemented by equations defining equilibrium and strain compatibility:

$$\partial_\beta\tau_\beta=0 \text{ and } \partial_x\gamma_y-\partial_y\gamma_x=0 \tag{5a,b}$$

Let us introduce new variables $\hat{\gamma}_\beta$ and $\hat{\tau}_\beta$ by

$$(\gamma_\beta,\tau_\beta)=(\hat{\gamma}_\beta,\hat{\tau}_\beta)\exp[-\alpha\mu\lambda(x,y)] \tag{6a,b}$$

where

$$\hat{\tau}_x^2+\hat{\tau}_y^2=k^2 \tag{7}$$

Here the constant k defines the yield stress in shear. In terms of the new variables $\hat{\gamma}_\beta,\hat{\tau}_\beta$, and λ the constitutive equations (2) become

$$\partial_x\hat{\gamma}_\beta-\alpha\mu\hat{\gamma}_\beta\partial_x\lambda=\frac{1}{\mu}\partial_x\hat{\tau}_\beta-\hat{\tau}_\beta\partial_x\lambda \tag{8}$$

In the limit $\alpha\to 0$, equation (8) turns into the constitutive equation for an elastic perfectly plastic material.

In the loading region the term $\partial_x\lambda$ should be positive. Indeed, since $\dot{\tau}>0$, we obtain from (3*a*), (4), and (6*b*):

$$\dot{\tau}=-v\partial_x\tau=-v\partial_x[(\hat{\tau}_x^2+\hat{\tau}_y^2)^{1/2}\exp(-\alpha\mu\lambda)]$$
$$=vk\alpha\mu\exp(-\alpha\mu\lambda)\partial_x\lambda>0 \tag{9}$$

which implies $\partial_x\lambda>0$.

Equation (7) suggests the introduction of the "stress function" $\hat{\omega}$ by the relations

$$\hat{\tau}_x=-k\sin\hat{\omega}, \quad \hat{\tau}_y=k\cos\hat{\omega} \tag{10a,b}$$

It is now convenient to introduce polar coordinates (r,θ).

[1] Department of Civil Engineering, The Technological Institute, Northwestern University, Evanston, Ill. 60201. J. D. Achenbach is a Fellow, ASME.

Manuscript received by ASME Applied Mechanics Division, November, 1981; final revision, January, 1982.

Manuscript received by ASME Applied Mechanics Division, November, 1981; final revision, January, 1982.

After some manipulation the governing equations (5*a*,*b*) and (8) are obtained in the form:

$$\cos(\hat{\omega}-\theta)\partial_r\hat{\omega}+\frac{1}{r}\sin(\hat{\omega}-\theta)\partial_\theta\hat{\omega}$$

$$=\alpha\mu[\sin(\hat{\omega}-\theta)\partial_r\lambda-\frac{1}{r}\cos(\hat{\omega}-\theta)\partial_\theta\lambda] \tag{11}$$

$$\cos(\hat{\omega}-\theta)\partial_r\gamma_x+\frac{1}{r}\sin(\hat{\omega}-\theta)\partial_\theta\hat{\gamma}_x$$

$$+\frac{k}{\mu}(\cos\theta\partial_r\hat{\omega}-\frac{1}{r}\sin\theta\partial_\theta\hat{\omega})=$$

$$=\alpha\mu\hat{\gamma}_x[\cos(\hat{\omega}-\theta)\partial_r\lambda+\frac{1}{r}\sin(\hat{\omega}-\theta)\partial_\theta\lambda] \tag{12}$$

$$-\sin(\hat{\omega}-\theta)\partial_r\hat{\gamma}_x+\frac{1}{r}\cos(\hat{\omega}-\theta)\partial_\theta\hat{\gamma}_x$$

$$+k(\cos\theta\partial_r\lambda-\frac{1}{r}\sin\theta\partial_\theta\lambda)=$$

$$=-\alpha\mu\hat{\gamma}_x[\sin(\hat{\omega}-\theta)\partial_r\lambda-\frac{1}{r}\cos(\hat{\omega}-\theta)\partial_\theta\lambda] \tag{13}$$

3 The Solution in the Loading Zone

As point of departure we assume that for small α, $\hat{\omega}$ does not depend on r, and that the function λ is independent of θ. In the sequel it will be shown that the solutions obtained on the basis of these assumptions have the proper behavior in the limit $\alpha\to 0$. With these assumptions (11) yields $\hat{\omega}=\theta$, and (12) and (13) reduce to:

$$\partial_\rho\hat{\gamma}_x+\frac{k}{\mu}\sin\theta=\alpha\mu\hat{\gamma}_x\partial_\rho\lambda \tag{14}$$

$$\partial_\theta\hat{\gamma}_x-k\cos\theta\,\partial_\rho\lambda=0 \tag{15}$$

where we have introduced

$$\rho=-ln(r/r_p) \tag{16}$$

Here r_p is the length of the plastic zone in the plane of the crack. Integration of (15) with respect to θ yields

$$\hat{\gamma}_x=k\sin\theta\,\partial_\rho\lambda, \tag{17}$$

where we have used that $\hat{\gamma}_x\equiv 0$ for $\theta=0$. Substitution of (17) into equation (15) results in

$$\frac{d^2\lambda}{d\rho^2}-\alpha\mu\left(\frac{d\lambda}{d\rho}\right)^2+\frac{1}{\mu}=0 \tag{18}$$

The appropriate solution to this equation is

$$\lambda=-\frac{1}{\alpha\mu}ln[\cosh(\alpha^{1/2}\rho+B)]+A, \tag{19}$$

where A and B are arbitrary constants. Substitution of (19) in (17) and (6*a*) gives γ_x as

$$\gamma_x=-\frac{k}{\mu}\alpha^{-1/2}e^{-\alpha\mu A}\sinh(\alpha^{1/2}\rho+B)\sin\theta \tag{20}$$

Just outside the zone of plastic deformation, the elastic strain is $\gamma_x=-(k/\mu)\sin\theta$. If it is assumed that the plastic strain is zero at $x=r_p$, continuity of γ_x at $x=r_p$ and θ small yields

$$\sinh B=\alpha^{1/2}e^{\alpha\mu A} \tag{21}$$

Clearly $\sinh B=O(\alpha^{1/2})$ and $\cosh B=O(1)$ as $\alpha\to 0$. For fixed ρ we then find in the limit $\alpha\to 0$

$$\sinh(\alpha^{1/2}\rho+B)\sim\alpha^{1/2}(\rho+1) \tag{22}$$

Substitution of (22) into (20) yields for small α

$$\gamma_x=\left[-\frac{k}{\mu}+ln(r/r_p)\right]\sin\theta+O(\alpha^{1/2}) \tag{23}$$

which tends to the solution for the elastic perfectly plastic case when $\alpha\to 0$. Equation (22) is, however, not valid when $\rho=0(\alpha^{1/2})$, i.e., when $r/r_p=0[\exp(-1/\alpha^{1/2})]$. Then $\sinh(\alpha^{1/2}\rho+B)\sim\sinh(\alpha^{1/2}\rho)$, and (20) yields as $\alpha\to 0$

$$\gamma_x\sim-\frac{k}{2\mu}\alpha^{-1/2}(r/r_p)^{-\alpha^{1/2}}\sin\theta \tag{24}$$

Equations (23) and (24) reveal the existence of an edge zone near the crack tip, defined by $r/r_p\sim 0[\exp(-1/\alpha^{1/2})]$. This zone vanishes in the limit $\alpha\to 0$. Inside the edge zone (24) is valid, while outside the edge zone (23) holds. It is now evident that a regular expansion with respect to $\alpha^{1/2}$, as alluded to in reference [2], cannot give a uniform transition from linear strain hardening to perfect plasticity.

It is noted that neither (23) nor (24) contains the external load via a stress intensity factor. The external load is, however, implicit in these expressions through r_p.

By virtue of the compatibility condition (5*b*), we have for $\theta\to 0$

$$\frac{d\gamma_y}{d\rho}=\frac{k}{\mu}\alpha^{-1/2}e^{-\alpha\mu A}\sinh(\alpha^{1/2}\rho+B) \tag{25}$$

Upon integration we find

$$\gamma_y=\frac{k}{\mu}\alpha^{-1}e^{-\alpha\mu A}\cosh(\alpha^{1/2}\rho+B)+C \tag{26}$$

Continuity of γ_y at $x=r_p$ gives

$$C=\frac{k}{\mu}(1-\alpha^{-1}e^{-\alpha\mu A}\cosh B) \tag{27}$$

Outside the edge zone, i.e., $\rho=o(\alpha^{-1/2})$, we can use the expansion

$$\cosh(\alpha^{1/2}\rho+B)=\cosh\beta+\alpha^{1/2}\rho\,\sinh B+\frac{1}{2}\alpha\rho^2\cosh B \tag{28}$$

By the use of (21) we then find from (26) and (27) in the limit $\alpha\to 0$

$$\gamma_y=\frac{k}{\mu}\left\{1-ln(r/r_p)+\frac{1}{2}[ln(r/r_p)]^2\right\}+0(\alpha^{1/2}) \tag{29}$$

which is just the solution for the elastic perfectly plastic case. Within the edge zone (26) and (27) yield

$$\gamma_y\sim\frac{k}{\mu}\alpha^{-1}\left[\frac{1}{2}(r/r_p)^{-\alpha^{1/2}}-1\right]+O(1) \tag{30}$$

The stresses corresponding to (30) follow from (6*a*) and (10*a*,*b*) as

$$\tau_x=-\frac{1}{2}ke^{-\alpha\mu A}[(r/r_p)^{\alpha^{1/2}}+(r/r_p)^{-\alpha^{1/2}}]\sin\theta$$

$$\tau_y=\frac{1}{2}ke^{-\alpha\mu A}[(r/r_p)^{\alpha^{1/2}}+(r/r_p)^{-\alpha^{1/2}}]\cos\theta$$

Acknowledgment

This work was carried out in the course of research sponsored by the U.S. Office of Naval Research under Contract No. N00014-76-C-0063.

References

1 Chitaley, A. D., and McClintock, F. A., "Elastic-Plastic Mechanics of Steady Crack Growth under Anti-Plane Shear," *Journal of the Mechanics and Physics of Solids*, Vol. 19, 1971, pp. 1–12.

2 Amazigo, J. C., and Hutchinson, J. W., "Crack Tip Fields in Steady Crack Growth with Linear Strain Hardening," *Journal of the Mechanics and Physics of Solids*, Vol. 25, 1977, pp. 81–97.

Approximate Stability Criteria for Some Second-Order Linear Differential Equations With Stationary-Gaussian Random Coefficients[1]

G. Ahmadi[2] and P. G. Glockner[3]

Approximate sufficiency conditions for almost sure stability of the equilibrium state of some second-order linear systems with stationary-Gaussian random coefficients are obtained in analytical form.

Introduction

Stability of stochastic differential equations was investigated by Samuels and Eringen [1], Bertram and Sarachik [2], and Kozin [3]. Caughy and Gray [4], Infante [5], Kozin and Wu [6], and Kozin and Prodromou [7] have developed improved regions for stability of linear differential equations with stationary random coefficients of different kinds. Stability of nonstationary stochastic differential equations was studied by Ahmadi [8, 9] and Ahmadi and Mostaghad [10, 11].

In the present work, stability of some second-order differential equations subjected to Gaussian random coefficients is considered. Approximate analytical expressions for the sufficiency conditions for almost sure stability of the equilibrium state are derived. It is shown that for a small damping coefficient, the present approximate results become quite accurate.

Analysis

The second-order differential equations

$$\ddot{x}+2\zeta\dot{x}+[c+f(t)]x=0, \tag{1}$$

$$\ddot{x}+[2\zeta+f(t)]\dot{x}+cx=0, \tag{2}$$

with ζ and c being constants and $f(t)$ being a zero-mean stationary ergodic process with finite second moments encountered in many engineering problems. The criteria for almost sure stability of the equilibrium state of equations (1) and (2), as obtained by Infante [5], are

$$\sigma^2<4\zeta^2, \tag{3}$$

$$\sigma^2<\frac{4\zeta^2}{1+\zeta^2}, \tag{4}$$

respectively, where the parameter c is taken to be equal to 1. In equations (3) and (4), σ^2 is the variance of $f(t)$. Kozin and Wu [6] obtained the following stability criterion

$$E\{\,|l-f(t)|\,\}<2\zeta(l+c-\zeta)^{1/2}, \tag{5}$$

for equation (1), where l is an arbitrary positive constant. Similarly, for the stability of equation (2), they found [6],

$$E\{\,|l-f(t)|\,\}<2\zeta(1-\alpha^2/c), \tag{6}$$

where

$$\alpha=\zeta+l/2. \tag{7}$$

In equations (5) and (6) $E\{\ \}$ stands for the expected value.

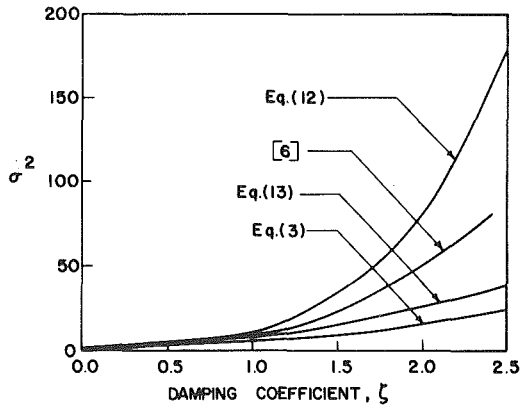

Fig. 1 Comparison of the stability prediction of equations (12) and (13) with the results of references [5, 6]

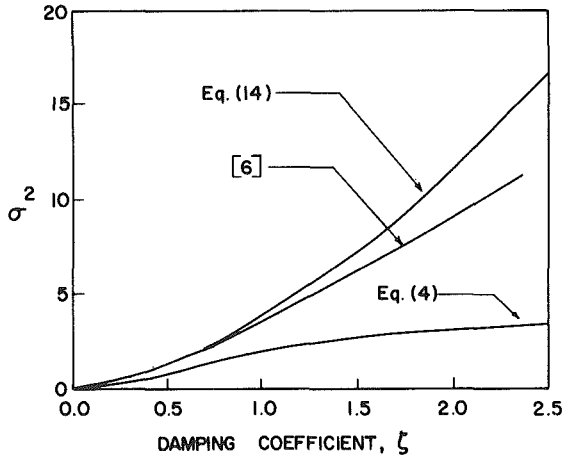

Fig. 2 Comparison of the stability limit according to equation (13) with the results of references [5, 6]

Stability criteria (5) and (6) are further developed in [6] and when $f(t)$ is Gaussian, and $c = 1$, the boundaries of the sufficiency stability criterion are obtained by a numerical optimization technique. These results, together with Infante's criteria (equations (3) and (4)) are reproduced in Figs. 1 and 2. When $f(t)$ is Gaussian, it can be shown

$$E\{\,|l-f(t)|\,\}=\sigma\sqrt{2/\pi}\,e^{-l^2/2\sigma^2}+2l\,\mathrm{erf}\,(l/\sigma), \tag{8}$$

where erf is the error function as defined in [12]. For small values of l/σ, using a Taylor series expansion, up to the second order in l, equation (8) becomes

$$E\{\,|l-f(t)|\,\}\simeq\sqrt{2/\pi}\left(\sigma+\frac{l^2}{2\sigma}\right). \tag{9}$$

Employing equation (9) in equation (5) and solving for σ one finds

$$\sigma^2<2\pi\zeta^2(l+c-\zeta^2)-l^2. \tag{10}$$

The optimum choice for l is

$$l=\pi\zeta^2, \tag{11}$$

and the approximate stability criterion for equation (1) becomes

$$\sigma^2<(\pi^2-2\pi)\zeta^4+2\pi c\zeta^2. \tag{12}$$

For small values of ζ, neglecting the fourth power of ζ, one obtains

$$\sigma^2<2\pi c\zeta^2. \tag{13}$$

Similarly, use of the approximate equation (9) in equation (6), after optimization, yields

[1] The results presented here were obtained in the course of research sponsored by the Natural Sciences and Engineering Research Council of Canada, Grants No. A-2736 and G-0106.

[2] Professor, Department of Mechanical and Industrial Engineering, Clarkson College of Technology, Potsdam, N.Y. 13676.

[3] Professor and Chairman, Department of Mechanical Engineering, the University of Calgary, Calgary, Alberta, Canada.

Manuscript received by ASME Applied Mechanics Division, August, 1981.

$$\sigma^2 < (2\pi - 4)\zeta^2 + \frac{4\zeta^2}{1 + \left(\frac{\pi}{2}\right)\left(\frac{\zeta^2}{c}\right)}, \tag{14}$$

which is the approximate expression for almost sure stability of the equilibrium state of equation (2). The corresponding optimum choice for l is given by

$$l = \frac{\pi\zeta^3/c}{1 + \left(\frac{\pi}{2}\right)\left(\frac{\zeta^2}{c}\right)}. \tag{15}$$

The predictions of equations (12), (13), and (14) for $c = 1$ are also shown in Figs. 1 and 2. It is observed that the approximate equations (12), (13), and (14) give remarkably accurate results for damping coefficients below 0.6. However, for $\epsilon > 1$ the error becomes rather large and equation (13) underestimates the critical variance whereas equations (12) and (14) overestimate the critical variances of the stability limit. This is, of course, expected since the values of l as given by equations (11) and (15) are no longer small for relatively large magnitudes of the damping coefficient.

Equations (12), (13), and (14) provide approximate sufficiency criteria for the almost sure stability of the equilibrium states of equations (1) and (2) for arbitrary values of the parameter c. These analytical results are quite easy to use for a first-order estimation of the stability limit.

Acknowledgments

The financial assistance provided by the Natural Sciences and Engineering Research Council of Canada in the form of an operating grant, Grant No. A-2736 and a strategic grant, Grant No. G-0106 is gratefully acknowledged.

References

1 Samuels, J. S., and Eringen, A. C., "On the Stochastic Stability of Linear Systems," *Journal of Mathematics and Physics,* Vol. 38, 1959, pp. 83–103.

2 Bertram, J. E., and Sarachik, P. E., "Stability of Circuit With Randomly Time Varying Parameters," *Trans. IRE, PGIT-5*, Special Supplement, 1959, pp. 260–270.

3 Kozin, F., "On Almost Sure Stability of Linear Systems With Random Coefficients," *Journal of Mathematics and Physics,* Vol. 42, 1963, pp. 59–67.

4 Caughy, T. K., and Gray, A. H. Jr., "On the Almost Sure Stability of Linear Dynamic Systems With Stochastic Coefficients," ASME JOURNAL OF APPLIED MECHANICS, Vol. 32, 1965, pp. 365–372.

5 Infante, E. F., "On Stability of Some Linear Nonautonomous Random Systems," ASME JOURNAL OF APPLIED MECHANICS, Vol. 35, 1968, pp. 7–12.

6 Kozin, F., and Wu, C. M., "On the Stability of Linear Stochastic Differential Equations," ASME JOURNAL OF APPLIED MECHANICS, Vol. 40, 1973, pp. 87–92.

7 Kozin, F., and Prodromou, S., "Necessary and Sufficient Conditions for Almost Sure Sample Stability of Linear Ito Equations," *SIAM Journal of Applied Mathematics*, Vol. 21, 1971, pp. 413–424.

8 Ahmadi, G., "On Stability of Nonstationary Stochastic Differential Equations," *Iranian Journal of Science and Technology*, Vol. 6, 1977, pp. 75–80.

9 Ahmadi, G., "On the Mean Square Stability of a Class of Nonstationary Coupled Partial Differential Equations," *Ingenieur-Archiv,* Vol. 48, 1979, pp. 213–219.

10 Ahmadi, G., and Mostaghel, N., "On the Stability of Nonstationary Nonlinear Random Systems," *International Journal of System Science,* Vol. 7, 1976, pp. 67–77.

11 Ahmadi, G., and Mostaghel, N., "On the Stability of Columns Subjected to Nonstationary Random or Deterministic Support Motion," *Earthquake Engineering and Structural Dynamics,"* Vol. 6, 1978, pp. 321–326.

12 Papoulis, A., *Probability, Random Variables and Stochastic Processes,* McGraw-Hill, New York, 1965.

Edge Effect in the Bending of Inextensible Plates

E. N. Kuznetsov[1]

In the uniaxial bending of an elastic plate, a boundary layer develops along each free edge in the form of a small ripple in the deformed midsurface. The layer provides a smooth transition from the zero transverse bending moment at the edge to the required value in the plate interior. For an inextensible plate, the formation of this type of a boundary layer is impossible. An alternative mechanism for providng this transition is identified and investigated.

Introduction

In a flexible plate with free edges that undergoes large deformation, boundary layers develop along the edges [1–3]. If the plate is deformed sufficiently, it behaves as a nearly inextensible one and approximates a developable surface except for the boundary layers where some additional localized deflections occur. This phenomenon can be easily traced using the example of a rectangular strip under uniaxial bending by a moment M. The strip would acquire a cylindrical form only if a transverse bending moment μM was to act along the curved edges (μ is Poisson ratio). However, even in the absence of the transverse moment, the deviation from the cylindrical shape is small and confined to a narrow longitudinal strip adjacent to each of the free edges. This boundary layer provides a smooth transition from the constant transverse bending moment in the interior of the plate to its zero boundary value at the free edges. The intrinsic mechanism of the boundary layer action (revealed in the preceding references) consists in the development of membrane stresses resisting the tendency toward transverse bending. As shown in [1–2], the maximum deviation of the deformed midsurface from the cylinder equals a certain fraction of the plate thickness depending only on the Poisson ratio (for $\mu = 0.32$ it is about 10 percent of the thickness).

However small, this deviation and the formation of an edge ripple is only possible for extensible plates. Note that homogeneous plates, regardless of their thickness, are always extensible so that when a thinner plate is said to more closely approximate an inextensible plate, this only means that the boundary layer width reduces. However, the ratio of the edge ripple amplitude to the plate thickness preserves and, more importantly, so does the aforementioned mechanism of the boundary layer action (membrane stresses in the ripple fibers *outside* of the developable surface).

For a truly inextensible plate, the *entire* deformed surface including its edges must be developable. Consider, for example, the uniaxial bending of a plate involving a very thin layer of material much stiffer than the rest of the plate. Although this layer, being made of a real material will still develop an edge ripple, its amplitude will measure no more than only about one-tenth of the *layer* thickness. This is inconsequential for the deformation of the plate as a whole and, in particular, with regard to the boundary conditions at its free edges. Thus, for all practical purposes, such a plate is inextensible, which precludes the formation of a boundary layer of the foregoing type. Obviously, in this case any attempt to evoke the previously described boundary layer mechanism (e.g., by introducing different Young's moduli of

[1]Professor, Department of General Engineering, University of Illinois, Urbana, Ill. 61801

Manuscript received by ASME Applied Mechanics Division, June, 1981; final revision, January, 1982.

$$\sigma^2 < (2\pi - 4)\zeta^2 + \frac{4\zeta^2}{1 + \left(\frac{\pi}{2}\right)\left(\frac{\zeta^2}{c}\right)}, \tag{14}$$

which is the approximate expression for almost sure stability of the equilibrium state of equation (2). The corresponding optimum choice for l is given by

$$l = \frac{\pi\zeta^3/c}{1 + \left(\frac{\pi}{2}\right)\left(\frac{\zeta^2}{c}\right)}. \tag{15}$$

The predictions of equations (12), (13), and (14) for $c = 1$ are also shown in Figs. 1 and 2. It is observed that the approximate equations (12), (13), and (14) give remarkably accurate results for damping coefficients below 0.6. However, for $\epsilon > 1$ the error becomes rather large and equation (13) underestimates the critical variance whereas equations (12) and (14) overestimate the critical variances of the stability limit. This is, of course, expected since the values of l as given by equations (11) and (15) are no longer small for relatively large magnitudes of the damping coefficient.

Equations (12), (13), and (14) provide approximate sufficiency criteria for the almost sure stability of the equilibrium states of equations (1) and (2) for arbitrary values of the parameter c. These analytical results are quite easy to use for a first-order estimation of the stability limit.

Acknowledgments

The financial assistance provided by the Natural Sciences and Engineering Research Council of Canada in the form of an operating grant, Grant No. A-2736 and a strategic grant, Grant No. G-0106 is gratefully acknowledged.

References

1 Samuels, J. S., and Eringen, A. C., "On the Stochastic Stability of Linear Systems," *Journal of Mathematics and Physics,* Vol. 38, 1959, pp. 83–103.

2 Bertram, J. E., and Sarachik, P. E., "Stability of Circuit With Randomly Time Varying Parameters," *Trans. IRE, PGIT-5*, Special Supplement, 1959, pp. 260–270.

3 Kozin, F., "On Almost Sure Stability of Linear Systems With Random Coefficients," *Journal of Mathematics and Physics,* Vol. 42, 1963, pp. 59–67.

4 Caughy, T. K., and Gray, A. H. Jr., "On the Almost Sure Stability of Linear Dynamic Systems With Stochastic Coefficients," ASME JOURNAL OF APPLIED MECHANICS, Vol. 32, 1965, pp. 365–372.

5 Infante, E. F., "On Stability of Some Linear Nonautonomous Random Systems," ASME JOURNAL OF APPLIED MECHANICS, Vol. 35, 1968, pp. 7–12.

6 Kozin, F., and Wu, C. M., "On the Stability of Linear Stochastic Differential Equations," ASME JOURNAL OF APPLIED MECHANICS, Vol. 40, 1973, pp. 87–92.

7 Kozin, F., and Prodromou, S., "Necessary and Sufficient Conditions for Almost Sure Sample Stability of Linear Ito Equations," *SIAM Journal of Applied Mathematics*, Vol. 21, 1971, pp. 413–424.

8 Ahmadi, G., "On Stability of Nonstationary Stochastic Differential Equations," *Iranian Journal of Science and Technology*, Vol. 6, 1977, pp. 75–80.

9 Ahmadi, G., "On the Mean Square Stability of a Class of Nonstationary Coupled Partial Differential Equations," *Ingenieur-Archiv,* Vol. 48, 1979, pp. 213–219.

10 Ahmadi, G., and Mostaghel, N., "On the Stability of Nonstationary Nonlinear Random Systems," *International Journal of System Science,* Vol. 7, 1976, pp. 67–77.

11 Ahmadi, G., and Mostaghel, N., "On the Stability of Columns Subjected to Nonstationary Random or Deterministic Support Motion," *Earthquake Engineering and Structural Dynamics,"* Vol. 6, 1978, pp. 321–326.

12 Papoulis, A., *Probability, Random Variables and Stochastic Processes,* McGraw-Hill, New York, 1965.

Edge Effect in the Bending of Inextensible Plates

E. N. Kuznetsov[1]

In the uniaxial bending of an elastic plate, a boundary layer develops along each free edge in the form of a small ripple in the deformed midsurface. The layer provides a smooth transition from the zero transverse bending moment at the edge to the required value in the plate interior. For an inextensible plate, the formation of this type of a boundary layer is impossible. An alternative mechanism for providng this transition is identified and investigated.

Introduction

In a flexible plate with free edges that undergoes large deformation, boundary layers develop along the edges [1–3]. If the plate is deformed sufficiently, it behaves as a nearly inextensible one and approximates a developable surface except for the boundary layers where some additional localized deflections occur. This phenomenon can be easily traced using the example of a rectangular strip under uniaxial bending by a moment M. The strip would acquire a cylindrical form only if a transverse bending moment μM was to act along the curved edges (μ is Poisson ratio). However, even in the absence of the transverse moment, the deviation from the cylindrical shape is small and confined to a narrow longitudinal strip adjacent to each of the free edges. This boundary layer provides a smooth transition from the constant transverse bending moment in the interior of the plate to its zero boundary value at the free edges. The intrinsic mechanism of the boundary layer action (revealed in the preceding references) consists in the development of membrane stresses resisting the tendency toward transverse bending. As shown in [1–2], the maximum deviation of the deformed midsurface from the cylinder equals a certain fraction of the plate thickness depending only on the Poisson ratio (for $\mu = 0.32$ it is about 10 percent of the thickness).

However small, this deviation and the formation of an edge ripple is only possible for extensible plates. Note that homogeneous plates, regardless of their thickness, are always extensible so that when a thinner plate is said to more closely approximate an inextensible plate, this only means that the boundary layer width reduces. However, the ratio of the edge ripple amplitude to the plate thickness preserves and, more importantly, so does the aforementioned mechanism of the boundary layer action (membrane stresses in the ripple fibers *outside* of the developable surface).

For a truly inextensible plate, the *entire* deformed surface including its edges must be developable. Consider, for example, the uniaxial bending of a plate involving a very thin layer of material much stiffer than the rest of the plate. Although this layer, being made of a real material will still develop an edge ripple, its amplitude will measure no more than only about one-tenth of the *layer* thickness. This is inconsequential for the deformation of the plate as a whole and, in particular, with regard to the boundary conditions at its free edges. Thus, for all practical purposes, such a plate is inextensible, which precludes the formation of a boundary layer of the foregoing type. Obviously, in this case any attempt to evoke the previously described boundary layer mechanism (e.g., by introducing different Young's moduli of

[1]Professor, Department of General Engineering, University of Illinois, Urbana, Ill. 61801

Manuscript received by ASME Applied Mechanics Division, June, 1981; final revision, January, 1982.

bending and stretching and subsequently setting their ratio to zero) is doomed to failure.

The objective of this study is to identify and investigate an alternative mechanism that provides a smooth transition of the transverse bending moment in inextensible plates.

Analysis

This goal can be achieved within the framework of a generalized theory of plates taking into account shear deformations. The governing system of equations of this theory [4] as applied to the problem in question (a rectangular plate bent in the x-direction) reads:

$$W = W^f - \beta^2 \nabla^2 W^f, \quad \beta^2 = \frac{t^2}{6(1-\mu)} \tag{1}$$

$$D \nabla^4 W^f = N W_{xx}, \quad D = \frac{\mathrm{E}t^3}{12(1-\mu^2)} \tag{2}$$

where W is the plate deflection, W^f is the deflection component due to flexure alone (disregarding the shear as is the case for the conventional plate theory), t is the plate thickness, N is the membrane force in the x-direction (other membrane forces as well as transverse loads are absent), E and μ are Young's modulus and Poisson's ratio, respectively, and subscripts x and y denote the corresponding partial derivatives.

To reveal the essence of the phenomenon in question in a simple way, assume that the foregoing plate has a very thin and stiff midsurface layer with a modulus of elasticity $\mathrm{E}^* >> \mathrm{E}$, but a thickness $t^* << t$ so that the overall flexural rigidity and, hence, the preceding governing equations are not affected. Under the action of a longitudinal bending moment $M_1 = M$ the plate bends into a cylinder of a radius R with some small deviation, $w = w(y)$, in the vicinity of the free edges. It is this deviation that produces a membrane force, N, of the magnitude

$$N = -(\mathrm{E}^* t^* + \mathrm{E}t)\frac{w}{R} = -k\mathrm{E}t\frac{w}{R} \tag{3}$$

where

$$k = 1 + \frac{\mathrm{E}^* t^*}{\mathrm{E}t}. \tag{4}$$

Following the version of the perturbation method employed in [2], the additional plate deflections are referred to the cylindrical surface corresponding to the middle region between the two boundary layers:

$$W^f = W_0^f + w^f \tag{5}$$

$$W = W_0 + w. \tag{6}$$

Since

$$W^f_{0xx} = \frac{1}{R} \tag{7}$$

it follows from equation (1) that

$$W_0 = W_0^f - \frac{\beta^2}{R} \tag{8}$$

Substituting expressions (5) and (6) into equations (1) and (2) and taking into account relations (3) and (8) yields

$$w = w^f - \beta^2 w^f_{yy} \tag{9}$$

$$D w^f_{yyyy} = -\frac{k\mathrm{E}t}{R^2} w \tag{10}$$

This system reduces to one equation in the unknown w^f:

$$w^f_{yyyy} - 4\alpha^4\beta^2 w^f_{yy} + 4\alpha^4 w^f = 0 \tag{11}$$

where

$$4\alpha^4 = \frac{12k(1-\mu^2)}{t^2 R^2} \tag{12}$$

The roots of the biquadratic characteristic equation are

$$\lambda_{1-4} = \pm\sqrt{2\alpha^2(\alpha^2\beta^2 \pm \sqrt{\alpha^4\beta^4 - 1})} \tag{13}$$

The subsequent analysis depends on the magnitude of the dimensionless parameter

$$\gamma^2 = 2\alpha^2\beta^2 = \frac{\sqrt{3k(1-\mu^2)}}{tR}\frac{t^2}{2(1-\mu)} = \sqrt{\frac{k(1+\mu)}{3(1-\mu)}}\frac{t}{R} \tag{14}$$

For a homogeneous plate ($k = 1$) this parameter is much smaller than unity (unless the radius of curvature becomes comparable to the plate thickness). If, indeed, γ^2 can be disregarded as compared to 1, the roots of the characteristic equation become

$$\lambda_{1-4} = \pm\sqrt{\pm 2i\alpha^2} \tag{15}$$

and the Fung and Wittrick [2] edge effect is obtained.

Being interested in the opposite extreme (approaching a truly inextensible plate) we assume the value of k sufficiently large to produce $\gamma^4 = 4\alpha^4\beta^4 >> 1$.

Then

$$\lambda_{1-4} = \pm\sqrt{2\alpha^2[\alpha^2\beta^2 \pm \alpha^2\beta^2\left(1 - \frac{1}{2\alpha^4\beta^4}\right)]} \tag{16}$$

$$\lambda_{1,2} = \pm\frac{\gamma^2}{\beta}, \quad \lambda_{3,4} = \pm\frac{1}{\beta} \tag{17}$$

and the general solution acquires the form

$$w^f = Ae^{-\gamma^2 y/\beta} + A_1 e^{-\gamma^2 y\beta} + Be^{-y/\beta} + B_1 e^{y/\beta} \tag{18}$$

To eliminate the growing exponentials (the solution must be finite and decaying toward the plate interior), the constants A_1 and B_1 must be set to zero, while the remaining constants are determined so as to provide the absence of the transverse bending moment and shear on the free edge ($y = 0$):

$$W^f_{yy} + \mu W^f_{xx} = 0 \tag{19}$$

$$W^f_{yyy} + (2-\mu)W^f_{xxy} = 0 \tag{20}$$

Upon the evaluation of A and B using expressions (5) and (7) the preceding solution becomes

$$w^f = \frac{\beta^2\gamma^2}{\gamma^2 - 1}\left(\frac{1}{\gamma^6}e^{\gamma^2 y/\beta} - e^{-y/\beta}\right)\frac{\mu}{R} \tag{21}$$

Results and Discussion

The transverse bending moment, M_2, and the total additional deflection (9) are determined as follows:

$$M_2 = D(W^f_{yy} + \mu W^f_{xx}) = \mu M\left[1 + \frac{\gamma^2}{\gamma^2 - 1}\left(\frac{1}{\gamma^2}e^{-\gamma^2 y/\beta} - e^{-y/\beta}\right)\right] \tag{22}$$

$$w = w^f - \beta^2 w^f_{yy} = -\frac{\mu}{R}\frac{\beta^2(\gamma^2+1)}{\gamma^4}e^{-\gamma^2 y/\beta} \tag{23}$$

In the limiting case of a truly inextensible plate both the parameters α and γ approach infinity and

$$w^f \to -\beta^2 e^{-y/\beta}\frac{\mu}{R} \tag{21'}$$

$$M_2 \to \mu M(1 - e^{-y/\beta}) \tag{22'}$$

$$w \to 0. \tag{23'}$$

As can be readily seen, in this limiting case the deformed surface remains perfectly cylindrical, while the transverse bending moment rapidly increases from $M_2 = 0$ on the edge to $M_2 = \mu M$ in the plate interior. For $\mu = 0.32$, moment M_2 reaches 0.99 of its maximum value at the distance $y = 2.28t$ from the edge. Comparing this to the known limitations of the theory (plate with shear) shows that the accuracy of the proposed solution should be quite reasonable.

Note that the described edge effect is *linear*, with all the components of displacements and internal forces being proportional to the external load from the very onset of loading. In this regard it is different in principle from the boundary layer investigated in [1-3] which is nonlinear and does not allow a continuous transition from the conventional linear plate theory [5].

The developed solution is rather general in that it covers the entire range of possible values of the parameter γ (14) for which expressions (15) and (16) represents the two extreme cases. It applies directly (or can be readily modified to apply) to the analysis of laminated plates of various structural composition.

Acknowledgment

The author wishes to thank Professor W. Brent Hall from the same department for many constructive discussions and suggestions on this paper.

References

1 Ashwell, D. G., "The Anticlastic Curvature of Rectangular Beams and Plates," *Journal of the Royal Aeronautical Society*, Vol. 54, 1950, p. 708.

2 Fung, Y. C., and Wittrick, W. H., "A Boundary Layer Phenomenon in the Large Deflection of Thin Plates," *Quarterly Journal of Mechanics and Applied Mathematics*, Vol. 8, 1955, pp. 191-210.

3 Ashwell, D. G., "The Boundary Layer in the Bending of Inextensible Plates and Shells," *Quarterly Journal of Mechanics and Applied Mathematics*, Vol. 16, 1963, pp. 179-191.

4 Donnell, L. H., *Beams, Plates and Shells*, McGraw-Hill Book Company, 1976.

5 Simmonds, J. G., and Libai, A., "Exact Equations for the Inextensional Deformation of Cantilevered Plates," ASME JOURNAL OF APPLIED MECHANICS, Vol. 46, 1979, pp. 631-636.

On Interactive Computation of Supersonic Boundary Layers With Wall Mass Transfer

J. Brandeis[1]

Nomenclature

a = local speed of sound
M = Mach number
p = pressure
Re = Reynolds number
T = temperature
U_∞ = free-stream velocity
u = streamwise velocity component
v = lateral velocity component
x = distance along the plate
y = distance normal to the plate
δ = boundary-layer thickness
δ^* = boundary-layer displacement thickness
ρ = density

Subscripts

AW = adiabatic wall
e = external
r = reference
w = wall
∞ = conditions far upstream

Introduction

Boundary-layer suction and injection, commonly used methods of controlling viscous layer growth, transition, and heat transfer are particularly applicable to control surface regions on wings and to jet engine inlets and diffusers. The effects of the wall mass transfer on boundary-layer development have long been calculated [1, 2] using the classical boundary-layer equations decoupled from the free stream. Recently, the boundary-layer equations have been used interactively with the potential outer flow [3-5] because the interaction was recognized as a significant factor in the boundary-layer development, especially in the presence of significant rates of mass transfer at the wall. The use of the interactive approach for solution of the flat-plate boundary layer with wall mass transfer may give rise to the following problem [6]. Under certain conditions the interactive solution shows thinning of the layer in reaction to injection at the wall, and thickening in response to suction. This behavior, devoid of physical meaning, is the consequence of an inappropriate initial condition for the interaction problem, which was shown by Garvine [7] to be of boundary-value type due to the ellipticity returned to the problem through interaction. Such solutions have been observed [7, 8] to exhibit branching behavior due to their sensitivity to the upstream condition. The same basic problem with wall mass transfer was also encountered by Smith and Stewartson, [9], and was noted by Werle, [5] who was able to avoid it by using a nonmarching (but iterative) interaction scheme.

The problem due to solution branching exists only when the boundary layer exhibits subcritical behavior (i.e., following Crocco [10] $d\delta^*/dp > 0$). For these cases, a noniterative method is proposed that makes local corrections to the matching, reflecting the changes in the wall boundary conditions due to variation in suction or injection level. The noniterative method is valid for modest rates of wall mass transfer, for which the upstream influence effect is small. The results computed using this method are compared with those computed using the general interactive approach. On this basis, the relative importance of the upstream influence is examined.

For the supercritical boundary layer ($d\delta^*/dp < 0$), the solutions are nonbranching and insensitive to the initial condition, even in the presence of wall mass transfer. Such a nonbranching solution was computed in reference [11], but it was not identified as supercritical. Supercritical boundary layers are usually associated with hypersonic or turbulent supersonic flows.

The qualitative difference in the behavior of the interactive solution for supercritical and subcritical boundary layers leads to an interesting observation concerning the location of possible separation points.

Method of Solution

All results presented here were obtained using the standard compressible boundary-layer momentum, continuity, and energy equations with the outer-edge compatibility relations

[1]NRC Research Associate, NASA Ames Research Center, Moffet Field, Calif. Present address: Lawrence Livermore National Laboratory, Livermore, Calif. 94550.

Manuscript received by ASME Applied Mechanics Division, June, 1981; final revision, February, 1982.

As can be readily seen, in this limiting case the deformed surface remains perfectly cylindrical, while the transverse bending moment rapidly increases from $M_2 = 0$ on the edge to $M_2 = \mu M$ in the plate interior. For $\mu = 0.32$, moment M_2 reaches 0.99 of its maximum value at the distance $y = 2.28t$ from the edge. Comparing this to the known limitations of the theory (plate with shear) shows that the accuracy of the proposed solution should be quite reasonable.

Note that the described edge effect is *linear*, with all the components of displacements and internal forces being proportional to the external load from the very onset of loading. In this regard it is different in principle from the boundary layer investigated in [1-3] which is nonlinear and does not allow a continuous transition from the conventional linear plate theory [5].

The developed solution is rather general in that it covers the entire range of possible values of the parameter γ (14) for which expressions (15) and (16) represents the two extreme cases. It applies directly (or can be readily modified to apply) to the analysis of laminated plates of various structural composition.

Acknowledgment

The author wishes to thank Professor W. Brent Hall from the same department for many constructive discussions and suggestions on this paper.

References

1 Ashwell, D. G., "The Anticlastic Curvature of Rectangular Beams and Plates," *Journal of the Royal Aeronautical Society*, Vol. 54, 1950, p. 708.

2 Fung, Y. C., and Wittrick, W. H., "A Boundary Layer Phenomenon in the Large Deflection of Thin Plates," *Quarterly Journal of Mechanics and Applied Mathematics*, Vol. 8, 1955, pp. 191-210.

3 Ashwell, D. G., "The Boundary Layer in the Bending of Inextensible Plates and Shells," *Quarterly Journal of Mechanics and Applied Mathematics*, Vol. 16, 1963, pp. 179-191.

4 Donnell, L. H., *Beams, Plates and Shells*, McGraw-Hill Book Company, 1976.

5 Simmonds, J. G., and Libai, A., "Exact Equations for the Inextensional Deformation of Cantilevered Plates," ASME JOURNAL OF APPLIED MECHANICS, Vol. 46, 1979, pp. 631-636.

On Interactive Computation of Supersonic Boundary Layers With Wall Mass Transfer

J. Brandeis[1]

Nomenclature

a = local speed of sound
M = Mach number
p = pressure
Re = Reynolds number
T = temperature
U_∞ = free-stream velocity
u = streamwise velocity component
v = lateral velocity component
x = distance along the plate
y = distance normal to the plate
δ = boundary-layer thickness
δ^* = boundary-layer displacement thickness
ρ = density

Subscripts

AW = adiabatic wall
e = external
r = reference
w = wall
∞ = conditions far upstream

[1]NRC Research Associate, NASA Ames Research Center, Moffet Field, Calif. Present address: Lawrence Livermore National Laboratory, Livermore, Calif. 94550.

Manuscript received by ASME Applied Mechanics Division, June, 1981; final revision, February, 1982.

Introduction

Boundary-layer suction and injection, commonly used methods of controlling viscous layer growth, transition, and heat transfer are particularly applicable to control surface regions on wings and to jet engine inlets and diffusers. The effects of the wall mass transfer on boundary-layer development have long been calculated [1, 2] using the classical boundary-layer equations decoupled from the free stream. Recently, the boundary-layer equations have been used interactively with the potential outer flow [3-5] because the interaction was recognized as a significant factor in the boundary-layer development, especially in the presence of significant rates of mass transfer at the wall. The use of the interactive approach for solution of the flat-plate boundary layer with wall mass transfer may give rise to the following problem [6]. Under certain conditions the interactive solution shows thinning of the layer in reaction to injection at the wall, and thickening in response to suction. This behavior, devoid of physical meaning, is the consequence of an inappropriate initial condition for the interaction problem, which was shown by Garvine [7] to be of boundary-value type due to the ellipticity returned to the problem through interaction. Such solutions have been observed [7, 8] to exhibit branching behavior due to their sensitivity to the upstream condition. The same basic problem with wall mass transfer was also encountered by Smith and Stewartson, [9], and was noted by Werle, [5] who was able to avoid it by using a nonmarching (but iterative) interaction scheme.

The problem due to solution branching exists only when the boundary layer exhibits subcritical behavior (i.e., following Crocco [10] $d\delta^*/dp > 0$). For these cases, a noniterative method is proposed that makes local corrections to the matching, reflecting the changes in the wall boundary conditions due to variation in suction or injection level. The noniterative method is valid for modest rates of wall mass transfer, for which the upstream influence effect is small. The results computed using this method are compared with those computed using the general interactive approach. On this basis, the relative importance of the upstream influence is examined.

For the supercritical boundary layer ($d\delta^*/dp < 0$), the solutions are nonbranching and insensitive to the initial condition, even in the presence of wall mass transfer. Such a nonbranching solution was computed in reference [11], but it was not identified as supercritical. Supercritical boundary layers are usually associated with hypersonic or turbulent supersonic flows.

The qualitative difference in the behavior of the interactive solution for supercritical and subcritical boundary layers leads to an interesting observation concerning the location of possible separation points.

Method of Solution

All results presented here were obtained using the standard compressible boundary-layer momentum, continuity, and energy equations with the outer-edge compatibility relations

$$\rho_e u_e \frac{\partial u_e}{\partial x} = -\frac{dp}{dx}$$

$$\rho_e u_e \frac{\partial T_e}{\partial x} = u_e \frac{dp}{dx} \tag{1}$$

and the appropriate conditions on u, v, and T at the surface. To ensure the validity and consistency of results, these equations were solved using two different finite difference codes: the methods of Reyhner et al. [12] and of Murphy [13], the latter using the generalized Galerkin method on the boundary-layer equations rewritten in terms of the Levy-Lees variable. The method of reference [13] incorporates a turbulent flow option. For the outer flow solution, the exact potential equation

$$(u^2 - a^2)\frac{\partial u}{\partial x} + uv\left(\frac{\partial u}{\partial y} + \frac{\partial v}{\partial x}\right) + (v^2 - a^2)\frac{\partial y}{\partial y} = 0$$

$$\frac{\partial u}{\partial y} - \frac{\partial v}{\partial x} = 0 \tag{2}$$

was solved using the method of two-family characteristics.

The two flows were coupled for interactive solution by matching pressure and slope along the matching line. Since only unseparated flows were considered, the displacement thickness was used as the matching line, with some results also recalculated using an outer streamline of the boundary layer for the matching line, initially corresponding to 0.98 U_e.

Solution for the Subcritical Case

To obtain a physical solution to the subcritical interaction problem with wall mass transfer, the initial condition for the pressure interaction must be correctly stated to satisfy the appropriate downstream condition in order to account for the upstream influence. This was done in [9] by making repeated streamwise passes of the solution, each time readjusting the initial condition. Equivalently, Werle [5] used an iterative approach that directly imposes the downstream condition during all stages of calculation. Both these approaches assume knowledge of the downstream condition.

In the present approach, the interactive solution to the problem with any distribution of wall mass transfer is obtained by making local adjustments at the matching line corresponding to the local change in the wall boundary condition, under the assumption that the upstream influence is small (i.e., for small rates of mass transfer). This is accomplished by imposing a local slope correction in the matching surface. This adjustment is proportional to the effect of the change of the wall condition and, in effect, constitutes an adjustment in the compatibility condition. The scheme for making the local slope correction is as follows.

Assume that interactive solution is known up to some station x_i. The first iteration at the next station, x_{i+1}, is obtained by computing the boundary layer for this step with the suction-injection velocity, v_w, and external pressure extrapolated from the preceding station, x_i. The second iteration is computed with the actual v_w for x_{i+1}. Now the

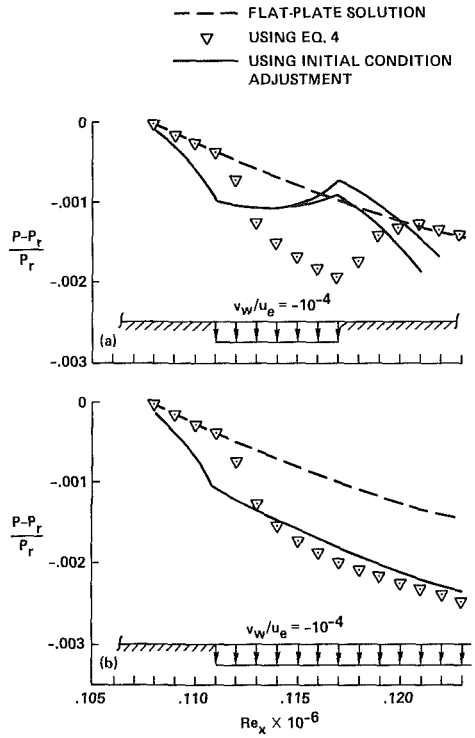

Fig. 1 Interactive boundary-layer computation-comparison of methods. Laminar flow, $M_\infty = 2.23$, T_{AW}: (a) slot suction; and (b) constant step suction.

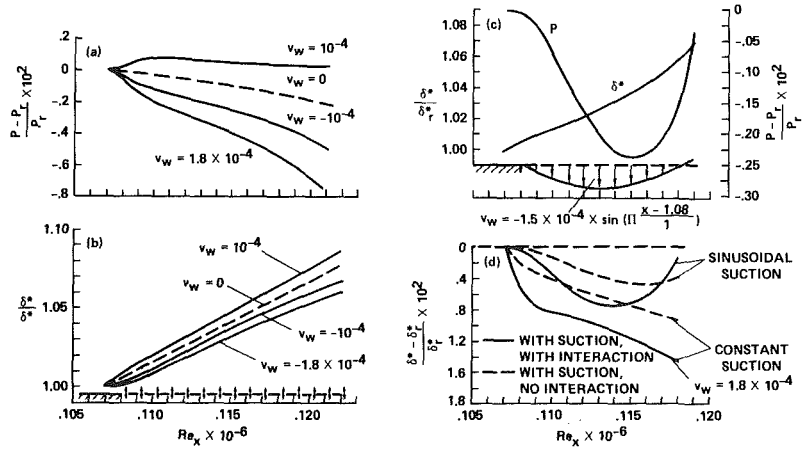

Fig. 2 Some results of interactive boundary-layer computation for laminar, flat-plate flow, $M_\infty = 2.25$, T_{AW}: (a) constant level of wall mass transfer – pressure distribution; (b) constant level of wall mass transfer – displacement thickness distribution; (c) sinusoidal suction; and (d) importance of interaction in the preceding cases.

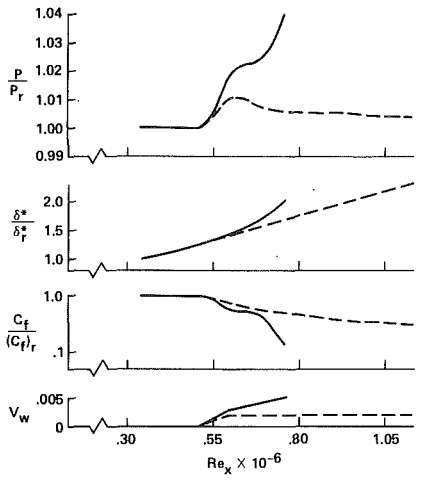

Fig. 3 Some results of interactive boundary-layer computation for turbulent flat-plate flow with $M_\infty = 2.23$, T_{AW}, for the two distributions of wall injection. (The solid and dashed lines refer to the corresponding injection levels shown in the lowermost plot.)

difference in the matching streamline displacement between the two iterations

$$\Delta\delta^*(x_{i+1}) = \delta^*(x_{i+1}, v_{w_{i+1}}) - \delta^*(x_{i+1}, v_{w_i}) \tag{3}$$

is taken as the local streamline slope correction (at constant pressure) due to the surface mass transfer. The interactive computation is resumed at this station after correcting the streamline location for "wall curvature effect" due to the wall mass transfer.

The need for the correction arose since the downstream compatibility condition was set for the case of no mass transfer at the wall (thus neglecting the upstream influence). The corresponding pressure could therefore be expected to be lower than that in the case in which injection was present at the wall. Thus, the encountered decrease in pressure due to "turning on" of injection would constitute the right response of the matching scheme to the incorrect initial condition.

The advantage of the present approach lies in its simplicity. Once the correct interactive solution has been obtained for the case of the flat plate with no wall mass transfer, solutions with arbitrary distributions of v_w may be obtained from the same initial condition, using the marching process and applying equation (3). No knowledge of the downstream boundary condition is required for each v_w distribution. Specification of the downstream condition may not always be possible for cases in which the downstream conditions do not return to the original (undisturbed) state. It should further be noted that due to this "parabolization" of the interaction problem, the computation need not be continued as far downstream as would be necessary to completely satisfy the downstream condition.

A comparison is presented in Fig. 1 between the method of equation (3) and that of repeated adjustment of initial condition, which does fully account for the upstream influence. The marching scheme was used for both. For the slot suction case (Fig. 1(*a*)) the downstream boundary condition on pressure may safely be inferred as the corresponding value for the case without wall mass transfer. (A similar condition for slot injection was imposed in reference [5].) The method of equation (3) clearly meets the downstream pressure condition. The two solution branches obtained by the shooting method and corresponding to slightly different initial conditions exhibit a downstream pressure gradient (negative) in excess of that observed for the case with no suction. The same trend may be observed in the results in [5], apparently caused by insufficient accuracy in imposing the downstream boundary condition. The significant discrepancy between the two solutions stems from the fact that the shooting method accounts for upstream influence, and the local interaction adjustment of equation (3) does not. This difference is especially pronounced in the present example, for the length of the slot is comparable with the interaction length. The discrepancy rapidly decreases as the length of the region in which wall mass transfer occurs increases. This is shown in Fig. 1(*b*) for steplike continuous wall suction distribution. Although here the downstream boundary condition was not obvious, it was taken to match dp/dx at the downstream end of the solution with no suction. It is seen that except in the region close to the onset of suction, the two sets of results are in good agreement.

Some more examples using the present approach are shown in Fig. 2 for a steplike suction-injection distribution in which equation (3) yields nonzero correction only at the discontinuity, and for a sinusoidal suction distribution where the wall boundary condition changes continuously, resulting in continuous contribution of equation (3) to the solution.

The relative importance of interaction and suction is seen from Fig. 2(*d*), which compares the displacement thickness calculated with and without interaction for the aforementioned sinusoidal and $v_w = -1.8 \times 10^{-4}$ suction distributions. It is clear that interaction effects and those of suction are of the same order of magnitude, and that they complement each other in thinning the boundary layer, when the correction, equation (3), is applied.

When applied to the problem of plate injection with v_w one order of magnitude greater than those in Fig. 2, the present approach still gave a fair approximation to the pressure rise at the onset of injection, but overestimated the downstream pressure distribution. The solution was improved by making another downstream correction of the form of equation (3). This now resembles the approach in reference [8] and though locally involving iteration, may still be more convenient than the fully interactive approach.

Solution for the Supercritical Case

As an example of supercritical solution, Fig. 3 shows the pressure, displacement thickness, and skin friction distribution for a turbulent boundary layer with $M_\infty = 2.23$ for two different injection rates. These results were computed by straightforward downstream marching of the interactive solution, with transition set at the start of computation.

It is interesting to note that the solution corresponding to the higher injection level breaks down due to approaching separation point. This breakdown occurs well into the blowing region. In contrast, Werle [5] in his study of injection-induced separation, always observed the separation point to occur upstream of the onset of blowing. Since his results were obtained for a subcritical boundary layer, they may easily be explained by the significant upstream influence shown. The mechanism for the upstream influence does not exist (at least in interactive computation) for supercritical boundary layers. Thus, the present finding is not incongruent with the results of reference [5].

Conclusions

The problem of interactive computation of boundary layers with wall mass transfer was considered. It was shown that the solution reacts differently to wall mass transfer for supercritical and subcritical boundary layers.

For the solution of the subcritical interaction with wall mass transfer, a method was proposed that is applied as local correction to the interaction while marching the solution downstream. This avoids the need for repeated iterations on the whole field, but the method ignores the upstream in-

fluence, and consequently is limited to modest rates of wall mass transfer.

For the supercritical interactive boundary layer with injection, the separation point was encountered within the blowing region. For the subcritical case, separation was previously shown to occur ahead of the blowing region.

References

1 Low, G. M., "The Compressible Boundary Layer with Fluid Injection," NASA TN 3404, 1955.

2 Rheinboldt, W., "On the Calculation of Steady Boundary Layers for Continuous Suction, With Discontinuously Variable Suction Velocity," NASA TT F-29, 1961.

3 Inger, G. R., and Swean, T. F., "Hypersonic Viscous-Inviscid Interaction with Vectored Surface Mass Transfer," *AIAA Journal*, Vol. 14, May 1976, pp. 859–866.

4 Gersten, K., and Paperfuss, H. D., "Second-Order Boundary Layer Flow with Hard Suction," *AIAA Journal*, Vol. 15, Dec. 1977, pp. 1750–1755.

5 Werle, M. J., "Supersonic Laminar Boundary Layer Separation by Slot Injection," *AIAA Journal*, Vol. 17, Feb. 1979, pp. 160–167.

6 Brandeis, J., "Computation of Supersonic Two-Dimensional Viscous Flows Using Multilayer Interactive Method," DSc. Thesis, 1979, Technion-I.I.T.

7 Garvine, R. W., "Upstream Influence in Viscous Interaction Problems," *The Physics of Fluids*, Vol. 11, July 1968, pp. 1413–1423.

8 Baum, E., "An Interaction Model of a Supersonic Laminar Boundary Layer on Sharp and Rounded Backward Facing Steps," *AIAA Journal*, Vol. 6, Mar. 1968, pp. 440–447.

9 Smith, F. T., and Stewartson, K., "On Slot Injection Into a Supersonic Laminar Boundary Layer," *Proceedings of the Royal Society of London*, Series A, Vol. 332, 1973, pp. 1–22.

10 Crocco, L., "Considerations of the Shock-Boundary Layer Interaction," *Proceedings of the Conference on High-Speed Aeronautics*, Polytechnic Institute of Brooklyn, Jan. 20–22, 1955, pp. 75–112.

11 Werle, M. J., and Wornom, S. F., "Numerical Studies of the Hypersonic Strong Interaction Boundary-Layer Equations," *AIAA Journal*, Vol. 9, Oct. 1971, pp. 2058–2060.

12 Reyhner, T. A., and Flugge-Lotz, I., "The Interaction of Shock Wave with a Laminar Boundary Layer," *International Journal of Non-Linear Mechanics*, Vol. 3, 1968, pp. 173–199.

13 Arieli, R., and Murphy, J. D., "Pseudo-Direct Solution to the Boundary Layer Equations for Separated Flow," AIAA Paper 79-0139, New Orleans, La., 1979.

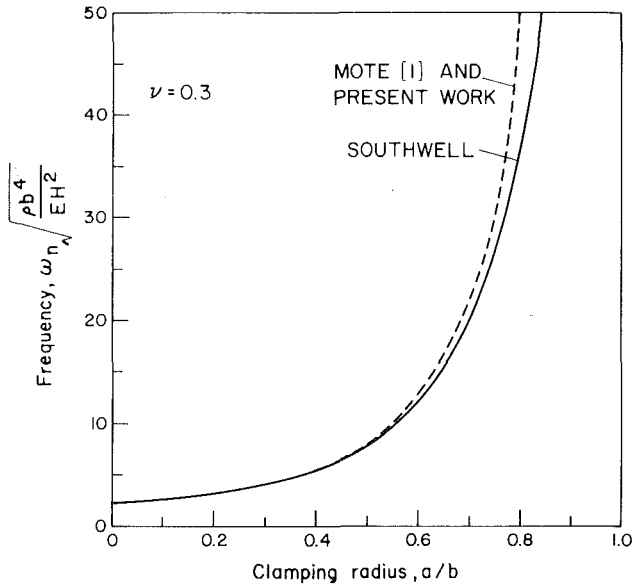

Fig. 1 Variation of frequency with clamping radius for $\lambda^2 = 1$

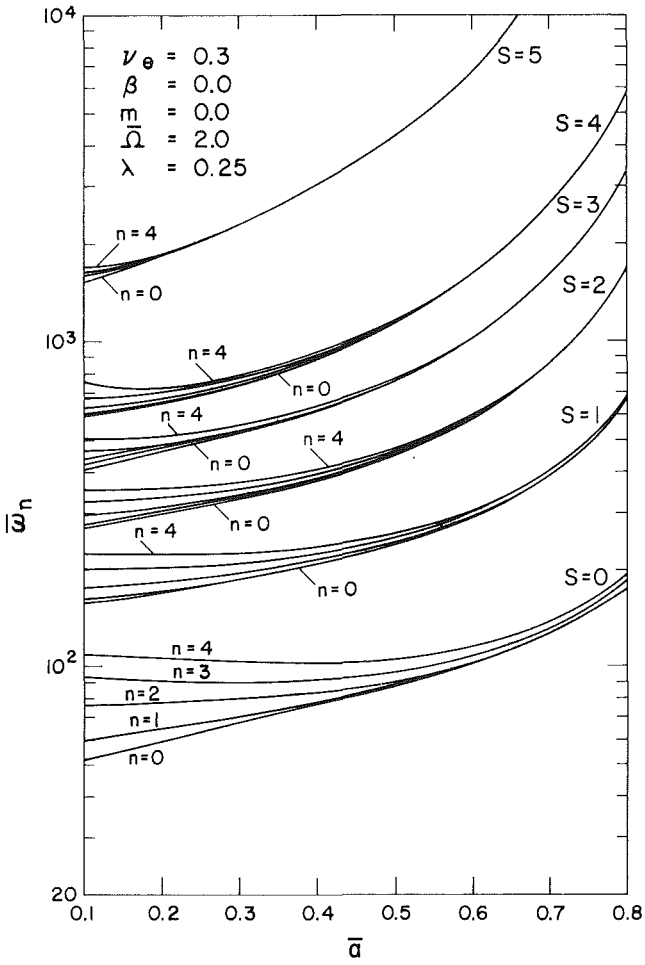

Fig. 2 Variation of frequency with clamping radius for $\lambda^2 = 0.25$

Vibration of a Rotating Orthotropic Disk

A. Rajguru[1] and V. Sundararajan[2]

Introduction

The vibration of a rotating isotropic circular disk is studied by Mote [1], Eversman and Dodson [2], and Barasch and Chen [3]. Ghosh [4] has formulated the vibration of a rotating orthotropic circular disk of uniform thickness neglecting the effect of bending stiffness. The present Note deals with the determination of the natural frequencies of a centrally clamped, rotating orthotropic disk with varying thickness and density which has applications in the design of composite fly wheels. The effect of the rigidity parameter (the ratio of the Young's modulus in the Θ direction to that in the *r* direction), the clamping radius, and thickness variation on the natural frequencies are analyzed.

Problem Formulation

A thin orthotropic disk with outer radius *b* and clamped at radius *a* rotating uniformly about the normal axis passing through and perpendicular to the center plane of symmetry is considered. The analysis is based on the plane state of stress assumption. The influence of shear and rotatory inertia is neglected. The material of the disk is homogeneous and polarly orthotropic. The thickness and density distributions are assumed to be symmetrical with respect to both the axis

[1]Central Planning Cell, Bharat Petroleum Corporation Limited, Bombay, India.

[2]Professor, Department of Mechanical Engineering, Indian Institute of Technology, Kanpur, India.

Manuscript received by ASME Applied Mechanics Division, March 1981; final revision, February 1982.

fluence, and consequently is limited to modest rates of wall mass transfer.

For the supercritical interactive boundary layer with injection, the separation point was encountered within the blowing region. For the subcritical case, separation was previously shown to occur ahead of the blowing region.

References

1 Low, G. M., "The Compressible Boundary Layer with Fluid Injection," NASA TN 3404, 1955.

2 Rheinboldt, W., "On the Calculation of Steady Boundary Layers for Continuous Suction, With Discontinuously Variable Suction Velocity," NASA TT F-29, 1961.

3 Inger, G. R., and Swean, T. F., "Hypersonic Viscous-Inviscid Interaction with Vectored Surface Mass Transfer," *AIAA Journal*, Vol. 14, May 1976, pp. 859–866.

4 Gersten, K., and Paperfuss, H. D., "Second-Order Boundary Layer Flow with Hard Suction," *AIAA Journal*, Vol. 15, Dec. 1977, pp. 1750–1755.

5 Werle, M. J., "Supersonic Laminar Boundary Layer Separation by Slot Injection," *AIAA Journal*, Vol. 17, Feb. 1979, pp. 160–167.

6 Brandeis, J., "Computation of Supersonic Two-Dimensional Viscous Flows Using Multilayer Interactive Method," DSc. Thesis, 1979, Technion-I.I.T.

7 Garvine, R. W., "Upstream Influence in Viscous Interaction Problems," *The Physics of Fluids*, Vol. 11, July 1968, pp. 1413–1423.

8 Baum, E., "An Interaction Model of a Supersonic Laminar Boundary Layer on Sharp and Rounded Backward Facing Steps," *AIAA Journal*, Vol. 6, Mar. 1968, pp. 440–447.

9 Smith, F. T., and Stewartson, K., "On Slot Injection Into a Supersonic Laminar Boundary Layer," *Proceedings of the Royal Society of London*, Series A, Vol. 332, 1973, pp. 1–22.

10 Crocco, L., "Considerations of the Shock-Boundary Layer Interaction," *Proceedings of the Conference on High-Speed Aeronautics*, Polytechnic Institute of Brooklyn, Jan. 20–22, 1955, pp. 75–112.

11 Werle, M. J., and Wornom, S. F., "Numerical Studies of the Hypersonic Strong Interaction Boundary-Layer Equations," *AIAA Journal*, Vol. 9, Oct. 1971, pp. 2058–2060.

12 Reyhner, T. A., and Flugge-Lotz, I., "The Interaction of Shock Wave with a Laminar Boundary Layer," *International Journal of Non-Linear Mechanics*, Vol. 3, 1968, pp. 173–199.

13 Arieli, R., and Murphy, J. D., "Pseudo-Direct Solution to the Boundary Layer Equations for Separated Flow," AIAA Paper 79-0139, New Orleans, La., 1979.

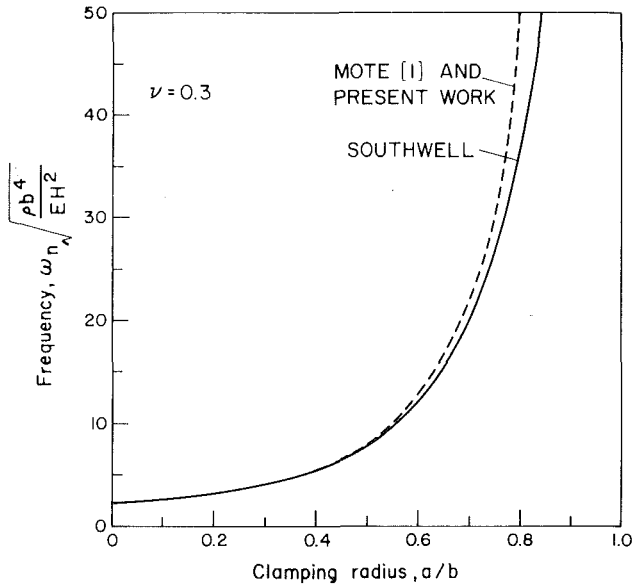

Fig. 1 Variation of frequency with clamping radius for $\lambda^2 = 1$

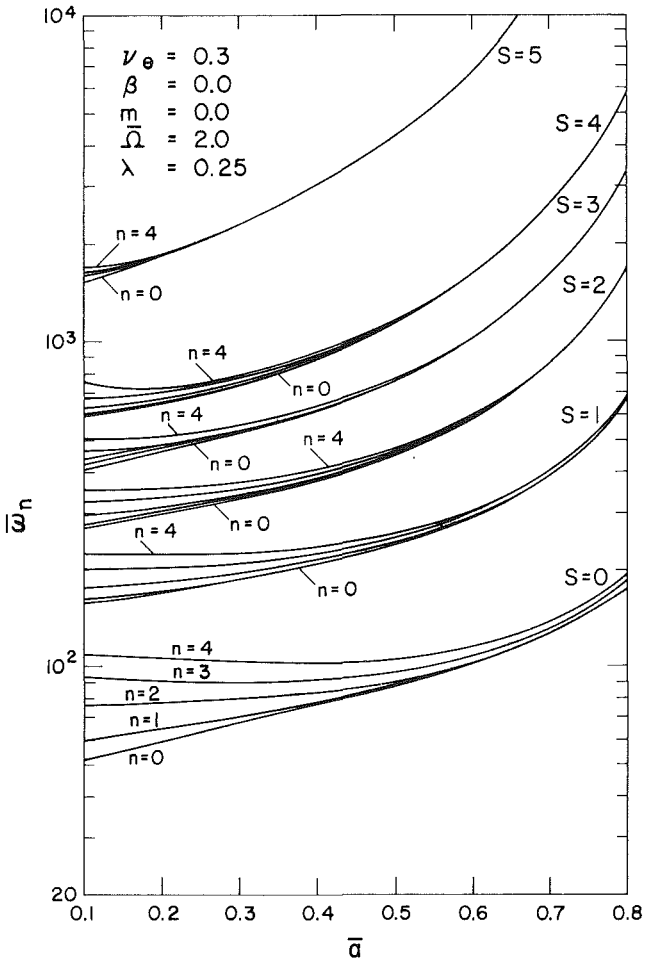

Fig. 2 Variation of frequency with clamping radius for $\lambda^2 = 0.25$

Vibration of a Rotating Orthotropic Disk

A. Rajguru[1] and V. Sundararajan[2]

Introduction

The vibration of a rotating isotropic circular disk is studied by Mote [1], Eversman and Dodson [2], and Barasch and Chen [3]. Ghosh [4] has formulated the vibration of a rotating orthotropic circular disk of uniform thickness neglecting the effect of bending stiffness. The present Note deals with the determination of the natural frequencies of a centrally clamped, rotating orthotropic disk with varying thickness and density which has applications in the design of composite fly wheels. The effect of the rigidity parameter (the ratio of the Young's modulus in the Θ direction to that in the *r* direction), the clamping radius, and thickness variation on the natural frequencies are analyzed.

Problem Formulation

A thin orthotropic disk with outer radius *b* and clamped at radius *a* rotating uniformly about the normal axis passing through and perpendicular to the center plane of symmetry is considered. The analysis is based on the plane state of stress assumption. The influence of shear and rotatory inertia is neglected. The material of the disk is homogeneous and polarly orthotropic. The thickness and density distributions are assumed to be symmetrical with respect to both the axis

[1]Central Planning Cell, Bharat Petroleum Corporation Limited, Bombay, India.

[2]Professor, Department of Mechanical Engineering, Indian Institute of Technology, Kanpur, India.

Manuscript received by ASME Applied Mechanics Division, March 1981; final revision, February 1982.

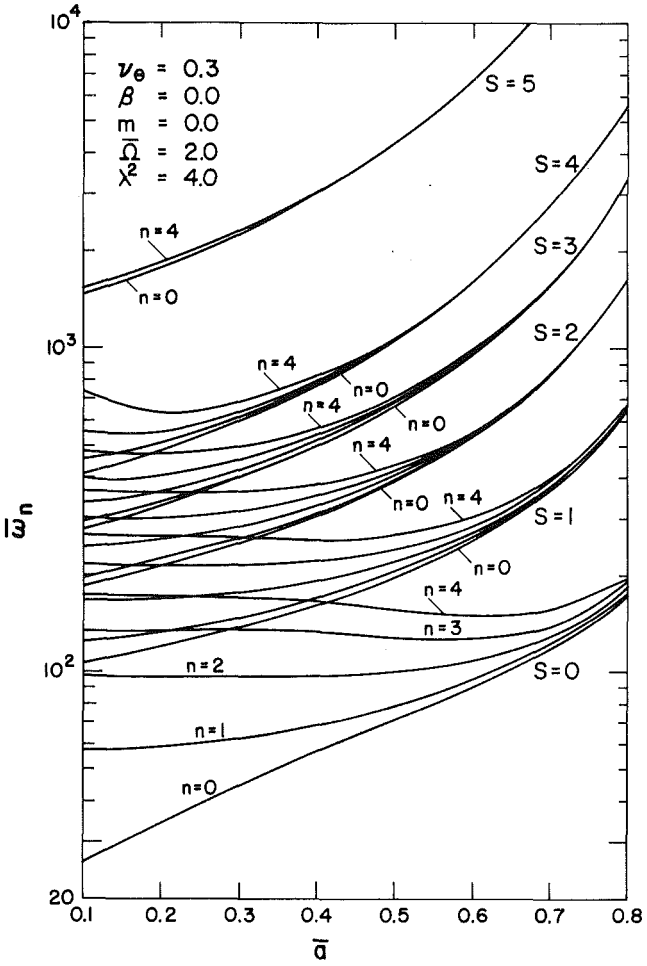

Fig. 3 Variation of frequency with clamping radius for $\lambda^2 = 4.0$

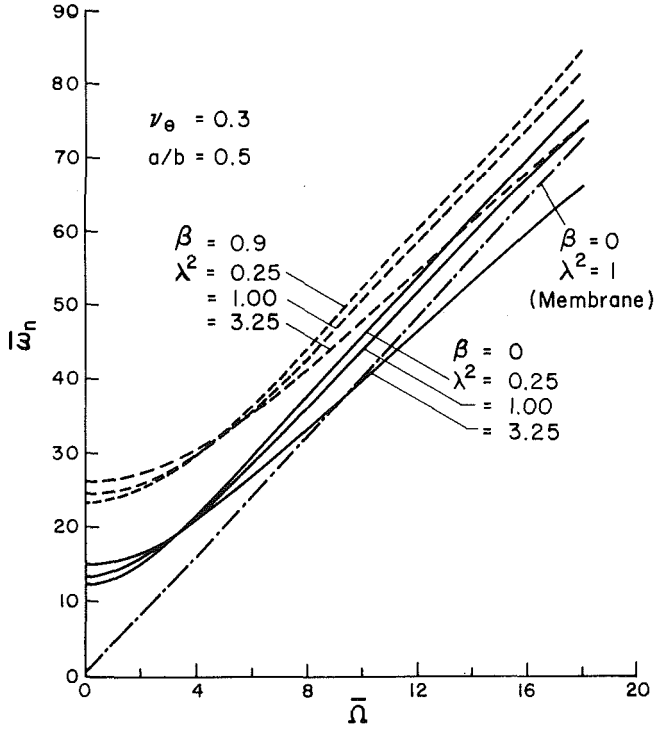

Fig. 4 Variation of frequency with rotational speed

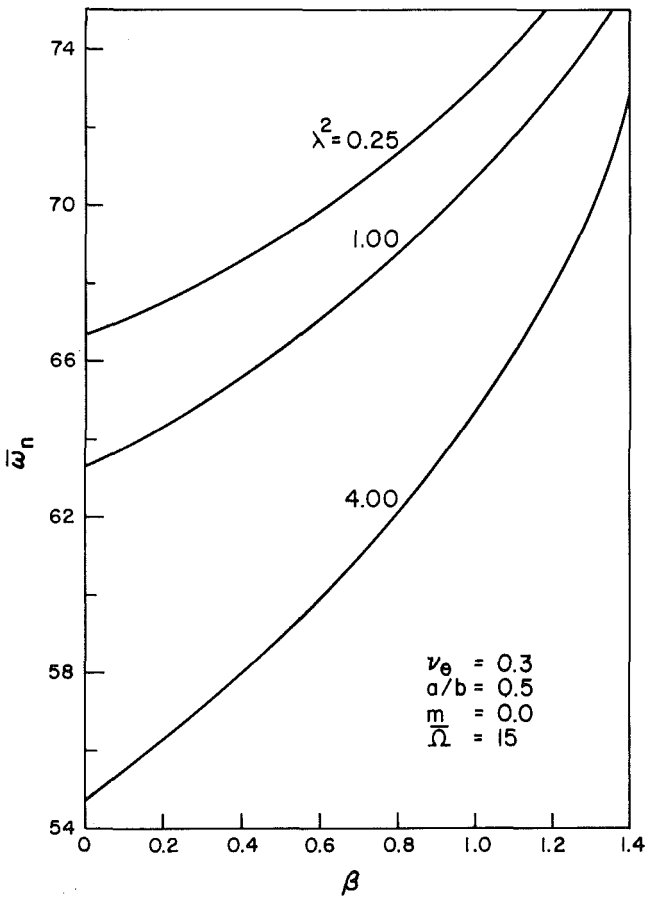

Fig. 5 Variation of frequency with thickness parameter

and the midplane of the disk. The thickness h and the density ρ are assumed to vary along the radius in the form

$$h = h_0\left(\frac{r}{b}\right)^{-\beta} \quad \text{and} \quad \rho = \rho_0\left(\frac{r}{b}\right)^{m} \tag{1}$$

Where h and ρ are the local thickness and mass density and h_0 and ρ_0 that at b. β and m are the thickness and density parameters.

Assuming that the plate is undergoing harmonic oscillations

$$w = W(y)\cos n\Theta \cos \omega_n t \tag{2}$$

the maximum potential energy V, which is the sum of the maximum potential energy due to bending ($V_{B\max}$) and due to rotation ($V_{R\max}$) can be written as

$$\begin{aligned} V_{\max} &= V_{B\max} + V_{R\max} \\ &= \frac{\pi}{2}\int_a^b \left[D_y\left(\frac{d^2W}{dy^2}\right)^2 + \frac{2D_1}{y}\frac{d^2W}{dy^2}\left(\frac{dW}{dy} - \frac{n^2}{y}W\right)\right. \\ &\quad + \frac{D_\theta}{y^2}\left(\frac{dW}{dy} - \frac{n^2}{y}W\right)^2 \\ &\quad \left. + \frac{4D_{y\theta}n^2}{y^2}\left(\frac{dW}{dy} - \frac{W}{y}\right)^2\right] y\,dy \\ &\quad + \frac{\pi}{2}\int_a^b \left[h\sigma_y\left(\frac{dW}{dy}\right)^2 + h\sigma_\theta n^2\left(\frac{W}{y}\right)^2\right] y\,dy \end{aligned} \tag{3}$$

where D_y and D_θ are the flexural rigidities in the r and Θ directions, D_y is the shear rigidity, and $D_1 = \nu_y D_\theta = \nu_\theta D_y$. The maximum kinetic energy is given by

$$T_{\max} = \frac{\pi}{2}\omega_n^2 \int_a^b \rho h W^2 y\,dy \tag{4}$$

The inplane stresses σ_r and σ_Θ of the orthotropic disk rotating with angular velocity Ω, satisfying the boundary conditions

$$u=0 \quad \text{at} \quad r=a \quad \text{and} \quad \sigma_r=0 \quad \text{at} \quad r=b$$

are given by [5]

$$\sigma_\gamma=\rho_0\Omega^2b^2c_3\left[\frac{\beta_1}{\beta_3}\left(\frac{y}{a}\right)^{\alpha_1+\beta-1}-\frac{\beta_2}{\beta_3}\left(\frac{y}{a}\right)^{\alpha_2+\beta-1}+\left(\frac{y}{b}\right)^{2+m}\right] \tag{5}$$

$$\sigma_\Theta=\rho_0\Omega^2b^2\left[c_3\left\{\frac{\alpha_1\beta_1}{\beta_3}\left(\frac{y}{a}\right)^{\alpha_1+\beta-1}-\frac{\alpha_2\beta_1}{\beta_3}\left(\frac{y}{a}\right)^{\alpha_2+\beta-1}+(3+m-\beta)\left(\frac{y}{b}\right)^{2+m}\right\}+\left(\frac{y}{b}\right)^{2+m}\right] \tag{6}$$

where

$$\alpha_{1,2}=-\frac{\beta}{2}\pm\sqrt{\frac{\beta^2}{4}+\lambda^2+\nu_\Theta\beta}$$

$$\lambda^2=\frac{E_\Theta}{E_y}, \quad c_3=\frac{-(3+m+\nu_\Theta)}{(9-\lambda^2)-\beta(3+m+\nu_\Theta)+m(m+6)}$$

$$\beta_1=\frac{\nu_\Theta^2-\lambda^2}{3+m+\nu_\Theta}\left(\frac{a}{b}\right)^{3+m+\nu_\Theta}+(\alpha_2-\nu_\Theta)\left(\frac{a}{b}\right)^{\beta}$$

$$\beta_2=\frac{\nu_\Theta^2-\lambda^2}{3+m+\nu_\Theta}\left(\frac{a}{b}\right)^{3+m+\nu_\Theta}+(\alpha_1-\nu_\Theta)\left(\frac{a}{b}\right)^{\beta}$$

and

$$\beta_3=(\alpha_1-\nu_\Theta)\left(\frac{a}{b}\right)^{1-\alpha_2}-(\alpha_2-\nu_\Theta)\left(\frac{a}{b}\right)^{1-\alpha_1}$$

It should be noticed that the stress expressions are not valid for combinations of λ^2, ν_Θ, m, and β which make

$$(9-\lambda^2)-\beta(3+m+\nu_\Theta)+m(m+6)=0$$

The mode shapes $W(r)$ in the radial direction are assumed as

$$W(y)=a_0(y-a)^2+a_1(y-a)^3+a_2(y-a)^4+\ldots\ldots \tag{7}$$

which satisfy the geometric boundary conditions.

Introducing the nondimensional quantities

$$\bar{y}=\frac{y}{b}, \quad \bar{a}=\frac{a}{b}, \quad \bar{\sigma}_y=\frac{\sigma_\gamma}{\rho_0\Omega^2b^2}, \quad \bar{\sigma}_\Theta=\frac{\sigma_\Theta}{\rho_2\Omega^2b^2}$$

$$\bar{\Omega}=\left[\frac{\Omega^2\rho_0h_0b^4}{8\bar{D}_y}\right]^{1/2}, \quad \bar{\omega}_n=\left[\frac{\omega_n^2\rho_0h_0b^4}{\bar{D}_y}\right]^{1/2}$$

and substituting equations (5), (6), and (7) into equations (3) and (4) and applying the Rayleigh-Ritz technique we obtain the eigenvalue equation:

$$([A]-\omega_n^2[I])\begin{Bmatrix}a_0\\a_1\\.\\.\\.\\.\end{Bmatrix}=0 \tag{8}$$

from which the natural frequencies are obtained.

Results and Discussion

The numerical solution of equation (8) is obtained considering the first six terms in equation (7). The natural frequencies ($\bar{\omega}_n$) of a stationary isotropic disk ($\lambda^2 = 1$) of constant thickness and density have been compared with the exact natural frequencies of Southwell [6] in Fig 1. For values of $a/b < 0.7$, the values compare very well whereas for values $a/b > 0.7$ the present estimate is higher than the exact value. The variation of $\bar{\omega}_n$ with a/b for orthotropic disks ($\lambda^2 = 0.25$, 4.0) rotating at a speed $\bar{\Omega} = 20$ are shown in Figs. 2 and 3. Frequencies are plotted for various nodal circles (s) and nodal diameters (n).

The natural frequencies of an isotropic rotating disk with $\beta = m = 0$ computed with the present technique compares very well with that of Barasch and Chen [3]. Figure 4 shows this variation in the case of an orthotropic disk for $\beta = 0, 0.9$. In a rotating disk $\bar{\omega}_n$ is controlled both by the bending stiffness and inplane stresses. Since the inplane stresses are proportional to the angular velocity, the bending rigidity is the controlling factor at low speeds and the inplane stresses at high speeds. The inplane stress σ_r due to rotation decreases with increase in λ^2 [5] and consequently $\bar{\omega}_n$ decreases with increasing λ^2 at high $\bar{\Omega}$. The variation of $\bar{\omega}_n$ with $\bar{\Omega}$ neglecting the bending stiffness, for $\lambda^2 = 1$, is also plotted in Fig. 4.

The variation of the natural frequencies with the thickness parameter β for various values of λ^2 is shown in Fig. 5.

References

1 Mote, C. D., Jr., "Free Vibration of Initially Stressed Circular Disks," ASME *Journal of Engineering for Industry*, Vol. 87, 1965, pp. 258-264.

2 Eversman, W., and Dodson, R. O., Jr., "Free Vibration of a Centrally Clamped Spinning Circular Disk," *AIAA Journal*, Vol.. 7, No. 10, 1969, pp. 2010-2012.

3 Barasch, S., and Chen, Y., "On the Vibration of a Rotating Disk," ASME JOURNAL OF APPLIED MECHANICS, Vol. 39, Dec. 1972, pp. 1143-1144.

4 Ghosh, N. C., "The Vibration of Rotating Aelotropic Elastic Disk," *Indian Journal of Physics*, Vol. 45, 1971, pp. 262-267.

5 Reddy, T. Y., and Srinath, H., "Elastic Stresses in a Rotating Anisotropic Annular Disk of Variable Thickness and Variable Density," *International Journal of Mechanical Sciences*, Vol. 16, 1974, pp. 85-89.

6 Southwell, R. V., "On the Free Transverse Vibration of a Uniform Circular Disc Clamped at Its Center; and on the Effects of Rotation," *Proceedings of the Royal Society* (London), Vol. 101, May 1922, pp. 133-153.

On the Effect of Axial Force on Dynamic Fracture of a Beam or a Plate in Pure Bending

C. Levy[1] and G. Herrmann[1]

Introduction

The dynamic fracture response of a long beam of brittle elastic material subjected to pure bending was recently studied by Freund and Herrmann [1] and Adeli, Herrmann, and Freund [2]. A one-dimensional model was generated under the assumptions that the crack-tip velocity was low enough such that the normal stress distribution caused by the propagating crack could be approximated by the static distribution appropriate for the instantaneous crack length and net-section bending moment [1]. Following this, the model was modified to include the effect of the induced axial force on the fracturing cross section [2].

Inclusion of the axial force was accomplished by modifying the fracture model stress-intensity factor (equations (11-13), [2]) and redefining the compliance coefficients (equation (23),

[1] Division of Applied Mechanics, Department of Mechanical Engineering, Stanford University, Stanford, Calif. 94305. G. Herrmann is a Fellow, ASME.

Manuscript received by ASME Applied Mechanics Division, September, 1981; final revision, March, 1982.

The inplane stresses σ_r and σ_Θ of the orthotropic disk rotating with angular velocity Ω, satisfying the boundary conditions

$$u=0 \quad \text{at} \quad r=a \quad \text{and} \quad \sigma_r=0 \quad \text{at} \quad r=b$$

are given by [5]

$$\sigma_\gamma=\rho_0\Omega^2b^2c_3\left[\frac{\beta_1}{\beta_3}\left(\frac{y}{a}\right)^{\alpha_1+\beta-1}-\frac{\beta_2}{\beta_3}\left(\frac{y}{a}\right)^{\alpha_2+\beta-1}+\left(\frac{y}{b}\right)^{2+m}\right] \tag{5}$$

$$\sigma_\Theta=\rho_0\Omega^2b^2\left[c_3\left\{\frac{\alpha_1\beta_1}{\beta_3}\left(\frac{y}{a}\right)^{\alpha_1+\beta-1}-\frac{\alpha_2\beta_1}{\beta_3}\left(\frac{y}{a}\right)^{\alpha_2+\beta-1}+(3+m-\beta)\left(\frac{y}{b}\right)^{2+m}\right\}+\left(\frac{y}{b}\right)^{2+m}\right] \tag{6}$$

where

$$\alpha_{1,2}=-\frac{\beta}{2}\pm\sqrt{\frac{\beta^2}{4}+\lambda^2+\nu_\Theta\beta}$$

$$\lambda^2=\frac{E_\Theta}{E_y}, \quad c_3=\frac{-(3+m+\nu_\Theta)}{(9-\lambda^2)-\beta(3+m+\nu_\Theta)+m(m+6)}$$

$$\beta_1=\frac{\nu_\Theta^2-\lambda^2}{3+m+\nu_\Theta}\left(\frac{a}{b}\right)^{3+m+\nu_\Theta}+(\alpha_2-\nu_\Theta)\left(\frac{a}{b}\right)^{\beta}$$

$$\beta_2=\frac{\nu_\Theta^2-\lambda^2}{3+m+\nu_\Theta}\left(\frac{a}{b}\right)^{3+m+\nu_\Theta}+(\alpha_1-\nu_\Theta)\left(\frac{a}{b}\right)^{\beta}$$

and

$$\beta_3=(\alpha_1-\nu_\Theta)\left(\frac{a}{b}\right)^{1-\alpha_2}-(\alpha_2-\nu_\Theta)\left(\frac{a}{b}\right)^{1-\alpha_1}$$

It should be noticed that the stress expressions are not valid for combinations of λ^2, ν_Θ, m, and β which make

$$(9-\lambda^2)-\beta(3+m+\nu_\Theta)+m(m+6)=0$$

The mode shapes $W(r)$ in the radial direction are assumed as

$$W(y)=a_0(y-a)^2+a_1(y-a)^3+a_2(y-a)^4+\ldots\ldots \tag{7}$$

which satisfy the geometric boundary conditions.

Introducing the nondimensional quantities

$$\bar{y}=\frac{y}{b}, \quad \bar{a}=\frac{a}{b}, \quad \bar{\sigma}_y=\frac{\sigma_\gamma}{\rho_0\Omega^2b^2}, \quad \bar{\sigma}_\Theta=\frac{\sigma_\Theta}{\rho_2\Omega^2b^2}$$

$$\bar{\Omega}=\left[\frac{\Omega^2\rho_0h_0b^4}{8\bar{D}_y}\right]^{1/2}, \quad \bar{\omega}_n=\left[\frac{\omega_n^2\rho_0h_0b^4}{\bar{D}_y}\right]^{1/2}$$

and substituting equations (5), (6), and (7) into equations (3) and (4) and applying the Rayleigh-Ritz technique we obtain the eigenvalue equation:

$$([A]-\omega_n^2[I])\begin{Bmatrix}a_0\\a_1\\.\\.\\.\\.\end{Bmatrix}=0 \tag{8}$$

from which the natural frequencies are obtained.

Results and Discussion

The numerical solution of equation (8) is obtained considering the first six terms in equation (7). The natural frequencies ($\bar{\omega}_n$) of a stationary isotropic disk ($\lambda^2 = 1$) of constant thickness and density have been compared with the exact natural frequencies of Southwell [6] in Fig 1. For values of $a/b < 0.7$, the values compare very well whereas for values $a/b > 0.7$ the present estimate is higher than the exact value. The variation of $\bar{\omega}_n$ with a/b for orthotropic disks ($\lambda^2 = 0.25$, 4.0) rotating at a speed $\bar{\Omega} = 20$ are shown in Figs. 2 and 3. Frequencies are plotted for various nodal circles (s) and nodal diameters (n).

The natural frequencies of an isotropic rotating disk with $\beta = m = 0$ computed with the present technique compares very well with that of Barasch and Chen [3]. Figure 4 shows this variation in the case of an orthotropic disk for $\beta = 0, 0.9$. In a rotating disk $\bar{\omega}_n$ is controlled both by the bending stiffness and inplane stresses. Since the inplane stresses are proportional to the angular velocity, the bending rigidity is the controlling factor at low speeds and the inplane stresses at high speeds. The inplane stress σ_r due to rotation decreases with increase in λ^2 [5] and consequently $\bar{\omega}_n$ decreases with increasing λ^2 at high $\bar{\Omega}$. The variation of $\bar{\omega}_n$ with $\bar{\Omega}$ neglecting the bending stiffness, for $\lambda^2 = 1$, is also plotted in Fig. 4.

The variation of the natural frequencies with the thickness parameter β for various values of λ^2 is shown in Fig. 5.

References

1 Mote, C. D., Jr., "Free Vibration of Initially Stressed Circular Disks," ASME *Journal of Engineering for Industry*, Vol. 87, 1965, pp. 258-264.

2 Eversman, W., and Dodson, R. O., Jr., "Free Vibration of a Centrally Clamped Spinning Circular Disk," *AIAA Journal*, Vol.. 7, No. 10, 1969, pp. 2010-2012.

3 Barasch, S., and Chen, Y., "On the Vibration of a Rotating Disk," ASME JOURNAL OF APPLIED MECHANICS, Vol. 39, Dec. 1972, pp. 1143-1144.

4 Ghosh, N. C., "The Vibration of Rotating Aelotropic Elastic Disk," *Indian Journal of Physics*, Vol. 45, 1971, pp. 262-267.

5 Reddy, T. Y., and Srinath, H., "Elastic Stresses in a Rotating Anisotropic Annular Disk of Variable Thickness and Variable Density," *International Journal of Mechanical Sciences*, Vol. 16, 1974, pp. 85-89.

6 Southwell, R. V., "On the Free Transverse Vibration of a Uniform Circular Disc Clamped at Its Center; and on the Effects of Rotation," *Proceedings of the Royal Society* (London), Vol. 101, May 1922, pp. 133-153.

On the Effect of Axial Force on Dynamic Fracture of a Beam or a Plate in Pure Bending

C. Levy[1] and G. Herrmann[1]

Introduction

The dynamic fracture response of a long beam of brittle elastic material subjected to pure bending was recently studied by Freund and Herrmann [1] and Adeli, Herrmann, and Freund [2]. A one-dimensional model was generated under the assumptions that the crack-tip velocity was low enough such that the normal stress distribution caused by the propagating crack could be approximated by the static distribution appropriate for the instantaneous crack length and net-section bending moment [1]. Following this, the model was modified to include the effect of the induced axial force on the fracturing cross section [2].

Inclusion of the axial force was accomplished by modifying the fracture model stress-intensity factor (equations (11-13), [2]) and redefining the compliance coefficients (equation (23),

[1] Division of Applied Mechanics, Department of Mechanical Engineering, Stanford University, Stanford, Calif. 94305. G. Herrmann is a Fellow, ASME.

Manuscript received by ASME Applied Mechanics Division, September, 1981; final revision, March, 1982.

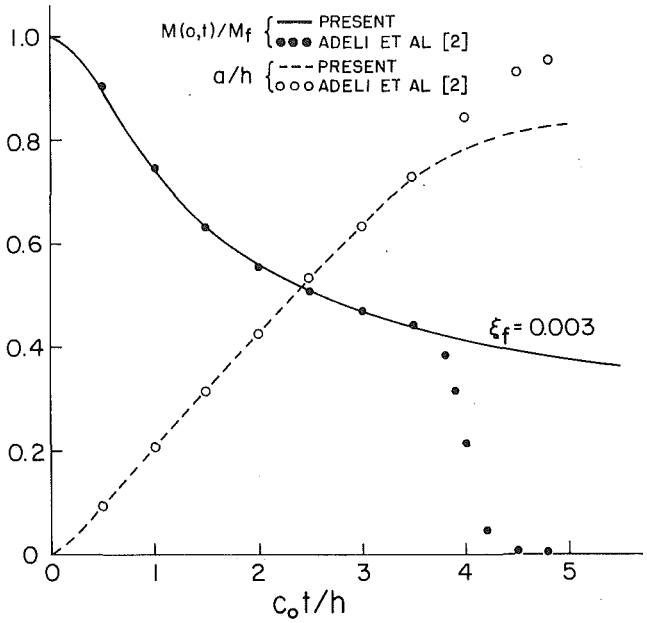

Fig. 1 Dimensionless moment and crack length versus time for the Euler-Bernoulli beam model

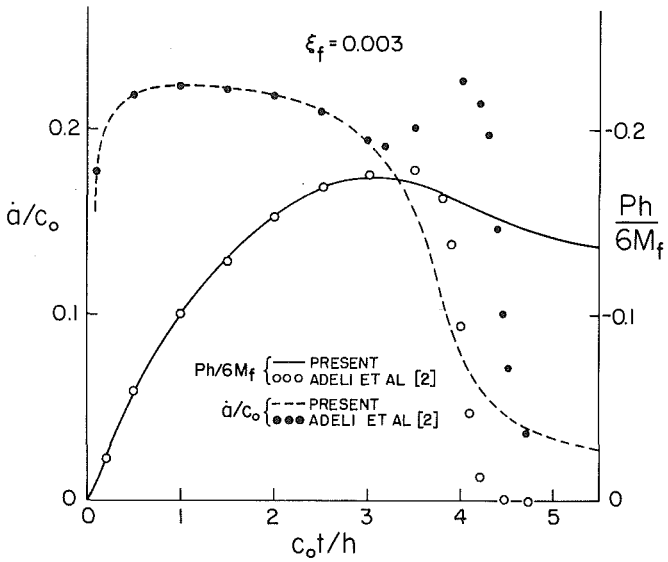

Fig. 2 Dimensionless crack speed ($\dot{a}/c_0$) and load on fracture cross section ($Ph/6M_f$) versus time ($c_0 t/h$) for the Euler-Bernoulli beam model

[2]). In so doing, the following shape functions were introduced in equation (13), [2].

$$g_t(\xi) = \frac{-5.7272 + 15.1184\xi}{(1-\xi)^{1/2}} \quad \text{for } 0.7 \le \xi \le 1 \qquad (1a,b)$$

$$g_b(\xi) = \frac{1.0363 - 0.5722}{(1-\xi)^{3/2}}$$

where $\xi = a/h$, a being the crack length and h being the beam depth. These functions led to the "bump" in the velocity versus time graph in Fig. 3 of [2]. For an infinitely long beam this bump should not appear, but does so due to an inconsistency in the $g_t(\xi)$ formula proposed in [2]; this Note attempts to correct this by defining a more consistent model.

Modification of the Shape Functions

An inconsistency exists if equation (1*a*) and the one-dimensional wave equation are used to correlate the induced discontinuity in displacement at the centerline and the net cross-section induced loading. This function is correct if the load were located at the "centerline" of the unbroken ligament [3]. Since the longitudinal wave equation is written with respect to the original centerline of the beam, by applying the load at the "centerline" of the remaining ligament implies an additional bending moment proportional to $p(t)$ times the unbroken ligament.[2] This can be taken care of by using a shape function proportional to $(1-\xi)^{-3/2}$, similar to $g_b(\xi)$ [3]. A more consistent set of formulas for $g_t(\xi)$ would then be

$$g_t(\xi) = \xi^{1/2}(1.99 - 0.41\xi + 18.7\xi^2 - 38.48\xi^3 + 53.85\xi^4) \qquad 0 \le \xi \le .6$$

and (2*a*,*b*)

$$g_t(\xi) = (1.7756 + 0.0526\xi)\left(\frac{\xi}{(1-\xi)^3}\right)^{1/2} \qquad 0.6 \le \xi < 1$$

[2] It should be noted that the formulas in [3] are true only for a semi-infinite crack in a half space. However, locally, deep cracks near the boundary do take on this characteristic. See, for instance, [3] pp. 2.10–2.11 for the form of the formulas used.

Because of the change in the interval length ([0,0.6] as opposed to [0,0.7]) a minor change in $g_b(\xi)$ is also required; thus,

$$g_b(\xi) = \xi^{1/2}(1.99 - 2.47\xi + 12.97\xi^2 - 23.17\xi^3 + 24.80\xi^4) \qquad 0 \le \xi \le .6$$

(2*c*,*d*)

$$g_b(\xi) = \frac{0.7083 - 0.0744\xi}{(1-\xi)^{3/2}} \qquad 0.6 \le \xi < 1$$

These functions would in turn modify (equation (20), [2]) to

$$\alpha_{bl} = \alpha_{tb} = \xi^2(1.98 - 1.91\xi + 16.009\xi^2 - 34.838\xi^3 + 83.933\xi^4 - 153.649\xi^5 + 256.722\xi^6 - 244.668\xi^7 + 133.548\xi^8)$$

$$\alpha_{tt} = \xi^2(1.98 - 0.544\xi + 18.649\xi^2 - 33.70\xi^3 + 99.261\xi^4 - 211.901\xi^5 + 436.838\xi^6 - 460.477\xi^7 + 289.982\xi^8) \qquad 0 \le \xi \le 0.6 \qquad (3a,b)$$

and equation (23), [2]) to

$$\alpha_{bl} = \alpha_{tb} = \sqrt{\xi}\left(0.0078 - \frac{0.1873}{(1-\xi)} + \frac{0.5796}{(1-\xi)^2}\right) - 0.1021 - 0.2ln\left(\frac{1+\sqrt{\xi}}{1-\sqrt{\xi}}\right)$$

$$\alpha_{tt} = -0.197ln(1-\xi) - 0.003\xi - \frac{(1.672 + 0.194\xi)}{1-\xi} + \frac{1.672\xi}{(1-\xi)^2} + 1.5633 \qquad 0.6 \le \xi < 1 \qquad (4a,b)$$

Using these shape functions leads to a more consistent model and provides results, shown in Figs. 1 and 2, that are more consistent qualitatively with those of [4] and [6].

Discussion of Results

Unlike the results in [2], the moment (Fig. 1) and the load (Fig. 2) tend to nonzero asymptotic values, a consequence of the fact that the beam is infinitely long. The results more readily confirm qualitatively the experimental observation of [4] and [6] for the moment and load, even though in both papers the measurements were not made at the fracturing cross section. It is noted that the crack length and crack velocity are also effectively arrested, confirming Kinra and Kolsky's observations for extremely long beams [6]; i.e., in the absence of end reflections the forward motion of the crack is arrested at 90–95 percent of beam depth. It should also be noted that the model confirms Kolsky's narrative in the discussion of his results in [5].

Acknowledgment

This research was supported in part by the U.S. Army Research Office under Grant DAAG29-78-G-0086 to Stanford University.

The authors would like to thank Prof. R. J. Clifton of Brown University for the helpful discussions on the results of this paper, and for the constructive comments of the reviewers.

References

1 Freund, L. B., and Herrmann, G., "Dynamic Fracture of a Beam or Plate in Plane Bending," ASME JOURNAL OF APPLIED MECHANICS Vol. 43, 1976, pp. 112–116.

2 Adeli, H., Herrmann, G., and Freund, L. B., "Effect of Axial Force on Dynamic Fracture of a Beam or Plate in Pure Bending," ASME JOURNAL OF APPLIED MECHANICS, Vol. 44, 1977, pp. 647–651.

3 Tada, H., Paris, P., and Irwin, G., *The Stress Analysis of Cracks Handbook*, Del Research Corp., Hellertown, Pa., 1973, pp. 9.1–9.4.

4 Bodner, S., "Stress Waves Due to Fracture of Glass in Bending," *J. of Mech. and Physics of Solids*, Vol. 21, 1973, pp. 1–8.

5 Kolsky, H., "Stress Pulse Propagated as a Result of the Rapid Growth of Brittle Fracture," *Eng. Fract. Mech.*, Vol. 5, 1973, pp. 513–522.

6 Kinra, V. K., and Kolsky, H., "The Interaction between Bending Fractures and the Emitted Stress Waves," *Eng. Fract. Mech.*, Vol. 9, 1977, pp. 423–432.

Stress Field in Orthotropic Accelerating Disks

G. Genta,[1] M. Gola,[1] and A. Gugliotta[1]

Nomenclature

h = disk thickness
r = radius
u = radial displacement
v = circumferential displacement
E = elastic modulus
G = tangential modulus
S_{ij} = elastic compliances in the radial and circumferential directions
β = ratio r_i/r_e
γ = shear strain
ϵ = linear strain
θ = polar angle
ν = Poisson ratio
ρ = density
σ = normal stress
τ = shear stress
$\dot{\omega}$ = angular acceleration
$(\ )_{,x}$ = derivative with respect to variable x.

Indexes:

c = circumferential direction
e = external, outer
i = inner
r = radial direction
L = principal longitudinal direction of the material ($\theta = 0$ deg)
T = principal transversal direction of the material ($\theta = 90$ deg)

1 Introduction

The stress field produced by an angular acceleration in an isotropic disk of any shape has been known for a long time [1], in the hypotheses of plane stress and material's linearity.

The stress field in an orthotropic accelerating disk has been solved in [2], but doubts are to be cast on the correctness of this solution.

The aim of the present work is to discuss the controversial aspects of the problem, to provide a new closed-form solution when it is possible, and to show more general results obtained via a numerical approach.

2 Analytical Approach

2.1 Fundamental Equations. A geometrically axisymmetrical disk is given, defined by polar coordinates (r, θ).

The thickness varies along the radius, and is indicated $h(r)$.

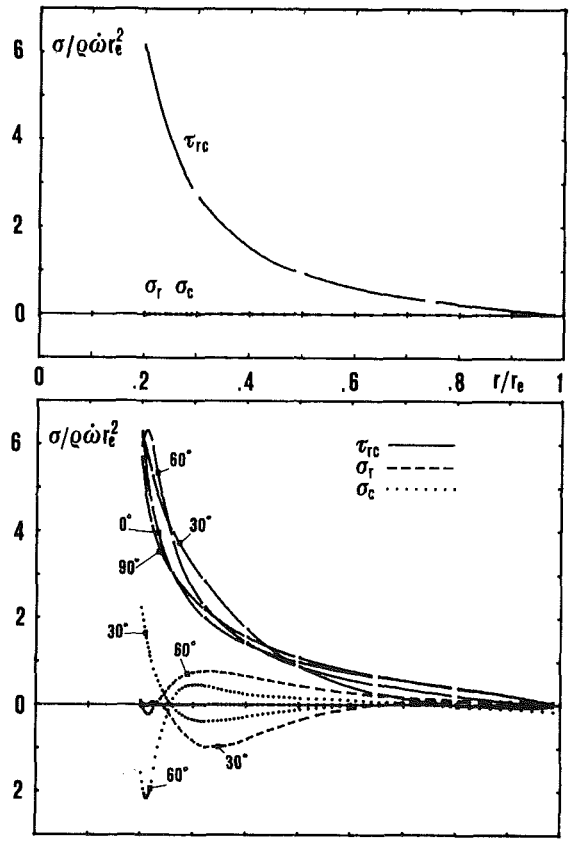

Fig. 1 Stress distribution in an accelerating disk of constant thickness made of orthotropic material. (*a*) Material satisfying equation (5); and (*b*) material not satisfying equation (5).

[1] Associate Professors, Instituto della Motorizzazione, Politecnico di Torino, 10100 Torino, Corso duca Degli Abruzzi 24, Italy. G. Genta is an Assoc. Mem. ASME; A. Gugliotta is a Mem. ASME.

Manuscript received by ASME Applied Mechanics Division, June 1981; final revision, November, 1981.

Discussion of Results

Unlike the results in [2], the moment (Fig. 1) and the load (Fig. 2) tend to nonzero asymptotic values, a consequence of the fact that the beam is infinitely long. The results more readily confirm qualitatively the experimental observation of [4] and [6] for the moment and load, even though in both papers the measurements were not made at the fracturing cross section. It is noted that the crack length and crack velocity are also effectively arrested, confirming Kinra and Kolsky's observations for extremely long beams [6]; i.e., in the absence of end reflections the forward motion of the crack is arrested at 90–95 percent of beam depth. It should also be noted that the model confirms Kolsky's narrative in the discussion of his results in [5].

Acknowledgment

This research was supported in part by the U.S. Army Research Office under Grant DAAG29-78-G-0086 to Stanford University.

The authors would like to thank Prof. R. J. Clifton of Brown University for the helpful discussions on the results of this paper, and for the constructive comments of the reviewers.

References

1 Freund, L. B., and Herrmann, G., "Dynamic Fracture of a Beam or Plate in Plane Bending," ASME JOURNAL OF APPLIED MECHANICS Vol. 43, 1976, pp. 112–116.

2 Adeli, H., Herrmann, G., and Freund, L. B., "Effect of Axial Force on Dynamic Fracture of a Beam or Plate in Pure Bending," ASME JOURNAL OF APPLIED MECHANICS, Vol. 44, 1977, pp. 647–651.

3 Tada, H., Paris, P., and Irwin, G., *The Stress Analysis of Cracks Handbook*, Del Research Corp., Hellertown, Pa., 1973, pp. 9.1–9.4.

4 Bodner, S., "Stress Waves Due to Fracture of Glass in Bending," *J. of Mech. and Physics of Solids*, Vol. 21, 1973, pp. 1–8.

5 Kolsky, H., "Stress Pulse Propagated as a Result of the Rapid Growth of Brittle Fracture," *Eng. Fract. Mech.*, Vol. 5, 1973, pp. 513–522.

6 Kinra, V. K., and Kolsky, H., "The Interaction between Bending Fractures and the Emitted Stress Waves," *Eng. Fract. Mech.*, Vol. 9, 1977, pp. 423–432.

Stress Field in Orthotropic Accelerating Disks

G. Genta,[1] M. Gola,[1] and A. Gugliotta[1]

Nomenclature

h = disk thickness
r = radius
u = radial displacement
v = circumferential displacement
E = elastic modulus
G = tangential modulus
S_{ij} = elastic compliances in the radial and circumferential directions
β = ratio r_i/r_e
γ = shear strain
ϵ = linear strain
θ = polar angle
ν = Poisson ratio
ρ = density
σ = normal stress
τ = shear stress
$\dot{\omega}$ = angular acceleration
$(\ )_{,x}$ = derivative with respect to variable x.

Indexes:

c = circumferential direction
e = external, outer
i = inner
r = radial direction
L = principal longitudinal direction of the material ($\theta = 0$ deg)
T = principal transversal direction of the material ($\theta = 90$ deg)

1 Introduction

The stress field produced by an angular acceleration in an isotropic disk of any shape has been known for a long time [1], in the hypotheses of plane stress and material's linearity.

The stress field in an orthotropic accelerating disk has been solved in [2], but doubts are to be cast on the correctness of this solution.

The aim of the present work is to discuss the controversial aspects of the problem, to provide a new closed-form solution when it is possible, and to show more general results obtained via a numerical approach.

2 Analytical Approach

2.1 Fundamental Equations. A geometrically axisymmetrical disk is given, defined by polar coordinates (r, θ).

The thickness varies along the radius, and is indicated $h(r)$.

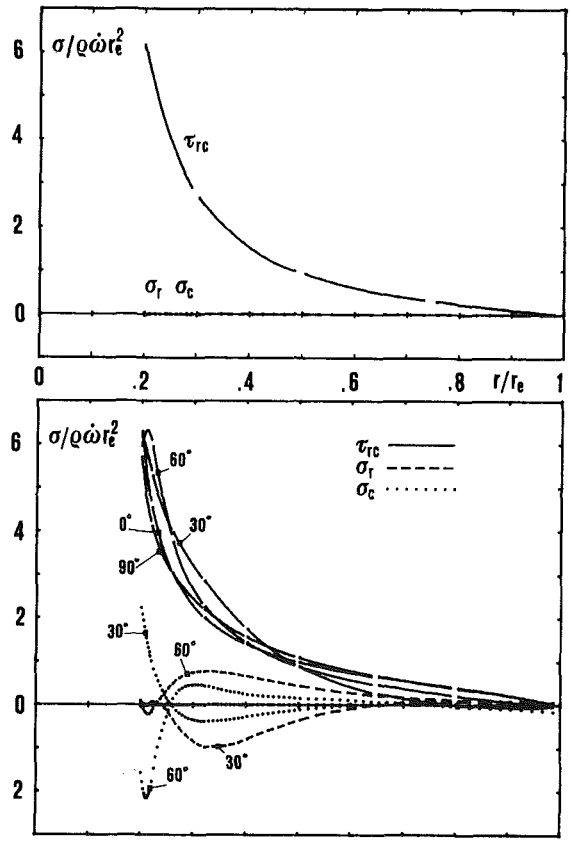

Fig. 1 Stress distribution in an accelerating disk of constant thickness made of orthotropic material. (a) Material satisfying equation (5); and (b) material not satisfying equation (5).

[1] Associate Professors, Instituto della Motorizzazione, Politecnico di Torino, 10100 Torino, Corso duca Degli Abruzzi 24, Italy. G. Genta is an Assoc. Mem. ASME; A. Gugliotta is a Mem. ASME.

Manuscript received by ASME Applied Mechanics Division, June 1981; final revision, November, 1981.

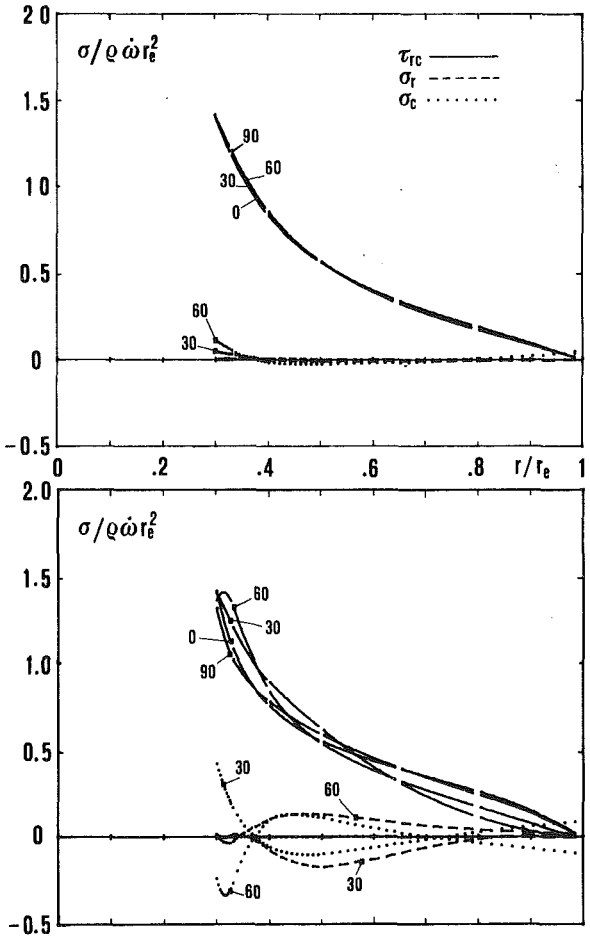

Fig. 2 Stress distribution in conical disks, ratio of inner rim thickness to outer rim thickness equal to 3.1. Respectively, same materials as in Figs. 1(*a*) & (*b*).

The equilibrium equations in the radial and in the circumferential directions are:

$$\begin{cases} \dfrac{1}{h}(\sigma_r h),_r + \dfrac{1}{r}(\sigma_r - \sigma_c) + \dfrac{1}{r}(\tau_{rc}),_\theta = 0 \\ \dfrac{1}{h}(\tau_{rc} h),_r + \dfrac{2}{r}\tau_{rc} + \dfrac{1}{r}(\sigma_c),_\theta - \rho\dot{\omega} r = 0 \end{cases} \tag{1}$$

Equations (1) have been obtained in the hypotheses that the stress state is plane and that only body forces due to the angular acceleration are present.

If the thickness h is constant with the radius, equation (1) reduces to equation (1) in [2].

The strain compatibility equation is:

$$(\epsilon_c),_{rr} + \frac{1}{r^2}(\epsilon_r),_{\theta\theta} + \frac{2}{r}(\epsilon_c),_r - \frac{1}{r}(\epsilon_r),_r + \\ - \frac{1}{r}(\gamma_{rc}),_{r\theta} - \frac{1}{r^2}(\gamma_{rc}),_\theta = 0 \tag{2}$$

The stress-strain relationship has, in the linear field, the general form:

$$\{\epsilon_r, \epsilon_c, \gamma_{rc}\}^T = [S]\{\sigma_r, \sigma_c, \tau_{rc}\}^T \tag{3}$$

where the compliance matrix $[S]$ is valid for the plane stress case, and its elements S_{ij} are in general point functions; thus r and θ play different roles according to the material type.

2.2 Axisymmetrical Material. If the material is isotropic and homogeneous, the solution of equation (1) is [1]:

$$\begin{cases} \tau_{rc} = (-\rho\dot{\omega}\displaystyle\int_r^{r_e} u^3 h\,du)/(r^2 h) \\ \sigma_r = \sigma_c = 0 \end{cases} \tag{4}$$

It is easy to verify that equation (1) holds also in the case of axially orthotropic material, provided that the radial and circumferential directions are the material's principal directions ($S_{13} = S_{23} = 0$).

If the material is isotropic but nonhomogeneous, the solution is expressed again by equation (4) where the density ρ is moved inside the integral symbol.

This conclusion is immediately arrived at, by observing the structure of the differential equation (1) in [1].

The same solution holds also in the case of orthotropic axisymmetrical materials.

2.3 Orthotropic, Nonaxisymmetric, and Homogeneous Material. This is the case solved in [2], but limited to the constant thickness. The present authors did not succeed in finding a closed-form solution valid for whatever material. It is, though, possible to find such closed-form solution in the special case where:

$$\frac{1}{E_L} + \frac{1}{E_T} + \frac{2\nu_{LT}}{E_L} - \frac{1}{G_{LT}} = 0 \tag{5}$$

and where the disk's thickness does not vary with the radius.

A material satisfying condition (5) has particular properties, already studied by De St. Venant [4] and Wolf [5]; specifically its characteristic is to produce an axisymmetrical stress field under the centrifugal accelerations in disks of any thickness shape [6-8]. If (5) is satisfied, and the disk has constant thickness, it is easy to verify that the stress field coincides with the one expressed by equations (4) for isotropic materials. Since equations (4) satisfy the equilibrium equations (1), it is sufficient to verify that they also satisfy the compatibility equations. Since the stresses are functions only of the radius, while the S_{ij}'s depend only on θ, and moreover since $\sigma_r = \sigma_c = 0$, the compatibility equation becomes:

$$S_{23}(\tau_{cr}),_{rr} + \frac{1}{r^2}(S_{13}),_{\theta\theta}\tau_{cr} \\ + \frac{(2S_{23} - S_{13})}{r}(\tau_{cr}),_r + \\ - \frac{1}{r}(S_{33}),_\theta(\tau_{cr}),_r - \frac{1}{r^2}(S_{33}),_\theta\tau_{cr} = 0 \tag{2b}$$

Introducing equation (5) into the expressions of the elastic compliances S_{ij} with angle θ for orthotropic materials, it follows:

$$\begin{cases} S_{13} = S_{23} = \sin\theta\cdot\cos\theta\cdot\left(\dfrac{1}{E_L} - \dfrac{1}{E_T}\right) \\ S_{33} = \dfrac{1}{G_{LT}} \end{cases} \tag{6}$$

With equations (6) and their derivatives, equation (2*b*) becomes:

$$(\tau_{cr}),_{rr} + \frac{1}{r}(\tau_{cr}),_r - \frac{4}{r^2}\tau_{cr} = 0 \tag{7}$$

Now, differentiating the first of equation (4) and substituting into equation (7), it becomes apparent that the compatibility equation is satisfied. The displacements are obtained by integrating the known relationships:

$$\begin{cases} \epsilon_r = (u)_{,r} \\ \epsilon_c = \dfrac{u}{r} + \dfrac{1}{r}(v)_{,r} \\ \gamma_{rc} = (v)_{,r} - \dfrac{v}{r} + \dfrac{1}{r}(u)_{,\theta} \end{cases} \tag{8}$$

and therefore giving the following circumferential (v) and radial (u) displacements:

$$\begin{cases} u = \dfrac{\rho\dot{\omega}}{8} \sin 2\theta \left(\dfrac{1}{E_L} - \dfrac{1}{E_T}\right)\left(\dfrac{r_e^4}{r} + \dfrac{r^3}{3}\right) \\ v = \dfrac{\rho\dot{\omega}}{8} \cos 2\theta \left(\dfrac{1}{E_L} - \dfrac{1}{E_T}\right)\left(\dfrac{r_e^4}{r} - \dfrac{r^3}{3}\right) + \dfrac{1}{G_{LT}}\left(r^3 + \dfrac{r_e^4}{r}\right) \end{cases} \tag{9}$$

While the stresses are functions only of the radius r, displacements depend also on θ. If the material does not satisfy condition (5), or if the thickness is not constant, the present authors could not find a closed form solution.

A numerical approach, illustrated in the following section, shows that in that case the stress field is no longer axisymmetrical, and that the normal stresses (radial and circumferential) are no longer zero.

3 Numerical Approach

The present authors described in [9] and [10] a finite element procedure particularly suitable for studying rotating disks. Use was made of semi-analytical annular elements, in which the radial and circumferential displacements were expressed by third-degree polynomials along the radius and by truncated Fourier series along the angle. The advantage was that at the interfaces the continuity was attained both for displacements and for stresses/strains.

For evident reasons of symmetry, the study of orthotropic rotating disks requires the trigonometrical terms of even order, sin ($2K\theta$) and cos ($2K\theta$), and moreover only sines for the circumferential displacements and only cosines for the radial displacements.

This basic program was adapted to the present case, by introducing circumferential body forces and by expressing radial and circumferential displacements both with sinusoidal and with cosinusoidal terms.

The displacement field, made more general in this way, can nevertheless be considered as the superposition of:

(a) a symmetrical part, i.e., the part necessary if centrifugal forces only are present (symmetry is relative to the material's principal axes);

(b) an antisymmetrical part, i.e., the part that contains sinusoidal terms for the radial displacements and cosinusoidal terms for the circumferential displacements.

In the resulting stiffness matrix, however, the symmetrical and the anti-symmetrical parts result to be uncoupled, therefore the stress field in an orthotropic disk can be separately studied in these two parts. The meaning of this uncoupling is also that circumferential forces will produce a purely antisymmetric displacement field.

A more general examination of the structure of the stiffness matrix shows that all the harmonics of even order are uncoupled from the odd-order harmonics; since the virtual work of the circumferential acceleration forces is due to the cosines of order zero, i.e., of even order, the most general displacement field that is needed to study the stress field due to angular and to centrifugal accelerations is:

$$\begin{Bmatrix} u \\ v \end{Bmatrix} = \sum_{n=0}^{M} \begin{bmatrix} \cos 2n\theta & 0 \\ 0 & \sin 2n\theta \end{bmatrix} \begin{Bmatrix} u_{2n}^S \\ v_{2n}^S \end{Bmatrix} + \sum_{n=0}^{M} \begin{bmatrix} \sin 2n\theta & 0 \\ 0 & \cos 2n\theta \end{bmatrix} \begin{Bmatrix} u_{2n}^A \\ v_{2n}^A \end{Bmatrix} \tag{10}$$

where apex S indicates the symmetric part, and apex A indicates the antisymmetric part.

Figures 1 and 2 show results obtained with the computer program elaborated on these grounds.

Fig. 1(a) refers to an accelerating plane disk in an orthotropic material which satisfies equation (5):

$$E_L = 40{,}000\ \text{MN/m}^2 \qquad E_T = 5000\ \text{MN/m}^2$$
$$G_{LT} = 4210.53\ \text{MN/m}^2 \qquad \nu_{LT} = 0.25$$

and having central hole with diameter equal to one-fifth of the outer diameter. As analytically shown before, the tangential stresses do not vary with angle θ, and the normal stresses are zero.

Fig. 1(b) refers to a disk geometrically equal, but made of a material having a different value for G_{LT}, and specifically $G_{LT} = 2000\ \text{MN/m}^2$, thus no longer satisfying equation (5). It appears that stresses now vary circumferentially.

Figures 2(a) and (b) refer to conical disks, with outer and inner thickness ratio equal to about one-third, and made of the same materials, respectively, of Figures 1(a) and (b). Since the disk has not constant thickness, the stresses are in all cases functions of the angle θ.

These solutions are completely different from the solutions proposed in [2]. The present authors have reason, thanks to analytical and numerical crossconfirmation, to trust their own solution, and moreover have noticed that the solution [2] is characterized by these facts:

1. Radial stresses do not go to zero on the free edges.

2. Normal stresses do not go to zero when the material satisfies equation (5).

3. Shear stresses are independent of angle θ, and equal to the ones in isotropic disks (Fig. 2 in [2]), even if normal stresses are nonzero and functions of θ; this evidently conflicts with the second of equations (1), since the presence of the derivative $(\sigma_c)_{,\theta}$ implies that τ_{rc} must be different from the value it takes in the isotropic case, in which $(\sigma_c)_{,\theta} = 0$.

4 Conclusion

The stress field due to angular acceleration of a disk made of an orthotropic material is independent of the circumferential angle θ if:

1. the material is axisymmetrical orthotropic,
2. the material satisfies condition (5) and the thickness is constant.

In these cases, the tangential stresses take the same values characterizing a disk of equal geometry and density, but made of an isotropic material.

If the disk has variable thickness with the radius, or if the material's parameters do not satisfy equation (5), the stress field is not axisymmetrical and normal stresses are nonzero. The present authors were not able to find a closed-form solution for this case, and the solution proposed in [2] does not seem to be correct. Therefore a numerical method was evolved for this purpose.

In the case of flywheels for energy storage, the stresses induced by the angular acceleration are in general much lower than the stresses due to the centrifugal field. However there are cases, such as thin disks carring a rim of relevant mass or flywheels designed to deliver high powers for short times [12], in which tangential stresses may reach higher values.

The situation can be made dangerous by the fact that the shear strength of some materials, such as filament wound composites, is very low. In the design of such rotors, the stresses due to angular acceleration must be considered.

References

1 Deresiewicz, H., "Acceleration Stresses in Disks of Variable Thickness," ASME JOURNAL OF APPLIED MECHANICS, Sept. 1975, pp. 727–729.

2 Yella Reddy, T., Lakshminarayana H. V., et al., "Elastic Stresses in an Accelerating Circular Disk," ASME JOURNAL OF APPLIED MECHANICS, Sept. 1974, pp. 817–819.

3 Lekhnitskii, S. G., *Theory of Elasticity of an Anisotropic Elastic Body,"* Holden Day, New York, 1963.

4 De St. Venant, B., "Memoire Sur la Distribution de Elasticite," *Journal des Math. Pures et Appl*: S2, t8, 1863.

5 Wolf K., "Ausbreitung der Kraft in der Halbebene und im Halbraum bei Anisotropen Material," *Zeit. Angew Mech*, Vol. 15, No. 249, 1935.

6 Genta G., and Gola, M. M., "The Stress Distribution in Rotating Orthotropic Disks," ASME JOURNAL OF APPLIED MECHANICS, Sept. 1981, pp. 559–562.

7 Genta, G., Gola, M. M., and Gugliotta, A., "Axisymmetrical Stress States in Orthotropic Rotating Disks," *V. Congr. Naz. AIMETA*, Palermo, Oct. 1980.

8 Genta, G., Gola, M. M., and Gugliotta, A., "Remarks on the Stress State in Rotating Orthotropic Disks," 1980 Flywheel Tech. Symp., Scottsdale, Ariz. Oct. 1980.

9 Belingardi, G., Genta, G., and Gola, M. M., "Una Applicazione del Principio dei Lavori Virtuali al Calcolo di Dischi Rotanti in Materiale Anisotropo," *V. Congr. Naz. AIAS*, Bari, Sept. 1977.

10 Belingardi, G., Genta, G., and Gola, M. M., "A Study of the Stress Distribution in Rotating, Orthotropic Discs," *Composites*, Apr. 1979, pp. 77–80.

11 Lakshminarayana, H. V., and Srinath, H., "Elastic Stresses in Rotating Orthotropic Disks of Variable Thickness," *Journal of Strain Analysis*, Vol. 8, no. 3, 1973 pp. 176–181.

12 Beedham, E., "Flywheel Generators for the JET Experiment," *GEC Journal of Science and Tech.*, Vol. 46, no. 3, 1980, pp. 128–138.

Boundary Layer Over a Rotating Disk Sector

M. Ungarish[1], A. Solan[2], M. Toren[3]

Introduction

Flow over rotating surfaces is usually modeled in two distinct geometries: full-circle axisymmetric disks or relatively narrow blades (e.g., [1]). In this paper we consider the laminar incompressible boundary layer flow over a rotating plane sector of wide angle (but significantly less than a full circle) and we show that the flow changes from the leading to the trailing edge from that characteristic of thin narrow blades to that characteristic of axisymmetric disks. The present paper is closely related to our previous paper which considered a similar problem for a stationary sector in a rotating fluid [2].

Consider a solid surface in the form of a disk sector of angle $\theta_s < 2\pi$ and infinite radius rotating about an axis perpendicular to the disk plane with angular velocity Ω in a fluid at rest. Near the leading edge, the dominant velocity is in the circumferential direction, forming a Blasius-type boundary layer which generates a secondary, radial flow. With increasing angular distance the radial component becomes comparable to the circumferential component and one may expect the flow pattern to approach that of a Von Karman type boundary layer, such as for an axisymmetric disk. As the solid surface moves, its trailing edge leaves a wake which is seen by the leading edge at its next revolution, such that at the leading edge the flow is slightly disturbed and is not purely circumferential. In a coordinate system rotating with the sector the problem is stationary, with an outer angular velocity Ω. Following the same steps as in [2], we obtain for the r-scaled velocity components a system of equations that are similar, but not identical, to those of [2] (for details see [3]). As in [2], we first assume an undisturbed flow approaching the leading edge at $\theta = 0^-$ and solve for the boundary layer over the solid surface $0 < \theta < \theta_s$, and then we solve the wake in the region $\theta_s < \theta < 2\pi$ and estimate the perturbation it causes in the oncoming flow.

Flow Over the Solid Sector

Near the leading edge, $\theta << 1$, the equations admit a solution in a series of functions of a similarity variable $z\theta^{-1/2}$ multiplied by ascending the powers of θ [1, 2], where the leading term for v is Blasius. Such series can be used for small θ but strongly diverge from about $\theta \approx 0.6$. In the other limit, as $\theta >> 1$, one may expect the dependence on θ to decay, leading to a classical Von Karman flow. To study the flow over the full range of θ we transform the governing equation into momentum-integral form:

$$\frac{d}{d\theta}\int_0^\infty uv\,dz + \int_0^\infty [3u^2 - (v-1)^2]\,dz = -\left.\frac{\partial u}{\partial z}\right|_0 \quad (1)$$

$$\frac{d}{d\theta}\int_0^\infty (v^2 - v)\,dz + 4\int_0^\infty u(v-1)\,dz = -\left.\frac{\partial v}{\partial z}\right|_0 \quad (2)$$

and assume $u = f(\theta)\Phi(\eta)$, $v = \psi(\eta)$, $\eta = z/\delta(\theta)$, where u and v are the r-called radial and circumferential velocity components and δ is the boundary layer thickness. Once Φ and ψ are assumed, the problem is reduced to a system of two coupled ordinary differential equations for $\delta(\theta)$, $f(\theta)$. Note that for $\theta \to 0$ the equations admit an initial solution of the form $\delta = a\theta^{1/2}$, $f = b\theta$ where a, b are constants that depend on the choice of Φ, ψ. This is the momentum-integral representation of the initial similarity solution of Blasius type [1, 2].

Four pairs of functions representing u and v were tried: (A) $\Phi = \sin \pi\eta$, $\psi = \sin \pi\eta/2$; (B) $\Phi = \eta(1-\eta)^2$, $\psi = 1 - (1-\eta)^2$; (C) Φ and ψ from Von Karman's rotating disk solution; and (D) $u = f(\theta)\,\eta(1-\eta)^2 + (1/6)\,[\delta(\theta) - 4f(\theta)]\,\eta(1-\eta)^3$, $v = 1 - (3/2)(1-\eta)^2 + (1/2)(1-\eta)^3$. (Here the u profile changes with θ.)

Some results of the numerical solution with the four assumed profiles (A-D) are shown in Fig. 1. Also shown are the asymptotic values for small θ (Blasius profile for v and the corresponding similarity solution for u), and for large θ (θ-independent Karman solution). The limit values of $(\partial v/\partial z)_0$ and $(\partial u/\partial z)_0$ are also given in Table 1.

Table 1 Aymptotic values of velocity gradients at wall

	$\theta \to 0$		$\theta \to \infty$	
Profile	$\theta^{-1/2}u_z(0)$	$\theta^{1/2}v_z(0)$	$u_z(\infty)$	$v_z(\infty)$
A	0.297	0.328	0.317	0.596
B	0.337	0.365	0.450	0.622
C (Karman)	0.343	0.430	0.510	0.616
D	0.707	0.323	0.543	0.537
Blasius	0.665	0.332	–	–

[1]Faculty of Mechanical Engineering, Technion-Israel Institute of Technology, Haifa, Israel. Presently at Department of Mathematics, Massachusetts Institute of Technology, Cambridge, Mass. 02139.

[2]Professor, Faculty of Mechanical Engineering, Technion-Israel Institute of Technology, Haifa, Israel. During 1981-1982: Department of Mechanical and Aerospace Engineering, Rutgers University, New Brunswick, N.J. 08903. Mem. ASME.

[3]Adjunct Senior Lecturer, Faculty of Mechanical Engineering, Technion-Israel Institute of Technology, Haifa, Israel.

Manuscript received by ASME Applied Mechanics Division, October, 1981; final revision, March, 1982.

The situation can be made dangerous by the fact that the shear strength of some materials, such as filament wound composites, is very low. In the design of such rotors, the stresses due to angular acceleration must be considered.

References

1 Deresiewicz, H., "Acceleration Stresses in Disks of Variable Thickness," ASME JOURNAL OF APPLIED MECHANICS, Sept. 1975, pp. 727–729.

2 Yella Reddy, T., Lakshminarayana H. V., et al., "Elastic Stresses in an Accelerating Circular Disk," ASME JOURNAL OF APPLIED MECHANICS, Sept. 1974, pp. 817–819.

3 Lekhnitskii, S. G., *Theory of Elasticity of an Anisotropic Elastic Body,"* Holden Day, New York, 1963.

4 De St. Venant, B., "Memoire Sur la Distribution de Elasticite," *Journal des Math. Pures et Appl*: S2, t8, 1863.

5 Wolf K., "Ausbreitung der Kraft in der Halbebene und im Halbraum bei Anisotropen Material," *Zeit. Angew Mech*, Vol. 15, No. 249, 1935.

6 Genta G., and Gola, M. M., "The Stress Distribution in Rotating Orthotropic Disks," ASME JOURNAL OF APPLIED MECHANICS, Sept. 1981, pp. 559–562.

7 Genta, G., Gola, M. M., and Gugliotta, A., "Axisymmetrical Stress States in Orthotropic Rotating Disks," *V. Congr. Naz. AIMETA*, Palermo, Oct. 1980.

8 Genta, G., Gola, M. M., and Gugliotta, A., "Remarks on the Stress State in Rotating Orthotropic Disks," 1980 Flywheel Tech. Symp., Scottsdale, Ariz. Oct. 1980.

9 Belingardi, G., Genta, G., and Gola, M. M., "Una Applicazione del Principio dei Lavori Virtuali al Calcolo di Dischi Rotanti in Materiale Anisotropo," *V. Congr. Naz. AIAS*, Bari, Sept. 1977.

10 Belingardi, G., Genta, G., and Gola, M. M., "A Study of the Stress Distribution in Rotating, Orthotropic Discs," *Composites*, Apr. 1979, pp. 77–80.

11 Lakshminarayana, H. V., and Srinath, H., "Elastic Stresses in Rotating Orthotropic Disks of Variable Thickness," *Journal of Strain Analysis*, Vol. 8, no. 3, 1973 pp. 176–181.

12 Beedham, E., "Flywheel Generators for the JET Experiment," *GEC Journal of Science and Tech.*, Vol. 46, no. 3, 1980, pp. 128–138.

Boundary Layer Over a Rotating Disk Sector

M. Ungarish[1], A. Solan[2], M. Toren[3]

Introduction

Flow over rotating surfaces is usually modeled in two distinct geometries: full-circle axisymmetric disks or relatively narrow blades (e.g., [1]). In this paper we consider the laminar incompressible boundary layer flow over a rotating plane sector of wide angle (but significantly less than a full circle) and we show that the flow changes from the leading to the trailing edge from that characteristic of thin narrow blades to that characteristic of axisymmetric disks. The present paper is closely related to our previous paper which considered a similar problem for a stationary sector in a rotating fluid [2].

Consider a solid surface in the form of a disk sector of angle $\theta_s < 2\pi$ and infinite radius rotating about an axis perpendicular to the disk plane with angular velocity Ω in a fluid at rest. Near the leading edge, the dominant velocity is in the circumferential direction, forming a Blasius-type boundary layer which generates a secondary, radial flow. With increasing angular distance the radial component becomes comparable to the circumferential component and one may expect the flow pattern to approach that of a Von Karman type boundary layer, such as for an axisymmetric disk. As the solid surface moves, its trailing edge leaves a wake which is seen by the leading edge at its next revolution, such that at the leading edge the flow is slightly disturbed and is not purely circumferential. In a coordinate system rotating with the sector the problem is stationary, with an outer angular velocity Ω. Following the same steps as in [2], we obtain for the r-scaled velocity components a system of equations that are similar, but not identical, to those of [2] (for details see [3]). As in [2], we first assume an undisturbed flow approaching the leading edge at $\theta = 0^-$ and solve for the boundary layer over the solid surface $0 < \theta < \theta_s$, and then we solve the wake in the region $\theta_s < \theta < 2\pi$ and estimate the perturbation it causes in the oncoming flow.

Flow Over the Solid Sector

Near the leading edge, $\theta << 1$, the equations admit a solution in a series of functions of a similarity variable $z\theta^{-1/2}$ multiplied by ascending the powers of θ [1, 2], where the leading term for v is Blasius. Such series can be used for small θ but strongly diverge from about $\theta \approx 0.6$. In the other limit, as $\theta >> 1$, one may expect the dependence on θ to decay, leading to a classical Von Karman flow. To study the flow over the full range of θ we transform the governing equation into momentum-integral form:

$$\frac{d}{d\theta}\int_0^\infty uv\,dz + \int_0^\infty [3u^2 - (v-1)^2]\,dz = -\left.\frac{\partial u}{\partial z}\right|_0 \quad (1)$$

$$\frac{d}{d\theta}\int_0^\infty (v^2 - v)\,dz + 4\int_0^\infty u(v-1)\,dz = -\left.\frac{\partial v}{\partial z}\right|_0 \quad (2)$$

and assume $u = f(\theta)\Phi(\eta)$, $v = \psi(\eta)$, $\eta = z/\delta(\theta)$, where u and v are the r-called radial and circumferential velocity components and δ is the boundary layer thickness. Once Φ and ψ are assumed, the problem is reduced to a system of two coupled ordinary differential equations for $\delta(\theta)$, $f(\theta)$. Note that for $\theta \to 0$ the equations admit an initial solution of the form $\delta = a\theta^{1/2}$, $f = b\theta$ where a, b are constants that depend on the choice of Φ, ψ. This is the momentum-integral representation of the initial similarity solution of Blasius type [1, 2].

Four pairs of functions representing u and v were tried: (A) $\Phi = \sin \pi\eta$, $\psi = \sin \pi\eta/2$; (B) $\Phi = \eta(1-\eta)^2$, $\psi = 1 - (1-\eta)^2$; (C) Φ and ψ from Von Karman's rotating disk solution; and (D) $u = f(\theta)\,\eta(1-\eta)^2 + (1/6)\,[\delta(\theta) - 4f(\theta)]\,\eta(1-\eta)^3$, $v = 1 - (3/2)(1-\eta)^2 + (1/2)(1-\eta)^3$. (Here the u profile changes with θ.)

Some results of the numerical solution with the four assumed profiles (A-D) are shown in Fig. 1. Also shown are the asymptotic values for small θ (Blasius profile for v and the corresponding similarity solution for u), and for large θ (θ-independent Karman solution). The limit values of $(\partial v/\partial z)_0$ and $(\partial u/\partial z)_0$ are also given in Table 1.

Table 1 Aymptotic values of velocity gradients at wall

	$\theta \to 0$		$\theta \to \infty$	
Profile	$\theta^{-1/2}u_z(0)$	$\theta^{1/2}v_z(0)$	$u_z(\infty)$	$v_z(\infty)$
A	0.297	0.328	0.317	0.596
B	0.337	0.365	0.450	0.622
C (Karman)	0.343	0.430	0.510	0.616
D	0.707	0.323	0.543	0.537
Blasius	0.665	0.332	–	–

[1]Faculty of Mechanical Engineering, Technion-Israel Institute of Technology, Haifa, Israel. Presently at Department of Mathematics, Massachusetts Institute of Technology, Cambridge, Mass. 02139.

[2]Professor, Faculty of Mechanical Engineering, Technion-Israel Institute of Technology, Haifa, Israel. During 1981-1982: Department of Mechanical and Aerospace Engineering, Rutgers University, New Brunswick, N.J. 08903. Mem. ASME.

[3]Adjunct Senior Lecturer, Faculty of Mechanical Engineering, Technion-Israel Institute of Technology, Haifa, Israel.

Manuscript received by ASME Applied Mechanics Division, October, 1981; final revision, March, 1982.

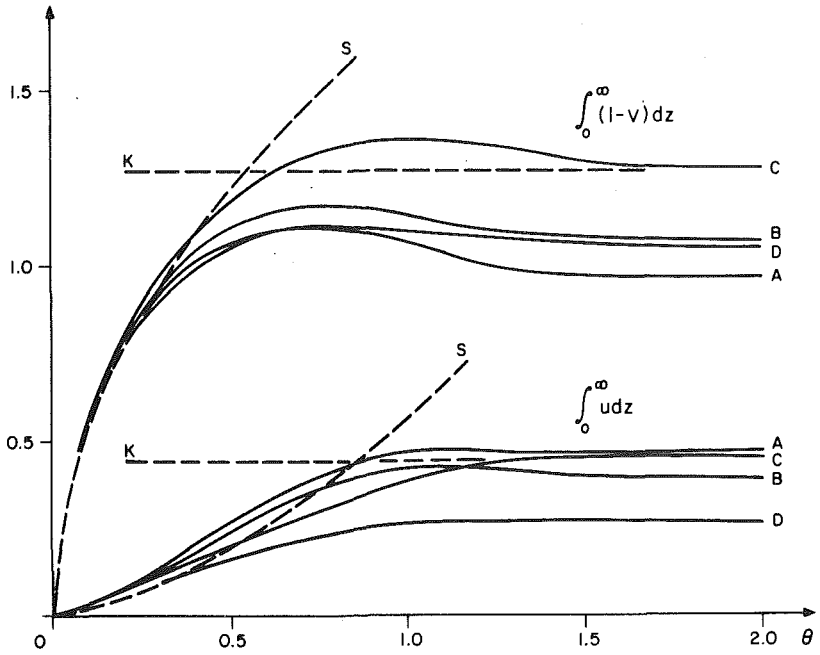

Fig. 1 Boundary layer over solid sector. *A–D* momentum-integral solution with assumed profiles *A–D*.
S **= leading term of initial similarity solution;** ***K*** **= von Karman axisymmetric solution**

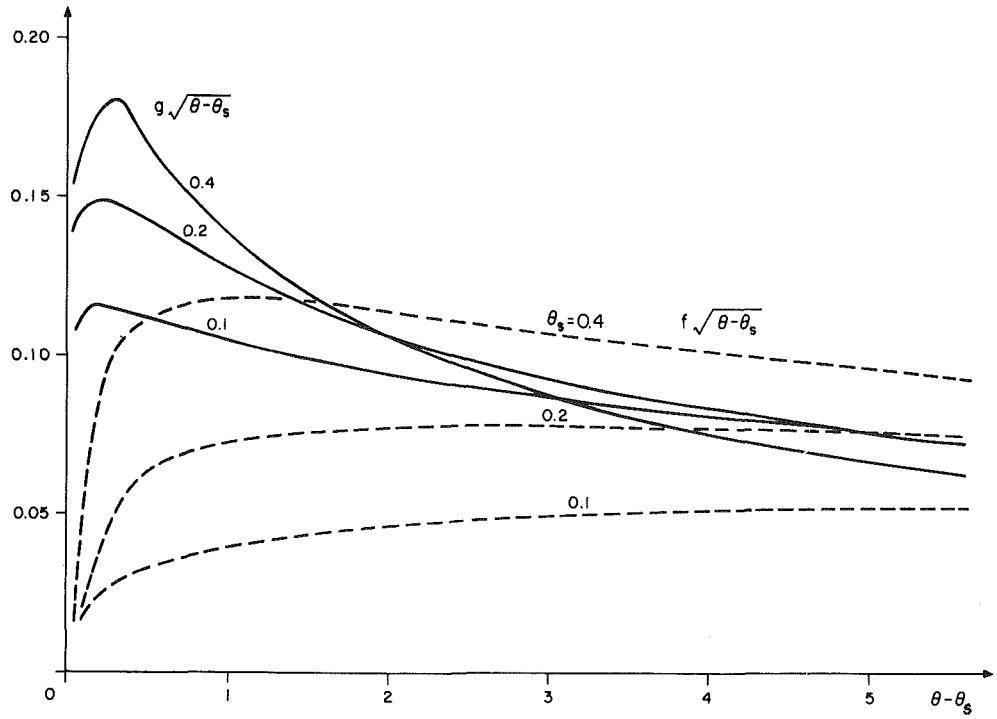

Fig. 2 Wake flow

All numerical results exhibit a Blasius-like behavior for small θ and tend to a constant value, like the Karman solution, for large θ. Although the values of the constants depend on the particular profile, the transition from the initial θ-dependent region to the final θ-independent region occurs for all profiles in the range $\theta \simeq 0.5$–1.2, i.e., within the first quadrant. Thus, it is interesting to note that although the problem is definitely nonaxisymmetric, the results tend after a relatively narrow angle to values that correspond to the axisymmetric solution. (A similar behavior was obtained in [2].)

In Fig. 1 all curves of $\int(1-v)\,dz$ show a slight overshoot. Obviously, the integral solution based on the Karman profile (*C*) approaches the "correct" asymptotic value for $\theta \to \infty$, but it is interesting to note that this solution also fits quite well the initial Blasius curve (*S*). Further, it appears that the continuous momentum-integral solution with profile *C* can be approximated fairly well by a simple intersection of the two

asymptotic curves (S and K). For the other profiles (A, B, D) the general behavior is quite similar to that of C, with the final values differing by not more than 30 percent. For $\int u dz$ the general trend of the four computed curves again approaches the asymptotic values, with slightly larger spread. (Recall that u is not imposed by the outer flow, but is induced by the rotational forces, thus its solution is more sensitive to the simplifying assumptions made in the integral solution.) Similar trends are observed in curves of u_{max}, $(\partial v/\partial z)_0$, and $(\partial u/\partial z)_0$ (not shown here, see reference [3]). In summary, all assumed profiles produce a solution that is Blasius-like for $\theta \to 0$ and Karman-like for $\theta \to \infty$, the transition occurring at about $\theta \simeq 0.5$–1.2. Quantitatively, profiles C and D are somewhat better than A or B. As an approximation, a simple intersection of the initial and final similarity solutions is quite adequate.

Referring back to the series solution for small θ [1], our attempt to compute it for finite θ showed that the series diverges from about $\theta \simeq 0.6$. From the momentum-integral solution we now see that this is approximately where the flow rather abruptly changes its behavior from the initial to the final form, which is accompanied by a change in the direction of the axial flow.

Flow in the Wake

In the preceding section it was assumed that the flow approaching the leading edge is undisturbed. To assess this assumption, we now attempt a momentum-integral solution of the wake flow, which will allow us to estimate the disturbance that the wake causes at the leading edge. The momentum-integral equations are again (1) and (2) with the right-hand terms equal to zero. The profiles assumed were $u = f(\theta)\Phi(\eta)$, $v = 1 + g(\theta)\Phi(\eta)$. Here we have now three unknowns; δ, f and g, since unlike the preceding problem, the scale of v is not imposed from the outside. This requires a third equation to close the system. It is convenient to use the azimuthal momentum equations evaluated at $z = 0$, with the assumed profiles. The initial conditions for the wake at $\theta = \theta_s^+$ are determined from the flow profiles of the boundary layer over the trailing edge of the solid sector at $\theta = \theta_s^-$, by requiring the integrals of $(v^2 - v)$, uv, and $(1 - v)$ to be continuous. These depend on the angle of the solid sector θ_s. Numerical solutions were obtained for small θ_s, for which the values of these integrals were approximated by the leading term (Blasius-like) of the boundary layer flow. The wake profile assumed was $\Phi(\eta) = e^{-\eta^2}$. (A different profile, $\Phi(\eta) = \frac{1}{2} + \frac{1}{2}\cos\pi\eta$, $(0 < \eta < 1)$ was also tried, with essentially similar results.)

The results for f and g versus $\theta - \theta_s$ (the angle from the trailing edge) are shown in Fig. 2. In particular, we can now estimate f and g, i.e., the scales of the two components of the velocity perturbation, induced by the wake at the leading edge, $\theta = 2\pi$. For example, for $\theta_s = 0.4$, the results are $u_{max}(\theta_s^-) = 0.112$, $f(\theta_s^+) = 0.136$, $g(\theta_s^+) = -0.868$, $f(2\pi) = 0.038$, and $g(2\pi) = -0.025$.[4] It can be seen that $g(\theta)$, which represents the v-component, decays rapidly and its value as it reaches the leading edge (at $\theta = 2\pi$) is small compared to the outer flow which is of order 0(1). The u-component, represented by $f(\theta)$, decays somewhat slower, and its value at the leading edge $f(2\pi)$, though small compared to unity, is not negligible compared to $u_{max}(\theta_s^-)$, i.e., it can be expected that the returning flow may have an effect on the boundary layer over the blade. Hence a detailed analysis of the interaction of the flow over the full circle appears to be a worthwhile topic for further study.

[4] For $\theta_s = 0.1$ the corresponding values are 0.028, 0.034, −0.868, 0.021, and −0.029.

Acknowledgment

This research was partially supported by the Fund for the Promotion of Research at Technion (Grant 030-278).

References

1 Morris, P. J., "The Three-Dimensional Boundary Layer on a Rotating Helical Blade," *Journal of Fluid Mechanics*, Vol. 112, 1981, pp. 283–296.

2 Toren, M., Solan, A., and Ungarish, M., "Rotating Flow over a Disk Sector," ASME JOURNAL OF APPLIED MECHANICS, Vol. 49, 1982, pp. 13–18.

3 Ungarish, M., Solan, A., and Toren, M., "Boundary Layer over a Rotating Disk Sector," Report TME-396, Faculty of Mechanical Engineering, Technion, Haifa, Israel, 1981.

Plastic Torsional Buckling of Thin-Walled Cylinders

D. W. A. Rees[1]

Introduction

In Donnell's original solution to the critical shear stress for which elastic torsional buckling occurs in short to moderately long thin-walled cylinders [1], it was found that no constraints were required to prevent longitudinal motion of the ends. The solution was shown to be in good agreement with the results of buckling experiments in which the ends of cylinders were either held perpendicular to the axis of twist (clamped) or were free to change their angle with the twisting action (hinged). The attempt that has been made to extend the elastic prediction to the torsional buckling stress for cylinders operating in the plastic range employs a plasticity reduction factor [2]. The extension implies that axial restraint is again unimportant when it is known that appreciable inelastic tensile strain will accumulate during plastic torsion when one end of the cylinder is completely unrestricted [3]. The second-order axial strain together with an associated diametral contraction prevent a state of pure shear from being achieved by the application of a shear stress alone. In combination with axial compression and internal pressure, which prevent second-order effects in a thin cylinder, a shear stress can sustain a state of pure shear which would be the proper starting point for an investigation into inelastic torsional buckling. However, the influence of diametral contraction on buckling is important only for the unrestrained condition when it is then equivalent to buckling by external overpressure [4]. An approximate state of pure shear can be achieved for a thin cylinder in which the accumulation of axial strain is prevented since diametral contraction is small and deformation before buckling occurs primarily by first-order shear. This approximation has been exploited for the present experimental investigation in which buckling is shown to depend on the degree to which axial extension is prevented.

Analysis

Second-order effects are due to the influence of the third deviatoric stress invariant J_3' in the yield criterion $f(J_2', J_3')$. The following form is assumed

$$f = J_2' + \frac{p}{Y} J_3' \tag{1}$$

where Y is the tensile yield stress and p is a constant which must lie in the range $-3 \le p \le 3/2$ to ensure convexity of the yield surface [5]. When the stress subspace is torsion τ, combined with tension σ, equation (1) becomes

[1] Department of Mechanical Engineering, Trinity College, Dublin 2, Ireland.

Manuscript received by ASME Applied Mechanics Division, May, 1981; final revision, February, 1982.

asymptotic curves (S and K). For the other profiles (A, B, D) the general behavior is quite similar to that of C, with the final values differing by not more than 30 percent. For $\int u dz$ the general trend of the four computed curves again approaches the asymptotic values, with slightly larger spread. (Recall that u is not imposed by the outer flow, but is induced by the rotational forces, thus its solution is more sensitive to the simplifying assumptions made in the integral solution.) Similar trends are observed in curves of u_{max}, $(\partial v/\partial z)_0$, and $(\partial u/\partial z)_0$ (not shown here, see reference [3]). In summary, all assumed profiles produce a solution that is Blasius-like for $\theta \to 0$ and Karman-like for $\theta \to \infty$, the transition occurring at about $\theta \simeq 0.5$–1.2. Quantitatively, profiles C and D are somewhat better than A or B. As an approximation, a simple intersection of the initial and final similarity solutions is quite adequate.

Referring back to the series solution for small θ [1], our attempt to compute it for finite θ showed that the series diverges from about $\theta \simeq 0.6$. From the momentum-integral solution we now see that this is approximately where the flow rather abruptly changes its behavior from the initial to the final form, which is accompanied by a change in the direction of the axial flow.

Flow in the Wake

In the preceding section it was assumed that the flow approaching the leading edge is undisturbed. To assess this assumption, we now attempt a momentum-integral solution of the wake flow, which will allow us to estimate the disturbance that the wake causes at the leading edge. The momentum-integral equations are again (1) and (2) with the right-hand terms equal to zero. The profiles assumed were $u = f(\theta)\Phi(\eta)$, $v = 1 + g(\theta)\Phi(\eta)$. Here we have now three unknowns; δ, f and g, since unlike the preceding problem, the scale of v is not imposed from the outside. This requires a third equation to close the system. It is convenient to use the azimuthal momentum equations evaluated at $z = 0$, with the assumed profiles. The initial conditions for the wake at $\theta = \theta_s^+$ are determined from the flow profiles of the boundary layer over the trailing edge of the solid sector at $\theta = \theta_s^-$, by requiring the integrals of $(v^2 - v)$, uv, and $(1 - v)$ to be continuous. These depend on the angle of the solid sector θ_s. Numerical solutions were obtained for small θ_s, for which the values of these integrals were approximated by the leading term (Blasius-like) of the boundary layer flow. The wake profile assumed was $\Phi(\eta) = e^{-\eta^2}$. (A different profile, $\Phi(\eta) = \frac{1}{2} + \frac{1}{2}\cos\pi\eta$, $(0 < \eta < 1)$ was also tried, with essentially similar results.)

The results for f and g versus $\theta - \theta_s$ (the angle from the trailing edge) are shown in Fig. 2. In particular, we can now estimate f and g, i.e., the scales of the two components of the velocity perturbation, induced by the wake at the leading edge, $\theta = 2\pi$. For example, for $\theta_s = 0.4$, the results are $u_{max}(\theta_s^-) = 0.112$, $f(\theta_s^+) = 0.136$, $g(\theta_s^+) = -0.868$, $f(2\pi) = 0.038$, and $g(2\pi) = -0.025$.[4] It can be seen that $g(\theta)$, which represents the v-component, decays rapidly and its value as it reaches the leading edge (at $\theta = 2\pi$) is small compared to the outer flow which is of order 0(1). The u-component, represented by $f(\theta)$, decays somewhat slower, and its value at the leading edge $f(2\pi)$, though small compared to unity, is not negligible compared to $u_{max}(\theta_s^-)$, i.e., it can be expected that the returning flow may have an effect on the boundary layer over the blade. Hence a detailed analysis of the interaction of the flow over the full circle appears to be a worthwhile topic for further study.

[4] For $\theta_s = 0.1$ the corresponding values are 0.028, 0.034, −0.868, 0.021, and −0.029.

Acknowledgment

This research was partially supported by the Fund for the Promotion of Research at Technion (Grant 030-278).

References

1 Morris, P. J., "The Three-Dimensional Boundary Layer on a Rotating Helical Blade," *Journal of Fluid Mechanics*, Vol. 112, 1981, pp. 283–296.

2 Toren, M., Solan, A., and Ungarish, M., "Rotating Flow over a Disk Sector," ASME JOURNAL OF APPLIED MECHANICS, Vol. 49, 1982, pp. 13–18.

3 Ungarish, M., Solan, A., and Toren, M., "Boundary Layer over a Rotating Disk Sector," Report TME-396, Faculty of Mechanical Engineering, Technion, Haifa, Israel, 1981.

Plastic Torsional Buckling of Thin-Walled Cylinders

D. W. A. Rees[1]

Introduction

In Donnell's original solution to the critical shear stress for which elastic torsional buckling occurs in short to moderately long thin-walled cylinders [1], it was found that no constraints were required to prevent longitudinal motion of the ends. The solution was shown to be in good agreement with the results of buckling experiments in which the ends of cylinders were either held perpendicular to the axis of twist (clamped) or were free to change their angle with the twisting action (hinged). The attempt that has been made to extend the elastic prediction to the torsional buckling stress for cylinders operating in the plastic range employs a plasticity reduction factor [2]. The extension implies that axial restraint is again unimportant when it is known that appreciable inelastic tensile strain will accumulate during plastic torsion when one end of the cylinder is completely unrestricted [3]. The second-order axial strain together with an associated diametral contraction prevent a state of pure shear from being achieved by the application of a shear stress alone. In combination with axial compression and internal pressure, which prevent second-order effects in a thin cylinder, a shear stress can sustain a state of pure shear which would be the proper starting point for an investigation into inelastic torsional buckling. However, the influence of diametral contraction on buckling is important only for the unrestrained condition when it is then equivalent to buckling by external overpressure [4]. An approximate state of pure shear can be achieved for a thin cylinder in which the accumulation of axial strain is prevented since diametral contraction is small and deformation before buckling occurs primarily by first-order shear. This approximation has been exploited for the present experimental investigation in which buckling is shown to depend on the degree to which axial extension is prevented.

Analysis

Second-order effects are due to the influence of the third deviatoric stress invariant J_3' in the yield criterion $f(J_2', J_3')$. The following form is assumed

$$f = J_2' + \frac{p}{Y} J_3' \tag{1}$$

where Y is the tensile yield stress and p is a constant which must lie in the range $-3 \le p \le 3/2$ to ensure convexity of the yield surface [5]. When the stress subspace is torsion τ, combined with tension σ, equation (1) becomes

[1] Department of Mechanical Engineering, Trinity College, Dublin 2, Ireland.

Manuscript received by ASME Applied Mechanics Division, May, 1981; final revision, February, 1982.

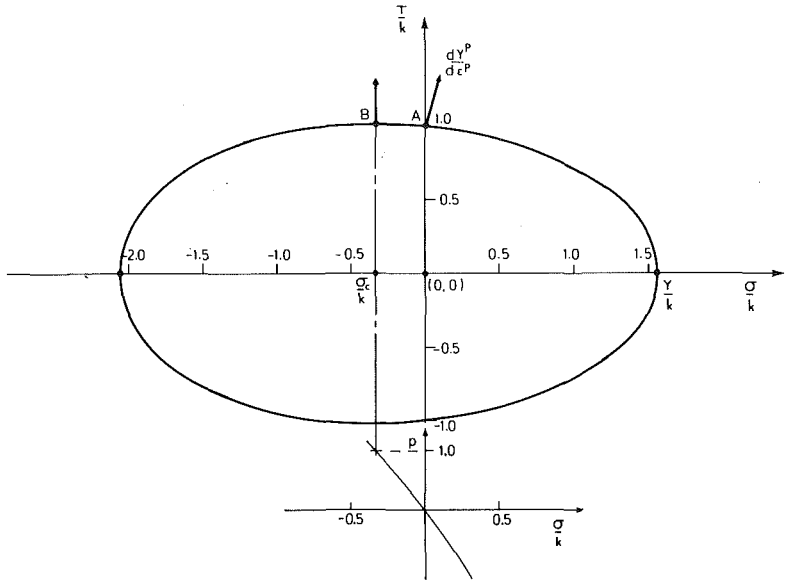

Fig. 1 Yield locus defined by equation (2) for $p = 1$ showing the direction of the plastic-strain increment vector $d\gamma^P/d\epsilon^P$ corresponding to unrestricted torsion at *A* and restricted torsion (pure shear) at *B*

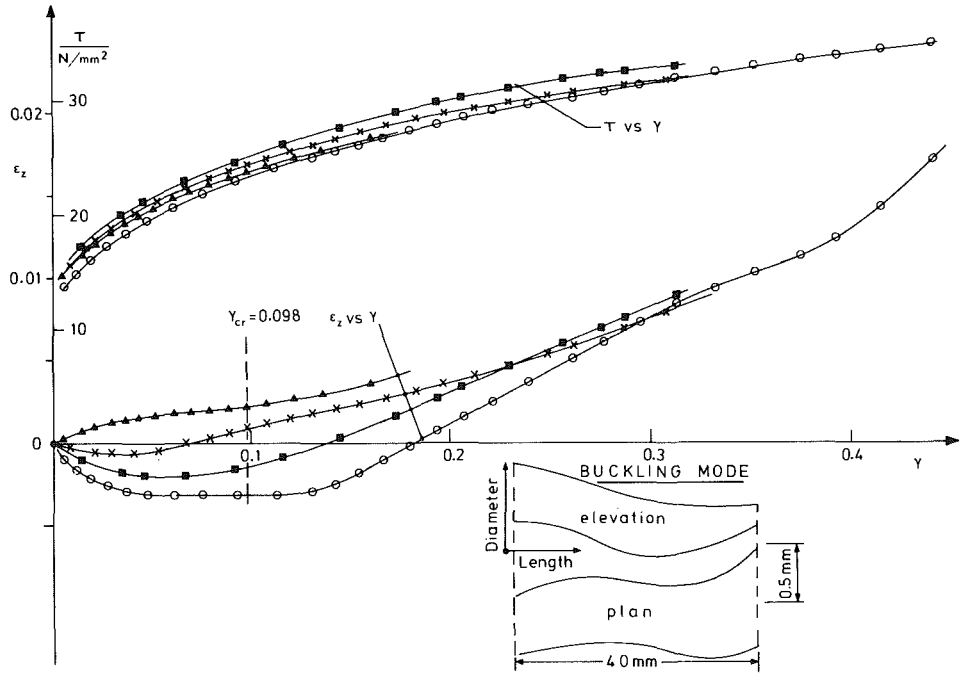

Fig. 2 Results from four torsion tests each approximating to a state of pure shear showing shear stress τ versus shear strain γ and axial strain ϵ_z versus shear strain. Typical buckling mode and critical shear strain prediction from equation (8) are also indicated. The plots include elastic strain components.

$$\left(\tau^2 + \frac{\sigma^2}{3}\right) + \frac{p\sigma}{3Y}(2\sigma^2/3 + \tau^2) = k^2 \tag{2}$$

where k is the shear yield stress in the absence of σ. Identifying equation (1) with the plastic potential f in the flow rule $d\epsilon_{ij}^p = d\lambda\, \partial f/\partial\sigma_{ij}$ the corresponding stress-incremental plastic strain relations are found

$$d\epsilon_z^p = \frac{d\lambda}{3}\left\{2\sigma + \frac{p}{Y}\left(\tau^2 + \frac{2\sigma^2}{3}\right)\right\}$$

$$d\epsilon_\theta^p = \frac{d\lambda}{3}\left\{-\sigma + \frac{p}{Y}\left(\tau^2 - \frac{\sigma^2}{3}\right)\right\}$$

$$d\epsilon_r^p = -\frac{d\lambda}{3}\left\{\sigma + \frac{p}{Y}\left(2\tau^2 + \frac{\sigma^2}{3}\right)\right\} \tag{3}$$

$$d\gamma^p = \frac{2d\lambda}{3}\left(3\tau + \frac{p}{Y}\sigma\tau\right)$$

where λ is a scalar multiplier and polar subscripts z, θ, and r refer to the axial, circumferential, and radial directions, respectively. The normal strain components preclude volume change since their sum $d\epsilon_{ii}^p = 0$ and, in an unrestricted cylinder where $\sigma = 0$, are proportional to $(d\gamma^p)^2$ which is the quadratic relationship that characterizes second-order strain [4]. The compressive stress σ_c necessary to suppress axial

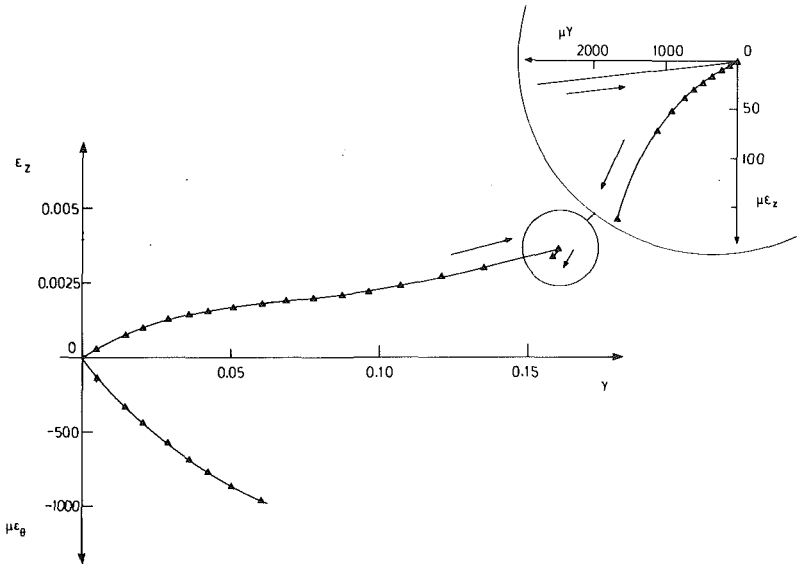

Fig. 3 Component strain paths for loading and unloading in torsion. Loading path shows increasing axial strain ϵ_z and small-order circumferential strain ϵ_θ with increasing shear strain γ. Unloading path shows small order of recovered axial and shear strains. The plots include elastic strain components.

strain is found by equating the first of equations (3) to zero. Then,

$$\sigma_c = \frac{3}{2}\left\{\frac{Y}{p} - \left(\frac{Y^2}{p^2} - \frac{2\tau^2}{3}\right)^{1/2}\right\}. \tag{4}$$

Now from equation (2) $Y^2 = 3k^2/(1+2p/9)$ which can be combined with equation (4) provided $\tau \approx k$ (i.e., $\sigma_c \approx 0$). The compressive stress is then found in dimensionless form

$$\frac{\sigma_c}{k} = \frac{q}{2p}\left(\frac{3}{q+2p}\right)^{1/2}\left\{1 - \left[1 - \frac{2p^2}{9} - \frac{4p^3}{81}\right]^{1/2}\right\}. \tag{5}$$

In the rule of isotropic hardening equation (5) implies that for deformation before buckling the axial strain is eliminated by a constant compressive stress. The solution, which is made possible by the unsymmetrical nature of the yield locus represented by equation (2), is shown graphically in Fig. 1 for the case $p = 1$. Due to the difference observed between tensile and compressive yield stresses the locus allows the normal direction of a plastic strain increment vector $d\gamma^p/d\epsilon^p$ to have an axial component at A (shown exaggerated) in the unrestricted case but not at B in the restricted case where $d\gamma^p/d\epsilon^p = \infty$.

Results and discussion

To ensure inelastic buckling, torsion tests were performed on cylinders manufactured from a commercial grade of pure aluminum to dimensions: 28.4 mm outside diameter, 25.4 mm inside diameter, and 75 mm parallel length. The compressive force necessary to restrict the second-order axial strain in annealed cylinders was found experimentally to be 500 g which was equivalent to the horizontal frictional force exerted on the end of the specimen by the bearing in the 100 kg sliding end of the torsion machine. Thus in this instance the free expansion of the cylinder during torsion is prevented by a frictional force that is the product of the coefficient of friction and the normal reaction at the sliding end of the test machine. This force produced a compressive stress of $\sigma_c = 3.8 \times 10^{-2}$ N/mm^2 and hence $\sigma_c/k = 0.0042$ for $k = 9.2$ N/mm^2 at the limit of elastic proportionality. Four tests were performed in which torques were applied incrementally through square-end registers and alignment plugs that maintained the condition of clamped ends during deformation. Axial and shear displacements on a 50-mm gauge length were continuously monitored from displacement transducers. Full details of the extensometer and preparation of the test specimen are given elsewhere [6].

Test results, presented in Fig. 2, shows good agreement between the shear stress-strain curves for each specimen. The magnitude of the axial strain when plotted against shear strain, shows that initially the compressive force was of the order necessary to suppress axial strain since in each curve $d\gamma/d\epsilon = \infty$. The degree of scatter indicates the sensitivity to slight differences in work-hardening characteristics where either tensile or compressive axial strain can result. Nevertheless a region of approximate isotropic hardening can be identified for plastic shear strains in the range $0 < \gamma < 0.12$. Thereafter an increasing compressive force would be necessary to maintain $d\gamma/d\epsilon = \infty$. If the ends were completely restrained the associated build up of compressive end force that would begin around $\gamma \approx 0.12$ would be expected to lead to buckling. It was at this point that buckling was judged to begin and this was confirmed from gauge diameter measurements that indicated ellipticity of the cross section (inset Fig. 2). In one test (Fig. 3) a post-yield strain gauge, bonded to the outer diameter in a circumferential direction, confirmed that a second-order diametral contraction was present which is consistent with the prediction of $d\epsilon_\theta^p$ from equation (3). The small magnitude of this strain (≈ 0.1 percent) corresponding to $\gamma \approx 6$ percent confirms that an approximate state of pure shear existed prior to buckling in each test.

To examine the recoverable strain in this specimen it was unloaded at a forward shear strain of 16 percent when the cross section was only slightly elliptical. The corresponding recovered axial and shear microstrains are plotted inset to enlarged scales in Fig. 3. Nonlinearity in this plot implies that the small order of recovered strain was composed of elastic and anelastic components. The former are found from the elastic constants for the material. However, in comparison with the forward strain, it is seen from Fig. 3 that recovered strain is negligibly small which confirms the irrecoverable second-order nature of axial strain resulting from a torsion test.

A prediction of the critical shear stress τ_{cr} at which elastic torsional buckling occurs is provided by Donnell's solution [1] to the associated equilibrium and compatibility equations.

For a hollow cylinder with clamped ends of length l, mean radius r, and wall thickness t that satisfies the inequality $50t/r < (l/r)^2 < 10r/t$ then

$$\tau_{cr} = \frac{0.82E}{(1-\nu^2)^{3/4}} \left(\frac{t}{r}\right)^{5/4} \left(\frac{r}{l}\right)^{1/2} \tag{6}$$

where E and ν are the usual elastic constants. Following Gerard [2], who extended the elastic solution to inelastic buckling through a plasticity reduction factor, $E/(1-\nu^2)^{3/4}$ is replaced by $E_s/(1-\nu_p^2)^{3/4}$ where $\nu_p = 1/2$ and E_s is the secant modulus at the point of buckling defined as

$$E_s = \bar{\sigma}_{cr}/\bar{\epsilon}^p_{cr} \tag{7}$$

where $\bar{\sigma}$ and $\bar{\epsilon}^p$ are the equivalent stress and equivalent plastic strain, respectively. Neglecting σ for simplicity, since $\sigma << \tau$, the isotropic hardening rule and equation (2) give $\bar{\sigma} = Y = \{3\tau^2/(1+2p/9)\}^{1/2}$. The work hypothesis for torsion, $W^p = \bar{\sigma}\bar{\epsilon}^p = \tau\gamma^p$ yields $\bar{\epsilon}^p = \{\gamma^2/3(1+2p/9)\}^{1/2}$. Equation (7) becomes $E_s = 3\ \tau_{cr}/(1+2p/9)\gamma^p_{cr}$ and substitution into equation (6) gives the critical plastic shear strain expression

$$\gamma^p_{cr} = \frac{26.5}{(9+2p)} \left(\frac{t}{r}\right)^{5/4} \left(\frac{r}{l}\right)^{1/2} \tag{8}$$

where constant $p \approx 0.015$ is estimated from $\sigma_c/k = 0.0042$ and the solution to equation (5), which is shown graphically in Fig. 1. Then from equation (8) $\gamma^p_{cr} = 0.098$ which is in reasonable agreement with the shear strain in Fig. 2 for which buckling was judged to begin. It is concluded that inelastic buckling under a condition of pure shear deformation is expressed quite well by equation (8). A solution for the unrestricted tube must account for the axial strain that accumulates from the start (3). The onset of buckling can then be detected either by direct diameter measurements or, possibly, from a change in the characteristic second-order dependence relation $\epsilon^p \alpha (\gamma^p)^2$. It is doubtful if the solution will depend wholly on specimen geometry in this case.

References

1 Donnell, L. H., "Stability of Thin Walled Tubes Under Torsion," NACA Rept. 479, 1933, pp. 1,24.

2 Gerard, G., "Compressive and Torsional Buckling of Thin Walled Tubes in the Yield Region," NACA Tech. Note 3726, Aug. 1956, pp. 1,35.

3 Billington, E. W., "Non-linear Mechanical Response of Various Metals II. Permanent Length Changes in Twisted Tubes," *J. Phys. D: Appl. Phys.*, Vol. 9, 1976, pp. 533,552.

4 Freudenthal. A. M., and Ronay, M., "Second-Order Effects in Dissipative Media," *Proc. Roy. Soc.*, Vol. 292A, 1966, pp. 14,50.

5 Betten, J., "Plastische Anisotropie und Bauschinger - Effekt; Allgemeine Formulierung und Vergleich mit Experimentell Ermittelten Fließorthkurven,, *Acta Mechanica*, Vol. 25, 1976, pp. 79,94.

6 Rees, D. W. A., "Biaxial Creep and Plastic Flow of Anistropic Aluminum," Ph.D. Thesis, CNAA (UK), 1976.

Axially Loaded Stiffened and Unstiffened Cylindrical Shells

I. Sheinman[1] and G. J. Simitses[2]

Introduction

In a previous publication [1], the present authors dealt with the same problem, but their objective was limited to finding critical conditions (limit point loads) only for imperfect stiffened cylinders under axial compression. The present paper extends the previous work and presents a solution methodology for finding not only the prelimit point behavior of the imperfect shell, but also its postlimit point behavior. This improvement leads to results, which explain very clearly the observed snapping phenomenon, including post-buckling strength and change of the mode during snapping.

The mathematical symbols and formulation are the same as those of [1]. Therefore, they will not be repeated, herein. There is one minor change in connection with boundary conditions, equation (15) of [1]. It is stated in [1] that the general computer program was written for the end conditions listed as equation (15). The program has been modified to allow $M_{xx} \neq 0$ at a boundary. This is done to accommodate the possibility of applying the constant axial stress resultant, $\bar{N}_{xx}$, not only through the reference surface (in which case $M_{xx} = 0$ for simply supported and free boundary conditions), but also as a uniform stress (in which case $M_{xx} = a_3 \bar{N}_{xx}$, for simply supported and free boundary conditions).

Solution Methodology

The solution methodology, employed herein, is an extension and modification of the one described in [1]. The changes allow one to obtain postlimit point equilibrium paths for every desired wave number, n (number of full waves around the circumference). The governing equations are expressed in terms of w (normal displacement component) and F (Airy stress function) (see [1]).

For finding prelimit point equilibrium positions, the applied load level, $\bar{N}_{xx}$, is taken as known, the linear ($n \equiv 0$)

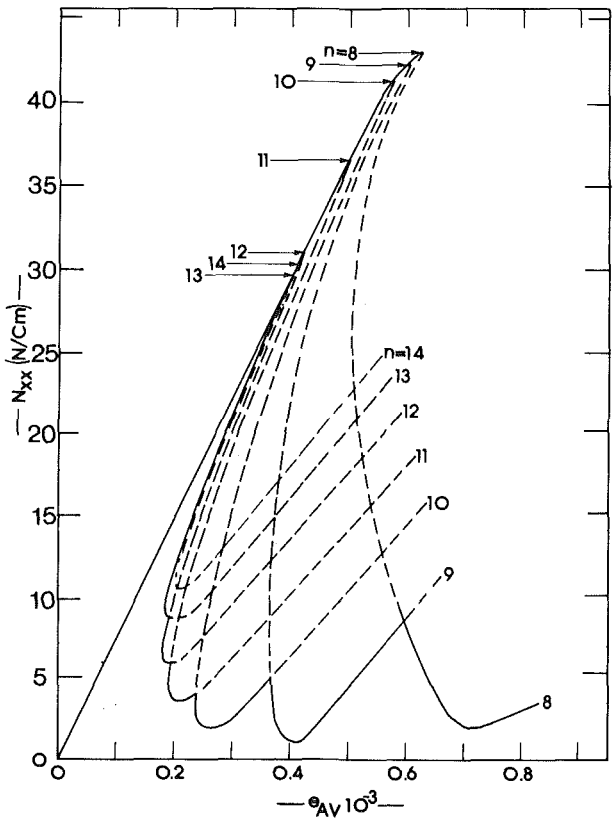

Fig. 1 Response characteristics of the unstiffened geometry ($\xi = 0.5$)

[1] Senior Lecturer, Department of Civil Engineering, Technion-Israel Institute of Technology, Haifa, Israel.

[2] Professor, School of Engineering Science and Mechanics, Georgia Institute of Technology, Atlanta, Ga. Mem. ASME.

Manuscript received by ASME Applied Mechanics Division, March, 1981; final revision, December, 1981.

For a hollow cylinder with clamped ends of length l, mean radius r, and wall thickness t that satisfies the inequality $50t/r < (l/r)^2 < 10r/t$ then

$$\tau_{cr} = \frac{0.82E}{(1-\nu^2)^{3/4}} \left(\frac{t}{r}\right)^{5/4} \left(\frac{r}{l}\right)^{1/2} \tag{6}$$

where E and ν are the usual elastic constants. Following Gerard [2], who extended the elastic solution to inelastic buckling through a plasticity reduction factor, $E/(1-\nu^2)^{3/4}$ is replaced by $E_s/(1-\nu_p^2)^{3/4}$ where $\nu_p = 1/2$ and E_s is the secant modulus at the point of buckling defined as

$$E_s = \bar{\sigma}_{cr}/\bar{\epsilon}^p_{cr} \tag{7}$$

where $\bar{\sigma}$ and $\bar{\epsilon}^p$ are the equivalent stress and equivalent plastic strain, respectively. Neglecting σ for simplicity, since $\sigma << \tau$, the isotropic hardening rule and equation (2) give $\bar{\sigma} = Y = \{3\tau^2/(1+2p/9)\}^{1/2}$. The work hypothesis for torsion, $W^p = \bar{\sigma}\bar{\epsilon}^p = \tau\gamma^p$ yields $\bar{\epsilon}^p = \{\gamma^2/3(1+2p/9)\}^{1/2}$. Equation (7) becomes $E_s = 3\ \tau_{cr}/(1+2p/9)\gamma^p_{cr}$ and substitution into equation (6) gives the critical plastic shear strain expression

$$\gamma^p_{cr} = \frac{26.5}{(9+2p)} \left(\frac{t}{r}\right)^{5/4} \left(\frac{r}{l}\right)^{1/2} \tag{8}$$

where constant $p \approx 0.015$ is estimated from $\sigma_c/k = 0.0042$ and the solution to equation (5), which is shown graphically in Fig. 1. Then from equation (8) $\gamma^p_{cr} = 0.098$ which is in reasonable agreement with the shear strain in Fig. 2 for which buckling was judged to begin. It is concluded that inelastic buckling under a condition of pure shear deformation is expressed quite well by equation (8). A solution for the unrestricted tube must account for the axial strain that accumulates from the start (3). The onset of buckling can then be detected either by direct diameter measurements or, possibly, from a change in the characteristic second-order dependence relation $\epsilon^p \alpha (\gamma^p)^2$. It is doubtful if the solution will depend wholly on specimen geometry in this case.

References

1 Donnell, L. H., "Stability of Thin Walled Tubes Under Torsion," NACA Rept. 479, 1933, pp. 1,24.

2 Gerard, G., "Compressive and Torsional Buckling of Thin Walled Tubes in the Yield Region," NACA Tech. Note 3726, Aug. 1956, pp. 1,35.

3 Billington, E. W., "Non-linear Mechanical Response of Various Metals II. Permanent Length Changes in Twisted Tubes," *J. Phys. D: Appl. Phys.*, Vol. 9, 1976, pp. 533,552.

4 Freudenthal. A. M., and Ronay, M., "Second-Order Effects in Dissipative Media," *Proc. Roy. Soc.*, Vol. 292A, 1966, pp. 14,50.

5 Betten, J., "Plastische Anisotropie und Bauschinger - Effekt; Allgemeine Formulierung und Vergleich mit Experimentell Ermittelten FließβOrthkurven,, *Acta Mechanica*, Vol. 25, 1976, pp. 79,94.

6 Rees, D. W. A., "Biaxial Creep and Plastic Flow of Anistropic Aluminum," Ph.D. Thesis, CNAA (UK), 1976.

Axially Loaded Stiffened and Unstiffened Cylindrical Shells

I. Sheinman[1] and G. J. Simitses[2]

Introduction

In a previous publication [1], the present authors dealt with the same problem, but their objective was limited to finding critical conditions (limit point loads) only for imperfect stiffened cylinders under axial compression. The present paper extends the previous work and presents a solution methodology for finding not only the prelimit point behavior of the imperfect shell, but also its postlimit point behavior. This improvement leads to results, which explain very clearly the observed snapping phenomenon, including post-buckling strength and change of the mode during snapping.

The mathematical symbols and formulation are the same as those of [1]. Therefore, they will not be repeated, herein. There is one minor change in connection with boundary conditions, equation (15) of [1]. It is stated in [1] that the general computer program was written for the end conditions listed as equation (15). The program has been modified to allow $M_{xx} \neq 0$ at a boundary. This is done to accommodate the possibility of applying the constant axial stress resultant, $\bar{N}_{xx}$, not only through the reference surface (in which case $M_{xx} = 0$ for simply supported and free boundary conditions), but also as a uniform stress (in which case $M_{xx} = a_3 \bar{N}_{xx}$, for simply supported and free boundary conditions).

Solution Methodology

The solution methodology, employed herein, is an extension and modification of the one described in [1]. The changes allow one to obtain postlimit point equilibrium paths for every desired wave number, n (number of full waves around the circumference). The governing equations are expressed in terms of w (normal displacement component) and F (Airy stress function) (see [1]).

For finding prelimit point equilibrium positions, the applied load level, $\bar{N}_{xx}$, is taken as known, the linear ($n \equiv 0$)

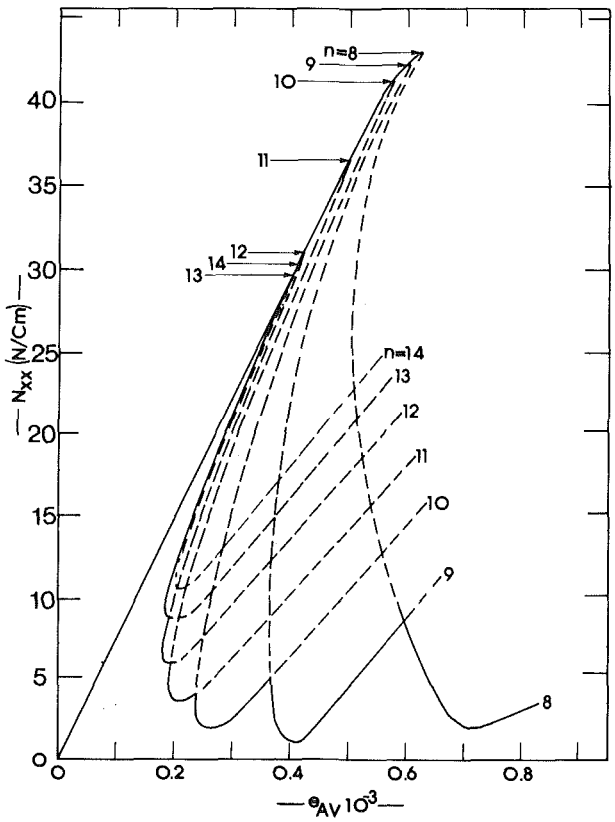

Fig. 1 Response characteristics of the unstiffened geometry ($\xi = 0.5$)

[1] Senior Lecturer, Department of Civil Engineering, Technion-Israel Institute of Technology, Haifa, Israel.

[2] Professor, School of Engineering Science and Mechanics, Georgia Institute of Technology, Atlanta, Ga. Mem. ASME.

Manuscript received by ASME Applied Mechanics Division, March, 1981; final revision, December, 1981.

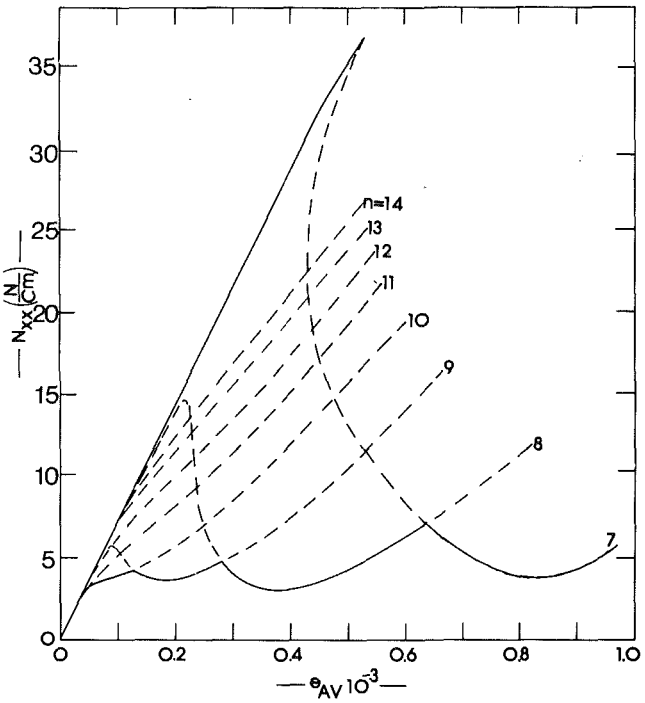

Fig. 2 Response characteristics of the unstiffened geometry ($\xi = 4.0$)

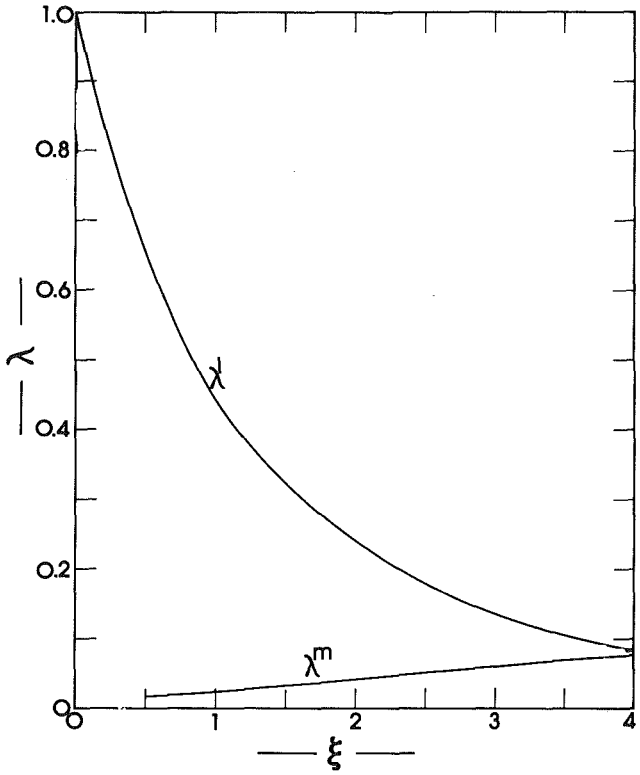

Fig. 3 Effect of imperfection parameter ξ, = on critical loads (unstiffened)

solution is taken to be the approximate solution, and the small corrections (in W_i's, and f_i's) are obtained through the solution of the linearized (with respect to the corrections) differential equations. Note that, in this range, the stiffness matrix is positive definite.

For finding postlimit point equilibrium positions (in a range of negative stiffness matrix), the numerical scheme is modified. The load parameter, $\bar{N}_{xx}$, is taken to be unknown, and one of the displacement parameters W_i replaces it as a known parameter. Great care must be exercised in choosing this W_i. This is done by observing how the various W_i's change with $\bar{N}_{xx}$ changes in the prelimit point range, and choosing a W_i that tends to increase in a smooth and continuous manner, but most importantly is one of the most dominant displacements terms. In this postlimit point range, the last converged, prelimit point solution is used as an initial estimate for finding the first postlimit point solution. From there on, in this same range, the previous solution is utilized as an initial estimate.

Numerical Results and Discussion

Numerical results are obtained for two geometries, one unstiffened and one stiffened. The geometry for both is described in the following:

(a) Unstiffened Cylindrical Shell.

R = 10.16 cm (4 in.); $h = 0.01016$ cm (0.004 in.);

L = 10.16 cm (4 in.);

E = 7.24×10^6 N/cm^2(10.5×10^6 psi); $\nu = 0.3$;

$$w^\circ(x,y) = h\xi\left[-\cos\frac{2\pi x}{L} + 0.1\sin\frac{\pi x}{L}\cos\frac{ny}{R}\right];$$

and *SS*-3 boundary conditions

(b) Ring and Stringer-Stiffened Cylindrical Shell

$R = 10.16$ cm (4 in.); $h = 0.1016$ cm (0.04 in.);

$L = 10.16$ cm (4 in.); $E = 7.24 \times 10^6$ N/cm^2(10.5×10^6 psi);

$\nu = 0.3$; $e_x = \pm 0.6096$ cm (0.24 in.);

$e_y = \pm 0.3048$ cm (0.12 in.); (+ for internal stiffeners)

$\lambda_{xx} = 0.910$; $\lambda_{yy} = 0.455$; $\rho_{xx} = 100$, $\rho_{yy} = 20$; with

$$w^\circ(x,y) = h\xi \sin\frac{\pi x}{L}\cos\frac{ny}{R};$$ *SS*-3 boundary conditions

Before discussing the results, a few more clarifying remarks about the geometry are needed. The unstiffened geometry is taken from [1] and [2]. Note that in these references only the critical load is given and not the complete behavior. The classical load for this case is 44.52 N/cm. Moreover, in this geometry, ξ is varied from zero to four, in order to study the effect of imperfection amplitude, ξ ($w^\circ_{max}/h = 1.1\xi$). Finally, results are generated for several values of n (number of circumferential full waves). This is needed to obtain a clear picture of the complete response, since the shell is very thin ($R/h = 1000$) and from experimental evidence the response is expected to be nonaxisymmetric.

The stiffened geometry corresponds to examples 14, 16, 18, 19, and 21 of [1]. Again, note that in [1], only limit-point loads were obtained. Moreover, in [1] *SS*-3 boundary conditions are used, but *SS*-3 with $M_{xx} = 0$. In the present work, *SS*-3 with $M_{xx} = a_3\bar{N}_{xx}$ boundary conditions are employed. The most important results are presented in graphical form. In the ensuing discussion, including conclusions, the statements are based on all generated data.

Figure 1 is a plot of $\bar{N}_{xx}$ versus average end shortening for $\xi = 0.5$ (unstiffened geometry). These data are generated for several values of full waves, n, around the circumference. From this figure, it is clear that, as the system is loaded quasi-statically from zero, the load-deflection curve is the same and independent of n. The limit-point load, $\bar{N}_{xx_{cr}}$ is definitely n-dependent. It is observed that the value of the total

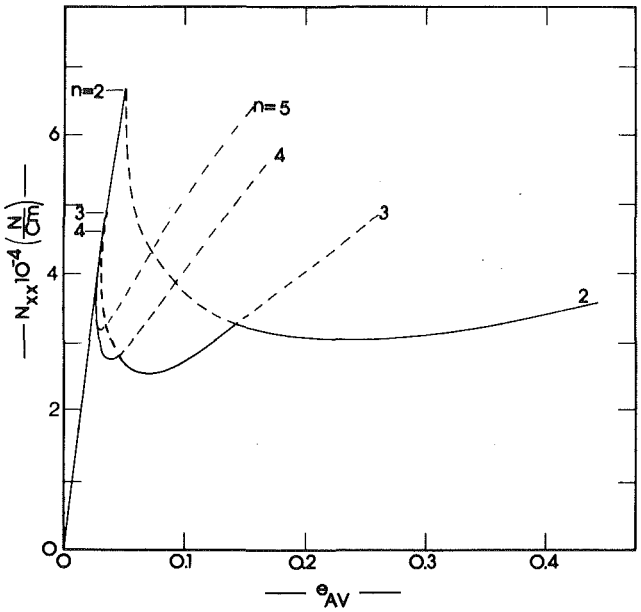

Fig. 4 Response characteristics of the externally stiffened geometry ($\xi = 1$)

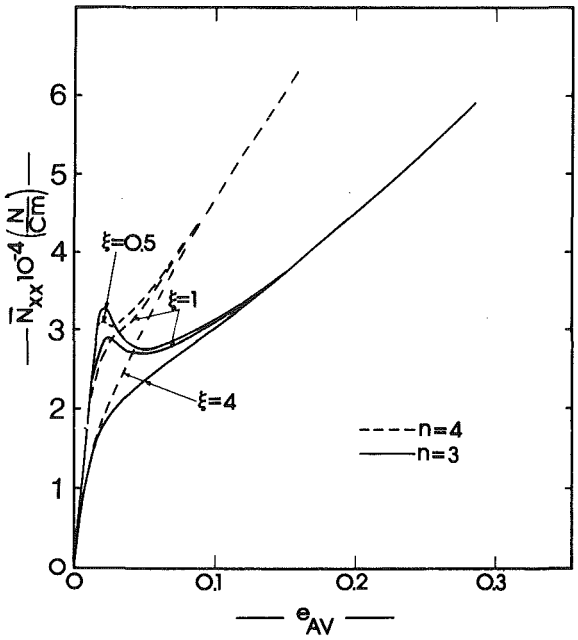

Fig. 5 Response characteristics of the internally stiffened geometry

potential corresponding to the lowest limit load (and associated n) is the smallest of all values corresponding to the same load and different n's (at an equilibrium position). For this value of ξ (which corresponds to $w^{\circ}_{\max} = 0.55\,h$), the limit point occurs at $\bar{N}_{xx} = 29.07$ N/cm [$\lambda^l = (\bar{N}_{xx_{cr}}/\bar{N}_{xx_{cl}}) = 0.653$]. In the postlimit point region, the unstable branch shows several changes from $n = 13$ to $n = 12$ to $n = 11$. These changes occur at the unstable portion of the curve. The change from $n = 11$ to $n = 10$, etc., to $n = 8$, occur at the stable portion of the curves. This implies that *if one can transverse the postlimit point branches*), he would move along the $n = 13$ (with decreasing load) curve, then along the $n = 12$ and $n = 11$ curves (with decreasing load). Then along the $n = 11$ curve, the system moves with increasing load until it reaches the $n = 10$ curve. Then it moves along the $n = 10$ curve until it intersects the $n = 9$ curve, etc. In reality, though, under dead weight loading, the system reaches the limit point, and then it snaps through (violent buckling) towards far stable equilibrium positions. During the snapping process, it is clear from this figure that the shell experiences changes in the circumferential mode, corresponding to various n-values.

For $\xi = 1$ and 2 the behavior is similar to that of Fig. 1. As ξ increases, changes in behavior take place, which behavior becomes similar to the one corresponding to $\xi = 4$, and plotted on Fig. 2. Note that for $n \geq 10$, there is no limit point instability, but for $n = 9$, 8, 7 there exist limit points. The response, though, as the system is loaded quasi-statically from zero, is along the $n = 10$ path and snapping takes place at the load level corresponding to unstable bifurcation (the $n = 10$ and $n = 9$ paths cross). Even for this imperfection amplitude ($\xi = 4$), violent buckling is predicted with change in circumferential mode. Finally, for the unstiffened geometry, Fig. 3 presents the effect of the imperfection amplitude, ξ on the limit point load, $\lambda^l = \bar{N}_{xx_{cr}}/\bar{N}_{xx_{cl}}$, and on the minimum load, $\lambda^m = \bar{N}_{xx_{\min}}/\bar{N}_{xx_{cl}}$. Note that $\bar{N}_{xx_{\min}}$ corresponds to the minimum equilibrium load in the postlimit point region. According to this figure, for $\xi \geq 4$, there is no possibility of snap-through buckling. The cylindrical shell simply deforms, with bending, from the initial application of the load.

For the stiffened geometries, the results are presented in Figs. 4 and 5. The classical values for $\bar{N}_{xx}$ are 61,680 N/cm for external positioning of the stiffeners and 34,660 N/cm for internal.

The results, for the external positioning of the stiffeners, are presented in Fig. 4. It is seen from this figure that the response is similar to the unstiffened geometry (Figs. 1 and 2), but the number of full waves is smaller (this is an effectively much thicker thin shell). Note that the lowest limit point corresponds to $n = 4$ for $\xi = 1$. Similar changes in behavior (to the unstiffened) are observed as ξ increases. Another important similarity to the unstiffened shell behavior, is that this configuration is also sensitive to initial geometric imperfections. When $\xi = 1$ (which means that $w^{\circ}_{\max} = h$), $\lambda^l = 0.77$ and when $\xi = 4$, $\lambda^l = 0.46$.

The results, for the internally stiffened configuration, are shown in Fig. 5. The dashed lines correspond to $n = 4$ and the solid lines to $n = 3$. Data for other n-values need not be shown on this figure. The three sets of curves correspond to $\xi = 0.5$, 1, and 4. Note that, for $\xi = 0.5$, limit-point instability occurs at $\bar{N}_{xx} = 31{,}170$ N/cm with $n = 4$. Also note that, during snap-through buckling, a change of circumferential mode occurs (to $n = 3$). The minimum equilibrium load in the postlimit point region corresponds to $n = 3$. On the other hand, for $\xi = 1$, snap-through buckling occurs at $\bar{N}_{xx} = 28{,}720$ N/cm because of the existence of an unstable bifurcated branch (corresponding to $n = 3$). The minimum equilibrium load, for $\xi = 1$ also, corresponding to $n = 3$. Finally, there is no possibility of a snapping phenomenon, for $\xi = 4$, neither through the existence of a limit point nor through the existence of an unstable bifurcated branch. It is observed that this configuration is not very sensitive to initial geometric imperfections. For $\xi = 0.5$, $\lambda^l = 0.9$ and for $\xi = 1.0$. $\lambda^l = 0.84$. This is attributed to two reasons: (*a*) internally stiffened configurations are less sensitive than externally stiffened ones and stiffened configurations are less sensitive than unstiffened ones, and (*b*) for this reported case, *SS*-3 with $M_{xx} = a_3 \bar{N}_{xx}$ boundary conditions are used, which has a stabilizing effect. The primary reason, though, is the former.

Acknowledgments

This work was performed under Contract No. F33615-79-C-3221 with the U.S.A.F., Aeronautical Systems Division (AFSC), Wright-Patterson Air Force Base. The financial

support provided by the United States Air Force is gratefully acknowledged.

References

1 Sheinman, I., and Simitses, G. J., "Buckling Analysis of Geometrically Imperfect Stiffened Cylinders under Axial Compression," *AIAA J.*, Vol. 15, No. 3, Mar. 1977, pp. 374-382.

2 Arbocz, J., and Sechler, E. E., "On the Buckling of Axially Compressed Imperfect Cylindrical Shells," ASME JOURNAL OF APPLIED MECHANICS, Vol. 41, Sept. 1974, pp. 737-743.

Coupled Flexural Torsional Vibration of an Eccentrically Stretched Strip

S. Suryanarayan[1] and A. Joshi[1]

Introduction

Flat rectangular strips subjected to an eccentric axial load exhibit coupled flexural torsional modes of vibrations. The coupling between the flexural and torsional modes depends on the axial load and the amount of eccentricity. Their effect is to increase the torsional frequency and decrease the flexural frequency.

Figure 1 shows a flat rectangular strip of uniform thickness on simple supports and stretched by an eccentric axial load which results in a linearly varying axial stress distribution. When (L/b) is sufficiently large, fibers normal to the z-axis can be assumed to remain straight and the transverse displacement "v" in the y-direction of any point on the strip can be given in terms of v_0, the lateral displacement of the cross section as a whole, and θ, its rotation, as $v_0 + x\theta$. The lateral force in the y-direction on an elemental fiber of length "dz" and area tdx, produced by the axial stress σ_{zz} is σ_{zz} $(\partial^2 v/\partial z^2)$ $tdxdz$. Integrating this term over the cross section, the net transverse force and torque which couple the transverse y-flexural and torsional motion, can be obtained. Taking these into account besides inertia, Euler bending, and St. Venant torsion of the strip, the governing equations can be written as,

$$-\mathrm{E}I_{xx}\frac{\partial^4 v_0}{\partial z^4} + N_z\frac{\partial^2 v_0}{\partial z^2} + N_z e\frac{\partial^2 \theta}{\partial z^2} - \rho A\frac{\partial^2 v_0}{\partial \tau^2} = 0 \qquad (1)$$

$$GJ\frac{\partial^2 \theta}{\partial z^2} + N_z e\frac{\partial^2 v_0}{\partial z^2} + \frac{N_z I_{yy}}{A}\frac{\partial^2 \theta}{\partial z^2} - \rho I_{yy}\frac{\partial^2 \theta}{\partial \tau^2} = 0$$

Where E is the Young's modulus, G the shear modulus, A the area of cross section of the strip, I_{xx} and I_{yy} the second moments of the area about the x and y axes, respectively, J the Saint Venant torsional stiffness, N_z the net axial load, e its eccentricity, ρ the density, and τ the time variable.

Solution and Discussion

For simply supported edges, v_0 and θ can be assumed to vary sinusoidally along the span and the governing equation (1) simplified to

$$\begin{bmatrix} (\lambda - \lambda_{f_0}) & -\bar{e} \\ -12\bar{e} & (\lambda - \lambda_{t_0}) \end{bmatrix} \begin{Bmatrix} \bar{v}_0/b \\ \bar{\theta} \end{Bmatrix} = 0 \qquad (2)$$

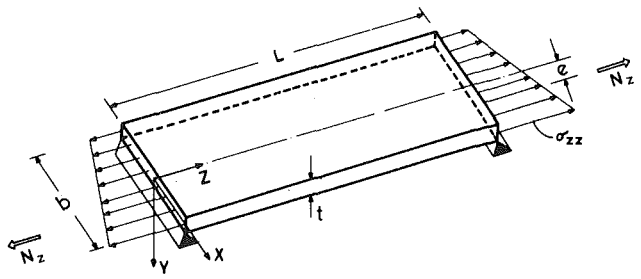

Fig. 1 An eccentrically loaded thin strip on simple supports

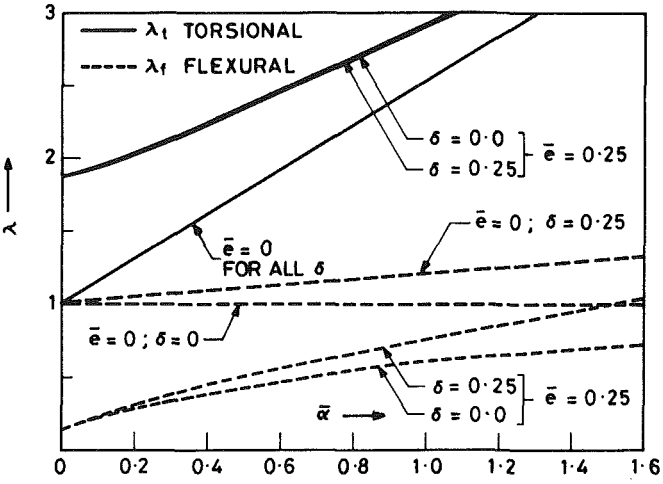

(a) λ VERSUS $\bar{\alpha}$ FOR $\delta = 0 ; 0{\cdot}25$ AND $\bar{e} = 0 ; 0{\cdot}25$

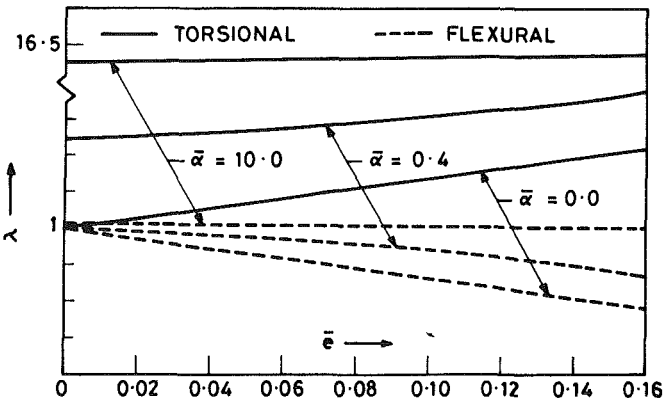

(b) λ VERSUS $\bar{e}$ FOR $\bar{\alpha} = 0 ; 0{\cdot}4 ; 10$ AND $\delta = 0{\cdot}0025$

Fig. 2 Variation of λ with $\bar{e}$ and $\bar{\alpha}$

where $\lambda(=\rho k^2 L^2/\mathrm{E}m^2\pi^2\epsilon_0)$ is the dimensionless frequency parameter, ϵ_0 the average axial strain, $\bar{e}$ $(=e/b)$ the eccentricity ratio, k the circular frequency, m the wave number and $\bar{v}_0$ and $\bar{\theta}$ are the maximum amplitudes of v_0 and θ, respectively. λ_{f_0} and λ_{t_0} are the values of λ for uncoupled flexural and torsional vibration, respectively, when the eccentricity is zero and can be expressed as

$$\lambda_{f_0} = 1 + \frac{m^2\pi^2\mathrm{E}I_{xx}}{N_z L^2} = 1 + \frac{\pi^2\bar{\alpha}\delta}{12}; \quad \lambda_{t_0}$$

$$= 1 + \frac{GJA}{N_z I_{yy}} = 1 + \frac{2\bar{\alpha}}{1+\mu} \qquad (3)$$

where μ is the Poisson's ratio of the material, $\delta(=(mb/L)^2)$ is a slenderness parameter and $\bar{\alpha}$ $(=(t/b)^2/\epsilon_0)$ is a dimensionless parameter representing the relative significance of

[1]Assistant Professor and Research Scholar, respectively, Department of Aeronautical Engineering, Indian Institute of Technology, Bombay, India.

Manuscript received by ASME Applied Mechanics Division, March, 1981; final revision, March, 1982.

support provided by the United States Air Force is gratefully acknowledged.

References

1 Sheinman, I., and Simitses, G. J., "Buckling Analysis of Geometrically Imperfect Stiffened Cylinders under Axial Compression," *AIAA J.*, Vol. 15, No. 3, Mar. 1977, pp. 374–382.

2 Arbocz, J., and Sechler, E. E., "On the Buckling of Axially Compressed Imperfect Cylindrical Shells," ASME JOURNAL OF APPLIED MECHANICS, Vol. 41, Sept. 1974, pp. 737–743.

Coupled Flexural Torsional Vibration of an Eccentrically Stretched Strip

S. Suryanarayan[1] and A. Joshi[1]

Introduction

Flat rectangular strips subjected to an eccentric axial load exhibit coupled flexural torsional modes of vibrations. The coupling between the flexural and torsional modes depends on the axial load and the amount of eccentricity. Their effect is to increase the torsional frequency and decrease the flexural frequency.

Figure 1 shows a flat rectangular strip of uniform thickness on simple supports and stretched by an eccentric axial load which results in a linearly varying axial stress distribution. When (L/b) is sufficiently large, fibers normal to the z-axis can be assumed to remain straight and the transverse displacement "v" in the y-direction of any point on the strip can be given in terms of v_0, the lateral displacement of the cross section as a whole, and θ, its rotation, as $v_0 + x\theta$. The lateral force in the y-direction on an elemental fiber of length "dz" and area tdx, produced by the axial stress σ_{zz} is σ_{zz} $(\partial^2 v/\partial z^2)$ $tdxdz$. Integrating this term over the cross section, the net transverse force and torque which couple the transverse y-flexural and torsional motion, can be obtained. Taking these into account besides inertia, Euler bending, and St. Venant torsion of the strip, the governing equations can be written as,

$$-\mathrm{E}I_{xx}\frac{\partial^4 v_0}{\partial z^4} + N_z\frac{\partial^2 v_0}{\partial z^2} + N_z e\frac{\partial^2 \theta}{\partial z^2} - \rho A\frac{\partial^2 v_0}{\partial \tau^2} = 0 \qquad (1)$$

$$GJ\frac{\partial^2 \theta}{\partial z^2} + N_z e\frac{\partial^2 v_0}{\partial z^2} + \frac{N_z I_{yy}}{A}\frac{\partial^2 \theta}{\partial z^2} - \rho I_{yy}\frac{\partial^2 \theta}{\partial \tau^2} = 0$$

Where E is the Young's modulus, G the shear modulus, A the area of cross section of the strip, I_{xx} and I_{yy} the second moments of the area about the x and y axes, respectively, J the Saint Venant torsional stiffness, N_z the net axial load, e its eccentricity, ρ the density, and τ the time variable.

Solution and Discussion

For simply supported edges, v_0 and θ can be assumed to vary sinusoidally along the span and the governing equation (1) simplified to

$$\begin{bmatrix} (\lambda - \lambda_{f_0}) & -\bar{e} \\ -12\bar{e} & (\lambda - \lambda_{t_0}) \end{bmatrix} \begin{Bmatrix} \bar{v}_0/b \\ \bar{\theta} \end{Bmatrix} = 0 \qquad (2)$$

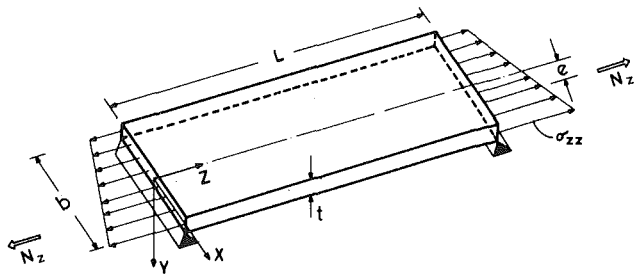

Fig. 1 An eccentrically loaded thin strip on simple supports

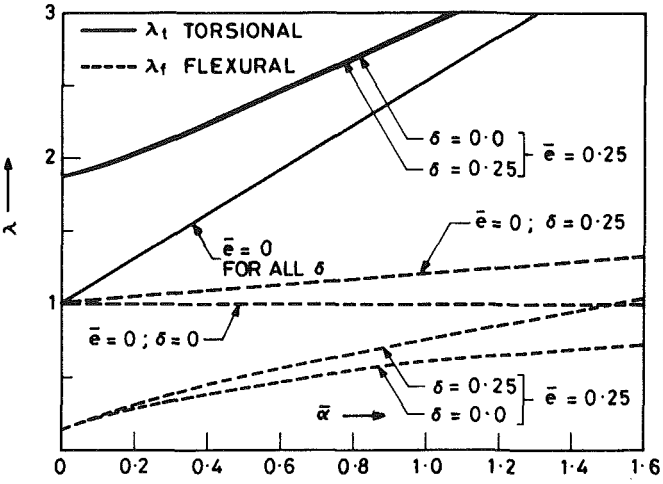

(a) λ VERSUS $\bar{\alpha}$ FOR $\delta = 0 ; 0{\cdot}25$ AND $\bar{e} = 0 ; 0{\cdot}25$

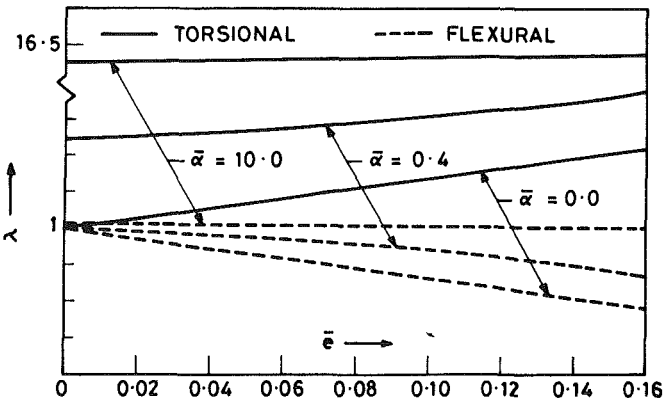

(b) λ VERSUS $\bar{e}$ FOR $\bar{\alpha} = 0 ; 0{\cdot}4 ; 10$ AND $\delta = 0{\cdot}0025$

Fig. 2 Variation of λ with $\bar{e}$ and $\bar{\alpha}$

where $\lambda(=\rho k^2 L^2/\mathrm{E}m^2\pi^2\epsilon_0)$ is the dimensionless frequency parameter, ϵ_0 the average axial strain, $\bar{e}$ $(=e/b)$ the eccentricity ratio, k the circular frequency, m the wave number and $\bar{v}_0$ and $\bar{\theta}$ are the maximum amplitudes of v_0 and θ, respectively. λ_{f_0} and λ_{t_0} are the values of λ for uncoupled flexural and torsional vibration, respectively, when the eccentricity is zero and can be expressed as

$$\lambda_{f_0} = 1 + \frac{m^2\pi^2 \mathrm{E}I_{xx}}{N_z L^2} = 1 + \frac{\pi^2\bar{\alpha}\delta}{12}; \quad \lambda_{t_0} = 1 + \frac{GJA}{N_z I_{yy}} = 1 + \frac{2\bar{\alpha}}{1+\mu} \qquad (3)$$

where μ is the Poisson's ratio of the material, $\delta(=(mb/L)^2)$ is a slenderness parameter and $\bar{\alpha}$ $(=(t/b)^2/\epsilon_0)$ is a dimensionless parameter representing the relative significance of

[1]Assistant Professor and Research Scholar, respectively, Department of Aeronautical Engineering, Indian Institute of Technology, Bombay, India.

Manuscript received by ASME Applied Mechanics Division, March, 1981; final revision, March, 1982.

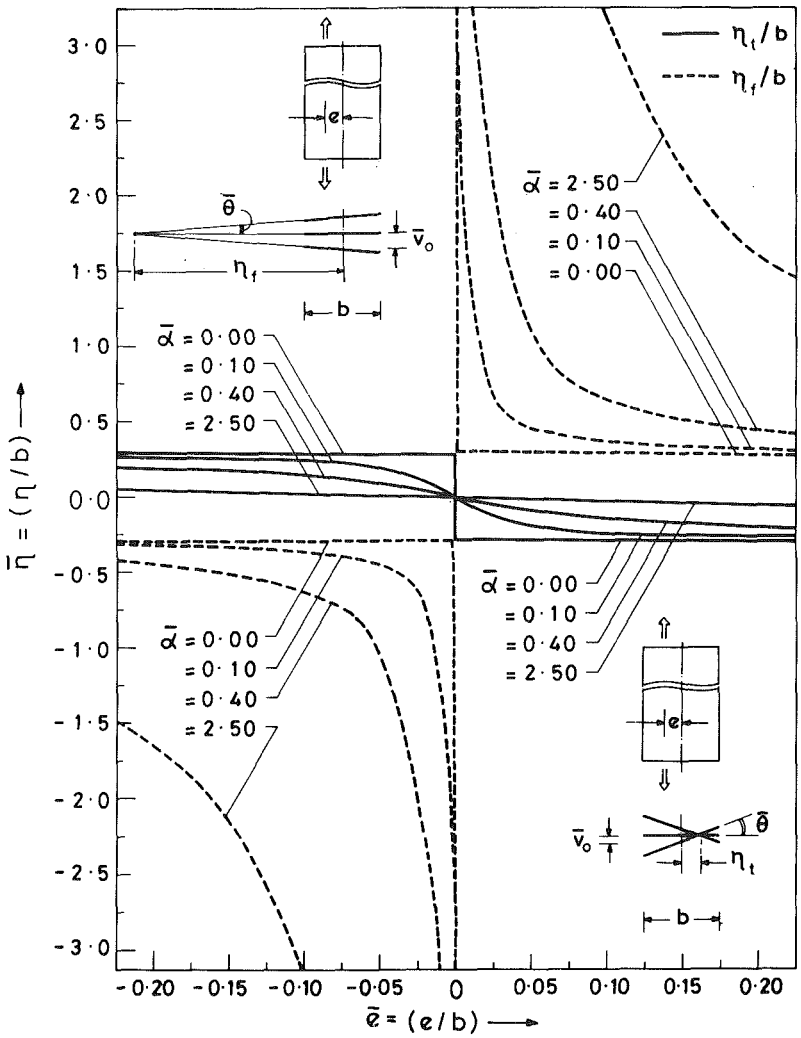

Fig. 3 Positions of the axes of rotation for the coupled transverse lateral and torsional modes, $\bar{\eta}$ versus eccentricity parameter $\bar{e}$ for $\bar{\alpha}=0$, 0.01, 0.4, and 2.5.

thickness effects (Euler bending and St. Venant torsion) with respect to the membrane effects produced by axial tension. The characteristic equation for λ can be obtained by setting the determinant of the square matrix in equation (2) to zero. This is quadratic in λ and can be solved for various values of $\bar{\alpha}$, δ, and $\bar{e}$. The two roots of λ in general represent a predominantly torsional (λ_t) and a predominantly flexural (λ_f) mode.

For the case of zero eccentricity, the vibration modes are uncoupled and the two roots are λ_{f_0} and λ_{t_0} respectively. Their variation with $\bar{\alpha}$ is given by the curves in Fig. 2 for which $\bar{e}$ is zero. When $\bar{\alpha}$ is zero we have, $\lambda_{t_0} = \lambda_{f_0} = 1$, which corresponds to the strip vibrating like a membrane. When the average axial strain ϵ_0 (or the tension in the strip) tends to zero, i.e., $\bar{\alpha} \to \infty$, we get $\lambda_{t_0} = 2\bar{\alpha}/(1+\mu)$ and $\lambda_{f_0} = \pi^2\bar{\alpha}\delta/12$, which are the St. Venant torsion and Euler bending frequency values of λ.

The effect of a typical eccentricity ratio $\bar{e}$ of 0.25 is also shown in Fig. 2. The effect of eccentricity is to raise the torsional frequency and to lower the flexural frequency. This effect is a maximum when the strip is a membrane ($\bar{\alpha}=0$) and reduces as thickness effects represented by nonzero values of $\bar{\alpha}$ become significant. It can also be seen that the slenderness parameter δ has got a significant effect on the flexural frequency but its effect on the torsional frequencies is felt only when $\bar{e} \neq 0$ and is marginal. For the case of $\bar{\alpha}=0$, the solution for the coupled frequenceis can be obtained as

$$\lambda_t = 1 + 2\sqrt{3}\bar{e}; \quad \lambda_f = 1 - 2\sqrt{3}\bar{e}. \tag{4}$$

For nonzero values of $\bar{\alpha}$ the solution of λ_t and λ_f can be written as

$$\lambda_t = 1 + \frac{2\bar{\alpha}}{1+\mu} + C; \quad \lambda_f = 1 + \frac{\pi^2\delta\bar{\alpha}}{12} - C. \tag{5}$$

where C is a correction factor given by,

$$C = \frac{\gamma}{2}\left[\left(1 + \frac{48(\bar{e})^2}{\gamma^2}\right)^{1/2} - 1\right]; \quad \gamma = \bar{\alpha}\left(\frac{2}{(1+\mu)} - \frac{\pi^2\delta}{12}\right) \tag{6}$$

It may be noted that for $\bar{\alpha}=0$, $C = 2\sqrt{3}\bar{e}$ as in equation (4). This explains the linear variation of λ with $\bar{e}$ in Fig. 2. The reduction in λ_f is same as the increase in λ_t. For large values of $\bar{\alpha}$ the effect of the axial strain and consequently the effect of eccentricity diminishes and λ_t and λ_f remain almost constant with $\bar{e}$. This is shown for $\bar{\alpha}=10$ in Fig. 2. The variation of λ with $\bar{e}$ for $\bar{\alpha}=0.4$ is also shown in Fig. 2.

When the vibration modes are uncoupled, the cross section of the strip rotates about the z-axis for the torsional mode and about an axis parallel to the z-axis at $x=\infty$ for the flexural model. When the modes get coupled because of the eccentric axial load these axes shift. The distance η of the axis of rotation from the center of the cross section can be obtained

from any one of the equations (2) as equal to $-\bar{u}_0/\bar{\theta}$. Figure 3 shows the variation of $\bar{\eta}$ $(=\eta/b)$ for various values of $\bar{\alpha}$. When $\bar{\alpha}=0$ we have

$$\bar{\eta}_f=\infty \text{ and } \bar{\eta}_t=0 \text{ for } \bar{e}=0$$

and

$$\bar{\eta}_f=-\bar{\eta}_t=1/2\sqrt{3}) \text{ for } \bar{e}\neq 0$$

Thus there is a step discontinuity at $\bar{e}=0$. This fact manifests itself in a very interesting manner in practice. When long and very thin strips loaded by uniform axial tension are tested for vibration, though one can get the pure flexural and torsional frequencies, pure torsional and flexural mode shapes as signified by $\bar{\eta}_t=0$ and $\bar{\eta}_f=\infty$ are difficult to achieve: Even a small error in the symmetry of loading causes a large shift in the axes of rotation as by the large slope of the $\bar{\eta}$ curve near $\bar{e}=0$ in Fig. 3. For large values of $\bar{\alpha}$, the variation of $\bar{\eta}_f$ with $\bar{e}$ becomes a rectangular hyperbola and that of $\bar{\eta}_t$ becomes a straight line.

Higher Modes for the Compressible Elastica on an Elastic Foundation

J. V. Huddleston[1]

Introduction

The paper by Nicolau and Huddleston [1] used a set of nonlinear differential equations and a numerical method to solve the problem of buckling of a compressible elastica on an elastic foundation. It assumed foundation moduli in the relatively compliant range where the first or critical mode of buckling is a single-half-wave configuration. As the foundation enters a stiffer range, however, multiple-half-wave buckling becomes critical. This Brief Note uses the theory of

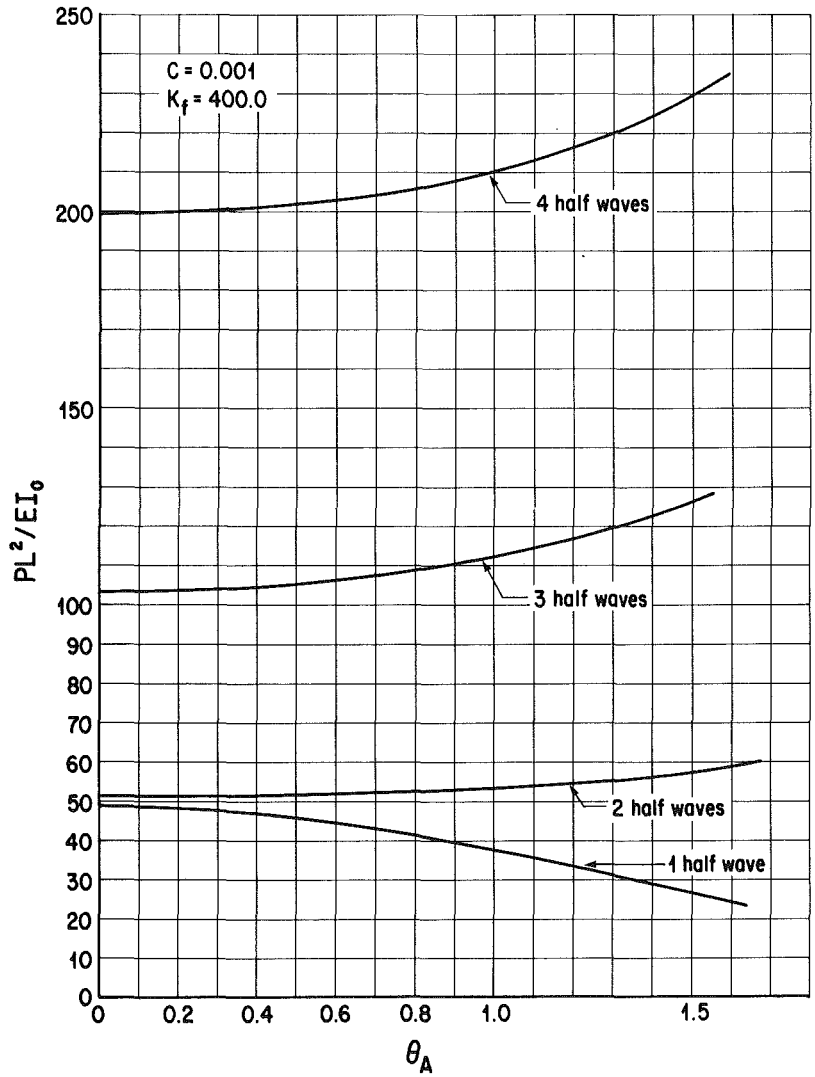

Fig. 1 P-θ_A curves for C = 0.001 and K_f = 400.0

[1] to correctly find the higher buckling loads and critical mode shapes and compares them with the classical predictions. It also uses the method of [1] to analyze the post-

[1]Professor of Engineering and Applied Sciences, State University of New York at Buffalo, Buffalo, N.Y. 14260. Mem. ASME.

Manuscript received by ASME Applied Mechanics Division, March 1981; final revision, October, 1981.

from any one of the equations (2) as equal to $-\bar{u}_0/\bar{\theta}$. Figure 3 shows the variation of $\bar{\eta}$ $(=\eta/b)$ for various values of $\bar{\alpha}$. When $\bar{\alpha}=0$ we have

$$\bar{\eta}_f=\infty \text{ and } \bar{\eta}_t=0 \text{ for } \bar{e}=0$$

and

$$\bar{\eta}_f=-\bar{\eta}_t=1/2\sqrt{3}) \text{ for } \bar{e}\neq 0$$

Thus there is a step discontinuity at $\bar{e}=0$. This fact manifests itself in a very interesting manner in practice. When long and very thin strips loaded by uniform axial tension are tested for vibration, though one can get the pure flexural and torsional frequencies, pure torsional and flexural mode shapes as signified by $\bar{\eta}_t=0$ and $\bar{\eta}_f=\infty$ are difficult to achieve: Even a small error in the symmetry of loading causes a large shift in the axes of rotation as by the large slope of the $\bar{\eta}$ curve near $\bar{e}=0$ in Fig. 3. For large values of $\bar{\alpha}$, the variation of $\bar{\eta}_f$ with $\bar{e}$ becomes a rectangular hyperbola and that of $\bar{\eta}_t$ becomes a straight line.

Higher Modes for the Compressible Elastica on an Elastic Foundation

J. V. Huddleston[1]

Introduction

The paper by Nicolau and Huddleston [1] used a set of nonlinear differential equations and a numerical method to solve the problem of buckling of a compressible elastica on an elastic foundation. It assumed foundation moduli in the relatively compliant range where the first or critical mode of buckling is a single-half-wave configuration. As the foundation enters a stiffer range, however, multiple-half-wave buckling becomes critical. This Brief Note uses the theory of

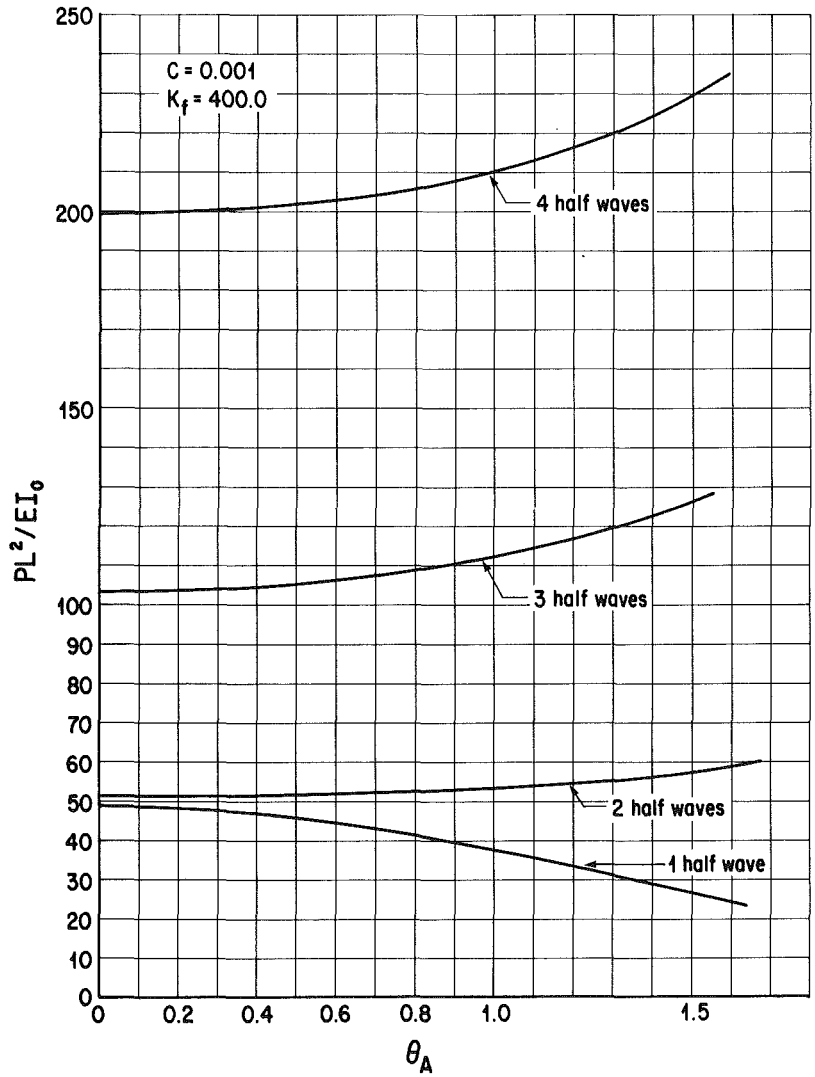

Fig. 1 P-θ_A curves for C = 0.001 and K_f = 400.0

[1] to correctly find the higher buckling loads and critical mode shapes and compares them with the classical predictions. It also uses the method of [1] to analyze the post-

[1]Professor of Engineering and Applied Sciences, State University of New York at Buffalo, Buffalo, N.Y. 14260. Mem. ASME.

Manuscript received by ASME Applied Mechanics Division, March 1981; final revision, October, 1981.

Table 1 Eigenvalues for $C = 0.001$ and various values of K_f (critical modes denoted by asterisks)

i	$K_f = 40.0$			$K_f = 400.0$			$K_f = 4000.0$			$K_f = 40000.0$		
	T_i (L)	T_i (M)		T_i (L)	T_i (M)		T_i (L)	T_i (M)		T_i (L)	T_i (M)	
		Lower	Higher		Lower	Higher		Lower	Higher		Lower	Higher
1	13.922*	14.006*	990.031	50.398	48.923*	990.027	415.154	298.411	989.990	4062.717	812.510	989.582
2	40.492	42.188	958.824	49.611*	51.223	958.808	140.800	133.362*	958.637	1052.690	546.524	956.757
3	89.277	98.991	901.459	93.330	103.073	901.410	133.858*	142.178	900.913	539.143	415.231*	895.264
4	158.167	196.812	803.441	160.447	199.231	803.296	183.244	222.891	801.814	411.217	418.956	783.152
5	246.902	443.346	556.816	248.361	447.418	554.201	262.951	complex	complex	408.854*	complex	complex

buckling behavior for different numbers of half waves and, for one combination of system parameters, traces the post-buckling process through its entire range.

The Linearized Problem

The boundary-value problem represented by equations (A), (B), and (C) of [1] can be linearized for the purpose of finding the buckling loads, as was done previously for the compressible elastica without reactive foundation by Huddleston [2]. This is achieved by replacing $\sin\theta$ by θ and $\cos\theta$ by unity in the differential equations:

$$\left.\begin{aligned}
&(1)\ \frac{d\theta}{dx} = \frac{M}{EI}\ ,\\
&(2)\ \frac{du_y}{dx} = \left(1+\frac{N}{EA}\right)\theta\ ,\\
&(3)\ \frac{d\xi}{dx} = 1+\frac{N}{EA}\ ,\\
&(4)\ \frac{ds}{dx} = 1+\frac{N}{EA}\ ,\\
&(5)\ \frac{du_x}{dx} = \frac{d\xi}{dx} - 1\ ,\\
&(6)\ \frac{dN}{dx} = -Q\frac{d\theta}{dx} + k_y u_y \theta\ ,\\
&(7)\ \frac{dQ}{dx} = N\frac{d\theta}{dx} - k_y u_y\ ,\\
&(8)\ \frac{dM}{dx} = Q\left(1+\frac{N}{EA}\right)\ ,
\end{aligned}\right\} \qquad (A)$$

Next assume that N = constant = $-P$ (this additional assumption was not necessary in [2]), so that, from (7),

$$\frac{dQ}{dx} = -P\frac{d\theta}{dx} - k_y u_y, \qquad (B)$$

and, from (8),

$$\frac{dM}{dx} = Q\left(1-\frac{P}{EA}\right). \qquad (C)$$

Now assume that EA is a constant, say EA_0, and combine equations (B) and (C):

$$\frac{d^2M}{dx^2} = -P\left(1-\frac{P}{EA_0}\right)\frac{d\theta}{dx} - k_y\left(1-\frac{P}{EA_0}\right)u_y. \qquad (D)$$

From (2),

$$\frac{d\theta}{dx} = \frac{1}{1-\dfrac{P}{EA_0}}\frac{d^2u_y}{dx^2}, \qquad (E)$$

and hence, from (1),

$$\frac{EI}{1-\dfrac{P}{EA_0}}\frac{d^2u_y}{dx^2} = M. \qquad (F)$$

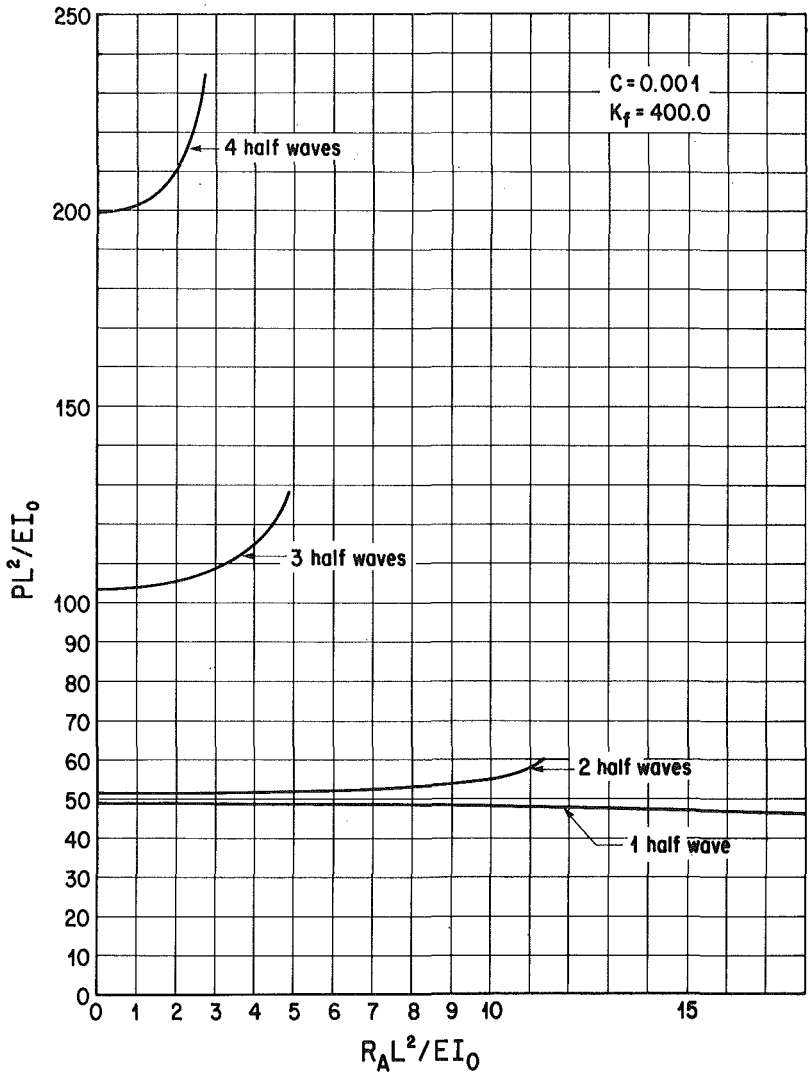

Fig. 2 P-R_A curves for $C = 0.001$ and $K_f = 400.0$

Now assume that EI is a constant, say EI_0, differentiate equation (F) twice, and substitute equations (D) and (E) to obtain:

$$\frac{EI_0}{1-\frac{P}{EA_0}}\frac{d^4u_y}{dx^4}+P\frac{d^2u_y}{dx^2}+k_y\left(1-\frac{P}{EA_0}\right)u_y=0. \quad (G)$$

Introducing the compressibility measure C defined by

$$C=\frac{I_0}{A_0L^2}, \quad (H)$$

one can rewrite equation (G) as follows:

$$\frac{d^4u_y}{dx^4}+\frac{P}{EI_0}\left(1-C\frac{PL^2}{EI_0}\right)\frac{d^2u_y}{dx^2}+\frac{k_y}{EI_0}\left(1-C\frac{PL^2}{EI_0}\right)^2u_y=0. \quad (I)$$

Equation (I) is the linearized fourth-order differential equation that reduces to the classical form for $C = 0$.

Next assume that k_y = constant = k_f to facilitate the solution of equation (I), and introduce the following dimensionless variables:

$$\left.\begin{aligned} U_y &= \frac{u_y}{L}, \\ X &= \frac{x}{L}, \\ T &= \frac{PL^2}{EI_0}, \\ K_f &= \frac{k_fL^4}{EI_0}. \end{aligned}\right\} \quad (J)$$

The dimensionless fourth-order differential equation is then

$$\frac{d^4U_y}{dX^4}+T(1-CT)\frac{d^2U_y}{dX^2}+K_f(1-CT)^2U_y=0. \quad (K)$$

Solution of equation (K) and use of boundary conditions on U_y and U_y'' at $X = 0$ and $X = 1$ gives the following eigenvalues:

For zero C:

$$T_i=\pi^2\left(i^2+\frac{K_f}{i^2\pi^4}\right), \quad i=1,2,\ldots, \quad (L)$$

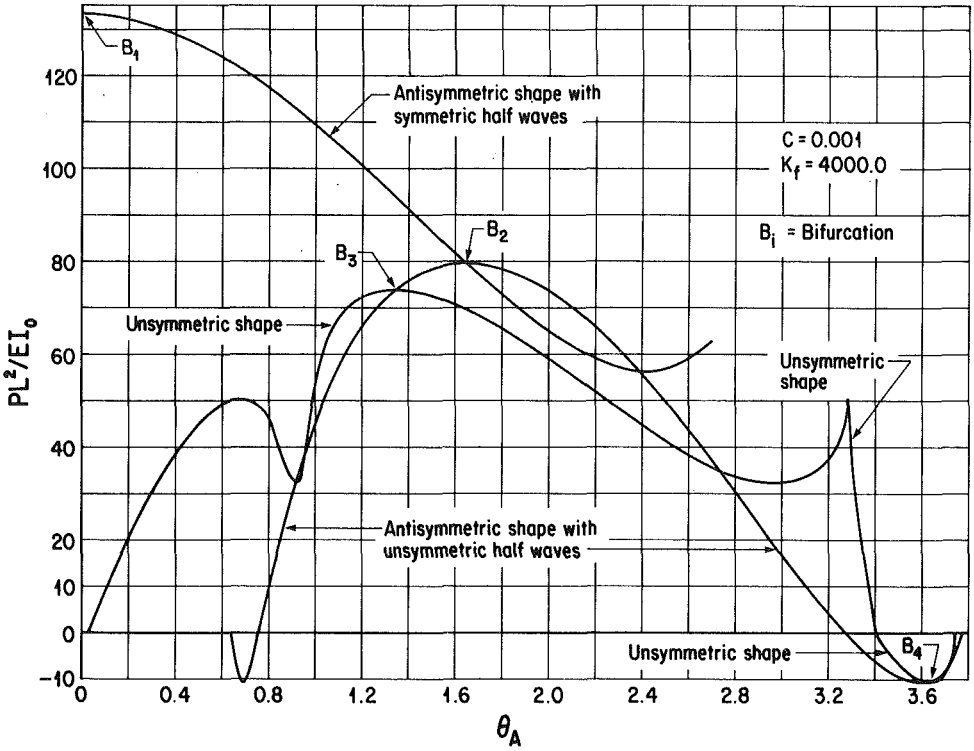

Fig. 3 P-θ_A curves for $C = 0.001$ and $K_f = 4000.0$

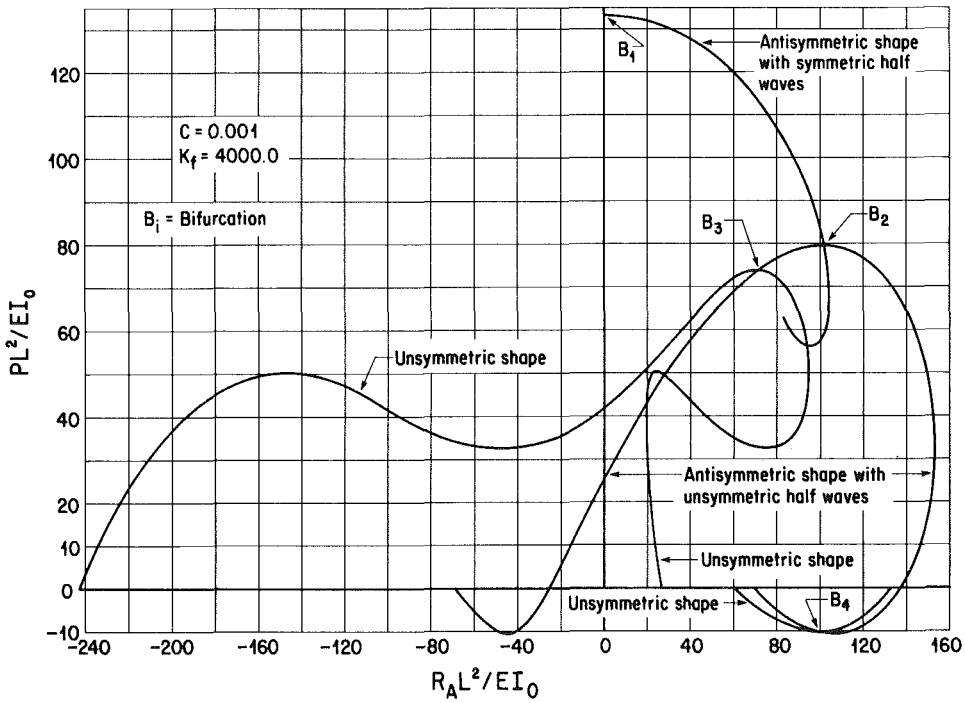

Fig. 4 P-R_A curves for $C = 0.001$ and $K_f = 4000.0$

and, for nonzero C:

$$T_i = \frac{(i^2\pi^2 + 2CK_f) \pm \sqrt{(i^2\pi^2 + 2CK_f)^2 - 4C(i^2\pi^2 + CK_f)(i^4\pi^4 + K_f)}}{2C(i^2\pi^2 + CK_f)}, \quad i = 0,1,2, \ldots . \quad (M)$$

Equation (L) agress with the eigenvalues found by Timoshenko and Gere [3], and equation (M) reduces to that found in [2] for the case $K_f = 0$.

Table 1 gives a comparison of the eigenvalues as determined by equations (L) and (M) for $C = 0.001$ (a moderately compressible elastica) and various values of K_f (ranging from compliant to very stiff). The value of i, of course, is the number of half waves into which the member buckles, and the

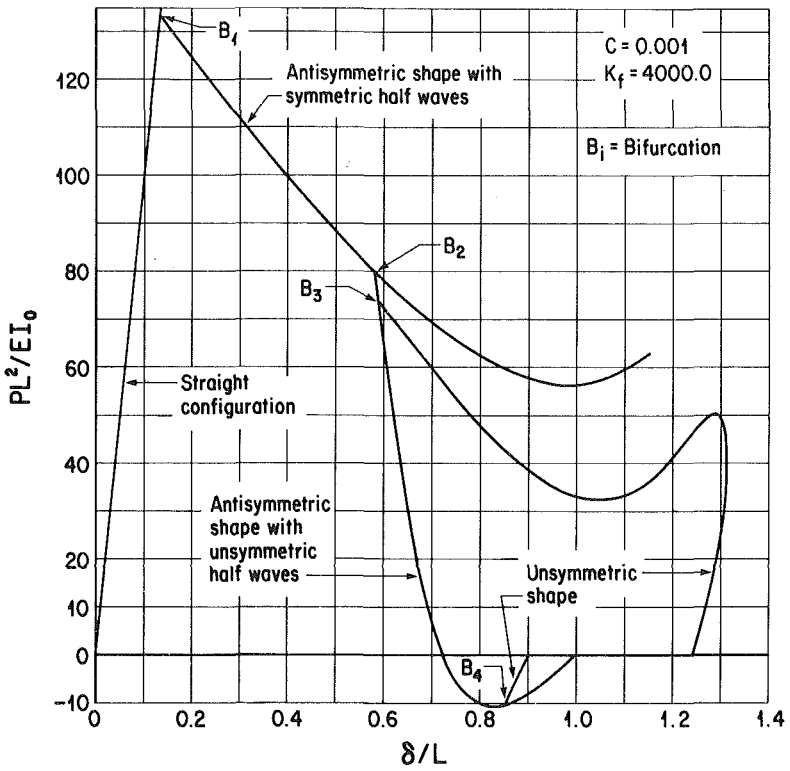

Fig. 5 P-δ curves for $C = 0.001$ and $K_f = 4000.0$

critical value is the lowest one given by each equation (denoted by an asterisk in Table 1). Already for $K_f = 400.0$, a case considered in [1], the classical theory predicts that the switch in the critical mode from one half wave to two half waves has occurred, but the corrected theory shows that the single half wave is still critical. Similarly, for $K_f = 4000.0$, the classical theory predicts three half waves but the corrected theory predicts two. Finally, for $K_f = 40000.0$, the classical predicts five and the corrected three.

Solutions of the Nonlinear Problem

Two cases have been selected from Table 1 for further study. One is the case of $C = 0.001$ and $K_f = 400.0$ considered in [1]. By means of the numerical algorithms used in that reference, the initial postbuckling curves for one, two, three, and four half waves have been determined from the nonlinear boundary-value problem. The curves of dimensionless force versus end rotation are plotted in Fig. 1, and the curves of dimensionless force versus dimensionless end reaction are plotted in Fig. 2. The one-half-wave curves, of course, reproduce results already reported in [1]. The reaction R_A in this Brief Note is the same as that symbolized by R_{VA} in [1].

A second case selected for further study is that of $C = 0.001$ and $K_f = 4000.0$, for which the exact theory predicts two half waves as the critical mode. The complete buckling and postbuckling process has been examined in this case, and the results are shown in Figs. 3,4, and 5. As the displacement δ of the movable end of the strut is increased, the force P increases, with θ_A and R_A remaining zero, until bifurcation B_1 ($P = 133.362$) is reached. At that point the member will buckle into either of two antisymmetric shapes each having two symmetric half waves. Assuming that the buckling begins with a positive θ_A, as shown in the figures, P decreases while θ_A and R_A increase. At point B_2, the system will bifurcate again into either of two antisymmetric shapes each having two unsymmetric half waves, but which of the two directions on the new paths it will take depends, as at B_1, on the imperfections of the particular system. If it branches with decreasing θ_A and R_A, another bifurcation point B_3 will be encountered shortly where totally unsymmetric shapes will become possible equilibrium configurations. It is apparent from Fig. 5, however, that unless compelled otherwise by external influences the system will continue on the antisymmetric path. If, at B_2, the system branches with increasing θ_A and R_A, the solution does not show another bifurcation point until B_4, which is in the negative-P regime, and it appears from Fig. 5 that the system would tend again to remain on the antisymmetric path. After returning to zero force, where the shape is symmetric with respect to the x-axis on either of the antisymmetric paths, the rest of the postbuckling process will follow along paths that can be inferred from the existing results by the kind of global analysis involving reflections and inversions that was carried out in [1].

References

1 Nicolau, A. M., and Huddleston, J. V., "The Compressible Elastica on an Elastic Foundation," ASME JOURNAL OF APPLIED MECHANICS, Vol. 49, 1982, pp. 577–583.

2 Huddleston, J. V., "Effect of Axial Strain on Buckling and Post-Buckling Behavior of Elastic Columns," *Developments in Theoretical and Applied Mechanics*, Vol. 4, *Proceedings of the Fourth Southeastern Conference on Theoretical and Applied Mechanics*, New Orleans, La., Feb. 1968, pp. 263–273.

3 Timoshenko, S. P., and Gere, J. M., *Theory of Elastic Stability*, second ed., Engineering Societies Monographs, 1961.

Journal of Applied Mechanics

Discussion

Energy-Release Rate in Elastic-Plastic Fracture Problems[1]

A. G. Herrmann[2] and G. Herrmann.[2] It is believed that the analysis and results presented in this paper cannot be correct for several different and independent reasons.

1 So-called path-independent integrals can be meaningfully discussed only for closed paths enclosing a defect. They are derived via Gauss theorem which requires closed surfaces or contours. The authors, however, consider an open path. The same inadmissible consideration is also applied, incidentally, in references [5] and [6] of the paper by the same authors. This renders their proof of path-independence invalid.

2 Path-independence of an integral means that the path can be absolutely arbitrary as long as it is closed. But the authors are not able to let their path enter or cross the process zone and thus the very foundation on which the J, L, and M integrals are based, as discussed in references [2] and [3] of the paper, are violated. The decomposition (equation (20) of the paper) implies that all integrals involving $\hat{J}_\alpha$, $\hat{L}_3$, $\hat{M}$, and I are taken around a crack tip. Even for a straight crack in static elasticity the contours for L and M are taken around the whole crack. (See e.g. reference [3] of the paper.)

3 Rice's J integral is based on the translational invariance requirement. In the purely elastic body, as a plane crack grows, the stress field around the crack moves with the crack tip. In the case of elastic-plastic fracture, however the plastic deformation (or process region) is left behind (as a wake) and thus translational invariance is violated.

4 For a curved crack considered by the authors, translational invariance is again obviously violated as the crack grows, which renders their results invalid.

5 It has been shown [1] that even for a plane crack only one component of the so-called J-vector (namely Rice's integral) is path-independent, while the other is indeed path-dependent. Thus authors' proof concerning path-independence is again invalid.

[1] By S. Aoki, K. Kishimoto, and M. Sakata, and published in the December, 1981, issue of the ASME JOURNAL OF APPLIED MECHANICS, Vol. 48, pp. 825–829.

[2] Division of Applied Mechanics, Stanford University, Stanford, Calif. 94305.

References

1 Herrmann, A. G., and Herrmann, G., "On Energy-Release Rates for a Plane Crack," ASME JOURNAL OF APPLIED MECHANICS, Vol. 48, 1981, pp. 525–528.

Authors' Closure

We appreciate the discussers' interest and comments. Their remarks are thought to come from the difference in the interpretation of the crack model adopted in the paper. The authors have considered that the fracture process region is of a finite size. Since the usual continuum mechanics cannot be applied to this region where microstructural processes take place, an attempt has been made to relate Φ (i.e., the time rate of the energy change referred to the fracture process region A_{end} near a crack tip) to the physical quantities in the regular region A, where the continuum mechanics work.

1. The fact that the values of $\hat{J}_\alpha$, $\hat{L}_3$, and $\hat{M}$ do not depend on the choice of $\Gamma + \Gamma_s$ for a prescribed Γ_{end} is proved by using a closed contour $(\Gamma + \Gamma_s)$· and Gauss theorem in the Appendix of the paper.

2. It is noted that the J, L, and M integrals are thought to be defined using a model with an infinitesimal fracture process region. In the fracture process region with a finite size as considered in this paper, the usual continuum mechanics do not work; therefore one cannot consider a path entering or crossing the process region.

We have focused our attention on one crack tip. If we consider both crack tips simultaneously, it would be possible to take Γ_{end} as the sum of Γ_{end} of each crack tip plus the path along the crack surfaces, and Γ as a contour surrounding the whole defects, i.e., a crack and both process regions (Γ_s is not necessary here because the crack surfaces are included in the Γ_{end}). In the case, the path Γ is the same as the path for L and M in [3].

3. It is obvious that the assumption of translational invariance does not hold in the case of elastic-plastic fracture. Therefore, the authors have considered deformation of the process region during crack extension. This fact reflects that Φ cannot be presented only by the translation component $\hat{J}_\alpha$ (see equation (20)). The $\hat{I}$ includes the energy change associated with the nonsteady deformation and contributes considerably to Φ.

4. The authors have also thought that translational invariance is violated for a curved crack. This is why Φ includes not only $\hat{J}_\alpha$, but also $\hat{L}_3$, $\hat{M}$, and $\hat{I}$ as shown in equation (20). It is thought that $\hat{L}_3$ is important in this case.

5. By introducing Γ_s, i.e., the path along the crack surfaces, we have obtained the path-independent (in the sense of the first comment of this Closure) $\hat{J}_\alpha$ integral.

On the Formulation of Strain-Space Plasticity with Multiple Loading Surfaces[1]

J. L. Kauschinger.[2] The authors are to be congratulated for their valuable contribution to the knowledge of constitutive modeling of nonlinear materials. It is clear that a formulation in strain space has important numerical advantages over a classical stress space model. It would appear that the authors next line of attack should be to present an approach for obtaining the appropriate material parameters from laboratory tests, and to propose functional relationships for modeling various materials.

While in general, a stress space formulation will require an inversion of the compliance matrix to obtain the stiffness, many times this inversion can be performed algebraically, as in the case of Prevost [4][3], and thereby the computational expense needed to obtain the stiffness is alleviated when performing finite element calculations.

When selecting the nesting rule used to harden the active yield surface, the only strict requirement is that the consistency condition be upheld. Although Prevost has arbitrarily selected a Mroz-type rule for use in his stress space formulation, the possibility of using Prager's Kinematic Rule is not excluded from his model [13]. It is true on the other hand, that when implementing Prager's Rule in a nested surface theory in conjunction with a Von Mises-type failure criterion, there must be a coupling between the translation of the present active surface and the next outer one, thereby increasing the computational effort. It should be emphasized that even in a strain space formulation the user must select some nesting rule. It is hoped that the hardening rule selected will portray the actual behavior of the material as measured in the laboratory. Undoubtedly, this comparison will represent the ultimate test of any functionals selected for use in a model.

Thus, while the advantages of a strain space formulation are many, particularly for monotonic loading, backtracking errors that develop during reversals when modeling an elastoplastic material cannot be eliminated when using either formulation. Therefore, it appears to this writer that the problems associated with implementing a classical stress space model are not as serious as the paper under discussion would seem to indicate. This conclusion was reached by this writer after implementing the Prevost Model [4] in a computer code for the purposes of simulating soil behavior.

Authors' Closure

The authors appreciate Kauschinger's interest in the subject paper and find themselves in general agreement with many of his observations. However, his comments about nesting rules deserve some further discussion, as does the question of backtracking error.

Although it has become customary in stress-space plasticity to require the various surfaces to nest as loading proceeds, this practice does not appear to stem from phenomenological considerations. Given the current stress and stress increment, after all, there is never any difficulty in determining the corresponding strain increment. Even if the stress happens to lie at a point where several yield surfaces cross, one simply finds the plastic contributions from each and sums them. However, when one is given the strain increment and needs to compute the corresponding stress increment, as typically happens in finite element programs, there arises a problem in determining which of the potentially active surfaces are in fact producing plastic strain. This difficulty comes about because the traditional loading criteria are based on the unknown stress increment. It was primarily to sidestep this issue that nesting rules were introduced in the first place. If one somehow contrives to force the yield surfaces to touch tangentially whenever they intersect, then at any given instant either all of the surfaces passing through the stress point will be active or else none of them will.

These considerations led Prévost [4, 13][1] to incorporate a nesting rule into his models for soil mechanics. Based on stress-space yield surfaces, these models lead directly to expressions for the elastoplastic compliance, which in turn are inverted through recourse to the nesting rule. This nesting rule has other ramifications, though, some of which are hard to conceptualize physically. For instance, if one tries to preserve Prager's kinematic hardening law by requiring each surface being loaded to move parallel to its own local normal, the surfaces outside of it must all somehow be made to move out of its way.

An alternative approach, as outlined in the subject paper, is to abandon nesting rules altogether. It should be emphasized that neither the stress nor strain-space models discussed therein make use of any such rule. Even so, it remains possible under fairly general conditions to obtain the elastoplastic stiffness. One particular class of models stands out among all those considered, namely, the ones based on uncoupled, nonnesting, strain-space loading surfaces. For models of this type, the loading surfaces act independently of one another and the stiffness is found quite simply by adding the contributions from each.

An additional advantage of these strain-space models is that the loading criteria are based on strain rather than stress. Thus one can determine whether there has been a loading reversal directly from the strain and strain increment, which can readily be calculated at the close of each time step. Stress-space models, on the other hand, require one to guess whether there has been a loading reversal before updating the stress. For this reason, the strain-space models should be somewhat less prone to backtracking error.

This promise of improved performance under loading reversals, while not compelling in and of itself, does lend support to the arguments in favor of the strain-space formulation. So, too, does the added flexibility that results from being able to use non-nesting loading surfaces. Of course, as Kauschinger intimates, a plasticity model is useful in any particular application only to the extent that its predictions agree with experimental results. The authors anticipate that the strain-space models will indeed prove useful in describing the constitutive behavior of real materials.

[1] By P. J. Yoder and W. D. Iwan, and published in the December, 1981, issue of the ASME JOURNAL OF APPLIED MECHANICS, Vol. 48, pp. 773–778.

[2] Graduate Student, Department of Civil Engineering, The University of Texas at Austin, Austin, Texas 78712.

[3] Numbers in brackets refer to references in Yoder and Iwan's paper.

[1] Numbers in brackets refer to references in the subject paper.

A Modified Strain-Energy Density Criterion Applied to Crack Propagation[1]

G. C. Sih[2] and E. E. Gdoutos[3]. First of all, the discussers wish to thank the authors for their candid view on applying the strain-energy density criterion to the angle crack problem. The selection of a suitable failure criterion to examine material damage caused by fracture and/or yielding is problematic, because the process can often be prejudiced by the investigator(s) on the basis of how well his or their experimental data agree with the theory. Generally speaking, it is not difficult to show that several competing failure criteria can be made to agree equally well with the data of a single physical problem but it becomes much more demanding to have a single criterion that can consistently explain a multitude of physical phenomena. Of equal importance is that approximations introduced through stress analysis should not be attributed to limitations of the failure criterion. This point was discussed in detail in 1974 [1] with reference to fracture experiments on beryllium. Needless to say, better accuracies are obtained when the complete strain-energy density expression is used rather than just the singular terms. Although the choice of number of terms affects the end results, it has no bearing on the original failure criterion. The so referred to "thinking ability" must indeed be left to the investigator.[4] The versatility of any criterion can only be judged by its *consistency* and *generality* in application.

More specifically, this discussion is intended to clarify the basic ideas behind the strain-energy density theory which apparently have escaped the attention of the authors. The concocted modifications outlined in the paper are found to be groundless and serve no useful purpose. Ironically, the authors' criticisms apply quite appropriately to their own work. For instance, the mean strain-energy density factor $\bar{S}$ as defined by equation (8) in the paper can hardly have more physical meaning than the strain-energy density factor S itself. For a linear elastic material, S can be written as [2]

$$S = S_v + S_d \tag{1}$$

in which S_v corresponds to the dilatational component and S_d to the distortional component. The former is assumed to govern fracture while the latter to yielding. More details on this will be given subsequently. In general, S is associated with the strain-energy density function dW/dV by the relation

$$\frac{dW}{dV} = \frac{S}{r} \tag{2}$$

with r being the linear distance locating a possible failure site.[5] Only in the case of a linear elastic material can S be computed from the stress-intensity factors. The expression in equation (2) applies to a typical material element at a distance[6] r_0 from the site of failure initiation, say a crack tip. The angular position of the element, denoted by θ, determines the direction of fracture or yielding. It suffices to use the singular term in the expansion of dW/dV if information is required only on failure inititation [3]. Of course the entire dW/dV field must be considered for determining the crack trajectory [4]. There is no sense to investigate one additional term at a time unless the truncation error is evaluated. The direction of the element that initiates fracture is assumed to correspond with $S_{\min}$ or $(dW/dV)_{\min}$ for a fixed r and the direction of the element that initiates yielding with $S_{\max}$ or $(dW/dV)_{\max}$. In this connection, the hypotheses A and B posed by the authors are inconsistent. One refers to the position of a specific element for which S possesses a relative minimum and the other considers the values of S for all the elements averaged from $\theta = 0$–360 deg. It is inconceivable how $\bar{S}$ could be claimed to have more physical meaning than S. What the authors have failed to recognize is that both $S_{\min}$ and $S_{\max}$ attain different critical values: one for the initation of fracture and the other for yielding. In a given problem, there may exist a number of $S_{\min}$. It is the maximum of $S_{\min}$ or $S_{\min}^{\max}$ where fracture will first initiate. Furthermore, the critical value of S or S_c can be related to K_{1_c} as

$$S_c = \frac{(1+\nu)(1-2\nu)}{2\pi \mathrm{E}} K_{1c}^2 \tag{3}$$

where E is Young's modulus and can be determined by the K_{1c} tests recommended by ASTM. While S_c can be interpreted as the fracture toughness of the material, $\bar{S}$ has no such meaning.

To be emphasized is that the strain-energy criterion as used by the authors in a concocted fashion represents only a special case of the more general theory [5] based on

$$\frac{dW}{dV} = \int_0^{\epsilon_{ij}} \sigma_{ij} d\epsilon_{ij} \tag{4}$$

In equation (1), dW/dV applies to all materials, either linear [3, 6]) (nondissipative) or nonlinear [7, 8] (dissipative). σ_{ij} and ϵ_{ij} are the stress and strain components referred to the rectangular Cartesian coordinates. It is worthwhile to review the following basic assumptions [5]:

(1) Yielding and fracture are assumed to coincide with *locations* of maximum of the local maximum and minimum of the strain-energy density function $(dW/dV)_{\max}$ and $(dW/dV)_{\min}$, respectively.

(2) Yielding and fracture are assumed to occur when the maximum of $(dW/dV)_{\max}$ and $(dW/dV)_{\min}$ reach their respective critical values.

(3) The amount of incremental growth r_1, r_2, . . . ,r_j, . . . ,r_c is governed by

$$\left(\frac{dW}{dV}\right)_c = \frac{S_1}{r_1} = \frac{S_2}{r_2} = \ldots = \frac{S_j}{r_j} = \ldots = \frac{S_c}{r_c} = \text{const.} \tag{5}$$

if the process of yielding and fracture leads to global instability,[7] i.e.,

$$r_1 < r_2 < \ldots < r_j < \ldots < r_c \tag{6}$$

and r_c corresponds to the critical ligament size of the material.

[1] Theocaris, P. S., and Andrianopoulos, N. P., and published in the March 1982 issue of the ASME JOURNAL OF APPLIED MECHANICS, Vol. 49, pp. 81–86.

[2] Professor of Mechanics and Director of Institute of Fracture and Solid Mechanics, Lehigh University, Bethlehem, Pa., Fellow ASME.

[3] Professor of Applied Mechanics, Democritus University of Thrace, Xanthi, Greece. Presently: Visiting Scientist at the Institute of Fracture and Solid Mechanics, Lehigh University, Bethlehem, Pa.

[4] Even in solving a quadratic equation involving two roots, the analyst must have the capability of recognizing that only one of them may be physically admissible.

[5] Failure does not necessarily initiate from an existing macrocrack. It can occur anywhere in the solid depending on the conditions assumed by the criterion.

[6] This is a limiting distance within which the influence of material microstructure must be accounted for.

[7] For a process that leads to arrest in yielding and/or fracture, the ratio S_c/r_c in equation (3) is replaced by S_0/r_0 such that $r_1 > r_2 > \ldots > r_j > \ldots > r_0$.

In contrast to the introductory remarks in the paper, the strain-energy density criterion is fundamentally different from the von Mises yield condition as it attempts to address material damage due to the simultaneous influence of yielding and fracture. The proportion of the distortional and dilatational energy component is weighed automatically by the stationary values of dW/dV regardless of whether the crack is in the elastic portion of the elastic-plastic material [8] or in the fully plastic material[8] [9]. The critical values of dW/dV for yielding and fracture are obviously different and *they occur at different locations*. This interpretation is perfectly clear and requires no modification. In fact, in the neighborhood of any point in a stressed solid, there exists a *local* $(dW/dV)_{\max}$ and $(dW/dV)_{\min}$. Their maximum values $(dW/dV)^{\max}_{\max}$ and $(dW/dV)^{\max}_{\min}$ corresponds to locations of yielding and fracture initiation. For the case of a crack in uniform tension, the former occurs at $\theta_{\max}=\cos^{-1}(1-2\nu)$ where ν is the Poisson's ratio and the latter at $\theta=0$ deg. The important point is that for ductile materials, yielding and fracture have to be addressed simultaneously.[9] The critical values of $(dW/dV)^{\max}_{\max}$ and $(dW/dV)^{\max}_{\min}$ denote the initiation of local yielding and fracture. There exists another pair of *global* stationary values of $(dW/dV)_{\max}$ and $(dW/dV)_{\min}$ whose critical values govern the global instability of the solid or specimen due to yielding and/or fracture. This condition corresponds to

$$\left(\frac{dW}{dV}\right)_c=\frac{S_c}{r_c} \tag{7}$$

where $(dW/dV)_c$ can be measured experimentally from the area under the true stress-strain curve [10]. Note that from equations (3) and (7), r_c can be determined. Hence, for any fracture process that involves crack initiation, slow growth, and termination at least two of the parameters in equation (7) will have to be specified for a given material. This procedure has been applied to a number of problems involving ductile fracture [11, 12].

Contrary to one's physical intuition, the authors' claim that the lowest applied stress for initiating fracture corresponds to $\beta=72$ deg rather than $\beta=90$ deg when the load and crack plane is normal to one another. This was based on $\bar{S}$ possessing a *weak* maximum at $\beta=72$ deg. They attempted to explain this effect by the influence of Mode I and II interaction for which the discussers cannot comprehend. Mode II prevails only because $\beta\neq 90$ deg. With reference to the work of Sih and Kipp (reference [13] in the paper), the $\beta\simeq 70$ deg phenomenon was clearly explained and attributed to the two-term approximation in the stress expression. The S-criterion cannot correct numerical inaccuracies. Sih and Kipp showed that the lowest failure stress indeed occurred at $\beta=90$ deg when the exact stress expansions were used while no change was made on the S-criterion. This serves as an excellent example of the danger of concocting analysis and forcing the results to agree with unexplained experimental data. Indeed, the experimental data of Williams and Ewing (reference [5] in the paper) exhibited the $\beta\simeq 70$ deg phenomenon. This effect was due to the Mode I and III interaction and not that of Mode I and II as claimed by the authors. In tensile specimens, there is the tendency for the crack to deviate from the plane normal to the specimen surfaces resulting in the additional influence of Mode III. In such a case, indeed, an exact three-dimensional analysis of the embedded flat elliptical crack solution confirmed [2] that the lowest failure stress corresponded to a Mode I and III loading situation rather then Mode I. This has been known in the open literature for some time.

Somewhat disconnected from the main body of the paper, the authors further concluded a paradox in the S-criterion that was concerned with predicting crack bifurcation [13] due to the dynamic effect of running cracks. Reference was also made to the $\beta\simeq 72$ deg phenomenon which, as explained earlier, refers to crack initiating under static loading. These two situations are clearly not the same and should not be confused with one another. In fact, it was shown in 1976 [14] that for $\nu=0.21$–0.24, the $S_{\min}$ condition did predict the range of half bifurcation angle of ± 18.84–± 15.52 deg. The results for $\nu=0.25$ was given in [13] and agree well with the S-criterion prediction. Again, it serves only a necessary condition but not sufficient to justify the verification of the criterion.

In conclusion, the discussers failed to see the advantage of the $\bar{S}$ approach which, in fact, tends to confuse the issue and leads to false conclusions. The semilobes represent no more than the graphical display of results and yield no additional information other than the location of $S_{\min}$. The three assumptions stated earlier for dW/dV are sufficiently general to describe the complex behavior of the damage process by fracture and/or yielding provided that the appropriate stress and/or strain analysis is performed.

[8] It has been shown that the condition $(dW/\mathrm{dV})_{\min}$ still governs the direction of crack growth when yielding at large takes place [9]. This result is shown numerically from the finite element solution of a crack in a fully plastic material.

[9] The modifications in the paper failed to recognize the simultaneous treatment of yielding and fracture and provided no improvements of any kind.

References

1 Sih, G. C., "Discussion on Some Observations on Sih's Strain Energy Density Approach for Fracture Prediction,"by Finnie, I., and Weiss, H. O., *International Journal of Fracture*, Vol. 10, 1974, pp. 279–283.

2 Sih, G. C., "A Three-Dimensional Strain Energy Density Factor Theory of Crack Propagation," *Mechanics of Fracture, Vol. II Three Dimensional Crack Problems*, by Kassir, M. K., and Sih, G. C., Noordhoff, The Netherlands, 1975, pp. XV–LIII.

3 Sih, G. C., "A Special Theory of Crack Propagation," *Mechanics of Fracture, Vol. I: Methods of Analysis and Solutions of Crack Problems*, Sih, G. C., ed., Noordhoff, The Netherlands, 1973, pp. XXI–XLV.

4 Kipp, M. E., and Sih, G. C., "The Strain Energy Density Failure Criterion Applied to Notched Elastic Solids," *International Journal of Solids and Structures*, Vol. 11, 1975, pp. 153–173.

5 Sih, G. C., "Experimental Fracture Mechanics: Strain Energy Density Criterion," *Mechanics of Fracture, Vol. VII: Experimental Evaluation of Stress Concentration and Intensity Factors*, by Sih, G. C., ed., Martinus Nijhoff, The Netherlands, 1981, pp. XVII–LVI.

6 Gdoutos, E. E., *Application of Strain Energy Density Theory to Crack Problems*, Martinus Nijhoff, The Netherlands, in press.

7 Sih, G. C., "Fracture Toughness Concept," ASTM Special Technical Publication, STP 605, 1976, pp. 3–15.

8 Sih, G. C., and Kiefer, B. V., "Nonlinear Response of Solids Due to Crack Growth and Plastic Deformation," *Nonlinear and Dynamic Fracture Mechanics*, Perrone, N., and Atluri, S. N., eds., ASME, Applied Mechanics Division, Vol. 35, 1979, pp. 136–156.

9 Sih, G. C., and Madenci, F., "Failure by Crack Growth and Gross Yielding: Strain Energy Density Criterion," Institute of Fracture and Solid Mechanics Technical Report No. IFSM-82-112, May 1982.

10 Gillemot, L. F., "Criterion of Crack Initiation and Spreading," *Journal of Engineering Fracture Mechanics*, Vol. 8, 1976, pp. 239–253.

11 Sih, G. C., and Matic, P., "A Pseudo-Linear Analysis of Yielding and Crack Growth: Strain Energy Density Criterion," *Proceedings of the International Conference on Defects, Fracture and Fatigue*, Sih, G. C., and Provan, J. W., eds., Martinus Nijhoff, The Netherlands, in press.

12 Sih, G. C., and Moyer, E. T., Jr., "Path Dependent Nature of Fatigue Crack Growth," *International Journal of Engineering Fracture Mechanics*, Vol. 16, 1982, in press.

13 Kalthoff, J. F., "On the Propagation Direction in Bifurcated Cracks," *Dynamic Crack Propagation*, Sih, G. C., ed., Noordhoff, The Netherlands, 1973, pp. 449–458.

14 Sih, G. C., "Dynamic Crack Problems: Strain Energy Density Fracture Theory," *Mechanics of Fracture, Vol. VI: Elastodynamic Crack Problems*, Sih, G. C., ed., Noordhoff, The Netherlands, 1976, pp. XVII–XLVII.

Authors' Closure

The authors wish to thank the discussers for the chance offered to clarify some basic ideas which drove to *one essential modification* of the *S*-criterion, introduced by Sih.

Before that, we have to clarify a few topics of secondary importance raised in the discussion.

1. We never attributed any limitations of the *S*-criterion to numerical inaccuracies introduced by the singular stress expressions. We just used the exact expressions, instead of the one, two-term, etc. approximations, usually used, which sometimes drive to a *"personalization"* of each term and to conclusions of the kind: "The first term affects the crack initiation, the second controls the crack direction . . ." [1]. There are no individual terms in nature. There are only individual stress fields represented algebraically by expressions more or less accurate. Thus, the senior of the discussers should not feel disappointed, if the *singular* predictions differ from the *exact* ones.

2. The versatility of a criterion is judged primarily by its *rationality* and then by its consistency and generality, as stated by the discussers. From a number of existing failure criteria, having the property of rationality, the best will be the criterion that also possesses consistency and generality. In our opinion, the original *S*-criterion seems to lack the property of rationality.

3. *Thinking ability* is asked from the crack, according to the original *S*-criterion. It does not answer the question "which minimum?" as misleadingly claim the discussers, but answers the question "why and how a minimum?" To the former question a good answer was given by Swedlow [2], the answer being independent of the thinking ability of the crack. The second discusser used this answer in at least one of his papers [3].

4. K_{II}-mode does not prevail for $\beta \neq 0$ deg. It just exists for $\beta \neq 0$ deg, 90 deg. It prevails for $\beta < 45$ deg, where all the criteria are (incidentally?) more or less problematic.

5. The discussers propose an experimental method for the determination of r_c. We have been waiting for it since 1974 [4]. Experimental results for the value of r_c will be helpful, if available, to compare them with the radius of the initial curve of the caustics, which was rationally proposed by us as the boundary of the core region [5, 6].

6. One's physical intuition is useful and productive but also dangerous. Intuitively, we agree with the discussers that it seems unphysical for a crack to propagate easier when $\beta \approx 72$ deg than when $\beta = 90$ deg; we were compelled by the results of extensive experiments performed in PMMA, PCBA, and 57-S Aluminum alloy. In all cases, this extremum was always present, stronger in the brittle PMMA and weaker in the other two ductile materials. We do not accept the discussers' explanation that this extremum is due exclusively to the presence of K_{III}. The contribution of K_{III} to the total strain-energy density is independent of angle β and, either S does not play a role in the fracture process (a fact that we do not believe), or the new explanation of the discussers is groundless.

7. Concerning the explanation given by Sih and Kipp (reference [13] in our paper), they explained the *theoretical* extremum of fracture load and not the *experimental* as the discusser's claim. Their statement that the extremum is due to the influence of the second term of the stress expressions is answered in our first remark. They surely know that this extremum in fracture-stress was also predicted [7] some years before the introduction of σ_ϑ-criterion [8], although a completely different algebraic description (by means of an asymptotic expansion) of the stress-field was used. However, the situation is somewhat confusing. Predictions of σ_ϑ and $\bar{S}$-criteria show an extremum somewhere around 70 deg, contrary to the *S*-criterion predictions. Experimental evidence is in favor of this extremum and the discussers felt obliged to fight this remarkable coincidence.

8. $\bar{S}_c$ is equally well connected with the toughness K_{Ic} of the material, as is S_c. Integration of equation (8) of the paper for $\beta = 90$ deg, immediately gives:

$$\bar{S}_c = \frac{(1+\nu)(3-4\nu)}{4\pi E} K_{Ic}^2$$

Having finished with the stuffing material, we will try to explain again our basic ideas that resulted in the introduction of the modified or $\bar{S}$-criterion. Let us consider a simple example. A specimen with a crack at $\beta = 90$ deg is loaded uniaxially in tension (Fig. 1). It is assumed that the critical value S_c of the strain-energy density is known. It is also known that $\vartheta_0 = 0$ deg. In the plane of energy-density, S_c is represented by a circle of constant radius S_c. As the external load increases, we consider an instant when the level of *S*-distribution around the crack tip is as shown in the figure. It is a possible situation since $S_{min} < S_c$. The elementary volume *A* ahead of the crack tip, where the crack is expected to propagate, can bear higher strain densities, according to *S*-criterion. But, what happens with the elementary volume at *B*? It, exactly, bears the critical density, but, still, denies to fail. Why? Other elementary volumes, corresponding to arcs *DE* and *FG*, are more stubborn. How can one accept such a behavior? There are two answers. Either the elementary volumes are entities that possess a *thinking ability* and they know that they have to fail only when they are in the "right" direction, or *S*, having an angular character, cannot serve as the critical quantity. At present, we cannot accept the first alternative. On the other hand, the second alternative (that *S* is irrelevant) can hardly be believed. Thus, we have modified the *S*-criterion, replacing S_{min} by the mean value $\bar{S}$ in the role of the decisive quantity for *crack initiation* and keeping S_{min} as the decisive quantity for *crack direction*. This modification removes the fundamental irrationalities of the original *S*-criterion, leaving its predictions unaffected.

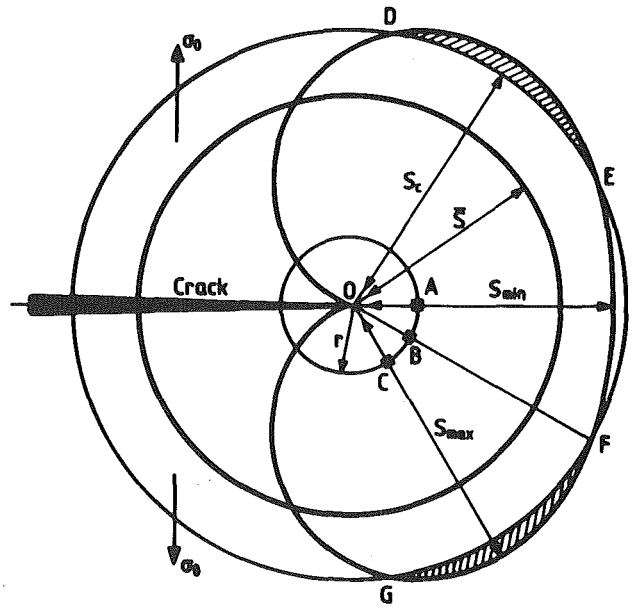

Fig. 1

How does the modified or $\bar{S}$-criterion work? At each load step the mean value of the strain-energy density stored around the crack-tip is geometrically represented by a circle. The crack initiates when the radius of this circle is greater or equal to the radius of the critical S, i.e., $\bar{S} \geqq S_c$. When this relation is fulfilled, the crack propagates to the direction of the minimum energy-density ($S_{\min}$) according to the fundamental laws of mechanics [9].

From a physical point of view, the introduction of $\bar{S}$ implies the necessity of the existence of a low-elastic, strain-energy density level in the neighborhood of the crack tip, which when achieved, permits the initiation of the various fracture and yielding mechanisms.

From the algebraic point of view, S is a positive quantity, increasing with the external load. Thus, S can reach a positive critical value (say S_c) only from below, and this obviously is first reached by the maximum value of S. Therefore, symbols like $S_{\min}^{\max}$ have only a formal value, not interpretable physically.

Let us return, again, to Fig. 1. Concerning the behavior of the elementary volumes corresponding to S-values between DE and FG, the discussers may say that these volumes are at the direction of yielding and thus they do not fracture, being already yielded. But, according to their words ". . . *yielding and fracture have to be addressed simultaneously*" not only for ductile materials, as they say, but for all materials. Perfectly brittle materials do not exist. Simple, the brittle or ductile part of the whole failure character of an individual material predominates more or less in each case. This situation is clearly exemplified in Fig. 1 where, at the given load-level, elementary volume A is still unaffected, B is a little yielded and a little fractured, and C is yielded, according to original S-criterion.

We feel that, exactly, such conclusions are "concocted." The problem asks for a more brave confrontation, where the fundamentally different influence of the two density components S_V and S_D on the failure process must be incorporated. In our opinion, this has already been done by the introduction of a new criterion, the T-criterion [10–12]. According to this criterion the distortional part S_D of the total strain-energy density is responsible for the creation of a yielded zone around the crack tip, as is described by the Mises yield condition, $S_D = \text{const}$. Outside the yielded area, dilational component S_V, being a module of normal stresses, initiates fracture processes like cleavage or hole growth and coalescence, according to modern concepts of fracture mechanics [13–15]. This approximation accurately describes the simultaneous but qualitatively different influence of S_D and S_V to the failure processes, and includes S or $\bar{S}$-criteria as limiting cases for purely brittle materials.

References

1 Cotterell, B., "Notes on the Paths and Stability of Cracks," *International Journal of Fracture Mechanics*, Vol. 2, 1966, pp. 526–533.

2 Swedlow, J. L., "Criteria for Growth of the Angled Crack," *ASTM, STP*, Vol. 601, 1976, pp. 506–521.

3 Gdoutos, E. E., "Biaxial Load Effects on Crack Propagation and Fracture Toughness," *Rev. Roumaine Science Technique*, Vol. 26, 1981, pp. 129–143.

4 Sih, G. C., "Strain-Energy-Density Factor Applied to Mixed Mode Crack Problems," *International Journal of Fracture*, Vol. 10, 1974, pp. 305–321.

5 Theocaris, P. S., "Experimental Determination of the Core Region in Mixed-Mode Fracture," *Proc. US-Greece Symposium on Mixed Mode Crack Propagation*, Sih, G. C., and Theocaris, P.S., Eds., Sijthoff and Noordhoff, 1980, pp. 21–36.

6 Theocaris, P. S., "The Caustics as a Means to Define the Core Region in Brittle Fracture," *Engineering Fracture Mechanics*, Vol. 14, 1981, pp. 353–362.

7 Williams, M. L., "On the Stress Distribution at the Base of a Stationary Crack," ASME JOURNAL OF APPLIED MECHANICS, Vol. 24, 1957, pp. 109–114.

8 Erdogan, F., and Sih, G. C., "On the Crack Extension in Plates Under Plane Loading and Transverse Shear," ASME *Journal of Basic Engineering*, Vol. 85, 1963, pp. 519–527.

9 Sih, G. C., "A Special Theory of Crack Propagation," *Mechanics of Fracture*, Vol. 1, Sih, G. C., Ed., Sijthoff and Noordhoff, 1973, pp. XXI–XLV.

10 Theocaris, P. S., and Andrianopoulos, N. P., "The Mises Elastic-Plastic Boundary as the Core Region in Fracture Criteria," *Engineering Fracture Mechanics*, Vol. 16, 1982, pp. 425–432.

11 Theocaris, P. S., Kardomateas, G., and Andrianopoulos, N. P., "Experimental Study of the T-criterion in Ductile Fractures," *Engineering Fracture Mechanics*, Vol. 16, 1982, in press.

12 Theocaris, P. S., "Ductile Fracture With Small Scale Yielding Studied by the T-criterion," to be presented at the *Proc. of VII SESA Conference*, Haifa-Israel, Aug. 1982.

13 McClintock, F. A., "A Criterion for Ductile Fracture by the Growth of Holes," ASME JOURNAL OF APPLIED MECHANICS, Vol. 35, 1968, pp. 363–371.

14 Rice, J. R., and Tracey, D. M., "On the Ductile Enlargement of Voids in Triaxial Stress Fields," *Journal of Mechanics and Physics of Solids*, Vol. 17, 1969, pp. 201–217.

15 Gurson, A. L., "Continuum Theory of Ductile Rupture by Void Nucleation and Growth: Part I—Yield Criteria and Flow Rules for Porous Ductile Media," ASME *Journal of Engineering Materials and Technology*, Vol. 39, 1977, pp. 2–15.

Journal of Applied Mechanics

Book Reviews

Finite Elements, An Introduction. By E. B. Becker, G. F. Carey, and J. T. Oden. Prentice-Hall, Englewood Cliffs, N.J., 1981. 258 Pages. Price /24.95.

REVIEWED BY T. BELYTSCHKO[1]

The finite element method has been the topic of approximately 30 books and monographs that have been published over the last 15 years. Nevertheless, many instructors still have difficulties in finding a text for advanced undergraduate or beginning graduate courses which will develop a sound, fundamental understanding of the method. This book presents a significant advance in that direction for those who wish a more rigorous, mathematical development.

The book consists of six chapters. The first two are devoted to one-dimensional problems, emphasizing the development of a symmetric variational formulation for second-order, two-point boundary value problems and the smoothness required in the space of approximating functions. In the third chapter, a finite element program for one-dimensional problems is described, including the FORTRAN statements. Chapters 4 and 5 repeat the same material for two-dimensional problems, including shape functions for triangles and quadrilaterals and numerical quadrature. Chapter 6 presents an introduction to three-dimensional problems, fourth-order problems, and time-dependent problems.

A notable feature of this book is that it develops the weak, or variational form, from the partial differential equations, rather than simply presenting the variational form as given; the latter approach bothers many of the better students who usually wonder where the variational form comes from. The concepts in this book are all developed with rigor, clarity, and conciseness. Once a student has mastered this book, he will certainly have a broader understanding of the mathematics of the finite element method than would be obtained from more conventional treatments.

In using this book in my class, I found two types of response. Engineering students with a modest mathematical background found the book a little difficult as an introduction; it requires simultaneously tackling the concepts of the weak form, finite element approximations, and notation and concepts to which they are unaccustomed. On the other hand, mathematically inclined students tend to find this book delightful. In addition to its value as a text, it is also recommended to finite element specialists who wish to familiarize themselves with the more recent developments in the mathematical aspects of the method. Even recently I have received papers submitted to the ASME JOURNAL OF APPLIED MECHANICS that deal with the continuity requirements and natural boundary conditions in the Galerkin method; this book presents an unambiguous, consistent development at an introductory level.

This book is the first volume of a series of six on finite elements. If the quality of this volume is maintained in the forthcoming volumes, it should prove a valuable contribution to the finite element literature.

Seismic Migration—Imaging of Acoustic Energy by Wave Field Extrapolation. By A. J. Berkhout. Elsevier, Amsterdam, 1980. pp. xii–339. Price $51.00.

REVIEWED BY Y.-H. PAO[2]

The purpose of this review is not to criticize Berkhout's book. Instead, it is intended to acquaint readers of the JOURNAL OF APPLIED MECHANICS with this seemingly mysterious topic.

Seismic migration is the construction of a vertical cross section of the ground from the time traces of signals recorded along a line of receivers. The signals are generated by either a single source, or a distribution of sources along the line of the receivers. Mathematically, the problem is formulated as the determination of the wave speed $c(x, y, z)$ and mass density $\rho(x, y, z)$ of an inhomogeneous half space $z \geq 0$, $-\infty < x, y < \infty$, from the known input at the surface, $P_0(x_0, y_0, 0, t)$, and the output $P(x, y, 0, t)$. The $P(x, y, z, t)$ satisfies a linear wave equation with a variable coefficient $c^2 \nabla^2 P = \partial^2 P / \partial t^2$.

The complexity of the problem apparently is far beyond the mathematical and computational tools currently available. In fact, this mathematical inverse problem may be ill-posed, for which the solutions are not stable, nonunique, or even nonexisting. Nevertheless, oil companies have to find oil, and do find them underground by seismic prospecting. Geophysicists specialized in this area have developed various approximate methods to map geological cross sections from records of map-generated seismic waves. The Migration is one of these methods.

A crude model for the cross section is a half space composed of many parallel layers, each having a constant wave speed $c(z_i)$, and density $\rho(z_i)$. A more refined model is to have nonparallel layers, and to allow c and ρ to vary laterally in x, y directions. Methods of seismic migration are developed to improve the lateral resolution of the data gathering and processing.

In this book, which is the first one devoted to the topic of seismic migration, the theory of migration is derived from first principles. Therefore, it contains some basic mathematics (Chapters 2–4) which are familiar to readers of the JOURNAL

[1]Professor, Department of Civil Engineering, The Technological Institute, Northwestern University, Evanston, Ill. 60201.

[2]Professor, Department of Theoretical and Applied Mechancis, Cornell University, Ithaca, N.Y. 14853.

OF APPLIED MECHANICS. The ensuing chapters discuss three methods to extrapolate downward wave fields, and the imaging of the cross sections (the inverse techniques). Chapter 11 compared different approaches to migration. To readers of the JOURNAL OF APPLIED MECHANICS, it would be benefical reading Chapter 11 first before reading Chapter 1, as the latter is incomprehensible to anyone outside the field of seismic prospecting. The last chapter (Chapter 12) discusses the limits of lateral resolution.

Most of the book is confined to two-dimensional scalar wave field $P(x, z, t)$. The three-dimensional case of scalar waves, $P(x, y, z, t)$ apparently is still not within the reach of prospecting seismologists, let alone the case of vector elastic waves, including P and S-wave conversions, in inhomogeneous media. This points a direction of research of a literally very rich area for readers of JOURNAL OF APPLIED MECHANICS who are well versed in the subject of wave propagations in solids.

Free Vibration Analysis of Rectangular Plates. By D.J. Gorman. Elsevier, North Holland, 1982. 324 Pages. Price $60.00.

REVIEWED BY A. LEISSA[3]

This work is a summarization and generalization of a number of previously published papers by Professor Gorman dealing with the free vibrations of rectangular plates. It presents the most comprehensive set of published analytical results to date for rectangular plates governed by classical plate theory; that is, the plates are limited to be homogeneous, isotropic, and thin, undergoing vibrations of amplitude less than the thickness, and free of inplane initial stresses. The book makes no comparisons with the voluminous numerical results found elsewhere in the literature, but stands upon the author's own accurate calculations.

Chapter 2 presents comprehensive eigenfrequencies for the six cases of rectangular plates having two opposite sides simply supported and the others simply supported, clamped, or free. These problems have "exact" solutions in the sense that the eigenfrequencies are obtained from frequency determinants of finite size, in this case having orders no larger than four, arising from the well-known Voigt-Levy solution of the equation of motion. For each of the six cases, 64 frequencies are presented for a/b and b/a = 1, 1.25, 1.5, ,2, 2.5, and 3 where a and b are the plate dimensions. For plates having free edges (3 cases), results are given for two values of Poisson's ratio (0.333 and 0.5).

Chapters 3–7 deal with the remaining 15 cases of plates having combinations of clamped, simply supported, and free edges. The method of superimposing infinite series of Voigt-Levy solutions previously developed by the author and others is utilized to solve these problems. Convergence studies were made to establish the accuracy of the frequencies to four significant figures. Numerical results for frequencies are given typically for the first 10 modes in each case, for values of a/b and b/a as listed in the foregoing. Where free edges are involved, Poisson's ratio is set at 0.333.

The last chapter is devoted to a series of problems involving rectangular plates having added point masses or supports, or line supports. Again the superposition procedure is used to solve the problems and results for frequencies are given.

Although the results for frequencies given throughout the book are typically quite comprehensive, considerably less information is supplied about the corresponding mode shapes.

The reviewer recommends the book highly to individuals who are interested in applying the superposition method to the analysis of eigenvalue problems for rectangular regions and/or who desire extensive, accurate numerical results for the free vibration of rectangular plates governed by classical theory.

[3]Department of Engineering Mechanics, Ohio State University, Columbus, Ohio 43210–1181.

Shock Waves and High-Strain-Rate Phenomena in Metals. Edited by M. A. Meyers and L. E. Marr. Plenum, New York, 1981. pp. xiii-1101. Price $95.00.

REVIEWED BY U. S. LINDHOLM[4]

This large volume (1100 pages) constitutes the proceedings of an international symposium held in Albuquerque, N. Mex. in June, 1980. There are a total of 58 papers divided into topical areas titled: High Strain Rate Deformation; Dynamic Fracture; Adiabatic Shearing; three sections on Shock-Waves Experimental Techniques, Fundamentals, and Microstructural and Mechanical Effects; Dynamic Compaction of Powders; and Explosive Metal Working and Welding. The editors have done an exceptionally fine job of editing and organizing the diverse papers in such a format that the volume presents a comprehensive state-of-the-art review of the subject while fulfilling the editors objective of making it a lasting reference and potential text for graduate education. The latter objective is achieved by a number of chapters contributed by the editors themselves as well as seven appendices providing supplemental basic information required for the design of shock-loading systems. The volume also achieves a balanced perspective for each topic from the points of view of physics, metallurgy, and mechanics.

In summary, this reviewer feels that this is perhaps the best collection of papers on the subject matter seen in recent years and reflects considerable extra effort by the editors to make it a self-contained treatise. It is well worth examination by all those active or interested in dynamic deformation or fracture.

Modern Fluid Mechanics. By Shih-I. Pai. Science Press, Beijing; distributed by Van Nostrand Reinhold Company, New York, 1981. pp. xx–570. Price $37.50.

REVIEWED BY J. S. WALKER[5]

This book on theoretical fluid mechanics falls into the large gap between the teaching textbooks on classical fluid mechanics and the research-oriented monographs that summarize recent developments in specific fields. The four chapters on basic concepts assume a knowledge of the traditional treatment and provide a novel and unifying approach to fluid properties, statics, dynamics, and dimensional analysis. The kinetic theory of gases is used to link continuum and molecular models. Throughout these chapters the author prepares the reader for the specific topics that follow.

The four chapters on specific areas of research treat gas

[4]Department of Materials Science, Southwest Research Institute, P. O. Drawer 28510, San Antonio, Texas 78284.

[5]Professor, Department of Theoretical and Applied Mechanics, University of Illinois, Urbana, Ill. 61801. Mem. ASME.

dynamics with chemical reactions, electromagnetic effects (plasma dynamics), radiation effects, and low densities (rarefied gas dynamics). A final chapter focuses primarily on continuum models for mixtures (two-phase flows and multiple-species models for plasmas). It includes brief mentions of non-Newtonian fluids, superfluids, biofluid mechanics, and relativistic fluid mechanics.

This book presents the basic concepts and equations of certain topics in modern theoretical fluid mechanics and provides insights and understanding so that the reader knows when and how to use these tools. The book should prove extremely valuable for both technology transfer and research preparation. From this book someone who wants to apply recent advances in fluid dynamics and who has a good background in classical fluid dynamics can obtain the knowledge and understanding of concepts and equations needed to apply results in the research literature. The researcher can also turn to this book as the first step toward original research in a new area. This book could be used as a text for an advanced course for graduate students who are at the transition point between course work and thesis research.

Compressible Flow. By S. Schreier. Wiley, New York, 1982. 577 Pages. Price $60.00.

REVIEWED BY M. MORDUCHOW[6]

A number of well-known and notable texts dealing specifically with compressible flows have appeared in the past. Mention may be made, for example, of the general compressible-flow texts of Shapiro, and of Liepmann and Roshko among others, of Ferri's book on supersonic-flow aerodynamics, of Stewartson's text on compressible laminar boundary layers, of the text of Hayes and Probstein, and of that of Dorrance, on hypersonic flow, and of the book of Vincenti and Kruger on physical gas dynamics. Due to the broad scope of compressible fluid dynamics, however, there remains of course room for further good texts on the subject. The book under review may be considered as in this category, its subject being primarily classical compressible flow. It is claimed on the book cover that this is the "first major new work" on compressible flow since 1972. Assuming that "work" here means "textbook" this may be close to true, but note must be made here at least of the 1976 text of Zucrow and Hoffman (*Gas Dynamics Vol. 1*, admittedly based at least in part on a well-known 1958 book of Zurcrow) and of the quite recent (1982) text of J.D. Anderson (*Modern Compressible Flow, With Historical Perspective*).

Although there are various ways, depending on individual tastes and interests, of treating the subject of compressible flow, the 577-page text of Schreier's can serve quite well as the basis of at least a one-year graduate course on compressible flow. It could also be used for self-study. In fact, the explanations here are sufficiently detailed so that the text may be considered as essentially self-contained, although a knowledge of vector analysis is assumed and a previous knowledge of basic incompressible fluid mechanics and elementary thermodynamics would be desirable. An appreciable variety of topics is covered, including: the Navier-Stokes equations; sound waves, shock waves, and expansion waves; steady and unsteady one-dimensional flows with and without shock waves; two and three-dimensional steady subsonic and supersonic flow; characteristics; transonic flow (in unusual detail); (classical) compressible laminar and turbulent boundary layers; real gas effects, especially dissociating boundary layers; and computational methods, with emphasis on numerical solution of ordinary differential equations and finite-difference solutions of the standard partial differential equations, with the addition of a more complicated example, involving supersonic flow. A set of 241 references and certain working tables for compressible flow calculations are included. Moreover, a set of useful and interesting exercises for each chapter is given at the end of the book.

In summary this book may be regarded as a quite useful addition to the textbook literature on compressible flows.

[6]Professor, Department of Mechanical and Aerospace Engineering, Polytechnic Institute of New York, 333 Jay Street, Brooklyn, N.Y. 11201.